NTech
Lehrstuhl für
Nukleartechnik

Technische Universität München

Experimental investigation and CFD validation of two-phase phenomena related to nuclear safety research during LOCA accidents

Suleiman Al Issa

Vollständiger Abdruck der von der Fakultät für Maschinenwesen der technischen Universität München zur Erlangung des akademischen Grades eines

Doktor-Ingenieurs (Dr.-Ing.)

Genehmigten Dissertation.

Vorsitzender	Univ.-Prof. Dr.-Ing. Carlo L. Bottasso
Prüfer der Dissertation:	1. Univ.-Prof. Rafael Macián-Juan, Ph.D.
	2. Univ.-Prof. Dr.-Ing. habil. Eckart Laurien, Universität Stuttgart
	3. Prof. David Aumiller, Ph.D. , University of Pittsburg, USA

Die Dissertation wurde am 12.06.2014 bei der Technischen Universität München eingereicht und durch die Fakultät für Maschinenwesen am 20.11.2014 angenommen.

Dedication

To the soul of my father, to my mother, and to the soul of my uncle.

Abstract

This work is concerned with the experimental investigation and CFD validation of two-phenomena that are of interest for nuclear safety research: steam bubble condensation in flowing sub-cooled water and counter current flow limitation (CCFL) in the hot-leg geometry of a pressurized water reactor. A detailed and exhaustive literature review of both phenomena is initially introduced. The reviews provide the knowledge base for the design of the experimental facilities and they show the state of the art and shortcomings regarding each subject. Consequently, the objectives of the current work were identified. The SCUBA test facility, with a vertical large-diameter and a transparent test section, was built to investigate the steam bubble condensation under different flow conditions. The COLLIDER test facility, with a 1/3.9 scale of a real PWR hot-leg pipe geometry, was built to investigate the countercurrent flow limitation conditions. Investigations in both facilities were intended to be in large diameter geometry (DN100 in SCUBA, DN200 in COLLIDER) in order to cover the lack of experimental data regarding this range of channel size. The concept, the design, and construction of both facilities were explained, including the design and the function of each sub-component. The link between the final research objectives and the design concepts was clarified through the construction of all components. High speed recording was used as the main measuring technique to capture the interface between different phases in both facilities. High-quality imaging of the air/water interface in COLLIDER provided a detailed look into the interfacial structure without further processing and was a valuable source for CFD simulations. Appropriate image-processing programs were developed in order to identify the bubbles and track them in SCUBA tests. These programs allowed a fully automatic and efficient processing of thousands of images and, thus, provided a powerful tool for the investigation of diluted bubbly flows in general. The programs were able to identify each detached bubble from the injected nozzle and track it until full condensation calculating all its parameters: equivalent diameter, aspect ratio, position, rising velocity, and consequently the bubbles' Reynolds and Nusselt numbers. Out of the large number of tracked bubbles, valuable information over bubble-size distributions and relative-velocity distributions were also calculated. Experimental investigations in SCUBA were carried out at atmospheric pressure using distilled water and steam. Steam was injected into water using different injection nozzles with different geometries in order to generate large bubbles ($5 < D_{eq} < 50$ mm) with different sizes and initial velocity vectors. Experiments were conducted at three different water superficial velocities, water subcooling temperatures, and steam superficial velocities for each of the four implemented injection nozzles. The resulting visual observations form the high-speed recording provided a unique look into the condensation of large steam bubbles under the condition of direct steam injection (no accompanying evaporation). The current experiments showed for the first time the effect of the bubbles surface structure upon the resulting heat transfer. Large bubbles with a large shape deformations and surface roughness showed an enhanced heat transfer against bubbles with a smoother surface generated on a heated surface. The effect of the gas turbulence and injection geometry upon the condensation rate was also clarified. The Nu-Re correlation was evaluated for each injection nozzle and for all obtained data and new correlations were developed to fit the new experimental data. The effect of the different flow conditions upon numerous bubbles parameters was discussed and explained in details. This included: the bubble-size distribution, the relative-velocity

distribution, bubbles' equivalent diameter, bubbles rising velocity, and bubbles paths. Through these explanations many facts were learned about the behavior of large bubbles under different flow conditions. The obtained raw images were processed to obtain 2D distributions of the time-averaged void fraction for each case. The resulting distributions can be obtained either for all injected steam or for detached bubbles only, providing a valuable data for CFD validations. Two representative cases of SCUBA tests were modeled and simulated using CFX12.1 by applying the two-resistance heat transfer model. This allowed the implementation and testing of the experimentally developed Nu-Re correlations against the existing ones in CFD codes. The comparison showed a clear improvement of CFD performance when using the new developed heat transfer correlations, and confirmed the experimentally observed enhancement of the heat transfer.

Experimental investigations in COLLIDER were carried out under atmospheric pressure using distilled water and filtered air. Systematic experimental tests were carried out and covered the low and medium water inlet velocities ($0.085 \leq J_{w,in}^{*0.5} \leq 0.305$) which are the most important range of values for reflux condensation during LOCA accidents. Experiments were carried out with $\Delta J_{w,in}^{*0.5} = 0.01$ in order to allow a precise identification of the onset of CCFL, and deflooding at each water inlet velocity. High-speed recording was implemented to capture high-quality images of the air/water interface and understand the mechanisms by which the CCFL occurs and disappears. Air flow was increased step-wise until the occurrence of the CCFL and then decreased gradually until de-flooding. During experiments, all flow parameters were recorded using the control and measuring system. Two main CCFL mechanisms were identified and explained in details: bend-CCFL and ADE-CCFL. Four regions of the occurrence of the CCFL were recognized according to the sub-phenomenon and mechanisms that lead into the CCFL occurrence. The experiments, along with the high-quality imaging of the interface, allowed identifying and sorting all observed flow patterns in such large-pipe and full hot-leg geometry for the first time. This improved the knowledge about this complicated phenomenon and linked all experimental descriptions to a clear and well-captured interface, and, thus, a lot of ambiguity that was noticed through the literature review was clarified. The experimental curve of the onset of CCFL for each of the two mechanisms, and de-flooding line was produced, and compared against results from previous works. The experimental investigations in COLLIDER shows the importance of experiments in a large-diameter geometry (the disappearance of slugging mechanism), and the effect of a real-pipe geometry against a rectangular cross section (the appearance of the ADE-CCFL mechanism). ADE-CCFL starts to occur lightly when $J_{w,in}^{*0.5} > 0.185$ and becomes significant for $J_{w,in}^{*0.5} > 0.265$. It occurs before the onset of bend-CCFL and thus it is important to identify for safety analysis. Most experimental investigations did not notice the ADE-CCFL, either because they were done in small-diameter geometry, a rectangular cross section, or was not experimentally identified. In order to evaluate the existing momentum transfer models and validate the performance of CFD codes against COLLIDER data, CFD simulations of two-representative cases were carried out. The mesh was produced using ANSYS ICEM 12.1 advanced meshing tool. A two-fluid free surface model was adopted for the simulations along with a drag coefficient out of literature. Transient simulations were conducted to validate the flow transitions during the onset of the hydraulic jump, the onset of ADE-CCFL, and the

onset of bend-CCFL at low and medium water inlet velocities. The simulations were validated against the air/water interface obtained by high-speed recording, and the pressure difference between the reactor vessel simulator and the steam generator simulator. The comparison results showed the ability of the current CFD codes to predict the onset of bend-CCFL. The drag and momentum transfer was clearly overestimated during the onset of the bend-CCFL. The onset of ADE-CCFL was not predicted using the current modeling. This showed the necessity of further work aimed at developing a different model to simulate the mechanism of ADE-CCFL (active droplets entrainment), and an enhanced momentum-transfer model (drag modeling) in order to enhance the results of bend-CCFL simulations.

Contents

Nomenclature

Latin Letters

A	Area
ax	Bubble's maximum extension in the horizontal direction.
ay	Bubble maximum extension in the vertical direction.
c	Constant.
D	Diameter.
F	Force.
f	Friction factor.
g	Gravity acceleration.
h	heat transfer coefficient.
H	Length of the horizontal part in hot-leg geometry.
I	Length of the inclined riser in hot-leg geometry.I
J	Superficial velocity.
k	Thermal conductivity.
L	Length of the horizontal part in hot-leg geometry/ or channel length.
lw	Water level.
m	Constant.
n	Bubble number.
N	Total number.
P	Pressure.
Q	Volume flow rate.
T	Temperature.
t	Time.
V,v	Velocity.

x	Cartesian coordinate.
y	Cartesian coordinate.
z	Cartesian coordinate.

Other Latin symbols

C_D	Drag coefficient.
C_P	Heat capacity at constant pressure (Water if no subscript)
D_{in}	Inner diameter.
D_s	Sauter mean diameter (for bubbles).
$\dot{m}$	Mass flow rate.
Δh_{fg}	Latent heat of vaporization.
a_i	Interfacial area concentration
f_s	Acquisition frequency for high speed recording [frame/s].
ṅ	Bubble number.

Non-dimensional numbers

Fo	Fourier number.
Fr	Froud number.
Nu	Nusselt number.
Pe	Péclet number.
Pr	Prandtl number.
Re	Reynolds number.
Ku	Kutateladze number
$J^{*0.5}$	Wallis parameter.

Greek letters

Δ	Difference.
Ψ	Probability function.

α	Void fraction.
θ	Inclination angle.
κ	κ-factor of the Pitot-tube.
μ	Dynamic viscosity.
ν	Kinematic viscosity.
ξ	Calibration factor in high speed recordings [mm/pixel]
ρ	Density.
σ	Surface tension.
τ	Shear stress.
ϵ	Calculation error [%].

Superscripts

*	Non-dimensional value

Subscripts

0	Initial value.
a	Air.
b,B	Bubble.
d	Drift.
c	Center-of-Mass (when used with coordinates).
C	Condensation.
crit	Critical gas velocity at which countercurrent flow limitation or other event occurs.
eq	Volume equivalent.
G,g	Gas.
in	Inlet, to denote velocities measured at the inlet.
k	To denote phases in general (k=l or g)
L,l	Liquid.

lam	Laminar flow.
lim	Limit value.
max	Maximum value.
min	Minimum value.
n	Bubble number n.
r, rel	Relative velocity between different phases (slip velocity).
s	Steam.
set	Set value at the controller input device.
t	Time instant.
test	Values measured within the test section.
turb	Turbulent.
w	Water.

Other

$\lvert \ \rvert$	Absolute value.
$\overline{\ }$	Time-averaged mean value.

Abbreviations

1D, 2D, 3D	1-, 2-, or 3-dimensional consideration.
ABS	Anti-Brand System
ADE-CCFL	CCFL caused by active droplets entrainment.
AIAD	The algebraic interfacial area density model.
Bend-CCFL	CCFL that occurs at the bend region of a hot-leg geometry.
BWR	Boiling water reactor.
CCFL	Countercurrent flow limitation.
CFD	Computational fluid dynamics.
DCC	Direct contact condensation.

DI	Distilled water.
DN	Diameter nominal.
HSC	High-speed Camera.
IFF	Interfacial friction factor.
IRWST	In-containment refueling water storage tank, a part of the passive safety system of Westinghouse advanced passive PWR plants.
LIM	Large interface model.
LOCA	Loss of coolant accident.
P, PI, PID	Proportional, Proportional-Integral, Proportional-Integral-Differential controller design.
RMS	Root mean square value.
RVs	Reactor vessel simulator.
SBLOCA	Small-break LOCA.
SGs	Steam generator simulator.
VOF	Volume of fluid approach.

A general introduction

Two-phase flow phenomena that take place during LOCA/SBLOCA design base accidents are of special importance for nuclear safety research. The increased interest in the development and validation of CFD codes for two-phase flows is also an important motivation for more elaborated and combined experimental/validation work in this area. Two-phase flows are still a challenge for both: experimental measurements and CFD simulations and, therefore, they are still a fertile domain for research and development of correlations and closure laws of the interfacial exchange of mass, momentum and thermal energy. Within this framework, two phenomena became a subject of interest: countercurrent flow limitation (CCFL) that can occur during reflux condensation phase of a LOCA and SBLOCA accidents, and steam bubble condensation, which can be encountered in some operational situations and many safety applications (like IRWST in a PWR). In both cases, the interphase topology plays an important role for enhancing our knowledge over the incorporated processes on the phenomenological level. Tracking of bubbles' shape, surface, and various parameters (diameter, position, velocity, etc.), besides the gas/liquid interface during CCFL occurrence; forms a solid ground for the development of CFD modeling. High speed camera recording (HSC) can be implemented in both cases, and by developing adequate image processing programs, it becomes possible to obtain all the necessary information about the behavior of the two-phase interface. HSC is also a non-intrusive measuring technique that allows the observation of the phenomenon´s occurrence without affecting its development. Two facilities were designed and constructed at the Institute of Nuclear Engineering (NTech) at TUM for experimental investigation of the two phenomena using HSC as a main measurement technique:

1. **SCUBA** (**S**team **C**ondensation **U**nder **B**ubbly flow and **A**tmospheric pressure conditions): for investigation of steam bubble condensation in subcooled flowing water in a relatively large-diameter (DN100) vertical pipe geometry.
2. **COLLIDER**: (**CO**untercurrent **LI**mitation in a **L**arge **D**iamet**ER** geometry): which is a test facility dedicated to the investigation of the countercurrent flow limitation phenomenon in a hot-leg large-diameter pipe geometry of a PWR.

The choice of carrying out the investigations in large-diameter geometry was a common design feature for both facilities. This choice resulted from the literature review (as chapter 1 will show), and from the fact that flow characteristics can differ substantially between small diameter and large diameter geometries. For instance, no transition into slug flow occurs in a large diameter vertical pipe, and transition of bubbly flows into churn flow occurs without passing through the slug flow regime. Additionally, flows near the pipes center stay away from any wall effects in comparison to small-diameters pipes. In a large-diameter pipe, the shear forces resulting from the fluid velocity gradient are also small near the pipe's center, while a strong shear field exists near the wall. This allows studying bubbles behavior in two distinctive flow conditions: under weak/or strong effect of shear forces, and consequently under different and distinctive turbulence conditions. The same applies for horizontal flows. Slugging plays an important role in the occurrence of CCFL in small pipes, while no slugging can happen in large-diameter pipes at the same non-dimensional parameters. Scaling effects

are crucial for CCFL occurrence, and thus it becomes important to identify the CCFL mechanisms in a geometry which is as close as possible to the full-scale geometry. During LOCA/SBLOCA accidents, the pressure in the primary loop drops rapidly and boiling can take place inside the reactor vessel. The large amount of generated steam during the accident should be condensed effectively. In advanced PWR designs, the IRWST tank serves as a large water inventory and a heat sink in which the steam can be directly injected and condensed. As the amount of leaked water increases, reflux condensation becomes an important passive cooling mechanism for the reactor core that is driven only by pressure difference and gravity. The occurrence of CCFL inside the hot-leg during this phase can inhibit the effectiveness of this mechanism partially or completely. The investigation of both phenomena within the current work will aim at fulfilling the following objectives:

- Construction of experimental facilities, measuring systems, and measurement techniques that allow the carrying out of the intended investigations and provide a unique experimental platform for the investigation of two-phase flows in general.
- Development of robust image-processing algorithms that allow automatic bubbles' identification, tracking, and calculation of needed flow parameters.
- Providing a detailed phenomenological study of the interfacial heat transfer (SCUBA) and CCFL mechanisms (COLLIDER). This should enhance the current knowledge over both investigated phenomena.
- Providing a qualitative and quantitative analysis of the studied phenomena. High quality HSC should deliver "CFD-grade" validation data.
- Development of new closure laws for the interfacial heat and mass transfer for application in CFD codes.
- Using experimental measurements and data to validate CFD codes and to test the newly-developed correlations.
- Identification of shortcomings and further necessary developments.

Chapters 1-9 will describe how these objectives were challenged in this work. Chapter 1 presents a detailed and extensive theoretical background and review of the literature linked to both phenomena. Chapter 2 describes the conceptual and design criteria, the design, construction, instrumentation and characteristics of both facilities. It explains how the design principles were linked into the final construction of diverse components. Chapter 3 describes the control and data acquisition system used to control test parameters, record flow variables, and maintain safety and reliable operation of the facilities. Chapter 4 is dedicated to high speed camera recording (HSC) since it was the main measuring technique used for acquisition of the two phases interface (steam bubbles in SCUBA, and air/water in COLLIDER). It gives a brief review of HSC and explains the self-developed procedures that were used to obtain bubbles parameters. Chapter 5 introduces the experimental investigations carried out in SCUBA. It lists test conditions, shows experimental results including visual observations, and quantitative measurements. It includes an extensive qualitative and quantitative analysis of the acquired data, provides explanations of the diverse noticed phenomena, identifies new observed ones, and proposes new correlations for the heat transfer between steam bubbles and the liquid. Chapter 6 implements the experimentally obtained heat transfer correlations into

CFD calculations using CFX12.1. It demonstrates the improved CFD performance via a comparison with the experimental data, and shows several useful simulation results. Chapter 7 presents the experimental investigations of CCFL in COLLIDER test facility. It provides a detailed visual and phenomenological description of the onset of CCFL and deflooding, identifies and explains the mechanisms by which the CCFL occurs and disappears, and provides a high quality acquisition of the air/water interface for all occurring flow patterns. Additionally the chapter concludes the criteria for the onset of CCFL and deflooding according to current experiments and compares that with previous works. Chapter 8 validates the performance of CFD codes against the obtained air/water interface in two representative experimental cases using ANSYS CFX12.1. It introduces a comparison between CFX results and experimental distribution of the air/water interface in the entire hot-leg geometry for the first time using such a scale. The chapter identifies some shortcomings and shows which mechanisms CFD codes can predict and which need a further development and validation. Chapter 9 shows the possibilities of future work in both facilities. Finally, an acknowledgement is provided with all credits and thanks, references are listed, and an appendix, which provides a plenty of visual observations over the behavior of large steam bubbles, is attached.

Chapter 1 Theoretical background

1.1 Steam bubbles condensation in subcooled water

1.1.1 Introduction

Phase-change phenomena are very important in many applications of industrial interest. Since the energy exchange occurs through latent heat at a constant temperature, high heat fluxes can be achieved with moderate temperature gradients [Didier 2006]. Condensation is one of such phase-change phenomena which is of a great interest for many industrial applications including the energy industry and the evaluation of the safety of power plants (nuclear power plants in particular). In this area, some of the most important applications are, for instance, direct contact condensation (DCC) in mixing type heat exchangers, thermal degasifies, sea water desalination, compact heat exchangers, in-containment refueling water storage tank (IRWST), and the condensation of steam in the form of jet flow or bubbly flow inside the suppression pool of passively safe boiling water reactor (BWR) designs [Cheng et al. 2006, Park et al. 2005]. An important phenomenon is the condensation of steam bubbles in water-cooled reactors [Hari et al 2004, Koncar et al 2003, Koncar et al 2004, and Zeitoun et al. 1997]. It is of importance for both power and research reactors regarding the safety of the low-pressure research reactors and the sump-cooling concept for advanced light water reactors [Koncar et al 2004]. It is well known that the presence of bubbles affects the reactor's reactivity, and, for instance, the reactor power. Furthermore the inception of two-phase instability is influenced by the presence of vapor in the subcooled boiling region. Therefore, a detailed understanding of the physical phenomena driving subcooled flow boiling is of considerable interest to improve the safety and performance of nuclear reactors. The capability of accurately predicting two-phase flow variables such as void fraction or the interfacial area concentration in the subcooled boiling region is of considerable interest also to BWR's safety evaluation [Bartel et al 2001, Okawa et al. 2005]. Since the condensation of steam bubbles is fundamental for subcooled boiling, a better understanding of this process through well designed experimental conditions will provide valuable data to develop new correlations, or improve those in use today, and contribute to a better understanding of the overall subcooled boiling process.

Table 1.1: A review of experimental investigation in which steam bubble condensation was studied

Article	ΔTsub [K]	Pressure [bar]	Liquid velocity [m/s]	Bubble diameter [mm]	Bubble life time [ms]
Prodanovic et al. (2002)	10,20,30, 40,60	1	0.08 – 0.83	0.59 – 2.68	1.43 – 18.4
Koncar et al. (2004)	7 – 46.5	~1.03	~0.235 – 0.684	0.69 – 1.14	~2
Kalman et al. (2006)	4.4 – 5.4	~1.2	~1	0.9 – 3.7 (collapsing)	1.4 – 4.8 (collapsing)
Zeitoun et al. (1997)	~10	~1	Stagnant	0.6 – 3.7	-
Lee et al. (2002)	11.5 – 21.3	1 – 2	~0.6 – 1.3 (average)	0.15 – 8 (predicted)	-
Cheng et al. (2006)	2.6 – 18.8	1 – 1.8	0.2 – 0.5	1 – 8	
Mayinger and Chen	12.5 – 40	0.25 – 2	0.02 downflow	Various due to pressure	6 – 19

(1986)	7.6 at 2 bar			nozzle: 1.6mm	
Kalman and Mori (2002), Kalman (2003)	3.3 – 7.4	~1.02	~ 0 (slowly circulating)	0.8 – 3.5 1 – 1.5	150 – 400
Warrier et al. (2002)	7 – 46.5	1.03			~6.4
Lucic et al. (2010)	4.5 – 11	1.15	0.22 – 0.3	2 – 3.5	~6
Lucas and Prasser (2007)	0.7 – 6.2	10 – 20.8	1	3 – 35	
Yuan et al. (2009)	8.7 – 25	~ 1.1	0.07 – 0.122	0.77 – 2.03	~ 3 – 6
Kim and Park (2011)	14.9 – 24.7	~1.05 – 1.13	-	3.5 – 6	~ 10 – 40

A review of series of experiments (summarized in Table 1) in which steam bubble condensation was investigated [Prodanovic et al. 2002, Warrier et al. 2002, Okawa et al. 2005, Okawa et al. 2003, Lee et al. 2002, Zeitoun et al. 1994], shows that there are few experiments that were carried out with a direct injection of steam bubbles under atmospheric pressure. In most cases, steam bubble condensation was studied as a secondary phenomenon during subcooled boiling. The dimensions of the test sections were generally small (<50 mm equivalent hydraulic diameter) and the subcooled water velocity was kept constant (sometimes stagnant), or it was varied within a limited range. Bubbles were generally small (under 5 mm) and, in a few cases, up to 8 mm. Consequently, an experimental investigation of this phenomenon at relatively low pressure using direct injection of steam bubbles into a subcooled liquid flow, and covering a wider range of main test variables (subcooling temperature, fluid velocity and bubble injection diameter) will increase the experimental data base in this field.

1.1.2 Bubbles condensation and factors affecting it

1.1.2.1 Condensation regimes

When a steam bubble comes into a contact with subcooled water, the bubble starts to shrink while moving in the fluid due to convective heat transfer across the steam/liquid interface and subsequent mass transfer. When the bubble diameter is below a certain value the bubble collapses and suddenly disappears in a short time due to the liquid inertia [Park et al. 2007]. However, as figure 1.1 shows, bubble condensation is mainly controlled by the heat transfer in the so-called thermal regime (convective heat transfer). The Rayleigh regime of bubble collapse, controlled by the inertia of the liquid, is not typical and often the collapse process is limited by the ability of the liquid to conduct the heat of condensation [Gumerov et al. 1996].

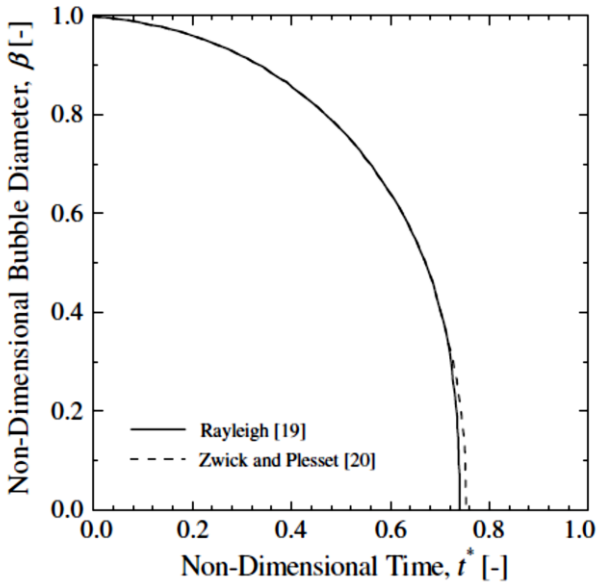

Figure 1.1 Time history of a bubble condensing in subcooled water [Park et al. 2007]

1.1.2.2 Physical Properties and system Pressure

The change of physical properties influences the condensation process directly via the change of various condensation parameters, and indirectly by affecting the bubble motion and properties of the bubble surface. A major change of physical properties happens when the system pressure changes. This is why some experiments are classified under low pressure and others under high pressure criteria. Closure laws should be also assigned to the pressure range in which the experiments were carried out. An essential quantitative difference between “high pressure” and “low pressure” conditions is the order of magnitude of the difference between the liquid and the vapor densities. Many closure laws describing the mass momentum and energy exchange at the gas/iquid interface do not apply equally to both high-pressure and low-pressure conditions [Koncar et al. 2004]. The bubble’s surface tension and liquid viscosity decreases under high pressures. The Morton number under saturation temperature conditions, which is one of the most important parameters characterizing the bubble motion, is less than the lower limit of most experimental databases usually carried out in ambient temperature water. Thus, the available correlations for bubble motion in ambient temperature conditions might not be applicable to the bubbles in such a low Morton number fluid [Okawa et al. 2003]. Brucker and Sparrow [Brucker et al. 1977] found that a bubble interface was more compliant at higher pressures owing to the decrease of its surface tension and liquid viscosity with the temperature and therefore was more susceptible to oscillations [Park et al. 2007]. Their experimental results for steam bubbles injected into still water under different pressure values showed also that bubble collapsing time increased with an increasing pressure [Park et al. 2007]. This may indicate different heat transfer coefficient magnitudes at different pressure levels. Fan and Tsuchiya [Fan et al. 1990] pointed out that their correlation for the terminal bubble rise velocity is reasonably accurate in a wide range of experimental

conditions with ambient water temperatures with the exception of bubbles in hot tap water. All these remarks indicate the importance of the chosen range of experimental investigation.

1.1.2.3 The flow field around the bubble

The characteristics of the flow field formed around the bubble have also influence upon bubble condensation.

- The flow past a bubble can heavily influence the thermal region of the bubble collapse governed by the convection, and consequently affect the condensation rate [Gumerov et al. 1996]. As the bubble condensates, a thermal layer grows around the bubble which leads, in turn, to a slowing down of the condensation process [Warrier et al. 2002]. The change of the flow field will affect the topology and the structure of this layer and thus the condensation process.
- The non-stationary nature of the thermal boundary layer around the bubble will also influence the bubble dynamics [Gumerov et al. 1996] and subsequently, both the bubble motion and the condensation process (bilateral interconnected influences).
- The relative velocity affects the lateral force acting on a bubble and the bubble rising velocity. As such, the lateral void distribution, and the cross-sectional area-averaged void fraction significantly depend upon the relative velocity.
- The oscillations observed in the path of the rising bubbles are related to the spatial development of the void fraction profile in the flow channel. Both the bubble rising velocity, and the rise path oscillations were found to have a strong relation to the bubbles' shapes [Fan et al. 1990, Clift et al. 1978].
- The condensation process itself can have an influence upon the interface condition and bubble motion [Okawa et al. 2005].

These observations show how the bubble condensation process is connected to the local flow parameters in the bubble's vicinity and how these parameters are interconnected and affecting each other bilaterally.

1.1.2.4 Bubble shape and diameter

Bubble geometrical characteristics, mainly bubble shape and bubble diameter, are important factors for bubble condensation. Together they determine an important factor for the bubble condensation process: the interfacial area of each bubble, and consequently the interfacial area concentration for the entire flow. The heat and mass transfer between bubbles and liquid is proportional to the surface area of the bubble, and thus the Nusselt condensation number is dependent upon the bubble diameter. Usually most correlations assume the bubbles to have a spherical shape, and even to resemble a rigid sphere. A rigid sphere is a rough assumption for the condensation of a vapor bubble [Kalman et al. 2006], since the flow field around a bubble -which has an interface with a certain surface tension- will differ from that around a rigid sphere. Additionally, the heat transfer mechanism in the inner side of the bubble surface is

completely different from a rigid sphere. Most Nusselt number correlations do not differentiate between spherical and non-spherical bubbles [Warrier et al. 2002], this leads to discrepancies in the calculation of the interfacial area concentration. It is well known that small bubbles are spherical but larger ones are ellipsoidal [Maurus et al. 2002, Okawa et al. 2003], and they become cap-shaped or very distorted when they are large enough ($D_{B,eq} > 10$ mm). Condensation is more prominent at the rear of the bubble, which has been observed as a sudden acceleration of the bubble while shrinking [Okawa et al. 2005]. The assumption of an equal condensation rate all over a single bubble's surface is thus an approximate assumption that helps to calculate a single heat transfer coefficient for a single bubble. The shape of the bubble eventually affects its motion: Small spherical bubbles follow a linear path, while larger deformed bubbles will follow spiral or zigzag paths [Okawa et al. 2003].

1.1.2.5 Existence of multiple bubbles

The existence of more than one bubble leads into bubbles interactions, which create different flow fields from those existing around a single bubble. The condensation of many bubbles in a volume means that the liquid absorbs more thermal energy. This results in a different distribution of the local subcooling temperature. Leading bubbles in a swarm often affect the behavior of the trailing ones. Bubbles envelopment by the wake created by leading bubbles changes the flow field around the trailing bubbles [Okawa et al. 2003, Kalman 2006] and consequently the condensation process. The increase of bubbles concentration usually leads to an increase in the overall heat transfer due to the increased bubbles' agitation and thus the heat transfer rate [Prodanovic 2002]. This means that the "swarm effect" should be considered when the bubbles concentration causes the flow to go beyond the "diluted bubbly flow" flow condition and becomes closer to a "dense bubbly" flow condition.

1.1.2.6 Water purity and initial distortion

Bubble motion significantly depends on the liquid purity [Fan et al. 1990, Clift et al. 1978]. However initial distortion has a counter effect and it was found that the bubble behavior in pure liquid can be similar to that in impure liquid if the initial distortion is sufficiently small [Tomiyama et al. 2001]. Since the initial distortion cannot be controlled, it is better to perform the experimental investigations in a similar liquid purity conditions to avoid discrepancies.

1.1.2.7 Dissolved gas effect

Dissolved gas may lower down the saturation temperature resulting in larger subcooling temperatures [Bartel et al. 2001]. The non-condensable gases effect upon steam bubbles condensation was rarely investigated. In most experimental investigations, dissolved gases were drawn out of the system by boiling water used to generate the steam for one hour before starting the experiments. The existence of dissolved gases will complicate the formulation of

closure laws and the modeling of the phenomenon. Additionally, the effect upon the final heat transfer rate should be systematically investigated at different concentration levels, which is out of the scope of the current work.

1.1.3 A review of previously carried-out experimental investigations

1.1.3.1 Test section geometry and size

Most experimental investigations handled steam bubbles condensation as a sub-phenomenon of subcooled boiling. This lead to an annular configuration in many cases [Prodanovic et al. 2002, Lee et al. 2002, Zeitoun et al. 1994]. In this configuration, the inner tube was used as heating rod in order to generate steam bubbles while the liquid flows in the annular space. This configuration resembles the flow conditions of the subcooled-boiling at the surface of PWR rod-bundle. A rectangular channel configuration was used in other cases [Warrier et al. 2002, and Lucic et al. 2004]. In these cases, one side of the rectangular cross section channel was used as a heating wall. Experiments that performed investigations in a stagnant liquid or slowly flowing liquid, used a rectangular large pool or container [Okawa et al. 2003, Mayinger und Chen 1986 & 1992, Kalman and Mori 2002, Kalman 2003]. A circular channel was used in one study where bubbles were generated by electrical heating of a part of the outer surface coated with a metallic oxide [Okawa et al 2005]. Glass (quartz or sapphire glass) was used for the construction of the test section for its transparency and heat resistance. Since most experiments have been executed under 1 bar, test section lengths are rarely longer as 1 m and even less than 0.2 m. These lengths are sufficient for the observation of steam bubbles condensation under atmospheric pressure as the bubble life time is very small and bubbles' path length is of the order of a few centimeters. The cross section dimensions were, however, different, and generally less than 50 mm equivalent hydraulic diameter. Bubbles generated under these conditions were small and less than 8 mm diameter. Distilled water is used in most experiments as a standard liquid. A summary of test sections' geometry and dimensions is given in table 1.2.

Table 1.2 Test section dimensions in some experimental investigations of subcooled boiling

Article	Geometry*	Length [m]	Diameter/cross section dimensions [mm]	Development length/ injection-measurement distance [m]	Test section material	Remarks
Prodanovic et al. (2002)	A	0.78	12.7/ 22	0.22	*Quartz glass*	
Koncar et al. (2004)	R	1.38	42.0×41.28	0.61 ($developmen$ $+0.3$ ($transition$)	*Glass*	*Distilled water*
Kalman et al. (2006)	C	0.16	20	1.465	*Sapphire glass*	*Deionized tap water*
Zeitoun et al. (1997)	R	0.4	250×300		*Pyrex glass*	*Stagnant /distilled water*

Lee et al. (2002)	A	2.376	19/ 37.5	0.28	$Glass$	$Distilled\ water$
Cheng et al. (2006)	A	0.3	12.7	0.34	$Plexiglas$	$Distilled\ water$
Mayinger and Chen (1986), Chen and Mayinger (1992)	C		1.6 mm $Nozzle$			$Degassed\ water$ $R113, ethanol,$ $and\ propanol$
Kalman et al. (2002, Kalman et al. (2003)	R	0.6	100×100		$Glass$	$Freon113$
Warrier et al. (2002)	R	1.83 (total) 0.3 (test)	16.33 mm^2	0.61 $(inlet)$ 0.3 $(outlet)$ $+2x0.3\ (transitio$	$Copper\ block\ a$ $pyrex\ glass$	$Distilled$ $and\ degassed\ w$
Lucic et al. (2004), Lucic and Mayinger (2010)	R	0.344 (test)	8×10	0.55 $(inlet)$ 0.35 $(outlet)$	$Stainless\ steel$ $with\ glass\ inse$	$Degassed\ water$
Lucas et al. (2007 & 2009)	C	8 – 9	$DN50$ $DN200$		$Steel$	$Water$
Yuan et al. (2009)	R		$Width$: 2mm			$Water$
Kim and Park (2011)	R	1 (0.6 test)	25×15	0.3 $(inlet)$ 0.1 $(outlet)$	$Glass\ and\ tefl$ $-\ coated\ heate$	$Deionized -$ $degassed\ water$
Zeitoun (1994) [from Park et al. (2007)]	A	1.15 (total) 0.31 (test)	12.7 (OD) 25.4 (ID)	0.34 $(inlet)$ 0.5 $(outlet)$	$Plexiglass,$ $stainless\ steel$ $and\ copper$	$Water$

* Geometry: A: Annular, R: Rectangular, C:Circular.

1.1.3.2 Measurements

High speed camera recording (HSC) was employed order to track bubbles parameters in most reviewed investigations (the double tip needle probes were used in Lee et al. 2002). The acquired images were analyzed to obtain different parameters such as: bubbles equivalent diameter, aspect ratio and bubble rising velocity. Camera resolutions varied from 256×256 to 1024×1024 pixel. Frame rate was generally larger than $1000\ \mathrm{frame/s}$ and up to $8000\ \mathrm{frame/s}$. The error in measuring bubbles equivalent diameter or bubble position was around 0.1mm. Temperatures were measured by k-type thermocouples. Micro-thermocouples; and Platinum resistance detectors were used for a better accuracy (± 1 K for k-type, and down to ± 0.2 K for micro-thermocouples). The better accuracy allows the accurate measurement of low-subcooling temperatures (< 3 K). Flow rates were measured by turbine flow meters or ultrasonic flow meters with errors around $\pm 0.5\%$. Pressure was measured by transducers with an accuracy of 0.5 kPa. Tables 1.3 and 1.4 lists measuring devices its accuracy.

Table 1.3: Measuring devices and corresponding measurement accuracy.

Article	Temperature	Error [K]	Flow rate	Error[%]	Pressure	Error [kPa]
Prodanovic et al. (2002)	K – Type	±1	Turbine flowmeter	±0.3%	Bourdon type guage	0.14
Koncar et al. (2004)	Micro thermocouples (K – type) 0.25mm diameter)	±0.2	Turbine flowmeter		Pressure tranducers (Omega PX202 – 100GV)	
Kalman et al. (2006)	K – Type	±1.5	Ultrasonic flowmeter	±0.5%	Transducers	±0.5
Zeitoun et al. (1997)	K – Type					
Lee et al. (2002)	Platinum resistance detector	±0.2	Turbine flowmeter	±1.9%	Tranducer (Validyne DP103 with CD15 demodulator)	±0.5
Cheng et al. (2006)	Calibrated platinum resistance J – type thermocouples	–	Calibrated rotameter	±2%		
Mayinger and Chen (1986), Chen and Mayinger (1992)	Interferometry and thermocouple	±7%				
Warrier et al. (2002)	K – Type	±0.2			Omega, Model PX202 – 100GV)	
Lucic and Mayinger (2010)	Interferometry					
Lucas et al. (2007 and 2009)	Thermocouple					
Yuan et al. (2009)	Thermocouple	±0.5			–	±0.25
Kim and Park (2011)	Microthermo – couples and RTDs	±0.2	Variable – area flow meter	±5%	DPI260 (DRUG Co.)	±1

Table 1.4 Video recording parameters and errors

Article	Video camera type	Resolution	Frame rate [frame/s]	Error
Prodanovic et al. (2002)	HYCAM K20S4		4000-8000	± 0.05m spatial resolution
Koncar et al. (2004)	HISIS 2000, KSV Instruments Ltd	256×256	1120	± 0.02 mm spatial resolution
Kalman (2006)		512×256	2000	± 0.1mm spatial resolution
Zeitoun et al. (1997)		1024×1024	1000	± 0.1mm spatial resolution
Lee et al. (2002)			25 kHz two-conductivity probe method	$+3\%$ (local void fraction measurement)
Cheng et al. (2006)	Kodak Ektapro EM Motion Analyzer	200×190	1000	± 0.1mm spatial resolution
Mayinger and Chen (1986), Chen and Mayinger (1992)				$\pm 10-20\%$ in heat transfer coefficient
Warrier et al. (2002)	HISIS 2000, KSV Instruments Ltd	256×256	1120	± 0.02 mm $->$ Nuc $-$ error: $\pm 28\%$
Lucic and Mayinger (2010)			20,000	
Lucas et al. (2007 and 2009)	Wire $-$ mesh sensor		2500	
Yuan et al. (2009)	Camera	512×512	5000	± 0.05
Kim and Park (2011)	AOS $-$ technologies	640×512	1000	Nuc $-$ error: $\pm 24.3\%$

1.1.3.4 Test conditions

Table 1.5 lists test conditions found within previously made investigations. Most experiments were conducted under ~ 1 bar with some at higher values up to 2 bars. Subcooling temperatures ranged from 4K up to 60 K. High subcooling temperatures can lead to a direct contact condensation rather than steam bubbles condensation. Bubbles were generated by electrical heating in most experiments with the exception of Mayinger and Chen 1986 & 1992, and Lucas and Prasser 2007 where steam was injected directly into the liquid. The resulting bubbles' diameters depends upon the heat flux and flow conditions. Small bubbles were generated in most experiments (less than 5 mm). The 8 mm bubbles in [Lee et al. 2002] results from coalescence .Liquid velocities were varied between $0-2$ m. s^{-1} and sometimes

they were kept constant or varied within a narrow range. The test conditions of the reviewed experiments show a dispersed set of experimental conditions in general. There was not an attempt of a systematic covering of a well-defined set of values for important thermal-hydraulic variables (subcooling temperature, liquid velocity, bubbles initial conditions, etc.). The use of steam injection instead of a heated surface to generate steam bubbles, isolates the condensation phenomenon from other phenomena such as evaporation, and prevents occurrence of a steep temperature gradient near the heated surface. It allows studying the heat transfer under homogeneous flow conditions around the investigated bubbles and thus the heat transfer coefficient can be more accurately defined.

Table 1.5 Test conditions and parameters' range.

Article	ΔTsub [C]	Pressure [bar]	Liquid velocity [m/s]	Bubble diameter [mm]	Bubble life time [ms]
Prodanovic et al. (2002)	10,20,30,40,6	1	0.08 – 0.83	0.59 – 2.68	1.43 – 18.4
Koncar et al. (2004)	7 – 46.5	~1.03	~0.235 – 0.684	0.69 – 1.14	~2
Kalman et al. (2006)	4.4 – 5.4	~1.2	~1	0.9 – 3.7 (collapsing)	1.4 – 4.8 (collapsing)
Zeitoun et al. (1997)	~10 (by vapor injection)	~1	Stagnant	0.6 – 3.7	–
Lee et al. (2002)	11.5 – 21.3	1 – 2	~0.6 – 1.3 (average)	0.15 – 8 (predicted)	–
Cheng et al. (2006)	2.6 – 18.8	1 – 1.8	0.2 – 0.5	1 – 8	
Mayinger and Chen (1986), Chen and Mayinger (1992)	12.5 – 40 (7.6 at 2 bar)	0.25 – 2	0.02 downflow	Various due to pressure: nozzl	6 – 19
Kalman and Mori (2002), Kalman (2003)	3.3 – 7.4	~1.02	~ 0 (slowly circula	0.8 – 3.5 1 – 1.5	150 – 400
Warrier et al. (2002)	7 – 46.5	1.03			~6.4
Lucic et al. (2004)	4.5 – 11	1.1	0.22 – 0.3	2 – 3.5	~7
Lucic and Mayinger (2010)	4.5 – 11	1.15	0.22 – 0.3	2 – 3.5	~6
Lucas and Prasser (2007)	0.7 – 6.2	10 – 20.8	1	3 – 35	
Yuan et al. (2009)	8.7 – 25	~ 1.1	0.07 – 0.122	0.77 – 2.03	~ 3 – 6
Kim and Park (2011)	14.9 – 24.7	~1.05 – 1.13	–	3.5 – 6	~ 10 – 40
Zeitoun (1994) [from Park et al. (2007)]	~2	1.03	~0.15		

1.1.3.5 Design of the test loop

The test loops used for investigation of subcooled boiling or steam bubbles condensation consisted of the following components:

- A test section with the heated surface for bubble generation.
- A separation tank: to separate gas form liquid.
- A storage tank for subcooled water.
- A pump.
- A pre-heater and heat exchangers to control subcooling temperature and condense the resulting steam.
- A filter for water purification.
- A degasifier to eliminate dissolved gases.
- Measuring devices, and measurement & control system.

Figure 1.2 shows a set of images indicated by the corresponding reference of the previously used test loops.

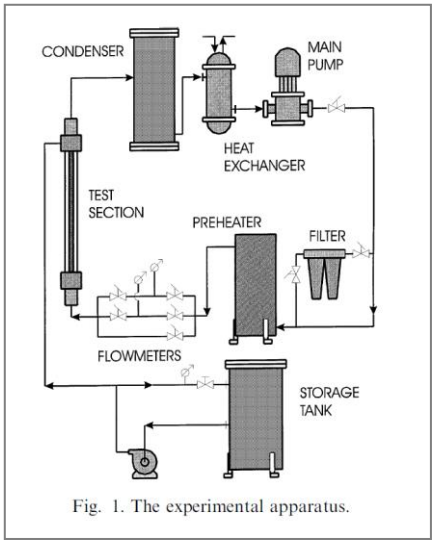

Fig. 1. The experimental apparatus.

Prodanovic et al. (2002)

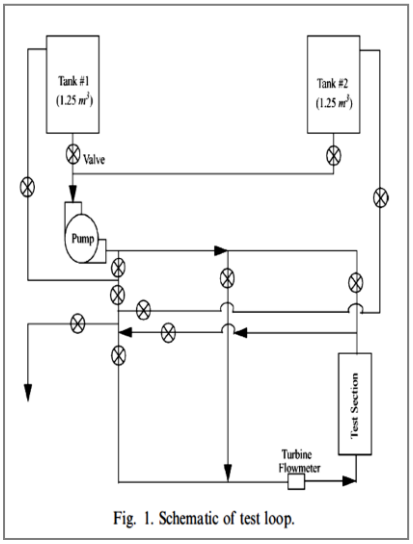

Fig. 1. Schematic of test loop.

Warrier et al. (2002)

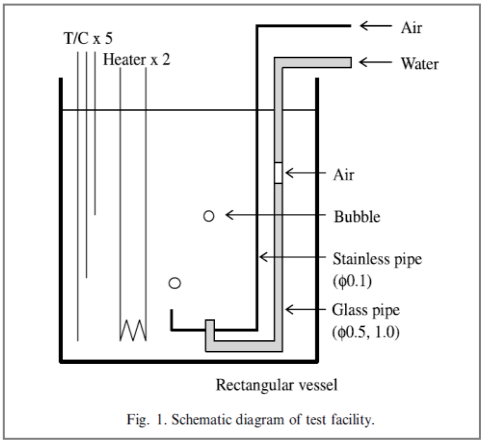

Fig. 1. Schematic diagram of test facility.

Okawa et al. (2003)

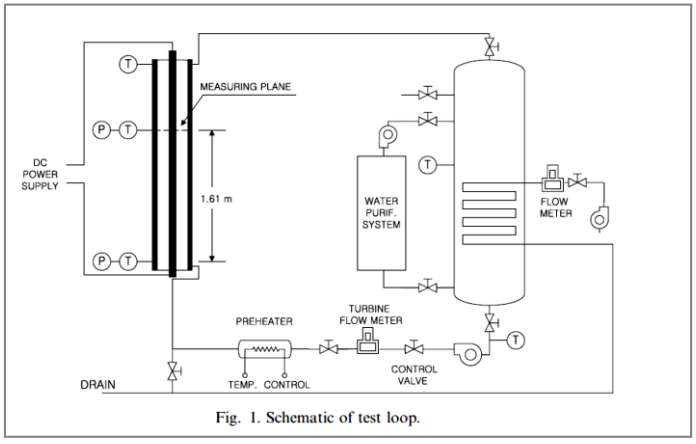

Fig. 1. Schematic of test loop.

Lee et al. (2002)

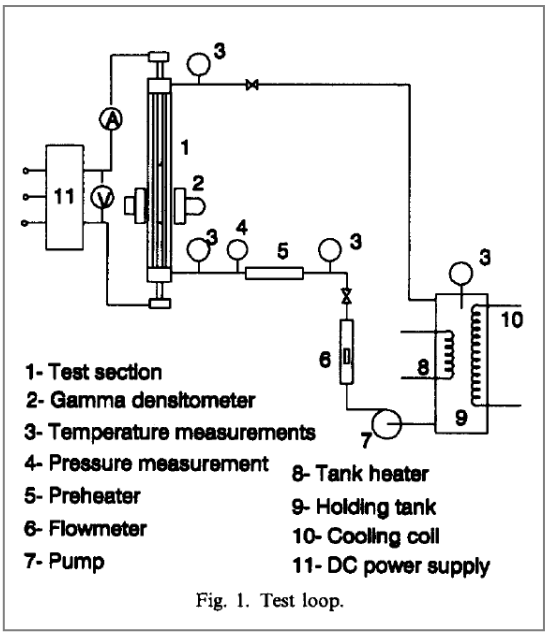

Fig. 1. Test loop.

Zeitoun et al. (1994)

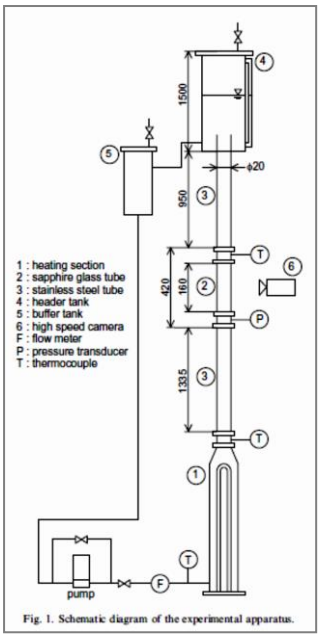

Fig. 1. Schematic diagram of the experimental apparatus.

Okawa et al. (2005)

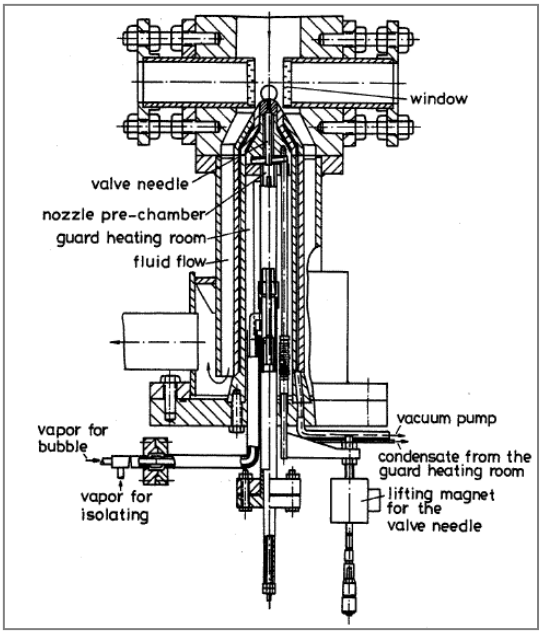

Mayinger und Chen (1986 & 1992)

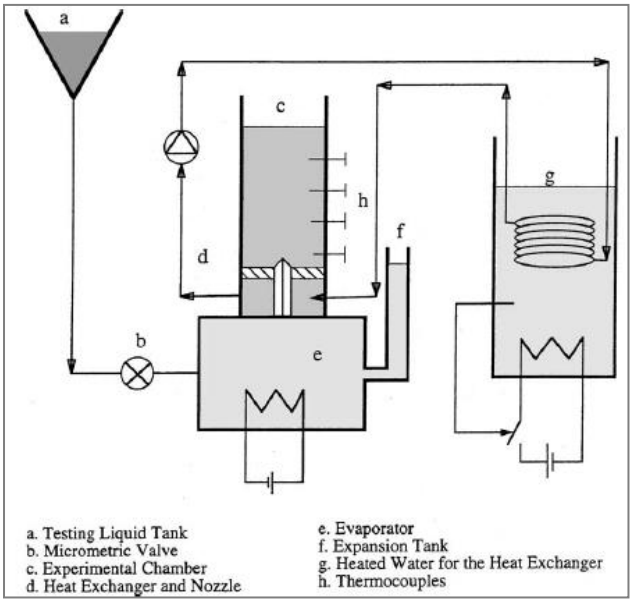

Kalman and Mori (2002), Kalman (2003)

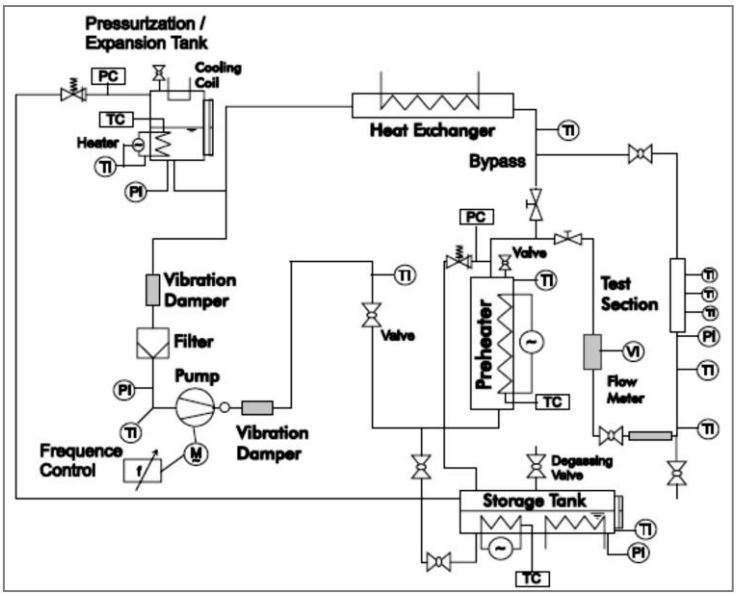

Lucic et al. (2004)

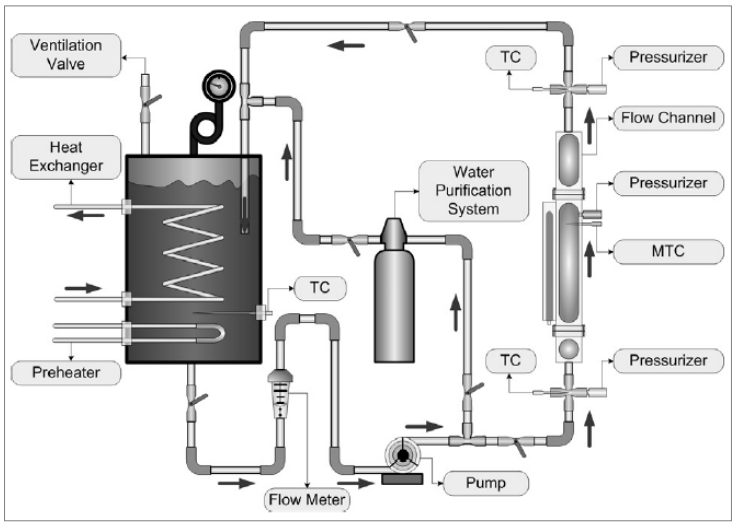

Kim and Park (2011)

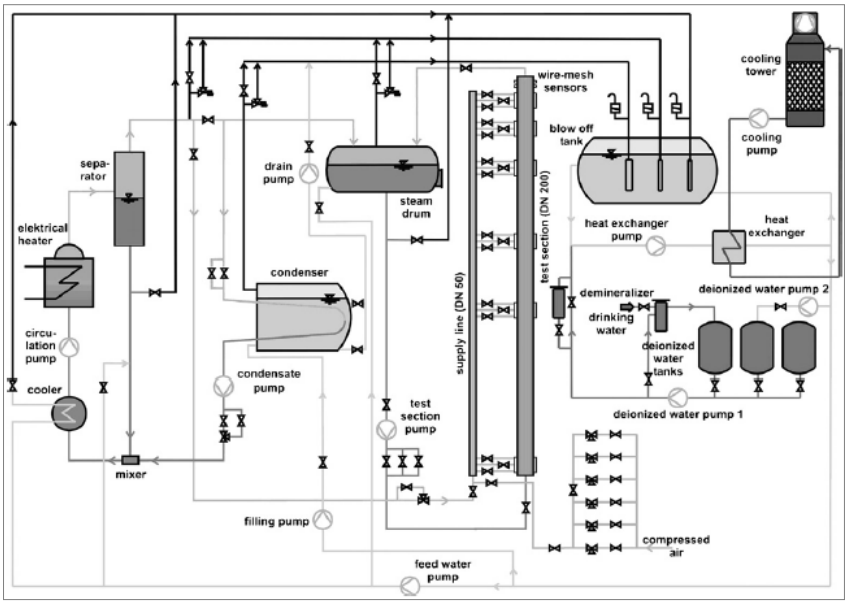

Lucas et al. (2007 and 2009)

Figure 1.2 Different schematics used by different researchers to study subcooled boiling or steam bubbles condensation

1.1.3.6 Test section arrangement

Test sections are transparent in order to allow optical observations. When the cross section is circular, a refraction correction is needed. This is usually achieved by constructing a square channel around the circular test section and filling it with water. Figure 1.3 shows the measurement arrangement and refraction correction adopted in the previously made investigations.

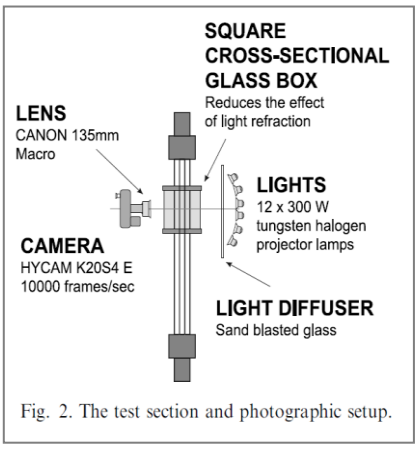

Fig. 2. The test section and photographic setup.

Prodanovic et al. (2002)

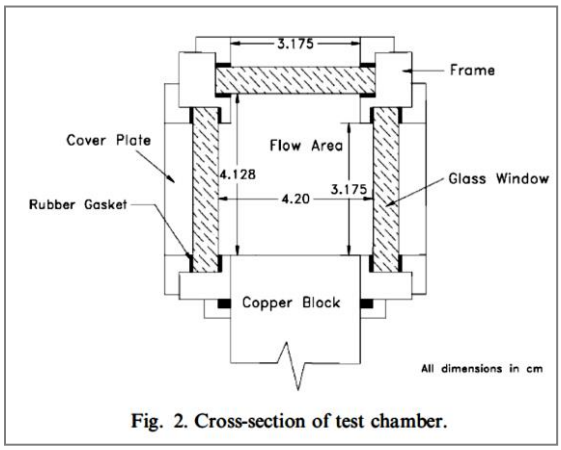

Fig. 2. Cross-section of test chamber.

Warrier et al. (2002)

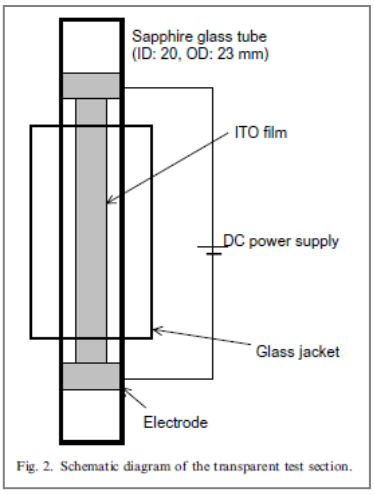

Fig. 2. Schematic diagram of the transparent test section.

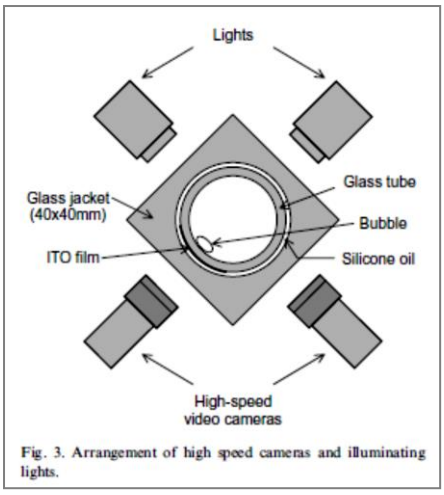

Fig. 3. Arrangement of high speed cameras and illuminating lights.

Okawa et al. (2005)

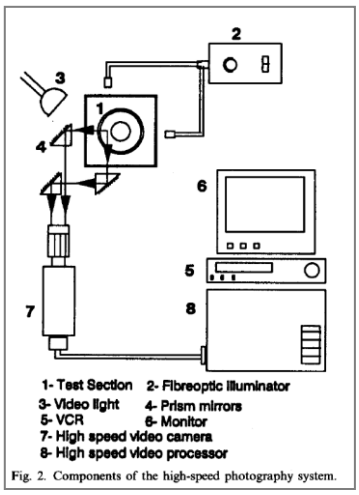

Fig. 2. Components of the high-speed photography system.

Zeitoun et al. (1994)

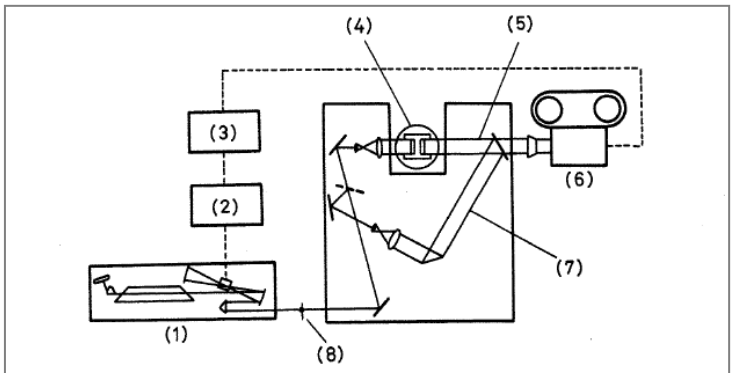

Figure 2. Optical setup of the holographic interferometer: (1) argon laser, (2) Bragg cell, (3) pulse unit, (4) test section, (5) object wave, (6) high-speed camera, (7) reference wave, (8) shutter.

Mayinger und Chen (1986 & 1992)

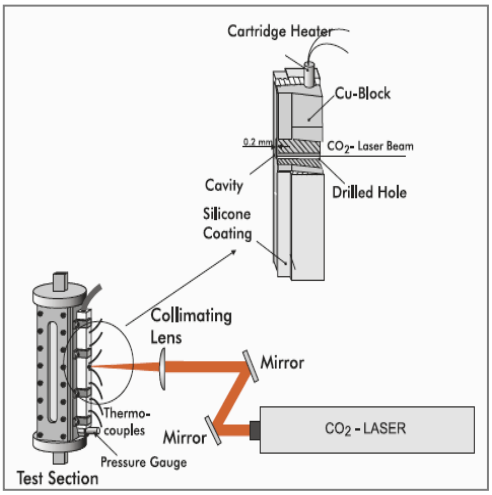

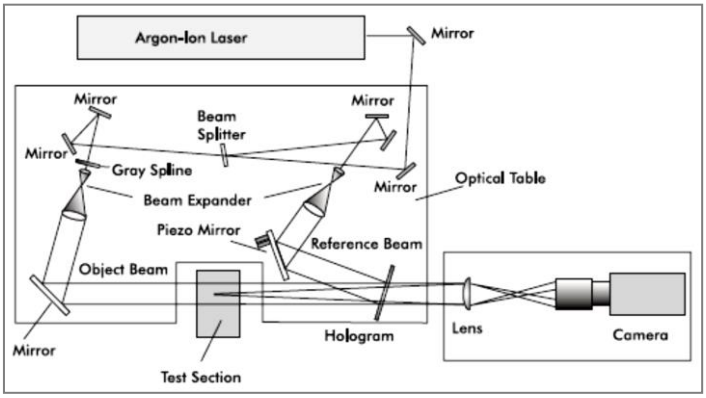

Lucic et al. (2004)

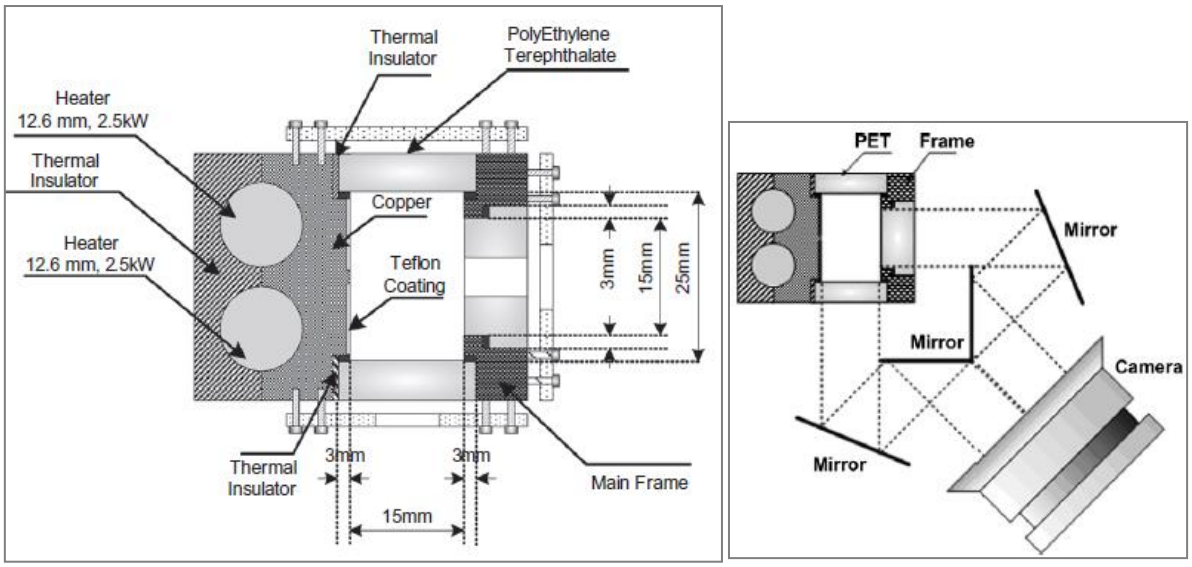

Kim and Park (2011)

Figure 1.3. Refraction correction for circular test section used by different authors. reference is shown at the bottom of each image.

Usually one camera was implemented to acquire the bubbles images (for shadowgraph techniques). However sometimes either two cameras were used [Okawa et al. 2005] or one camera with a double-image acquisition arrangement [Zeitoun et al. 1994, and Kim and Park 2011]. Mayinger und Chen (1986 & 1992) and Lucic et al. (2004) applied holographic interferometry using one camera.

1.1.4 Modeling

The governing equations used in bubbly flow simulations consist of the basic equations describing the conservations of mass, momentum and energy and the constitutive equations for closure laws [Okawa et al. 2003]. Among the various mathematical formulations of two-phase flow, the two-fluid model is considered the most accurate one. In this formulation, both phases are separately described in terms of averaged phasic mass, momentum and energy equations. Moreover, the interactions between different phases are modeled by interfacial transfer terms to account for interfacial mass, momentum and energy transport [Zeitoun et al. 1994]. Modeling of the interfacial phenomena requires accurate knowledge of a number of important parameters: the interfacial area concentration and the heat transfer coefficients [Zeitoun et al. 1994]. Two-phase flow parameters measured locally are necessary for the accurate solution of the interfacial area transport equation for the closure of the two-fluid model. This applies clearly to the simulation of bubble condensation, since it is a phenomenon depending upon local flow parameters [Bartel et al. 2001, Yeoh et al. 2005]. Additionally, experimental data over the behavior of vapor bubbles is of a significant importance for the development of improved mechanistic modeling of forced convective subcooled flow boiling [Okawa et al. 2003]. Even though bubble evaporation and condensation are usually considered to be symmetrical phenomena, preliminary work has shown that under the same conditions of mass flux, void fraction and subcooling, the average bubble size, and

consequently the interfacial area concentration, is dependent on whether vapor generation or condensation is taking place [Zeitoun et al. 1994]. This supports experimental investigations that isolate the condensation from the evaporation process in order to achieve a more accurate modeling of interfacial heat and mass transfer. Such investigations are of special interest for the development of CFD codes which always seek a better and more accurate modeling of the basic mass, momentum and heat transfer terms.

1.1.4.1 Heat transfer coefficient and interfacial area concentration

For a bubble with $D_{B,eq}$ equivalent diameter, the condensation heat transfer coefficient h_c is calculated as follows:

$$h_C = \frac{k_L.Nu_c}{D_{B,eq}} \tag{1.1}$$

The condensation Nusselt number Nu_c is dependant upon bubbles Reynolds number Re_b, Prandtl number Pr and sometimes the void fraction α, Jacob number Ja, and Pecelt numbers Pe were considered:

$$Re_b = \frac{V_{rel}D_{B,eq}}{\nu_l} \tag{1.2}$$

$$Pr = \frac{C_{P,l}\mu_l}{k_l} \tag{1.3}$$

$$Ja = \frac{\rho_l C_{p,l}\Delta T_{sub}}{\rho_g \Delta h_{fg}} \tag{1.4}$$

$$Pe = Re_b Pr \tag{1.5}$$

Table 1.6 gives set of correlations used for the calculation of the Nusselt condensation number for steam bubbles:

Table 1.6 Correlations for condensation Nusselt Number

Name /author	Correlation	Range of applicability
Zeitoun (1994)	$Nu_C = 2.04Re_b^{0.61}.Ja^{-0.308}.\alpha^{0.328}$	$2266 < Re_b < 7953$
Ranz-Marshall (1952)	$Nu_C = 2 + 0.6Re_b^{0.5}.Pr^{0.33}$	$2 < Re_b < 800$
Akiyama (1973)	$Nu_C = 0.37Re_b^{0.6}.Pr^{0.33}$	
Hughmark (1967)	$Nu_C = 2 + 0.6Re_b^{0.5}.Pr^{0.33}$	$0 < Re_b < 450$ $0 < Pr < 250$
	$Nu_C = 2 + 0.27Re_b^{0.5}.Pr^{0.33}$	$Re_b > 450$ $0 < Pr < 250$

Chen and Mayinger (1992)	$Nu_C = 2 + 0.6Re_b^{0.6}.Pr^{0.5}$	$Before\ \ detachment$ $100 < Re_b < 1000$
	$Nu_C = 0.185Re_b^{0.7}.Pr^{0.5}$	$After\ detachment$ $0 < Re_b < 10000$
Gnielinski (1975)	$Nu^2 = Nu_{min} + \left(Nu_{lam}^2 + Nu_{turb}^2\right)^{0.5}$ $Nu_{min} = 2\ for\ a\ sphere$ $Nu_{lam} = 0.664Re_b^{0.5}.Pr^{0.33}$ $Nu_{turb} = \frac{0.037Re_b^{0.8}.Pr}{1 + 2.443Re_b^{-0.1}.(Pr^{2/3} - 1)}$	$For\ flow\ around$ $solid\ sphere$ $0 < Re_b < 10^6$ $0.7 < Pr < 600$
Clift, Grace, Weber (1978)	$Nu = 1 + \frac{0.725}{Pr^{0.139}}.(1 + \frac{1}{Pe})Pe^{0.472}$	
Kutateladze (1979)	$Nu_C = 2 + 0.03Re_b.Pr^{1/3} + 0.35Re_b^{0.58}.Pr^{0.35}$	$Flow\ around\ a\ sphere$ $, quasi - isothermal$ $and\ stationary\ flows$ $1 < Re_b^{0.54}Pr^{1/3} < 10^3$
Kelly, Kazimi (1982)	$Nu = \max(\frac{12}{\pi}Ja, 0.7Re_b^{0.5})$	$Water - steam\ flows$
Hori, Toda (1991)	$Nu_c = 0.02Re_b.Pr$	
Isenberg and Sideman (1970)	$Nu_c = \frac{12}{\pi}Re_b^{0.5}.Pr^{1/3}$	
Trace code 2000	$Nu_c = 116.\sqrt{Pr}$	$Re_b > 10000$
	$Nu_c = 0.185Re_b^{0.7}.\sqrt{Pr}$	$400 < Re_b < 10000$
	$Nu_c = 2 + 0.6(0.4Re_b^{0.5} + 0.4Re^{2/3})$	$Re_b < 400$
Ruekenstein (1959)	$Nu_c = \sqrt{\frac{4}{\pi}(Re_b.Pr)^{0.5}}$	
Warrier (1999)	$Nu_C = 0.6Re_b^{0.5}.Pr^{0.33} \times (1 - 1.2Ja^{0.9}Fo_0^{0.66})$	$20 < Re_b < 700$
Lucic and Mayinger (2010)	$Nu_{av} = 1.46Re_b^{0.61}.Pr^{0.33}Ja^{-0.31}$	$1000 < Re_b < 3400$ $10 < Ja < 30$
Yuan et al. (2009)	$Nu_C = 0.6Re_b^{0.5}.Pr^{0.33} \times (1 - Ja^{0.1}Fo_0)$	$355 < Re_b < 1770$ $20 < Ja < 60$ $Pr = 1.7$

		$1000 < Re_b < 6000$
Kim and Park (2011)	$Nu_{av} = 0.257 Re_b^{0.7}.Pr^{04564} Ja^{-0.2043}$	$18 < Ja < 36$
		$1.87 < Pr < 2.03$

Zeitoun (1994), Ranz-Marshall (1952) and Akiyama (1973) are among the most used correlations in literature. Ranz-Marshall is frequently used in CFD codes. It is important to note that some correlations are based on flow around a solid sphere or were originally for droplets (Ranz-Marshall 1952). Usually bubbles with an equivalent diameter above 10 mm have a deformed shape. Depending on the bubble size, such deformations determines the contact area of the bubble with the subcooled fluid, which has a direct impact on the heat transfer rate. The effect of the bubbles Reynolds number range is not always considered and most investigations lies in the low range values ($Re_B < 10000$) with some exceptions. Zeitoun correlation incorporates the void fraction and the Jacob number, which impose some iterative calculation. The interfacial area concentration is incorporated in all interfacial transfer terms. It can be calculated either as a result of the solution of transport equations, or as a formula based on the bubble's diameter, which is the most adopted approach. If bubbles were considered to have a spherical shape with an equivalent diameter $D_{B,eq}$, the following formula can used:

$$a_i = \frac{6\alpha}{D_{B,eq}} \tag{1.6}$$

Although the hypothesis of spherical bubble is not ideal, this formula/assumption is widely implemented [Zeitoun et al. 1997, Zeitoun et al. 1994, Koncar et al. 2004]. Considering a bubbles size distribution instead of an average bubbles' equivalent diameter will enhance the accuracy of such correlations, however the average bubbles diameter (the assumption of a monodispersed bubbly flow) was frequently used by adopting the mean Sauter diameter D_s. Zeitoun and Shoukri [Zeitoun et al. 1997] give following formula for calculating the D_s.:

$$\frac{D_s}{\sqrt{\sigma/g\Delta\rho}} = \frac{0.0683(\rho_L/\rho_G)^{1.326}}{Re^{0.324}\left(Ja + \frac{149.2(\rho_L/\rho_G)^{1.326}}{Bo^{0.487}.Re^{1.6}}\right)} \tag{1.7}$$

The maximum bubble diameter for the bubbles after evaporation and detachment off the heated wall was also applied as a characteristic bubbles' diameter. The bubble diameter decrease after detachment and beginning of the condensation was approximated by a linear function of the radial position from the fuel rod center (case of subcooled boiling in PWR rod bundle, Koncar et al. 2004). The maximum bubble diameter was also calculated using some empirical correlations such as Unal's mechanistic model (1976). Some authors have used this maximum bubble diameter along with the interfacial area concentration distribution of Nukiyama to calculate the interfacial area concentration [Koncar et al. 2003, Ha et al. 2005]:

$$a_i = \frac{3.6\alpha}{D_{max}} \tag{1.8}$$

Since the maximum bubble diameter is usually calculated out of the bubbles evaporation model, the implicit errors will be transferred into the calculations of bubbles condensation. The existence of a steep temperature gradient near the heated wall makes the assumption of using a homogeneous bulk temperature (used to estimate the subcooling temperature) around the bubble, not accurate.

1.2 Counter current flow limitation CCFL

1.2.1 Definition and occurrence of CCFL

Gas/liquid two-phase stratified flows in horizontal channels are frequently encountered in practical applications such as nuclear reactors, oil and gas pipelines, and steam generation and refrigeration equipment, reflux condensers, packed columns, heat pipes, etc [Navarro 2005, Ghiaasiaan et al. 1997, De Sampiano 2008, Wallis and Dobson 1973]. The accurate prediction of the pressure gradient and void fraction in gas/liquid two-phase stratified flow is of both scientific and technological interests [Wong and Yau 1997]. If the liquid and gas are flowing in opposite directions the flow is a countercurrent flow. A stratified countercurrent flow of gas and liquid is only stable for a certain range of mass flow rates. If the gas mass flow rate increases too much, the liquid flow is stopped, and then it will be carried over by the gas and partially or totally flows in the opposite direction. This phenomenon is known as countercurrent flow limitation (CCFL). Onset of CCFL corresponds to the limiting condition where the flow rates of neither the gas nor the liquid can be further increased without changing the flow pattern, and limiting the liquid flow rate [Wongwises 1996, Navarro (2005), Wongwises (1998a)], or it is the limiting point of stability of the countercurrent flow indicated by the maximum gas mass flow rate at which the down flowing liquid mass flow rate is equal to the inlet liquid mass flow rate [Deendarlianto et al. 2011]. This limiting condition–known also as onset of flooding- can happen in vertical or horizontal geometry. The phenomenon plays an important role in several equipment of the chemical and mechanical industries. Countercurrent flows of water and steam are of a great importance in the field of safety analysis of nuclear reactors [Wintterle et al. 2008, Wang and Kondo 1990, Navarro 2005 , Wongwises 1996, Ohnuki 1986, Jeong 2002, Miniani et al. 2010 ,Kim and No 2002]. CCFL can occur in the hot-leg of a pressurized water reactor PWR during a loss of coolant accidents, LOCA or SBLOCA and in the event of loss of residual heat removal system (loss of RHR). Three Mile Island accident in 1979 drew attention to the importance of CCFL phenomenon in reactor safety. Due to CCFL, no coolant flowed from pressurizer to the primary circuit during the accident at Unit 2. In the case of a LOCA or a SBLOCA, the supply of cooling water into the reactor core is limited partially or totally by the occurrence of CCFL at the upper tie plate, reactor vessel down comer, pressurizer surge line, in tubes of the steam generator and hot leg pipe, depending on the situation [Jeong 2002, Navarro 2005, Gargallo et al. 2005, Deendarlianto et al. 2011, Wongwises 1996, Ohnuki et al. 1988]. Also, it is important that the reflux condensation will not be stopped during the loss of RHR event, therefore the prediction of CCFL is one of the most important issues for the evaluation of nuclear safety. The most important safety issues in CCFL studies are

- The specification of conditions leading to its occurrence (Onset of CCFL)
- The prediction of gas and liquid flow rates once CCFL takes place (Partial delivery and zero liquid penetration)

1.2.2 Onset of CCFL

In a hot-leg geometry (see Figure 1.16) a smooth stratified establishes at low liquid and gas superficial velocities. As the gas velocity increases, disturbances start to appear at the interface. Small waves initiate and grow. Instabilities, hydraulic jump, wave growth, droplets entrainment, and chaotic interface movement appearance and development leads eventually to CCFL occurrence. The identification of the CCFL onset mechanism and corresponding CCFL onset correlation is the first important step in studying CCFL phenomenon. Siddiqui et al. (1986) performed several experiments in vertical-to-horizontal pipes and studied the effect of pipe diameter, bend curvature radius, horizontal part length, entrance geometry and slight inclination of the horizontal part on the flooding phenomenon. They found that flooding is caused by unstable wave formation at the hydraulic jump which forms near bend. As the air flow rate was increased the location of the hydraulic jump moved closer to the bend, and eventually slugging occurred and caused the onset of flooding. They observed that flooding in the bend geometry occurred at gas flow rates much smaller than those needed to produce flooding in a vertical pipe with the same diameter. Flooding coincides with unstable wave formation and slugging near the bend. A slight upward inclination of the channel will reduce the air flow rate needed to cause flooding while equal downward inclinations induce the opposite effect. Ardron and Banerjee (1986) developed a theoretical model to predict the onset of flooding in horizontal to vertical or near-horizontal to vertical geometry. Their model assumes that smooth stratified flow exists near the bend with a free fall at the water outlet. They found flooding to coincide with slugging downstream of the bend where the liquid thickness is deepest. Ohnuki (1986) performed several experiments in hot-leg geometry and with different geometrical characteristics of the bend and riser exit to the upper tank. Geometrical parameters were as follows:

L[m]	Geometry	D[mm]	Riser		Water level in upper tank	L/D	I/D	$J_G[m/s]$	$J_L[m/s]$
			I	θ					
$0.01 - 0.4$	$Circular$	26	$0.038 - 0.6$	$40\|45$	$0.1\|0.02$	$0.38 - 5.9$	$1.5 - 11.76$	$Air\ 0.6 - 9.6$	$0 - 0.34$
		51						$Air\ 4.3 - 10.0$ $Steam\ 7.3$	$0 - 0.124$
		76						$Air\ 7.1 - 12.4$ $Steam\ 7.74 - 17.9$	$0 - 0.083$

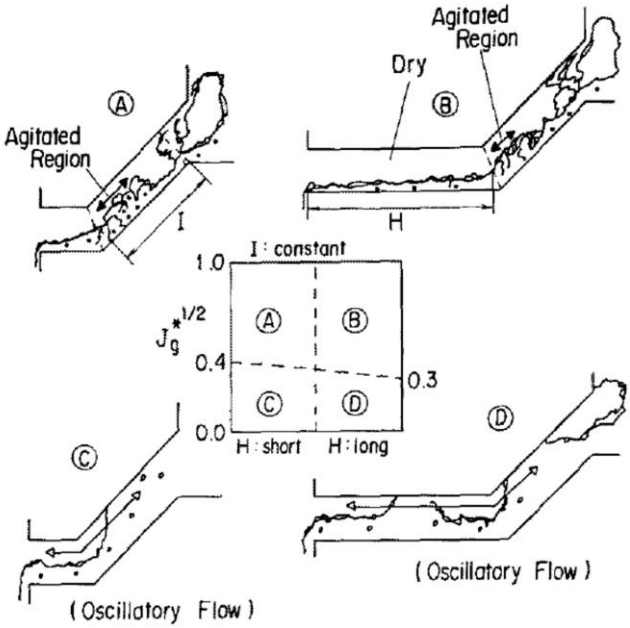

Figure 1.4 Agitation region and flow patterns during CCFL. Ohnuki (1986)

The mechanism by which CCFL happened was different according to the length of the horizontal part and according to the gas superficial velocity as follows:

- For inclined riser without horizontal part the mechanism depends upon $J_G^{*0.5}$. Over a certain limit the flow is annular and unstable disturbed waves were blown into the upper tank. Below the limit the flow becomes oscillatory with periodic plugging and fluctuating water delivery.
- For inclined riser with horizontal part. The limit shifts towards smaller $J_G^{*0.5}$ values. The agitated region at the bend becomes shorter and roll waves become smaller. The limit becomes dependent upon the horizontal length. At large L/D values CCFL location shifts towards the lower tank.
- Increasing riser length makes the agitated region larger and CCFL location shifts to the bend.

The flow transition into unstable periodic plugging flow causes deviation from linearity in CCFL correlation as figure 1.5 shows. The figure excludes geometrical parameters effects by adopting $J_G^{*0.5}/C$ and $J_L^{*0.5}m\ /C$ as coordinates. This indicates the need for different CCFL correlation according to different CCFL mechanisms.

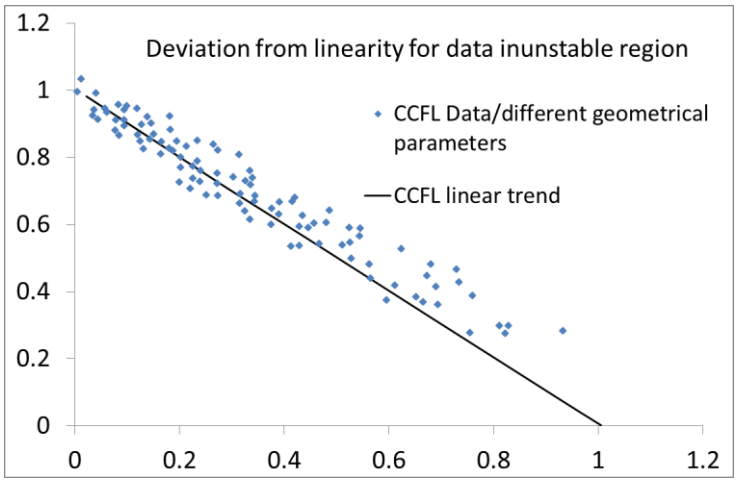

Figure 1.5 $J_G^{*0.5}/C$ Vs. $J_L^{*0.5}m/C$ during CCFL, geometrical effects are excluded and the effect of flow stability under specific gas flow rate is brought in. Ohnuki (1986)

Ohnuki et al. (1988) studied countercurrent flow in a hot-leg geometry in which he used two types of horizontal channels: without and with Hutze, (a Hutze is a secondary pipe used for hot leg ECC injection in some German PWRs):

L[m]	Geometry	D [mm]	Riser		L/D	I/D	$J_G[m/s]$	$J_L[m/s]$
			I	θ				
0.23	*Circular A*	25.4	0.06	50	9.1	2.36	1.25 − 4.2	0 − 0.04
0.23	*Circular B (with Hutze)*	25.4	0.06	50				

As gas velocity increases, an instable roll-wave grows near the bend. At high gas superficial velocities the roll-wave breaks into droplets and blown by air flow into upper tank. At low J_G, the crests of the roll-waves reaches sometimes the upper wall of the channel forming froth or slug flow

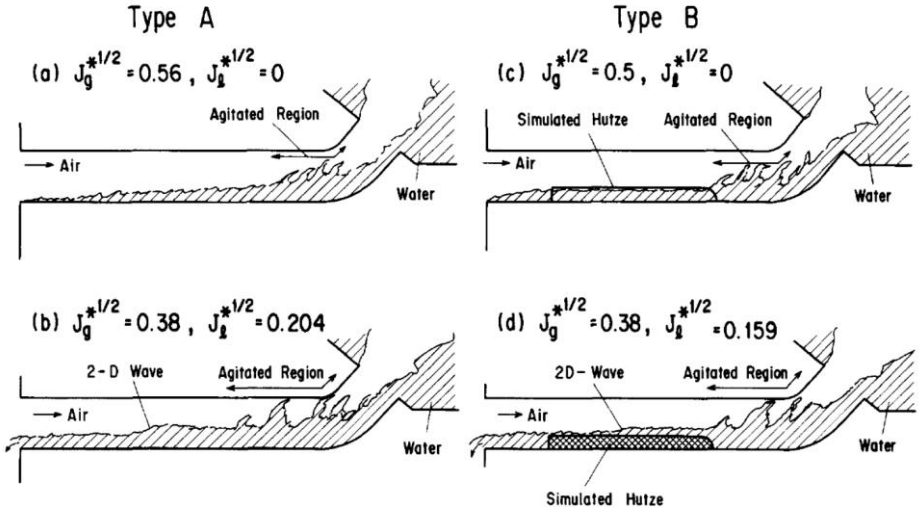

Figure 1.6 Agitation region during CCFL. Ohnuki (1988)

The continuous roll-waves intrusion into the upper tank results in CCFL occurrence. The most agitated region was identified near the bend as shown in Figure 1.6. Wang and Kondo (1990) gave a description of the CCFL phenomenon in the following facility

L[m]	Geometry	Cross section		L/D	$J_G[m/s]$	$J_L[m/s]$
		Height [mm]	**Depth [mm]**			
0.5	*Rectangular*	20,35,50	35	25,14.3,10	*No info*	*No info*
1.5		35	35	42.9		

They described CCFL in three regions according to the liquid fraction α_L:

- $\alpha_L < 0.25$: Instable wave formation leads into CCFL onset.
- $0.25 < \alpha_L < 0.75$: Instable large wave growth and slugging
- $\alpha_L > 0.75$: Immediate slugging happens without wave formation.

The classification according to the liquid fraction (or liquid level) is not frequent. The liquid superficial velocity is more relevant and used by many authors as the rest of this section shows. However the classification can be also related to liquid velocities since the friction is higher at higher liquid velocities causing the liquid level to rise. Kawaji et al. (1991) conducted experiments with vertical-to-inclined pipes containing bend of different inclination angles. They found the flooding mechanism to be dependent upon the water flow rate:

- $J_L^{*0.5} < 0.4$: flooding is initiated by the formation of a hydraulic jump and subsequent slugging downstream of the bend.
- $0.4 < J_L^{*0.5} < 0.7$ The hydraulic jump location shifts toward the horizontal pipe exit away from the bend. Flooding occurs due to slugging.
- $J_L^{*0.5} > 0.8$ Flooding occurs in the vertical section exit near the liquid entrance due to active liquid entrainment.

They suggested that the flooding mechanism for intermediate to high liquid flow rates in vertical-to-downwardly-inclined pipes is the breakup of a turbulent jet-like liquid flow near the elbow and the carryover of droplets by the countercurrent gas flow into the upper tank. They also noted that flooding in vertical-to-downwardly-inclined pipes required higher gas flow rates than in vertical or vertical-to-horizontal pipes at low to moderate liquid flow rates ($J_L^{*0.5} < 0.7$). This is mainly due to the extra gravity component that adds in case of downwardly-inclined pipes and due to the fact that CCFL for $J_L^{*0.5} < 0.7$ is governed by slugging within horizontal channel while the flooding mechanism happens at the vertical section exit for $J_L^{*0.5} > 0.7$ independently from geometrical conditions in the horizontal channel. Ghiaasiaan (1994) reports that the mechanism responsible for flooding in horizontal and near-horizontal channels is the growth of interfacial waves which leads to the formation of slugs. Lopez de Bertodano (1994) analyzed the occurrence of CCFL in hot-leg geometry and stated that the hydraulic jump observed in the down-scaled experiments is not relevant in the full-scale ones. His computations at three different pressures $0.3, 1.5, and\ 7$ MPa show that because of small L/D no hydraulic jump will appear. CCFL will always be located at the upper exit of the riser near the steam generator (entrance flooding according to Choi and No 1995). This result was found to be consistent with the full-scale flooding data of Ohnuki et al. (1988) where no hydraulic jump occurred. Choi and No (1995) suggested two mechanisms of flooding in nearly horizontal pipes: "inner flooding" and "entrance flooding". Figure 1.7 illustrates both mechanisms.

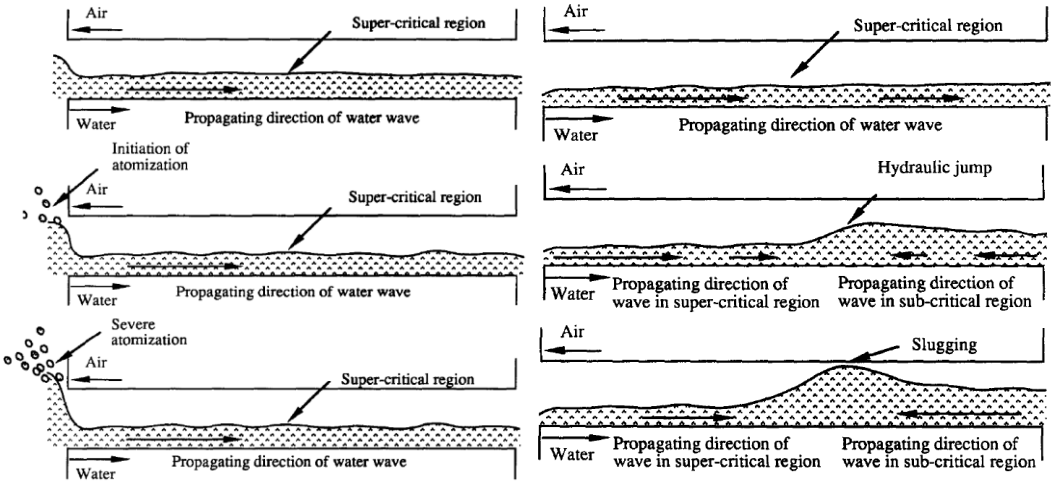

Figure 1.7 Different flooding mechanisms in near-horizontal channels: Left: entrance flooding mechanism by active liquid entrainment ($\theta_{\text{Inclination}} = 0.92^{o}$), Right: inner flooding by slugging ($\theta_{\text{Inclination}} = 0.69^{o}$). Choi and No (1995).

- Inner flooding: is initiated by unstable wave growth (slugging) at some location within the pipe. The location depends upon liquid superficial velocity and inclination angle.
- Entrance flooding is always observed to take place at the entrance of the water flow without slugging. It is caused by active entrainment of droplets.

Choi and No injected water into the pipe by the head difference which restricted the water flow rate within a narrow range and provided limited number of data for high water flow rates where entrance flooding occurs. They found that the initiation of flooding greatly depends on the method of introducing the water into the pipe for the high inclinations and high water flow rates. Wongwises (1996) found that the CCFL mechanism is a function of the water superficial velocity. He made his study in the following hot-leg geometry:

L[m]	Geometry	D[mm]	Riser dimensions **I**	**θ**	Inlet	**L/D**	**I/D**	$\mathbf{J_G}[m.s^{-1}]$	$\mathbf{J_L}[m.s^{-1}]$
0.557|0.832|1.41|2.82	*Circular*	64	1.215	50|75|90	*Porous, inner*	8.7|13|22|44	19	2.2 − 15.4	0|0.0124|0.0248|0.0311

1. $J_L^{*0.5} < 0.2$: A hydraulic jump happens near the bend at low J_L, and away from the bend but moving towards the bend at higher J_L. An instable large roll-waves grow at the jump crest and breaks into droplets which are blown into upper tank causing CCFL.
2. $0.2 < J_L^{*0.5} < 0.35$:
    1. $J_L^{*0.5}$ slightly greater than 0.20: the unstable wave is formed at the hydraulic jump near the bend and grows into froth slug. The slug is pushed strongly like froth in the air direction.
    2. $J_L^{*0.5} > 0.2$: An unstable wave is formed at the hydraulic jump in the horizontal part and grows into slug. The slug is pushed swiftly in the air direction.
3. $J_L^{*0.5} > 0.35$: Water thickens near the lower tank and droplets are carried by air. Then a sudden slug is formed and pushed strongly in the air direction.

In general CCFL was caused by slugging and large roll-waves breaking into the upper tank at low and medium liquid velocities while immediate slugging was caused by droplets entrainment at high liquid velocities. Kang et al (1999) studied countercurrent stratified flow during reflux condensation condition. His experimental set-up had the following geometrical characteristics:

L[m]	Geometry	D[mm]	Riser		L/D	I/D	$J_G[m/s]$	$J_L[m/s]$
			I	θ				
$0.7-3.388$	*Circular*	40	0.648	35	$17.5-84.7$	16.2	0.3316 -9.2840	0.0133 -0.2255
0.928 -3.388	*Circular*	80	0|0.623	0|35	11.6 -42.35	7.79	0.7958 -6.1009	0.0033 -0.3747

In a similar way to Wongwises (1996), The CCFL mechanism was classified into three regions according to the liquid superficial velocity. It was noted that the onset of CCFL depends upon the water flow rate while the zero liquid penetration is independent of the inlet water flow rate as Figure. 1.8 shows.

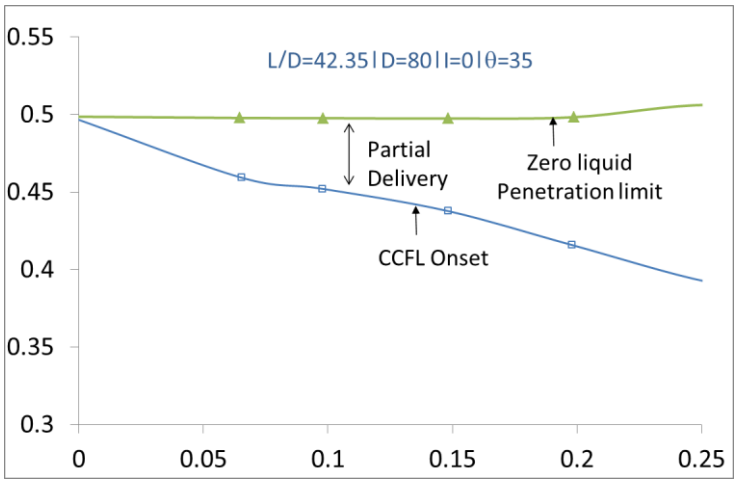

Figure 1.8 Onset of CCFL and Zero liquid penetration. Kang et al (1999).

Figure 1.9 shows a typical onset of CCFL curve where different regions are identified by different trends of the critical gas superficial velocity:

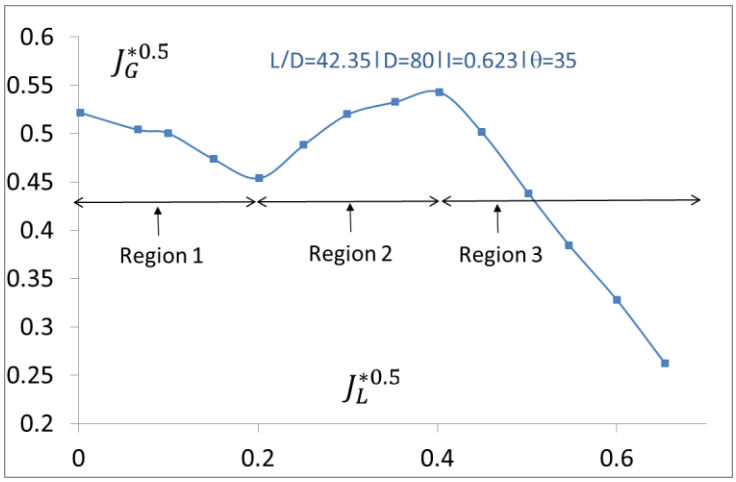

Figure 1.9 Onset of CCFL as function of the liquid superficial velocity. Kang et al (1999)

- $J_L^{*0.5} < 0.2\, m/s$: An unstable roll-wave appears at the crest of a hydraulic jump within the horizontal section. The location of the hydraulic jump depends on the liquid superficial velocity. It appears near the bend at low liquid velocities and away from the bend at higher velocities.
- $0.2 < J_L^{*0.5} < 0.4\, m/s$: No hydraulic jump occurs within the pipe. A supercritical flow throughout the horizonta1pipe is maintained. The depth of water layer increases near the lower tank and water droplets are entrained in the upper region of the pipe. Large amplitude roll-waves develop near the lower tank and move quickly toward the bend decreasing the effective air flow area and increasing the air f1ow velocity which results in restricted water flow.
- $0.4 < J_L^{*0.5} < 0.7\, m/s$ No hydraulic jump in the horizontal pipe and no increase of water layer depth at the horizontal pipe outlet were observed. CCFL occurs near the upper exit of the riser due to active entrainment of water droplets into the upper tank

This description is somehow close to the Wongwises' one especially the description of 1st region, which is rather identical. The fact that Kang et al. did not notice a hydraulic jump in the medium liquid superficial velocities range is probably due to the lower inclination angle which can help inducing a supercritical flow where no hydraulic jump occurs. Consequently, slugging happens at the liquid outlet due to active liquid droplets entrainment at medium liquid superficial velocities leading into flooding while active liquid droplets entrainment at the liquid inlet leads to flooding at higher velocities. The latter was not noted by Wongwises mainly because the third liquid superficial velocity region investigated by Kang $J_L^{*0.5} > 0.4$ was not reached in Wongwises experiments where $J_L^{*0.5} < 0.35$. Gargallo et al. (2005) Studied flooding in horizontal channels and noted that subcritical flow is a precondition for flooding occurrence. The onset of flooding coincides with the transition from supercritical flow to subcritical flow through a hydraulic jump (Figure 1.10). A hydraulic jump forms near the end of the test section and propagates towards the liquid inlet during onset of floodingl.

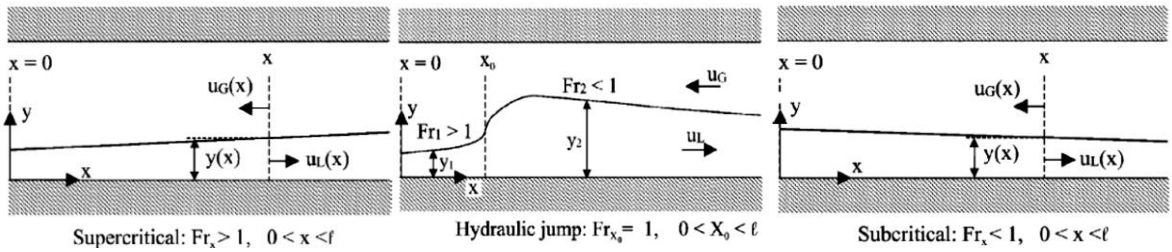

Figure 1.10 Transition from supercritical to subcritical flow through a hydraulic jump. Schematic: Gargallo (2005)

However they found that the occurrence of a hydraulic jump is a necessary but not sufficient condition. Flooding occurs in a countercurrent horizontal flow only if the liquid flow is subcritical and if the constant value of the Wallis correlation is approximately 0.7 or higher. Thus, a Flooding of a subcritical flow occurs if $J_L^{*0.5} + J_G^{*0.5} = 0.7$. Experimentally they found that flooding took place at values of the Wallis constant C from 0.6 to 0.7. Also, they obtained experimental points, for which the transition occurs at values of the Wallis constant larger than 0.7. For these points the value $C = 0.7$ was reached at supercritical flow conditions and

flow reversal did not occur before a hydraulic jump appeared. Navarro (2005) studied CCFL under following geometrical conditions

L[m]	Geometry	D[mm]	Riser		L/D	I/D	$J_G[m/s]$	$J_L[m/s]$
			I	θ				
0.1|0.3|0.5|0.8	*circular*	54	0.1|0.3|0.5	30|50|70|90	1.85 − 14.8	1.85 − 9.26	0.6 − 8	0.022 − 0.22
0.35|0.8	*circular*	36	0.35|0.8	50	9.72 − 22.22	9.72 − 22.22		
0.42|0.8	*circular*	44	0.1	50	9.54 − 18.18	2.27		

Navarro identified three mechanisms for the onset of CCFL. They agree in general with the previous descriptions of Wongwises (1996) , Kang et al (1999). Navarro experiments covered only the1st and 2nd regions of liquid superficial velocities studied by Wongwises (1996). Low and medium liquid flow rates lie in the region $J_L^{*0.5} < 0.35\ m/s$ according to Navarro description. Navarro's high liquid flow rate region is similar to Kang's 3rd region description $J_L^{*0.5} > 0.4\ m/s$.

- Low liquid flow rate: CCFL occurs at the horizontal pipe close to the bend due to the formation of a hydraulic jump.
- Intermediate liquid flow rates: CCFL occurs near the lower tank with the formation of a slug at this position,
- High liquid flow rates: CCFL occurs at the upper exit of the riser due to the air flow area reduction

Navarro found partial delivery not to depend on the injected water flow rate and is only influenced by the geometrical parameters. Figure 1.11 shows Illustration of the onset of CCFL curve, Zero liquid penetration and partial delivery line.

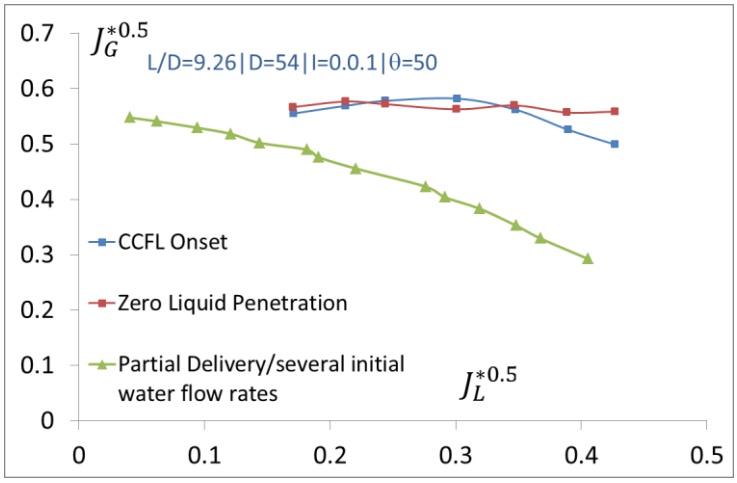

Figure 1.11 Partial delivery as function of the water superficial velocity. Navarro (2005)

Deendarlianto et al (2011) described the mechanism in the following hot-leg geometry:

L[m]	Geometry	Cross Section		Riser		L/D^*	I/D^*	$J_G[m/s]$	$J_L[m/s]$
		Height [mm]	**Depth [mm]**	**I[m]**	**θ**				
2.12	*Rectangular*	250	50	0.23	50	8.48	0.92	0.18 $-$ 0.34 kg/s	0.1 $-$ 0.9 kg/s

* based on the height of the channel as equivalent to diameter in circular channels.

They noticed that a hydraulic jump appears near the bend at low J_L ,while it appears at the water outlet and moves towards the bend at higher J_L. A wave suddenly grows at the channel end and slugging develops resulting in CCFL occurrence. Flooding was noted to coincide with slugging. Miniami et al (2010) studied CCFL in hot-leg geometry that had the following geometrical characteristics.

L[m]	Geometry	D[mm]	Riser		L/D	I/D	$J_G[m/s]$	$J_L[m/s]$
			I	**θ**				
0.43	Circular	50	0.6	50	8.6	12	$0-7.4$	0.09|0.17|0.26

The CCFL characteristics were found strongly connected with flow patterns. Two partial deliveries lines with different Wallis constants were identified: inclined line and horizontal line. The difference comes from different CCFL mechanisms that happen at the riser and at the horizontal part. Figure 1.12 shows both lines.

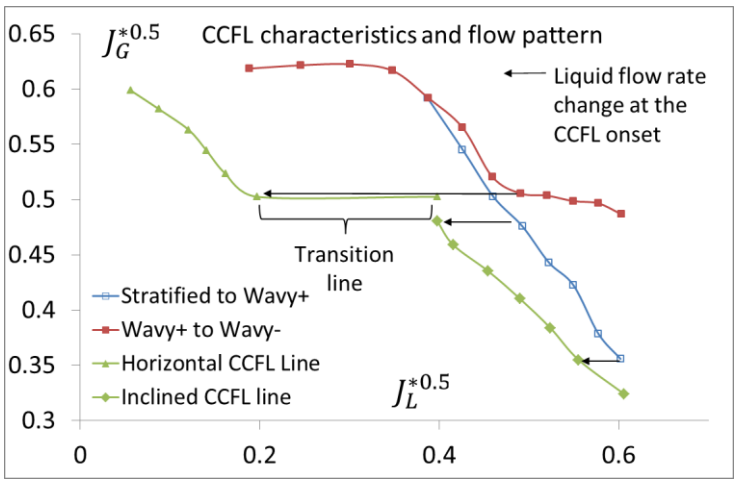

Figure 1.12 CCFL characteristics change according to flow pattern change. Minami et al. (2010a)

Figure 1.13 shows different observed flow patterns along with a pattern map while increasing gas velocity. The CCFL occurrence mechanism was found to be dependent upon water flow rate. For comparison purposes it should be noted that the entire investigated water flow rate range by Minami et al (2010a) lies within the third regions described by Wongwises (1996) and Kang (1999)

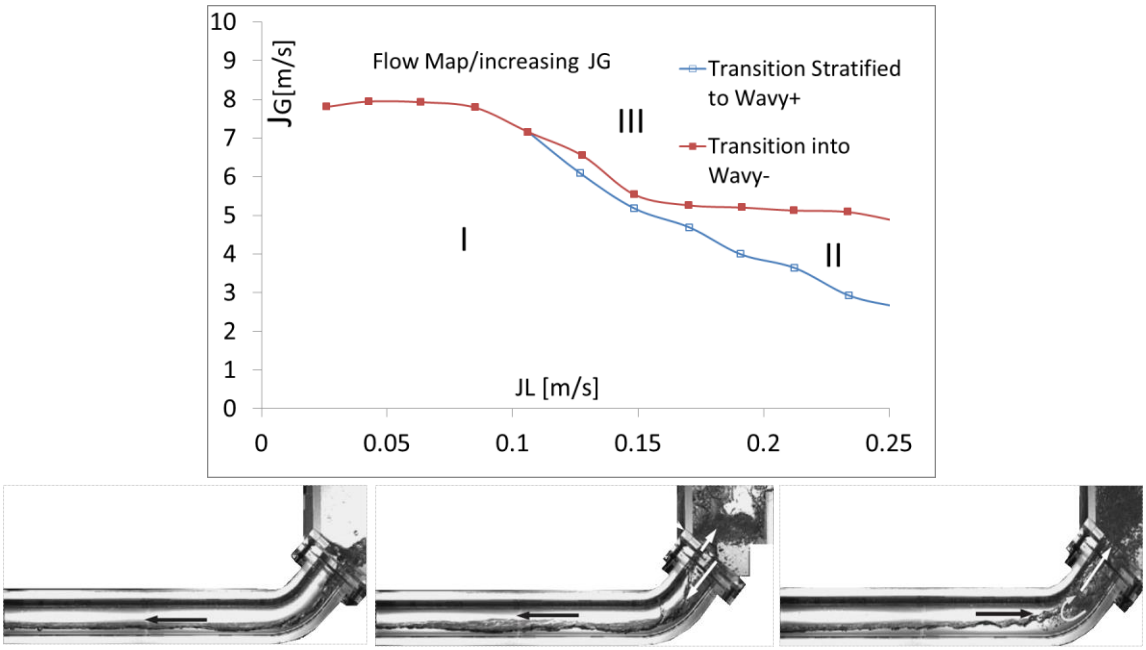

Figure 1.13 Top: flow pattern map while increasing gas velocity. Bottom: flow patterns while Increasing J_G Left: Stratified flow, Middle: Positive wavy Flow, Right: Negative wavy flow in the horizontal section and annular-mist flow in the elbow and the inclined section. Gas superficial velocities (from left to right):($J_G^{*0.5} = 0, 0.5, 0.58$ m/s),($J_L^{*0.5} = 0.49$). Minami et al. (2010a)

- $J_L^{*0.5} < 0.43$: A sudden transition from stratified into negative wavy occurs in the horizontal part and to annular-mist in the riser due to the intrusion of waves generated in the horizontal section into the bend. CCFL occurs at the bend due to the breaking of the instable waves into the upper tank.
- $0.36 < J_L^{*0.5} < 0.49$: The onset of flooding at the upper end of the inclined section was stochastic, and the occurrence of slugging in the horizontal part was dependent upon $J_L^{*0.5}$
- $J_L^{*0.5} > 0.43$: At low gas superficial velocities CCFL happened at the upper exit of the riser. The accompanied instability to CCFL occurrence induces positive waves in the horizontal part and oscillatory periodic plugging behavior at the bend (This is similar to Ohnuki description for CCFL mechanism in inclined riser without a horizontal part). At higher gas superficial velocities ($J_G^{*0.5} > 0.48 - 0.5$) the CCFL location was shifted to the bend and the flow maintained negative wavy pattern in the horizontal part and annular-mist in the bend region.

In the third region different CCFL mechanisms occur according to gas superficial velocity in agreement with Ohnuki et al. (1988) description. The limit of ($J_G^{*0.5} \sim 0.48 - 0.5$) also agrees somehow with Ohnuki limit($J_G^{*0.5} \sim 0.3 - 0.4$). The reason for different values may come from the way this value was determined. In Ohnuki's study, the limit separates between oscillatory and stable flow, in Minami's it was determined at the onset of transition to negative wavy in the horizontal part and to annular-mist in the bend region. The two phenomena may not happen at the same limit, or in other words: the flow becomes unstable at lower gas superficial velocities than those required for full transition to annular-mist at the bend. By

decreasing J_G , the deflooding was noticed to be dependent upon liquid velocity as well. Figure 1.14 shows deflooding flow map.

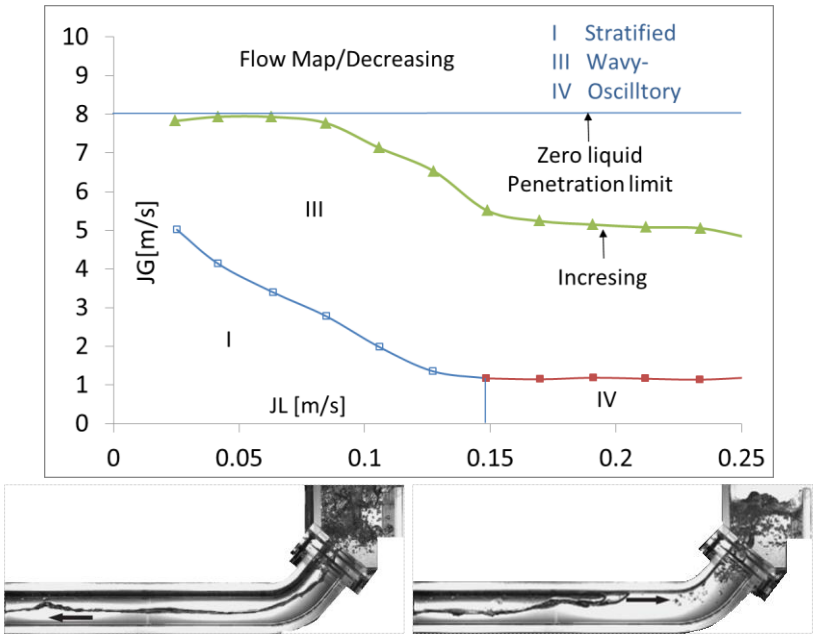

Figure 1.14 Top: flow pattern change while decreasing J_G. Bottom: Oscillatory flow behavior: periodic Plugging ($J_G^{*0.5} = 0.041$ m/s $J_L^{*0.5} = 0.49$ m/s). Miniami et al. (2010).

- $J_L^{*0.5} > 0.49$ m/s The flow pattern transit to oscillatory flow. The CCFL characteristics follows the ‘‘horizontal-section CCFL line.’’
- $J_L^{*0.5} < 0.49$ m/s The flow pattern in the horizontal section transits from negative wavy to stratified flow as J_G is decreased. The transition takes place at a lower J_G than the transition from stratified to wavy flows when increasing J_G which indicates a hysteresis effect.

Figure 1.15 gives an overview of the possible CCFL onset mechanisms against the liquid superficial velocity according to three authors who gave description of the phenomenon in different liquid superficial velocities.

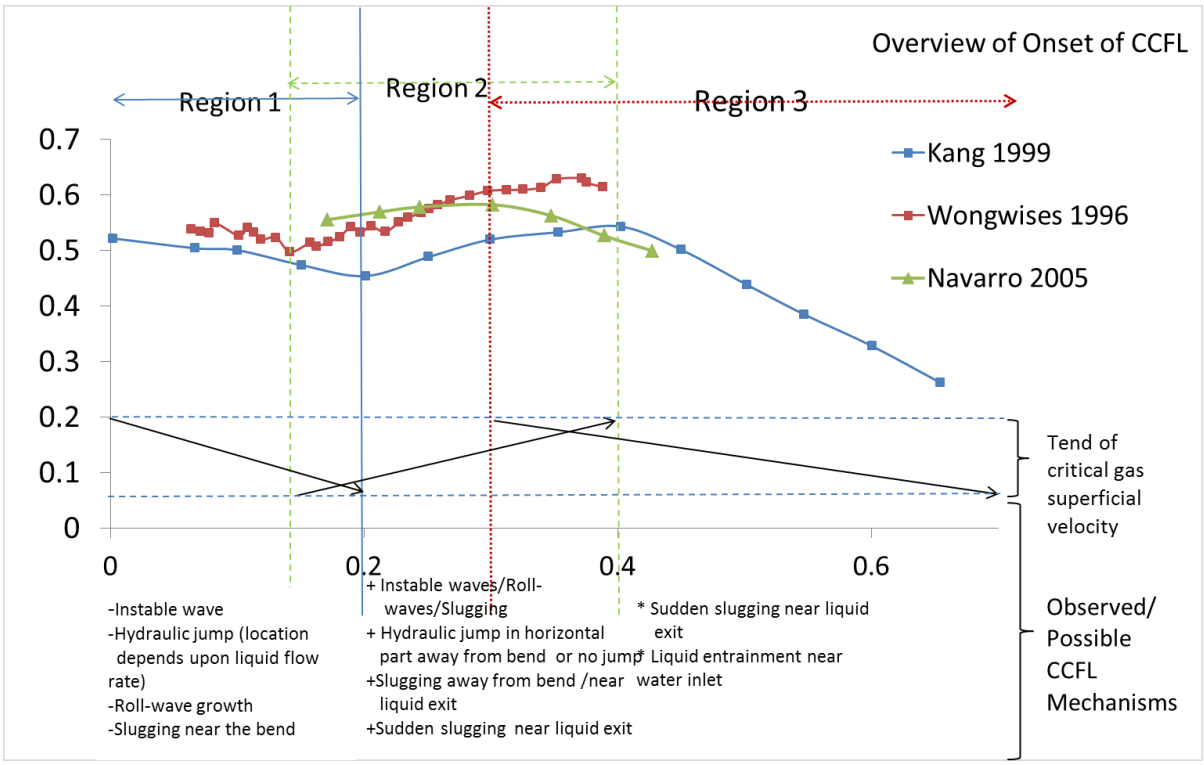

Figure 1.15 Overview of the onset of CCFL, Trend of the critical gas superficial velocity, and different possible CCFL mechanisms in different regions.

Table 1.7 summarizes a large number of CCFL correlations along with some important geometrical parameters. Most of these correlations have the form used by Wallis et al. (1961) and use Wallis parameters defined in equation (1.9).

$$J_{G,L}^{*0.5} = \sqrt{J_{G,L} \cdot \sqrt{\frac{\rho_{G,L}}{gD(\rho_L - \rho_G)}}} \tag{1.9}$$

Table 1.7 CCFL correlations according to several authors and references

Authors	Horizontal length L[m]	Inclined riser length l[m]	Inclination Angle θ[m]	Diameter D[mm]	Correlation	Correlation Parameters
Wallis (1961)	–	–	–	–	$mJ_L^{*1/2} + J_G^{*1/2} = C$	$m = 0.8 - 1.0$ $C = 0.7 - 1.0$ Vertical flow
Wallis (1969)	–	–	–	–	$J_L^{*1/2} + J_G^{*1/2} = 1$	- Analytical: Liquid film Model, Low liquid momentum
Pushkina and Sorokin (1969)	–	–	–	–	$mK_L^{*1/2} + K_G^{*1/2} = C$	$Ku_{G,L}^{*0.5} = J_{G,L} \cdot \left(\frac{\rho_{G,L}^2}{g\sigma(\rho_L - \rho_G)}\right)^{0.25}$

Best fit to experiment, Vertical flow, thin film layer

Richter (1987)	0.914	–	45	203.2	$J_L^{*1/2} + J_G^{*1/2} = 0.7$	-
Krolewski (1980)	0.584	0.305	45 90	50.8	$0.78J_L^{*1/2} + J_G^{*1/2} = 0.53$	-
Ohnuki (1986)	0.01 ↓ 0.4	0.038 0.6	40 45	26 51 76	$0.75J_L^{*1/2} + J_G^{*1/2} = C$	$C = \ln\left(\frac{L}{D}.\frac{1}{I}\right)^{-0.066} + m$
	m = 0.88 for a circular exit to the upper tank, and m = 0.81 for an elliptical exit					
Siddiqui et al. (1986)	24D ↓ 95D	–	90	36.5 ↓ 47	$J_G^{*1/2} = 0.45$	
Ardron and Banerjee (1986)	1.82 ↓ 2.36	–	90	36 ↓ 47	$J_G^{*0.5} = 1.444 - 0.004\lambda - \cosh\left(\lambda^{0.057}(Fl_P^*)^{-0.02}\left(J_L^{*1/2}\right)\right.$	$Fl_p^* = \frac{\upsilon_g}{\upsilon_L}\sqrt{\frac{\rho_G}{\rho_L}}$ $\lambda = \frac{H(Re^*)^{-0.2}}{D}$ $Re^* = \frac{D}{\upsilon_G}\sqrt{\frac{gD(\rho_L - \rho_G)}{\rho_G}}$
Ohnuki (1988)	0.26	0.06	50	25.4	$0.75J_L^{*1/2} + J_G^{*1/2} = C$	$C = \ln\left(\frac{L}{D}.\frac{1}{I}\right)^{-0.066} + 0.88$
Kawaji et al. (1989)	0.1 ↓ 2.54	–	90	51	-	-
UPTF (Weiss et al. 1992)	7.197	1.27	50	750	$J_L^{*1/2} + J_G^{*1/2} = 0.7$	-
	1:1 PWR hot-leg geometry					
Lopez de Bertodano (1994)	0.4	–	50	26 ↓ 76	$J_G - J_L > 0.487\left(\frac{(\rho_L - \rho_G)/\rho_G \,.\, gD\cos(\theta).\alpha_G}{8/\pi\left(y/D\left(1-\frac{y}{D}\right)\right)^{\frac{1}{2}}}\right)$ $0.798J_L^{*1/2} + J_G^{*1/2} = 0.619$	
	Analytical/Empirical: Best fit to Model calculations					
Choi and No (1995)	2.16	–	0 ↓ 1	40 60 70	$0.64J_L^{*1/2} + J_G^{*1/2} = 0.58$	-
MHYRES A (Geffraye et al. 1995)	2.645 ↓ 2.473	1.06 ↓ 1.194	50	75 ↓ 352	$J_G^{*1/2} = 0.52, \quad J_G^{*1/2} = 0.61$	
Zapke and Kröger (1996)	2		60 ↓ 90	30	$mJ_L^{*1/2} + J_G^{*1/2} = kZ_L^n$	$Z_L = \frac{\sqrt{D\rho_L\sigma}}{\mu_L}$
	Air, Argon, Helium, Hydrogen, Water, Methanol, Isopropanol and Aqueous Methanol solutions					
Wongwises (1996)	0.557 ↓ 2.816	1.26	50 75 90	64	-	-
Chun et al.(1999)	0.7 ↓ 3.388	0.623 ↓ 0.648	35	40 ↓ 80	$0.397J_L^{*1/2} + J_G^{*1/2} = C$	$C = 0.603 - 0.00234(L/D)$

Kang et al. (1999)	0.7 ↓ 3.39	0.623 ↓ 0.648	35	40 ↓ 80	$0.397J_L^{*1/2} + J_G^{*1/2} = C$	$C = 0.603 - 0.00234(L/D)$ Low inlet water Flow $J_L^{*0.5} < 0.2$
Chun and Yu (1999)	2.2	–	0.25 ↓ 0.5	83	$0.6J_L^{*1/2} + J_G^{*1/2} = 0.52$	
Yu et al.(2000)	$mJ_L^{*1/2} + J_G^{*1/2} = C$ $m = \alpha\left(0.38 + 4.14\exp\left(-\frac{\alpha}{0.14}\right)\right), \quad C = 0.6\alpha^{0.6} - 0.00234(L/D)$					
Kim and No(2002)	–	–	–	–	$0.614J_L^{*1/2} + J_G^{*1/2} = C$	$C = 0.635 - 0.00254(L/D)$
Jeong (2002)	$J_L^{*1/2} + J_G^{*1/2} = 0.85$					
Navarro (2005)	0.1 ↓ 0.8	0.1 ↓ 0.5	30 ↓ 90	36 ↓ 54	$J_G^{*0.5} = F_0 - F_1 J_G^{*0.5} - F_2 J_G^*$ For head = 0 and UPTF dimensions: $J_G^{*0.5} = 0.5963 - 1.17J_G^* - 0.2452J_G^{*1/2}$	
$F_0 = -0.04722\theta - 1.5649\,10^{-4}\left(\frac{L}{D}\right)^2 - 0.16539\left(\frac{H + D\cos\left(\frac{\theta}{2}\right)}{D}\right)^{0.2} + 0.78375$ $F_1 = 0.5070^{0.2} - 0.26015\left(\frac{L}{D}\right)^{0.46} - 0.00121\left(\frac{I}{D}\right)^{1.2}$ $F_2 = -1.03549\theta - 0.5881\left(\frac{L}{D}\right)^{0.3} + 0.20163\left(\frac{L.\theta}{D}\right)^{0.7}$						head is the water head in the upper tank
Analysis of 356 Data point for CCFL						
Minami et al.(2010a)	0.43	0.06	50	58	$J_L^{*1/2} + J_G^{*1/2} = 0.7$	-

1.2.3 The effect of the water superficial velocity

The previous section showed the effect of the liquid superficial velocity upon onset of CCFL in detail. Onset of flooding has strong dependence upon inlet liquid velocity, while partial delivery and zero liquid penetration have less dependency. The liquid velocity effect upon the onset of flooding in last section can be summarized as follows: A hydraulic jump is formed in the channel and the position of the hydraulic jump will depend upon the inlet flow rate. It will be close to the bend at relatively low liquid velocities while it happens away from the bend and near or at the water outlet for higher liquid flow rates. At higher inlet liquid flow rates no hydraulic jump is formed and the flow is supercritical along the whole channel. In the intermediate flow rates there were different observations; Wongwises (1996) observed a hydraulic jump with a position depending on the inlet liquid flow rate while Kang et al. (1999) did not observe any hydraulic jump and the flow was supercritical and flooding happening by a different mechanism. This difference can be attributed to the inclination angle ($\theta = 35^o$in Kang et al. while $\theta = 75^o$in Wongwises) low inclination angle in Kang's experiments may have caused supercritical flow while a higher angle in Wongwises' induced more turbulence and consequently a hydraulic jump could have been formed. This can be supported by the observations of Navarro (2005) who did not notice a hydraulic jump except

for $\theta = 90^o$ and for low liquid flow rates. However, it should be mentioned that the absence of hydraulic jump in Navarro experiments can be also a result of low L/D ratios in comparison with those in Kang et al and Wongwises. Lopez de Bertodano (1994) states that for short L/D ratios there is no hydraulic jump. At high liquid flow rates the flooding happens at the riser exit to the upper tank due to active water droplets entrainment or at the pipe exit by sudden slugging.

1.2.4 Geometrical effects

Navarro (2005) Ohnuki (1986) and Ohnuki et al (1988) state that studies in hot-leg geometry demonstrate some inconsistencies in the extrapolation of results obtained in down-scaled experiments into full scale dimensions. Since most of studies of CCFL phenomenon are executed in down-scaled geometries, it becomes of interest to find out the influence of different geometrical parameters on the CCFL. It becomes also interesting to show the dimensions of a real PWR hot-leg geometry since all geometrical effects should be considered in relative to this geometry. Figure 1.16 shows the dimensions of a full-scale hot-leg according to the configuration of many Westinghouse and combustion engineering reactors [Lopez de Bertodano 1994].

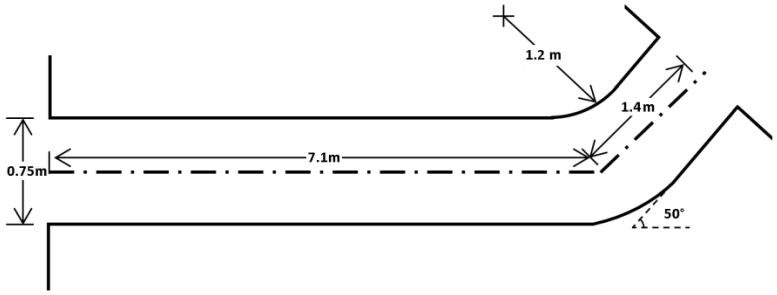

Figure 1.16. Full-Scale Hot-leg geometry in a PWR, Lopez de Bertodano (1994)

The upper exit to the steam generator is circular and the elbow is fine rounded. The full-scale hot-leg has the following characteristics:

Full-scale hot-leg geometry

L[m]	Geometry	**D**[mm]	Riser		**L/D**	**I/D**
			I[m]	**θ**		
7.1	Circular	750	1.4	50^o	9.47	1.87

1.2.4.1 Channel diameter

The diameter of the channel affects the interfacial area and the contact area with the wall and consequently the relative importance of interfacial forces to other friction and surface tension forces. Different effects were reported by different authors.

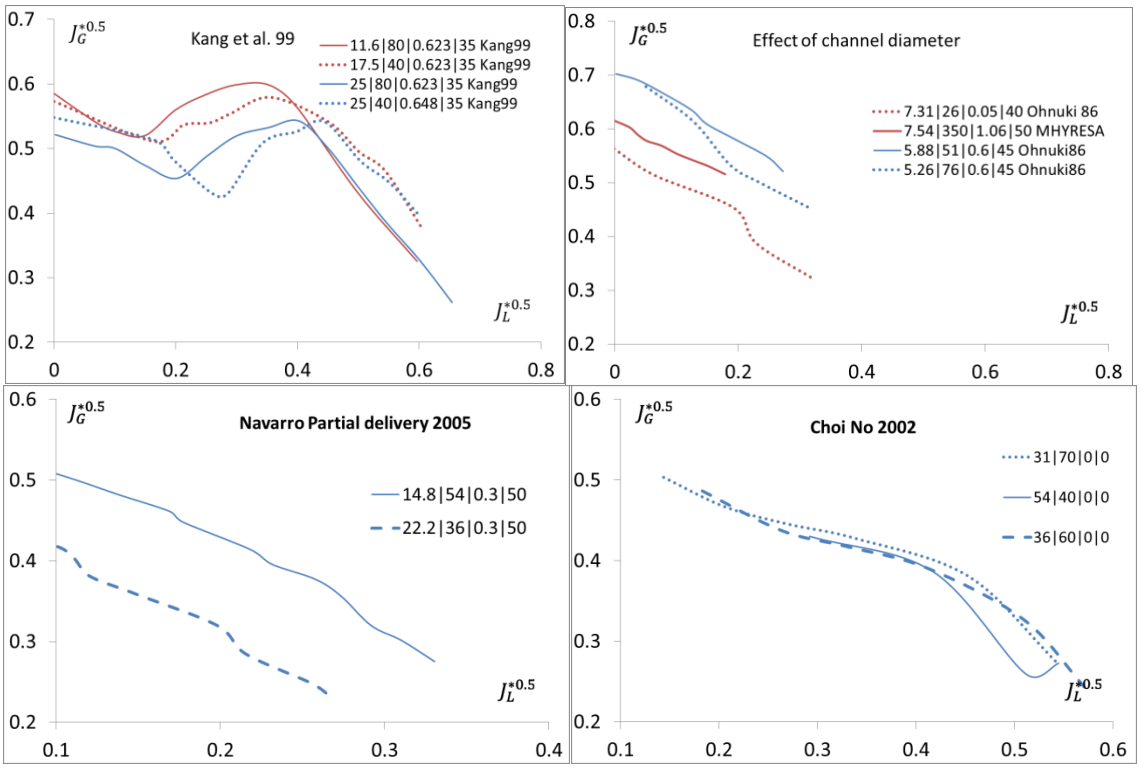

Figure 1.17 Different trends of onset of CCFL or partial delivery at different channel diameters. Reference: see graph title or legend.

There exists no clear trend, some researchers found that higher gas superficial velocities are required for larger diameters in order to initiate the CCFL [Navarro 2005 ,Kang et al 1999, Taitel and Duckler 1976]. Navarro explains that larger diameters produces smaller drag and thus higher gas velocities are needed to initiate flooding. Kang reports that no difference can be seen except for large L/D values. However others like Ohnuki (1986) ,Ohnuki et al. (1988) ,and Choi and No (1995) found negligible effects, while it was the opposite trend in the case of Lopez de Bertodano (1994) who used a reduced factor in slugging correlation (resulting in lower $J_{G,crit}$) to fit experimental results for experiments with large diameters. This makes it hard to fix the diameter effect. It appears that for down-scaled experiments higher $J^*_{G,crit}$ values are needed at larger diameters but this trend may change at very large diameters according to de Bertodano's conclusions.

1.2.4.2 Length and length to diameter ratio

The length of the horizontal part affects the available length for wave development, the gradient of the water depth and consequently the liquid depth variation along the channel. Unlike the effect of the diameter, there were consistent results regarding the effect of the L/D ratio. Many authors: Navarro (2005) ,Kang et al. (1999) ,Kim and No (2002) ,Wongwises (1996) ,and Ohnuki (1986), reported that the critical gas superficial velocity $J^*_{G,crit}$ decreases with increasing the channel length to diameter ratio L/D, or the channel length L. Also the zero liquid penetration limit decreases by increasing L/D. The main reason is the increased friction which leads to a higher liquid depth near the bend within the channel and

consequently an earlier initialization of CCFL through slugging formation at the hydraulic jump crest. For very long channels this effect becomes smaller ($L/D > 105$ Ghiaasiaan (1994)). These results make the L/D ratio an important factor in hot-leg geometry design.

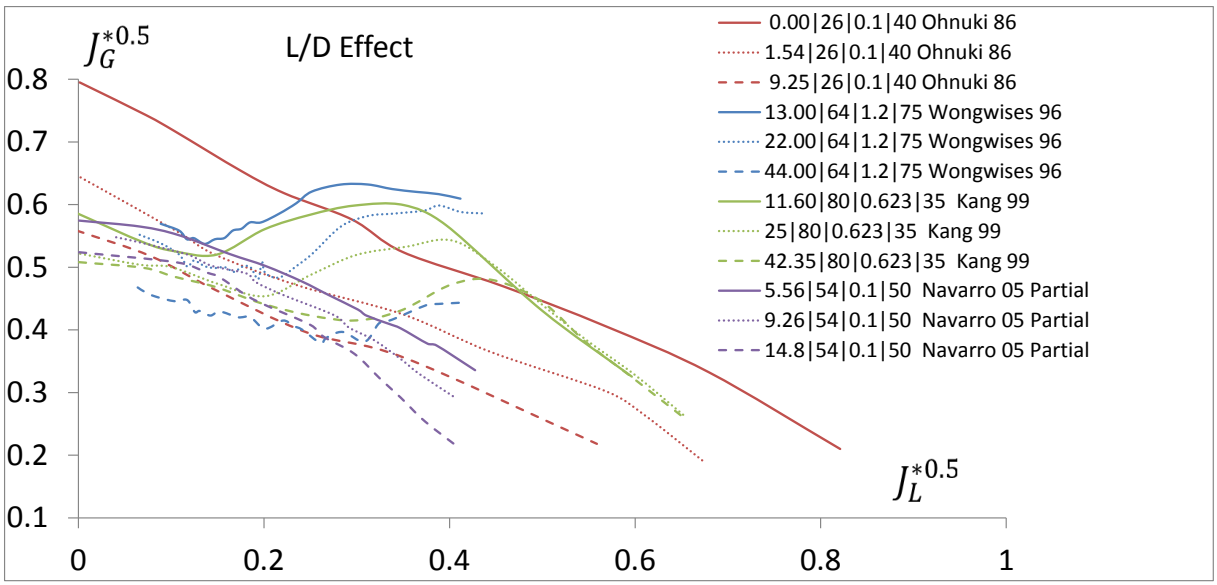

Figure 1.18 Onset of CCFL (or partial delivery) at different L/D ratios. Reference: see legend. Legend format: L/D | D[mm]|I[m]| θ| Author

1.2.4.3 Inclination Angle

The inclination angle is the angle between the riser and the horizontal part in the hot-leg geometry. The inclination angle affects the liquid flow conditions at the lower end of the riser (the entrance into the horizontal channel) such as acceleration, velocity, turbulence and flow criticality. Figure 1.19 shows the inclination angle's effect upon the onset of CCFL from two references. The available data is limited since it is easier to carry out experiments with a fixed riser angle.

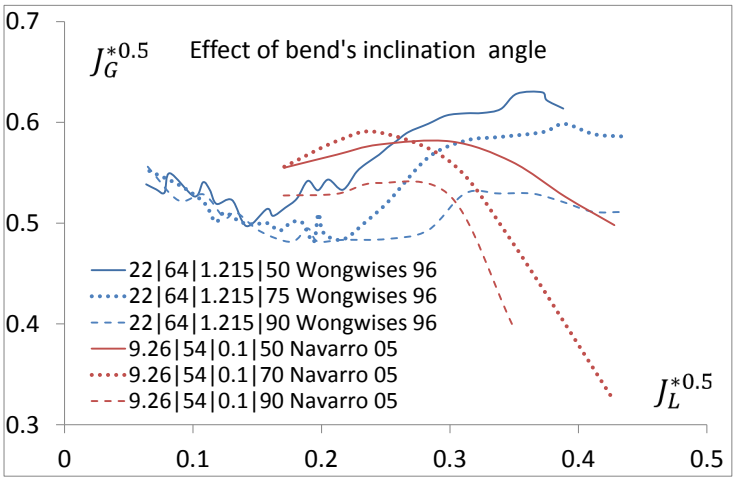

Figure 1.19 The onset of CCFL at different inclination angles. Reference: see legend. Legend format: L/D | D[mm]|I[m]| θ| Author

Wongwises (1996) and Navarro (2005) reported similar results, $J^*_{G,crit}$ becomes lower with increasing inclination angle. The effect is clearer in the middle and high liquid superficial velocities as figure 1.19 shows. The reason for this behavior is that larger inclination angles produce more turbulence at the bend because of the flow direction change, while lower angles cause the flow to be smoother. The effect is low for $\theta < 90^o$ and becomes larger when θ is closer to 90^o. The effect is also more apparent at high liquid velocities. Ohnuki (1986) noted that higher $J^*_{G,crit}$ are needed at higher inclination angles. However his remarks are connected with large riser length which makes CCFL mechanism totally controlled by the riser rather than the horizontal part. Kim and No (2002) compared a large number of data within a narrow range of low liquid superficial velocities, where the inclination angle effect is small. In near-vertical channels: (can be seen as equivalent to a riser without/or with very short horizontal part) Wongwises (1998) noted that the onset of CCFL happens at higher $J^*_{G,crit}$ for higher inclination angle from horizontal position (⇔ lower angles from vertical position). The result of Wongwises (1998) may explain Ohnuki (1986) results which oppose in its trend other results in hot-leg geometry. Ohnuki hot-leg geometry consisted of long inclined riser length and short horizontal part length with the flooding mechanism is mainly governed by the riser.

1.2.4.4 Riser length

The riser affects the liquid flow characteristics as it arrives to the bend. A longer riser will allow a longer distance for the development of flow and will increase the flow velocity at the bend since the liquid will flow through higher elevation at the same inclination angle. Figure 1.20 shows the effect of the riser's length according to different authors.

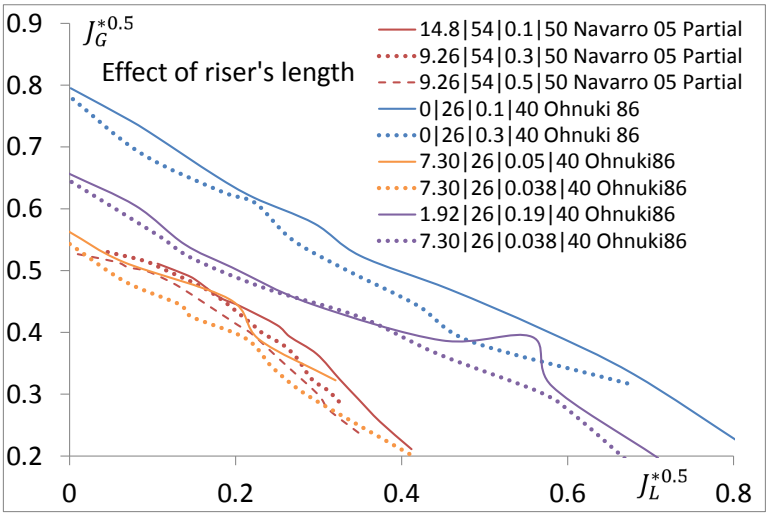

Figure 1.20 CCFL data (partial delivery) at different inclination angles. Reference: see legend. Legend format: L/D | D[mm]|I[m]| θ| Author

According to Ohnuki et al (1988) there exist a limit of the riser length ($I = 0.2$ m) below which there is no effect of the riser length, and above it, the increase of the inclined riser length will lead into an increase of $J^*_{G,crit}$. The reason for this is the shift of CCFL mechanism from the bend into the riser exit when increasing the riser length. Kang et al (1999) speculated about the existence of a saturation length, above which there is no effect of the riser, this can be expected as the length at which the CCFL mechanism is completely controlled by the riser

with no effect of the horizontal part (The CCFL mechanism is then an active droplets entrainment at the riser exit). This is confirmed by Ohnuki (1986) results who did not notice an effect of the inclined riser for tests without horizontal part where flooding happens at the riser upper exit. Navarro (2005) showed partial delivery results for values above $0.2\ \mathrm{m}$. Lower $J^*_{G,crit}$. were observed for higher I values. Navarro results are in contradiction to Ohnuki's ones. The reason can come from using larger channel diameter where CCFL mechanism remains controlled by the horizontal part (instable wave development) and the shift of the CCFL mechanism to the riser did not happen. In this case larger riser length will induce more turbulence at the bend resulting in increased restriction of the liquid flow during partial delivery at the same gas velocity.

1.2.4.5 Geometry at the bend and riser exit.

The shape of the upper exit of the riser into the upper tank was found to have an influence on the onset of CCFL. A circular exit requires higher $J^*_{G,crit}$.while an elliptical one requires lower values according to Ohnuki (1986). In the same investigation, Ohnuki found the effect of the shape of the bend to be negligible. The existence of an edge/step at the liquid entrance enhances the liquid turbulence and consequently leads into an earlier onset of CCFL according to Ghiaasiaan (1994), Lopez de Bertodano (1994), and Kang et al (1999). This indicates the need for a well-defined entrance conditions for liquid flow. Other differences at the liquid entrance like the use of porous or inner injection [Wongwises 1996], or upper closed or opened end [Ghiaasiaan et al. 1998] have different effects which are recognizable at high liquid superficial velocities or high inclination angle respectively. In relevant hot-leg experimental set-up these injection types are not adopted.

1.2.4.6 Hutze effect

Gargallo (2005) reports that in some German PWRs hot-leg design, ECC injection is performed via a secondary pipe called Hutze having an equivalent diameter of $320\ \mathrm{mm}$. This secondary pipe affects the effective hydraulic diameter and plays as an obstacle for liquid flow. Wang and Mayinger (1995) reported that the ECC-injection pipe induces considerable disturbances in the horizontal part near the bend where the onset of CCFL usually takes place. Ohnuki et al. (1988) reported that the existence of Hutze is considered to be one of the reasons to cause the discrepancy between experiment and empirical correlations. The Hutze effect becomes smaller when decreasing J^*_G as Figure 1.21 shows. The effect can be eliminated by considering hydraulic diameters and areas instead of nominal diameter and areas in the calculation of non-dimensional superficial velocities $J^*_{k=G,L}$. A comparison between a Wallis-like onset of CCFL correlation and experimental data from down-scaled hot-leg geometry without Hutze and with Hutze, shows some better agreement when considering hydraulic diameter in the calculation of $J^*_{k=G,L}$.

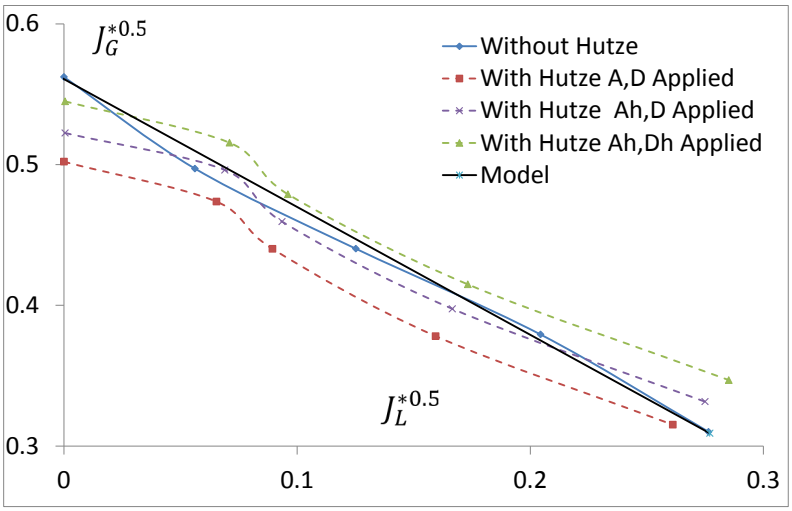

Figure 1.21 Different results for flooding curve using different diameters in the calculation of the non-dimensional superficial velocities . Ohnuki et al (1988)

1.2.5 Initial water level in the horizontal channel

The existence of an initial water level within the hot leg results in an earlier occurrence of CCFL. Kang et al. (1999) reported that the existence of initial stagnant water works as an obstacle for liquid flow. The magnitude of the hydraulic jump that results from the sudden liquid deceleration becomes larger. The higher magnitude of the hydraulic jump increases the water level near the bend and the gas velocity. Consequently, an earlier growth of unstable waves at the hydraulic jump crest happens and CCFL is initialized at lower gas flow rates. Yu et al. (2000) developed CCFL correlation that considers the effect of initial water level (via initial void fraction α_0) and confirms Kang's results:

$$\alpha_0\left(0.38 + 4.14\,exp\left(-\frac{\alpha_0}{0.14}\right)\right)J_L^{*1/2} + J_G^{*1/2} = 0.6{\alpha_0}^{0.6} - 0.00234(L/D) \qquad (1.10)$$

The onset of CCFL occurs at lower gas flow rates if the initial water level is not zero or $\alpha_0 < 1$. Kang et al. (1999) experimental data on the onset of CCFL show this effect clearly. The differences that appear in Figure 1.22 agree satisfactorily with calculations of Yu et al. (2000) correlation. Kang's data are given along with the initial water hold up defined in (1.11). It is remarkable that the initial water level affects the onset of CCFL strongly.

$$h_{L,0}/D = 1 - \alpha_0 \qquad (1.11)$$

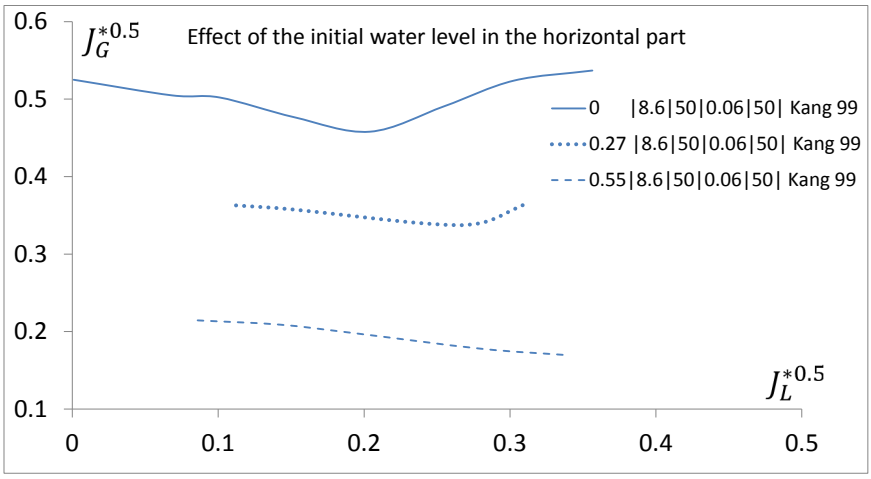

Figure 1.22 Onset of CCFL at different initial water level in the horizontal channel. Kang et al. (1999). Legend format: $1-\alpha_0|$ L/D | D[mm]|I[m]| θ| Author

1.2.6 Water head in the upper tank

During reflux condensation, water condenses in the steam generator and flows back into the hot-leg horizontal part by gravity. This led some authors to investigate the effect of the liquid head in the upper tank upon CCFL. Ohnuki (1986) found no influence upon the results for liquid heads between $2-10$ cm. Navarro (2005) observed no difference when the water head was smaller than 4 cm, but a lower zero liquid penetration limit and lower $J^*_{G,crit}$ were observed for water heads larger than 4 cm , however the differences were quit small ($<6\%$). It should be mentioned that data of Ohnuki (1986) and Navarro (2005) are rather partial delivery data and not onset of CCFL. Figure 1.23 illustrates the above results.

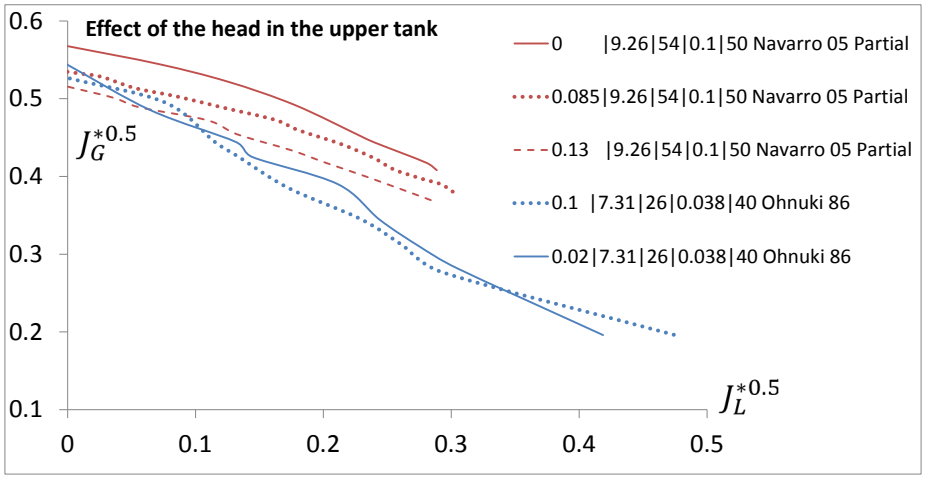

Figure 1.23 Partial delivery at different liquid head values in the upper tank of a hot-leg geometry. Reference: see legend. Legend format: H[m]| L/D | D[mm]|I[m]| θ| Author

1.2.7 Physical properties

Since countercurrent limitation's mechanisms incorporate strong interfacial momentum transfer between gas and a liquid phases, some physical properties of both fluids becomes of special interest to the CCFL occurrence. Among various physical properties of the gas and

liquid: gas density, liquid density, and liquid viscosity play an important role, while liquid surface tension, and gas viscosity are of minor importance. During a LOCA or SBLOCA, changes of the system pressure and temperature bring significant changes to gas density and water viscosity. Water density variations by pressure or temperature are small; this makes the gas density and water viscosity the most important physical properties that should be taken into consideration in a gas/water system. The gas density affect the amount of momentum exchange between gas and liquid phase while liquid viscosity will affect the friction factor and eventually the momentum transfer as equation (1.12) of the interfacial shear stress shows:

$$\tau_i = f_i\left(\frac{1}{2}\rho_G(V_G - V_L)^2\right) \tag{1.12}$$

Studies on the viscosity and surface tension effects upon CCFL are rare. Some authors Zapke and Kröger (1996), Ghiaasiaan et al. (1997) and Suzuki and Ueda (1977) found that liquid viscosity has an important effect on the onset of CCFL while surface tension and gas viscosities have minor effects. Major density differences take place in the gas phase when the system pressure changes, or when the gas phase is steam (as in a LOCA or SBLOCA) and not air as in most experimental investigations. Chun and Yu (1999) reports that higher $J^*_{G,crit}$ are needed for steam/water system in comparison to an air/water system:

$$V_{G,crit} = \sqrt{\frac{(\rho_L-\rho_G)gH_G cos\theta C_{P,crit}}{\rho_G}}\frac{\sqrt{\left(\frac{4}{\pi}+f_i\right)(1-C_C)+C_C}-1}{4/\pi+f_i-1} \tag{1.13}$$

Where C_C is the condensation factor related to the condensing steam properties. Since:

$$\frac{\rho_{Water}}{\rho_{Steam}} > \frac{\rho_{Water}}{\rho_{air}}$$

$J^*_{G,crit}$ is higher in case of steam/water flow according to equation (1.13). Ohnuki (1986) states that the non-dimensional superficial velocity should compensate for the fluid properties and he observed no difference between steam/water and air/water data. Another major density difference can arises from the system pressure change .Increasing system pressure tends to increase the critical gas velocity needed for the onset of CCFL according to Deendarlianto et al. (2011) and Ohnuki et al (1988). Figure 1.24 shows experimental results at different system pressure from both authors. Differences are not clear enough and do not follow the trend reported by authors over the whole liquid velocity range. For Deendarlianto's data no significant or even clear difference can be seen.

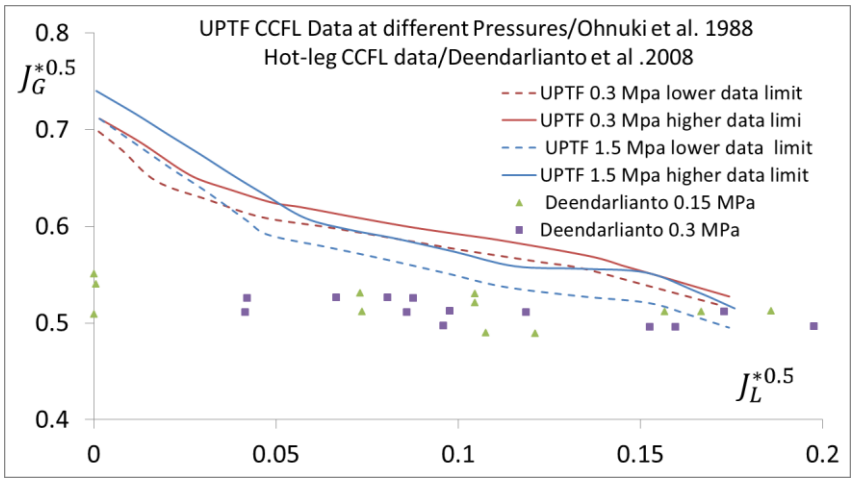

Figure. 1.24 Pressure effect upon CCFL. Reference: see legend.

1.2.8 Hysteresis

The hysteresis effect corresponds to the fact that the gas superficial velocity which is needed for the onset of CCFL while increasing the gas velocity is different from that necessary for termination of CCFL while decreasing the gas velocity (known also as deflooding). This was reported by many authors [Gargallo 2005, Ohnuki et al. 1988, Krolewski 1980, and Gardner 1983, Celata et al. 1991, Hewitt and Wallis 1966 and Becker and Letzter 1978]. All observations sates that deflooding happens at lower gas superficial velocities than those required for the onset of CCFL. That is why CCFL correlation should be assigned to flooding or deflooding. Figure 1.25 shows an example of hysteresis effect according to Minami et al. (2010a).

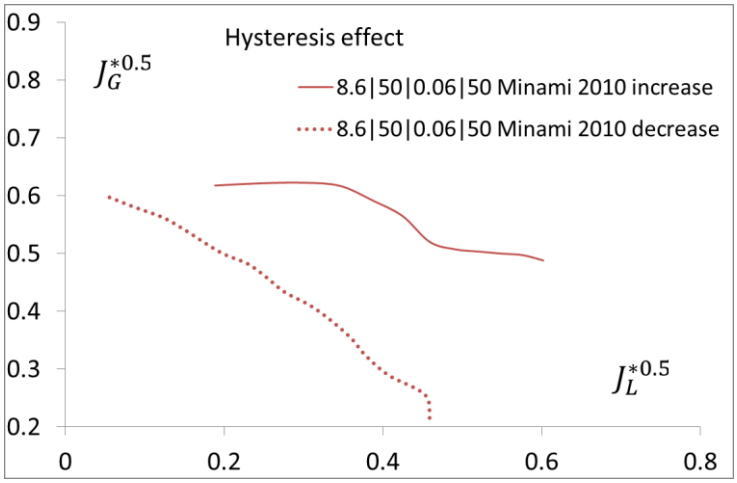

Figure. 1.25 Hysteresis effect, the onset of flooding and deflooding according to Minami et al. (2010a).

1.2.9 Condensation effect

Since CCFL phenomenon is linked to safety analysis in PWR during LOCA and SBLOCA accidents, and especially during reflux condensation phase, the expected gas/liquid

combination is condensed water/steam flow. The water and steam are expected to be near saturation conditions. Gargallo (2005) reports that during hot-leg injection in a PWR, the coolant is injected approximately one degree subcooled from the saturation temperature at accident conditions, while steam is slightly superheated. Under these conditions some steam will condense in the hot-leg. Steam condensation in the hot leg will increase the liquid depth. The liquid flow reaches the critical depth faster, and that will cause an earlier onset of CCFL. However, Gargallo states that the calculation of condensation rates requires the estimation of suitable heat transfer coefficients, and since the flow is unsteady and the interface motion is complex, accurate correlations are necessary to predict heat transfer and further work is needed here. Tien (1977) found that steam condensation greatly affects the CCFL phenomenon and can lead to earlier onset of CCFL. Wang and Kondo (1990) reported that steam condensation in UPTF tests contribute to the appearance of periodic plugging which is unstable flow condition that cause large fluctuations of the liquid delivery into the lower tank. Chun and Yu (1999) studied and modeled the condensation in a near-horizontal channel. They state that during a LOCA, the emergency core cooling (ECC) water is subcooled, and steam condensation reduces the effective steam mass flow which affects the CCFL occurrence. Their model predicted lower local gas velocities at the onset of flooding when the condensation happens. However, results shown in figure 1.26 do not show significant or clear effect.

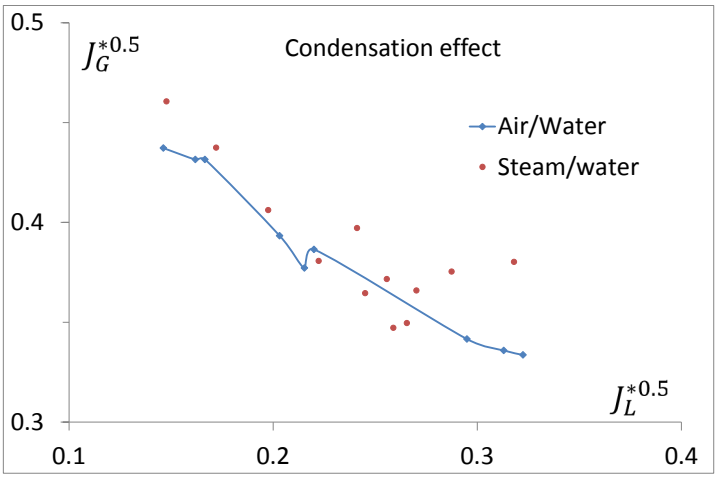

Figure 1.26 Onset of CCFL in air/water and steam/water tests. Chun and Yu (1999)

Chun and Yu developed a new correlation for onset of slugging assuming that CCFL coincides with slugging. In the new correlation, a factor was added to account for condensation. The factor considers the average velocity of the condensing steam as follows:

$$V_{G,crit} = \sqrt{\frac{(\rho_L-\rho_G)gH_G cos\theta C_{P,crit}}{\rho_G}} \frac{\sqrt{\left(\frac{4}{\pi}+f_i\right)(1-C_C)+C_C}-1}{4/\pi+f_i-1} \quad (1.14)$$

$$C_{P,crit} = 1+\frac{16}{9\pi}\frac{DH_G}{S_i^2}\left(1-\frac{2H_l}{D}\right)\left(1+\frac{\left(\sqrt{4/\pi+f_i}-1\right)^2}{4/\pi+f_i-1}\right) (C_{P,crit} = 1\ for\ rectangular\ duct)$$

$$C_C = \frac{\rho_G}{\rho_L}\frac{3.72V_C^2}{gH_G cos\theta C_P}, V_C = average\ speed\ of\ condensing\ steam$$

Chun and Yu reports that it is difficult to determine the condensation effect experimentally. They found that the condensation factor increases when the system pressure, the pipe

diameter, or the subcooling are increased. Consequently, the effect of steam condensation on the onset of CCFL will also increase accordingly.

1.2.10 Shear Stress

The interfacial shear stress in two-phase flow is one of the main factors governing transport phenomena like heat and mass transfer and it is important for flow modeling in these cases [Wongwises 1998, Chun and Kim 1995]. Interfacial shear stresses are usually calculated by using an interfacial friction factor (IFF) in similar way to the calculation of shear stresses near the wall (equation 1.12). Good knowledge of this factor is important for calculation of two phase flow pressure drops, and flow transition criteria including the flooding point [Chun and Kim 1995]. Modeling of countercurrent flow by analytical models showed that the stability limit is very sensitive to the ratio of interfacial shear stress to smooth surface friction factor f_i/f_s [Wang and Kondo 1990]. The major factor which affects the interfacial shear stress is the relative or gas superficial velocity and flow regime [Chun and Kim 1995]. Lee et al. (1983) and Ohnuki et al. (1988) reported that the flow pattern change from 3D waves into large roll-wave will cause a major increase of the interfacial friction factor. Wongwises (1998) studied the interfacial friction factor in a 5^o inclined long channel and noted that the interfacial friction factor decreases with increased liquid Reynolds number while decreasing with increased gas Reynolds number, the latter decrease was attributed to the change of the flow pattern in which the boundary layer effects become less important than the interfacial shape effect.

1.2.11 Different estimations of the interfacial friction factor (IFF)

Many correlations assume similarity between gas wall friction and interfacial friction. Some of these correlations are listed in table 1.8. This assumption is made for smooth or smooth wavy flow. The existence of large amplitude waves and the transition into roll-waves flow changes the ratio dramatically and the assumption that the interfacial friction factor decrease with increasing liquid Reynolds number becomes unsuitable for hot-leg models. At high gas velocities ($V_G > 5\ m/s$) it should be assumed that interfacial friction factor increases with increasing liquid Reynolds number. This coincides with the formation of large roll-waves and onset of CCFL. Also at high gas velocities the IFF becomes a function of the interface geometry rather than the Reynolds number. Countercurrent IFF is larger than concurrent IFF; and this is due to the larger shear at the interface and the interface geometry. This implies that more attention should be paid to this factor in countercurrent flows. There is no correlation that clearly corresponds to flow patterns that can exist in the bend region. In fact, most of correlations were developed for horizontal channel flow. Gargallo (2005) indicates that there is a lack of appropriate correlations for IFF in the literature, and further investigations should be done in this field. Jeong (2002) also reports that the development of accurate correlation for IFF in countercurrent flows is important. Wongwises (1998) states that the investigation of the interfacial shear stress in a countercurrent flow with pipe geometry, was limited in comparison to oncurrent flow or countercurrent in a rectangular channels. Since IFF is linked to the flow interfacial characteristics, this imposes that IFF can affect or change the existing flow pattern and vice versa. An example of this effect was introduced in the work of Baik and

Hanratty (2003), when the addition of solvable Polymer tended to reduce drag, and consequently changed the flow pattern from a slug into stratified. These effects need further investigations, since in case of LOCA accidents a considerable amount of insulation fibers mix with water and affect its characteristics.

Table 1.8 Different estimations of the IFF in con- and countercurrent flows

Authors	IFF correlation	Flow/Geometry
Linehan (1968)	$f_i = 0.23\ 10^{-5} Re_L + 0.0131$	Air/water, concurrent
Taitel and Duckler (1976)	$\frac{f_i}{f_G} = 1$ $f_G = \begin{cases} 0.046\ Re_G^{-0.2} & turbulent\ flow \\ \frac{16}{Re_G} & laminar\ flow \end{cases}$	Concurrent pipe
Cheremisinoff and Davis (1979)	$f_i = \begin{cases} 0.0142 & small\ amplitude\ waves \\ 0.008 + 2\ 10^{-5} Re_L & Roll\ waves \end{cases}$ $Re_L = \frac{J_L}{\nu_L} \frac{\pi D^2}{4 S_i}$	Concurrent, rectangular duct
Lee and Bankoff (1983)	$f_i = \begin{cases} 0.012 + 5.174\ 10^{-4} \left(\frac{Re_G - Re_G^*}{10^3}\right) & 23\ 10^3 < Re_G < \\ 0.012 + 2.694\ 10^{-4} \left(\frac{Re_L}{10^3}\right)^{1.534} \left(\frac{Re_G - Re_G^*}{10^3}\right) & Re_G < \end{cases}$ $Re_G^* = 1.837\ 10^5\ Re_L^{-0.184}$	Countercurrent Rectangular duct
Krwalski (1984)	$f_i = \begin{cases} 0.96\ (Re_G^+)^{0.52} & smooth\ sufrace \\ 7.5\ 10^{-5} (1-\alpha)^{-0.25} Re_G^{0.3} Re_L^{0.83} & Wavy\ surface \end{cases}$ $Re_G^+ = \frac{J_G D}{\nu_G}$	Countercurrent, pipe
Kim et al (1985)	$f_i = 0.56\ 10^{-5} Re_L + 0.084$	Steam/water countercurrent, rectangular duct
Kim et al (1985)	$f_i = 0.14\ 10^{-5} Re_L + 0.021$	Steam/water countercurrent, rectangular duct
Andritsos and Hanratty (1987)	$\frac{f_i}{f_G} = \begin{cases} 2 & smooth\ liquid\ surface\ \ V_G < V_{G,t} \\ 1 + 15 \left(\frac{h_L}{D}\right)^{0.5} \left(\frac{V_G}{V_{G,crit}} - 1\right) & V_G > V_{G,t} \end{cases}$ $f_G = 0.046\ Re_G^{-0.2}, V_{G,crit} = 5 \left(\frac{\rho_{Go}}{\rho_G}\right)^{0.5}$	Countercurrent,pipe

	$\frac{f_i}{f_G} = 1.84$	
Ohnuki (1987)	$f_G = \begin{cases} \frac{16}{Re_G} & Laminar\ flow \\ 0.079\ Re_G^{-0.25} & Re_G < 10^5 \\ 0.0008 + 0.05525\ Re_G^{-0.237} & Re_G \geq 10^5 \end{cases}$	Countercurrent, hot-leg geometry
	$f_i = 0.01(X)^{0.25(0.8+X)}$	
Chun and Kim (1995)	$X = 0.02\left(\frac{V_r}{\sqrt{gD}}\right)^{2/3} Re_{relative}^{1/3}\left(\frac{D_L}{D+D_L}\right)^{1/2}$	Countercurrent air/water horizontal
Wang and Mayinger (1995)	$f_i = \begin{cases} 0.015 & concurrent\ flow \\ 0.02 & countercurrent\ flow \end{cases}$	-
Wongwises (1998)	$f_i = 10^{15.51} Re_G^{-1.8} Re_L^{-1.442} \alpha_L^{2.18}$	Near-horizontal pipe air/water countercurrent flow
Kadri (2009)	$\frac{f_i}{f_G} = \begin{cases} 2 & smooth\ liquid\ surface\ V_r < V_{r,cr} \\ 5 & wavy\ liquid\ surface\ V_r < V_{r,cr} \\ 5 + 15\left(\frac{h_L}{D}\right)^{0.5}\left(\frac{V_r}{V_{r,crit}} - 1\right) & V_r > V_{r,cr} \end{cases}$ $V_{r,crit}$ *critical relative velocity at which waves become unstal*	Concurrent pipe flow

1.2.12 Pressure Drop

At the onset of CCFL a sudden increase of pressure drop occurs. All authors who investigated CCFL phenomenon noted this. The two-phase pressure drop increases slightly until the onset of flooding is reached, and then it starts to increases suddenly as a result of flow instability [Wongwises 1996]. A sudden decrease of the pressure drop was also observed in the case of deflooding while decreasing the gas velocity as Navarro (2005) reports. Figure 1.27 gives an illustration of the pressure drop during flooding and deflooding according to Navarro (2005)

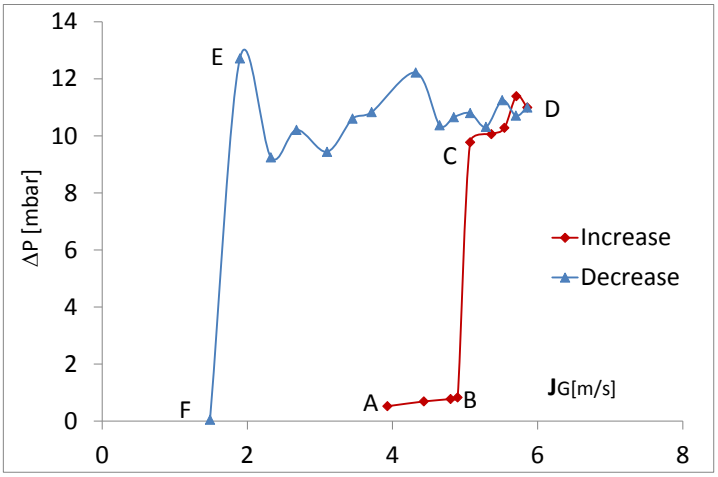

Figure 1.27 Illustration of pressure drop during flooding (A-D) and deflooding (D-F). Navarro (2005)

An abrupt increase B-C in Figure 1.27 corresponds to the onset of flooding while the abrupt decrease E-F corresponds to deflooding. The point of sudden pressure loss increase can help the experimental identification of critical gas velocity at which CCFL starts.

1.2.13 Void fraction

The void fraction was measured and correlated to the gas superficial velocity in many experimental investigations. The (J_G^*, α) relation was used as a closure law in CCFL analytical models, however it is of interest to link the gas superficial velocity to the void fraction since various experimental techniques can be used to measure α which can help estimation of correspondent J_G^*. In general this correlation takes the following exponential form:

$$J_G^* = m.\alpha^c \tag{1.15}$$

Where: m, c are experimental constants. It was remarkable that there was no fixed place where the void fraction was measured. In general the void fraction was measured near to the bend or at the location of the hydraulic jump (or equally: the deepest position of the water level), however no specific definition of distance from the bend was given which resulted in different correlations. Additionally, there was no clear link between correlations and flow pattern; although it is expected that different trends are also caused by different flow patterns. Table 1.9 summarizes the existing correlations for gas superficial velocity versus void fraction. Figure 1.28 plots these correlations on a logarithmic scale.

Table 1.9 Correlations of the gas superficial velocity versus void fraction at the onset of CCFL or slugging

Author(s)	Correlation	Notes
Taitel and Duckler (1976)	$J_G^* = \alpha^{5/2}$	Solitary wave, equilibrium void fraction
Mishima & Ishii (1980)	$J_G^* = 0.487\alpha^{3/2}$	Most dangerous wave
Wallis & Dobson (1973)	$J_G^* = 0.5\alpha^{3/2}$	Air/water slugging, stationary water
Siddiqui et al (1986)	$J_G^* = 0.2\alpha^{3/2}$	Void fraction at the crest of the hydraulic jump
Hori et al. (1985)	$J_G^* = 0.75\alpha^3$	200 mm pipe
Choi and No (1995)	$J_G^* = 0.36\alpha^{3/2}$	Near-horizontal channel, low liquid superficial velocity, void fraction at deepest location $J_L^{*0.5} < 0.4$
Hihara et al (1985)	$J_G^* = 2.8\alpha^{4.8}$	Void fraction higher than 0.5
Wongwises (1996)	$J_G^* = 0.82.\alpha^{2.75}$	$J_L^{*0.5} < 0.35$, void fraction

		measured70 mm from the bend
Navarro (2005)	$J_G^* = 1.453\alpha^{2.823}$	0.01 m from the bend
	$J_G^* = 0.854\alpha^{3.005}$	In the middle between the first and third measurements
	$J_G^* = 0.562\alpha^{3.185}$	0.01 m from connection with lower tank

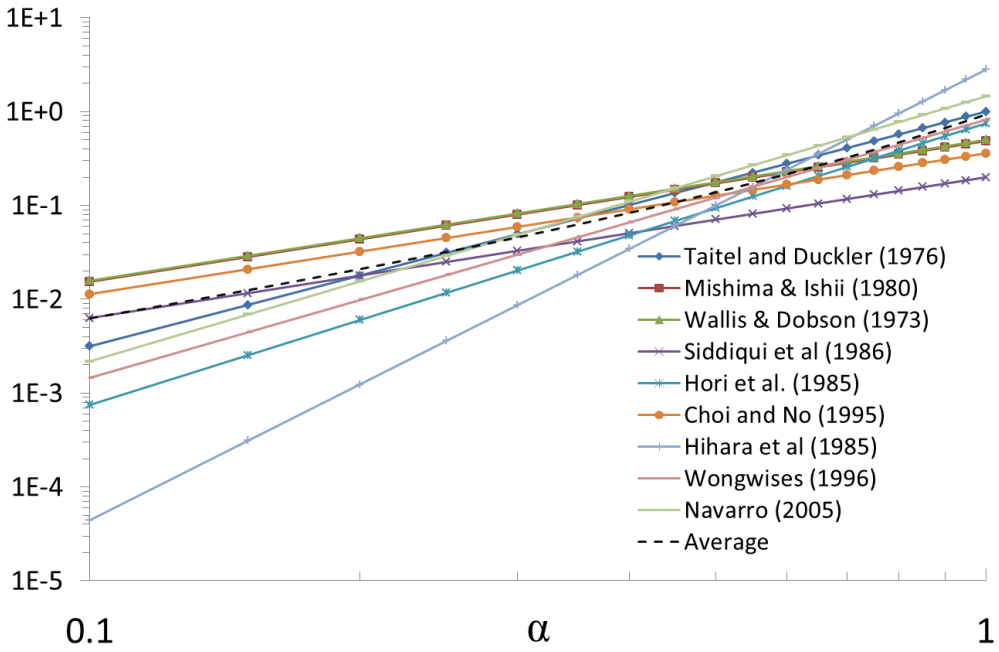

Figure 1.28 A Plot of all correlations in table 1.9.

Figure 1.29 Plots the correlations against some available data from literature. It can easily seen that data are concentrated in the range $\alpha = 0.5 - 0.8$ where onset of CCFL can happen. The correlations of Taitel and Duckler (1976) and Wongwises (1996) seem to be in best agreement with data points over the entire void fraction range.

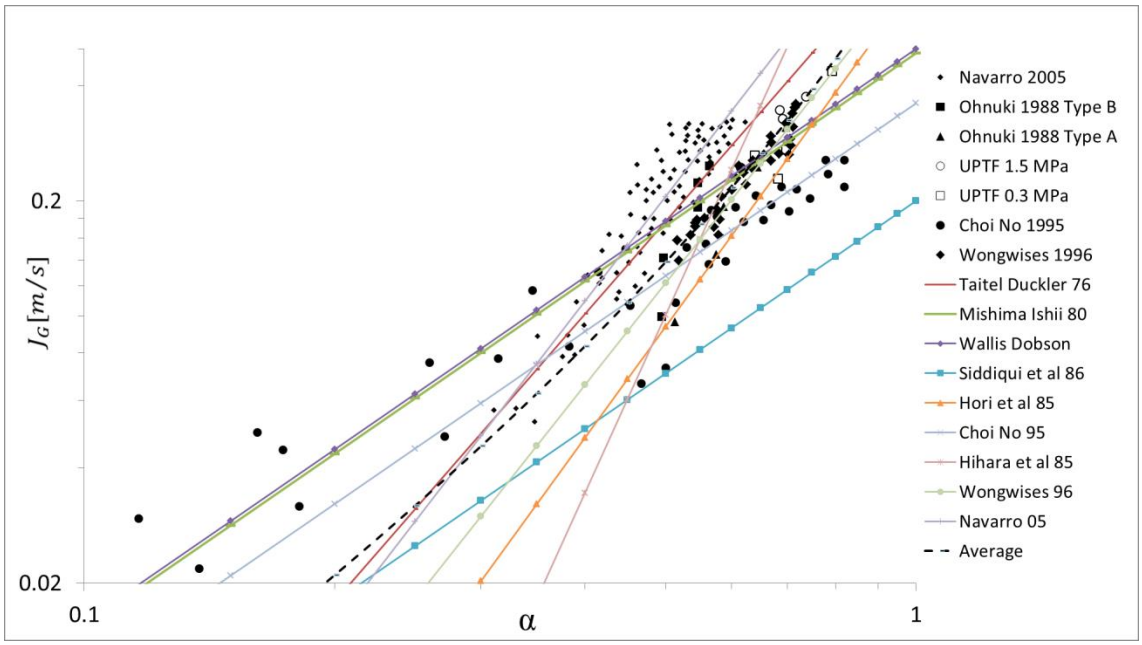

Figure 1.29 A comparison between all correlations in table 1.9 and some data from literature

1.2.14 Data bank of CCFL data

In order to have a clear overview about available data and CCFL correlations a large set of CCFL data were collected, grouped, and analyzed in this section. Since the L/D ratio has the most clear and consistent effect upon CCFL, data points were classified according to this criteria in four groups $L/D = 0-5, 5-10, 10-25, > 40$. The data sets are shown for each group in two Figures: in the first one: CCFL lines are plotted for the available data. In the second one data points and existing CCFL correlations were plotted together. This facilitates the presentation of the behavior of different data sets in the first figure -rather than a scattered collection of data points- along with the most important geometrical parameters in the following format:

$$L/D \mid D[mm] \mid\mid I/D \mid \theta$$

In the second figure, large number of CCFL correlations were shown against the available data points. For the correlations that need geometrical parameters as an input, average values of these parameters in each group were used. That is why it is important to understand the prediction of the correlations in these graphs as an approximate estimation for data with different geometrical parameters. As it can be noticed from different graphs, the effect of L/D parameters is still present within each group. It is also important to consider the effect of other parameters already discussed in previous sections. An important notice here is that some CCFL data may not be "onset of CCFL" data but rather a partial delivery or even deflooding. This concerns data in the first group $L/D = 0-5$ besides some data in the second and fourth group $L/D = 5-10$ and $L/D > 40$. In figures where data were plotted against CCFL correlations, a general trend (or best fit) was also calculated for the corresponding data points. These correlations should be understood as best fit for large number of experimental data in each group for the onset of CCFL. In case of partial delivery data, a different best fit was

calculated. The fact that onset and partial delivery data are analyzed together comes from literature where the general term "CCFL data" was used to refer to both: onset of flooding or partial delivery. The classification and analysis of the data allowed the identification of the nature of data when no clear indication was mentioned in the source.

1.2.15 Data Analysis and developed CCFL correlations

- First group: $L/D = 0 - 5$

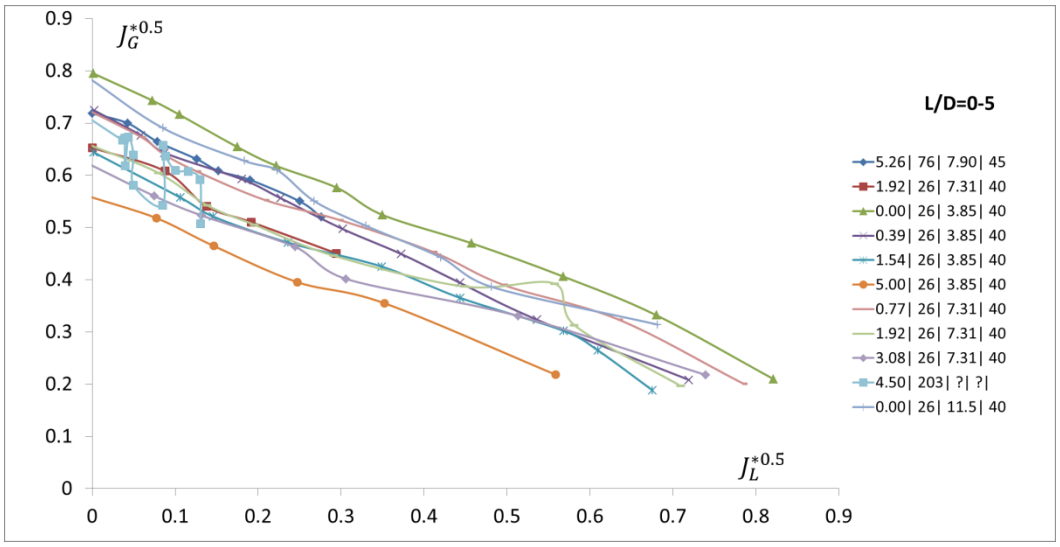

Figure 1.30 CCFL data for $0 < L/\mathrm{D} < 5$. Data here are mostly partial delivery.

For this range of L/D, the critical gas superficial velocity decreases continuously with increasing liquid superficial velocity for the entire value range. This is mainly due to the fact that most obtained data for this range of L/D were either partial flooding or deflooding data. Generally, data are well arranged according to L/D ratio between $L/D = 0$ and $L/D = 5$. The data set of $L/D = 5.26$ does not follow this classification mainly because of the higher D value which imposes higher $J_{G,crit}^{*0.5}$ in comparison to other data series of similar L/D value. As it can be seen from Figure 1.31 most CCFL correlations follow the general trend of the data except for Wallis (1969) which overpredicts all presented data and Krolewski (1986) which underpredicts all presented data.

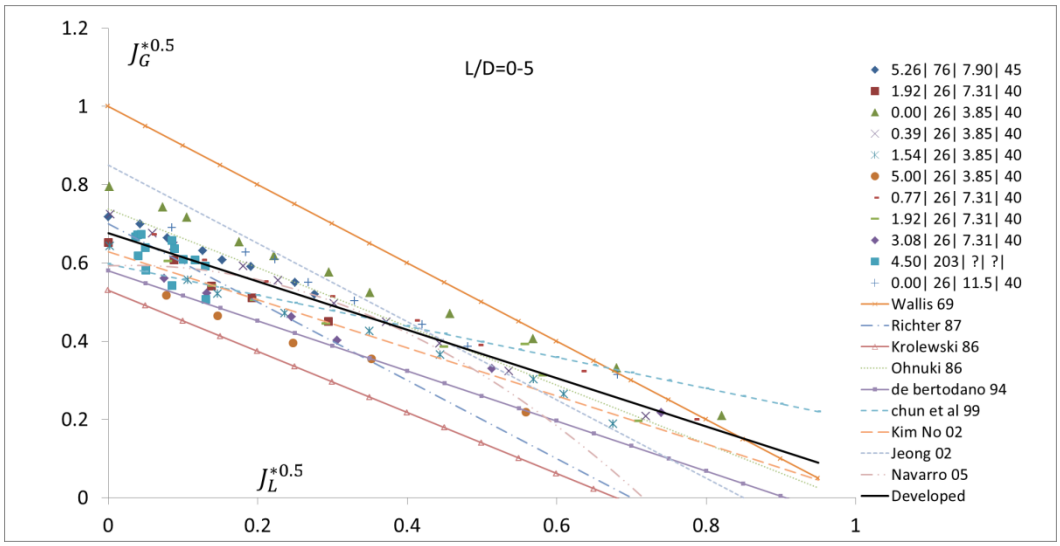

Figure 1.31 CCFL data for $0 < L/\mathrm{D} < 5$ along numerous number of CCFL correlations. Developed trend is shown in black.

A trend that fit existing data in this range of $L/D$was developed and shown in figure 1.31 as a black line. The trend has the following equation:

$$J_G^{*\,0.5} + 0.62\, J_L^{*0.5} = \ 0.75 - 0.03\frac{L}{D} \qquad (1.16)$$

Figure 1.32 shows scattering of the relative error [%]of equation (1.16) for data points in this group. The error falls well within $\pm 20\%$ for most data points.

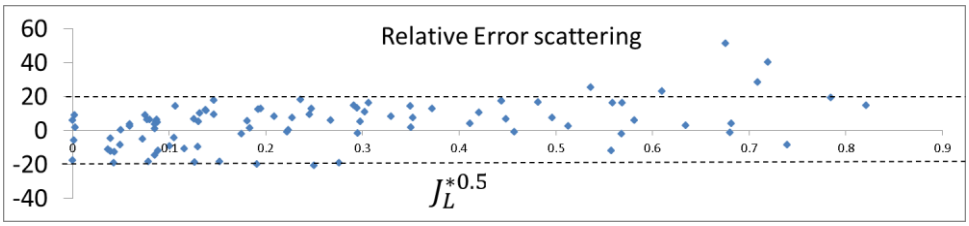

Figure 1.32 Relative error distribution for developed CCFL correlation (1.16), $0 < L/\mathrm{D} < 5$.

- Second Group: $L/D = 5 - 10$

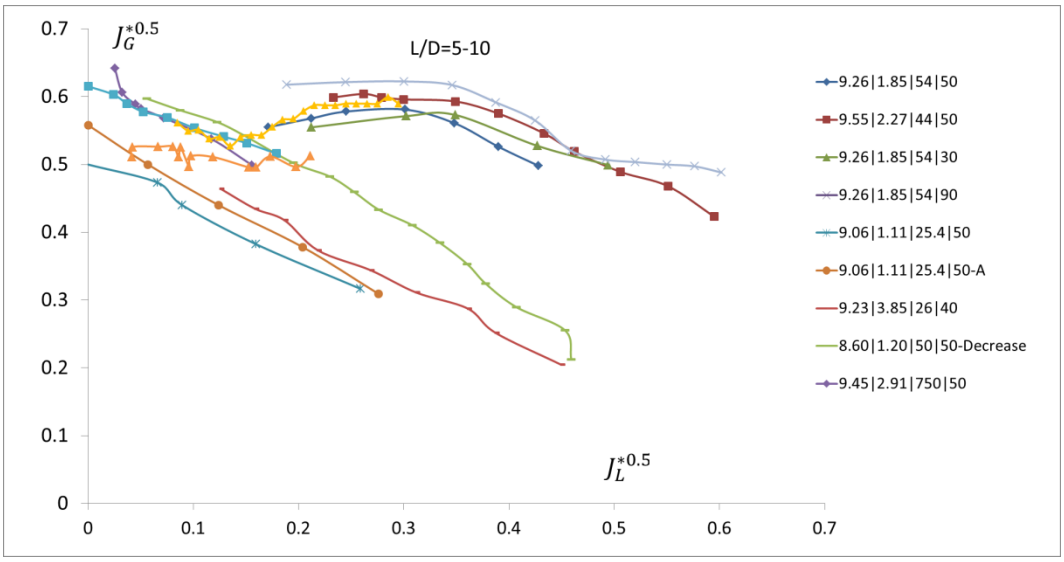

Figure 1.32 CCFL data for $5 < L/\mathrm{D} < 10$. Data here are mixed: onset of CCFL (those with changeable trend with liquid velocity) and partial delivery (a constant decreasing trend over the entire liquid velocity range)

Figure 1.32 shows two tendencies within this group. In the first tendency, the critical gas velocity rises in the range $0.2 < J_L^{*0.5} < 0.35$ and decreases thereafter. In the second one critical gas superficial velocity decreases for the entire range of $J_L^{*0.5}$. The data that follows the second tendency comes from Ohnuki et al. (1988) and Ohnuki (1986) besides a deflooding data from Minami et al (2010a). In fact Ohnuki et al. (1988) and Ohnuki (1986) data are rather a partial delivery data that have similarity with deflooding data and both follow a linear trend. The data that follows the first tendency are onset of flooding and tendency changes with liquid superficial velocity. Figure 1.33 shows that most available CCFL correlations predict partial delivery CCFL data well, while none of available correlations will predict the onset of flooding properly even at low liquid superficial velocities.

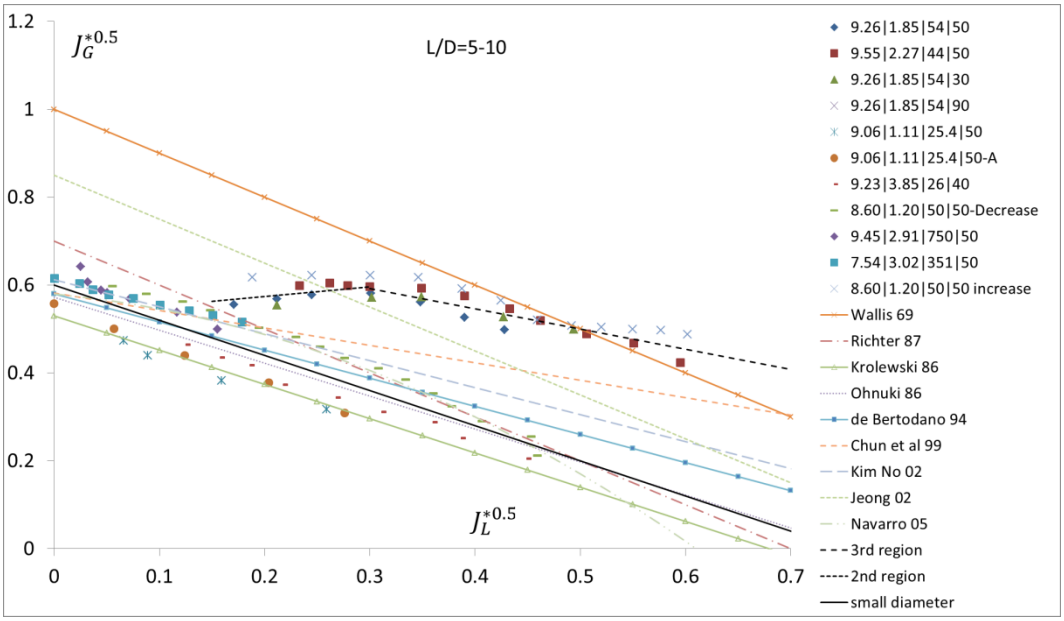

Figure 1.33 CCFL data for $5 < L/\mathrm{D} < 10$ along with numerous CCFL correlations. Developed trends are shown in black.

- Third group $L/D = 10 - 25$

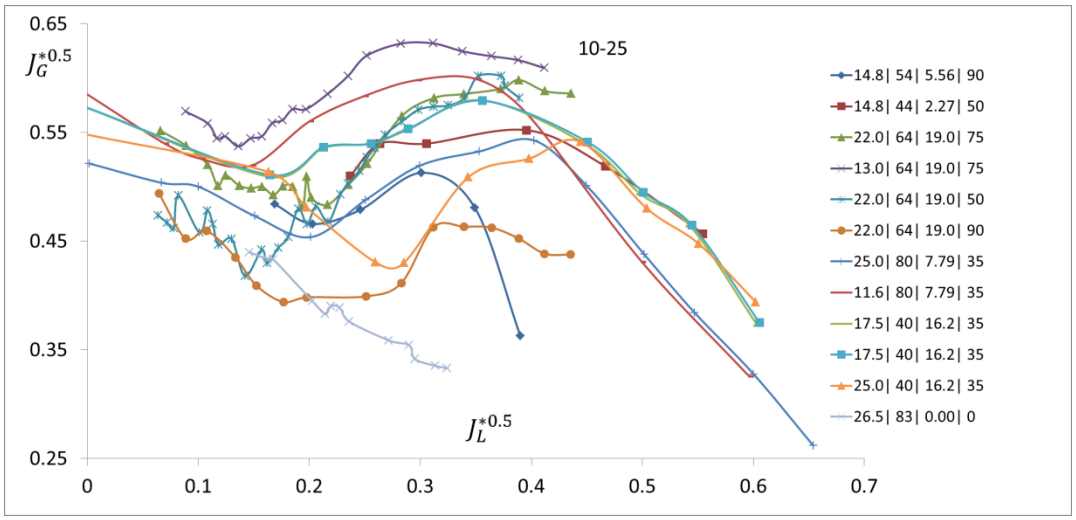

Figure 1.34 CCFL data for $10 < L/\mathrm{D} < 25$. Data here are mostly onset of CCFL.

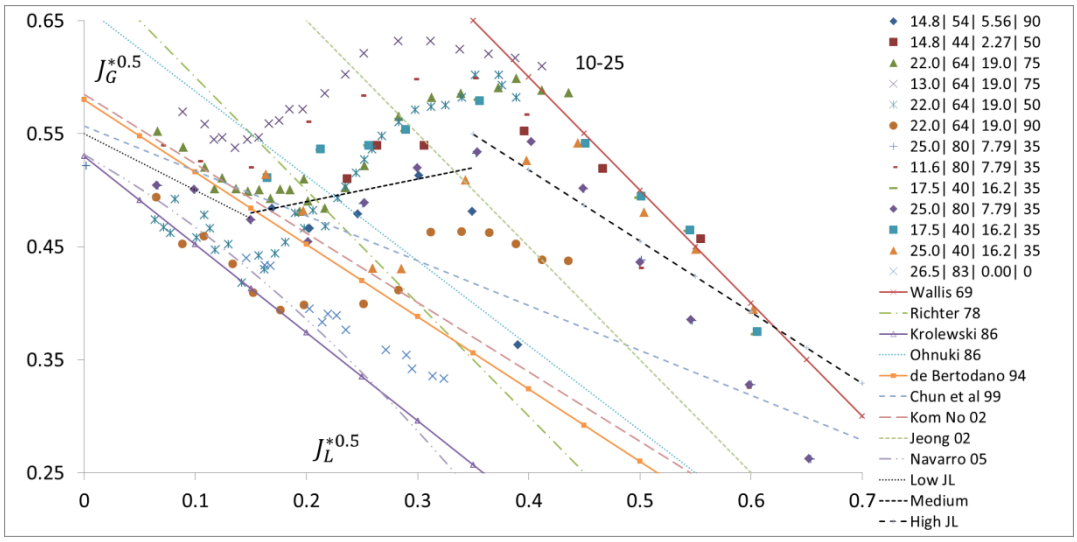

Figure 1.35 CCFL data for $10 < L/\mathrm{D} < 25$ along with numerous CCFL correlations. Developed trends are shown in black.

The data in this group corresponds to the onset of CCFL. Figure 1.34 shows three regions with three different trends:

- 1st region: critical gas velocity $J_{G,crit}^{*0.5}$ increases with increasing $J_L^{*0.5}$
- 2nd region: $J_{G,crit}^{*0.5}$ decreases with increasing $J_L^{*0.5}$
- 3rd region : $J_{G,crit}^{*0.5}$ decreases with increasing $J_L^{*0.5}$.

Data are well classified according to L/D ratio. Figure 1.35 shows that most of CCFL correlations predict the onset of CCFL only in the first region of low liquid superficial velocity $J_L^{*0.5} < 0.2$ No proper correlations exist for second and third regions. If the following

onset of CCFL set of correlations was adopted for $5 < L/D < 40$, the relative error falls within $\mp 20\%$ for most data as figure 1.36 shows.

$$\left.\begin{array}{ll} J_G^{*0.5} + 0.48 * J_L^{*0.5} = 0.68 - 0.0067\, L/D & J_L^{*0.5} < 0.15 \\ J_G^{*0.5} - 0.38 * J_L^{*0.5} = 0.68 - 0.013\, L/D & 0.15 < J_L^{*0.5} < 0.3 \\ J_G^{*0.5} + 0.71 * J_L^{*0.5} = 0.93 - 0.0067\, L/D & J_L^{*0.5} > 0.3 \end{array}\right\} \quad (1.17)$$

$$J_G^{*0.5} + 0.8 * J_L^{*0.5} = 0.6 \qquad \text{partial delivery+deflooding} \quad (1.18)$$

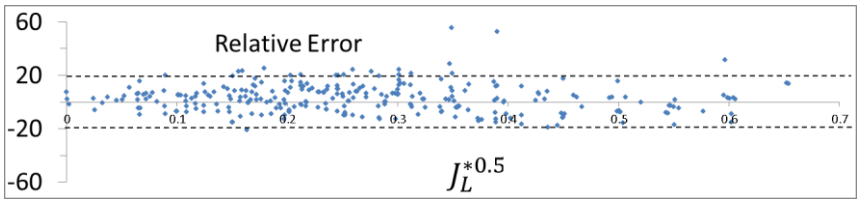

Figure 1.36 Relative error distribution for developed CCFL correlations (1.17 &1.18) $5 < L/\mathrm{D} < 40$.

- Fourth group $\mathrm{L/D} > 40$

Figure 1.37 shows three regions for the onset of CCFL and a decreasing trend over the entire liquid velocity range for partial delivery (or deflooding) data. Once again, the available correlations predict well partial delivery data while the onset of CCFL is predicted only in the low liquid superficial velocity.

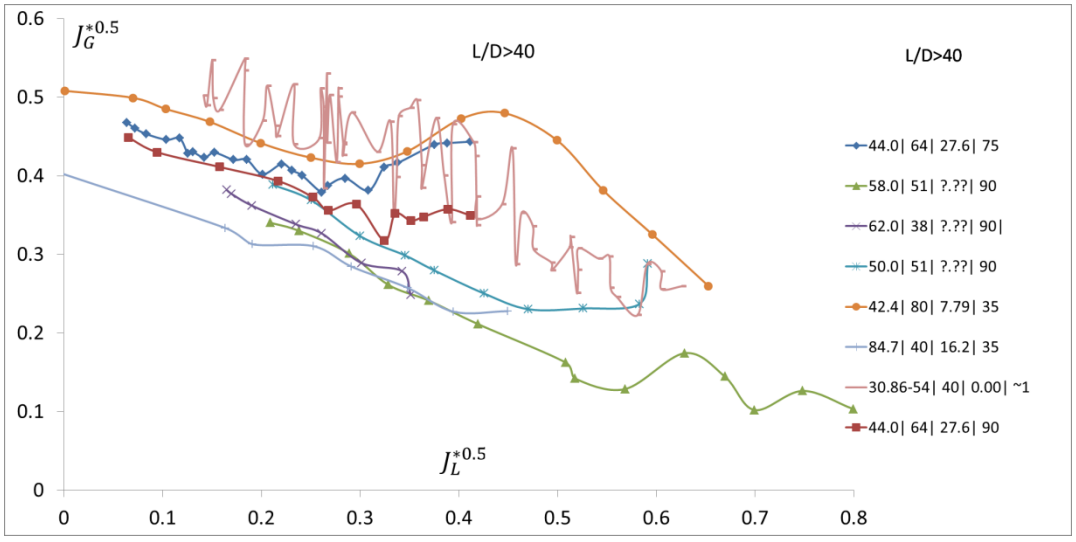

Figure 1.37 CCFL data for $\mathrm{L/D} > 40$. Data here are mostly onset of CCFL.

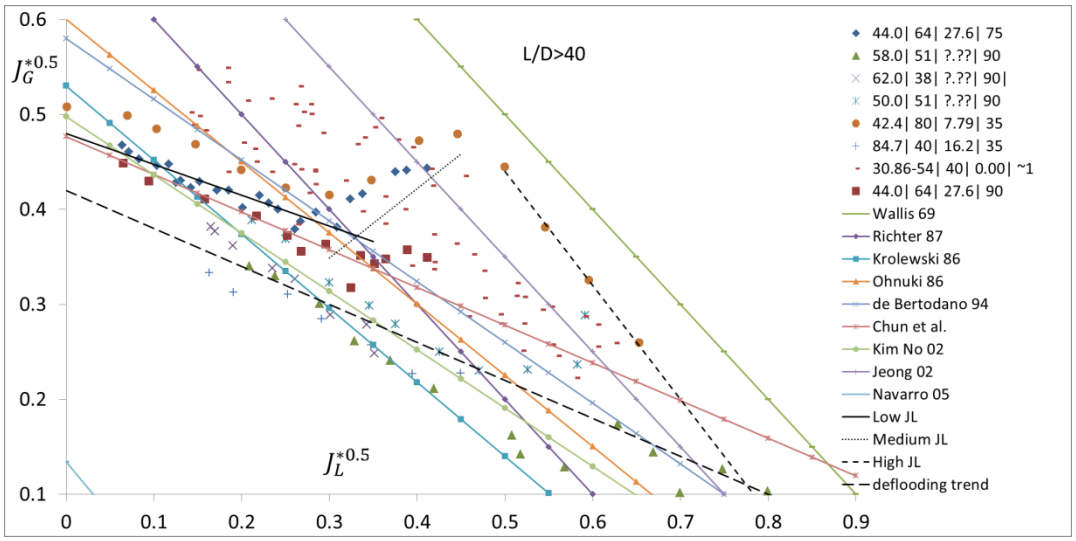

Figure 1.38 CCFL data for $L/D > 40$ along with numerous CCFL correlations. Developed trends are shown in black.

If the following onset of CCFL correlations set was adopted for $L/D > 40$, relative error falls within $\mp 20\%$ for most data (data from Choi and No 1995 in horizontal channel were excluded)

$$\left.\begin{array}{ll} J_G^{*0.5} + 0.39 * J_L^{*0.5} = 0.49 & J_L^{*0.5} < 0.3 \\ J_G^{*0.5} - 0.66 * J_L^{*0.5} = 0.16 & 0.3 < J_L^{*0.5} < 0.45 \\ J_G^{*0.5} + 1.2 * J_L^{*0.5} = 1.04 & J_L^{*0.5} > 0.45 \end{array}\right\} \quad (1.19)$$

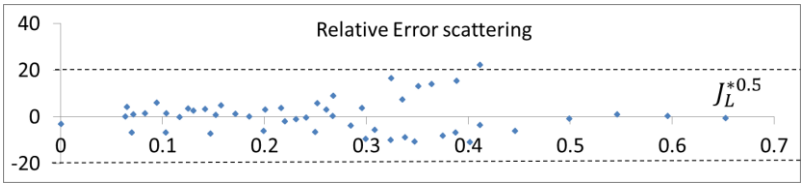

Figure 1.39 Relative error distribution for developed CCFL correlations (1.19). $L/D > 40$.

No L/D dependency was included in the correlations due to lack of enough number of data. However it can be seen that considerable change of the correlations parameters happen at large L/D in comparison to correlations set (1.17). Also, a change of the boundaries of the three regions of liquid superficial velocity happens. The first and second region extends into larger $J_L^{*0.5}$ values as Figure 1.38 shows. The over mentioned analysis shows that available CCFL correlations predict partial delivery data and deflooding data well. The prediction becomes more accurate when the correlation considers the effect of L/D ratio. However, the prediction of onset of CCFL is not satisfactory. In the third and fourth data groups (corresponding to $L/D = 10 - 25$ and $L/D > 40$) available correlations predicted the onset of flooding only at low liquid superficial velocities ($J_L^{*0.5} < 0.2$) but all available correlations do not predict neither the trend nor the values of critical gas superficial velocity (onset of CCFL) at medium and high liquid superficial velocities. The new developed set of correlations for the onset of CCFL for $5 < L/D < 40$ and $L/D > 40$ can predict the onset of CCFL with a relative error within $\mp 20\%$ for most available data.

1.2.15.1 Summary of correlations for the onset of CCFL

Developed correlations for the onset of CCFL depending upon the revised data bank can be summarized as follows:

For $5 < L/D < 40$

$$\left.\begin{array}{ll} {J_G^*}^{0.5} + 0.48 * {J_L^*}^{0.5} = 0.68 - 0.0067\, L/D & {J_L^*}^{0.5} < 0.15 \\ {J_G^*}^{0.5} - 0.38 * {J_L^*}^{0.5} = 0.68 - 0.013\, L/D & 0.15 < {J_L^*}^{0.5} < 0.3 \\ {J_G^*}^{0.5} + 0.71 * {J_L^*}^{0.5} = 0.93 - 0.0067\, L/D & {J_L^*}^{0.5} > 0.3 \end{array}\right\} \quad (1.17)$$

For $L/D > 40$

$$\left.\begin{array}{ll} {J_G^*}^{0.5} + 0.39 * {J_L^*}^{0.5} = 0.49 & {J_L^*}^{0.5} < 0.3 \\ {J_G^*}^{0.5} - 0.66 * {J_L^*}^{0.5} = 0.16 & 0.3 < {J_L^*}^{0.5} < 0.45 \\ {J_G^*}^{0.5} + 1.2 * {J_L^*}^{0.5} = 1.04 & {J_L^*}^{0.5} > 0.45 \end{array}\right\} \quad (1.19)$$

Using these correlations, the onset of CCFL can be determined when the gas velocity is increased beyond the corresponding critical gas velocity for the first time. If the gas velocity is decreased thereafter, the criteria for deflooding should be checked to determine whether a partial delivery or deflooding exists. The partial delivery condition will persist until the velocity is lower than the deflooding limit. If the deflooding occured, no CCFL will happen again until the onset of CCFL limit defined by the correlations above is crossed again. This kind of test is important for system safety codes.

1.2.15.2 Summary of correlations for deflooding

Developed correlations for deflooding are summarized as follows:

For $L/D < 5$

$${J_G^*}^{0.5} + 0.62\, {J_L^*}^{0.5} = 0.75 - 0.03\, \frac{L}{D} \quad (1.16)$$

For $5 < L/D < 40$

$${J_G^*}^{0.5} + 0.8 * {J_L^*}^{0.5} = 0.6 \quad (1.18)$$

These correlations determines the gas velocity below which, the deflooding will occur. (water flow rate into reactor vessel is equal to inlet water flow rate).

1.2.16 Conclusions

The previously introduced review leads to the following conclusions:

- CCFL is caused by the following mechanisms:

1. Instable wave growth at a hydraulic jump crest leading into slugging and roll-waves formation. Roll-waves flow into the bend and breaks there into droplets. Water is carried into the upper tank as droplets or lumps of water pushed by air flow.
2. Active liquid entrainment near the lower tank that lead into sudden slug formation. The slug is pushed by the air flow into the upper tank carrying the liquid in the opposite direction.
3. Active liquid droplets entrainment near the water entrance without slugging.
4. Periodic plugging at the riser. Large plugs accumulate and then pushed at once into the upper tank by air pressure. The periodic occurrence leads into continuous carryover of the water into the upper tank.

- The first and third mechanisms are recognized as inner and entrance flooding by Choi and No (1995). The second mechanism is also caused by slugging (inner flooding) but the slug is caused by liquid entrainment rather than instable wave growth. The periodic plugging shares features with large roll-wave mechanism, however the oscillatory/periodic feature and the dependency of the water carryover on transportation of large portions of water rather than droplets or mist (as in annular-mist flow) can distinguish it from previous mechanisms.
- Flow patterns during CCFL were well classified in the horizontal channels due to extensive investigation. However, it seems that there should be some more effort to classify visual observations in the bend and inclined riser regions.
- Description of the detailed succession of events (in particular visual observations) can deviate from one author to another even when descriptions and flow conditions lead to the conclusion that they are describing same phenomenon. This is mainly due to already existing deviations in description of visual phenomenon and flow patterns.
- Onset of flooding is highly influenced by the geometrical parameters
  - Lower $J_{G,crit}^{*0.5}$ values are required for higher L/D (or horizontal part length)
  - Higher inclination angles require lower $J_{G,crit}^{*0.5}$ values except for long riser length and short horizontal length where the trend is reversed.
  - Riser length effect is not enough clear though some data shows lower $J_{G,crit}^{*0.5}$ for longer I.
  - Channel diameter effect is also not clear enough. However, data in down-scaled experiments showed higher $J_{G,crit}^{*0.5}$ values foe larger diameters.
- Entrance conditions affect initial perturbation and consequently a delayed/early instable wave formation.
- Water head has minor effect upon CCFL while initial water level in the horizontal part has strong effect.
- CCFL Data should be always introduced along with above geometrical parameters besides water head and initial water level in the horizontal part. Various CCFL data cannot be compared correctly without a good knowledge of these parameters.
- Condensation, physical properties effects upon CCFL should be considered, in particular the condensation effect.

- There exist a clear connection between a specific flooding mechanism and suitable flooding correlation.
- Existing CCFL correlations predict partial delivery and the onset of CCFL at low liquid superficial velocities. However, there were no suitable correlations for the onset of CCFL in medium and high liquid velocities.
- There was ambiguity regarding "CCFL data" or "flooding data" terms. This expression was used to refer for both: the onset of CCFL and the partial delivery after the onset of CCFL. Some data were imported sometimes from other literature as "CCFL data" or "flooding data" without enough knowledge of being onset or partial delivery data. Some authors even developed "CCFL correlation" for deflooding data and compared it with correlations which were developed for the onset of CCFL or partial delivery. Partial delivery and deflooding data differ considerably from the onset of CCFL. That is why it is important to use "CCFL data" term carefully.
- The attempt was made to introduce a set of correlations for onset of CCFL and deflooding over the entire range of $J_L^{*0.5}$ and for different L/D ratios. Resulting errors were within $\mp 20\%$ for most data points that come from hot-leg geometry experiments. These correlations can help users of system safety codes to determine the CCFL-condition within the hot-leg of a PWR during accidents.

Chapter 2 General construction concepts of SCUBA and COLLIDER test facilities

2.1 General concepts

Within the frame of the current work, two facilities have been planned for the investigation of two-phase flows related to nuclear safety. These are: steam bubble condensation in flowing subcooled water and CCFL in large-diameter hot-leg pipe geometry, both at low pressure. In order to guarantee that the facilities will serve the objectives of the work and to maintain an effective and economic construction process, general concepts were set for the design of both facilities. These concepts are summarized as follows:

- Facilities should be optimized to serve main research goals in the first place, meanwhile they should be available for generic two-phase flows research within the geometrical characteristic each facility has.
- SCUBA should be optimized for investigation of two-phase flows in a vertical and a relatively large-diameter pipe geometry using high-speed recording as the main -but not the only- measuring technique.
- SCUBA should be highly flexible to assemble/reassemble for future test modifications.
- In order to minimize costs/efforts COLLIDER will shares a part of the water loop with SCUBA .
- COLLIDER will be fully transparent to allow optical observation in all parts. This will allow further possible investigations in all parts.
- COLLIDER should be designed to allow a possible replacement of the hot-leg pipe
- COLLIDER can accept the addition of extra storage tank capacities to increase the range of experimental test conditions in the future.
- Both facilities should be equipped with up-to-date measuring techniques of high accuracy.
- Test parameters in both facilities are monitored and controlled by a full automatic system that guarantees a precise set of the experimental parameters, mainly:

$$\text{SCUBA: } J_w, T_w, J_s \qquad \text{COLLIDER: } J_w, J_a$$

All those design principles resulted in the requirements and construction characteristics described in the following two sections.

2.2 SCUBA characteristics

SCUBA was designed with the following characteristics:

1. Working fluid: distilled water. This is the water used in most PWRs.
2. Pressure: atmospheric pressure. The construction of a pressurized loop will arise many difficulties with the construction and certification in addition to high costs. Experiments under high pressure were already performed at other facilities and investigations at low pressure are also within the objectives of this work.

3. Water temperature: $90° - 98°\,\mathrm{C}$. The loop is open to the atmospheric pressure and boiling temperature should be avoided (cavitation at the pump). Since low subcooling temperatures are required, high water temperatures should be reached. $98°\,\mathrm{C}$ is the maximum achievable water temperature that can be realized without risking a cavitation at the pump.
4. Water superficial velocity: a maximum of $1.5\,\mathrm{m.s^{-1}}$ was set as a target. Most of available data for steam bubble condensation was obtained in experiments with a water superficial velocity below $1\,\mathrm{m.s^{-1}}$. This leads to provide data in a comparable velocity range, and add new data at higher water velocities to expand the available data range.
5. Test section diameter: $100\,\mathrm{mm}$ value was chosen. This choice was based on the idea of performing experiments in a relatively large diameter geometry. Investigations in small diameters are numerous and can possess different flow characteristics such as the possibility of slug formation. A diameter larger than $100\,\mathrm{mm}$ was not considered regarding the large maximum water superficial velocity of $1.5\,\mathrm{m.s^{-1}}$. Larger diameter values will result in a large water volume flow rate and a requirement for a more powerful and an expensive pump.
6. Material: a special plastic synthetic material (PVDF) was chosen for the construction of SCUBA. Since the facility will be operated at high temperatures, thermally durable material are required. Stainless steel is the first choice in this regard. However, it is heavy and hard to handle in a small laboratory. PVDF can withstand temperatures up to $130°\,\mathrm{C}$ under continuous operation conditions without experiencing changes of its mechanical/chemical properties. It will guarantee the quality of the distilled water (no iron contamination, rust building) and make the loop lighter and easier to handle (assemble/disassemble/drill perforations, etc.).
7. A fully-developed turbulent flow should be maintained at the injection position. This was accomplished by the addition of a flow straightener at a sufficient distance upstream of the test section.
8. The storage tank, the preheater, and phase separation tank were integrated into one tank component. This minimizes costs and construction efforts.
9. Steam is provided via a small steam pressure vessel using electrical heating. The steam flow is controlled automatically and injected via different injection nozzles into the flowing water. This was achieved by adopting an injection kit with an interchangeable injection nozzle.
10. The steam superficial velocity should cover a range between $0.08 - 0.25\,\mathrm{m.s^{-1}}$. Higher flow rates will result in very large steam content and pressure fluctuations within the test section.

2.2.1 The water loop

Figure 2.1 shows two concepts which were considered for the design of SCUBA's water loop. The first concept (Figure. 2.1, left) with an open upper plenum facilitates the insertion of measuring instrumentations into the experimental part. However, the opening into atmospheric pressure along with the use of hot water with fairly large volume flow rates will require a large plenum and will complicate the overall design (continuous release of steam vapor into the laboratory). The second concept (Figure. 2.1, right) is more compact but it requires that all measuring devices to be inserted via perforations in the loop piping system. Considering all previous factors, the final design of the water loop followed the second design.

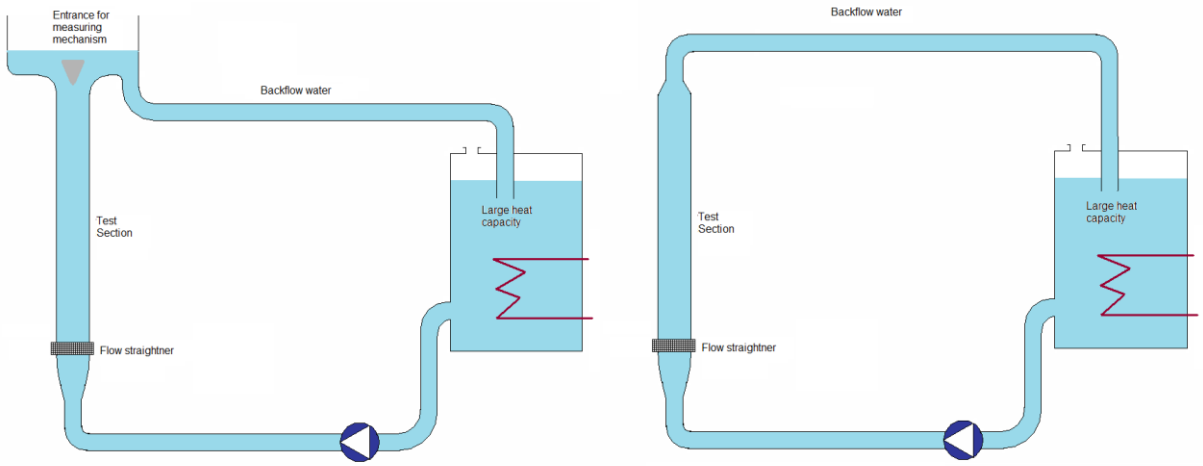

Figure 2.1 Two different concepts, both are opened to atmospheric pressure with different characteristics.

Figure 2.2 shows the final 3D design of the loop. The water tank was divided into two volumes by a thin wall. The volumes are connected at the bottom, and at the top of the tank (see Figure 2.3). The small volume receives the backflow water, separates gas from liquid (if any exists), and has two immersed heaters for regulating the water temperature (functioning as a preheater). The large volume has the remaining three immersed heaters and provides enough volume for the water to mix and homogenize before it arrives at the outlet. The outlet is placed at approximately two thirds of tank's height from the tank's bottom. This prevents the returning cold water to mix with the outlet water and provides enough mixing distance. The water tank is equipped with 5 cylindrical titanium heating elements each has a 4kW heating power. Titanium guarantees the water purity. The total heating power (20 kW) was calculated based on the power required to heat $1m^3$ of 20°C water up to 98°C within 4-5 hours. Each heating element is a cylinder of 44.5 mm diameter and 875 mm heated length (see figure 2.4). The power distribution over five elements avoids hot spots that can occur in heating bundles, and distributes the generated heat evenly within the tank volume allowing a better control of the water temperature.

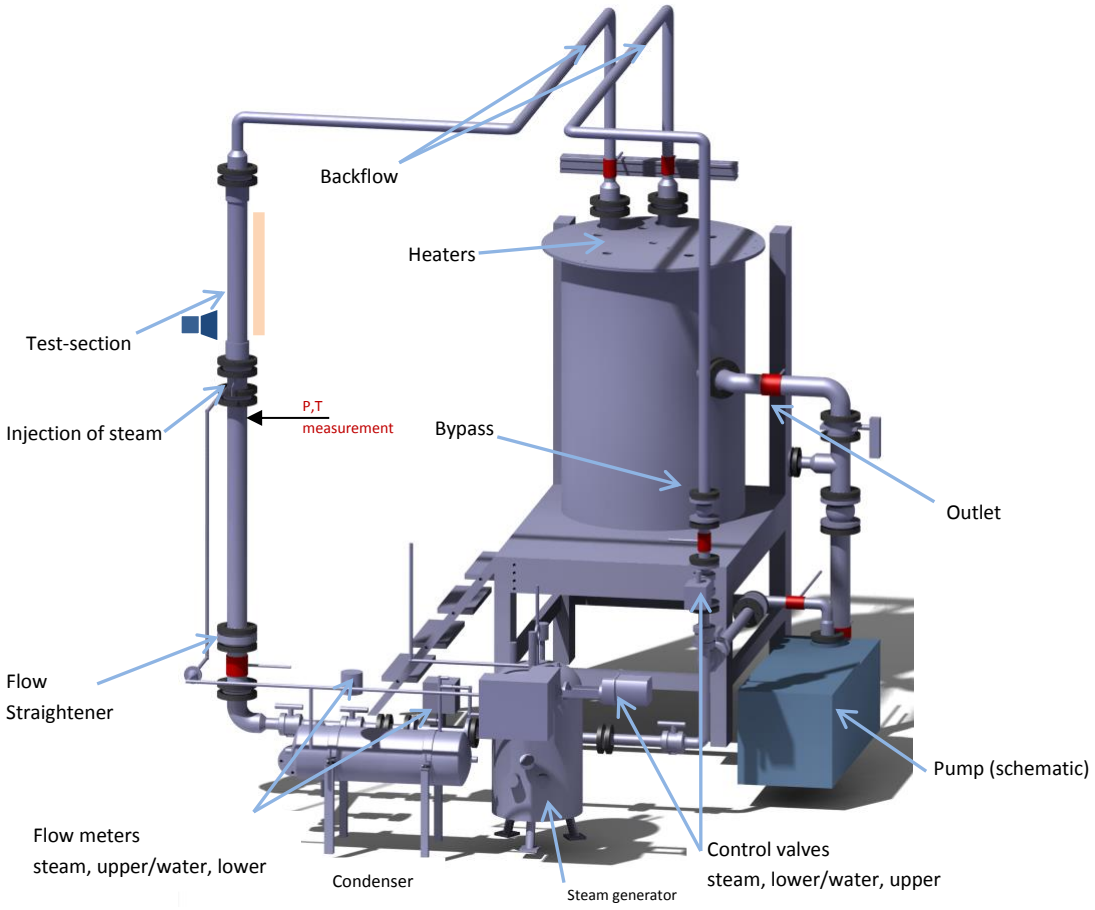

Figure 2.2 3D representation of test facility SCUBA.

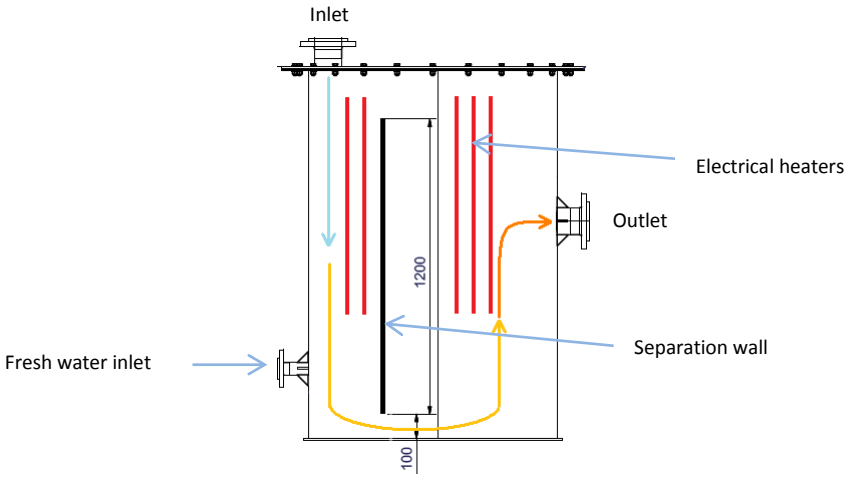

Figure 2.3 A schematic drawing of the storage tank along with immersed heating rods (depicted as red bars). The water circulation within the tank is also illustrated

The water tank was placed at higher elevation (about 2 m) than the pump in order to guarantee a safe pump operation up to 98 C without experiencing cavitation at the pump's suction side. In order to prevent cavitation at a specific temperature and a flow rate, a minimum head at the suction side is required. This is well known as $NPSH_r$ (required net positive suction head) value and should be determined by the manufacturer. For a better protection against cavitation, the pump was equipped with an inducer at the suction side (see

figure 2.5). It generates a local increase of the fluid pressure at the pump propeller providing better safe margin from the cavitation and increasing the maximum allowed void content from 5% into 20% .

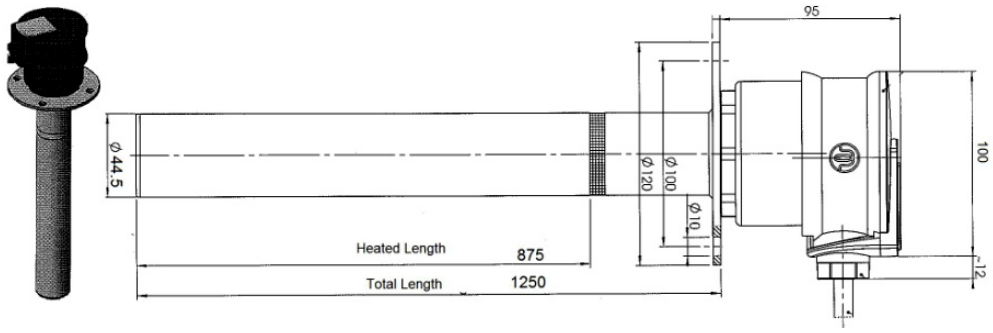

Figure 2.4 A drawing of one heater element.

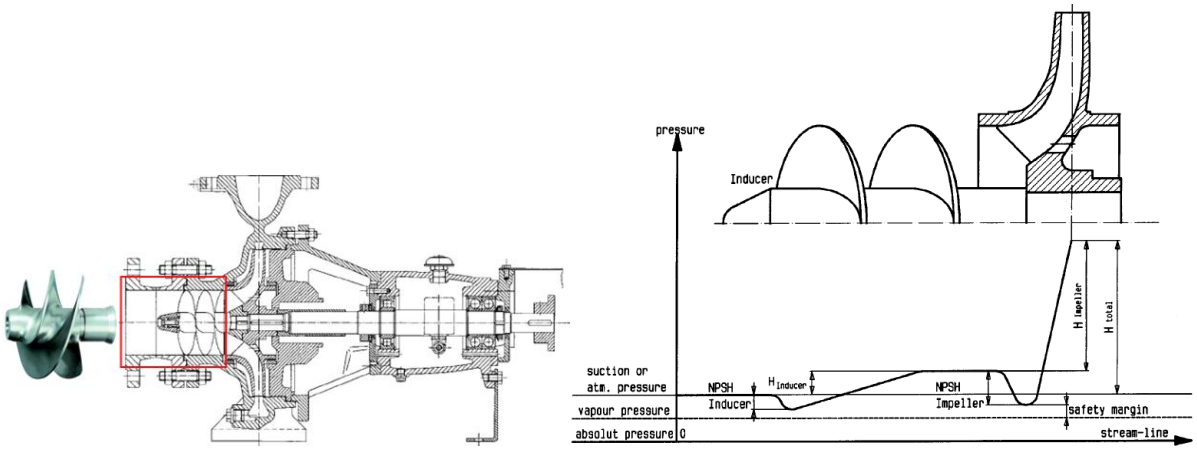

Figure 2.5 Left: Centrifugal pump equipped with an inducer. Right: Illustration of the inducer's contribution to the $NPSH_r$. [VOGEL-INDUCER Technology, ITT industries, datasheet information]

The piping system is also made of PVDF and was assembled via welding junctions where changing loop segment is irrelevant. However the test section and some other parts were rather flanged in order to allow flexibility for future modifications. The current design of SCUBA allows changing the entire vertical test section as desired. The water is pumped from the storage tank and split into two paths: the bypass and the test section. The bypass flows simply back to the storage tank providing a secure operation of the water loop (if the test section was accidently blocked). Additionally it provides a better possibility to control the flow within the test section. The test section path flows through a regulated valve, a flow meter, a flow straightener, the transparent test section pipe, and finally it returns to the storage tank. The backflow water coming from both flow paths is directed into two closed-end pipes. The pipes are immersed about 1 m within the storage tank and each of them has numerous 1 cm diameter holes in their side walls. This prevents formation of large waves, vibrations and disturbances as the backflow water pours into the tank, and allows the backflow water to be redistributed gently within the water volume. Two extensions were built within the water loop: one after the flow meter and one at the pump's suction side. They allow using the water loop for COLLIDER facility when required. The test section is made of 1m of transparent

polycarbonate (PC) pipe that has a $104mm$ inner diameter and 3 mm wall thickness. The PC material can withstand temperatures up to $130\ \mathrm{C}$ for neutral fluids. The pipe was connected to the loop using special connectors that allows it to be flanged into other parts. A honeycomb flow straightener (figure 2.6) was installed $2\mathrm{m}$ upstream of the test section (see Figure 2.2). It helps forming a fully-developed turbulent velocity profile at the injection position. The use of the straightener allows eliminating swirls and help developing a uniform flow field. As a result, it justifies the assumption of a uniform water velocity distribution around the condensing bubbles near the pipe's center

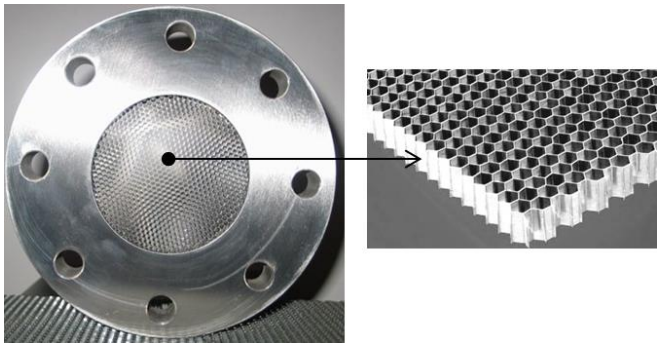

Figure 2.6 An illustration of the honeycomb flow straightener installed upstream of the test section in SCUBA.

Plastics tend to expand much more than metals. Since the loop was made of plastic material, thermal expansions are not negligible and should be treated to prevent them from affecting the integrity and geometry of the loop. Two measures were applied: the use of rubber compensators and bending-legs. Figure 2.7 illustrates the principle of using bending legs. Thermal expansions are simply compensated by light inclination of the smaller extension of the leg; which is fixed to the wall and allowed to slide along pipe direction. Bending legs were applied where small inclinations of the pipes can be tolerated. They appears in red color in Figure 2.2.

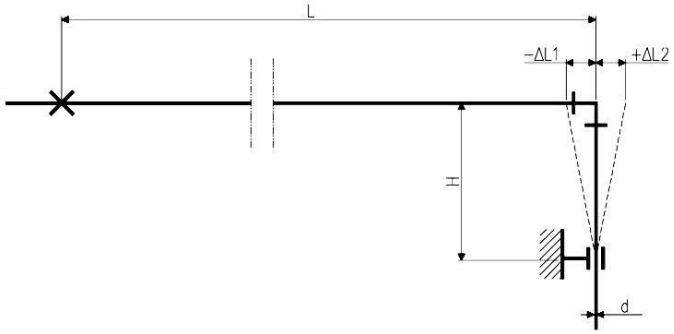

Figure 2.7 Illustration of the use of the bending leg principle to overcome thermal expansions.

Rubber compensators were installed in pipe segments where the bending legs are not applicable (ex. no sufficient H value as depicted in figure 2.7), or where inclination of the pipe cannot be tolerated. This is the case within the test section where it is important to keep the test section vertical.

2.2.2 The steam loop

The steam is provided via a small steam generator that has a total water capacity of 80 liter, this capacity is sufficient for running experiments continuously for about 3-4 hours within the desired steam superficial velocities range $0.3 - 0.3\ \mathrm{m/s}$ and without the need to resupply the vessel with fresh water (which adds water with a high dissolved air content). The vessel was designed to withstand a maximum absolute pressure of 2.5 bar, which is sufficient to overcome pressure losses until the injection point. The vessel was equipped with following devices:

- Two electrical heaters each has 5 kW electrical power.
- Feeding valve for distilled water.
- Steam outlet at the top of the vessel.
- Drain at the bottom.
- Safety valve: functioning according to the rupture disk principle that breaks when pressure exceeds the maximum design pressure of 2.5 bar.

The steam flowing out of the steam generator has two possible paths: one drives the steam into the injection point and the other discharge the steam through a bypass into a condenser in case of an overpressure. The path into the condenser is opened by actuating on/off valve when the pressure overpasses a certain limit below the maximum allowed pressure (a limit of 2-2.1 bar was practically used to keep a safety margin from the 2.5 bar maximum). The path into the injection point passes through, a control valve, a cyclone droplets separator, and a flowmeter. The control valve opening can be set continuously between $0\% - 100\%$ which allow-along with the feedback signal from the flowmeter- to control the steam flow rate inside the injection path. The cyclone separator is installed before the flowmeter in order to ensure that the steam is dry at the measuring and the injection points. A suitable development length is ensured between the cyclone separator and the flowmeter ($15D_{in}$). After passing the flowmeter, the steam can be directed either into the injection point or dumped into the condenser via a manual valve. The condenser has 11 kW cooling power and it was constructed in order to condense the entire steam flow when needed. The condenser is not needed for the experiments but it allows a feasible and safe operation of the steam loop. All the steam can be condensed when it is not injected into the water loop or when the overpressure-bypass valve opens due to an overpressure inside the steam vessel. The condenser was used for the calibration of the steam flow meter at low flow rates (see section 2.2.3.2.1). The entire steam vessel and attached pipes (DN15 stainless steel pipes) are insulated using rockwool to keep the steam dry until the injection point. A detail of the steam injection kit can be seen in Figure 2.8. Four injection nozzles with different geometries were implemented. There are two nozzles which inject steam centrally and vertically. They have an inner nozzle diameter of 4 and 6 mm, and labeled as CIN4mm, and CIN6mm. The third nozzle has two 4 mm horizontal injection holes and is labeled as HIN2X4mm. The fourth nozzle has two arms, each arm has two parallel sets of eight 0.8mm holes and it is labelled as HIN32X0.8mm.

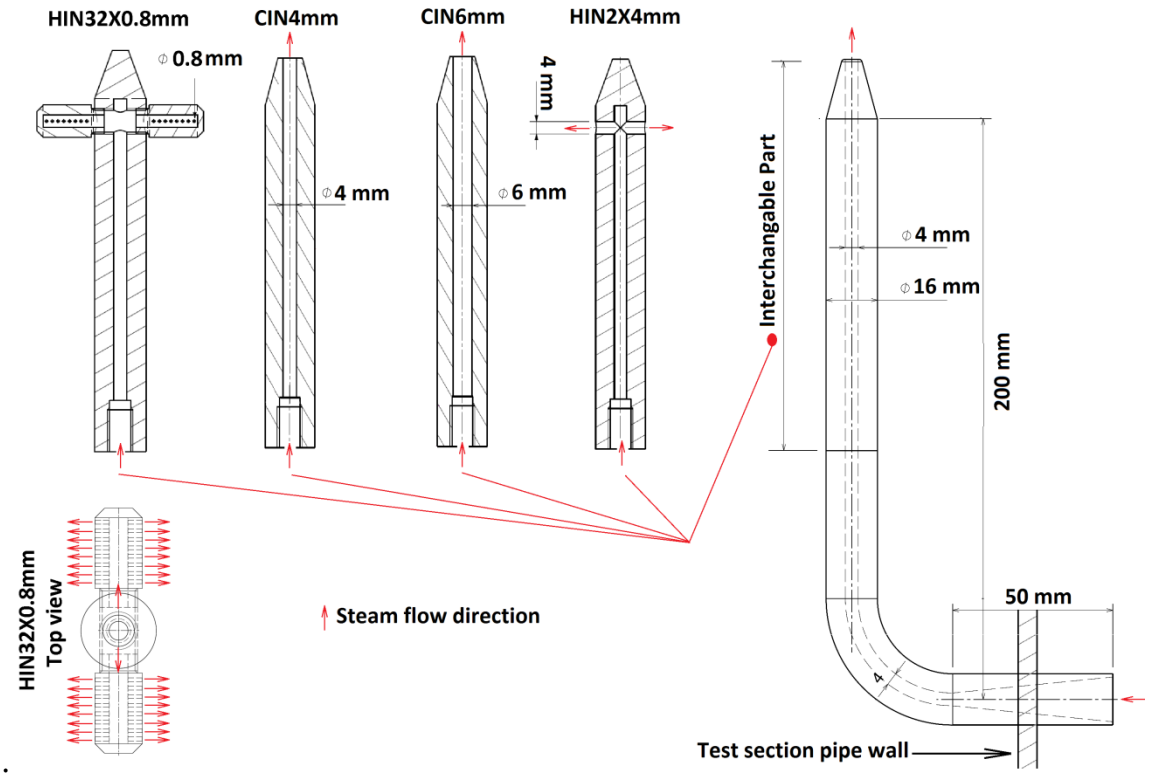

Figure 2.8 Design and geometry of the steam injection kit along with the different applied injection nozzles. Red arrows indicate the steam flow direction.

2.2.3 Measuring devices in SCUBA

Following flow parameters were controlled/measured in SCUBA experiments:

- Water temperature.
- Water static pressure at injection point (≡steam saturation temperature).
- Water velocity.
- Steam velocity.
- Bubbles parameters: Diameter, velocity…etc.

Bubble parameters are measured via high speed recording and shadowgraph techniques that are described in chapter 4. Following sections describe measuring devices used for the rest of the flow parameters.

2.2.3.1 Water loop

The temperature was measured with a Pt100 resistance thermometer which has $\pm 0.5°$ C accuracy within the measuring rang ($90° - 100°$ C). The thermometer tip is inserted into the center of the pipe near the test section entrance. This temperature is considered a representative of the water bulk temperature. A more precise measurement will require a movable thermometer along the pipe radius and is planned for future work. The static pressure near the injection position was measured by a capacitive ceramic absolute pressure transducer

which has an accuracy of of $\pm 0.5\%$. The transducer is placed about 50 cm below the steam injection position. It measures the static pressure at the injection point with a small hydrostatic pressure difference (~ 0.05 bar) which can be subtracted for the calculation of the saturation temperature. A similar transducer was used to estimate the water level inside the water tank. Its signal controls the opening/closing of the feed water valve into the water tank, and switches off the pump if the water level falls close to the outlet level. A float switch was installed inside the water tank in order to switch off the electrical heaters if the water level falls below the heated length of the rods. The water flow rate was measured via an ultrasonic flow meter which is suitable for application in distilled water with a high accuracy ($\pm 0.5\%$). The flowmeter has four built-in senders/receivers that allow a precise measurement of the flow rate in comparison with external clamp-on sensors (1.5% geometrical installation factors is added). The flowmeter was installed with the required $15D_{in}/3D_{in}$($D_{in} \equiv$ pipe's inner diameter) development lengths before/after the device in order to guarantee the accuracy of the measurements. The water flow rate was measured inside the DN50 pipe so that the flowmeter can measure as lower flow rates as possible (the low cut-off limit is linked to the water velocity inside the flowmeter). According to this configuration the flowmeter can measure flow rates as low as 0.7 l/s. No calibration was necessary for SCUBA tests, however a calibration was needed for COLLIDER in order to measure flow rates as low as 0.4 l/s.

2.2.3.2 Steam loop

The water temperature inside the steam generator was measured with a RTD Pt100 that has $\pm 0.5°$ C accuracy. The RTD was placed between the electrical heaters to provide a feedback value for controlling the water temperature and heating power. The steam pressure was measured with a piezoresistive cell which has $\pm 0.5\%$ accuracy. The device was mounted on top of the vessel and coupled with the bypass valve that opens when the pressure inside the vessel exceeds a preset value of 2 bar. The steam is then released into the condenser until the pressure decreases below the preset limit. The water level is measured with a capacitive level sensor that indicates the actual water level within the vessel. If the water falls below a certain limit the feedwater valves opens to prevent the heaters from operation without a sufficient water level. The water overflow (when the water level inside the pressure tank exceeds the maximum allowed height) was monitored using a vibration limit switch. The piezoelectrically activated vibration of a vibrating fork is damped when the fork comes into contact with water. The function is independent of fluctuations in the physical properties of the medium such as electrical conductance. The steam flow rate was measured via a vortex-meter which is capable of measuring steam mass flowrates as low as 4.3 kg/h. Since the desired lowest value is even lower than this value, an experimental calibration shown within the next section was performed. It should be noted that for measurements in this range of mass flow rates, no other device was found. The described in next section calibration allows to measure the average steam flow rate with an acceptable accuracy.

2.2.3.2.1 Calibration of the steam flowmeter rate at low flow rates

The calibration was achieved by conducting the entire steam flow after the flowmeter into the condenser. Since the condenser has a cylindrical shape, and it is placed in a horizontal position, all the condensate will flow via the outlet which is placed at the lowest point of the condenser. The flow rate was set constant and the condensate was gathered measured over 10 minutes time. The condensate volume was then measured using measuring tubes with ± 0.375 ml accuracy. By dividing the condensate volume by the condensation time and accounting for the water density, the average steam mass flow rate can be calculated $\dot{m}_{real}$. The set value of the steam mass flow rate $\dot{m}_{set}$ by the automatic control system is then compared with the real value $\dot{m}_{real}$ obtained out of the condensate measurementand the ratio between the set value and the real value is calculated. This ratio was found to be a linear function of the set value for mass flow rates lower than 3.3 kg/h, while the ratio is 1 for values larger than 3.3 kg/h. In another words the flowmeter measures steam mass flow rates precisely down to 3.3 kg/h (lower than the manufacturer's limit, which is a typical feature of many precise measuring devices), while it measures only a percentage of the mas flow rate values lower than 3.3 kg/h. Table 2.1 illustrates this calibration. More than one measurement was done when a considerable deviation between measured values for the same set value was noticed. Figure 2.9 shows the final obtained calibration curves used in SCUBA experiments.

Table 2.1 Calibration of the steam flowmeter.

Value set (controller) [kg/h]	Flowmeter reading (set) [kg/h]	Condensate mass[g]	Measuring Time [min]	Flow rate condensate (real) [kg/h]	set/real ratio
0.4	0.38	323	10	1.94	
0.4	0.40	255	7.5	2.04	
0.4	0.40	315	10	1.89	
0.4	0.39	311	10	1.87	
0.4	0.40	304	10	1.82	
	$0.39 \pm 1.6\%$			$1.91 \pm 4.3\%$	$0.2 \pm 5.9\%$
0.7	0.69	376	10	2.26	
0.7	0.70	376	10	2.26	
0.7	0.68	358	10	2.15	
0.7	0.70	184	5	2.21	
0.7	0.69	355	10	2.13	
	$0.69 \pm 0.7\%$			$2.20 \pm 2.7\%$	$0.31 \pm 3.4\%$
1.0	0.99	388	10	2.33	
1.0	0.99	412	10	2.47	
1.0	0.99	421	10	2.53	
1.0	0.99	412	10	2.47	
1.0	0.99	404	10	2.42	
	$0.99 \pm 0.0\%$			$2.44 \pm 3.0\%$	$0.41 \pm 3.0\%$
1.5	1.49	437	10	2.62	
1.5	1.49	448	10	2.69	
1.5	1.49	446	10	2.68	
1.5	1.49	446	10	2.68	
1.5	1.49	440	10	2.64	

	$1.49 \pm 0.2\%$			$2.66 \pm 1.1\%$	$0.56 \pm 1.3\%$
2.0	1.99	459	10	2.75	
2.0	1.99	480	10	2.88	
2.0	1.99	479	10	2.87	
2.0	1.99	476	10	2.86	
2.0	1.99	471	10	2.83	
	$1.99 \pm 0.1\%$			$2.84 \pm 1.8\%$	$0.70 \pm 1.9\%$
2.5	2.48	383	7.5	3.06	
2.5	2.48	377	7.5	3.02	
2.5	2.49	378	7.5	3.02	
2.5	2.49	383	7.5	3.06	
2.5	2.86	406	8.0	3.05	
	$2.56 \pm 6.5\%$			$3.04 \pm 0.7\%$	$0.84 \pm 7.3\%$
3.0	2.98	538	10	3.23	
3.0	2.99	541	10	3.25	
3.0	2.98	536	10	3.22	
3.0	2.99	537	10	3.22	
3.0	2.99	541	10	3.25	
	$2.99 \pm 0.2\%$			$3.23 \pm 0.4\%$	$0.92 \pm 0.6\%$
4.0	3.98	495	7.5	3.96	
4.0	3.99	500	7.5	4.00	
	$3.98 \pm 0.3\%$			$3.98 \pm 0.7\%$	$1.00 \pm 1.0\%$
5.0	5.02	633		5.06	0.99

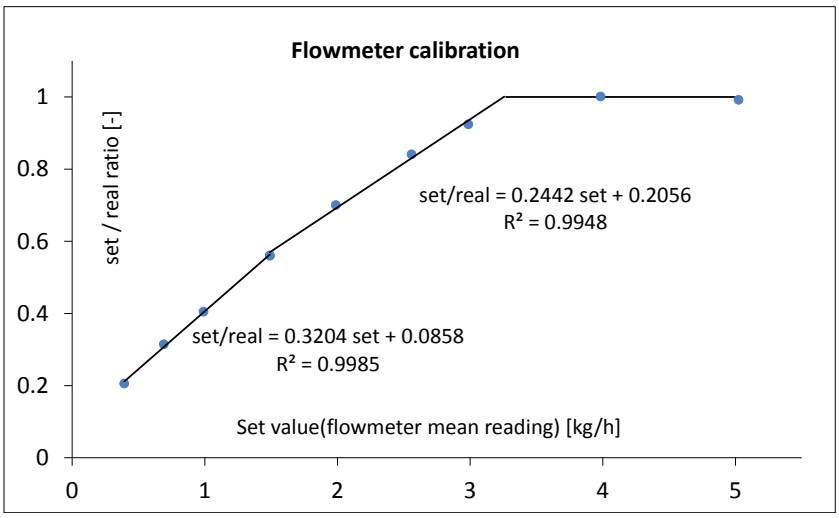

Figure 2.9 Calibration of the steam flowmeter's mean mass flowrate.

As figure 2.9 shows, a linear correlation was found between $\frac{\dot{m}_{set}}{\dot{m}_{real}}$ and $\dot{m}_{set}$ on the steam flow controller:

$$\frac{\dot{m}_{set}}{\dot{m}_{real}} = m.\dot{m}_{set} + c$$

$m, and\ c$ are determined through calibration. Two trends were fitted into the calibration results:

$$\frac{\dot{m}_{set}}{\dot{m}_{real}} = 0.2442\,\dot{m}_{set} + 0.2056 \qquad \dot{m}_{set} < 1.5 \text{ kg/h} \tag{2.1}$$

$$\frac{\dot{m}_{set}}{\dot{m}_{real}} = 0.3204\,\dot{m}_{set} + 0.0858 \qquad 3.3 > \dot{m}_{set} \geq 1.5 \text{ kg/h} \tag{2.2}$$

This allowed the measurement of the average steam mass flow rate within $\pm 6\%$ accuracy for the targeted measuring range

$$0.4 < \dot{m}_s < 4 \text{ [kg/h]}$$

2.2.4 SCUBA pre-tests

After the accomplishment of all construction works in SCUBA including: the construction of all components, piping system, instrumentation, and the control system; the facility went through some preliminary tests to ensure that it functions according to the design requirements. First tests were performed with cold water to test the loop's integrity and the functionality of the instrumentation/control systems and the loop stability (vibrations within the test section). Afterwards the water was heated gradually to test the sustained integrity, cavitation occurrence in the pump, and functionality of all measuring devices under elevated temperatures. The validity of counter-expansion measures was tested as well. As a result of the hot tests a small inclination was observed in the vertical test segment (~$4\ m$ long segment) at high temperatures ($> 96°\ C$). An additional rubber compensator was built into the test section. The added compensator solved the inclination problem. Another issue happened at the storage tank cover which bulked excessively upwards at high temperatures. This happens due to the fact that the outer non-heated flange of the cover remained relatively colder than the inner part exposed to the heat of the water inside the tank. The issue was later solved by installing a heat-durable plastic hose coil loop over the non-heated part. The hose gets hot water out of the bypass segment (no effect upon flowrate inside the test section) and heats that part up to similar temperatures of the inner part. The extracted water runs back into the water tank causing no water loss. The steam flow rate controller was adjusted manually (try and error) to achieve an optimized response to the set value. Another issue was the calibration of the steam flowmeter at low mass flow rates shown in previous section. Initial tests were also done using the high speed camera to test the optimized set-up. As a result of the pre-tests SCUBA was proved to function safely with stable test parameters. The achievable range of test parameters was set and following test matrix was used for experiments with the exception of the HIN32X0.8 nozzle:

SCUBA test Matrix			
Water superficial velocity [m/s]	0.4	0.6	1.0
Steam superficial velocity [m/s]	0.09	0.14	0.22
Water temperature [°C]	94	96	98

For the HIN32X0.8 nozzle no tests were performed at $J_L = 1.0\ \mathrm{m.s^{-1}}$ due to the high rate of DCC at the nozzle (no detached bubbles). Instead, a third measurement was performed at $J_L = 0.2\ \mathrm{m.s^{-1}}$.

2.3 COLLIDER Characteristics

COLLIDER (Countercurrent fLow LImitation in a large DiametER) was designed according to the following criteria:

1. Working fluid: distilled water, this is the working fluid in most PWRs.
2. Water temperature: room temperature.
3. Water superficial velocity: it was chosen to cover the low- and mid- range of water velocity values according to Wallis parameters. This results in the following range : $0.1 < J_w^{*0.5} < 0.4$.
4. Air superficial velocity: It was chosen to start from values considerably below the onset of CCFL along the entire range of inlet water velocities, and up to values that are higher than the highest reported values for onset of CCFL in literature, so that all possible phenomena from supercritical flow until the onset of CCFL can be recorded and observed. This resulted in a targeted range $0.36 < J_a^{*0.5} < 0.7$ (Wallis parameters).
5. Scale: Most CCFL test facilities are down-scaled of the real dimensions found in PWRs. however –as it was explained within the theoretical review, there is little high-quality and detailed observations in pipe hot-leg geometry at large diameters. Most studies were conducted in small diameters which infer scaling effects upon results plus a change of the observed phenomena. For instance, the formation of slugs is very common in diameters less than 100 mm and they play a major role in the onset of CCFL. On the other hand, it is hard for slugs to appear in a large diameter pipes (> 200 mm) due to the fact that at the same Wallis non-dimensional water velocity the relative height of the water inside the pipe will be much lower and surface tension forces will have lower effect. Scaling effects are crucial for CCFL investigations and specially when extrapolating into real PWR dimensions. All previous reasons led to the choice of a 200 mm pipe which results in a $1/3.9$ downscale of a real 1:1 full scale. All other components were dimensioned according to this scale so that the entire facility will be a 1/3.9 downscaled hot-leg model of a real PWR.
6. Pressure: Experiments were chosen to be carried out under atmospheric pressure. Many reasons led to this choice:
    a. Simplicity of the design, most investigations concentrate upon phenomenological investigations under low pressure rather than studying the physical properties effect.
    b. CCFL tests were already executed at high pressure in comparable scale facilities [Deendarlianto et al. 2011].
7. Material: Plexiglas was chosen as a standard material in all facilities under room conditions that require optical observations. There is a good working experience with this material in the market and the difficult large hot-leg pipe with the $50°$ bend was

possible to be manufactured with fully smoothed entrance. The entire facility including the reactor vessel simulator, the hot-leg, and the steam generator simulator was made transparent. The main aim was to observe the entire phenomenon even at the boundaries without obstructions. However this choice will make it possible to conduct additional experimental work at the facility, such as the investigation of impinging jet entrainment inside the reactor tank. This serves the generic goal of constructing a facility that can be used beyond the main design purpose.

2.3.1 COLLIDER description

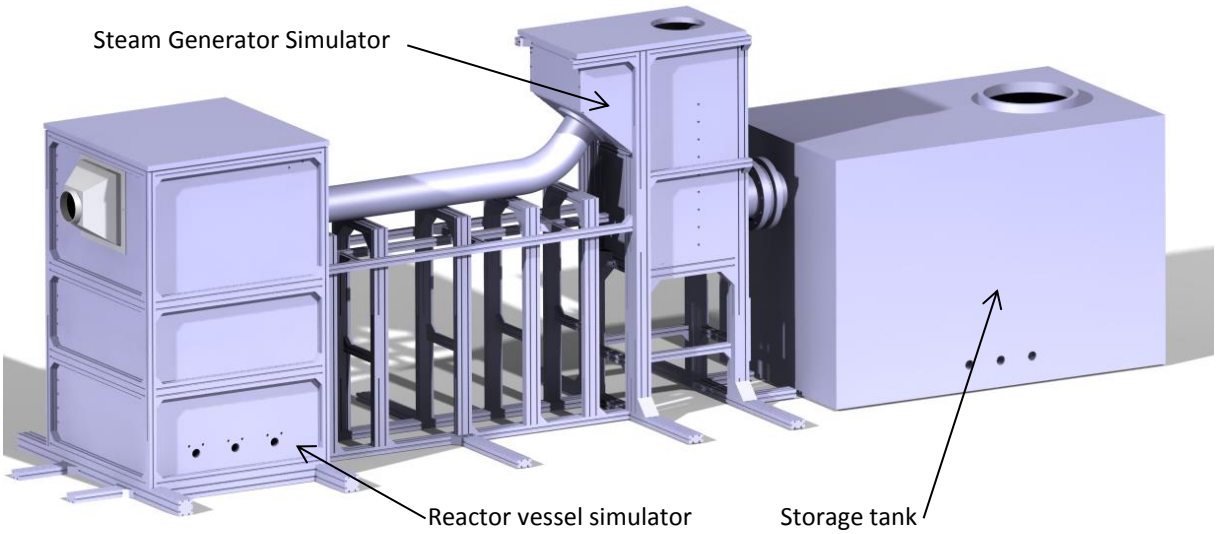

Figure 2.10 3D Illustration of COLLIDER test facility

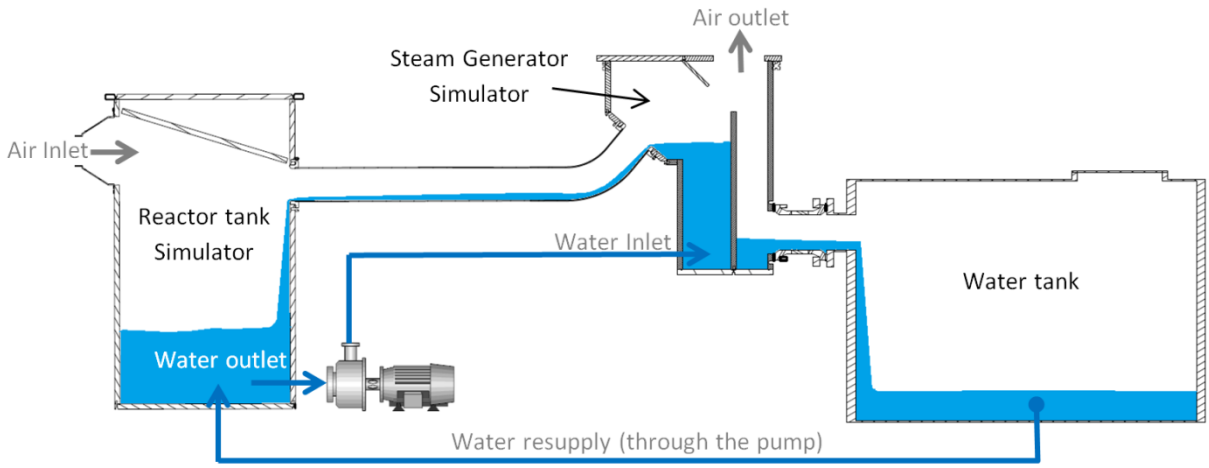

Figure 2.11 A cross section in COLLIDER showing water and air flow directions.

Figure 2.10 shows a 3D drawing of COLLIDER facility. Figure 2.11 shows a drawing made in the middle plane of COLLIDER and it gives a general distribution water/air within the different components. COLLIDER consists of a steam generator simulator, a reactor vessel simulator, a hot-leg, a water tank, and piping system. The drawing shows also positioning of the water/air inlet and outlet, as well as the water circulation and connection into the pump. In the following a more detailed description is given for the different components.

1. The Hot-leg pipe: a DN200 mm Plexiglas pipe (actual $190\,mm$ inner diameter) that is scaled exactly according to a real PWR hot-leg section shown in following table:

Hot-leg dimensions

	L[m]	Geometry	**D**[mm]	Riser		**L/D**	**I/D**
				I[m]	**θ**		
Full scale	7.1	Circular	750	1.4	50º	9.47	1.87
COLLIDER	1.8	Circular	190	0.356	50°	9.47	1.87

Figure 2.12 shows the exact positioning of these dimensions in COLLIDER's hot-leg

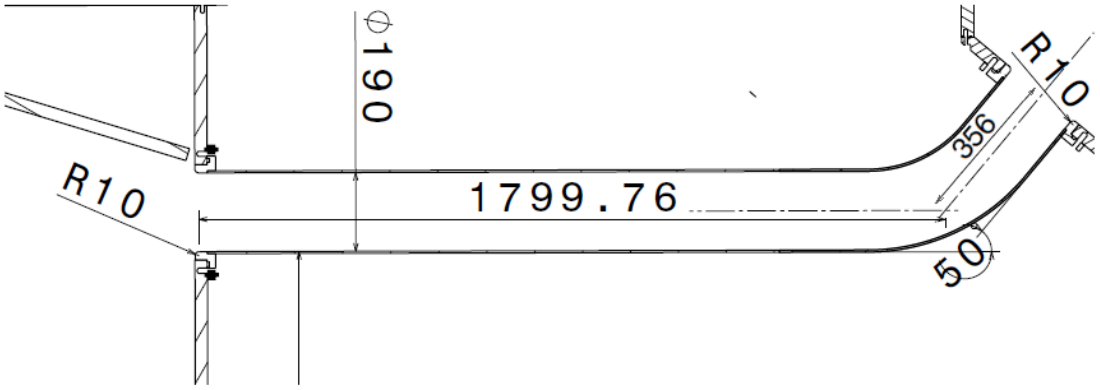

Figure 2.12 Dimensions of COLLIDER's hot-leg

2. Steam generator simulator was designed to represent half of the dome-shaped bottom of a real PWR steam generator. The design was simplified by replacing the dome shape with inclined surfaces to facilitate the manufacturing process (Figure 2.10). The dimensions were scaled to match the scales of the bottom of PWR steam generator. Figure 2.13 shows the dimensions of this component. The Steam generator has two DN50 water inlets near the bottom (in order to avoid water large swirls at the surface). The junction between the SG and the hot-leg was made seamless, rounded and smoothed so that no flow disturbances can occur as the water flows into the hot-leg riser. A separation wall divides the SG volume into two parts: the left part receives inlet water at the bottom and allows it to rise above the hot-leg inlet so that the water flow under gravity into the hot-leg pipe. The right volume receives backflow water (droplets, lumps of water, air/water mixture) when CCFL occurs. the right volume has a large DN250 opening into the water tank so that all backflow water flows back into the water tank instantaneously. A deflection inclined plate was mounted at the top of the steam generator in order to deflect the path of the droplets downwards away from the air outlet. However initial tests showed that a droplets separator (demister) was necessary. A stainless steel mesh was installed at the air outlet as shown in figure 2.13.

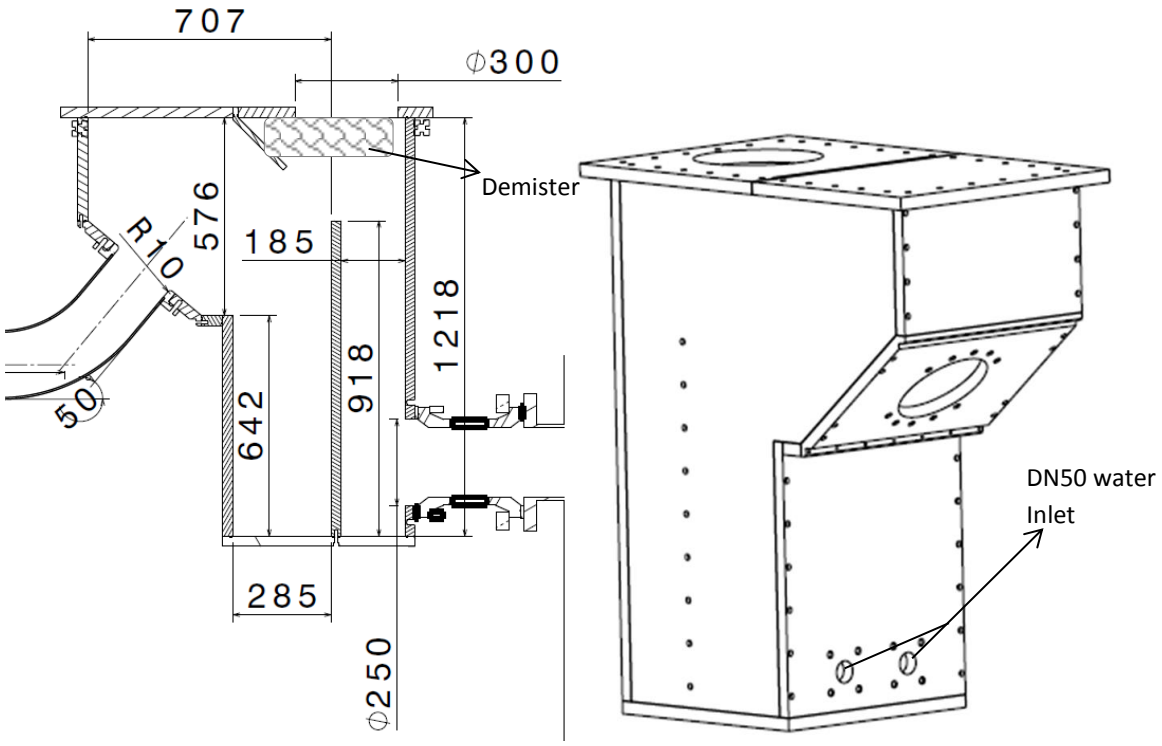

Figure 2.13 Dimensions of the steam generator simulator. values are in [mm]. the SG has a 500 mm depth in the perpendicular direction to the drawing's plane.

3. Measuring tank: The 1/3.9 scale resulted in 1 m^3 reactor tank simulator. The tank was made with a rectangular cross section to simplify the measurement of water volume change rate relying on water level measurement, and to allow an easy optical observation. The volume will be enough for water supply during a full CCFL test (i.e. starting from superficial state until onset of CCFL) even at the highest water flow rate. The tank was equipped with 3 DN50 junctions at the bottom. One of them was used for water outlet and another for installation of a pressure sensor. The third remains an extra extension for future modifications. The tank includes an inclined plate to direct the air into the hot-leg and elimination of large swirls.

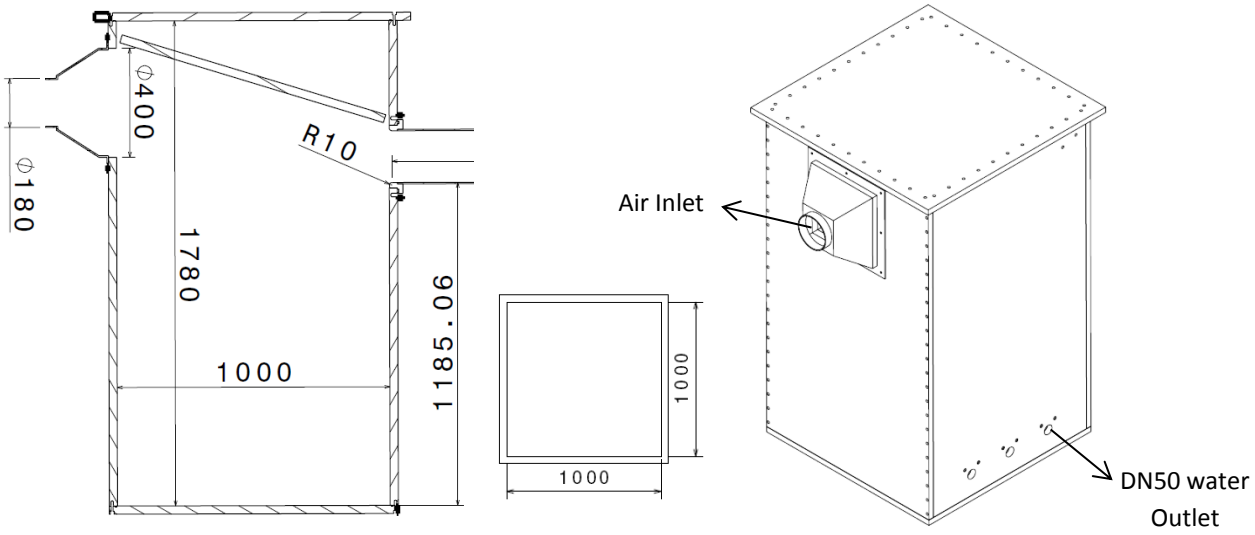

Figure 2.14 Dimensions of the reactor tank simulator (left). Cross section dimensions (middle). Dimensions are in mm. Angles in degrees.

4. Piping system: Figure2.15 shows a scheme of the piping system in COLLIDER. It uses the pump, the flowmeter, and the regulation valve from SCUBA water loop. The suction line into the pump and the outlet into COLLIDER are made via extensions in SCUBA at the pump suction side and after the water flowmeter. The system configuration allows to pump water either from the reactor vessel or from the water tank, and to direct pumped water into the steam generator or into the water tank. It allows almost all possible connections between the three existing tanks by manipulating two ball valves and one three-way valve as Figure 2.15 shows.

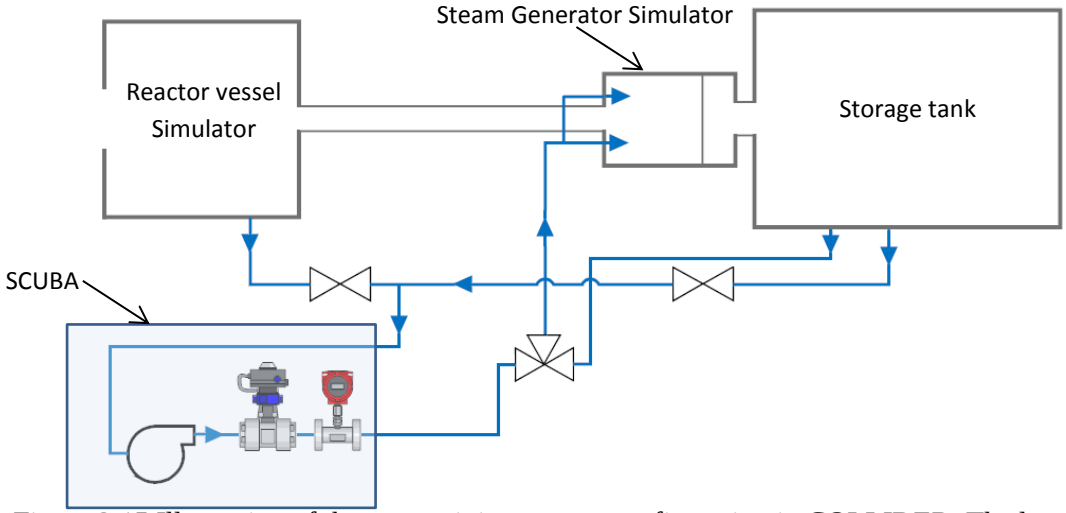

Figure 2.15 Illustration of the water piping system configuration in COLLIDER. The layout of the facility is drawn in a top view.

Figure 2.15 shows a schematic representation of the piping system. COLLIDER was connected with the pump and water flowmeter in SCUBA's loop via a flexible DN50 hoses. The scheme shows the rest of the piping system that allows all possible test procedures between all three tanks. As it was shown within the review, the initial conditions and the inlet

geometries are crucial for the CCFL phenomenon. A special care should be paid to the construction of these parts to avoid any kind of steps that can disturb the inlet flow . Figure 2.16 shows details of the inlet and outlet of the hot-leg pipe. As it can be seen, these parts are fully smooth, rounded, and seamless.

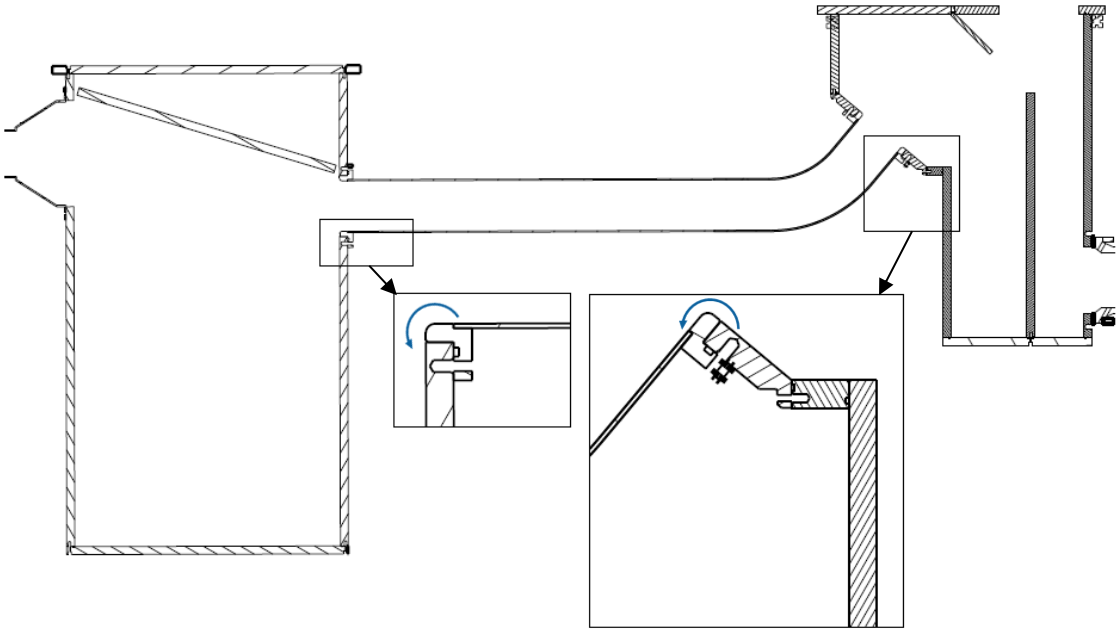

Figure 2.16 Details of the water inlet/outlet in the hot-leg of COLLIDER. All edges are rounded and smoothed to guarantee a smooth undisturbed flow at the entrance and exit of the hot-leg pipe.

2.3.2 Measuring devices in COLLIDER

COLLIDER shares a part of its water loop with SCUBA, including the ultrasonic water flowmeter, and water temperature which were described before. Air flow rate is measured via a Pitot tube (Figure 2.17). The applied device has 4 measuring positions along the measuring pipe diameter. Each of these measuring positions is exposed to the total pressure upstream the tube and the static pressure downstream the tube. The pressure difference is measured by an integrated precise pressure-difference device and the air flow rate is then proportional to the square root of the pressure difference as equation 2.3 shows.

$$Q = \kappa . A . \varepsilon . \sqrt{\frac{2\Delta p}{\rho_a}} \qquad (2.3)$$

Where κ, ε are κ-factor of the Pitot-tube and expansion factor respectively.these are provided by calibration from manufacturer.Performing the Measurement at four different radial positions gives an accurate value of the flow rate and account for existing velocity profile. The air flowmeter was installed into a specially designed plastic DN180 pipe with a sufficient development length in order to guarantee an undisturbed and fully developed velocity profile at the measurement point:

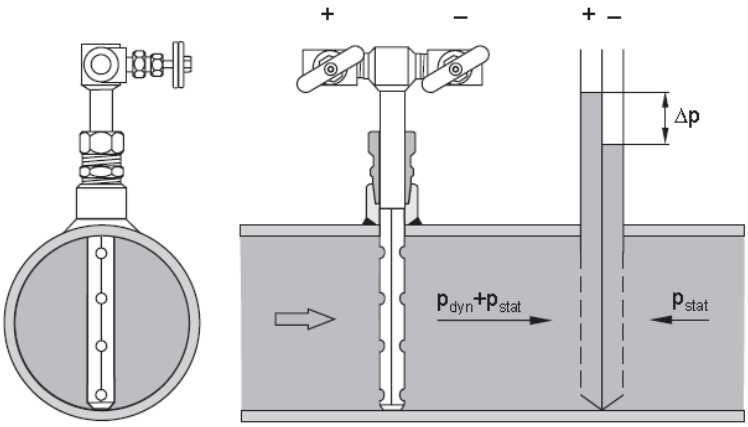

Figure 2.17 Measurement of the air flow rate: Details of the applied Pitot-tube. [Endress+Hauser Deltatop DP62D data sheet]

Applying this method, the flowrate was measured with 1.1% accuracy in experimental range of flow rate

$$0.36 < J_a^{*0.5} < 0.7$$

The pressure difference between reactor vessel tank and the steam generator tank is measured via a deflectable metal diaphragm that allows a more precise measurement of the pressure difference. The deflection is transferred vial oil into a semiconductor resistance bridge that converts this value into a current signal. This device provides a measuring error between $\pm 7.15\% - \pm 0.5\%$ for the measuring range $1 - 15$ mbar.

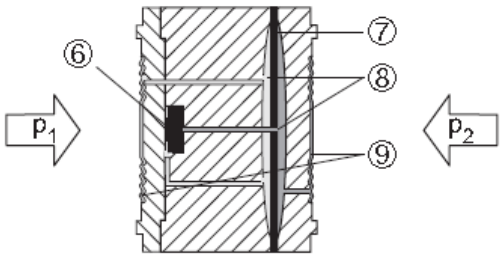

Figure 2.18 Measuring principle of the pressure difference sensor. 6: Sensing element, 7:middle diaphragm , 8:filling oil 8 , 9:process isolating diaphragm [Endress+Hauser Deltabar S PMD70/75, FMD76/77/78 Data sheet]

The water level inside the measuring tank/reactor vessel simulator is measured via two precise pressure transducers: one is located in the air, and the other in the water near the tank's bottom. The difference between these two measurements is directly proportional to the average water level in the tank. The pressure sensors are capacitive ceramic absolute pressure transducers which has an accuracy of of $\pm 0.15\%$ of the measuring range, within the applied measurement range. Taking into consideration the subtraction process-to calculate the pressure difference- the error of the estimated pressure difference value ranges between $\pm 0.65 - \pm 1.8\%$. This results in a ± 0.36 mm maximum error of the average water level. As the water level inside the reactor vessel simulator is always wavy

(due to the falling water stream from the hot-leg and air circulation inside the RVS) the measurement of the water level using a pressure transducer is the most accurate for estimation of the average water level under these conditions. The average water level indicates the flow balance into the RVS ($water\ inlet\ from\ the\ hot-leg-water\ outlet$).The separate measurement of the absolute pressure in air and water gives the possibility to determine the air pressure inside the RVS. Table 2.2 summarizes the measuring devices used in COLLIDER along with corresponding accuracy.

Table 2.2: Measuring devices in COLLIDER

Parameter	**Device**	**Error**	**Note**
Water temperature	Pt 100	$\pm 0.5°\,C$	-
Water velocity	Ultrasonic	$\pm 0.5\%$	With calibration at low flow rates ($J_L^{*0.5} < 0.135$)
Air velocity	Pitot Tube	$\max \pm 1.1\%$	
Water level in RVs	Capacitive ceramic absolute pressure transducers	$\max \pm 0.36$ mm	Two transducers are applied – one in air and one in water
Pressure difference between RV-SG	capacitive metallic differential pressure transducer	$\pm(0.5\% - 7.15\%)$	Error dependent upon pressure difference

Chapter 3 Monitoring and control of the experimental parameters

In order to monitor, log, and control experimental parameters a control system was constructed. The System consists of :

1. Facilities active components: Pump, ventilators, and heating elements.
2. Facilities control devices: control valves, actuators, and power thyristors.
3. Measuring devices described before.
4. Two electrical control units (for power devices).
    4.1 Electrical control unit1: It provides electrical three phase $400V$ and two phase $230V$ power supply, switching relays, safety switches, electrical monitoring devices, power manual switches, and continues/alternating $24V$ voltage supply for measuring devices and some on/off valves.
    4.2 Electrical and control unit2: It provides three phase 400V and two phase 230V power supply, switching relays, safety switches, electrical monitoring devices, power thyristors to control steam electrical heaters continuously. The unit includes a physical programmable controller (IMAGO500) that can receives analog input measurements from the steam generator, process it, and generates driving signals for electrical heaters, control valve, safety valve, and feed water supply valve. Measured values and generated outputs besides set values are presented via an LCD screen and button manual input.
5. An Input/output unit.
6. Signals wiring.
7. Control program and associated software and drivers.

LabVIEW was used to build the control program. LabVIEW was developed by NI (National Instruments) and thus fully compatible with all related hardware, especially theDAQ. Using this program, it is possible to read analog or digital signals, process it, save it, generate analog or digital signal and implement all kinds of signal processing, signal controlling in a graphical environment and thus providing a powerful tool to work with measurements and control. As the first three components were already described before, this section will describe the last components 4, and 5. Figure 3.1 shows a schematic representation of this control system . The two electrical control units are not shown in his schema and they are explained in next chapter. Measuring devices provides measurements in form of a standard $4-20\ mA$ output signal or a voltage output $0-10$ Volt signal. The data acquisition unit (DAQ) receives these analog signals and transforms them into digital signals. The DAQ transfers the digitalized signals into the PC via a standard USB connection. The program can then transform these signals from current/voltage values into meaningful physical values depending on the calibration of each measuring device. The program contains all necessary controllers to control desired experimental parameters. These controllers generate the suitable driving signals into the active components and actuators and are transformed into current/voltage values inside the program. These signals go via the USB into the DAQ and are converted into analog signals via the suitable integrated module.

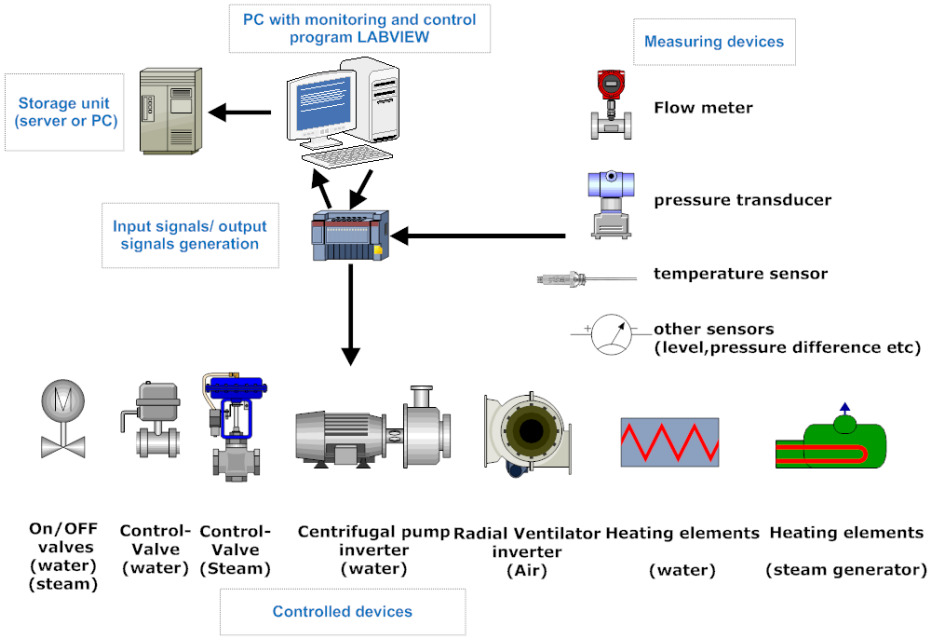

Figure 3.1 A schematic representation of the monitoring, data acquisition and control system in SCUBA and COLLIDER

3.1 Data acquisition unit

Figure 3.2 Data acquisition unit [http://sine.ni.com/nips/cds/view/p/lang/en/nid/207534]

Figure 3.2 shows the data acquisition unit(DAQ) NI cDAQ-9178 used to receive measurements signals and generates control signals. The unit is an 8-slot NI Compact DAQ USB chassis designed for small, portable, mixed-measurement test systems. cDAQ-9178 can be combined with up to eight NI C Series I/O modules for a custom analog input, analog output, digital I/O, and counter/timer measurement system. Modules are available for a variety of sensor measurements including thermocouples, RTDs, strain gages, load and pressure transducers, torque cells, accelerometers, flow meters, and microphones. NI Compact DAQ systems combine sensor measurements with voltage, current, and digital signals to create a custom, mixed-measurement systems with a single, simple USB cable back to the PC, laptop, or notebook [http://sine.ni.com/nips/cds/view/p/lang/en/nid/207534]. This makes it an optimal device for our application at the laboratory. In order to build the current control system, following modules were integrated to DAQ (Figure 3.3):

- NI 9208 current input C Series module: For analog current input signals. It has 16 channels of ±21 mA input with a built-in 50/60 Hz noise rejection.
- NI 9476: For remote on/off switching. It is a 32-channel, 500 µs sourcing digital output module. Each channel is compatible with 6 to 36 V signals, based on the external power supply, and features 1000 V (RMS) withstand isolation from channel to earth ground.
- The NI 9207 combination voltage and current input C Series module: For analog current and voltage input. It has eight channels of ±21.5 mA input and eight channels of ±10 V input with built-in 50/60 Hz noise rejection.
- The NI 9265: For analog current output. It is a 4-channel, 0 to 20 mA, 100 kS/s simultaneously updating C Series analog output module. The NI 9265 is ideal for interfacing and controlling industrial current-driven actuators at high rates.

Figure 3.3 the Input/output modules used within the data acquisition unit of the control system. Left to right: NI 9207, NI 9476, NI 9208, NI 9265[http://sine.ni.com/nips/cds/view/p/lang/en/nid/208808].

3.2 Control program

Labview was chosen as a programming language because of its versatile capabilities and its compatibility with National Instruments hardware which is automatically recognized when the program is installed (plug and play). Once plugged, it becomes possible to configure a certain device by means of built-in routines and functionalities. Labview allows building a graphical user interface which is of great advantage in such applications. Figure 3.4 shows a simplified structure of the designed control program.

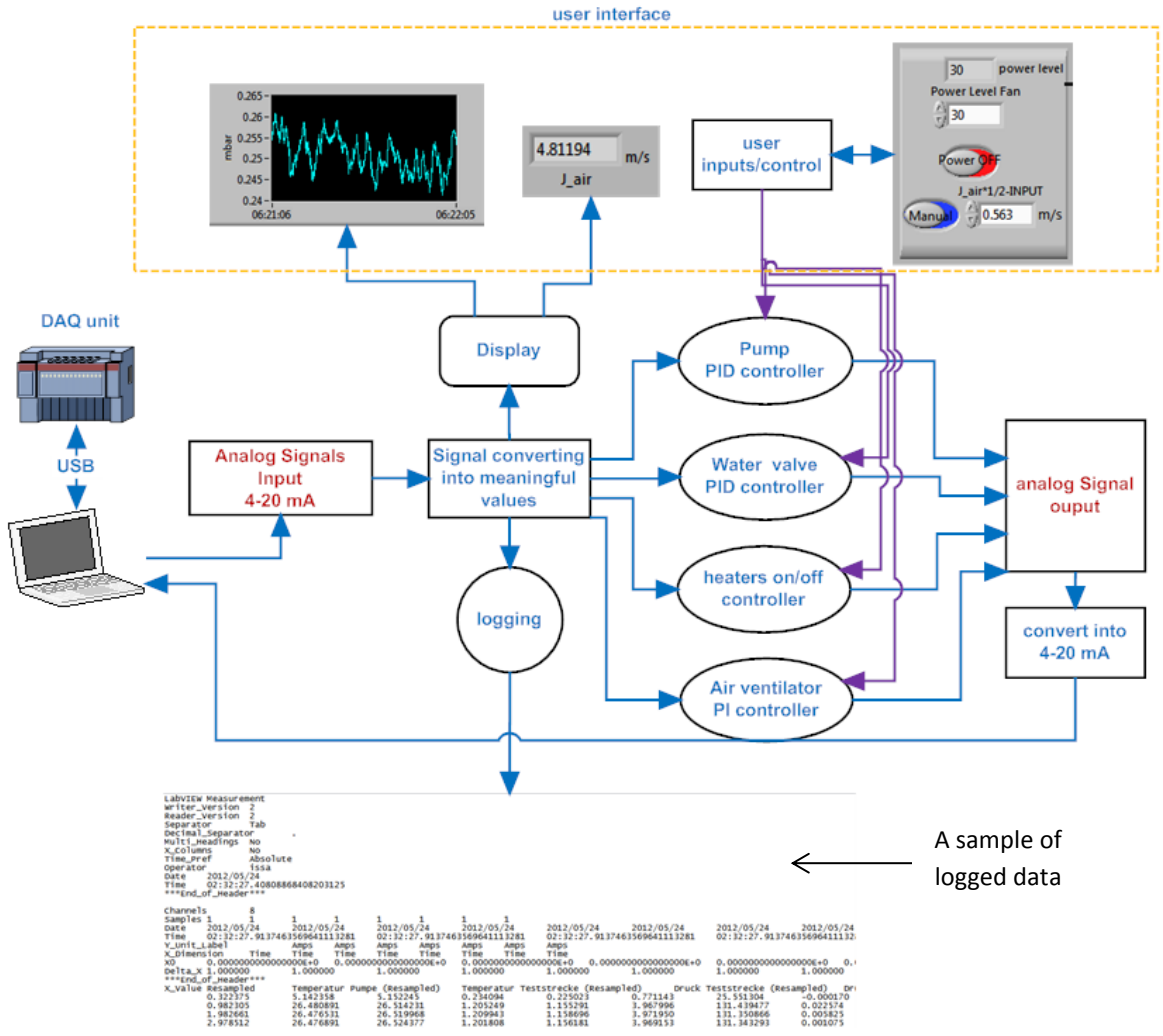

Figure 3.4 A schematic representation of the structure of the control Labview-based program.

The control program works according to the following steps and subroutines::

- Grabbing of input signals: The program receives digital inputs in form of current/voltage signals from the DAQ. Each value is linearly proportional to the measured parameter
- Converting current/voltage values into meaningful physical values: temperature, pressure, flow rates and level values. This is done relaying upon calibration curve of each measuring device.
- Processing of obtained values: addition/subtraction/root square/building matrixes/….etc. these extracted values can then be saved according to user-input log time into the work PC or used within the controllers.
- Building control feedback loops that included PID,PI, ON/OFF controllers for active components: pump, ventilator, heating elements (steam, and water), and control valves. These controllers set and maintain experimental parameters at desired user values. PI controllers were used for controlling loops containing flowmeters such as water/steam/air velocities. PI controllers provide a more stable response since they do not include a differential part that is highly affected by fluctuations of flow rates. PID

controller was used to control temperature (and thus saturation pressure) inside the steam generator. Parameters of the PID controllers were determined either by:

- Conducting a standard calibration procedure: performing a step-input and analyzing the output response characteristics.
- Try/error procedures relying on some empirical relations.

- Generation of the output analog driving signals: these were either a standard $4-20\ mA$ signals or on/off (0/24 V) signals:
  - Continues control of: pump and ventilator rotation per second.
  - Position of steam control valve and water control valve.
  - Heaters in steam generators (with help of installed power thyristors).
  - On/off control signals for on/off powering of all electrical devices from the user interface. On/off control was used for following devices as well:
    - Water supply into steam generator and water storage tank.
    - For each individual heating element in water storage tank: As each heating element out of the five 4kW elements can be either switched on or off, no continuous control is possible. Instead, power was set into six power levels: 0,4,8,12,16, and 20 kW. The suitable power level was determined depending on two parameters: the temperature difference between the measured water temperature and the user set-temperature and the rate at which the water temperature rise for each corresponding power level ($\mathrm{K/s}$). the latter was determined experimentally by running the loop at the corresponding power level and measuring the corresponding temperature change rate which will account for all affecting factors as heat loss and mixing inside the tank. This allowed a satisfactory control of the set temperature ($\mp 0.5\ K$).
    - Safety steam bypass valve within the steam line.
- User interface: A schematic representation of both facilities appears in the background to help the identification of monitored graphs, values, and controls. The interface shows:
  - Numerical instantaneous values of measured experimental values.
  - Graphical representation of some measured values as flow rates, temperatures, , water level and pressures. These graphs shows the parameter change within 60 seconds history and thus helps the user to determine the type of response for each occurring change in the experimental facilities.
  - Converted flow parameters according to different scale/definition/ to facilitate the determination of actual flow conditions (for ex Wallis parameters for water/air in COLLODER)
  - On/Off switches for all electrical components.
  - Manual control of all active components: Pump/ventilator/automated valves.
  - Input of the set values of flow parameters for automatic controllers: hot water temperature in SCUBA, water temperature inside steam generator, and all flow rates.

Figure 3.5 shows a screen snapshot of the developed interface. The schema of SCUBA and COLLIDER can be seen as a schematic drawing of water/air/steam circulation. The water tanks were integrated with a visual changing water level to help monitoring these levels easily. Switch controls can be seen for each component. The graphical graphs shows 60 seconds plot of each monitored variable. The log file control can be seen at the bottom. logging control is possible online .

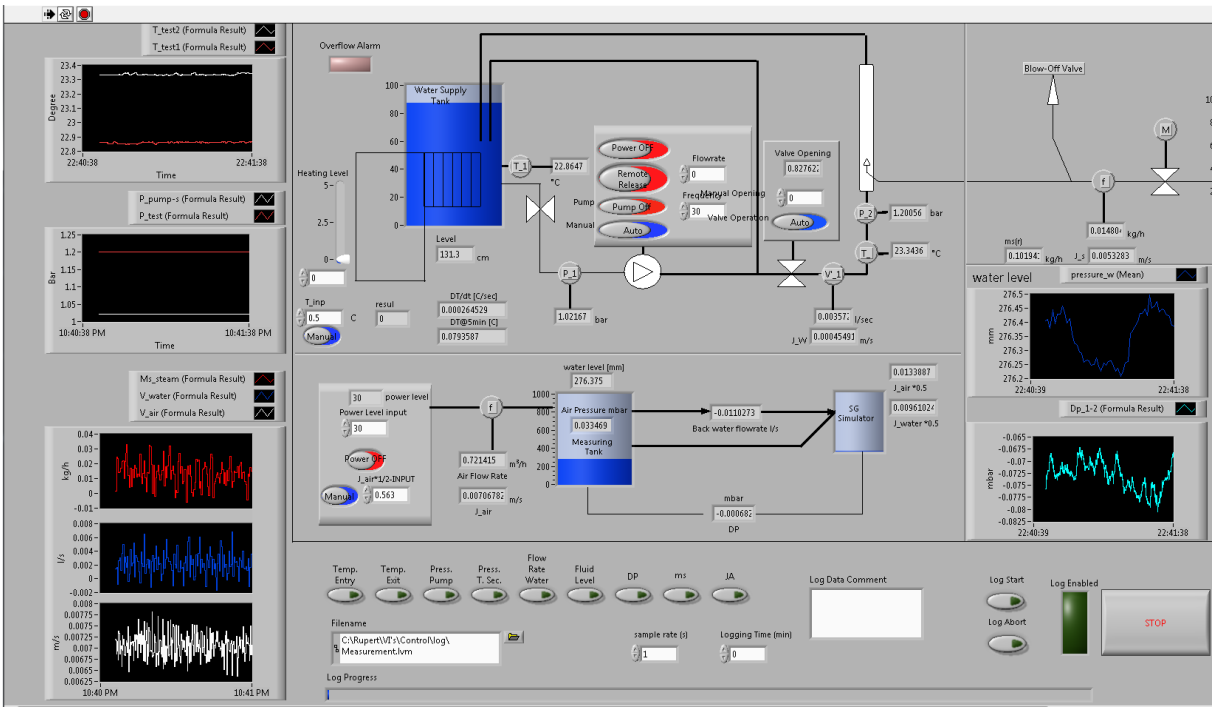

Figure 3.5 A snapshot of the control program user's interface.

3.3 Electrical control units

3.3.1 Unit1

Figure 3.6 illustrates a general schematic representation of the electrical control unit1. The main purpose of this unit is to control power supply for all electrical power units: heaters, pump, ventilator, and to provide the basic electrical protection. The unit provides also the power supply for measuring devices, valves, relays, and inverters. It includes also all safety control relays and some controllers for some devices. This unit was designed according to the following three levels:

1. Power supply and protection:
    - Power switches (400 VAC supply): Main power switch, individual on-board manual power switches for each device.
    - Basic electrical protection: differential current switches for heating elements and motor protection for pump and ventilator.
    - Low voltage supply: 230 VAC Supply for some switches, magnetic valves and measuring devices. 24VAC, 24VDC Supply for powering measurement devices and relays.

2. Safety relays:. These are relays that control safe operation of both loops such as: low pressure (low water level, dry run) at pumps suction side, low water level in SCUBA water tank, pump overheating, temperature inside heating elements..etc. These relays receive the driving signal from different independent controllers that relies upon a measured signal value: pressure, temperature, or water level. Many devices have its own controller that is independent from the control program and thus cannot be affected by the user.
3. External/user control: External on/off switching of all devices and driving signals for continuous control that comes from control program and user input.

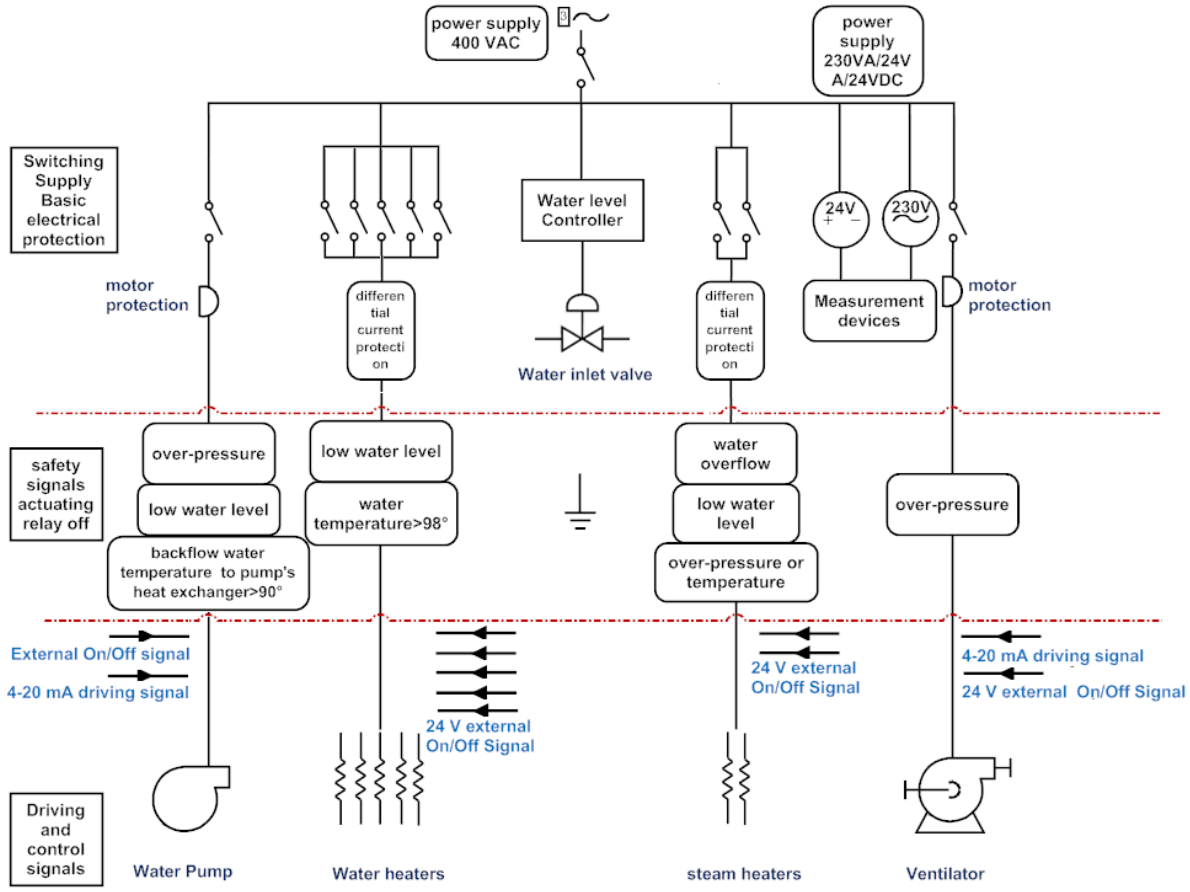

Figure 3.6 Schematic representation of the electrical control unit1. Unit 1 provides 3phase 400VAC, 230VAC, 24VAC, 24VDC supply for electrical devices, measurement devices

The water level controller that controls the DI water level in the water storage tank was integrated into this unit. It receives a pressure signal from the bottom of the water storage tank and converts it into water level value. It delivers three outputs for safety relays of: pump's low water level, heaters' low water level, and water overflow. It also actuates the DI feed water inlet magnetic valve on or off. The Heating elements are also provided with a physical controller that receives temperature signal from the water tank and switch off heating elements when temperature is above $98° C$ or above a preset temperature. It also switches heaters off when the built-in internal temperature sensor exceeds $100°C$ providing a built-in anti-brand-system (ABS) for extra safety. Figure 3.7 shows a real image of the control unit 1.

Figure 3.7 Electrical control unit 1. Left: open view with all components and internal connections. Right: closed view.

3.3.2 Unit2

Electrical control unit 2 controls power supply into the steam generator and includes a physical controller (IMAGO500, independent from the control program) for steam generation. The unit has two power thyrisotrs in order to control power supply into heating elements continuously; which enables the steam controller to set the temperature (and thus saturation pressure) precisely within the steam generator. The unit provides 230 VAC, 24 VAC, and 24 VDC for measuring devices, switches, and control valves attached to the steam generator. The IMAGO500 controller is capable of receiving different kinds of measurement signals (voltage/current, analog/digital) processing it, building PID,PI,I or switch controllers, and generating driving signals in a similar way to the built control program. The reason why the steam generation was controlled via a physical controller rather than a user-built controller is to guarantee an extra level of safety. The preset values in the physical controller are protected and well configured so that any failure of any measuring device lets the steam generation stops immediately and the open all safety valves. Figure 3.8 shows a schematic representation of this unit. Figure 3.9 shows a real image of the unit.

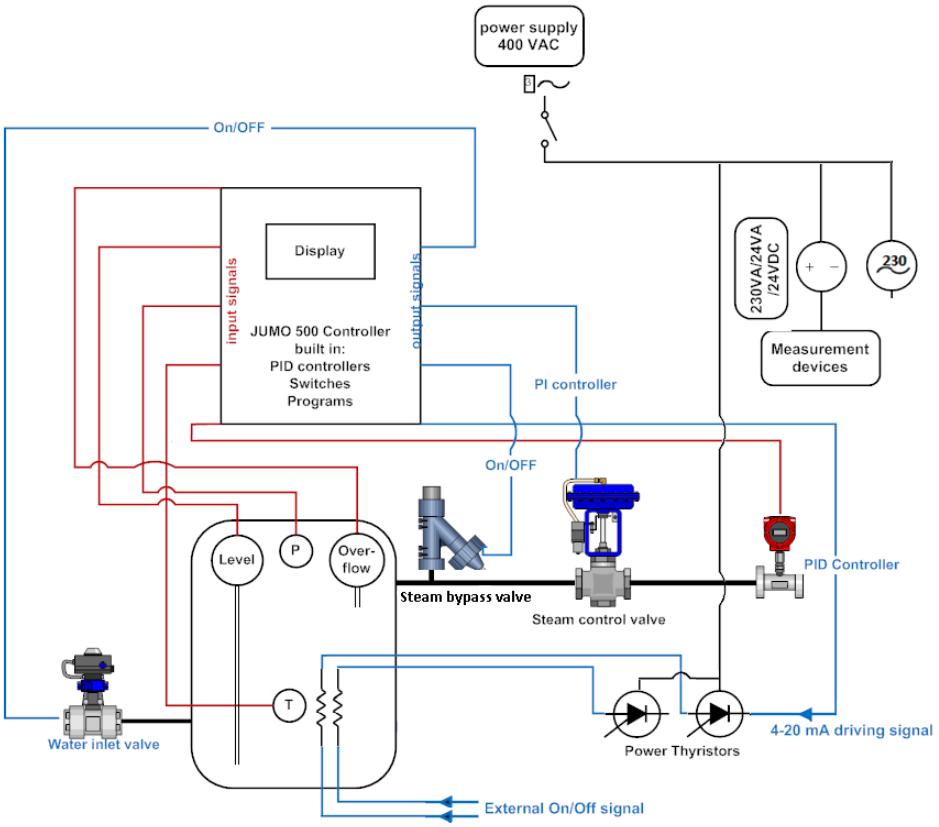

Figure 3.8 electrical control unit 2. Input signals are shown in red. Output signals are shown in blue. The type of the applied controller is written for each control signal.

Figure 3.9 Electrical control unit 2. Left: Open, power thyristors can be seen at the upper-right corner. Right: The interface of the controller.

Chapter 4 High speed recording (HSC)

The use of high speed recording to investigate bubbles behavior is frequent. The technique is non-intrusive and provides an excellent look into some bubbles characteristics or behavior that cannot be easily observed via other techniques, such as the bubble shape, surface structure, distortion, and bubble movement. In case of most other techniques that is applied into an opaque channel like: gamma/neutron/fast X-ray tomography, needle probes, or wire mesh sensors, only reconstructed results of the over mentioned characteristics can be retrieved. Reconstruction errors exist, and final reconstructed results cannot be judged via the behavior observed directly by the experimentalist through videos and images provided by the HSC. This is a unique advantage of using HSC over other techniques, and is very favorable in the field of bubbles behavior investigations. However HSC has also its limits and restrictions. Using one camera delivers only a 2D projection of the observed volume-of-interest. And thus all measurements obtained from these projections should consider this fact. For instance the existence of a dense bubbles' swarm where bubbles are screening each other, limits the ability to automatically track bubbles diameters via this technique, and if the density of the bubbles is very high only the behavior of the bubbles at the front side of the flow can be studied. This can be improved in some cases by using more than one camera. A second camera from a second perpendicular direction is the most applied set-up and sometimes third one was placed to acquire images from atop. The development of more advanced and complicated image-processing procedures can also help to avoid this limitation, however not in the case of densely-distributed bubbly flows. Most elaborated investigations of bubbles behavior that were performed using HSC were carried out with air bubbles. Air bubbles has a smooth surface and a constant volume and thus experiments with air bubbles are a simple case- compared to condensing steam bubbles- to start with in order to develop bubbles identification and tracking algorithms. Additionally there exists a sufficient amount of data in the literature over the behavior of single air bubbles in a stagnant liquid such as rising or terminal velocities and movement behavior which are performed by many investigators. This makes them a favorable test case for the verification of the developed procedures, by using the already known characteristics to validate the results of the procedures. Table 4.1 lists some of investigations found in literature over air bubbles rising in a stagnant water. All these investigations were carried out via injecting air bubbles into a stagnant water using different injection methods. The table gives basic characteristics of the applied HSC in each case and specially the achieved resolution and measurement error. Most of studies use a frame rate between $30 - 1000$ frame/second. Error of the bubbles' diameter estimation was typically between $2\% - 8\%$, while the estimation of bubbles velocity was little bit higher due to multiple error sources (length and time). Some studies used a fixed camera with a high spatial resolution to track bubbles geometrical parameters and a second moving camera with a lower spatial resolution to track bubbles velocity. Some investigations used two high-resolution cameras to acquire a 3D acquisition of the bubble surface.

Table 4.1 A comparison of different high-speed recording experiments out of literature.

Article	Video camera type	Resolution	Frame rate [f/s]	Measurement Error	Injection nozzle diameter[mm]	Bubble diameter range[mm]
Wu et al (2002)	Kodak Ektapro Motion Analyzer, 1000 HRC+3D imaging system	512×384	1000	$\pm 0.01\ mm$ bubble diameter ($\sim 1\%$)	0.31-0.44	$1 - 2$
Tomiyama et al (2002)	2 HSCs Kodak Motion Corder Analyzer SR-1000	512×512	250	$5.2\% - 6.8\%$ for bubble velocity and $2.9\% - 8\%$ for diameter	$0.51, 0.90, 1.45\ and\ 3.19$	$0.7 - 5.5$
Sam et al. (1995)	Moving Camera: for terminal velocity (Sony, Hi8-V801) - Stationary camera (Canon, EOS-lOOOF) for bubble size and shape	-	30	∓ 0.1 mm spatial resolution $(4 - 11\%)$	$(17, 70, 203\ and\ 508) \times 10^{-3}$	$0.9, 1.5, 2.2\ and\ 2.7$
Patro et al (2000)	Two monochrome VHS video cameras one for shape and size and one for velocity	$1.4 \times 2cm$ for $110mm$ lens $2.9 \times 4cm$ for $55mm$ lens $21.4 \times 30.0cm$ Terminal velocity	250			$0.36 - 4.40$
Okawa et al (2002)	Two High-speed video camera (Speedcam 512 Weinberger	1024x1024	250	± 0.1 mm diameter $(3 - 17\%)$ $\pm 2\ mm.s^{-1}$ terminal velocity	$0.1 - 1$	$0.6 - 3.7\ mm$
Celata et al (2005)	HIGH-speed video camera (Speedcam 512 Weinberger)	512 x 512	1000	$\pm 5.2\%$ for terminal velocity and $\pm 10.0\%$ average rms for the diameter	$5.0, 4.0, 2.5, 1.8, 0.9\ and\ 0.5$	$0.1 - 6mm$

Many of investigations used special programs for calculation of bubbles parameters such as the bubble size, shape, and terminal velocity. In these cases no description of the used-programs was provided. Those who developed their own procedures for bubbles identification did not provide a detailed description of this procedure and in general the focus was laid upon analysis of the obtained results and flow characteristics (terminal velocity, temperature effect, initial distortion and bubbles motion) more than the description of the used algorithms. In many cases there was no identification of the error resulting from processing the results, and thus one cannot judge the accuracy of the measured parameters regarding this error. In many cases, a single bubble was tracked. This case does not require the development and test of complicated tracking schemes since only one bubble exists in all acquired images (if the noise removal treatment was working properly) . In most cases only one camera was used to acquire raw images. The use of a second camera is expensive and in the case of a single bubble it will not bring a lot of additional information especially regarding the measurement of the geometrical parameters. Tomiyama et al. (2002) mentioned a maximum difference of 10% for the aspect ratio when another camera was deployed in the perpendicular direction. A considerable added-value of the use of a second camera can be achieved when images are recorded from the top, however which this is usually not a practically achievable set-up. In order to give an idea over the resolution by which bubbles were recorded using HSC a set of figures obtained from different investigations in the literature were provided in Figure 4.. Some processed images were also provided.

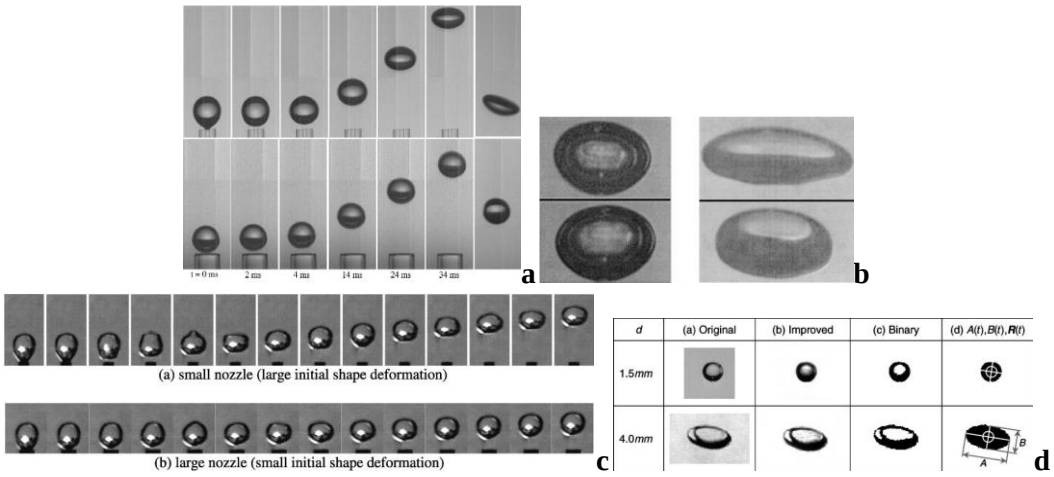

Figure 4.1: Examples of the HSC raw images captured by different authors. a: Wu et. Al. (2002), b:Patro et al (2000).c+d: Tomiyama et al. (2002).(c: raw, d:some processed images)

4.1 Bubble identification and tracking's procedures

This section will describe briefly the main algorithms implemented in the developed procedures used for the current work. The actual procedures contain a lot of programming solutions that cannot be shown within the current scope of this chapter. These procedures were first verified and applied into the case of air bubbles since it is a simpler case as steam bubbles. Section 4.1.4 will show the verification done through experiments. These experiments were performed using air injected into still DI water and by applying different sizes of injection nozzles. The objective of these experiments was to verify the developed

procedures and to provide an initial piece of information about the resulting bubbles size and behavior from different injection nozzle sizes. This was carried prior to the steam bubbles experiments to help designing the injection nozzles for experimental investigation of the steam bubbles.

4.1.1 Subtraction of background out of raw images

A frequent used method to subtract the background noise is to record an image without bubbles (so called a reference image) and then subtract it from all images with bubble. This method is easy but has its disadvantages. For instance, there exists no guarantee for a specific pixel in the reference image to have the same intensity in all subsequent images that contain bubbles for many reasons: mechanical vibration, optical reflections from the surrounding and by the bubbles themselves, unsteady light source, etc. This will cause the subtraction process to leave some noise that can be attached to the actual bubbles image. In order to avoid this case and to build a procedure that is independent form all small optical variations, and vibrations that can occur during experiments another method was adopted. Since bubbles appear as dark moving spots in the recorded images; it becomes possible to subtract them using intensity. Intensity variations between different mages can be taken into consideration by setting a dynamic limit. This means that each image can be scanned to calculate the minimum and the maximum intensities. Depending upon these two values, the intensity limit can be defined as a ratio of the full existing range:

$$if\ I_{xy} < \delta_{\text{limit}}(I_{max}[n] - I_{min}[n]) \Rightarrow P(x,y)\ belongs\ to\ a\ possible\ bubble,$$
$$else\ set\ P(x,y) \rightarrow white$$

Setting the limit δ_{limit}, is done manually by applying the filter to few arbitrary images and finding out the optimal value. Once this limit is set, it remains constant for all images acquired in the same experiment with the same set-up, focus, and lighting. Figure 4.2 shows how the variation of this limit influences the identified part of the bubble and amount of remaining noise. There exists always an optimal choice for this limit in each experiment that balances between the accuracy of bubbles extraction and amount of remaining noise. In figure 4.2, image (e) represents the optimal choice for the value of this limit. Values below do not extract the whole area of the bubble and values above get a lot of remaining noise as in image (f)

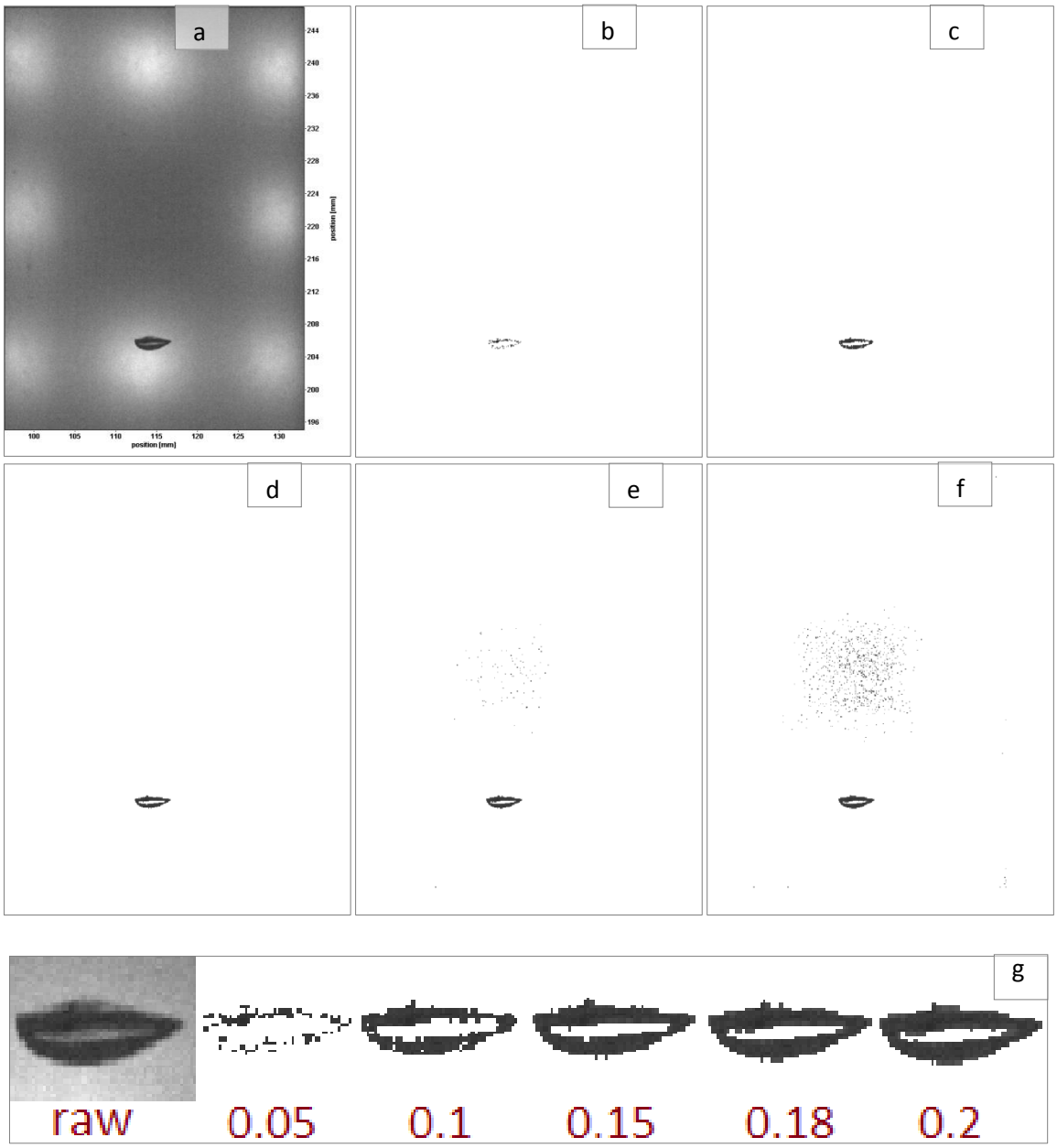

Figure 4.2: The influence of the intensity limit upon the extracted bubble's area and the amount of remaining noise: (a): Raw image, (b-f) processed images with different intensity limits: 0.05, 0.1, 0.15, 0.18 and 0.2 (b-f respectively). Image (g) shows the recognized bubble area in each case more clearly.

4.1.2 Bubble identification bubbles' parameters calculation

After the subtraction of the background by the intensity limit, the processed mage will contain the extracted bubbles and few remaining noise spots. Figure 4.2 (e) shows this typical case. At this point of the identification procedure all remaining dark pixels belong to a possible bubble. The elimination of the remaining noise using an intensity differences is not ideal, since some bubbles pixels can appears with a similar intensity to noise pixels. The first step for a further processing is to identify each separate group of remaining non-white pixels (dark spots). In this way, the procedure will have the ability to apply other criteria for a further processing. The procedure scans the image, and search for non-white pixels. Once one is found, the

procedure starts to search for all non-white pixels connected to this pixel and then gives all these pixels the same identifier (=number). This is repeated until all pixels belonging to the same spot are assigned by the same identifier. Then the rest of the image is scanned, and the same treatment is repeated until all image pixels are scanned and all spots are identified. At the end of this treatment, each of the image's pixels will be assigned either with a number n if belongs to a dark spot (=possible bubble), or 0 if it belongs to a white pixel (=water). Now the area of each spot n can be calculated as follows:

$$A_n = \sum_{identifier(P(x,y))=n} \xi^2 \quad (4.1)$$

Where ξ is the calibration factor [mm/pixel]. After the calculation of the area of each spot n, an area limit can be applied to eliminate the residual noise.

$$if\ A_n < A_{limit} \Rightarrow set\ all\ I(x,y)_{identifier=n}\ to\ white$$

This limit takes advantage of the fact that the majority of the remaining noise after the intensity limit is applied consists of spots with a remarkably smaller area than real bubbles as it can be seen in Figure 4.2(e). This limit depends upon flow conditions in each experiment and should be set carefully after examining some of the acquired images. Once it is set, it applies to all images of a specific experiment if the optical set-up was not changed considerably during the experiment (small variations do not affect this limit). Pixels that belong to noise are set into white pixels. After application of this limit a clean processed image that is composed of identified bubbles and white background should be obtained.

Figure 4.3(b) shows the result of applying the area limit to the image shown in figure 4.2(e). All noise is removed and only bubble the image remains. Figure 4.3(d) shows another example that includes many bubbles.

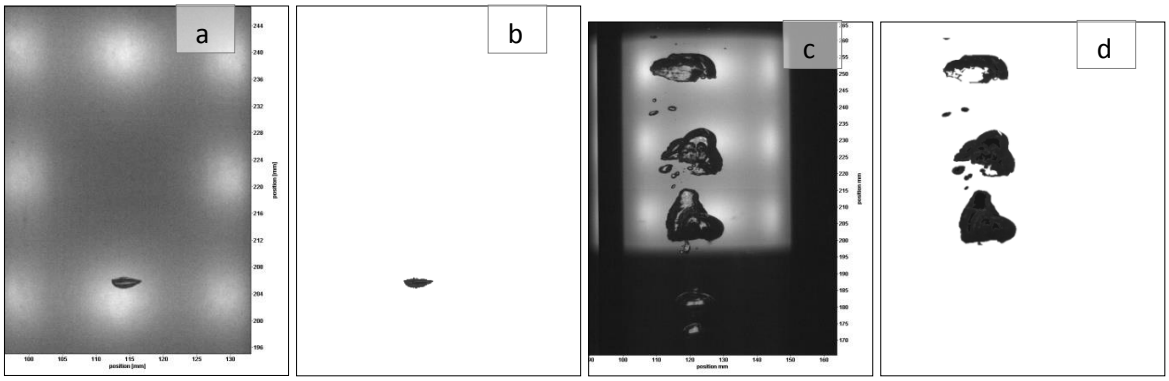

Figure 4.3 Application of the intensity limit and area limit to raw images. Images (a)+(b): case of a single bubble. Images (c)+(d): case of many bubbles. Note: In addition to the intensity and area limits, the white reflection at the bubbles center was filled automatically by a further processing.

After the application of the area limit all remaining spots are then considered as bubbles and pixels of each bubble have the same unique identifier. However some bubbles have a lot of white reflections at their centre as it can be seen in figure 4.2(g). The existence of these reflections can affect the correct calculation of bubbles parameters considerably. Pixels of the white reflections do not have the bubble identifier and thus are not considered into the

calculation of the bubbles area and other parameters. In order to overcome this problem, a special algorithm was developed to automatically fill the majority of these reflections. The algorithm search for white pixels that appears near bubbles center. If these spots are completely encircled inside the same bubble, they are given the same identifier of the same surrounding bubble and are artificially coloured by a dark colour. This part of the procedure uses complicated algorithms that cannot be explained within the current section. Figure 4.3 (b)+(d) shows the result of the application of this treatment (also compare Figure 4.2(e) and Figure 4.3 (b)). Most of the white reflections are attached to the corresponding bubble except when these reflections are not fully encircled by the bubble (Figure 4.3 (d), the last bubble on top). After the raw images pass through the intensity limit, the area limit and filling procedure of the white reflections, bubbles' parameters can be calculated according to the following equations:

The maximum horizontal and vertical axes for each bubble, $ax_{n,t}, ay_{n,t}$ (assuming an elliptical bubble shape, they represent the horizontal and vertical axis of the ellipse). Their ratio gives the aspect ratio of the corresponding bubble:

$$\left.\begin{aligned} ax_{n,t} &= \max(x) - \min(x)|_{identifier(x,y)=n} \\ ay_{n,t} &= \max(y) - \min(y)|_{identifier(x,y)=n} \end{aligned}\right\} \quad (4.2)$$

Position of the bubble: there are two methods:

First: considers the center of above both axes $ax_{n,t}, ay_{n,t}$: this method is more accurate for small air bubbles:

$$\left.\begin{aligned} x_{n,t} &= \frac{\max(x)+\min(x)}{2}\Big|_{identifier(x,y)=n} \\ y_{n,t} &= \frac{\max(x)+\min(x)}{2}\Big|_{identifier(x,y)=n} \end{aligned}\right\} \quad (4.3a)$$

Second: considers the center-of-mass of the identified bubble: this method is more accurate for large or highly-deformed bubbles:

$$\left.\begin{aligned} x_{n,t} &= \frac{\sum x|_{identifier(x,y)=n}}{\sum 1|_{identifier(x,y)=n}} \\ y_{n,t} &= \frac{\sum y|_{identifier(x,y)=n}}{\sum 1|_{identifier(x,y)=n}} \end{aligned}\right\} \quad (4.3b)$$

Circle equivalent diameter: of the bubble area, $D_{eq,n,t}$

$$D_{eq,n,t} = \sqrt{\frac{4.A_{n,t}}{\pi}} \quad (4.4)$$

Ellipse equivalent diameter

$$D_{eq,n,t} = \sqrt{ax_{n,t}.ay_{n,t}} \quad (4.5)$$

4.1.3 Bubbles tracking

If more than one bubble is present, a tracking procedure is required to track a specific bubble through different frames and calculate further parameters such as the rising velocity, lateral velocities, and movement path. The most well-known algorithm to achieve such a purpose is to perform a 2D cross-correlation between each two successive frames. However this method is extremely time-consuming and does not serve the objective of processing large number of images effectively. Moreover, this algorithm is required when lot of bubbles exist in the same frame with a considerable amount of overlapping, and thus a very precise treatment is required. In order to simplify this step, a more simplified approach was considered. In this approach bubbles are treated as moving points whose vertical/lateral displacements between two successive frames are limited by a specific number of pixels. This assumption is also supported by the use of a high frame rate and low probability of overlapping. The tracking procedure searches in frame $\mathrm{t}+1$ for bubbles $\acute{n}$ that can match a bubble n in frame t. The search criteria are defined by a search-box as follows:

$$x_n - x_{lim} < x_{\acute{n}} < x_n + x_{lim}, \quad and \quad y_n - y_{lim} < y_{\acute{n}} < y_n + y_{lim} \tag{4.6}$$

Where x_{lim}, y_{lim} are limits which are set manually according to each flow condition Practically the criterion is valid for all bubbles acquired in the same experiment and thus it does not need to be changed a lot. However, this criterion is valid when bubble displacement between two successive frames is small; this is valid when images are recorded at a high frame rate. Results should be checked to assure that the procedure is identifying bubbles correctly. Despite the manual setting of the search criteria limits and the need to check results this method is extremely robust and fast in comparison to a 2D cross correlation. The time needed to check the results and determine the optimal limits is very small (1-2 hours depending on the amount of processed data). The procedure can process the results from 100000 images in a 10 minutes time. Figure 4.4 illustrates the functionality of the tracking algorithm. The tracking algorithm provides an additional filtering to the identified bubbles. If some noise was dark enough to escape the intensity limit filter, and large enough to escape the area limit filter, it can still be filtered after the tracking is performed. This kind of noise can come from air bubbles that stick to the outer wall of the test section (for example: inside the aquarium), or can arise from some arbitrary reflections during the experiments. In both cases these parts are either stationary or do not appear through many frames. After running the tracking procedure, the number of instances “frames count” through which each bubble exist, and the total travel path can be obtained. Consequently bubbles of very low “frames count” or very short traveling path can be easily neglected. The combined filters applied in the identification and the tracking procedures allow an automated time-efficient and accurate processing of a large number of frames (10000-100000 frames). This makes the HSC along with the procedures a powerful tool for investigation of bubbly flows that do not have a lot of overlapping.

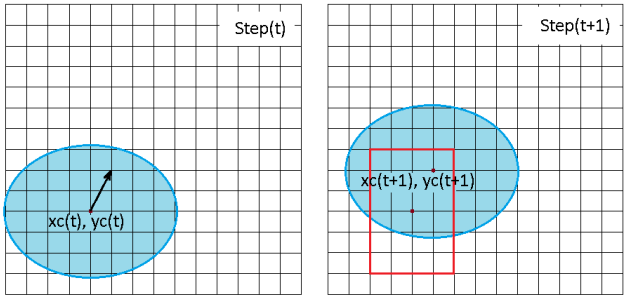

Figure 4.4: Illustration of the third step of the procedure.

4.1.4 Verification through experiments

The experiments which are described in next sections were carried out to test and verify the work of the described procedures in a well-studied case: air bubbles rising in a stagnant water column. In these experiments, air is injected via different nozzles size into the water column generating a single bubble or a train of bubbles. The objective of these experiments was to verify and develop the performance of the identification and tracking algorithms (main objective), and to study the effect of the nozzle size upon the resulting bubble size (secondary objective). The use of different nozzle sizes also allowed the generation of different bubbles sizes which was essential for the verification of the calculation of bubbles rising velocity. The result of the relation between the nozzle size and the average equivalent diameter of the obtained bubbles is irrelevant to the current work. However these experiments provided a pre-knowledge for the design of the steam injection nozzles.

4.1.4.1 Experimental Set-up

Experiments were carried out in a circular transparent pipe of 100 mm inner diameter. The pipe has a length of 1m which allows bubbles to reach their terminal velocity at the upper end. The pipe was filled with distilled water, and was surrounded by a water jacket in order to avoid image distortion through pipe geometry. Although the experiments could have been done within the rectangular surrounding aquarium (without the pipe), this set-up was used to be identical with the test section in which the steam bubbles condensation is going to be investigated. Air was injected into the bottom of the pipe through different nozzles with different inner diameters: $2, 3, 4, 5, 6,$ and 8 mm were applied in order to generate bubbles with different sizes. As a result, bubbles with an equivalent diameter between $3 - 9$ mm were generated. Experiments were conducted under atmospheric pressure and room temperature. A high speed camera (LaVision Imager Pro 4M with max 1279 frame/second @ 2016×2016 pixels) was used to record the movement and size of the bubble. Air flow was supplied directly from a pressure tank controlled by a valve and a bypass (Figure 4.5).

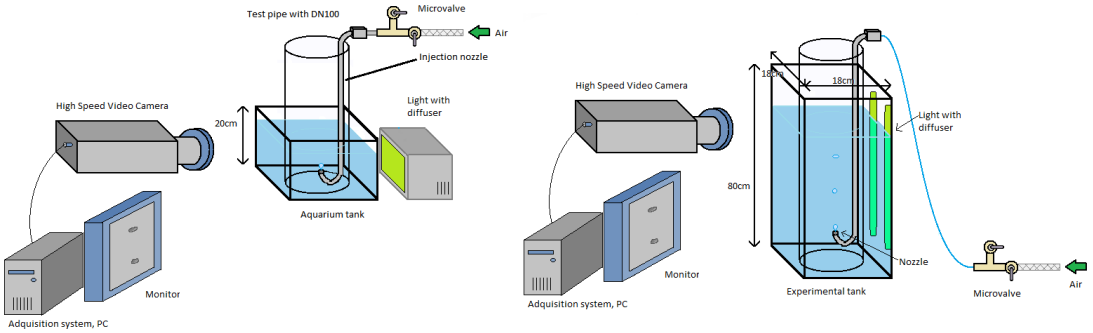

Figure 4.5 Experimental set-up. Left: The set-up adopted for train of bubbles. Right: the set-up adopted for a single bubble.

Two set-ups were used according to the objective of the experiment. Figure 4.5 (left) shows the set-up used for studying the case of a train of bubbles. The camera was placed close to the injection nozzle to capture the bubbles during growth and detachment off the injection nozzle (10×10 cm window). This case was used to test capability of the procedure to track more than one bubble simultaneously and in the case of a volume change. The terminal velocity was not controlled in these experiments because the camera is close to the injection (no enough rising distance) and the effect of the initial air velocity is not neglected. Figure 4.5 (right) shows the set-up used for studying the case of a single bubble. The camera was placed close to the top of the pipe to measure the terminal velocity. This case was used to verify if procedure is capable of correctly predicting the bubbles' terminal velocity. Both experimental set-ups are well used literature and thus enough pre-knowledge is available for the verification of the developed algorithms before application into the case of steam bubbles.

4.1.4.2 Existence of multiple bubbles: Train of bubbles

Figure 4.6 shows typical raw images from the $2,\ 3, 4, 5, 6$ and 8 mm nozzles. Processed images after the application of the intensity limit, and area limit filters (second row), and the filling algorithm (third row). All background was taken away, bubbles were extracted well and white reflections inside bubbles were filled automatically.

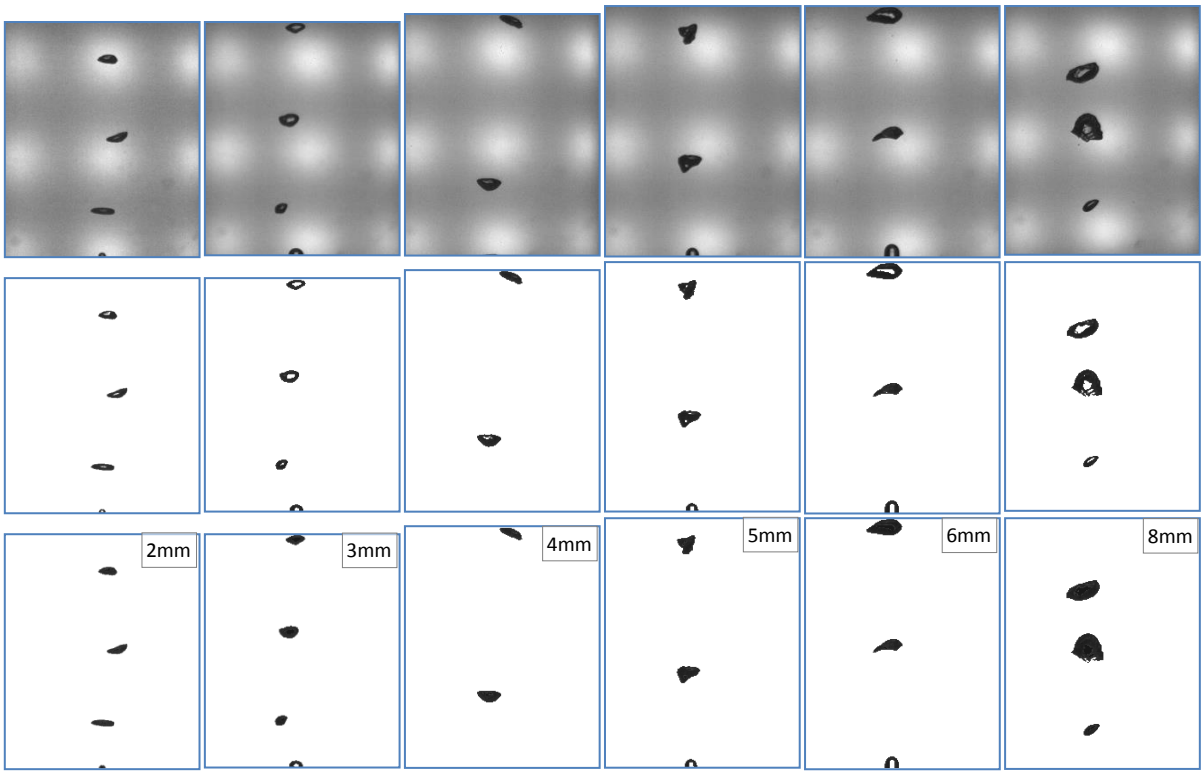

Figure 4.6 Raw images and processed images from different nozzle sizes. Upper row: raw images, Middle row: intensity and area limit filters applied, white reflections comes at the center of bubbles, lower row: the filling algorithm fills most of the white reflections.

Figure 4.7 shows paths of all tracked bubbles during 0.5 second. The paths show that multiple bubbles were tracked correctly by the procedure. Paths that do not start from the injection point belong to bubbles that were already detached at the HSC acquisition. The bubbles behaviour and movement can be judged and evaluated from these paths.

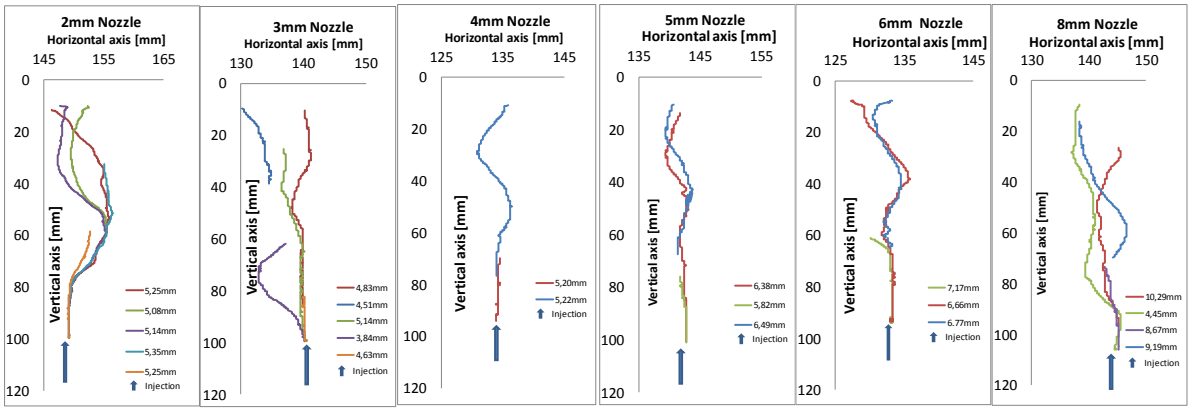

Figure 4.7 Paths of all tracked bubbles during 0.5 second of acquisition from different injection nozzles.

Figure 4.8 shows the growth of the bubble diameter along time during detachment. The fluctuations of the bubbles diameter after detachment are within $\pm 16\%$ of the average value. These fluctuations are caused by shape deformations that change the bubble's projected area (see figure 4.9). The correct average diameter can still be well estimated in case of a constant bubble volume (air bubble). When a volume change happens, like in the case of bubble growth at the injection nozzle and bubble condensation, the effect of the volume change upon

the bubble equivalent diameter are remarkably larger than those caused by shape fluctuations (as it can be seen in figure 4.8). In these cases, the instantaneous equivalent diameter can be used to estimate the bubble's growth or shrinking rate. The accuracy of the obtained bubble diameter depends also on the spatial resolution, this can be seen in figure 4.8 by comparing the plots obtained in the case of the 2mm injection nozzle (0.152 mm/Pixel) and the 3mm injection nozzle (0.333 mm/pixel).

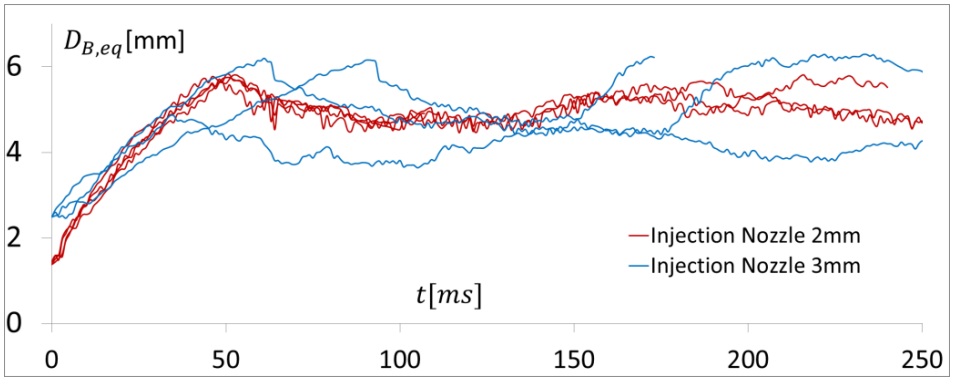

Figure 4.8 Tracking of bubbles equivalent diameter during growth and detachment of the injection nozzle. Fluctuations of the equivalent diameter after the detachment are due to shape fluctuations (figure 4.9).

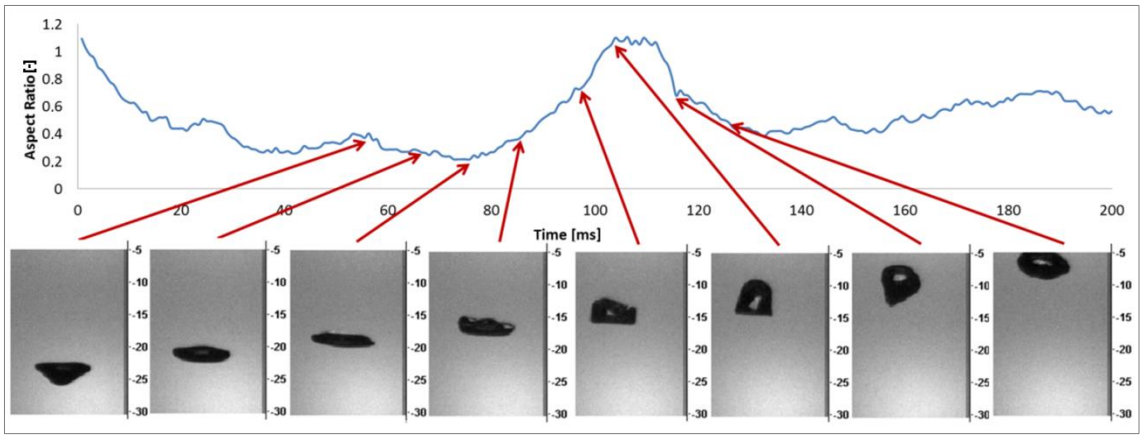

Figure 4.9 Fluctuations of the bubble shape and aspect ratio after detachment off the injection nozzle. Shape fluctuations affect the 2D projected area and eventually the instantaneous equivalent diameter.

Figure 4.9 shows fluctuations of the aspect ratio as a result of the periodic change bubble shape deformation after the detachment off the injection nozzle. These fluctuations were an interesting observation through the air bubbles experiments. They indicated that even in a still water and with a relatively low injection gas velocity, bubbles can suffer a considerable amount of shape deformations and diameter fluctuations. These deformations were sometimes (as shown in figure 4.9) sudden and large. They indicated a behaviour that may be also noticed within steam bubbles experiments. Through these experiments the functionality and performance of the tracking procedure was tested and developed.

4.1.4.3 Gentle injection of a single bubble, verification of the terminal velocity

In this case only one single bubble was recorded during an acquisition time of 0.5 seconds. This was accomplished by controlling the injection valve and the bypass valve in order to maintain a bubbles-generation frequency as low as possible to assume a non-zero initial velocity. The aim of these experiments is to validate weather the procedure is able to reproduce correct terminal velocities of the studied bubbles in comparison with those already reported in literature under similar conditions. For this purpose the acquisition window of 10 cm length was placed 60 cm above the injection nozzle (see figure 4.5, right). A distance of 60 cm from the injection allows the bubble to reach its terminal velocity.

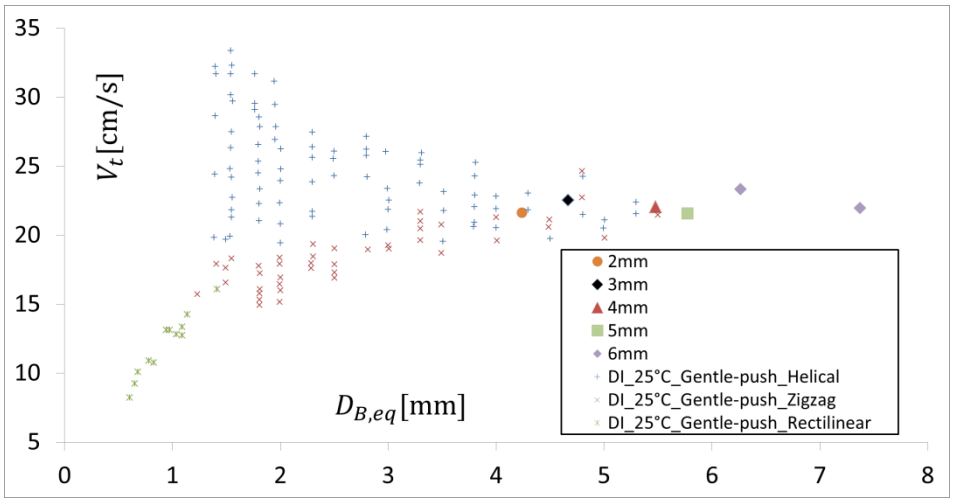

Figure 4.10 Terminal velocities from injection nozzles 2,3,4,5 and 6mm in comparison with reference experimental study [Tomiyama et al. 2002] (series with +,× markers).

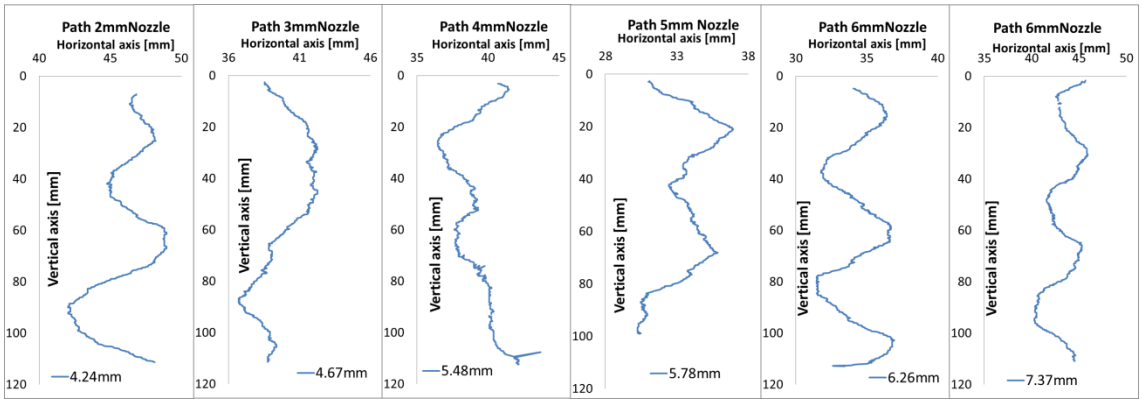

Figure 4.11 Paths of the bubbles injected from different nozzles. The average diameter of the resulting bubble appears in the legend of each plot.

Figure 4.10 shows the resulting terminal velocities from different bubbles sizes against measurements obtained by Tomiyama et al. 2002 under similar conditions. As it can be seen, the terminal velocities from the developed procedure agree well with Tomiyama et al. 2002 results, and this gives an indication that procedure calculates this parameter correctly. Figure 4.11 shows the path of the bubbles. Most bubbles follow a zigzag or a helical path which also agrees with Tomiyama et al. 2002 observations over the path of the bubbles. Due to injection

method (a direct injection via a nozzle), bubbles with an equivalent diameter below 4 mm cannot be generated. However since the objective was to verify the procedure's ability to calculate bubbles' rising velocities correctly rather than the investigation of the terminal velocity, the size of the generated bubbles within this study were sufficient. Figure 4.12 shows the bubble's instant rising velocity and the development of the final velocity calculated according to equations (4.7) and (4.8). As can be seen from the development of the final velocity, the bubble reaches its terminal velocity which remains constant thereafter. This indicates that bubbles reached the terminal velocity and thus the calculated results in this experiment can be compared to other results.

$$V_n(t) = \frac{K.f_s.(y_n(t+3)-y_n(t-3))}{(5t)} \tag{4.7}$$

$$V_{n,final}(t) = \frac{K.f_s.(y_n(t)-y_n(1))}{(t-1)} \tag{4.8}$$

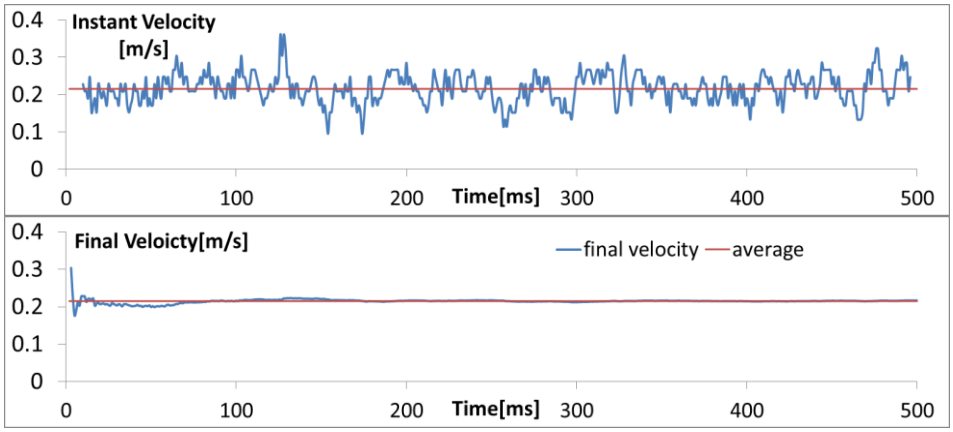

Figure 4.12: Left: instantaneous axial velocity along time, Right: final axial velocity along time.

4.1.4.4 Estimation of image processing error depending upon air experiments data

The uncertainty in the evaluation of the bubble equivalent diameter is caused by three error contributions: systematic error in the digital image procedure (half a pixel), calibration, and recognition procedure. The last uncertainly depends upon the method adopted to calculate the bubbles' equivalent diameter:

$$\frac{dD_{eq,n}}{D_{eq,n}} = 0.5\frac{dax_n}{ax_n} + 0.5\frac{day_n}{ay_n} \quad \text{(If eq. (4.5) was adopted)} \tag{4.9}$$

$$\frac{dD_{eq,n}}{D_{eq,n}} = 0.5\frac{dA_n}{A_n} \quad \text{(If eq. (4.4) was adopted)} \tag{4.10}$$

Analyzing numerous images, the maximum error made for the identification procedure is about 2 pixels for each of the vertical and horizontal directions. The contribution of this error is then between 1% and 6% for all the range of bubbles analyzed. Figure 4.12 illustrates the calculation of the identification error: the identified bubble area by the identification procedure is superimposed on the area that is manually extracted depending on human eye. In

this way the term dA_n, in equation (4.10) is the difference between the number of pixels counted in each case.

Figure 4.12 Illustration of the error made by the identification procedure. Left to right: Raw image, identified bubble's area, manually identified bubble, and superimposed images (green pixels represent those not counted by the procedure).

Table 4.2 shows the identification error for several bubbles in several experiments where the circle equivalent diameter was used.

Table 4.2 Error of diameter estimation.

nozzle diameter [mm]	Calibration [mm/pixel]	Calibration error[%]	Systematic error[%]	Identification Error[%]	Total error[%]
3mm	0.152	0.95	3.26	1.45	3.69
4mm	0.152	0.95	2.78	1.10	3.14
4mm	0.152	0.95	2.78	5.74	6.45
6mm	0.152	0.95	2.06	0.95	2.46

The root sum squares method was used in order to combine all errors as follows:

$$\epsilon_{total} = \sqrt{\epsilon_{calibration}^2 + \epsilon_{systematic}^2 + \epsilon_{identification}^2} \tag{4.11}$$

Total error is between $2-7\%$ which agree well with reported error in literature. This error can be achieved even when multiple and large bubbles with white reflections were tracked. Sometimes the bubble has a reflection that extends to its periphery (figure 4.3(d), the bubble on top). In this case the white area is not completely surrounded by the bubble and no automatic fill will take place. As a result, it will be cut out from the bubble's area underestimating the diameter calculation if the circle equivalent method was adopted (equation 4.5). In this case the ellipse equivalent diameter yields better results (equation 4.4) since it depends only upon vertical/horizontal maximum extensions of the bubble. However the ellipse equivalent diameter can be applied in the case of light deformed elliptical bubbles (equivalent diameter below 10 mm). For applications where large and highly deformed bubble exists, the circle equivalent diameter is the only choice since the bubbles stop to have an ellipsoidal shape. In these cases white reflections will account for a lower percentage of the bubble's area even if they occurred at the bubble's periphery and were not recognized by the filling algorithm. This is because large bubble deformations do not allow bubble to have a smooth surface and thus they will be smaller in size.

4.1.4.5 The application of the identification and tracking procedures

The previously described identification and tracking procedures were implemented using Delphi XE programing language. Delphi allows a feasible treatment of bitmap images and an easy access into each image pixel. The raw images are first handled by the identification procedure. The identification procedure requires the location of images (folder name), the intensity limit, and the size limit The identification procedure yields the first output file that contains: instance number, the bubble number, the bubble area and equivalent diameter, the bubble position of the center-of-mass, the axial and lateral maximal extensions and information about bubble detachment. The file consists of lines that start with the instance number and bubble number and then rest of the data. The bubble number distinguishes between bubbles in each instance (same bubble number in two instances does not necessarily mean the same bubble). These output files are then used by the tracking procedure to track bubbles. The tracking procedure requires the search limits $x_{lim}y_{lim}$, the "minimum frame count", and the "total path length" limits (other limits are required for handling steam bubbles, see section 4.1.5.6). The result of the tracking procedure will be saved into a different output files that contain all info for each tracked bubble that accomplish the tracking criteria arranged according to the time from the first tracking instance until the last tracking instance. In each instance, all info about the bubble equivalent diameter, position, extensions, aspect ratio is given. Additionally the rising velocity (or the lateral velocity) and total "frame count" for each bubble are obtained. For bubbles with a volume change (air/steam bubbles emerging at the nozzle tip, condensing bubbles), the change rate of the bubble diameter can be calculated and listed along with other data. For condensing steam bubbles, the tracking program calculates Reynolds and Nusselt number for each condensing and detached bubble. The results are automatically calculated considering all different physical properties (saturation temperature, steam density, viscosity, etc) which are calculated for each case depending upon the measured flow parameters and built-in correlations. The calculation of the bubble-size and bubbles relative velocities distributions was also included for steam bubbles. This reduced the time-cost of handling a large amount of data for steam bubbles considerably (27 cases/injection nozzle and around 1500-2000 bubbles /injection nozzle).

4.1.4.6 Additional treatment for steam bubbles

The tracking of steam bubbles brings additional difficulties to the tracking procedure. Since the steam bubbles are condensing continuously, their shape and size are changing fast and at high rates. The presence of breakup adds additional treatment challenges to the required procedures. Additional sources of error can be listed for handling steam bubbles:

- Volume change that can occurs either by condensation or by breakup.
- Abrupt change of volume and position after a large deformation or a breakup.
- Recognition of detached and non-detached bubbles.
- Appearance of air bubbles within the aquarium as the water temperature rises.
- Short-living bubbles.

- Estimation of rising velocity and diameter change rate correctly.

As it can be seen from the list above, lot of issues complicate the case. There are two approaches to handle those problems:

- Invest a lot of time developing a highly-sophisticated algorithm that can assure an ideal solution for all issues altogether. This solution will consume lot of effort and increase processing time as well.
- Solving the problems as much as sufficient and efficient making use of the good statistics (tracking lot of bubbles) to assure the correctness of the final results.

In fact the first solution cannot be achieved in practice because the amount of difficulties is beyond finding a general solution for each case. The implemented approach was to equip the procedure with some measures that eliminate a lot of errors, and rely on optical observations and processing of large number of data to avoid biases resulting from processing. For steam bubbles the following additional treatment was implemented:

- A volume change limit was imposed upon tracking of steam bubbles: This can be expressed by the following criteria:

$$-0.3 < \frac{dA_B}{A_B} < 0.05$$

  The left-hand negative limit prevents continuing the tracking after breakup. This means if a volume change with a value below -0.3 occurs, this is most likely to be a result of a breakup and the bubble will not be further tracked even if the position criteria (equation 4.6) is valid. The right-hand positive limit prevents an erroneous tracking in general. This means that if the volume difference is beyond 5% in one frame ($6.67 \times 10^{-4} s$) the tracking will stop.
- As a result of the previous criteria, breakup fragments are tracked then as new bubbles separately.
- Some bubbles can be tracked for a limited number of instances. Very small-lived bubbles and noise that is recognized as bubbles can also be tracked but for a short time. In order to filter out these cases and prevent it from imposing large uncertainties upon results, a minimum "frame count" was imposed. A value of 10 ($1\ instance = 6.67 \times 10^{-4} s$) was found to be a good criteria. This limit ensures also that the diameter change rate and velocities are calculated over a sufficient time interval.
- Steam bubbles grow first at the injection before detachment. This enables the procedure to identify the bubbles which are still attached to the injection nozzle. Only detached bubbles are tracked to investigate the heat transfer.
- The calculation of the bubbles' rising velocity suggests that the bubble moves for a sufficient distance. In some cases small bubbles –and some medium-size bubbles - can be trapped within a turbulence preventing them from moving vertically. Some bubbles' fragments after breakup can also have short-traveling distance. They show a low rising velocity upon detachment. For CIN4mm, CIN6mm and HIN2X4mm

injection nozzles, results from such bubbles can be recognized in ln(Nu)-ln(Re) plots at low Reynolds values where they show a constant trend. This is because the calculation of Nu number for these bubbles is less sensitive to the total traveled distance than the calculation of Reynolds number. A simple filtering of these results can be done by excluding points that scatter beyond $\pm 15\%$ from the main ln(Nu)-ln(Re) linear trend. However for HIN32X0.8mm nozzle, this was not sufficient because of the high exit velocity of the steam, and smaller bubbles that were easily trapped in turbulences. For this specific case an additional limit upon the traveled distance was applied and successfully filtered all the erroneously calculated rising velocities (=Reynolds number). The same limit was tested for the previous results and was found to have the same effect as the $\pm 15\%$ scatter filtering.

Chapter 5 Experimental investigations in SCUBA

This chapter will contain the results and discussions of the experimental investigation of steam bubbles condensation carried out at the experimental facility SCUBA. This will include: the optical observations, the evaluation of the Nu-Re correlation, bubble-size distributions, relative velocities distributions, and the effect of the flow conditions upon results. The chapter also discusses other important bubbles' features such as: the bubbles diameter against time, the bubbles path and motion, and bubbles' rising velocities. It discusses and shows the interconnected effects between all these parameters. Finally the optical recordings were used to obtain the time-averaged 2D void fraction distributions which are a valuable source for CFD validation.

5.1 Test conditions

Table 5.1 shows an overview of the testing conditions regarding: water superficial velocity, steam superficial velocity, and water temperature, which were pre-set parameters for experiments for all injection nozzles. This set of parameters form a $3 \times 3 \times 3$ test matrix that result in a systematic investigation of the flow conditions. Table 5.1 shows also the measured local saturation temperature (corresponding to the local measured pressure) and the corresponding subcooling temperature. The water head above the injection nozzle and the pressure variation coming from the pump at different water superficial velocities has put limitation upon performing all experiments at the same pressure. The pressure at the injection point varies between $1.1 - 1.5$ bar. Higher water velocities require a higher pump rotation, increasing the static pressure at the injection point. Consequently, saturation temperature at injection is not constant but a function of the local static pressure. This made it difficult to set a constant subcooling temperature for each case. Instead, experiments were performed at fixed water temperatures resulting in a varied subcooling temperatures ($\sim 6° - 15°$ C). In the case of HIN32X0.8mm nozzle, no measurements were performed at $J_w = 1$ m. s^{-1} since no bubbles exist at this water superficial velocity due to the high DCC rate at the injection nozzle (small holes leads to high exit steam velocities). Consequently a third measurement at $J_w = 0.2$ m. s^{-1} was performed instead. For comparison with other cases, results from $J_w = 0.4, 0.6$ m. s^{-1} can be considered.

Table 5.1. Experimental test conditions (Tests 100-108 were performed at $J_w = 0.2$ m. s^{-1})

$J_w[m.s^{-1}]$	$J_s[m.s^{-1}]$	$CIN4mm$ [#]	$T_{test}[°C]$	$\Delta T_{sub}[K]$	$CIN6mm$ [#]	$T_{test}[°C]$	$\Delta T_{sub}[K]$	$HIN2X4mm$ [#]	$T_{test}[°C]$	$\Delta T_{sub}[K]$	$HIN32X0.8mm$ [#]	$T_{test}[°C]$	$\Delta T_{sub}[K]$
0.4	**0.09**	1	94.0	8.2	28	93.4	8.9	55	93.9	8.4	82	93.7	8.7
0.4	**0.09**	2	96.0	6.2	29	96.2	6.6	56	96.2	6.4	83	96.5	6.4
0.4	**0.09**	3	98.1	5.6	30	97.8	6.1	57	97.9	5.9	84	97.7	6.7
0.4	**0.14**	4	94.1	8.2	31	93.4	8.6	58	94.0	8.2	85	93.7	8.7
0.4	**0.14**	5	96.0	6.2	32	96.2	6.6	59	96.1	6.4	86	95.9	6.5
0.4	**0.14**	6	98.0	5.7	33	97.6	6.1	60	97.9	6.0	87	97.8	5.8
0.4	**0.22**	7	94.0	8.3	34	93.8	8.4	61	93.7	8.5	88	93.9	8.6
0.4	**0.22**	8	96.1	6.4	35	96.2	6.6	62	96.2	6.5	89	96.4	6.2
0.4	**0.22**	9	98.1	5.8	36	98.0	6.0	63	98.2	5.9	90	97.9	6.2
0.6	**0.09**	10	94.0	9.9	37	94.2	9.6	64	93.9	10	91	93.8	10.3
0.6	**0.09**	11	96.2	7.7	38	96.2	7.7	65	96.2	7.7	92	96.2	7.9
0.6	**0.09**	12	98.0	6.9	39	97.7	7.3	66	97.9	6.9	93	97.9	7.6
0.6	**0.14**	13	93.9	10.0	40	94.1	9.9	67	93.9	10.0	94	93.6	10.5
0.6	**0.14**	14	96.0	7.8	41	96.0	7.9	68	96.0	7.9	95	95.8	8.3
0.6	**0.14**	15	97.9	7.0	42	97.9	7.3	69	98.1	6.8	96	97.7	7.6
0.6	**0.22**	16	94.0	9.9	43	94.2	9.7	70	94.0	9.9	97	93.7	10.4
0.6	**0.22**	17	96.0	7.8	44	96.2	7.8	71	96.3	7.7	98	96.2	7.9
0.6	**0.22**	18	97.9	7.1	45	97.9	7.3	72	97.7	7.0	99	98.0	7.3
1	**0.09**	19	94.1	14.9	46	93.9	15.1	73	93.9	15.1	100	94.1	9.5
1	**0.09**	20	96.0	13.0	47	96.1	13.0	74	96.4	12.6	101	96.1	7.5
1	**0.09**	21	98.1	11.6	48	97.8	11.5	75	98.3	11.4	100	98.0	5.7
1	**0.14**	22	94.1	15.0	49	93.9	15.1	76	94.1	14.9	103	94.2	9.5
1	**0.14**	23	96.0	13.0	50	95.9	13.1	77	96.2	12.9	104	96.0	7.7
1	**0.14**	24	98.0	11.5	51	97.6	11.6	78	98.3	11.3	105	97.9	5.7
1	**0.22**	25	94.1	14.9	52	93.9	15.1	79	94.1	14.9	106	94.2	9.4
1	**0.22**	26	96.1	12.9	53	96.2	12.8	80	96.6	12.5	107	96.2	7.4
1	**0.22**	27	98.1	11.6	54	97.8	11.5	81	98.3	11.4	108	98.0	5.6

$J_w = 0.2\ [m.s^{-1}] \downarrow$

5.2 Experimental results

Experiments were conducted according to the test conditions shown in table 5.1. HSC was used to record 3000 images at $1500\ frame/sec$ for each case. The resulting spatial resolution was around 0.32 mm/pixel in each measurement. For the calculation of the relative velocity of rising bubbles, the water superficial velocity was subtracted from the measured bubble rising velocity, thus calculating bubble Reynolds and Nusselt numbers as follows:

$$Re_B = \frac{(v_B - v_l).D_{B,eq}}{v_l} \quad , \quad Nu = \frac{\rho s h_{fg} D_{B,eq}}{2.\lambda_l \Delta T_{sub}} \times \left|\frac{dD}{dt}\right| \quad \left|\frac{dD}{dt}\right| = \left|\frac{\Delta D}{\Delta t}\right|_{D_0 \to 0.4D_0} \quad (5.1)$$

The limit $0.4D_0$ was chosen to determine the boundary of thermal condensation as reported by Park et al. (2007) .An inertial condensation can take place below this limit .This limit will also help to avoid the influence form dissolved air (if any exist) within the steam phase inside the bubbles. Since the fraction of these gases within the bubble volume will remain low when the bubble diameter is larger than $0.4D_0$. The water used to generate the steam was boiled for some time before injection which minimized the air content. It was noticed that remaining air volume fraction from a 20 mm bubble is less than 1 %. Figure 5.1 is illustrating this fact (remaining air accounts for tiny bubbles of around 0.32 mm diameter).

Figure 5.1 Snapshots illustrating remaining air (mixed with some background noise) after full condensation (snapshots are same 1-7 instances shown in Figure 7, left graph, the bubble on top)

5.2.1 Visual observations

Figures 5.2-5.10 show snapshots of fully detached bubbles condensing in different water superficial velocities, steam superficial velocities, and subcooling temperatures (water temperature $98° C$ is constant in all cases). The snapshots were taken at constant time intervals ($dt = 6.67 \times 10^{-3}$ s $= 10 \times 1/1500$) and thus the number of snapshots until full condensation gives an idea about bubble's lifetime in each case. Despite being raw, unprocessed images, these snapshots show high quality resolution of the bubble surface structure (spatial resolution was 0.32 mm/pixel). It is noticeable that bubbles at low steam injection velocities have a smoother surface in comparison to bubbles at higher steam injection velocities. This can be especially noted for central injection nozzles CIN4mm and CIN6mm (Figures 5.2-5.5). Turbulence is higher inside the gas phase at higher injection velocities; and the effect upon the bubble's surface structure and condensation mechanism is large. Figures 5.2-5.5 (right image) show that bubbles at higher steam injection velocities condense faster than bubbles at lower steam injection velocities. A quantitative analysis of this observation is shown in next sections. The surface of bubbles at high steam velocities appears to be rough and covered with many micro vibrations which act as heat transfer enhancer, making the heat transfer more effective and resulting in higher Nusselt numbers compared to predictions of most correlations reported in literature. These bubbles with rough surface and tiny vibrations will be referred to as "shivering bubbles" to indicate this phenomenon.

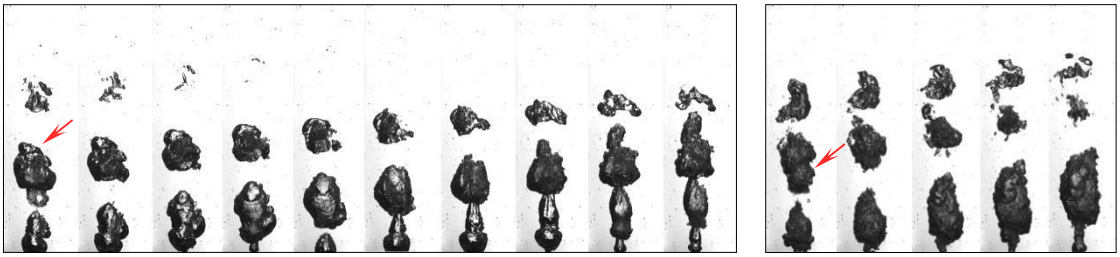

Figure 5.2 Snap shots for condensing steam bubbles from CIN4mm injection nozzle.
Flow conditions: $J_L = 0.4\ m.s^{-1}$, $T_L = 98°\ C, dt = 6.67 \times 10^{-3}$ s,
Left: $J_S = 0.09\ m.s^{-1}, \Delta T_{sub} = 5.6°\ K$, Right: $J_S = 0.21\ m.s^{-1}, \Delta T_{sub} = 5.8°\ K$

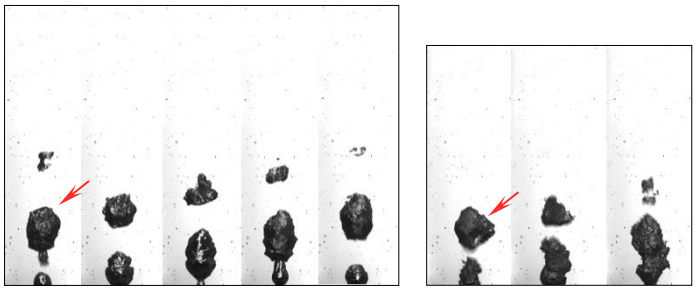

Figure 5.3 Snap shots for condensing steam bubbles from CIN4mm injection nozzle.
Flow conditions: , $J_L = 1.0\ m.s^{-1}, T_L = 98°\ C, dt = 6.67 \times 10^{-3}$ s.
Left: $J_S = 0.09\ m.s^{-1}, \Delta T_{sub} = 11.6°\ K$, Right: $J_S = 0.21\ m.s^{-1}, \Delta T_{sub} = 11.6°\ K$

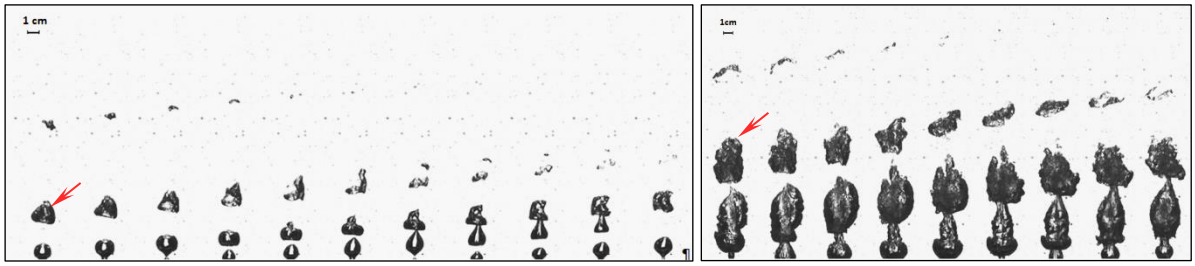

Figure 5.4 Snap shots for condensing steam bubbles from CIN6mm injection nozzle.
Flow conditions: $J_L = 0.4\ m.s^{-1}, T_L = 98°\ C, dt = 6.67 \times 10^{-3}$ s.
Left: $J_S = 0.08\ m.s^{-1}, \Delta T_{sub} = 6.1°\ K$, Right: $J_S = 0.22\ m.s^{-1}, \Delta T_{sub} = 6.0°\ K$

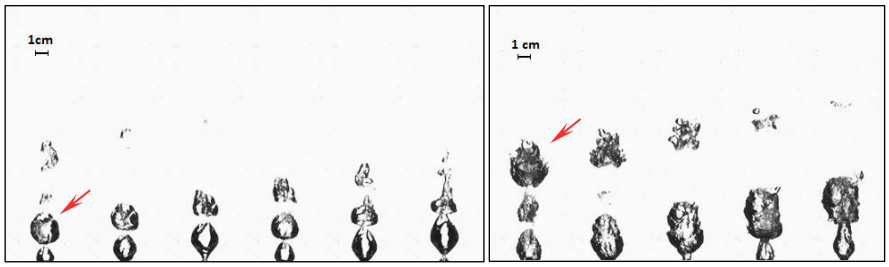

Figure 5.5 Snap shots for condensing steam bubbles from CIN6mm injection nozzle.
Flow conditions: $J_L = 1.0\ m.s^{-1}, T_L = 98°\ C, dt = 6.67 \times 10^{-3}$ s.
Left: $J_S = 0.09\ m.s^{-1}, \Delta T_{sub} = 11.5°\ K$, Right: $J_S = 0.22\ m.s^{-1}, \Delta T_{sub} = 11.5°\ K$

The bubbles are large ones and deviate a lot from spherical shape. The deformation of the bubbles increases the interfacial area and thus the heat transfer rate into the fluid. The initial velocity of steam bubbles detached off central injection nozzles is highly affected by the steam inlet velocity. The amount of turbulence inside the gas phase is also affected by steam injection velocity. Comparing snapshots from CIN4mm and CIN6mm at low steam injection

velocities (Figures 5.2-5.5, left plot) shows that bubbles resulting from CIN6mm are smoother. This can be also seen from the amount of light reflections at the bubbles surface. Next section shows that this difference will result in lower heat transfer rate for the bubbles coming out from CIN6mm nozzle. On the other hand, the horizontal injection nozzle (HIN2X4mm) results in higher direct contact condensation at the nozzle yielding smaller bubbles. Additionally the horizontal injection does not allow the bubbles to gain a high rising velocity or high amount of turbulence inside the gas phase. This results in smoother, and more rounded bubbles in general (bubbles at high steam injection velocities are still however highly deformed as figure 5.6, bottom shows). The water velocity has a larger effect upon condensation compared to central injection. At high water flow rates and low steam injection velocity small rounded bubbles are generated (Figure 5.7, left) while almost no bubbles at high steam injection velocities were generated since all steam has already condensed at the nozzle. Even little detached portions of steam will condense very fast (figure 5.7, right).

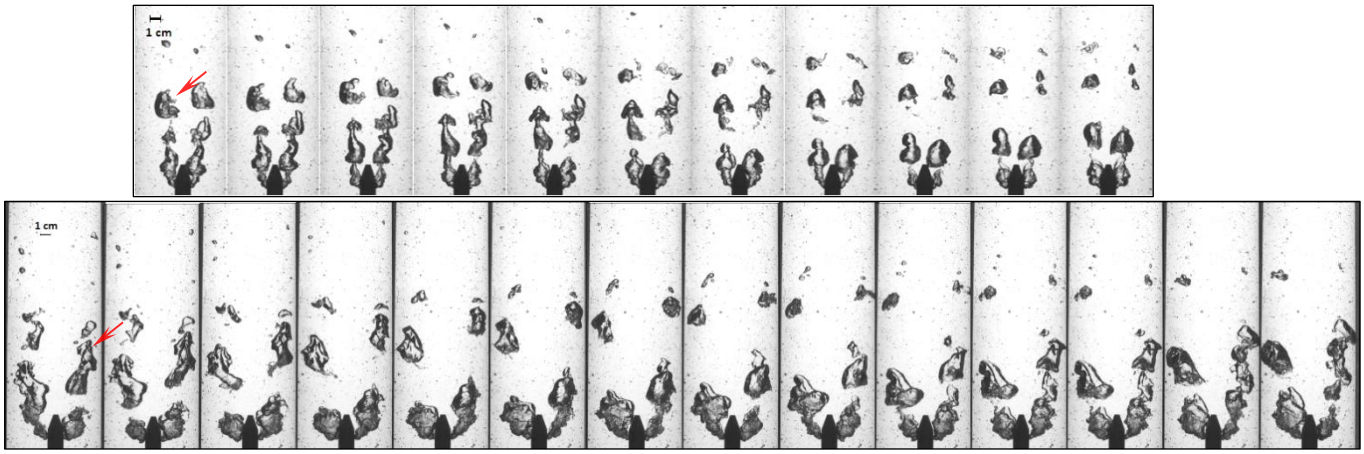

Figure 5.6 .Snap shots for condensing steam bubbles from HIN2X4mm injection nozzle. Flow conditions: HIN2X4mm nozzle, $J_L = 0.4\ m.s^{-1}, T_L = 98°\ C, dt = 6.67 \times 10^{-3}$ s, up: , $J_S = 0.09\ m.s^{-1}, \Delta T_{sub} = 5.9°\ K$, bottom: $J_S = 0.22\ m.s^{-1}, \Delta T_{sub} = 5.9°\ K$

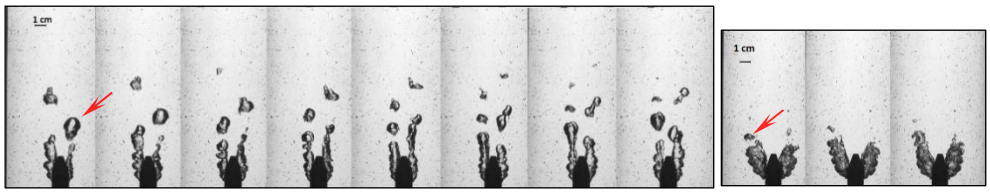

Figure 5.7 Snap shots for condensing steam bubbles from HIN2X4mm injection nozzle. Flow conditions: HIN2X4mm nozzle, $J_L = 1.0\ m.s^{-1}, T_L = 98°\ C, dt = 6.67 \times 10^{-3}$ s, Left: $J_S = 0.09\ m.s^{-1}, \Delta T_{sub} = 11.4°\ K$, Right: $J_S = 0.22\ m.s^{-1}, \Delta T_{sub} = 11.4°\ K$

The current observations show that it is possible to generate different bubble sizes, geometries and surface structure when different injections nozzles are used. This provides the possibility to investigate steam bubble condensation under different conditions. Application of more different injection nozzles is planned in order to enlarge the current database.

Figure 5.8 Snap shots for condensing steam bubbles from HIN32X0.8mm injection nozzle. Flow conditions: $J_L = 0.2\ m.s^{-1}, T_L = 98°\ C, dt = 6.67 \times 10^{-3}\ s$
up: , $J_S = 0.09\ m.s^{-1}, \Delta T_{sub} = 5.7°\ K$, bottom: $J_S = 0.22\ m.s^{-1}, \Delta T_{sub} = 5.6°\ K$

Figure 5.9 Snap shots for condensing steam bubbles from HIN32X0.8mm injection nozzle. Flow conditions: $J_L = 0.4\ m.s^{-1}, T_L = 98°\ C, dt = 6.67 \times 10^{-3}\ s$
up: , $J_S = 0.09\ m.s^{-1}, \Delta T_{sub} = 6.7°\ K$, bottom: $J_S = 0.22\ m.s^{-1}, \Delta T_{sub} = 6.2°\ K$

Figure 5.10 Snap shots for condensing steam bubbles from HIN32X0.8mm injection nozzle. Flow conditions: $J_L = 0.6\ m.s^{-1}, T_L = 98°\ C, dt = 6.67 \times 10^{-3}\ s$
up: , $J_S = 0.09\ m.s^{-1}, \Delta T_{sub} = 7.6°\ K$, bottom: $J_S = 0.22\ m.s^{-1}, \Delta T_{sub} = 7.3°\ K$

5.2.2 $Nu - Re$ Correlation

Nusselt numbers against Reynolds bubble numbers were calculated for all tracked bubbles in each investigated case according to Equations (5.1). Additionally, the probabilistic distribution functions of bubble equivalent diameters and bubble relative velocities were made to offer a better idea about the characteristics of the investigated bubbles, and to help understanding the influence of different initial flow conditions. In order to exclude the influence of some measurements that deviate from the main trend line of Nu-Re, points which deviate more than 15% from the initial, unprocessed trend line were excluded from the calculation of the final trend line. These points are marked as red points and labeled as "scatter" within the plots.

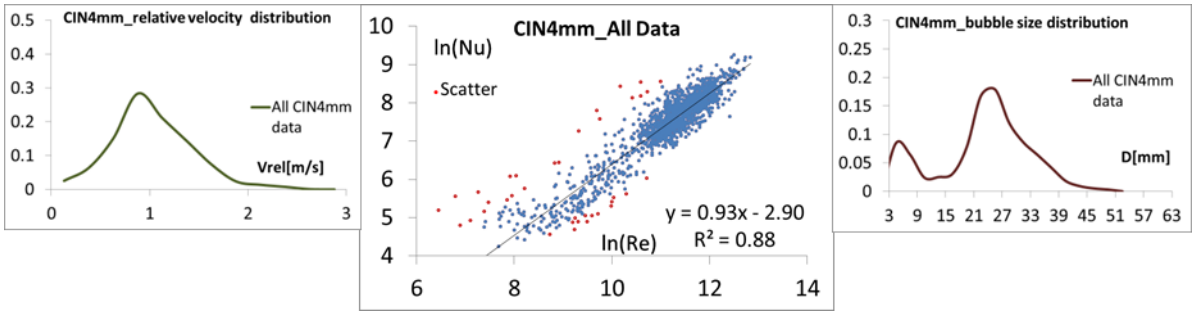

Figure 5.11 Nu-Re Correlation from CIN4mm injection nozzle data. A linear regression that correlates the logarithmic values of Nu, Re is also shown.

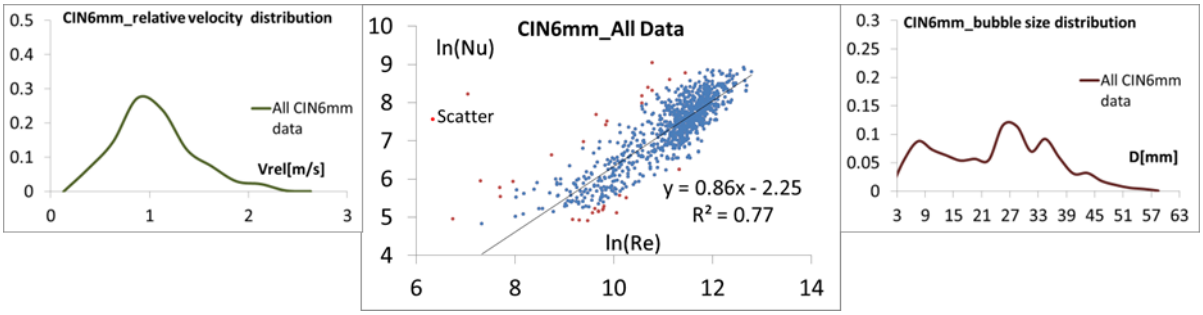

Figure 5.12 Nu-Re correlation for CIN6mm injection nozzle. A linear regression that correlates the logarithmic values of Nu, Re is also shown.

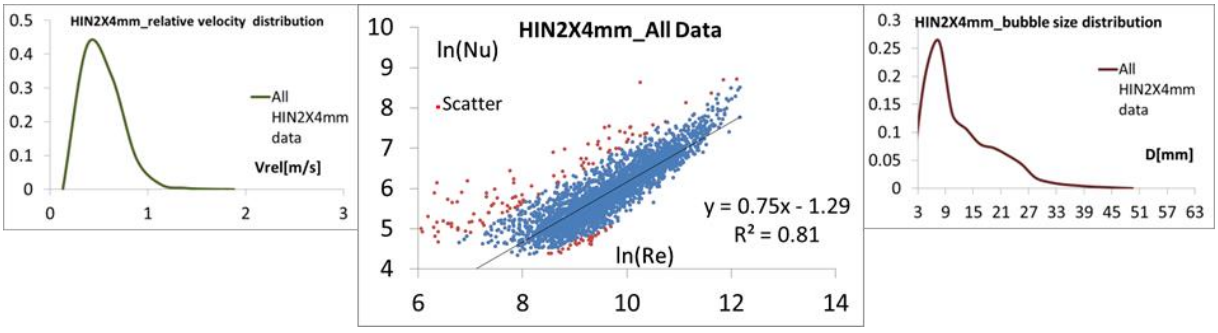

Figure 5.13 Nu-Re correlation for HIN2X4mm injection nozzle. A linear regression that correlates the logarithmic values of Nu, Re is shown.

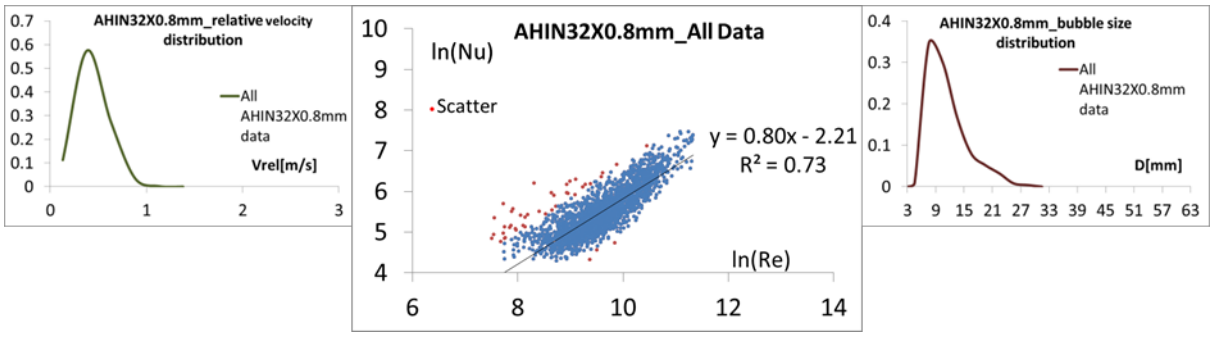

Figure 5.14 Nu-Re correlation from HIN32X0.8mm injection nozzle. A linear regression that correlates the logarithmic values of Nu, Re is shown. [Note: the vertical axis scale of both distributions is higher than in previous plots due to the shift towards smaller bubbles sizes]

Figures 5.11-5.14 show the Nu-Re correlation for each injection nozzle along with the distribution of the bubbles' equivalent diameter and the bubbles' relative velocity. As can be seen from bubble size distributions, most tracked bubbles for CIN4mm and CIN6mm are large bubbles that concentrate between 21-40 mm ($\overline{D_{B,eq}} = 23.2$ mm for CIN4mm and 24.2 mm for CIN6mm). A smaller secondary peak appears for both cases around $\overline{D_{B,eq}} = 7$ mm and it is generated by fragmentation of large bubbles (fragments that are tracked for enough time after defragmentation). Bubbles are slightly larger for CIN6mm. The larger nozzle diameter results in lower steam velocities that enable the formation of larger bubbles at the injection nozzle. Nonetheless, it can be seen from the linear fit of ln(Nu)-ln(Re) that the bubbles generated by CIN4mm have higher condensation rates than those generated by CIN6mm. This is due to the fact that at the same steam superficial velocities, CIN4mm -with its lower outlet area- results in higher steam velocities and, therefore, higher gas turbulence and rougher bubble surfaces (see previous section). This leads into higher Nusselt numbers, although the relative velocities and bubble sizes are rather similar. The relative velocity distributions show remarkably high values in comparison with those predicted by most empirical correlations of rising bubbles in stagnant deionized (DI) water. They are around 1 m/s for CIN4mm and CIN6mm and they are tightly related to the bubble size. The cases of HIN2X4mm and HIN32X0.8mm are quite different. The bubbles are remarkably smaller ($D_{B,eq} < 27$ mm, $with\ \overline{D_{B,eq}} = 12.3$ mm for HIN2X4mm and $\overline{D_{B,eq}} = 11.4$ mm for HIN32X0.8mm) resulting in lower relative velocities (around $0.5\ \mathrm{m.s^{-1}}$). The horizontal injection contributes also to the lower values in these cases. Consequently, bubbles have smoother surface, lower turbulence, and thus lower Reynolds and Nusselt numbers. The linear fit in Figures 5.13 and 5.14, shows lower values than that the of CIN4mm and CIN6mm nozzles. The slope approaches values reported in literature (0.7, Kim and Park 2011, and Chen and Mayinger 1992) although it remains a little higher due to large bubble deformations. The Nu-Re correlation for each injection nozzle is:

$$Nu = 0.0550\ Re^{0.93} \quad \text{[CIN4]}$$

$$Nu = 0.1054\ Re^{0.86} \quad \text{[CIN6]}$$

$$Nu = 0.2753\ Re^{0.75} \quad \text{[HIN2X4]} \qquad (5.2)$$

$$Nu = 0.1097\ Re^{0.80} \quad \text{[HIN32X0.8mm]}$$

$$Re_B = 3 \times 10^3 - 2.7 \times 10^5, D_{B,eq} = 5 - 50 \text{ mm}, \quad Pr = 1.75 - 1.9, \quad Ja = 16 - 35$$

No dependency upon the Prandtl number was included, for the physical properties of the fluid cannot be changed in order to implement its influence in the correlation. Nevertheless, such a dependency was investigated in the literature, and it was usually found to be proportional to $Pr^{0.33}$.

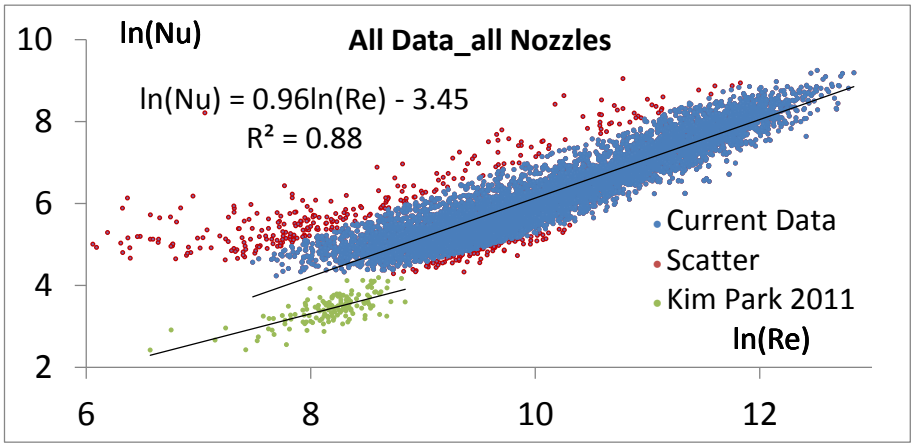

Figure 5.15 Nu-Re correlation from all injection nozzles. A linear regression that correlates the logarithmic values is shown. Data from Kim and Park 2011 at smaller bubble sizes $D_{B,eq} = 0.6 - 8$ mm and no direct injection is also shown.

Figure 5.15 shows Nu-Re correlation for all injection nozzles. The correlation corresponds to 7075 measurements (without calculation of scatter points). A similar measurement cannot be found in literature, however Kim and Park 2011 provided the next close measurements (only bubble condensation, and a considerable amount of measuring data points) and those are shown also in Figure 5.15. The remarkable lower values in Kim and Park measurements (37% lower than current measurements) corresponds to lower bubble size ($3.5 - 6$ mm) and lower rising velocities. The bubbles were generated by evaporation on a heated wall and not by direct injection, which significantly lowers the resulting relative velocity, gas turbulence, and bubble deformations. Table 5.2 summarizes Nu-Re correlation of condensing bubbles found in the literature. It is noticeable that most of these correlations cover lower Reynolds numbers and smaller bubbles. However a trend of increasing dependency upon Reynolds number can clearly be noticed. The comparison of the correlations from Chen and Mayinger (1992) after detachment (Re_B up to 10^4, $Nu \propto Re_B^{0.7}$) against correlations in which the Reynolds numbers are lower, e.g. that of Ranz-Marshall (1952) (Re_b up to 800 $\mathrm{Nu} \propto \mathrm{Re}^{0.5}{}_b$), provides an indication that the dependency upon Reynolds numbers grows higher as the Reynolds number increases.

$$Nu = 0.03175\, Re^{0.96} \quad \text{[highly deformed large bubbles]} \tag{5.3}$$

$$Re_B = 2 \times 10^3 - 2.7 \times 10^5, D_{B,eq} = 5 - 50 \text{ mm}, \quad Pr = 1.75 - 1.9, \quad Ja = 16 - 35$$

If Prandtl's dependency was considered as $Pr^{0.33}$ then the correlation reads:

$$Nu = 0.02603\, Re^{0.96} Pr^{0.33} \quad \text{[highly deformed large bubbles]} \tag{5.4}$$

$$Re_B = 2 \times 10^3 - 2.7 \times 10^5, D_{B,eq} = 5 - 50 \text{ mm}, \quad Pr = 1.75 - 1.9, \quad Ja = 16 - 35$$

It should be noted that the newly derived correlation does not intends to replace those found in Table 5.2, because of the difference in flow conditions and bubble generation mechanism. Yet, it provides a correlation applicable in high Reynolds number situations. The dependency upon the Jacob numbers was not included in the developed correlation, because the dependency upon the Jacob number is weak and can hardly be noticed taking into account the current experimental range (Ja=16-35). A rough estimation of the Jacob number dependency places it close to $Ja^{-0.29}$ (similar to those found in Table 5.2). Nevertheless, this estimation has a very high uncertainty (>100%) and, consequently, it was not included in our correlations.

Table 5.2 Correlations for condensation Nusselt number out of literature

Name /author	Correlation	Range of applicability
Ranz-Marshall (1952)	$Nu_C = 2 + 0.6Re_b^{0.5}.Pr^{0.33}$	$2 < Re_b < 800$
Hughmark (1967)	$Nu_C = 2 + 0.6Re_b^{0.5}.Pr^{0.33}$	$0 < Re_b < 450, 0 < Pr < 250$
	$Nu_C = 2 + 0.27\, Re_b^{0.5}.Pr^{0.33}$	$Re_b > 450, 0 < Pr < 250$
Chen and Mayinger (1992)	$Nu_C = 2 + 0.6Re_b^{0.6}.Pr^{0.5}$	Before detachment, $100 < Re_b < 1000$
	$Nu_C = 0.185Re_b^{0.7}.Pr^{0.5}$	After detachment, $0 < Re_b < 10^4$
Zeitoun (1994)	$Nu_C = 2.04Re_b^{0.61}.Ja^{-0.308}.\alpha^{0.328}$	$2266 < Re_b < 7953$
Lucic and Mayinger (2010)	$Nu_{av} = 1.46\, Re_b^{0.61}\, Pr_l^{0.33}\, Ja^{-0.31}$	$Re_b \approx 1000 \ldots 3400\,, Ja \approx 10 \ldots 30$
Yuan et al. (2009)	$Nu_c = 0.6\, Re_b^{0.5}\, Pr_l^{1/3}(1 - Ja^{0.1}\, Fo_{b,0})$	$Re_b = 335 - 1770, \text{Pr} \approx 1.7$ $Ja = 20 - 60$
Kim and Park (2011)	$Nu_c = 0.2575\, Re_b^{0.70}\, Pr^{-0.4564} Ja^{-0.2043}$	$Re_b \approx 1000 - 6000, Pr = 1.87 - 2.03, Ja = 18 - 36$

As can be noticed in Figures 5.11-5.15, there exist always some scatter points at low Reynolds number, when the Nusselt number is nearly constant. These points are caused mostly by erroneous tracking or by inaccurate calculation of their rising velocity by the processing software. Nonetheless some points originate from little fragments that separate from larger bubbles and are then tracked as new bubbles. Since these fragments are generated after a considerable time from the beginning of the bubble's condensation, they tend to have a higher air content, which reduces their condensation rate. Additionally, these fragments have a small size and they have a small relative velocity upon defragmentation, which also slows down their condensation.

5.2.3 Uncertainty analysis of $D_{B,eq}$, Re_B, and Nu experimental values

In order to determine the uncertainty of the bubble diameter, the original bubble image (marked in red) is superimposed with the image of the processed bubble as figure 5.16 shows.

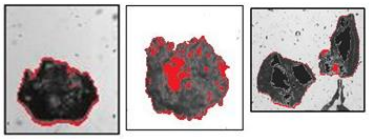

Figure 5.16 Error estimation of the bubble's recognized area

The difference in pixels is manually counted and the diameter's uncertainty is then:

$$\frac{\mathrm{dD_B}}{\mathrm{D_B}} = 0.5\frac{\mathrm{dA}}{\mathrm{A}} = 0.5\frac{\text{red pixels}}{\text{red pixels+black pixels}} \tag{5.5}$$

The overall uncertainty of Reynolds number is

$$\frac{dRe}{Re} = \frac{dv_B}{v_B} + \frac{dv_L}{v_L} + \frac{dD_B}{D_B} = \left(\frac{2dy_c}{\Delta y_c} + 2\frac{dt}{t}\right) + \frac{dv_L}{v_L} + \frac{dD_B}{D_B} \tag{5.6}$$

$\frac{dv_L}{v_L} = 0.5\%$ (section 2.2.3.1). The time-error is as a maximum 1/ frame rate ≡ 0.07%. The maximum error of vertical bubble's position y_C is 6.6%. The overall uncertainty of Nusselt number is

$$\frac{dNu}{Nu} = 2\frac{dD_B}{D_B} + 2\frac{dt}{t} + \frac{dT_{sub}}{T_{sub}} \tag{5.7}$$

Error! Reference source not found.5.3 shows examples for different bubble shapes and sizes. The uncertainty of the Reynolds number was 16.5%-33% with 25% average. The uncertainty of Nusselt number was 7%-40% with 24% average. The larger values of uncertainties are expected for large bubbles with a high shape deformation. However, these values are not far away from uncertainties reported for smaller bubbles. Kim and Park (2011) report an error of 24.3% for bubble Nusselt numbers ($D_{B,eq} = 0.8 - 6$ mm and dual-image processing).

Table 5.3 Uncertainty evaluation of $D_{B,eq}$, Re, and Nu, for different representative cases.

Case →	**19**	**17**	**2**	**24**	**15**	**42**	**50**	**46**	**36**	**28**	**55**	**55**
Bubble Shape	*Small, round*	*Medium, round*	*large (jet)*	*Fuzzy*	*flat*	*Small, round*	*Medium, round*	*large (jet)*	*Fuzzy*	*flat*	*Medium, round*	*large (jet)*
$\frac{dD}{D}$ [%]	6.0	10.2	6.6	12.8	14.6	10.5	8.9	18.9	11.6	9.9	2.9	3.3
$\frac{dRe}{Re}$ [%]	19.3	23.5	19.9	26.1	27.9	23.8	22.2	32.2	24.9	23.2	16.2	16.6
$\frac{dNu}{Nu}$ [%]	13.5	21.9	14.7	27.1	30.7	22.5	19.3	39.2	24.8	21.3	7.4	8.1

5.2.4 The influence of flow conditions

The influence of the steam superficial velocity and the water superficial velocity upon the condensation rate (Nu-Re correlation) is discussed next. Since results of CIN4mm and CIN6mm are similar, and the same for results from HIN2X4mm and HIN32X0.8mm, only cases CIN4mm and HIN2X4mm are shown. As the statistics of selected results are not as good as those for all results, the criteria to identify scatter points was tightened in order to follow the main trend of the measurements. Points with deviations of more than 10% off the initial trend line were excluded from the calculation of the final trend line. Points that deviate from the linear trend come from inaccurate measurements of the bubbles' equivalent diameter or the relative velocity. The measurement of these both parameters is affected by bubbles' deformation.

5.2.4.1 The effect of the steam superficial velocity

Figure 5.17 shows selected data according to the steam superficial velocity from the CIN4mm nozzle. Each of the plots gathers all the information from all water temperatures and water superficial velocities that have the corresponding steam superficial velocity. It can be clearly seen that higherJ_s's lead to higher bubble sizes, and a higher heat transfer rate (compare the slope of linear fit for each case in Figure 5.17). This confirms the visual observations that higher steam injection velocities cause a higher deformation of the bubbles and a rougher surface bringing a clear enhancement of the heat transfer. Relative velocities follow the trend of the bubbles size and they are higher for larger bubble sizes.

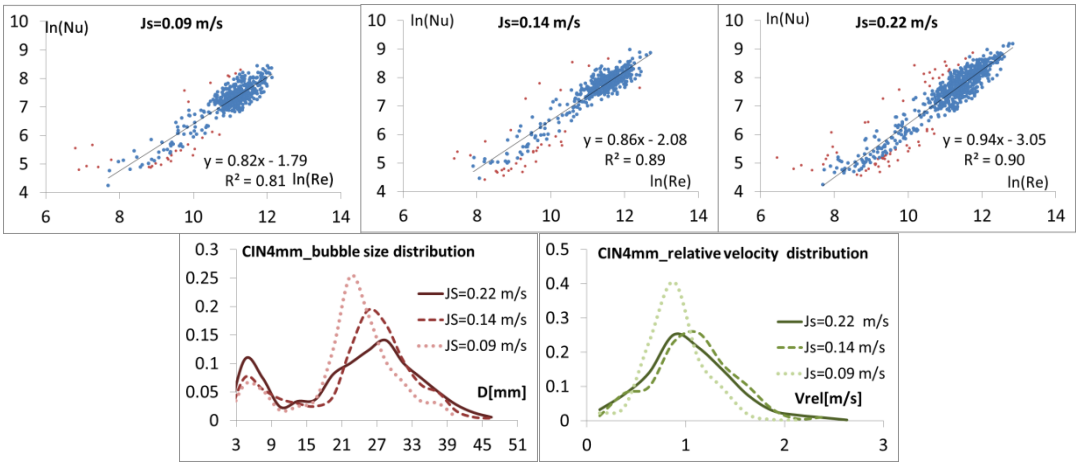

Figure 5.17 Influence of the steam superficial velocity upon results, CIN4mm injection nozzle.

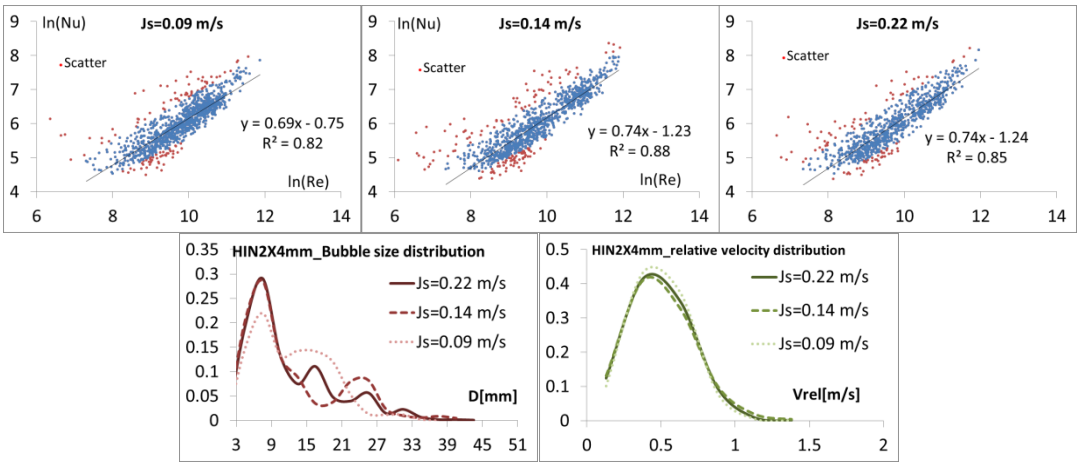

Figure 5.18 Influence of the steam superficial velocity upon results, HIN2X4mm injection nozzle.

Figure 5.18 shows data obtained from the HIN2X4mm nozzle. The horizontal injection removes the dependency upon steam velocity. Bubble size distributions are similar for all steam velocities and relative velocities distributions are almost identical. A little difference occurs for the smallest injection velocity ($J_s = 0.09\ \mathrm{m.s^{-1}}$), when bubbles are relatively smaller compared to the other two cases ($J_s = 0.14, and\ 0.22\ \mathrm{m.s^{-1}}$).

5.2.4.2 The effect of the water superficial velocity

Figure 5.19 shows selected results according to the water superficial velocity from the CIN4mm nozzle. Unlike the steam superficial velocity, the water superficial velocity does not have a clear influence upon the condensation rate of the bubbles. This can be seen from the comparison of the slope of the linear fit of $J_L = 0.4\ and\ 0.6\ \mathrm{m.s^{-1}}$. The third case with $J_L = 1.0\ \mathrm{m.s^{-1}}$is clearly different. The difference comes from resulting bubble size distribution in this case, which concentrates around a single peak with $\overline{D_{eq}} = 24$ mm .

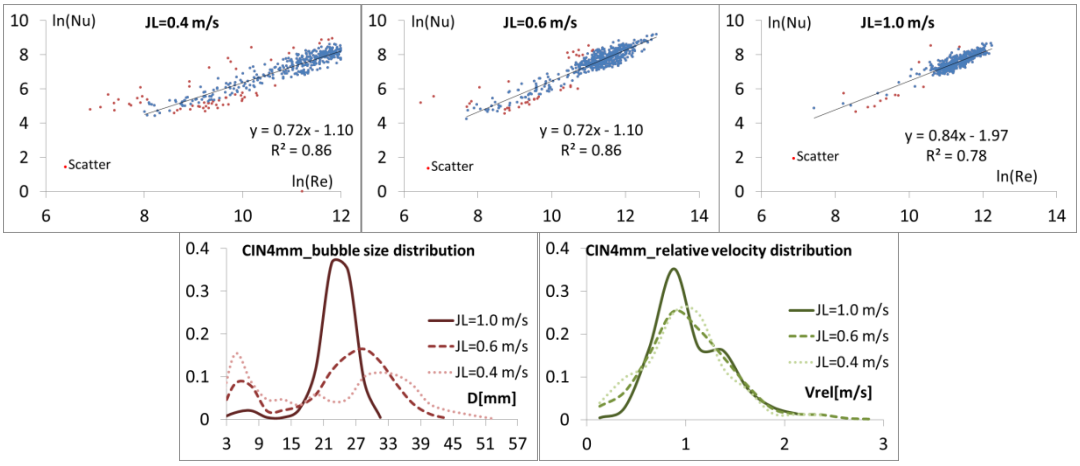

Figure 5.19 Influence of the water superficial velocity upon results, CIN4mm injection nozzle.

The higher water velocity in this case induces a higher direct contact condensation at the nozzle. Additionally, the high water velocity tears the bubbles off the steam plume before they can grow into larger bubbles. As the bubbles in this case are relatively smaller than those at $J_L = 0.4\ and\ 0.6\ \mathrm{m.s^{-1}}$, they do not tend to defragment and no secondary peak is noticed

at small bubbles' diameters. The relative velocities distributions are similar for $J_L = 0.4\ and\ 0.6\ \mathrm{m.s^{-1}}$, while they shift towards lower values for $J_L = 1.0\ \mathrm{m.s^{-1}}$due to lower bubble sizes. Figure 5.20 shows the results for the HIN2X4mm nozzle. The bubble size distribution shifts towards lower values as the water velocity increases. The relative velocity follows this trend as well. The case with highest water velocity $J_L = 1.0\ \mathrm{m.s^{-1}}$ is also characterized by the formation of smaller bubbles and the concentration of the bubble size around one peak. The effect of the water superficial velocity is minimal. The condensation rate is similar for $J_L = 0.4$ and $J_L = 0.6\ \mathrm{m.s^{-1}}$ (see the slope of the linear fit). However, the case of the highest water superficial velocity is remarkably different due to the smaller size of the bubbles. The slope of the ln(Nu)-ln(Re) correlation $(= 0.6)$ in this case is significantly lower and it coincides with the reported values in the literature $(0.5 - 0.6)$. This confirms once again the fact that the high dependency upon Reynolds in these experiments is influenced by the large size of the bubbles producing a highly deformed, rough surface structure, and high gas turbulence.

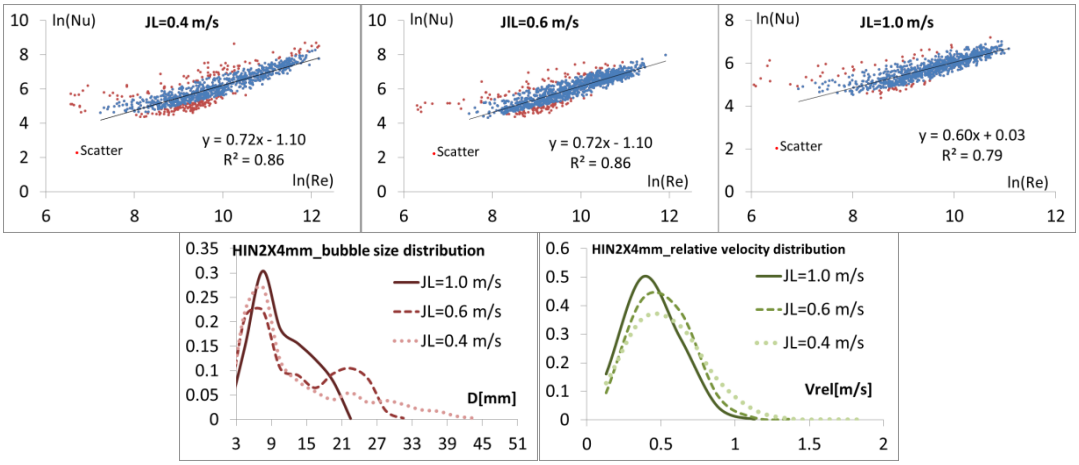

Figure 5.20 Influence of the water superficial velocity upon results, HIN2X4mm injection nozzle.

5.2.5 Bubble equivalent diameter

The development of bubble equivalent diameter along time is an important parameter that shows some important aspects of the condensation process. It shows for instance the bubble fluctuations via the instantaneous changes of the bubble equivalent diameter. Through this one can estimate the amount of shape fluctuations of each bubble. These plots give also a look into the condensation rate of each individual bubble along with the knowledge of the corresponding diameter. This helps to evaluate the condensation rate according to bubble size and time simultaneously. The change of condensation rate that is sometimes blurred through the scatter within Nu-Re plots can be seen more clearly within these plots.

5.2.5.1 Fluctuations and influence of steam and water superficial velocities.

Figures 5.21-5.26 shows development of the bubble diameter [mm] against time [ms]for different nozzles and at different flow conditions. Figure 5.21 shows CIN4mm results at three different steam injection velocities in two cases: $J_L = 0.4\ \mathrm{m.s^{-1}}, 1.0\ \mathrm{m.s^{-1}}$. The comparison of

plots in the upper and the lower row shows that bubbles at higher water velocity have lower initial diameter as a result of the increased DCC at the injection nozzle. However the most remarkable difference is the smoother development of the bubbles diameter at higher water velocities. This means that shape fluctuations are suppressed by the higher water flow field around the bubble and it means that gas flow inside the bubble is forced to be more uniform by the influence of the surrounding higher water velocities. This result can be noticed also in CIN6mm and HIN2X4mm nozzles as well (Figures 5.23 And 5.25). The effect can be also seen in Figures 5.22, 5.24, and 5.26 where plots at different water velocities and same steam injection velocity are shown. This is an interesting fact, since it opposes the fact that the turbulence inside the liquid phase increases as the water velocity increases. Furthermore it can be clearly noticed that bubble deformation is a function of its initial diameter. Bubbles with a larger initial diameter experience larger fluctuations of its equivalent diameter (shape fluctuations). Steam injection velocities or injection direction (initial deformation) do not seem to have a large impact upon shape fluctuations as much as the initial diameter or the water velocity have. However, it should be kept in mind that the surface structure (see last section) is highly affected by steam injection velocity. This leads to the following conclusions:

- Bubbles shape fluctuations are proportional to bubbles initial diameter.
- In pipe geometry and concurrent flows, bubbles experience larger shape fluctuations when they rise in flows of lower liquid velocities. Higher velocities of surrounding liquid suppress the surface deformations.
- Steam injection velocity has a minor effect upon shape fluctuations or bubbles shape deformation however they have a large effect upon surface structure roughness.
- Injection direction (initial deformation) has no effect upon the shape deformation.

Another fact that can be seen from the plots is the increased condensation rate as the steam injection velocity increases. This can be seen in Figures 5.21, and 5.23 by comparison of the lifetime of bubbles of the same initial diameter at different steam injection velocities. This fact was shown in previous sections via the increased Nusselt number dependency upon Reynolds number. However it can be also clearly noticed that this effect disappears in the horizontal injection nozzle HIN2X4mm (Figure 5.25). Bubbles of the same initial diameter condense in similar way for all three different values of steam injection velocities. Shape fluctuations increases as bubble diameter increases, this makes large bubbles experience an increased defragmentation. Also a higher defragmentation rate is seen at lower water velocities. Consequently, more small bubbles ($D_{B,eq} < 10$ mm) can be seen as steam injection velocity increases and water velocity decreases. This result can be seen in bubbles size distributions in previous section 5.24 where the small secondary peak around $D_{B,eq} = 7$ mm is higher as the steam injection velocity increases and water velocity decreases. An interesting fact about these small bubbles however can be seen here. All Figures shows a remarkably slowed condensation rate of the small bubbles in comparison to larger bubbles. A slowed condensation rate results partially from the fact that lower shape fluctuations and surface roughness are found at smaller bubbles. However a close look into the bubble diameter along time shows that some of these diameters have almost a close-to-horizontal trend (extremely low condensation). This fact was seen in Nu-Re plots as bubbles of low Reynolds number but

with almost constant Nusselt number. Here, the origin of these points can be seen. It comes from small bubbles fragments that were torn from larger bubbles and thus the air ration inside these fragments is already increased by the previous condensation of the larger bubble. As these fragments starts to condense, the air content slows down the condensation rate. Additionally, these fragments are believed to have lower rise velocities upon defragmentation, and thus contributing to the observed lower condensation rate.

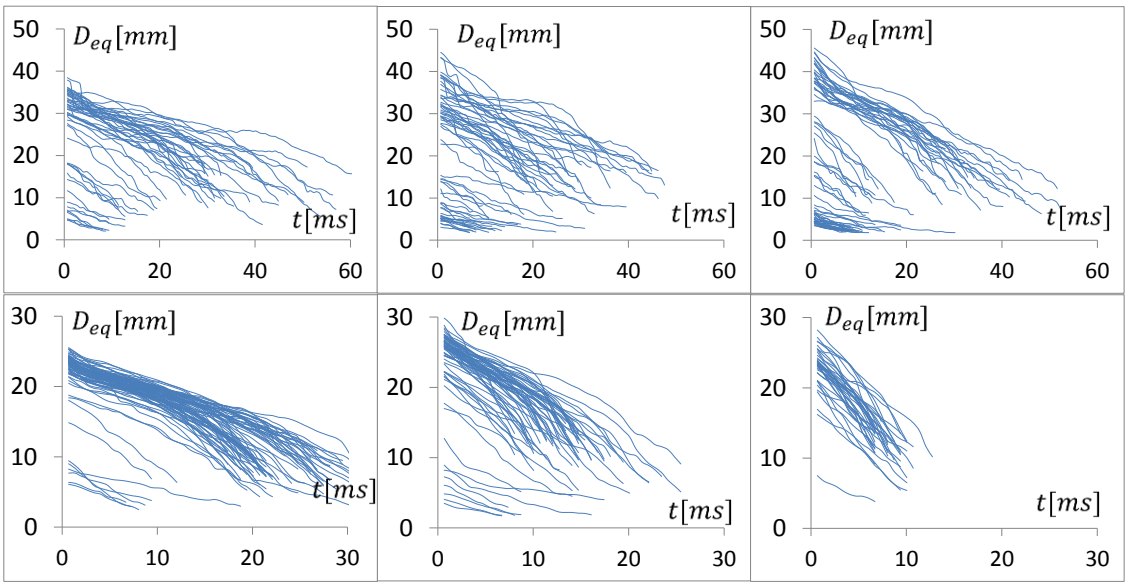

Figure 5.21 Bubble diameter against time at different steam injection velocities for **CIN4mm**.
Left: $J_S = 0.09\ m.s^{-1}$, Middle: $J_S = 0.14\ m.s^{-1}$ Right: $J_S = 0.22\ m.s^{-1}$
Upper row: $J_L = 0.4\ m.s^{-1}, T_L = 96°\ C, \Delta T_{sub} \approx 6.3\ K$,
lower row: $J_L = 1.0\ m.s^{-1}, T_L = 98°\ C, \Delta T_{sub} \approx 11.5\ K$,

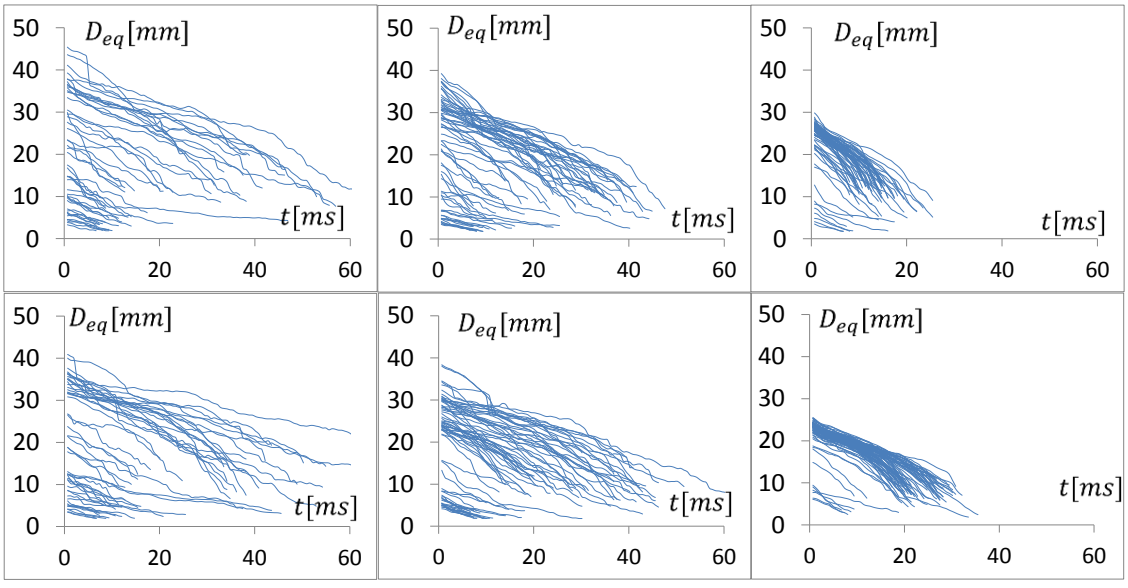

Figure 5.22 Bubble diameter against time at different water velocities for **CIN4mm**.
Left: $J_L = 0.4\ m.s^{-1}$, Middle: $J_L = 0.6\ m.s^{-1}$ Right $J_L = 1.0\ m.s^{-1}$
Upper row: $J_S = 0.14\ m.s^{-1}, T_L = 98°\ C, \Delta T_{sub} = 5.7\ K(left), 7\ K\ (middle), 11.5\ K\ (right)$
Lower row: $J_S = 0.09\ m.s^{-1}, T_L = 98°\ C, \Delta T_{sub} = 5.6\ K(left), 6.9K\ (middle), 11.6\ K\ (right)$

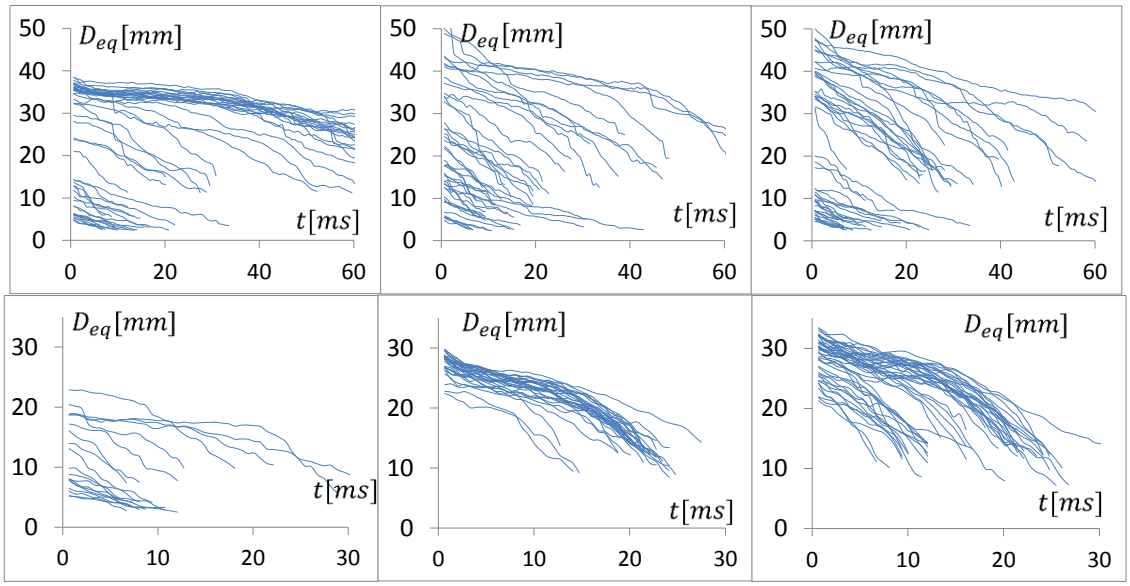

Figure 5.23 Bubble diameter against time at different steam injection velocities for **CIN6mm**.
Left: $J_S = 0.09\ m.s^{-1}$, Middle: $J_S = 0.14\ m.s^{-1}$ Right: $J_S = 0.22\ m.s^{-1}$
Upper row: $J_L = 0.4\ m.s^{-1}, T_L = 96°\ C, \Delta T_{sub} \approx 6.6\ K$,
lower row: $J_L = 1.0\ m.s^{-1}, T_L = 98°\ C, \Delta T_{sub} \approx 11.5\ K$,

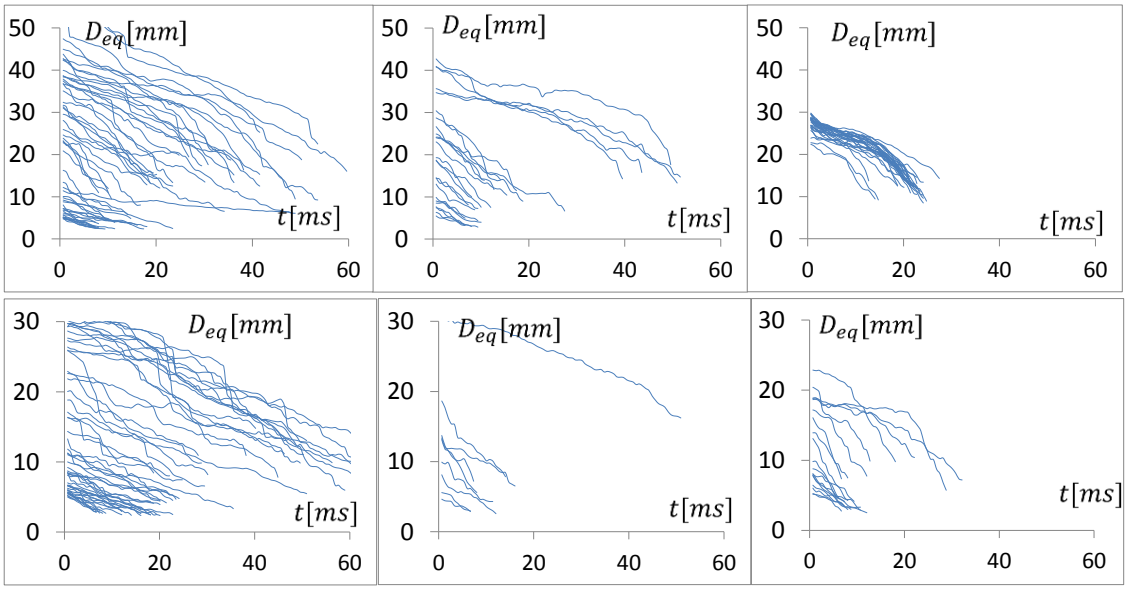

Figure 5.24 Bubble diameter against time at different water velocities for **CIN6mm**.
Left: $J_L = 0.4\ m.s^{-1}$, Middle: $J_L = 0.6\ m.s^{-1}$ Right $J_L = 1.0\ m.s^{-1}$
Upper row: $J_S = 0.14\ m.s^{-1}, T_L = 98°\ C, \Delta T_{sub} = 6.1\ K(left), 7.3\ K\ (middle), 11.6\ K\ (right)$
Lower row: $J_S = 0.09\ m.s^{-1}, T_L = 98°\ C, \Delta T_{sub} = 6.1\ K(left), 7.3K\ (middle), 11.5\ K\ (right)$

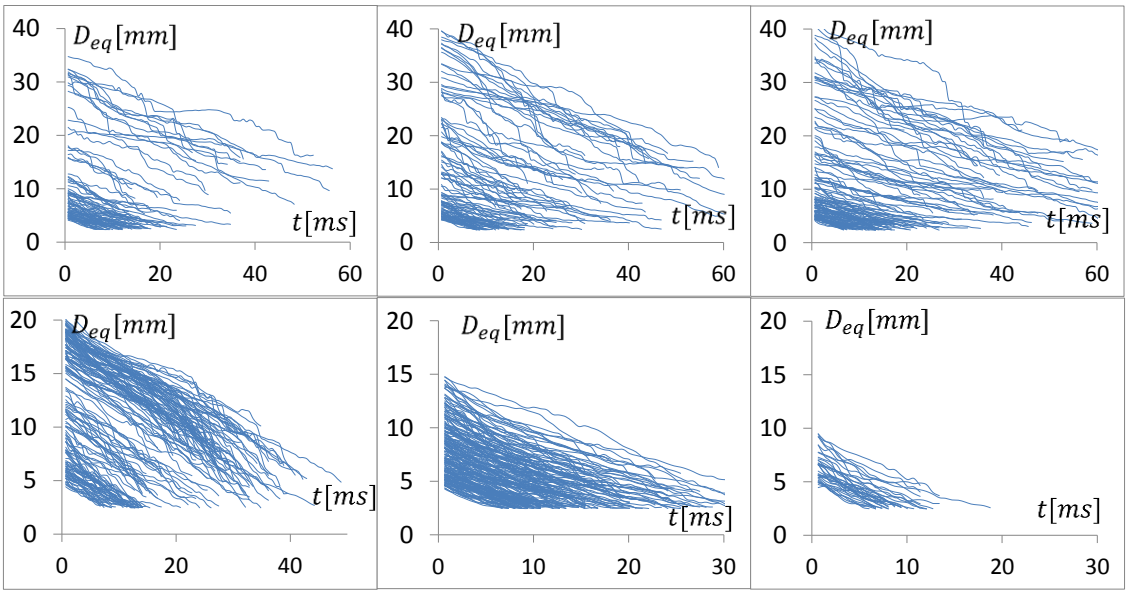

Figure 5.25 Bubble diameter against time at different steam injection velocities for **HIN2X4mm**.
Left: $J_S = 0.09\ m.s^{-1}$, Middle: $J_S = 0.14\ m.s^{-1}$ Right: $J_S = 0.22\ m.s^{-1}$
Upper row: $J_L = 0.4\ m.s^{-1}, T_L = 96°\ C, \Delta T_{sub} \approx 6.4\ K$,
lower row: $J_L = 1.0\ m.s^{-1}, T_L = 98°\ C, \Delta T_{sub} \approx 11.4\ K$,

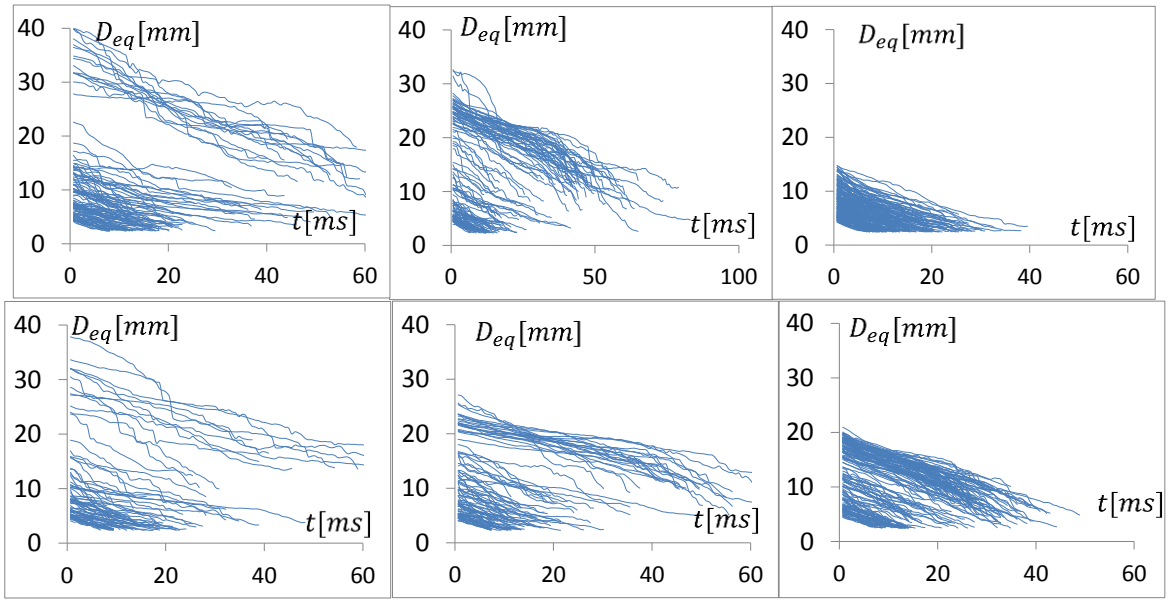

Figure 5.26 Bubble diameter against time at different water velocities for **HIN2X4mm**.
Left: $J_L = 0.4\ m.s^{-1}$, Middle: $J_L = 0.6\ m.s^{-1}$ Right $J_L = 1.0\ m.s^{-1}$
Upper row: $J_S = 0.14\ m.s^{-1}, T_L = 98°\ C, \Delta T_{sub} = 6.0\ K(left), 6.8\ K\ (middle), 11.3K\ (right)$
Lower row: $J_S = 0.09\ m.s^{-1}, T_L = 98°\ C, \Delta T_{sub} = 5.9\ K(left), 6.9K\ (middle), 11.4\ K\ (right)$

5.2.5.2 Influence of the subcooling temperature.

Subcooling temperature affect two issues: bubbles initial diameter and bubble condensation time. Even a small difference of $0.5°\ K$ have a visible effect upon the results.(compare Figure 5.27 upper row, second and third plots at $\Delta T_{sub} = 6.2$ K, and $\Delta T_{sub} = 5.7$ K respectively, and lower row, , second and third plots at $\Delta T_{sub} = 13$ K, and $\Delta T_{sub} = 11.5$ K respectively). Low

subcooling temperatures results in the formation of larger bubbles, and a larger bubbles lifetime. This can be seen clearly from all Figures in this section. However an interesting fact emerges from the classification of bubbles diameter according to the subcooling temperature: The comparison of bubble diameter along time shows that bubbles of the same size experience more shape fluctuations at lower subcooling temperatures. This result can be observed for all results from all nozzle types. An explanation for this observation can be as following: shape fluctuations appears as deformations off the elliptic or circle shape of the bubble images (2D projections), if a shape deformation starts to form at some position of the bubble periphery, there is a concurrence between the speed of formation and the condensation of the bubble. Since the bubble is condensing, the deformation can emerge if the condensation rate of that part of the bubble where the deformation starts allows it to happen. If the rate of the formation of the bubble periphery deformation is equal to the rate of disappearance -as a result of condensation and loss of mass-, then the deformation will not appear. As the condensation rate will be higher at higher subcooling temperatures, the suppression of shape deformations is higher at higher subcooling temperatures. As a conclusion of results from this section and previous section bubble deformation is a function of following parameters:

- Initial bubble size: deformation increases as it increases.
- Adjacent fluid velocity: deformation decreases as it increases.
- Subcooling temperature: deformation increases as it increases.

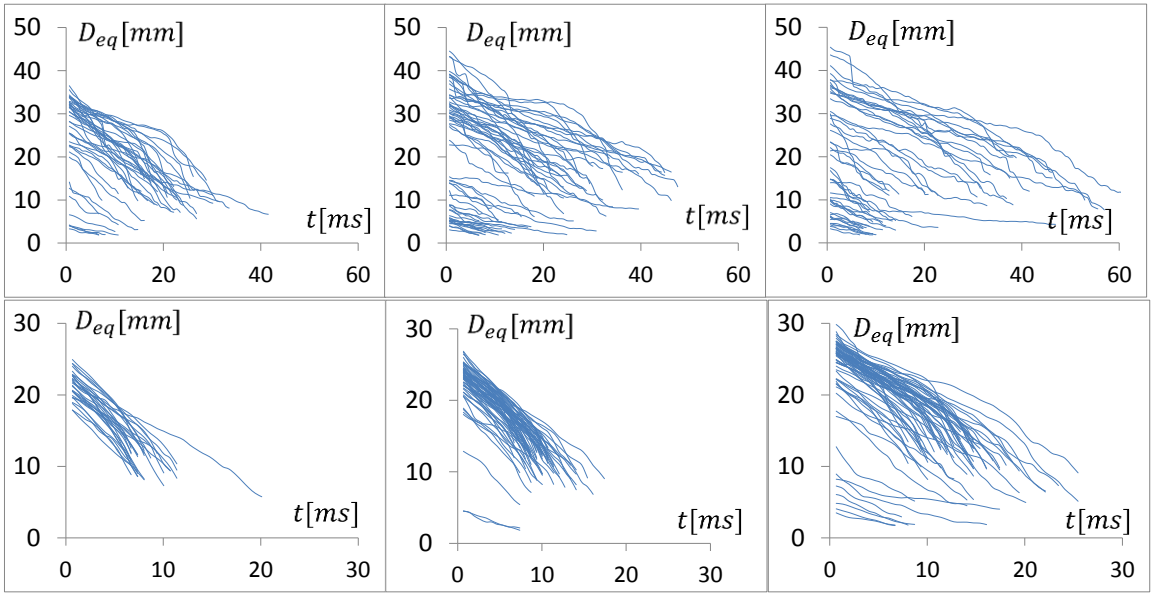

Figure 5.27 Bubble diameter against time at different subcooling temperatures for **CIN4mm**.
$J_S = 0.14\ m.s^{-1}$, Upper row $J_L = 0.4\ m.s^{-1}$, Lower row $J_L = 1.0\ m.s^{-1}$
Upper row: Left:$\Delta T_{sub} = 8.2\ K$, Middle: $\Delta T_{sub} = 6.2\ K$ Right: $\Delta T_{sub} = 5.7\ K$
Lower row: Left:$\Delta T_{sub} = 15\ K$, Middle: $\Delta T_{sub} = 13\ K$ Right: $\Delta T_{sub} = 11.5\ K$

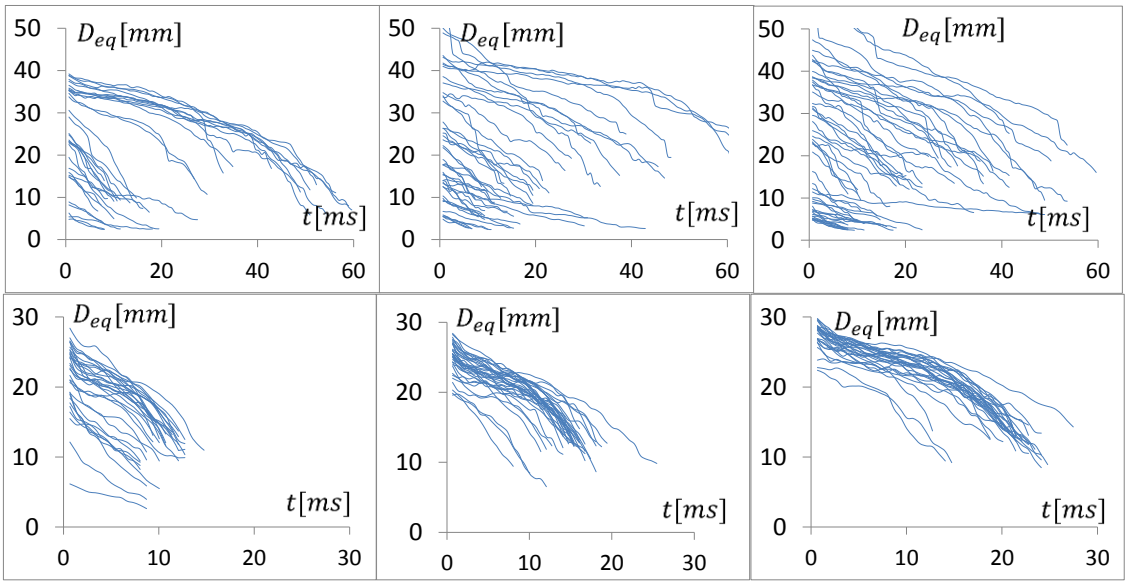

Figure 5.28 Bubble diameter against time at different subcooling temperatures for **CIN6mm**.
$J_S = 0.14\ m.s^{-1}$, Upper row $J_L = 0.4\ m.s^{-1}$, Lower row $J_L = 1.0\ m.s^{-1}$
Upper row: Left:$\Delta T_{sub} = 8.6\ K$, Middle: $\Delta T_{sub} = 6.6\ K$ Right: $\Delta T_{sub} = 6.1\ K$
Lower row: Left:$\Delta T_{sub} = 15.1\ K$, Middle: $\Delta T_{sub} = 13.1\ K$ Right:$\Delta T_{sub} = 11.6\ K$

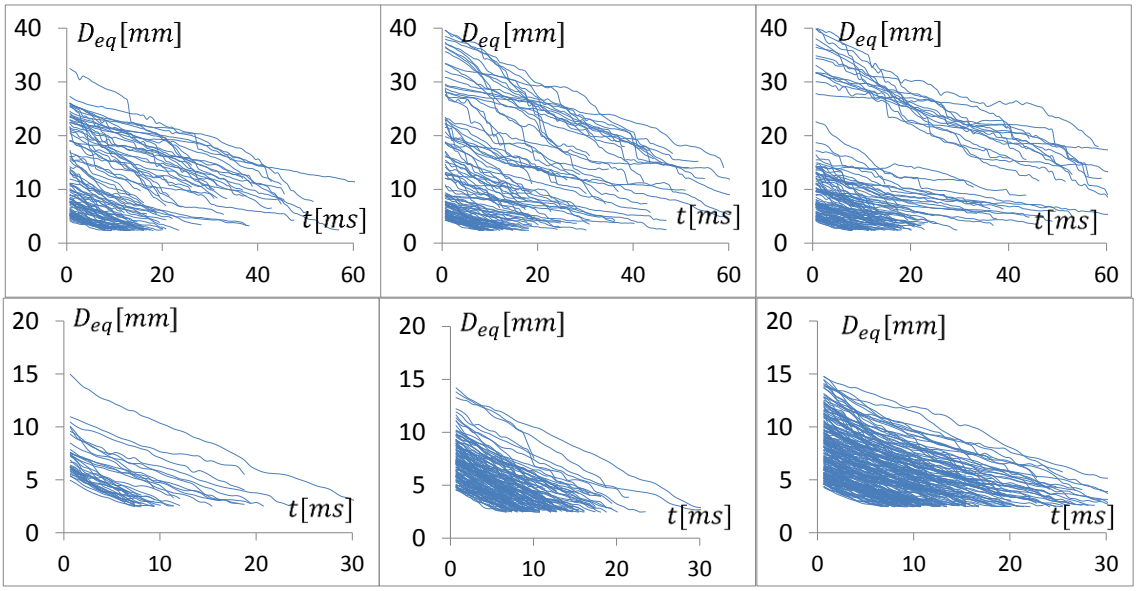

Figure 5.29 Bubble diameter against time at different subcooling temperatures for **HIN2X4mm**.
$J_S = 0.14\ m.s^{-1}$, Upper row $J_L = 0.4\ m.s^{-1}$, Lower row $J_L = 1.0\ m.s^{-1}$
Upper row: Left:$\Delta T_{sub} = 8.2\ K$, Middle: $J_S = \Delta T_{sub} = 6.4\ K$ Right: $\Delta T_{sub} = 6.0\ K$
Lower row: Left:$\Delta T_{sub} = 14.9\ K$, Middle: $\Delta T_{sub} = 12.9\ K$ Right: $\Delta T_{sub} = 11.3\ K$

5.2.7 Bubbles motion and path

5.2.7.1 Bubbles paths

Figures 5.30, 5.32, 5.33, and 5.34 show (x_c, y_c) plots of the center-of-mass of all tracked bubbles for each corresponding case. These plots represent the path of the corresponding bubble. The path does not start from the injection but from the detachment point of each tracked bubble. The upper row of each figure shows bubbles' paths from the CIN4mm nozzle, while the lower row shows it from the HIN2X4mm nozzle. In figure 5.30, The first column shows the path for all tracked bubbles from all flow conditions (i.e. from all water temperatures, steam injection velocities, and water velocities), the second column shows the paths only from $J_L^{*0.5} = 0.4\ \mathrm{m.s^{-1}}$, and the third column shows the paths only from $J_L^{*0.5} = 1.0\ \mathrm{m.s^{-1}}$. The shorter paths at higher water velocities are mainly due to the higher subcooling temperatures. This is not related to the effect of the water velocity but rather to the loop characteristics which results in higher static pressure at the injection point at higher water velocities (the increase of the static pressure comes from the pump). The general tendency of the bubbles lateral movement is to move away from the injection point. This results in diverging trajectories away from the injection nozzle. The divergence increases as the bubbles move upwards. In the case of the CIN4mm larger bubbles are existent (see bubble size distribution comparison between CIN4mm and HIN2X4mm Figure 5.31, left plot). Large bubbles break up resulting in bubbles fragments that follows chaotic trajectories (short lines with non-uniform path direction, Figure 5.30 CIN4mm, $J_L = 0.4\ \mathrm{m.s^{-1}}$). The divergence is generally higher for the HIN2X4mm nozzle than the CIN4mm nozzle. This is mainly due to the injection direction which is vertical in CIN4mm and horizontal in HIN2X4mm. This shows the effect of the initial velocity upon the bubble movement. The divergence is also higher at lower water velocities as at higher water velocities in the case of the HIN2X4mm nozzle due to the effect of the water velocity. The bubble size distribution of the HIN2X4mm nozzle in Figure 5.31, shows that smaller bubbles are generated at higher water velocities, however the bubbles size distributions are not very different as in the case of the CIN4mm nozzle, which indicates that the smoother trajectories in the HIN2X4mm, $J_L = 1.0\ \mathrm{m.s^{-1}}$ are not caused only by the fact that smaller bubbles are generated, but also by the effect of the surrounding water flow. It seems that the higher water velocities enforce the bubbles to travel in straight lines despite the higher liquid turbulence in the case of higher water velocities. Another effect can come from the higher condensation rates related to the higher subcooling temperatures at higher water velocities. This can inhibit the effects of the transversal bubble forces (lift force and turbulent dispersion force). In order to further assert this explanation the bubble paths were sorted according to the initial bubble size. These are presented in Figure 5.32 for the CIN4mm nozzle and in figure 5.33 for the HIN2X4mm nozzle. As a separation limit the bubble threshold diameter of $D = 5.8\ \mathrm{mm}$ for the lift force was used. It separates between bubbles where the lift force works towards the center of the pipe ($D > 5.8\ \mathrm{mm}$) and where it works towards the wall of the pipe ($D < 5.8\ \mathrm{mm}$). A third group for very large bubble was also presented ($D > 15\ \mathrm{mm}$). Figure 5.32 shows that :

- Small bubbles $D < 5.8\,\text{mm}$ are mainly generated by fragmentation from larger bubbles, they have chaotic trajectories; do not follow a general trend, and they have short trajectories.
- Medium bubbles: $5.8\,\text{mm} < D < 15\,\text{mm}$ are also fragments of larger bubbles in this case (The start point of their trajectories are remarkably higher than the lowest detachment point of the all the bubbles trajectories, compare with Figure 5.30). However they have longer trajectories and tend to move near the center of the pipe.
- Large bubbles $D > 15\,\text{mm}$: they compose the main fraction of the bubbles generated by the CIN4mm nozzle. They move clearly in nearly straight trajectories with an outwards movement along the vertical direction.

Figure 5.33 shows the trajectories from the HIN2X4mm:

- Small bubbles $D < 5.8\,\text{mm}$ are also generated as fragments from larger bubbles, they also have short trajectories. However they seem to have pit longer paths as the case of the CIN4mm nozzle due to the lower condensation rate. The trajectories of the small bubbles follow the movement of the larger bubbles.
- Medium bubbles: $5.8\,\text{mm} < D < 15\,\text{mm}$ are either fragments of larger bubbles or generated directly from the injection nozzle. Their trajectories tend to be concentrated in straight lines near the center of the pipe, however with a remarkable outward movement for the larger bubbles (~bubbles with the longest trajectories).
- Large bubbles $D > 15\,\text{mm}$: they have a more clear outward movement despite that a large concentration of straight trajectories near the pipe's center is noticeable. They move clearly in nearly straight trajectories which diverge outwards along the vertical direction.

The above remarks from the bubble-size resolved trajectories show that within current experiments: larger bubbles tend to have straighter trajectories as smaller bubbles generated out of fragmentation. This confirms the previous discussion that the straighter trajectories at higher water velocities are not the result of the smaller bubbles sizes rather than the combined effect of the water velocity and the higher condensation rate. Bubbles generated from the CIN4mm nozzle (Figure 5.30 upper row, middle plot, $J_L = 0.4\,\text{m.s}^{-1}$) move in straight path directly after the detachment until they lose the initial vertical velocity gained from the steam injection. Afterwards, they start to move outwards from the nozzle center. Smaller bubbles from $J_L = 1.0\,\text{m.s}^{-1}$ case start this outwards movement already at detachment. Smaller bubbles will not gain as much momentum from the injection process as the larger bubbles (compare the narrow bottom of the flame from $J_L = 0.4\,\text{m.s}^{-1}$ with the wider one from $J_L = 1.0\,\text{m.s}^{-1}$).

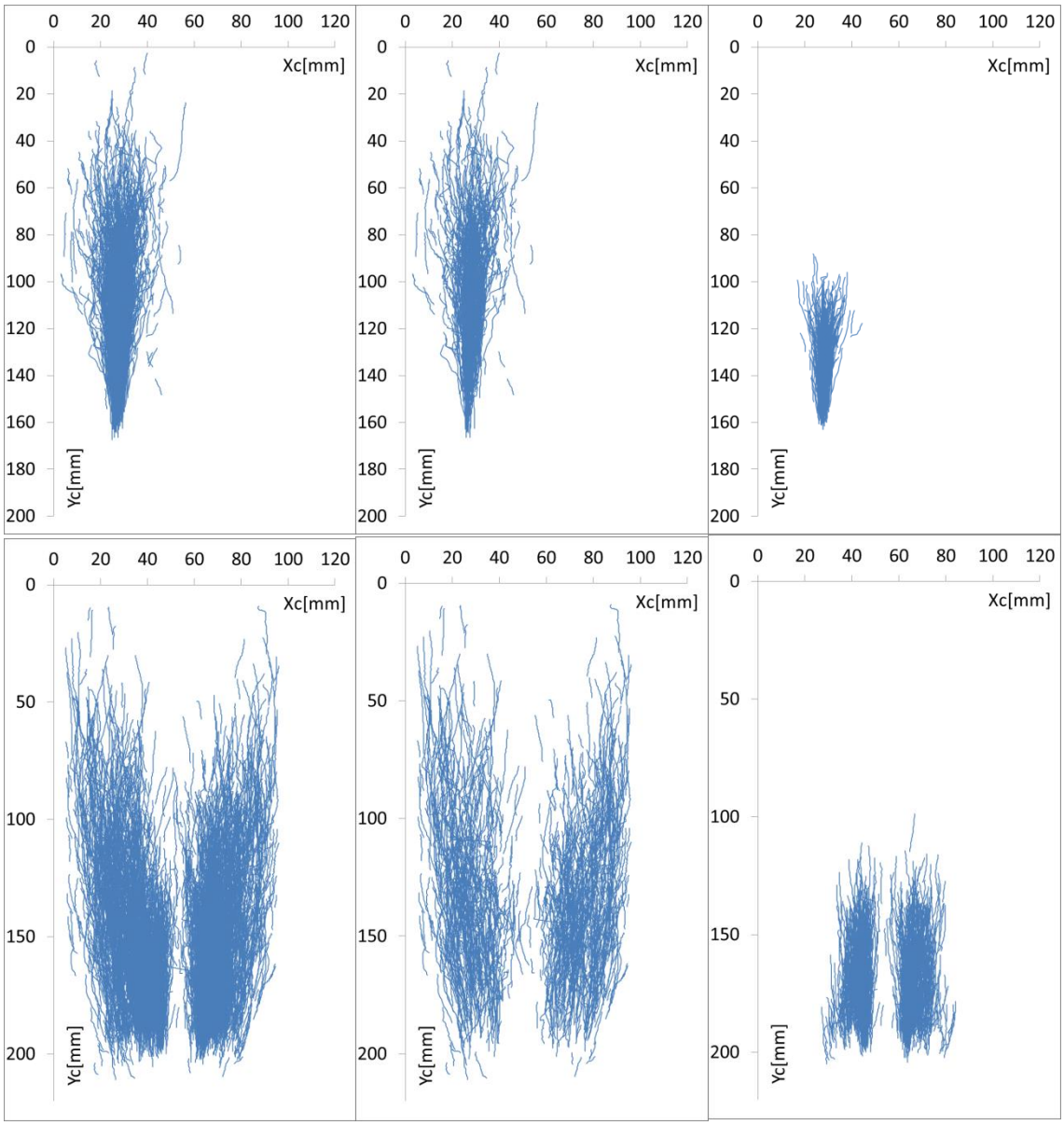

Figure 5.30 Steam Bubbles' path after detachment.
Upper row: CIN4mm nozzle, Lower row:HIN2X4mm nozzle

Left: All paths .Middle: paths at $J_L = 0.4\ \mathrm{m.s^{-1}}$, Right paths at $J_L = 1.0\ \mathrm{m.s^{-1}}$

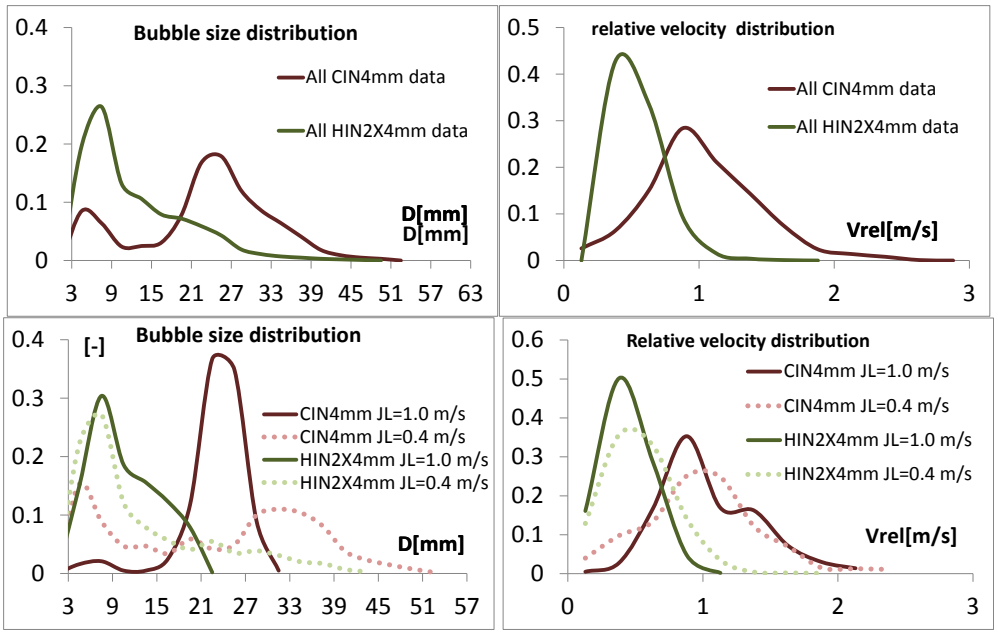

Figure 5.31 A comparison of the bubbles size distribution and bubbles relative velocity between the CIN4mm and HIN2X4mm nozzles at different water velocities.

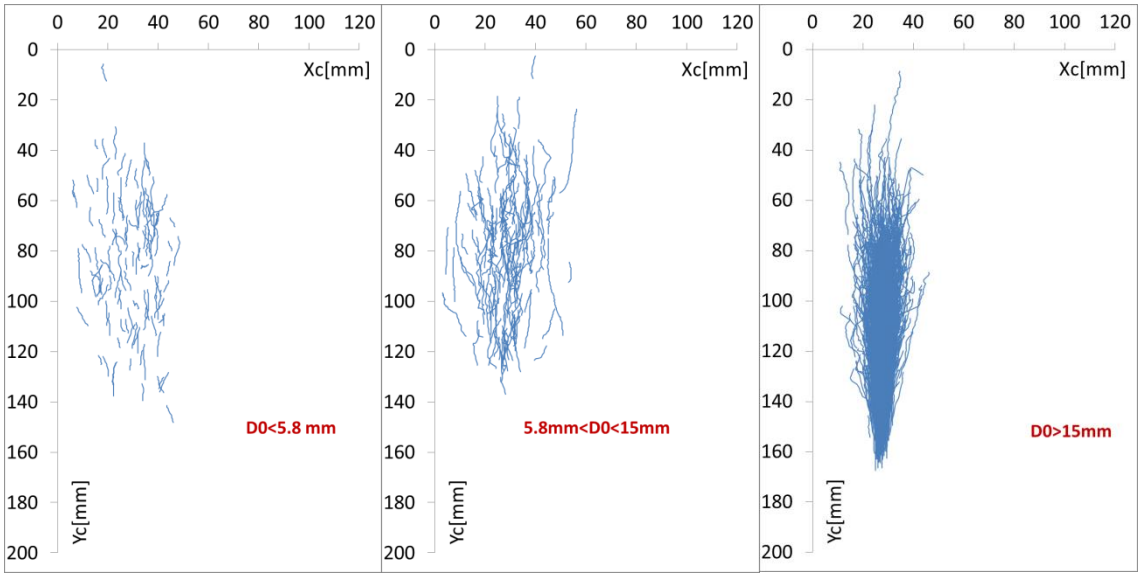

Figure 5.32 Steam Bubbles' path after detachment sorted according to the initial bubble diameter, CIN4mm nozzle.

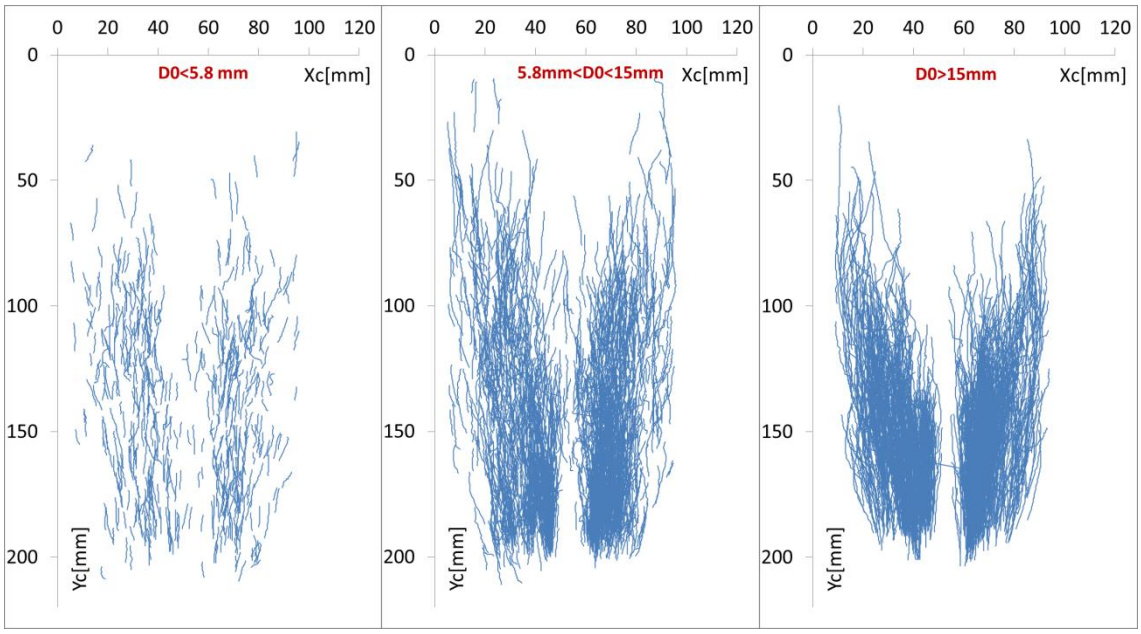

Figure 5.33 Steam Bubbles' path after detachment sorted according to the initial bubble diameter, HIN2X4mm nozzle.

In figure 5.34 The first column shows the path for all bubbles from all flow conditions, the second column shows the paths only for $J_s^{*0.5} = 0.09\ \mathrm{m.s^{-1}}$, and the third column shows the paths only for $J_s^{*0.5} = 0.22\ \mathrm{m.s^{-1}}$. It can be clearly seen that for both injection nozzles bubbles at higher steam injection velocities tend to have a higher outwards movement. For the CIN4mm nozzle the initial injection velocity is vertical and thus this effect cannot be caused by the initial injection. High steam injection velocities generate a higher turbulence inside the bubbles. This gas turbulence affects the bubbles deformation and movement. In this case, higher gas turbulence contributes to a higher lateral movement of the bubbles as figure 5.34, upper row shows. For the HIN2X4mm nozzle a clear lateral displacement occurs following the higher horizontal steam injection velocity. The effect of the initial steam velocity upon the movement of the generated bubbles is obvious. However even after the initial displacement, a more pronounced outward movement occurs at higher steam injection velocity. This can be returned partially to the increased gas turbulence within the generated bubbles in similar way to the CIN4mm case. Finally the trajectories at higher steam injection velocities deviates are more curved and twisted due to the effect of higher bubbles deformation at higher bubble sizes.

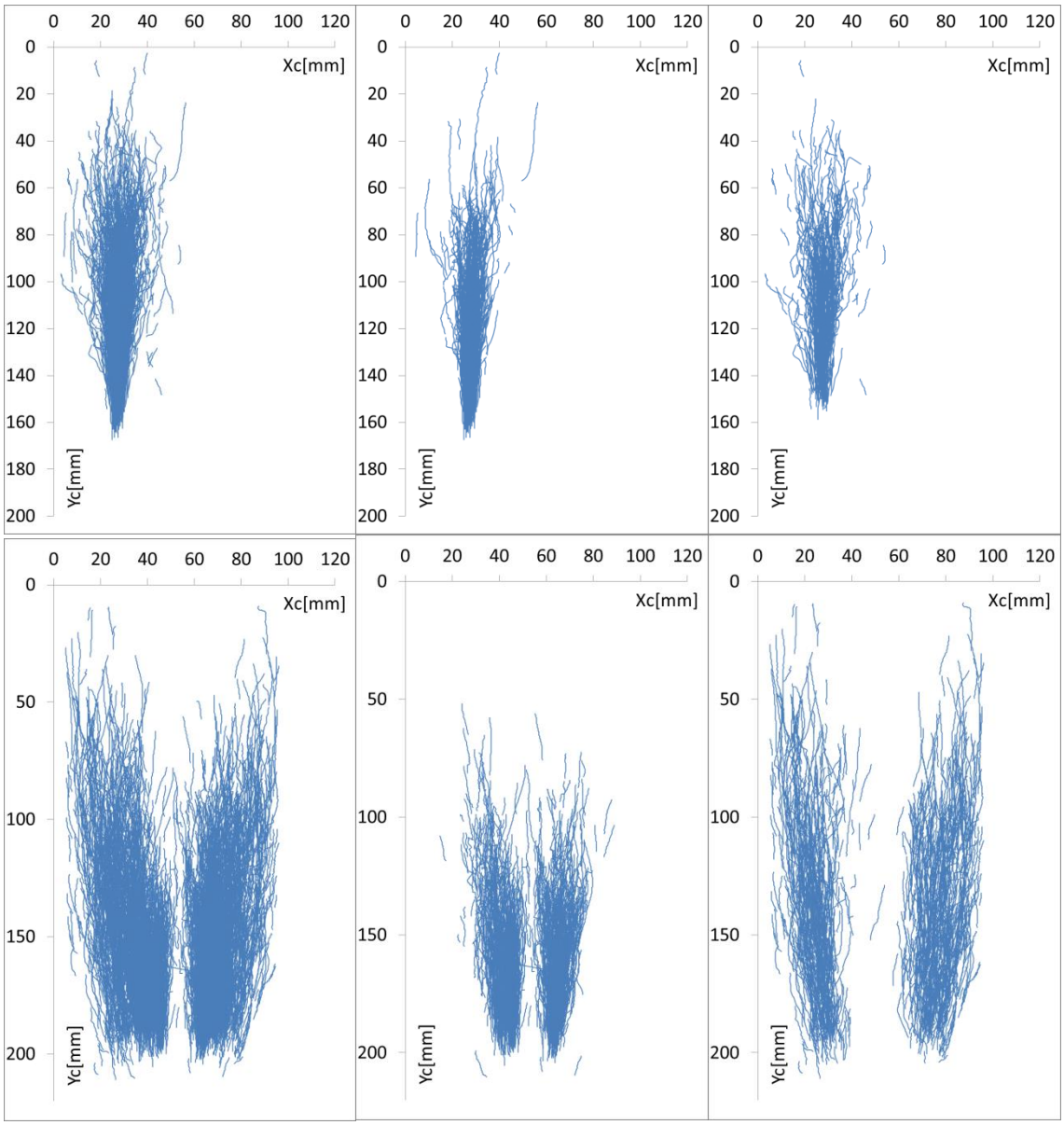

Figure 5.34 Steam Bubbles' path after detachment.
Upper row: CIN4mm nozzle, lower row:HIN2X4mm nozzle.
Left: All paths .Middle: paths at $J_s = 0.09\ \mathrm{m.s^{-1}}$, Right paths at $J_s = 0.22\ \mathrm{m.s^{-1}}$

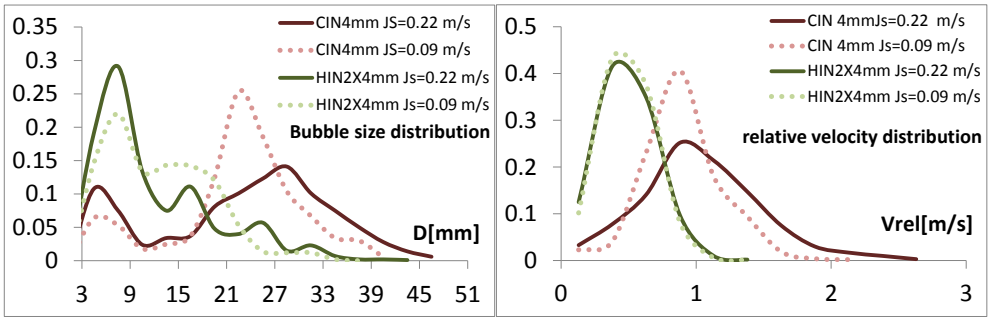

Figure 5.35 A comparison of the bubbles size distribution and bubbles relative velocity between the CIN4mm and HIN2X4mm nozzles at different steam injection velocities.

From the above discussion following conclusion can be stated over steam bubbles movement:

- Bubbles movement is affected by the initial conditions and mainly by the value of the injection velocity and the direction of the injection. Generally the turbulence resulting from the injection process increases the bubbles lateral movement (CIN4mm). The initial horizontal injection contributes to the outward lateral movement of the bubbles (HIN2X4mm).
- Flow conditions around the bubbles also affect their movement, and for instance bubbles experience increased lateral movement as the surrounding liquid velocity decreases, whereas the opposite occurs as the steam injection velocities increase.
- Sorting of the bubbles' paths according to the bubble initial diameter does not shows no clear effect of the bubbles lift force (weather a clear outward movement for $D_0 < 5.8\,\text{mm}$, and inward movement for $D_0 > 5.8\,\text{mm}$). This is mainly because the condensation path is largely affected by vertical forces and turbulence rather than lateral forces. However, the sorting shows that larger bubbles do have straighter trajectories than smaller bubbles. This can represent an effect of the lift force, compensating the effect of the outward movement caused by the gas turbulence and subsequent deformation.
- It is quite complicated to explain each trajectory within the Figures. This is due to the fact that a main influence upon the bubbles movement and the instantaneous change of its path comes from the bubble deformation, which plays a major role in the bubbles condensation as well.
- A more detailed investigation of the movement of the steam bubbles seems to be necessary, in particular the effect of various lateral forces upon the final bubble movement and trajectory.

5.2.7.2 Bubbles' rising velocity

Figures 5.36-5.43 shows the vertical position of the center-of-mass of the tracked bubbles against time. The vertical position is the position taken directly from the Bubble images files where the y index starts at the top of the image and increases downwards. That is why the vertical index is decreasing while the bubbles are rising upwards. The absolute value of the slope of the plotted lines within each figure represents the rising velocity of the corresponding tracked bubbles. The vertical index was left as it is in order to remain representative of the absolute position of the bubble among all plots. Additionally the start point and the end point of each line indicate the positions at which the bubble was first and last tracked. This convention does not affect the final goal of presenting these plots which is the comparison between the slope of different lines and change of the slope remains the same. The data within the plots are sorted according to the water velocity and steam injection velocity to illustrate the effect of flow conditions upon this parameter. Within each figure there two plots are shown: one shows the data through 1s of acquisition and gives an idea about the general behavior of the rising velocity, and the second zooms the data into 0.4 s period to show the details of the individual lines. Figures 5.36-5.39 shows data from the CIN4mm nozzle, while Figures 5.40-5.43 shows data from the HIN2X4mm nozzle.

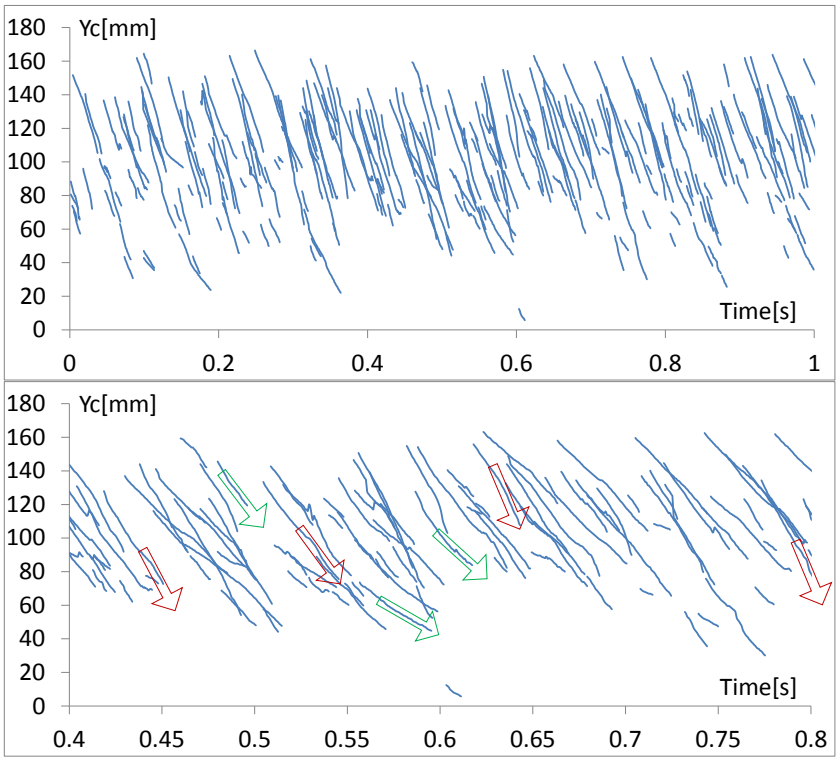

Figure 5.36 Bubbles' center-of-mass vertical position against time $y(t)$, CIN4mm nozzle $J_L = 0.4\ \mathrm{m.s^{-1}}$. Upper plot: 1s of recording. Lower plot: 0.4 s. The slope of each line represents the rise velocity of one bubble. Red arrow: Acceleration, green arrow: deceleration.

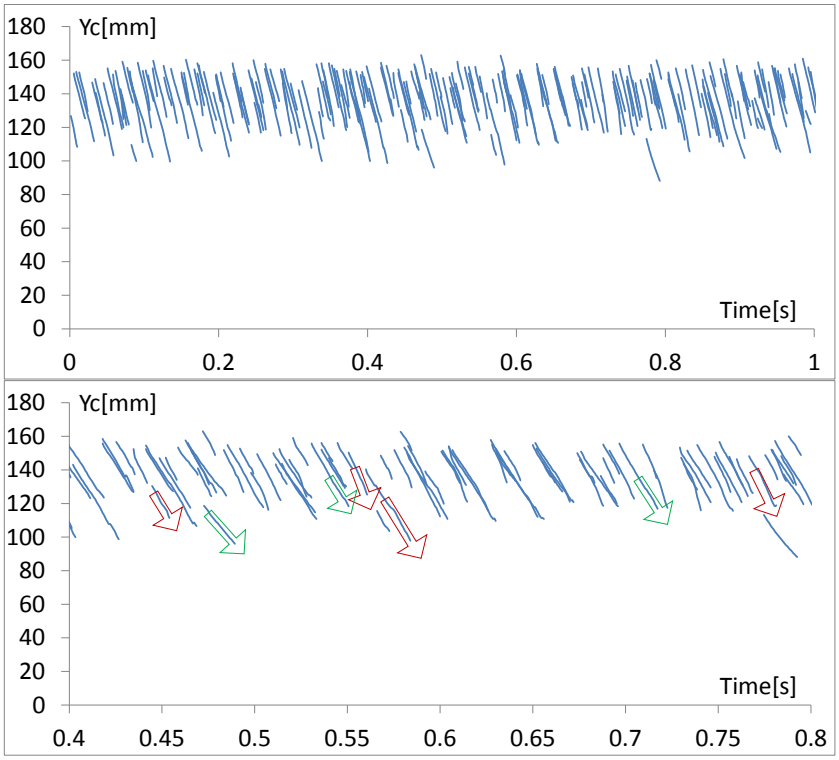

Figure 5.37 Bubbles' center-of-mass vertical position against time $y(t)$, CIN4mm nozzle $J_L = 1.0\ \mathrm{m.s^{-1}}$. Upper plot: 1s of recording. Lower plot: 0.4 s. The slope of each line represents the rise velocity of one bubble. Red arrow: Acceleration, green arrow: deceleration.

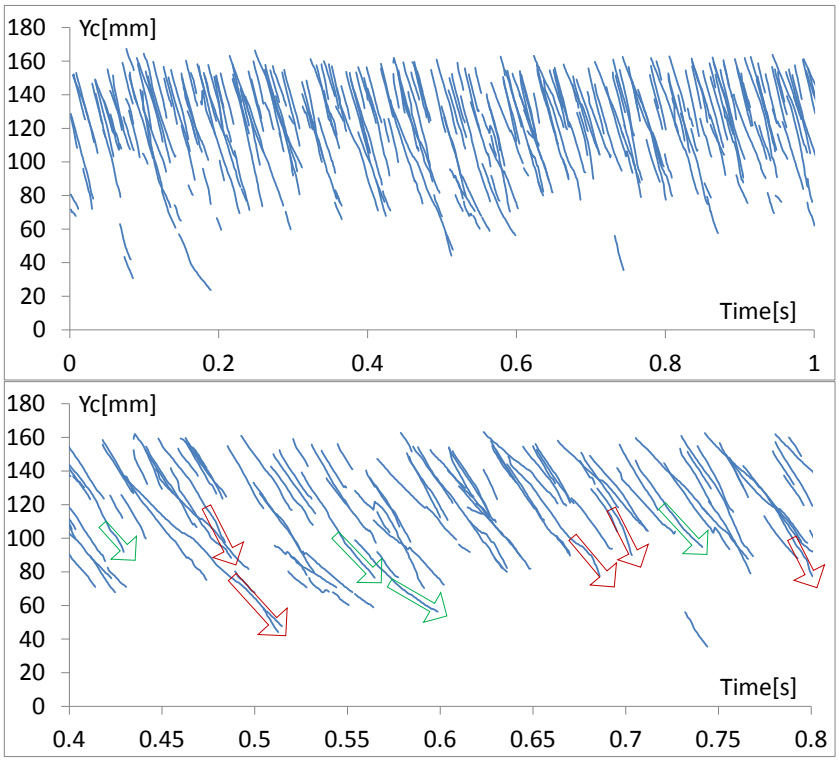

Figure 5.38 Bubbles' center-of-mass vertical position against time $y(t)$, CIN4mm nozzle $J_s = 0.09\ \mathrm{m.s^{-1}}$. Upper plot: 1s of recording. Lower plot: 0.4 s. The slope of each line represents the rise velocity of one bubble. Red arrow: Acceleration, green arrow: deceleration.

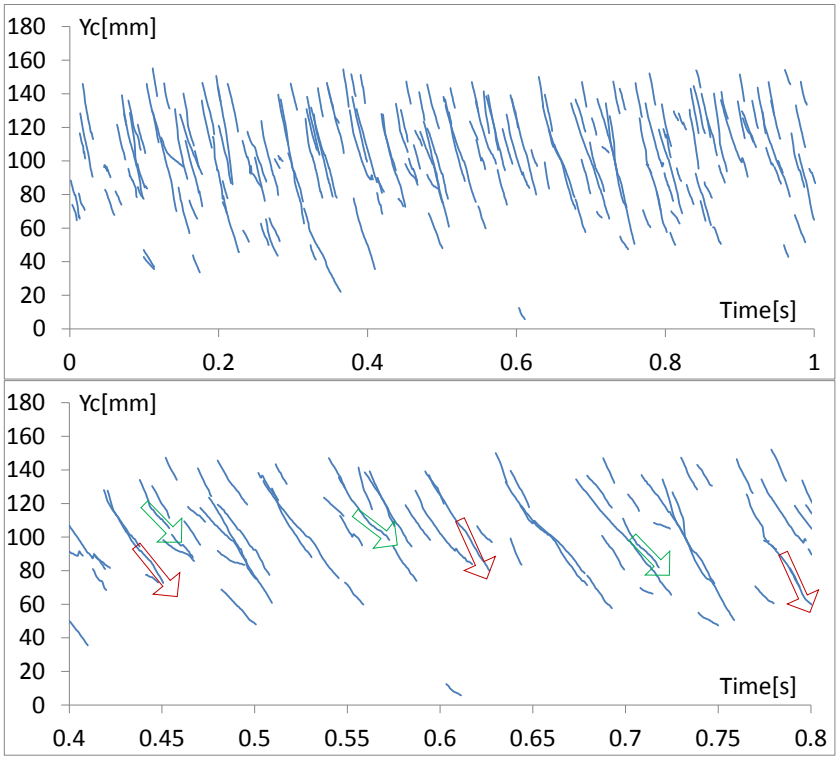

Figure 5.39 Bubbles' center-of-mass vertical position against time $y(t)$, CIN4mm nozzle $J_s = 0.22\ \mathrm{m.s^{-1}}$. Upper plot: 1s of recording. Lower plot: 0.4 s. The slope of each line represents the rise velocity of one bubble. Red arrow: Acceleration, green arrow: deceleration.

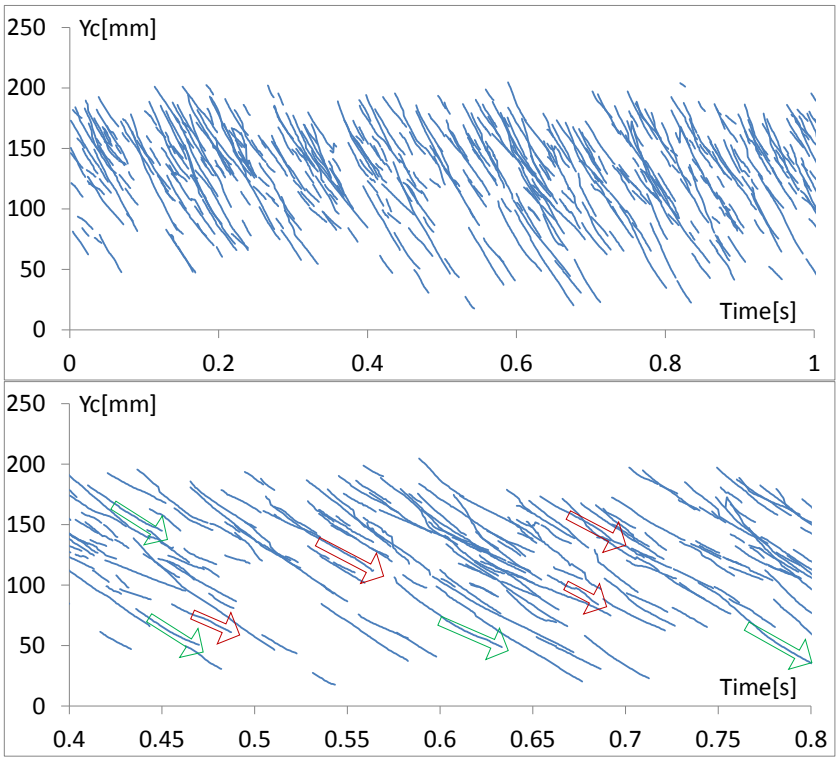

Figure 5.40 Bubbles' center-of-mass vertical position against time $y(t)$, HIN2X4mm nozzle $J_L = 0.4\ \mathrm{m.s^{-1}}$. Upper plot: 1s of recording. Lower plot: 0.4 s. The slope of each line represents the rise velocity of one bubble. Red arrow: Acceleration, green arrow: deceleration.

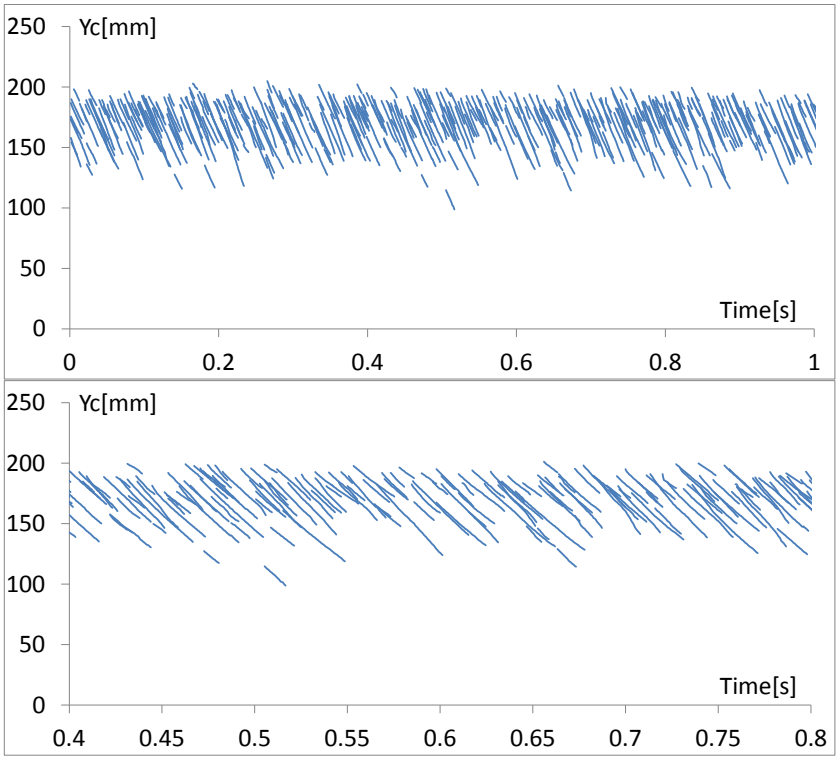

Figure 5.41 Bubbles' center-of-mass vertical position against time $y(t)$, HIN2X4mm nozzle $J_L = 1.0\ \mathrm{m.s^{-1}}$. Upper plot: 1s of recording. Lower plot: 0.4 s. The slope of each line represents the rise velocity of one bubble.

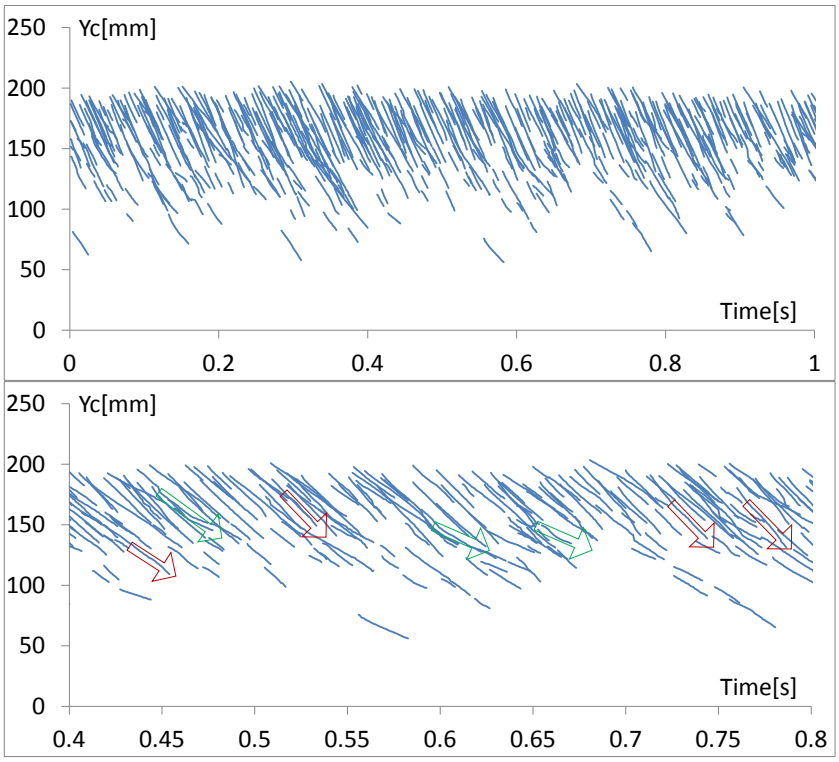

Figure 5.42 Bubbles' center-of-mass vertical position against time $y(t)$, HIN2X4mm nozzle $J_s = 0.09\ \mathrm{m.s^{-1}}$. Upper plot: 1s of recording. Lower plot: 0.4 s. The slope of each line represents the rise velocity of one bubble. Red arrow: Acceleration, green arrow: deceleration.

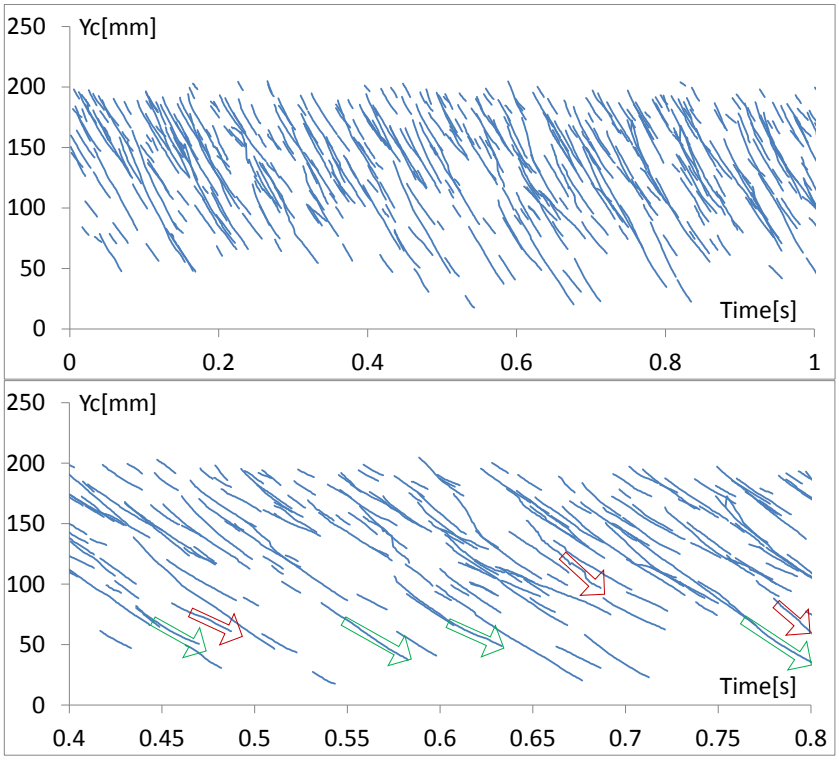

Figure 5.43 Bubbles' center-of-mass vertical position against time $y(t)$, HIN2X4mm nozzle $J_L = 0.22\ \mathrm{m.s^{-1}}$. Upper plot: 1s of recording. Lower plot: 0.4 s. The slope of each line represents the rise velocity of one bubble. Red arrow: Acceleration, green arrow: deceleration.

The following can be noticed from the above presented plots:

- In general, the rising velocities calculated according to equation 4.8 (between $t = t(D = D_0) - t(D = 0.4D_0)$) are proved to be consistent within these plots. The overall inclination of each line is a good representative of the corresponding bubble velocity. The plots show a lot of parallel lines indicating similar rising velocities for similar bubbles. Despite large deformations the bubbles suffer, the overall slope matches the instantaneous slope over the entire condensation time with exceptions.
- Some bubbles show a systematic change of the rising velocity near the end of the condensation time. The change however can be positive(acceleration) or negative (deceleration). These changes are not drastic, and are mainly due to bubbles changing its shape, or condensation rate during condensation process. the fact that the rising velocity is calculated only until $t(D = 0.4D_0)$ can neutralize these effects. Nevertheless some sudden changes do occur where a sudden and large change of the bubble's shape or diameter occur. These are a result of the bubble deformation, movement, shape projection and mistakes from applied identification and tracking procedures.
- The changes of the rising velocities occurs more frequently at lower water velocities and higher steam injection velocities, tightly combined to the notes over the bubble movement from the bubbles path plots (see section 5.2.7.1).
- The lines at high water velocities ($J_L = 1\ \mathrm{m.s^{-1}}$) shows a remarkable parallel lines with a minimal change of the lines slope. This is due to two factors. First: The Bubble-size distributions are concentrated around a single peak in this case (see Figure 5.31) and thus similar rising velocities are expected. Second: As it was illustrated in the last section, bubbles' paths at higher water velocities seems to be straightened by the surrounding liquid flow field resulting in a less fluctuating trajectory and thus a more constant rising velocity.
- Within the presented plots there is no systematic acceleration or deceleration of the bubble s it rises, but rather a tendency towards a constant velocity. This means that the bubble does not change its rising velocity as it condenses and getting smaller, or it does not show a larger rising velocities at the beginning when it possess a larger diameter and thus a larger buoyancy, and this occurs despite the fact that larger bubbles do have larger relative velocities as the relative velocities distributions show. In order to explain this phenomenon there is some suggestions to be made: The effect of the added mass force and the visual observations that shows higher deformation at higher bubble diameters. The first is the effect of the added mass force: as the bubble condense a condensate mass envelope the bubble throughout the condensation. In order to accelerate this mass a work should be excreted and this can counter the acceleration of the bubble when it is at the beginning of the condensation process. This effect however should be numerically tested and validated. The second reason can be the bubble large deformation at larger diameters. Surface shape deformations, and surface roughness can add more drag to the bubble movement preventing it from a further acceleration. However one obvious reason for the constant rinsing velocities is also the short lifetime of steam bubbles. One can suggest that even acceleration is going to take place, the short available time for the bubble make it difficult to see its effect. As it was shown within the already presented plots, some bubbles suffer from a

deceleration as well, which suggest that the main factor affecting bubble speed is the shape deformation and development of the whole condensation process. Similar to the bubbles movement issue a further investigation is required.

5.2.8 Time-averaged 2D distributions of void fractions

Another parameter that can be deduced from the raw images is the time-averaged steam flames. These plots give a useful and close imprint of the time-averaged steam fraction 2D distributions within the projected plane of the camera chip. Since the swarm effect is minimal within current experiments (due to the frequent existence of one bubble or a train of bubbles), these plots can be considered as a good approximation of the time-averaged void fraction 2D distribution within the center plane of the pipe. They can be used to validate numerical calculations of the void fraction regarding: shape and extension of the steam flames out of the injection nozzles, and the trend of the directional decrease/increase. If the intensity within an image frame t at specific location/pixel (x, y) was considered as a function:

$$I_t(x, y)$$

The following probability function can be defined:

$$\Psi_t(x, y) = \begin{vmatrix} 1 & I_t(x, y) \neq 0 \\ 0 & I_t(x, y) = 0 \end{vmatrix} \quad (5.8)$$

The Time-averaged probability at each pixel will represent –to some extent- the value of the average void fraction within the mid-plane at that pixel as follows:

$$\overline{\alpha}(x, y) = \frac{\sum_0^{N_{max}} \Psi_{t(x,y)}}{N_{max}} \quad (5.9)$$

$$\mathrm{N_{max}} = \text{total number of averaged instances } (= 3000 \text{ in current work})$$

This definition of the void fraction was frequently used to define the local time-averaged void fraction from the data obtained from measuring devices like the needle probe. It should be mentioned that these distributions are not ideal. For instance the center of some bubbles tends to have lower intensity (white reflection that is not handled by the filling procedure). These result in lower probability within the center of the maximum area of the distribution. This can be easily noticed from distributions which do not have this feature (compare first flame and– from left- in Figure 5.44 as an example). Figures 5.44-5.49 show the result of equation 5.9 for nozzles CIN4mm, and HIN2X4mm. Each figure corresponds to one water superficial velocity. The flames within each figure are arranged according to the water temperature and then according to the steam injection velocity. This means that flames 1-3 (from left) corresponds to the water temperature $T_w = 94°C$, flames 4-6 corresponds to $T_w = 96°C$, and flames 7-9 corresponds to $T_w = 98°C$. Flames at each water temperature are arranged according to the steam superficial velocity with the first corresponds to $J_s = 0.09\ \mathrm{m.s^{-1}}$, the second corresponds to $J_s = 0.14\ \mathrm{m.s^{-1}}$ and the third corresponds to $J_s = 0.22\ \mathrm{m.s^{-1}}$. The color index is shown within each figure, pure blue corresponds to and area occupied with

water during the entire 2s acquisition time and pure red corresponds to an area occupied with steam bubbles the entire 2s acquisition time. The shape and void fraction distribution within the resulting flames takes into consideration the bubbles which are still attached to the injection nozzle in order to give a realistic shape of steam flames. For distributions of only detached bubbles see equation 5.10 and 5.11 at the end of this section.

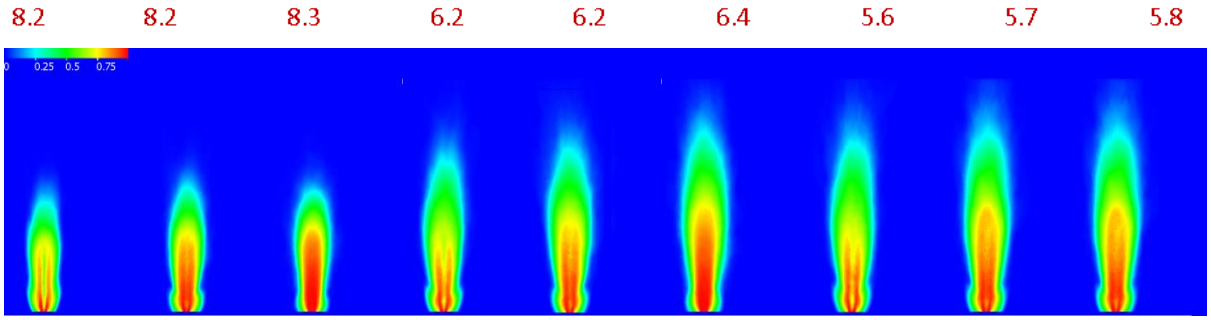

Figure 5.44: Time-averaged steam flames according to equation (5.9). CIN4mm nozzle, $\boldsymbol{J_L = 0.4\ \mathrm{m.s^{-1}}}$. Left to right: flames are arranged according to the water temperature $T = 94°, 96°, 98°$ C, and then according to the steam superficial velocity $J_s = 0.09, 0.14, 0.22\ \mathrm{m.s^{-1}}$.The red numbers above show the corresponding subcooling temperature in [k].

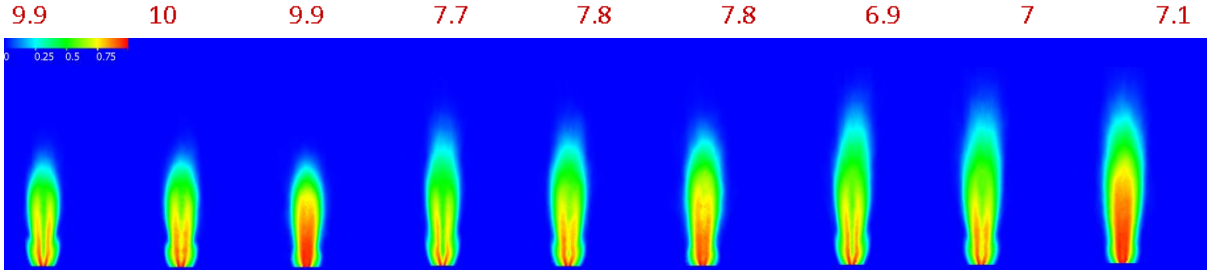

Figure 5.45: Time-averaged flames according to equation (5.9). CIN4mm nozzle $\boldsymbol{J_L = 0.6\ \mathrm{m.s^{-1}}}$. Left to right: Flames are arranged according to the water temperature $T = 94°, 96°, 98°$ C, and then according to steam superficial velocity $J_s = 0.09, 0.14, 0.22\ \mathrm{m.s^{-1}}$. The red numbers above show the corresponding subcooling temperature in [k].

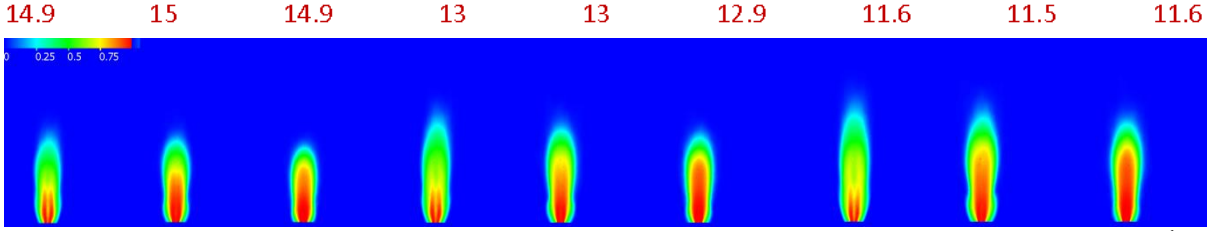

Figure 5.46: Time-averaged flames according to equation (5.9). CIN4mm nozzle $\boldsymbol{J_L = 1.0\ \mathrm{m.s^{-1}}}$. Left to right: Flames are arranged according to the water temperature $T = 94°, 96°, 98°$ C, and then according to the steam superficial velocity $J_s = 0.09, 0.14, 0.22\ \mathrm{m.s^{-1}}$. The red numbers above show the corresponding subcooling temperature in [k].

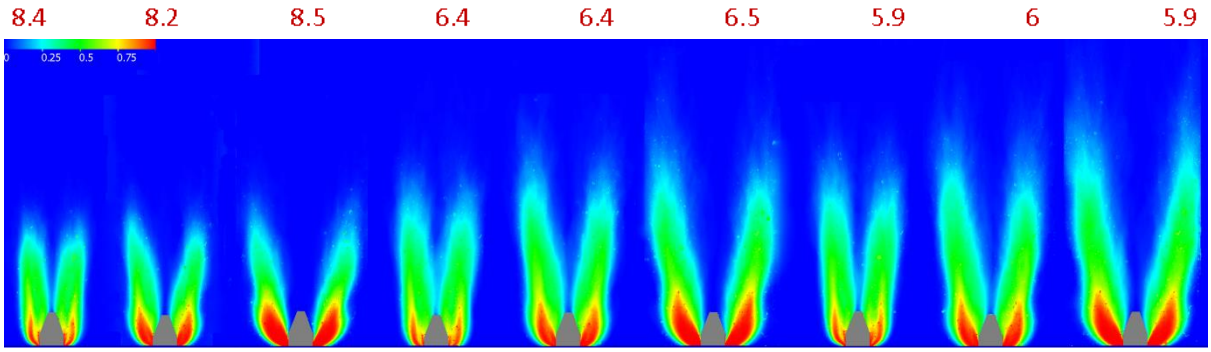

Figure 5.47: Time-averaged steam flames according to equation (5.9). HIN2X4mm nozzle $\boldsymbol{J_L = 0.4\ m.s^{-1}}$. Left to right: flames are arranged according to the water temperature $T = 94°, 96°, 98°$ C, and then according to the steam superficial velocity $J_s = 0.09, 0.14, 0.22\ \mathrm{m.s^{-1}}$. The red numbers above show the corresponding subcooling temperature in [k].

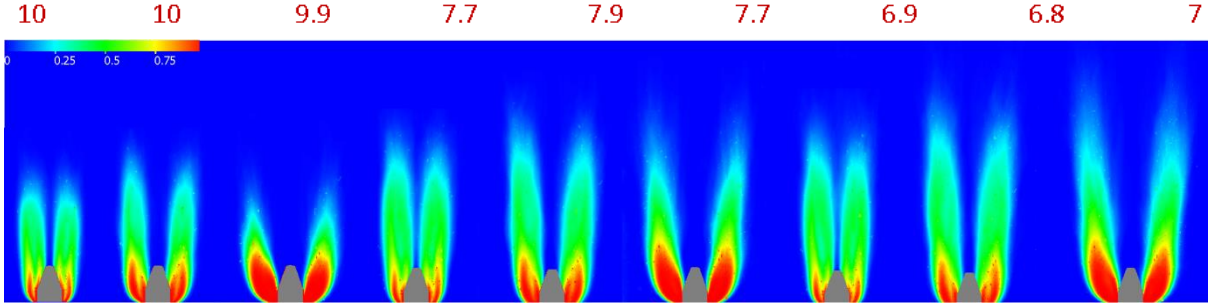

Figure 5.48: Time-averaged steam flames according to equation (5.9). HIN2X4mm nozzle $\boldsymbol{J_L = 0.6\ m.s^{-1}}$. Left to right: flames are arranged according to the water temperature $T = 94°, 96°, 98°$ C, and then according to the steam superficial velocity $J_s = 0.09, 0.14, 0.22\ \mathrm{m.s^{-1}}$. The red numbers above show the corresponding subcooling temperature in [k].

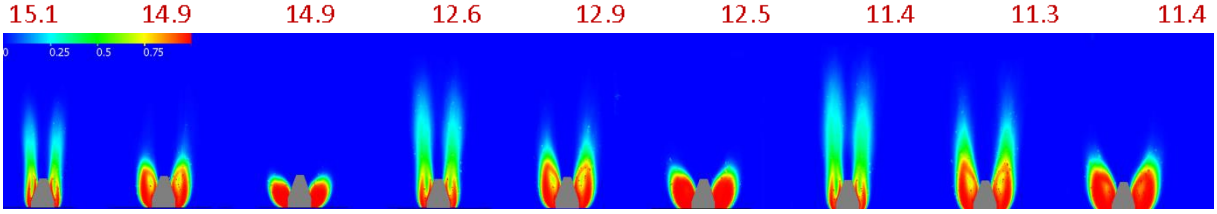

Figure 5.49: Time-averaged steam flames according to equation (5.9). HIN2X4mm nozzle $\boldsymbol{J_L = 1.0\ m.s^{-1}}$. Left to right: flames are arranged according to the water temperature $T = 94°, 96°, 98°$ C, and then according to the steam superficial velocity $J_s = 0.09, 0.14, 0.22\ \mathrm{m.s^{-1}}$. The red numbers above show the corresponding subcooling temperature in [k].

The final shape and void fraction distribution is a result of the competition of the following factors:

- Flow conditions: Steam and water superficial velocities and water temperature (subcooling temperature).
- Bubble size and rising velocities.

These factors lead to a competition among:

- Amount of injected steam.
- Ratio of the direct contact condensation and thus the ratio of remaining bubbles that can travel upwards and extend the flame vertically.
- The resulting condensation rate of the detached bubbles.

For a better comparison the subcooling temperatures were shown above each figure and they correspond to the flames in the figure below in the same order. Figure 5.50 shows the bubble size distributions at different steam and water velocities for all nozzles.

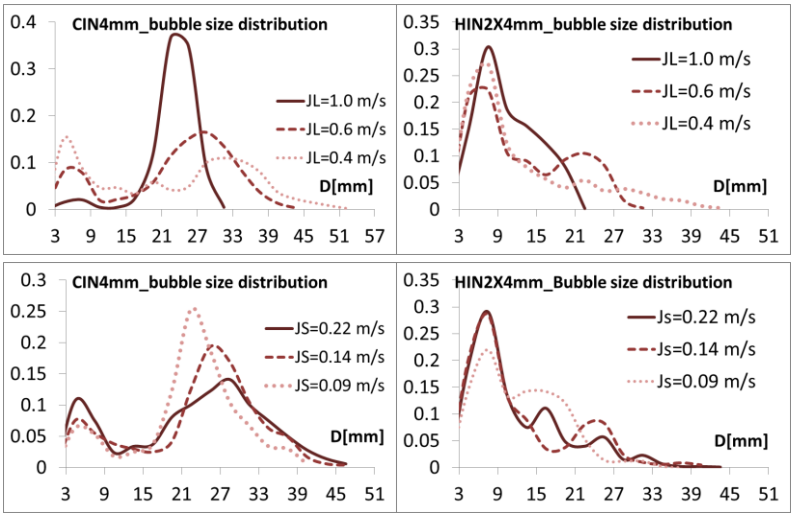

Figure 5.50 Upper row: Bubble size distribution according to the water superficial velocity. lower row: Bubbles size distribution according to the steam superficial velocity.

For CIN4mm nozzle following remarks can be seen:

- The flames get smaller in vertical and horizontal directions as J_L gets higher. This effect is caused by the fact that the bubble size distribution shifts towards lower values as J_L increases. This affects the horizontal extension of the flames and can be noticed even close to the injection point (where the bubbles are the start of condensation). Another reason in the increased subcooling temperature and in particular the case of $J_L = 1.0\ \mathrm{m.s^{-1}}$ where the bubbles size is also remarkably lower (see Figures 5.44 vs 5.46 and 5.47 vs 5.49).
- The decrease of the subcooling temperature causes the flames to get larger in vertical and horizontal direction. This result is trivial.
- In general: higher void fraction values are noticed near the center of the flames at higher steam superficial velocities even if the flame does not get larger in size. this can be seen in Figures: 5.44, and 5.45.
- As the steam superficial velocity increases the amount of injected steam is also increased. However this will generates higher injection velocities and thus higher condensation rates. Both effects balance the result and it can be seen that many of the flames at $J_s = 0.09\ ,\ and\ 0.14\ \mathrm{m.s^{-1}}$ are similar in size (Figures 5.44 and 5.45). At $J_L = 1.0\ \mathrm{m.s^{-1}}$ (Figure 5.46) the flames becomes smaller at highest steam superficial

velocity. This is due to the lower bubble sizes which cause the bubbles to condense in a shorter distance.

For HIN2X4mm nozzle, the effect of the turbulence from steam injection is minimized.

- At $J_L = 0.4\ \mathrm{m.s^{-1}}$ (Figure 5.47) flames are larger size and vertical extension as the steam injection velocity increases. At $J_L = 0.6\ \mathrm{m.s^{-1}}$(Figure 5.48) this effect can be seen except for the last case of $J_s = 0.22\ \mathrm{m.s^{-1}}$ where the vertical extension of the steam flame is less than that of the case of $J_s = 0.14\ \mathrm{m.s^{-1}}$. The reason lies with the increasing rate of direct contact condensation DCC as the water velocity increases. The same effect can be seen in the case of $J_L = 1.0\ \mathrm{m.s^{-1}}$ (Figure 5.49) between the cases of $J_s = 0.14\ \mathrm{m.s^{-1}}$and $J_s = 0.22\ \mathrm{m.s^{-1}}$.
- At $J_L = 1.0\ \mathrm{m.s^{-1}}$ (Figure 5.49) there exist a special case at low steam injection velocity. Here remarkably small bubbles are generated. These bubbles (see section 5.2.2) are smooth and more rounded and they have low condensation rate that allows them to rise a considerable distance before they completely condense. This explains why the flames vertical extension is large at low steam injection velocities.
- As it was mentioned in previous sections, the amount by which the twin flames diverge from each other increases by increasing the steam injection velocity. This is a natural effect of the steam horizontal injection. Meanwhile, the divergence is minimized by increasing the water velocity forcing the bubbles to travel in straight paths.

The previously presented flames incorporate both: detached bubbles and bubbles (and steam film) still attached to the injection nozzle. However, another set of void fraction distributions can be obtained by excluding the none-detached bubbles from the calculation of the distributions. These distributions are useful for CFX simulations since only the detached bubbles are considered in mono-dispersed or multi-dispersed approaches. The non-detached bubbles and the steam film that are still attached to the injection point should be modeled using direct contact condensation and require the steam phase to be considered as a continuous phase (not as a dispersed phase, particles). A model that combines both phenomena at the same time is thus not possible. These distributions are obtained as follows:

$$\Psi_t^d(x,y) = \begin{cases} 1 & I_t(x,y) \neq 0 \ \cap \ (x,y) \in detached\ bubble \\ 0 & I_t(x,y) = 0 \end{cases} \tag{5.10}$$

The time-averaged probability at each pixel is calculated as follows:

$$\overline{\alpha}^d(x,y) = \frac{\sum_0^{N_{max}} \Psi_t^d(x,y)}{N_{max}} \tag{5.11}$$

$$\mathrm{N_{max}} = \text{total number of averaged instances } (= 3000 \text{ in current work})$$

Figures 5.51 and 5.52 show an example of the resulting distribution in two cases #18 and #72. The lower part of the resulting distributions is taken as an input for CFX simulations (see section 6.3). As it can be seen form the resulting distributions, the detachment point has a 2D spatial distribution, it starts slightly close to the nozzle and approach a maximum at a certain

distance range. The distributions for CFD must be taken at the point where the bubbles-flame starts to shrink. Prior this point, the distribution is a combination of already-detached bubbles and bubbles that detached earlier and condensed upon reaching the corresponding point.

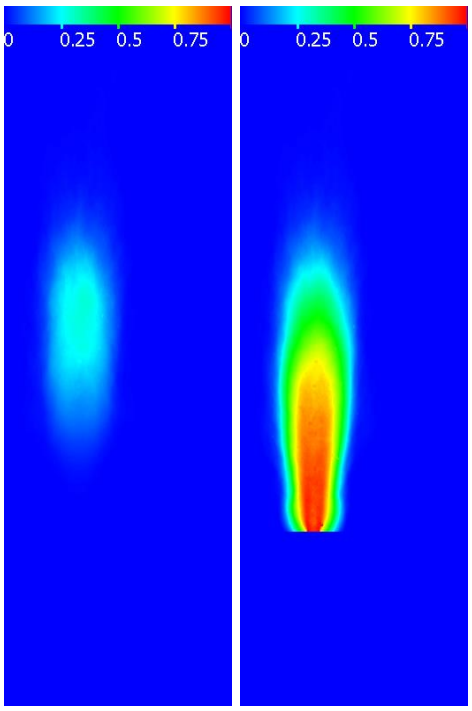

Figure 5.51 The time-averaged void fraction distribution of CIN4mm nozzle case 18. Left: Only detached bubbles, right detached and non-detached steam.

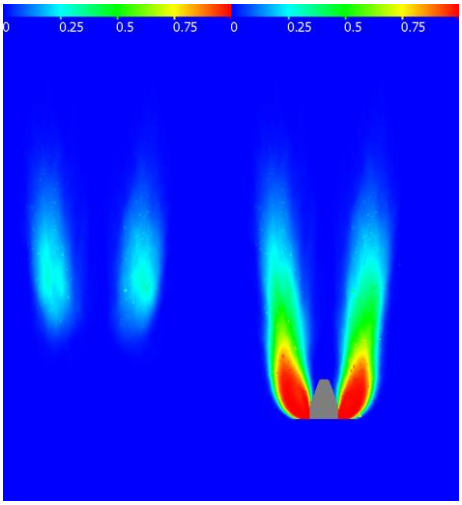

Figure 5.52 The time-averaged void fraction distribution of CIN4mm nozzle case 18. Left: Only detached bubbles, right detached and non-detached steam.

5.2.9 Conclusions of SCUBA experimental Results

SCUBA enabled a thorough experimental investigation of steam bubbles condensation at low pressure using direct injection of steam bubbles into a subcooled liquid flow, and covering a

wide range of flow parameters (subcooling temperature, fluid velocity, steam injection velocity, and bubbles diameter). The investigations covered the none-researched range of large steam bubbles ($D_{B,eq} > 8\,\mathrm{mm}$) with high Reynolds numbers in a large diameter (DN100) pipe geometry. Flow conditions were varied systematically according to a predefined test matrix in order to study the influence of flow conditions upon the condensation process. The investigations along with presented results and plots provide a phenomenological explanation for the condensation process under these conditions as a stand-alone phenomenon. It also tackles the effect of steam injection on the condensation process. The heat transfer between the bubbles and the liquid was evaluated by deriving new best-fit correlations based on the measured values of the Reynolds and Nusselt numbers. These correlations are suitable for larger bubble size, high Reynolds number, and large deformation and they do not replace those developed for different flow conditions and range of applicability (see table 5.2). However, the new correlations extend the already available database for the validation of interfacial heat and mass transfer correlations which is of large interest for safety equipment in nuclear reactors (e.g. IRWST). These were implemented to improve the performance of CFD simulations as chapter 6 will show. The analysis of the experimental results showed also new and interesting observations for large bubbles with high Reynolds number such as: rough and vibrating bubble surfaces that lead into an enhanced heat transfer. The amount of covered visual illustrations and analyzed parameters give a very detailed and deep look into this subject and show the capabilities that the test facility, the developed programs and HSC technique can provide for further investigations. Additional knowledge can be still acquired if the local liquid velocity can be measured in the future. This will allow a better calculation of the bubbles relative velocities and minimize the data scatter that was seen in Nu-Re plots.

Chapter 6 CFX Simulation of some of SCUBA test cases

In order to evaluate the functionality of the obtained Nu-Re correlations in previous section, some CFD simulation was carried out for some steam experiments to validate the steam fraction distribution against experimental data. Within these computations the performance of the newly obtained correlations was compared to the already existing Nu-Re correlation. Within experiments the steam is directly injected into the pipe's center. A direct contact condensation (DCC) occurs first followed by detachment of steam bubbles off the steam flame/ or film that is formed and attached to the injection nozzle. Bubbles start to condense within the flowing water directly after detachment. It is highly complicated to simulate the entire process of: DCC, bubbles detachment, and bubbles condensation, and additionally; only the last phenomenon is of interest for the current work. The simulation of the DCC requires also a quite different treatment and modeling (steam should be treated as a continuous phase), while during steam bubbles condensation steam is a dispersed phase with a specific average bubble diameter. In order to facilitate the modeling process, only the condensation of the steam bubbles will be simulated and compared with experiments. For this purpose new steam flames (void fraction distributions) were generated from the recorded images that correspond only to the fully detached steam bubbles. Out of these 2D distributions the steam distribution at the bottom of the resulting flame was extracted and used as an initial void fraction distribution for the numerical simulations. The steam was considered as a mono-dispersed gas phase with an average bubble diameter that is obtained out of the experimental bubble-size distributions. Relying on this approach CFD simulations and experiments can be well comparable. The rest of the parameters were taken out of the experiments: the water temperature, the water mass flow rate, and the static pressure at the injection point (=saturation temperature). Following sections give a detailed description of the applied geometry, meshing and physical models.

6.1 Geometry

The simple geometry of a quarter of the pipe was used. Figure 6.1 shows the applied geometry. Since only the detached bubbles are o be simulated, the injection nozzle was not accounted for in the built geometry. The 90° of the pipe geometry was used to allow an easy meshing of the pipe's cross section, mainly to allow creating a fine mesh near the center of the pipe easily.

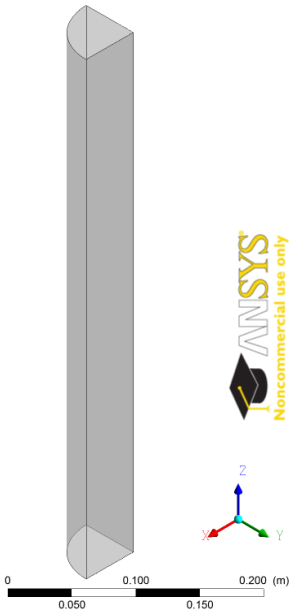

Figure 6.1 Geometry of the calculation domain for SCUBA CFX simulations.

6.2 Meshing

Figures 6.2-6.3 shows the meshing scheme. ANSYS ICEM 12.1 was used in order to block the cross section and allow creating a well-discretized mesh near the center of the pipe using hexahedral meshing elements. The meshing within the cross section was refined near the center region (square-like region) where most of the condensation process occurs. The meshing was also refined near the pipe's outer wall using suitable "inflation factors" in order to create a mesh that is more refined near the wall. The meshing in the axial direction was made using a 1 mm step which is quite sufficient for the intended purpose. The resulting mesh consists of 540417 hexahedral volume mesh element and 570500 nodes. A more refined mesh does not produce more accurate results.

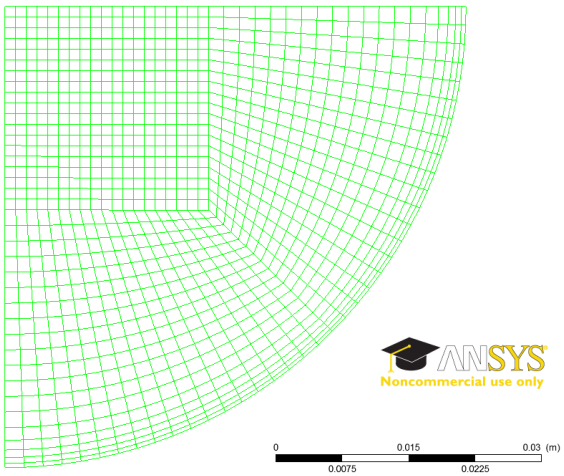

Figure 6.2 The mesh in the cross section of the pipe. The mesh is refined towards the center and the pipe’s wall.

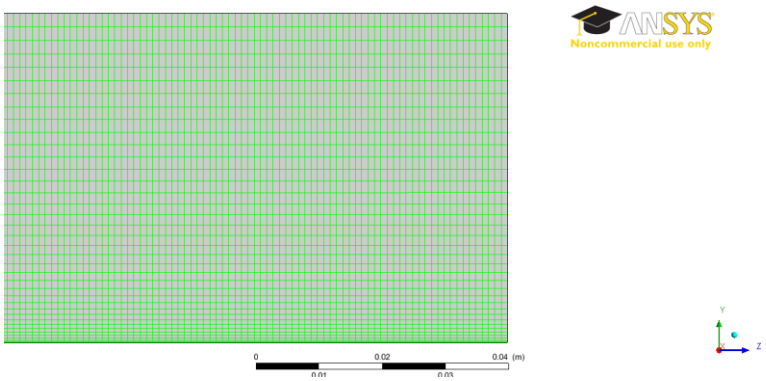

Figure 6.3 the mesh along the axis of the pipe. Mesh refinement towards the pipe's outer wall can be clearly seen.

6.3 Boundary conditions

Figure 6.4 shows the adopted boundary conditions. At the inlet (entrance of the pipe) a constant mass flow rate of water of a constant temperature is assumed. A steam void fraction distribution was calculated out of the experimental data and a 2D steam fraction profile was provided at the inlet, figure 6.5 shows an example of such a distribution in the case of CIN4mm nozzle. The steam saturation temperature is determined by the local existent static pressure. The static pressure itself was considered as a function of the axial elevation $f(z)$, assuming a constant average static pressure at the outlet. The constant value will be equal to the experimentally measured static pressure at the injection plus the water head at the outlet (0.5 m of water head). The steam velocity was also taken from experimental data by adding the water velocity to the average bubbles relative velocity obtained from the relative velocities distributions. A wall with non-slip condition was considered at the pipe's wall. A symmetry condition was applied to the two remaining walls.

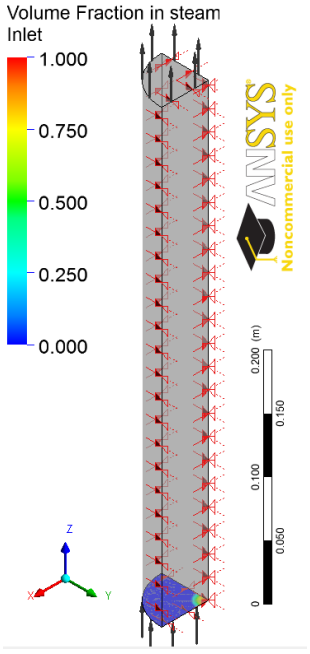

Figure 6.4 Boundary conditions.

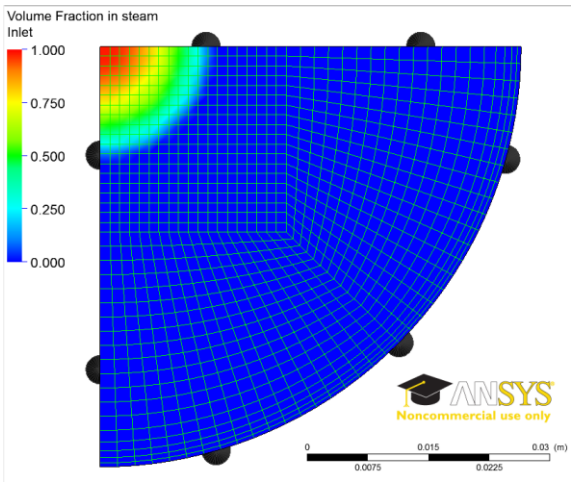

Figure 6.5 An example of the void fraction distribution applied at the inlet.

In order to set the void fraction distribution at the inlet, the time-averaged void fraction distributions of the detached bubbles were used. The development of the normalized average void fraction along the vertical axis was calculated out of these distributions as figures 6.6 and 6.7 shows. This plot was used to determine the point at which the axial void fraction begins to decrease. The relative void fraction shown in over-mentioned figures start to increase from the lowest detachment point, and then it increases as more bubbles detach. It reaches a maximum at the point where no more detachment occurs and thus this point was considered to represent the point above it only condensation occurs. A radial void fraction distribution was extracted at this point and implemented into the inlet as a boundary void fraction profile(see figure 6.5).

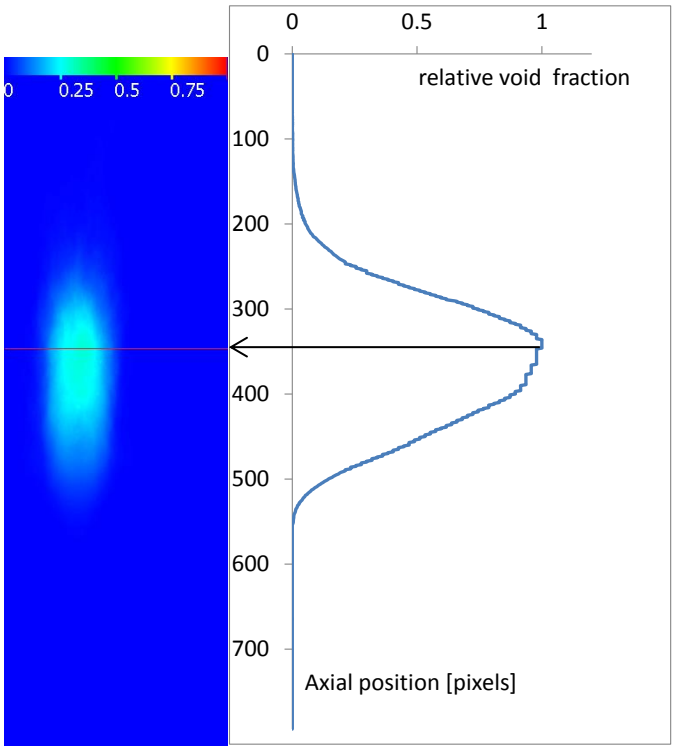

Figure 6.6 Extraction of the initial void fraction distribution from experimental data case #18. Left: experimental time-averaged and detached steam bubble 2D distribution. Right: the axial development of the void fraction and the point at which it starts to decrease.

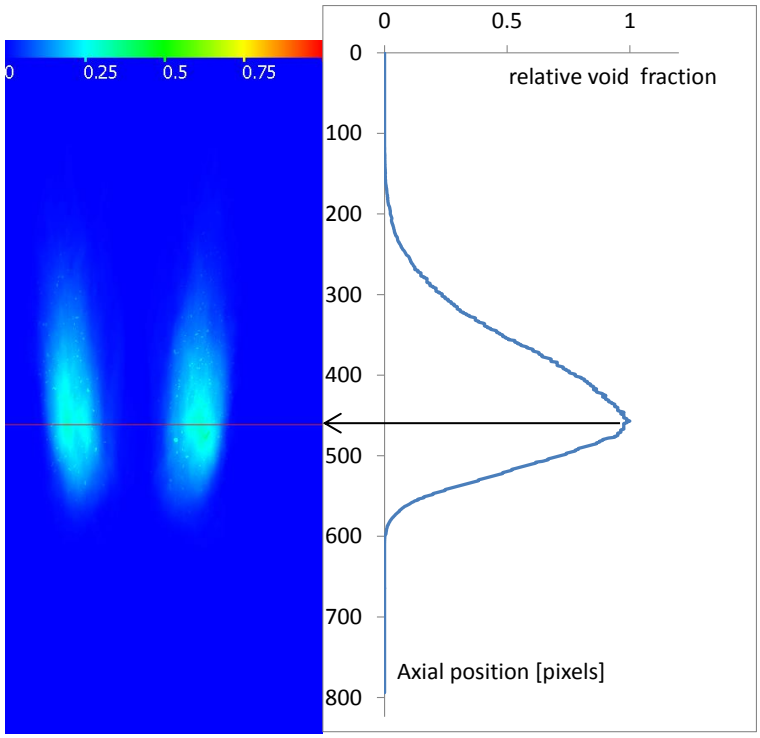

Figure 6.7 Extraction of the initial void fraction distribution from experimental data case #72. Left: experimental time-averaged and detached steam bubble 2D distribution. Right: the axial development of the void fraction and the point at which it starts to decrease.

6.4 Physical models

Two-fluid model was applied to the main domain with two materials: water as a continuous phase and steam as a dispersed phase. A mono-dispersed steam bubbles with an average bubble diameter $\overline{D}$ derived out of the experiments was applied. Buoyancy force for density differences was considered. Following bubble forces were considered for the interfacial momentum transfer:

- The Grace drag force: with void fraction correction exponent 4. A large value was adopted to allow rising velocities to stay as constant as possible and thus close to experiments. Lower exponent value leads to a fast decrease of the rising velocity.
- The virtual added mass force with 0.5 coefficients.
- The turbulent dispersion force: Defined according to Lopez de Bertodano with 0.5 coefficient.

The Tomiyama lift force has a small effect since it is a lateral force. As already explained in section 5.2.7.1 the effect of the lift force cannot be clearly seen from the experimental results even when the results are sorted according to the initial bubble diameter and the Tomiyama lift force critical diameter. Two-phase $k-\varepsilon$ turbulence model was adopted. As most of the condensation and bubble movement occurs near the pipe's center, the $k-\varepsilon$ model can perform satisfactory in these conditions .The heat transfer from the gas phase into the liquid phase was treated using the two resistance model. Using this model, two heat resistances can be defined on the liquid side, and on the gas side. The resistance on the gas side is usually

assumed to be zero, and thus the resistance on the liquid side defined through the heat transfer coefficient allows to implement the desired Nu-Re correlation. Among the built-in correlations Ranz-Marshall is the most implemented throughout most of the commercial CFDs including CFX12.1. The experimental Nu-Re correlation was implemented to compare the effect of the enhanced heat transfer.

6.5 Initialization

The calculation domain was initialized by filling it with water which has a velocity and a temperature equal to the experimental values. The steam void fraction distribution, and steam velocity were provided at the inlet. The steam temperature was calculated as a function of the static pressure, which is calculated as a function of the axial *z* coordinate considering the the experimentally measured value at the injection point. This will results in the correct experimental subcooling temperature at the inlet.

6.6 Numeric

Steady state simulations were carried out with the upwind advection scheme for numeric. This scheme allows getting a stable solution. First order numeric was considered for turbulence calculation, also for simplicity and fast calculations, besides that no complicated liquid turbulence profile is expected near the pipe's center (turbulence within the gas phase cannot be considered in such a simulation). A physical time scale of 5 ms was considered for the solution. The convergence criteria were 10^{-5} in these calculations.

6.7 Results

Table 6.1 shows the experimental cases which were simulated. Each simulation case was carried out using two Nu-Re correlations: the first was taken out of the experiments, and the other was CFX12.1 built-in Ranz-Marshall correlation.

Table 6.1 Flow conditions of the simulated cases

Case	$J_w[m.s^{-1}]$	$J_s[m.s^{-1}]$	$T_{test}[°C]$	$\Delta T_{sub}[K]$	$\overline{D}[mm]$	$V_{steam}[\mathrm{m.s^{-1}}]$
#18	0.6	0.22	98	~7	24	1.62
#72	0.6	0.22	98	7.3	13	1.1

6.7.1 CIN4mm case #18

Figure 6.8 shows a comparison of the steam fraction distribution between the experimental (left), CFX12.1 calculations using the experimental Nu-Re correlation (middle), and CFX12.1 calculations using Ranz-Marshal built-in correlation for the same flow conditions. As it can be seen the use of the built-in Ranz-Marshall correlation will result in a large deviation from

realistic experimental distribution. Meanwhile, the use of the improved experimental Nu-re correlation (5.2, CIN4mm case) yields a result that approaches the experiments.

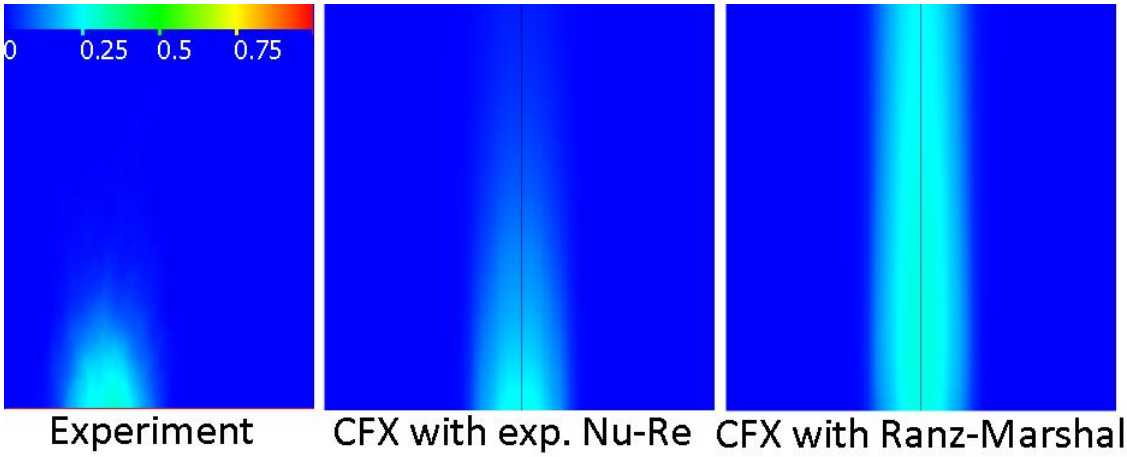

Figure 6.8 A comparision between: Left: experimental distribution of the time-averaged steam fraction of the detached bubbles, Middle: CFX simulation using experimental Nu-Re (Equation 5.2 [CIN4mm]), and right: CFX simulation using Ranz-Marshall corelation. The color scale within the experimental results applies for all plots.

The reason behind that the experimental distribution is still shorter that the simulated one, even with the enhanced Nu-Re correlation, is the steam rising velocity. Most built-in correlations for handling drag are optimized for smaller bubbles (in comparison to the bubbles size within these calculations), and thus the simulation did not reflect the experimental fact that the bubbles rising velocity was nearly constant (see figure 6.9 for steam velocity using experimental and Ranz-Marshall correlation). The rising velocity decreases due to the drag and even when the void fraction correction exponent set to 4. The rising velocity influences the bubble Reynolds number directly and consequently the Nusselt number and the heat transfer rate between the steam bubbles and the liquid. From this discussion it is found that the formulation of the momentum transfer and bubble forces affecting the bubbles axial velocity should be modified to adapt to the range of large deformed bubbles. Figure 6.10 shows the distribution of the water temperature. The distribution is rather uniform and has slight variations (within 1 K). Therefore, the assumption of a constant water bulk temperature was justified and a local measurement of the water temperature can be neglected. Figure 6.11 shows the water velocity, here a considerable variation can be seen. Since the local water velocity is essential to definition of the bubbles Reynolds number, an improvement of the experimental results is necessary and can be achieved via a local measurement of the water velocity. This can be done in the future using PIV technique.

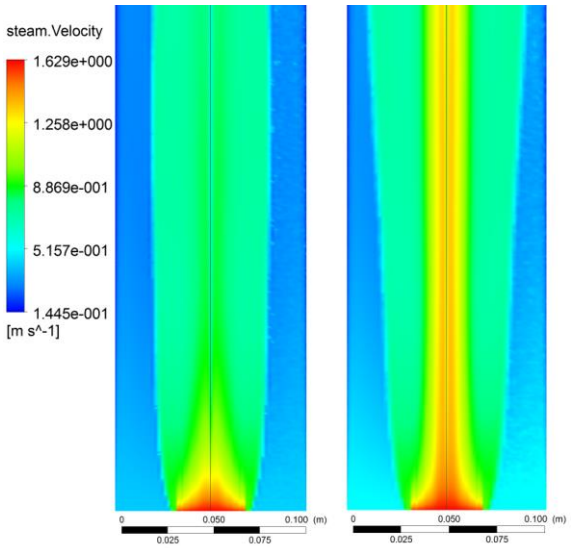

Figure 6.9 CFX calculations of the steam velocity: Left: experimental Nu-Re applied, and right: Ranz-Marshall correlation applied.

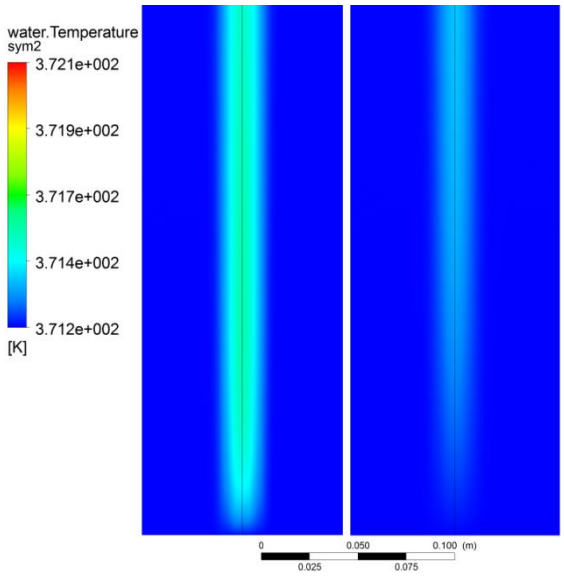

Figure 6.10 CFX calculations of the water temperature: Left: experimental Nu-Re applied, and right: Ranz-Marshall correlation applied.

.

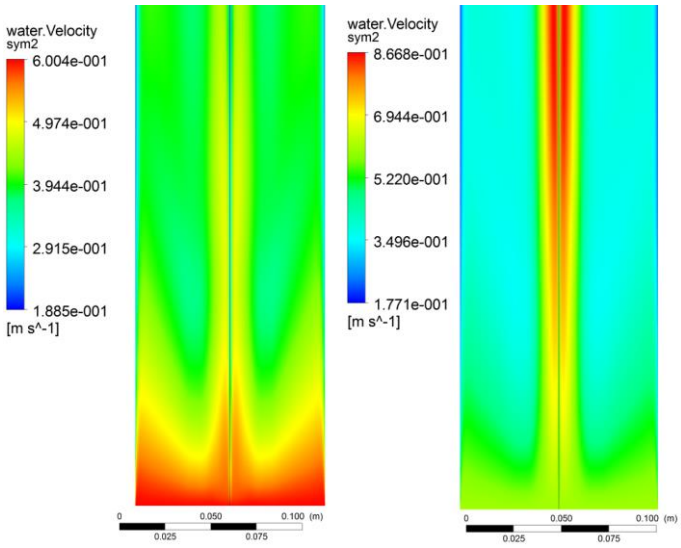

Figure 6.11 CFX calculations of the water velocity: Left: experimental Nu-Re applied, and right: Ranz-Marshall correlation applied.

6.7.2 HIN2X4mm case #18

Figure 6.12 shows a comparison of the steam fraction distribution between the experimental (left), CFX12.1 calculations using the experimental Nu-Re correlation (middle) (5.2, HIN2X4mm case), and CFX12.1 calculations using Ranz-Marshal built-in correlation for the same flow conditions. As it can be seen, the CFX simulation with the experimental Nu-Re agrees quite well with experimental data while the calculation using Ranz-Marshall correlation results in a large deviation.. The only clear deviation between experimental distribution and CFX with experimental Nu-Re is the divergent steam flame in experiments. This deviation can be neglected since the reson for it is the initial horizontal steam velocity gained from horizontal injection in HIN2X4mm nozzle. This velocity was not considered within the simulations and that caused the simulated flames to come vertical. The agreement in this case is clearly better than case#18 dur to the lower bubble diameter (13mm vs 24 mm) which makes the momentum transfer models perform better in this case. Figure 6.13 shows the steam velocity in both previously mentioned simulations. As it can be seen, the decrease rate of the steam velocity in the axial direction is less (taking into consideration the size of the flame).

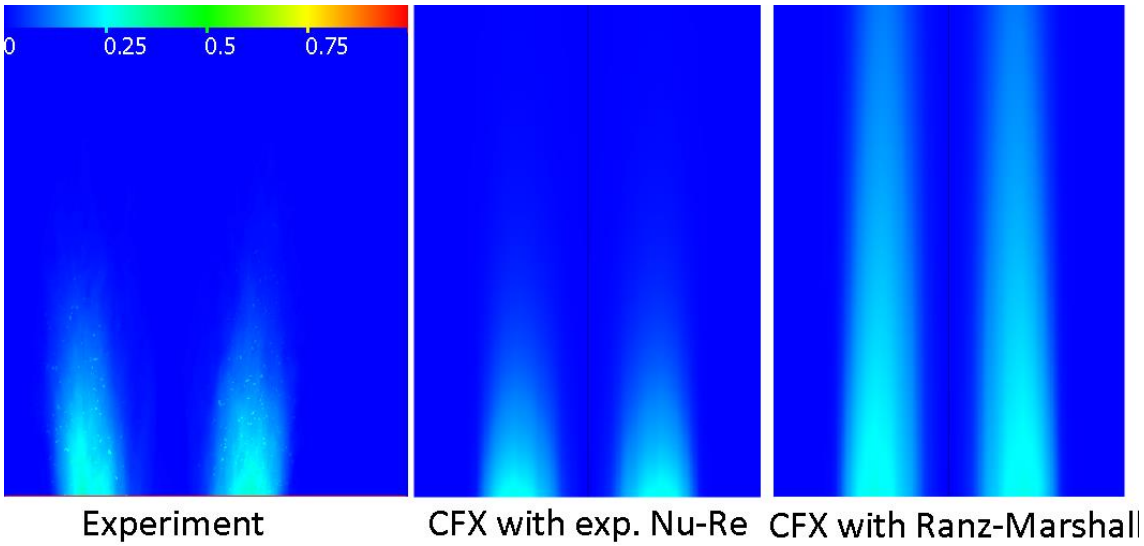

Figure 6.12 A comparison between: Left: experimental distribution of the time-averaged steam fraction of the detached bubbles, Middle: CFX simulation using experimental Nu-Re (Equation 5.2 [HIN2X4mm]), and right: CFX simulation using Ranz-Marshall correlation. The color scale within the experimental results applies for all plots.

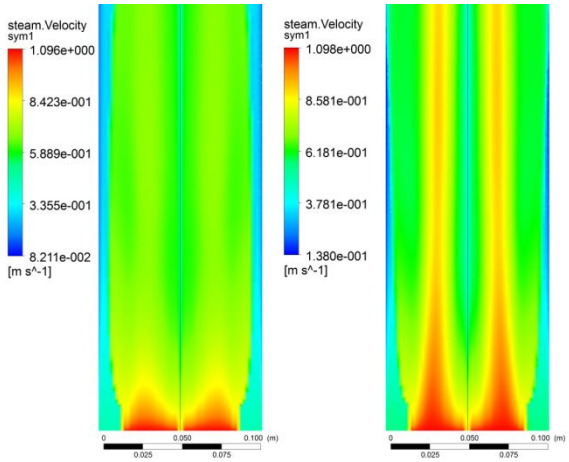

Figure 6.13 CFX calculations of the steam velocity: Left: experimental Nu-Re applied, and right: Ranz-Marshall correlation applied.

Figures 6.14 and 6.15 shows the distribution of the water temperature and the water velocity in both simulation cases. Same notes in previous case apply to this case. The water temperature changes are minimal while an enhancement of the measurement of the local water velocity would be required to enhance the experimental data.

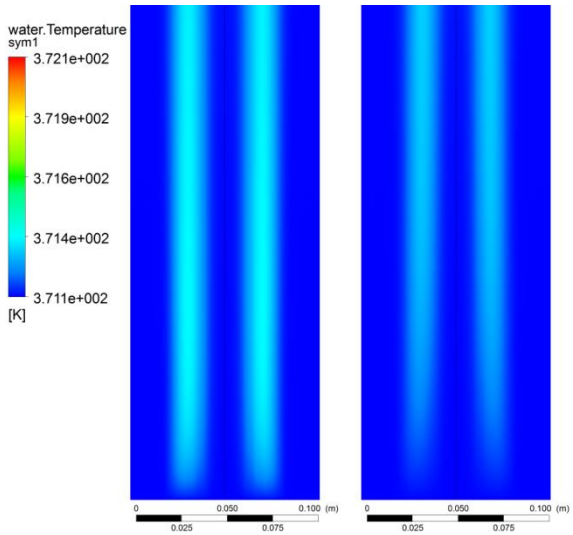

Figure 6.14 CFX calculations of the water temperature: Left: experimental Nu-Re applied, and right: Ranz-Marshall correlation applied.

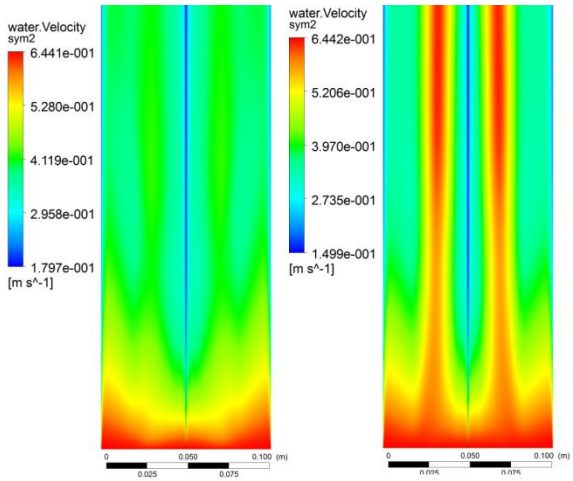

Figure 6.15 CFX calculations of the water velocity: Left: experimental Nu-Re applied, and right: Ranz-Marshall correlation applied.

6.7.3 The effect of the drag coefficient

In this section the effect of the void fraction correction exponent in Grace Drag force will be shown. As it was mentioned in previous section, the reason of adopting the value 4 was the fact that as this value was getting larger as it allows the steam velocity to maintain its initial value more along the vertical path of the bubbles. This is well explained in Figure 6.18 (CIN4mm #18) and 6.19 (HIN2X4mm #72). It is clear that the larger coefficient (void fraction correction exponent) value makes the steam velocity decrease by a lower decrease rate. This enhances the heat transfer and results in a better agreement with experimental data. Figures 6.16 and 6.17 Show the normalized void fraction for two values of this coefficient: 4 (adopted in previous simulations) and 1for comparison. The steam flame will extend further in the axial direction because of the reduced heat transfer at the lower value of this coefficient.

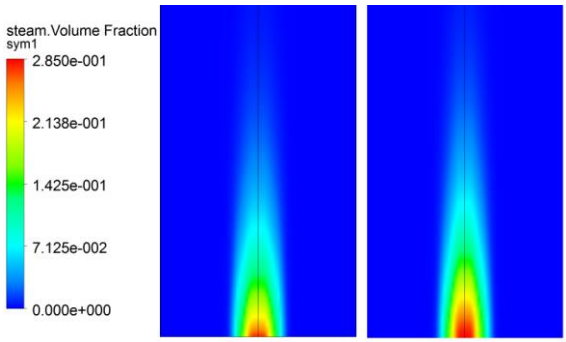

Figure 6.16 The influence of the void fraction correction exponent in Grace drag force upon results (normalized void fractions), case#18. Left: coefficient=4, right: coefficient=1.

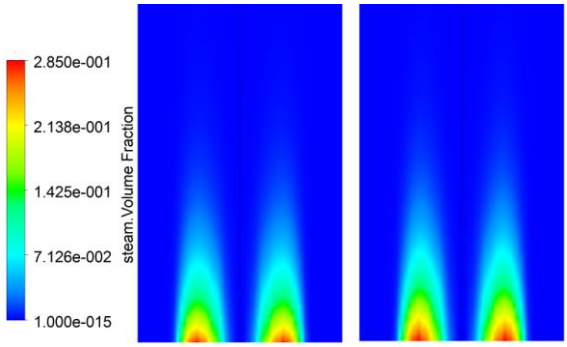

Figure 6.17 The influence of the void fraction correction exponent in Grace drag force upon results (normalized void fractions), case#72. Left: coefficient=4, right: coefficient=1.

The void fraction correction exponent was set originally to account for the fact that large bubbles tend to rise faster at high void fractions (densely distributed fluid particles) because they are dragged along by the wakes of other bubbles. The Ishii Zuber correlation uses a positive exponent of 2 in this regime. A value of 4 has been used successfully by some investigators [ANSYS CFX-Solver Modeling Guide 2009]. In our case, no densely distributed bubbly flow exists, however it is expected that the large deformed bubbles creates sufficient turbulence in its wake that yields the same final effect as in densely distributed fluid particles mentioned before. This makes the use of this coefficient physically justified.

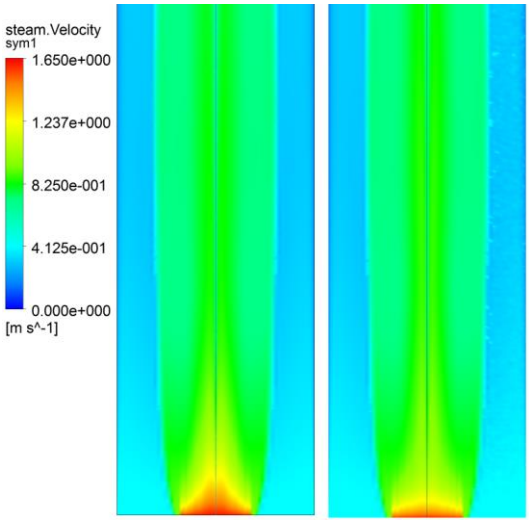

Figure 6.18 The influence of the void fraction correction exponent in Grace drag force upon steam velocity results, case#18. Left: coefficient=4, right: coefficient=1.

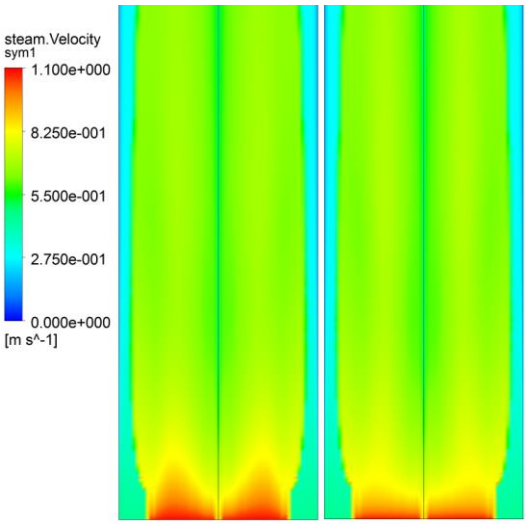

Figure 6.19 The effect of void fraction correction exponent in Grace drag force upon steam velocity results, case#72. Left: coefficient=4, right: coefficient=1.

6.7.4 Conclusions of the CFD simulations of steam bubble condensation

The CFD simulations of two cases of SCUBA experiments shown in the previous chapter confirm the validity of the newly developed NU-Re correlations. The performance of CFX was clearly enhanced via the use of the new correlations and this can be seen from the comparisons with experimental data. These simulations along with the experimental data show the efficiency of combined experimental and CFD validation work. The simulations enabled us to add more useful knowledge for both experiments and simulations:

- Through simulations it was demonstrated that the use of the bulk water temperature is justified and no need for a local temperature measurement regarding these experiments.
- However, the local measurement of the water velocity was asserted to be the next step to enhance the current experimental results as the local velocity has large variations along the pipe radius.
- We learned that large deformed bubbles that are generated in train (as they are detached from the steam plume at the injection nozzle) enhance the drag of the following bubbles and rise faster than predicted by drag correlations for a single bubble. This effect was accounted for by using a large value of the void fraction correction exponent within the drag definition. The results confirm that simulations using larger value agree better with experiments.

Chapter 7 Experimental investigations at COLLIDER test facility

This chapter will present the experimental results obtained from the COLLIDER test facility regarding:

- Phenomenological description of the CCFL: The experimental observations and identification of the various flow patterns and phenomena that occurs during the onset of CCFL and deflooding.
- The identification of CCFL mechanisms.
- The experimental determination of the onset of CCFL and the deflooding limits.
- High speed recordings that illustrate all described flow patterns, flow transitions, phenomena, and mechanisms.

7.1 Test Conditions

All experiments were carried out under atmospheric pressure ~ 1 bar and room temperature. Distilled water was used in all tests. Air was driven from the facility surrounding through a filter, preventing dust from accumulating inside the facility. The water flow rate at low flow conditions ($J_{w,in}^{*0.5} < 0.135$) was calibrated. the calibration was done by setting a constant opening of the control valve and pumping water from the storage tank into the RVs at a constant rotation speed of the pump. The change rate of the water level within the RVs was measured by ± 0.36 mm ($\equiv 0.36 \times 10^{-3} m^3$). The average rate provided a good estimation of the average flow rate at this opening. The average value was determined at several openings and yielded a calibration chart shown in Figure 7.1 For more accuracy a second order fit was used. The accuracy of the measured flow rate according to this method is comparable to the accuracy of the flow meter.

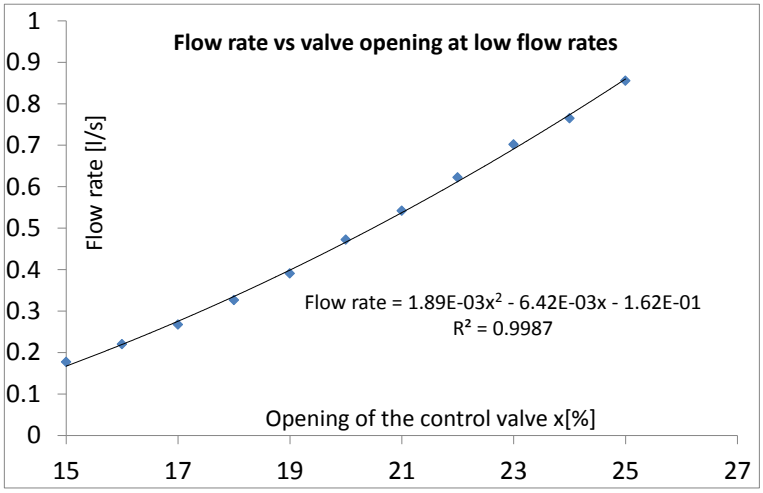

Figure 7.1 Calibration of the water flow rate against the control valve opening.

Experiments were conducted for water inlet velocities $J_{w,in}^{*0.5} = 0.085$ to 0.305 with $\Delta J_{w,in}^{*0.5} = 0.01$ in order to achieve accurate plots of the onset of CCFL and deflooding. This range covers the low and medium water inlet velocities according to the literature review (section 1.1) and is the most important for LOCA-related onset of CCFL.

7.2 Experimental procedure

There exist two possibilities of conducting the experiments:

1. Pumping water from storage tank into the SGs. The water flows through the hot-leg pipe to the RVs. The inlet water flow rate is measured with the ultrasonic flow meter. The actual flow rate into the RVs is estimated via the water level change rate. The backflow water rate after onset of CCFL is determined by subtracting the actual flow rate into the RVs from inlet water flow rate.
2. Pumping water from the RVs into the SGs. The water flows through the hot-leg into the RVs. The water level in the RVs remains constant as long as it receives the same inlet flow rate. After onset of CCFL, the water level starts to decrease. The change rate of the water level in the RVs is an estimation of the backflow water flow rate. The difference between the inlet flow rate and the backflow rate determines the actual flow rate into the RVs.

In both cases, the air flow rate will be gradually increased until onset of CCFL is reached, and then gradually decreased until deflooding happens. Since the determination of the flow rate through change rate of the water level is not as accurate as measuring the flow rate by a flow meter, it becomes difficult to determine the point of the onset of the CCFL using the first method. In order to determine whether a CCFL has already started or not, a considerable change of the water level should be measured. In the second method, the water level remains practically constant (within measuring devices accuracy) until a change in the hot-leg such as the transition into a subcritical flow, or the onset of CCFL occur. The decrease of the water level will accurately indicate the occurrence of CCFL. Thus the second method was adopted in this study. The test procedure followed following steps:

- The water is pumped into the RVs until it reaches a certain level (sufficient to compensate for the water level decrease after the onset of CCFL).
- The water is pumped from the RVs into the SGs through the pump and the flow meter and into the SGs. It flows then into the RVs and forms a smooth and undisturbed supercritical flow within the hot-leg.
- The air is blown from the air blower through the air flow meter into the RVs and then through the hot-leg into the SGs. It exits the SGs via the air outlet and droplets demister.
- The air flow rate is controlled automatically and increased in small constant steps ($\Delta J_G^{*0.5} = 0.01$) and for almost a constant time periods (≈ 30 seconds)
- Visual observations are registered and the control program logs all experimental parameters (flow rates, water level, and pressure difference) each1 s.
- Once the CCFL occurs, the air velocity is maintained for 30 seconds and then reduced gradually until the deflooding happens (water level stops decreasing in RVs).
- The air velocity is decreased gradually ($\Delta J_G^{*0.5} = 0.01$)until the lowest the air velocity is reached again (stable supercritical flow is reestablished).
- In cases where the CCFL is intense and fluctuations of air flow rates are high preventing a controlled decrease of the air flow, a manual and gradual decrease of the blower

rotation speed is used until the reestablishment of a smooth, supercritical flow within the hot-leg.

During intense CCFL occurrence, a large blockage of the air path occurs at the bend. This increases the pressure difference to the extent that the air blower cannot afford maintaining the air velocity anymore. The air velocity fluctuates a lot because of turbulences and chaotic changes of resistance at the bend. This makes it difficult for the control system to control/decrease the air velocity using a constant step change ($\Delta J_{w,in}^{*0.5} = 0.01$). Any small decrease of the blower rotation speed through the control system will decrease the blockage (air resistance) at the bend accordingly leaving the air velocity constant. The only possibility to induce an automatic air velocity decrease is to perform a large step decrease. In these cases a manual decrease of blower rotation speed was used instead in order to observe the gradual disappearance of the CCFL.

7.3 Phenomenological description of onset of the onset of CCFL/deflooding at different water inlet velocities

From a phenomenological point of view, the descriptions of the successive events that lead into the onset of the CCFL/deflooding vary according to the water inlet velocity. This section provides a detailed description of the onset of CCFL and deflooding at different water inlet velocities including: visual observations of the air/water interface, and the time development of the recorded flow parameters: the air velocity, the pressure difference between the RVs and the SGs, and the water level within the RVs. Four main regions were recognized within the current experiments:

1. Gradual onset of CCFL at low water inlet velocities ($J_{w,in}^{*0.5} = 0.085 - 0.125$). CCFL happens gradually at bend region.
2. Sudden onset of CCFL:($J_{w,in}^{*0.5} = 0.135 - 0.175$): CCFL occurs suddenly at the bend.
3. Dual mode: $J_{w,in}^{*0.5} = 0.185 - 0.265$): A slight CCFL occurs first at the water inlet as a result of active droplets entrainment. A sudden intensive CCFL occurs later at the bend.
4. Water inlet CCFL:($J_{w,in}^{*0.5} = 0.275 - 0.305$): CCFL happens first at water inlet accompanied with periodic behavior. A sudden and severe CCFL occurs later at the bend region.

Within the provided descriptions following terms were used:

- Water inlet: The junction between the steam generator simulator and the hot-leg where water flows into the hot-leg.
- Water exit: The junction between hot-leg and reactor vessel simulator.
- Bend-CCFL: Countercurrent flow limitation that takes place at the bend region as a result of transition from supercritical into subcritical flow and formation of large roll-waves, annular churn flow, or periodic plugging at the bend region and the riser.

- ADE-CCFL: Countercurrent flow limitation that takes place at water inlet as a result of strong active droplets entrainment that form a continuous droplet jet transporting water back into the SGs.

Section 7.5 gives a more clear and detailed visual description of the last two terms.

7.3.1 First region $J^{*0.5}_{w,in} = 0.085 - 0.125$

Figure 7.2 shows the time development of the normalized values of: the water level in reactor vessel simulator (blue), the pressure difference between the reactor vessel simulator and the steam generator simulator (red) and air velocity (in yellow) in this region during the gradual increase of the air velocity until CCFL occurrence and decrease until deflooding. The parameters values were normalized using to the maximum value of each parameter in each experiment.

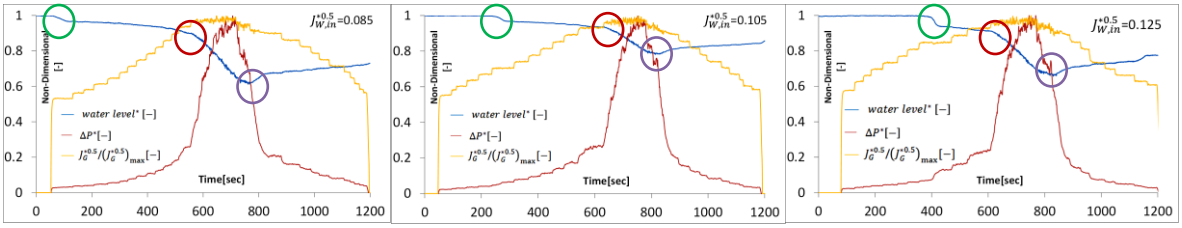

Figure 7.2 Development of normalized: $J^{*0.5}_G$(yellow), ΔP(red), and Water level in RVs (blue) along time for region 1($J^{*0.5}_{w,in} = 0.085, 0.105, 0.125$ left to right respecitively). The supercritical/subcritical transition is marked by a slight decrease of the water level before the CCFL occurrence (green circle). Pressure difference increases in this region gradually. Red circle: Onset of bend-CCFL, purple circle: deflooding.

7.3.1.1 First region, Onset of CCFL

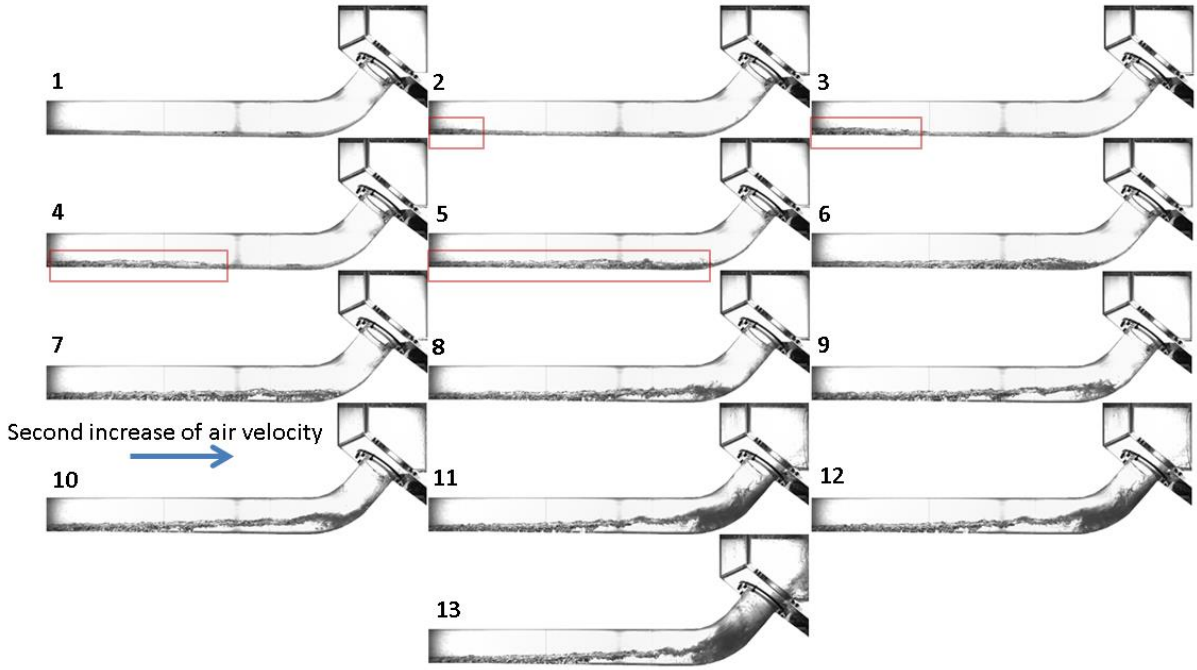

Figure 7.3 A successive set of images that show the air/water interface during the onset of CCFL in the first region. Images were recorded with 10 frames/second frequency using a wide-angle objective. The red rectangles show the advancing hydraulic jump from the water exit towards the bend.

At low air velocities the flow is a supercritical one, characterized by a smooth surface and a slight increase of the water thickness towards the water exit (Figure 7.3, 1). Water droplets and water recirculation starts to occur near water exit $J_G^{*0.5} = 0.42 - 0.47$ (value increases as $J_{w,in}^{*0.5}$ increases). Consequently, a water thickening happens near the water exit (Figure 7.3, 2), . Following the water thickening and local increase of air velocity, a hydraulic jump occurs initially near the water exit at $J_G^{*0.5} = 0.45 - 0.50$ (Figure 7.3, 3). As soon as the jump occurs, it moves towards the bend and the flow within the hot-leg transits from a supercritical to a subcritical flow immediately (Figure 7.3, 3-7). The occurrence of the hydraulic jump traps some water within the hot-leg resulting in a slight decrease of the water level (Figure 7.2, green circle). The air velocity, at which the hydraulic jump and corresponding water level decrease occur, increases as the water inlet velocity increases. The hydraulic jump locates at the bend region and the flow within the horizontal part of the hot-leg becomes wavy (Figure 7.3, 7-9). Small roll-waves start to form at the bend region. Roll-waves at the bend appear at $J_G^{*0.5} = 0.50 - 0.53$ and grow gradually with the increasing air velocity. The waves break into the riser and the droplets start to reach the SGs (Figure 7.3, 11). A gradual increase of the roll-waves' amplitude and the air blockage at the bend region cause a gradual increase of the pressure difference between RVs-SGs (figure 7.2, the red line). Eventually, CCFL occurs as a result of formation of large roll-waves at $J_G^{*0.5} = 0.57 - 0.52$ (Figure 7.3, 11-13). The flow at the riser becomes an annular churn flow. Continuous carry-over of water droplets and small portions of water cause a net water flow back into the SGs. The water level starts to suffer an apparent and large decrease (figure 7.2, the blue line; the red circle indicates the onset of CCFL). The intensity of CCFL grows by increasing the air velocity.

7.3.1.2 First region, Deflooding

Decreasing air velocity decreases the intensity of the annular churn flow and the roll-waves at the bend region gradually. Eventually there is not enough air flow to support the formation of such events at the riser. The annular churn flow disappears and large roll-waves remain at the bend with decreasing amplitudes as the air velocity decreases. This is usually accompanied with deflooding where no more water is carried out in the opposite direction $J_G^{*0.5} = 0.52 - 0.53$. When the deflooding occurs the water level stops to decrease. This is indicated by the purple circle in Figure 7.2. Roll-waves become smaller and smaller until they vanish and only a hydraulic jump remains at the bend at $J_G^{*0.5} = 0.45 - 0.48$. A further decrease of the air velocity causes the jump to move away from the bend at $J_G^{*0.5} = 0.41 - 0.42$ and eventually towards the water exit where it vanishes. The flow transits back to a supercritical flow occurs at $J_G^{*0.5} < 0.42 - 0.41$.

7.3.2 Second region $J_{w,in}^{*0.5} = 0.135 - 0.175$

Figure 7.4 shows the time development of the normalized values of: the water level in reactor vessel simulator (blue), the pressure difference between the reactor vessel simulator and the steam generator simulator (red) and air velocity (in yellow) in this region during the gradual increase of the air velocity until CCFL occurrence and decrease until deflooding. The parameters values were normalized using to the maximum value of each parameter in each experiment.

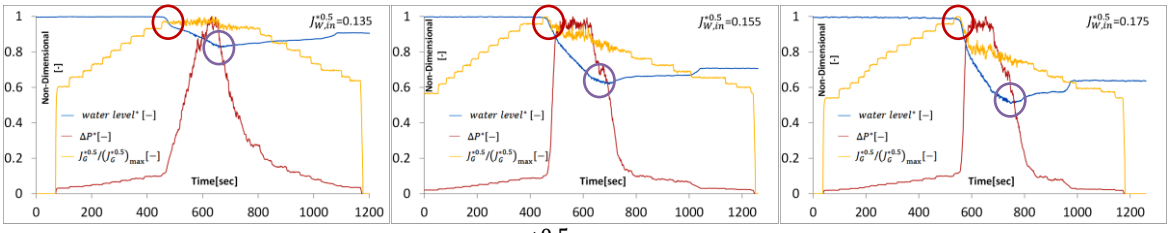

Figure 7.4: Development of the normalized $J_G^{*0.5}$(yellow), ΔP(red), and Water level in RVs (blue) along time for region 2($J_{w,in}^{*0.5} = 0.135, 0.155, 0.175$ left to right respecitively).

Supercritical/subcritical transition coincides with a sudden occurrence of the bend-CCFL. The increase of the pressure difference is sharp. Red circle: Onset of bend-CCFL, purple circle: deflooding.

7.3.2.1 Second region, Onset of CCFL

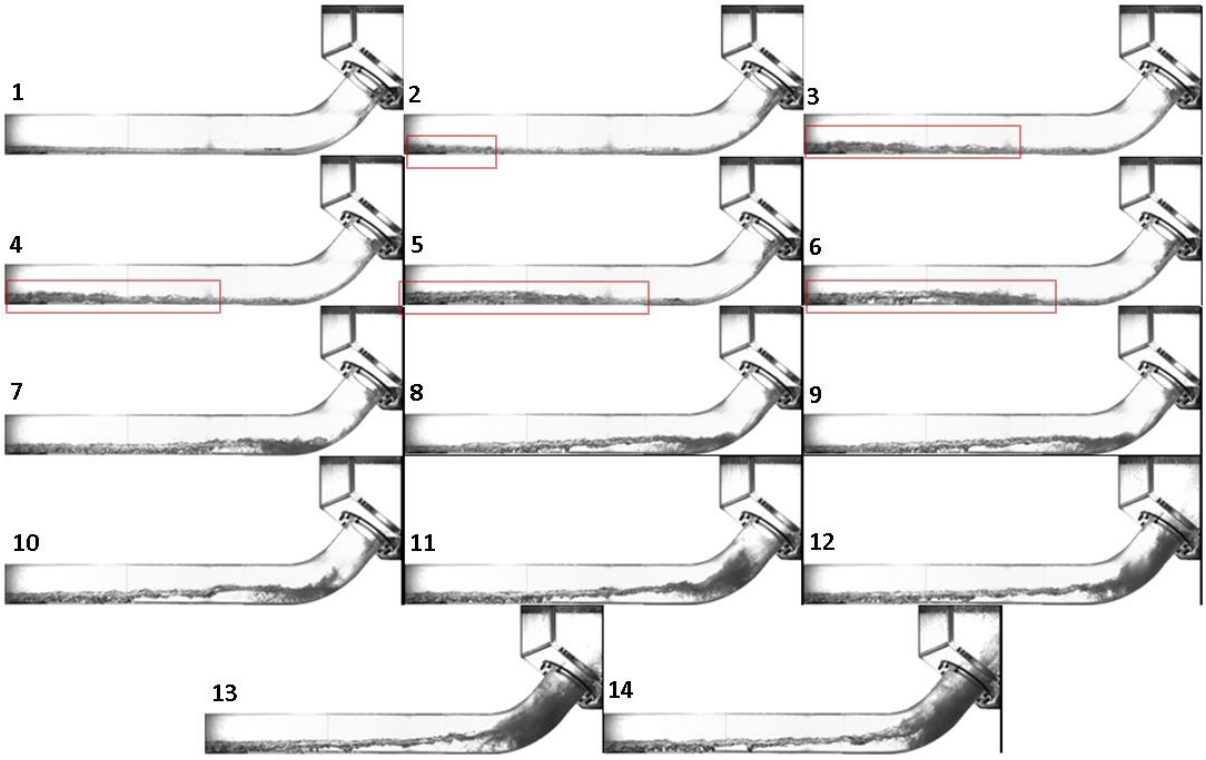

Figure 7.5 A set of successive images that show air/water interface during the onset of CCFL in the second region. Images were recorded with 10 frames/second frequency using a wide-angle objective. The red rectangles show the advancing hydraulic jump from the water exit towards the bend.

At low air velocities the flow is a supercritical flow as in the last region. However, the water thickness is higher due to the higher inlet water flow rate (Figure 7.5, 1). The formation of water droplets at the water exit plays a more important role in the process of water thickening and subsequent hydraulic jump formation. Water droplets start to appear near the water exit at higher air velocities ($J_G^{*0.5} = 0.47 - 0.48$) in comparison to the last region. This is caused by the higher water inlet velocities which require higher air velocities in order to create a sufficient shear force to extract water droplets out of the water surface. The water droplets fly in the opposite direction and fall into the water stream near the water exit. As a result, a local thickening of water level happens there (Figure 7.5, 2) .A local recirculation area forms at the water exit ($J_G^{*0.5} = 0.50 - 0.54$, with higher values required at higher $J_{w,in}^{*0.5}$). At this point, the further increase of the air velocity does not lead to the formation of a hydraulic jump that travels into the bend region and initiating a wavy flow within the hot-leg horizontal section, and roll-waves at the bend. In this region, a further increase of the air velocity increases the intensity of the water thickening and water droplets entrainment at the water exit, the water flow within the horizontal section becomes turbulent (Figure 7.5, 3,4) .However at a specific air flow rate , a slight increase of the air velocity ($\Delta J_G^{*0.5} = 0.01$) leads into a sudden formation of large roll-waves that emerges simultaneously at the water exit and moves at once into the bend region transforming the flow into a subcritical flow immediately and

initiating the CCFL (Figure 7.5, 5-11, the time step between these instances is small, however many Figures were shown to see the transition, the time required for this transition be seen also from the time passed during the sharp increase of the pressure difference in Figure 7.4, middle plot $J_{w,in}^{*0.5} = 0.155$) . The large roll-waves at the bend break into the riser where an strong annular churn flow occurs and the onset of bend-CCFL happens at $J_G^{*0.5} = 0.52 - 0.55$ (Figure 7.5, 11-14). The sudden occurrence of CCFL, the hydraulic jump, the large roll-waves, and the formation of an intense annular churn flow at the bend/riser differentiates this region from the last one. Also the water thickening at the water exit is caused by water droplets entrainment, and the formation of the hydraulic jump and transition into subcritical flow follows the formation of small roll-waves rather than the displacement of the hydraulic jump into the bend. The sudden blockage of the air flow path results in a sharp increase of the pressure difference (Figure 7.4, the red line). The increase of the pressure difference becomes steeper as the water inlet velocity increases. The water level also suffers a sudden decrease at the onset of CCFL (Figure 7.4, the blue line). There is no initial slight decrease of the water level as observed in the last region since the formation of the hydraulic jump occurs simultaneously along with the occurrence of the CCFL. The backflow of the water happens -as in the first region- as a result of the continuous carry-over of water droplets and small portions of water resulting from the broken roll-waves and annular churn flow into the SGs (see section 7.4).

7.3.2.2 Second region, Deflooding

Decreasing the air velocity causes the intensity of annular flow and the large roll-waves to decrease gradually. This leads eventually into deflooding. The annular churn flow disappears at the bend and only large roll-waves remains ($J_G^{*0.5} = 0.51 - 0.47$). A further decrease of the air velocity causes roll-waves to become smaller and smaller. They move eventually along with the hydraulic jump into the near-bend region and vanish there($J_G^{*0.5} = 0.45 - 0.46$). A further decrease of air velocity will reduces the waves' intensity until a sudden transition from subcritical into supercritical flow happens at a rather constant air value ($J_G^{*0.5} = 0.45$). The hydraulic jump moves towards the water exit and vanishes while the flow returns into supercritical condition immediately. (see section 7.4)

7.3.3 Third region $J_{w,in}^{*0.5} = 0.185 - 0.265$

Figure 7.6 shows the time development of the normalized values of: the water level in reactor vessel simulator (blue), the pressure difference between the reactor vessel simulator and the steam generator simulator (red) and air velocity (in yellow) in the third region during:

- The gradual increase of the air velocity until CCFL occurrence and
- The gradual decrease until deflooding.

The parameters values were normalized using to the maximum value of each parameter in each experiment. The water level decrease resulting from ADE-CCFL is marked by a rectangular.

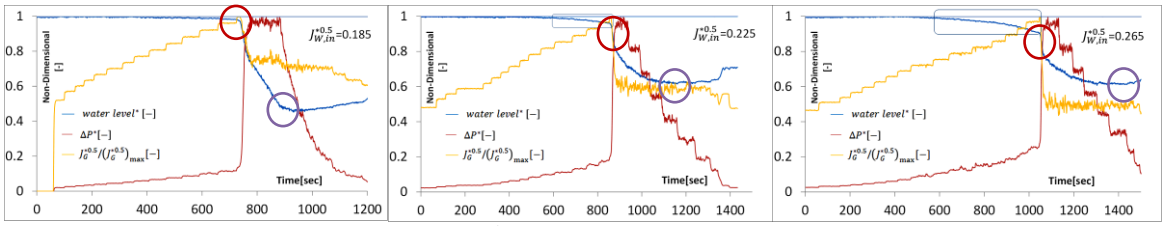

Figure 7.6 Development of normalized $J_G^{*0.5}$(yellow), ΔP(red), and Water level in RVs (blue) along time for region 3($J_{w,in}^{*0.5} = 0.185, 0.225, 0.265$ left to right respecitively). Supercritical/subcritical transition coincides with the bend-CCFL. At $J_{w,in}^{*0.5} = 0.185$ ADE-CCFL coincides with bend-CCFL. for $J_{w,in}^{*0.5} > 0.185$. ADE-CCFL occurrence precedes bend-CCFL and is marked by a blue rectangle. Red circle: Onset of bend-CCFL, purple circle: deflooding

7.3.3.1 Third region, Onset of CCFL

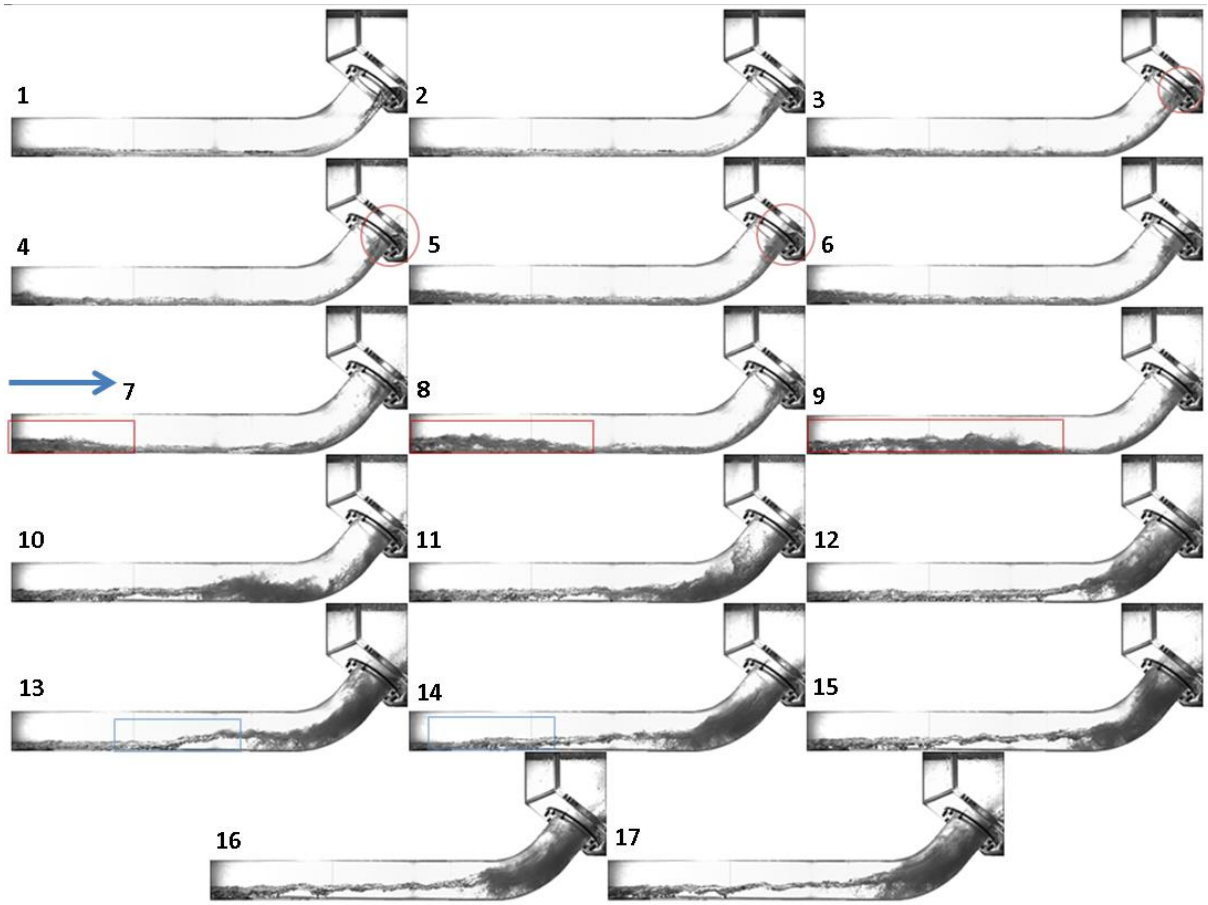

Figure 7.7 A successive set of images that show the air/water interface during the onset of CCFL in the third region. Images were recorded with 10 frames/second frequency using a wide-angle objective. The red circle indicates a light onset of ADE-CCFL. The red rectangles show the advancing small roll-waves from the water exit towards the bend. The blue rectangle shows the retreating water front after the onset of the bend-CCFL.

At low air velocities the flow is a supercritical flow. However, the water thickness is higher and the water stream begins to acquire a 3D structure. A flow pattern appears like a constant wavy surface from the side. In reality the water stream periodic divergence and convergence cause this phenomenon (Figure 7.7, 1,see section 7.4 for more detailed Figures). Droplets

start to appear at $J_G^{*0.5} = 0.47 - 0.48$ near the water exit. Following the increased inlet water flow rate, the water film thickness near the water inlet becomes thicker, and some water droplets and disturbances appear at the water inlet at $J_G^{*0.5} = 0.47 - 0.41$ (Figure 7.7, 3, red circle, value decreases with increasing $J_{w,in}^{*0.5}$). Disturbances of the water film at the water inlet make it easy to shear water droplets out of the water surface even at low air velocities in comparison with the situation at the water exit. The water film at the water exit is smoother and thus higher air velocities are required. The appearance of the water film thickening and recirculation area near the water exit is delayed until $J_G^{*0.5} = 0.51 - 0.57$ (recirculation) and $J_G^{*0.5} = 0.54 - 0.55$ (water film thickening) (increased values with increased $J_{w,in}^{*0.5}$). The hydraulic jump appears a bit later at $J_G^{*0.5} = 0.54 - 0.58$ (figure 7.7, 4-6). This is mainly due to the increased water kinetic energy which requires higher air velocities in order to induce a recirculation area, water thickening, and eventually a hydraulic jump. Active droplets entrainment appears at the water exit at ($J_G^{*0.5} = 0.54 - 0.50$ increased values with increased $J_{w,in}^{*0.5}$) and it contributes effectively to the later formation of the hydraulic jump. The hydraulic jump in this region remains initially near the water exit and does not travel to the bend region (Figure 7.7, 6). Small roll-waves -supported by active droplets entrainment near the water exit-appears at the surface of the hydraulic jump and disappear locally near the water exit $J_G^{*0.5} = 0.57 - 0.58$, and $J_{w,in}^{*0.5} > 0.205$, however, only an intensified active droplets entrainment occurs when $J_{w,in}^{*0.5} < 0.205$. At the water inlet, active droplets entrainment starts at $J_G^{*0.5} = 0.51 - 0.46$ (value decreases as $J_{w,in}^{*0.5}$ increases) accompanied with an increased disturbance in the water film there (water seems to resemble water flow over a little obstacle causing the interface to become vibrating and shedding droplets, Figure 7.7, 3-4, red circle). The formation of water droplets at the water exit spread into the horizontal part of the hot-leg at $J_G^{*0.5} = 0.54 - 0.51$ and $J_{w,in}^{*0.5} > 0.205$ (value decreases as $J_{w,in}^{*0.5}$ increases,). The flow in horizontal part becomes more disturbed with a rippled surface at $J_G^{*0.5} = 0.57 - 0.54$ and $J_{w,in}^{*0.5} > 0.215$ (value decreases as $J_{w,in}^{*0.5}$ increases). At higher water inlet velocities ($J_{w,in}^{*0.5}$>0.225) a light annular flow starts to appear sporadically at the riser even before onset of bend-CCFL. The active droplets entrainment at the water inlet starts to transport a sensible amount of water back into the SGs, causing the onset of a light CCFL at the water inlet. This phenomenon will be called as Active Droplets Entrainment CCFL (ADE-CCFL) and it starts at $J_G^{*0.5} = 0.58 - 0.53$, (value decreases with increased $J_{w,in}^{*0.5}$, Figure 7.7 5, red circle). A further increase of air velocity causes small roll-waves at the water exit, which were locally disappearing, to grow in amplitude causing an increased local blockage of the air flow (Figure 7.7, 7, red rectangular). As the roll-waves become large enough they travel towards the bend transforming the flow into subcritical flow immediately and initiating intense bend-CCFL at the bend region (Figure 7.7, 8-11, red rectangular). The onset of the bend-CCFL is sudden and even faster and more intensive that the previous region. Figure7.7, 13 and 14 blue rectangular shows the retreating water front back towards the water exit after the initial onset of the CCFL. The initial transported large amount of water flows back under gravity as the CCFL settles at the bend. Large turbulent roll-waves, intense and foamy annular churn flow occurs at the bend ($J_G^{*0.5} = 0.57 - 0.59$, value increases as $J_{w,in}^{*0.5}$ increases, figure 7.7,, 12-17) . When $J_{w,in}^{*0.5} > 0.215$, The intense CCFL

starts to block the entire cross section of the pipe at the riser periodically (figure 7.7, 12, 15, and 17). Considerable lumps of water consisting of waves' crests, droplets, and small water portion from the water surface are pushed at once into SGs causing the water to flow back at high flow rates (see the sharp reduction of the water level within the reactor vessel in figure 7.6, middle+right.). Since the CCFL occurs initially by ADE-CCFL mechanism at the water inlet, followed by Bend-CCFL at higher air velocities, this region is characterized by a dual-mode region.

7.3.3.2 Third region, Deflooding

Once the bend CCFL occurs, the air velocity drops immediately due to limited power of the blower and sudden increased pressure-loss. This happens due to the increased flow resistance at the bend region (Figure 7.6, all plots, yellow line). Nevertheless, the CCFL persists and the reduction of the flow area at the bend region keeps the air velocity locally high at this point. Decreasing the blower rotational speed decreases blockage ratio and the pressure loss together, leaving the air velocity constant (see Test procedure section 7.2). The decrease of the blower's speed cause the intensity of bend-CCFL to decrease gradually until no more annular churn flow or periodic plugging exist. The large roll-waves remain at the bend and breaks into the riser ($J_G^{*0.5} = 0.46 - 0.42$, lower values as $J_{w,in}^{*0.5}$ increases). The amplitude of the large roll-waves decreases and moves to near-bend at $J_G^{*0.5} = 0.45 - 0.42$. A further decrease of blower power causes the roll-waves to become small and eventually it disappear leaving a hydraulic jump at the bend. Finally, the hydraulic jump moves towards the water exit and vanishes. The flow returns back into supercritical flow. This happens constantly at the same blower power and air velocity $J_G^{*0.5} \approx 0.44$.

7.3.4 Fourth region $J_{w,in}^{*0.5} = 0.275 - 0.305$

Figure 7.8 shows the time development of the normalized values of: the water level in reactor vessel simulator (blue), the pressure difference between the reactor vessel simulator and the steam generator simulator (red) and air velocity (in yellow) in the third region during the gradual increase of the air velocity until CCFL occurrence and the gradual decrease until deflooding.

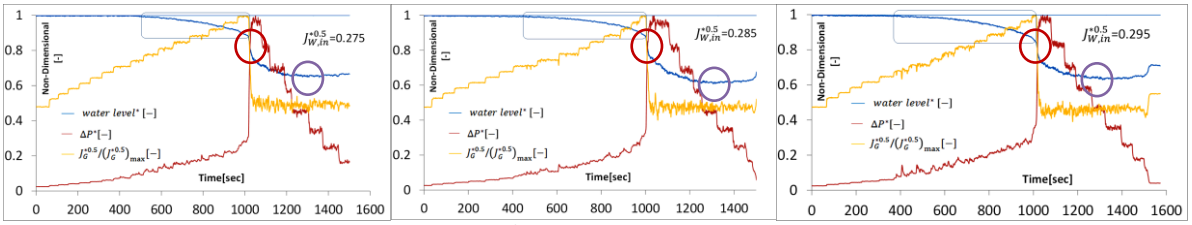

Figure 7.8: Development of normalized $J_G^{*0.5}$(yellow), ΔP(red), and Water level in RVs (blue) along time for region 4($J_{w,in}^{*0.5} = 0.275, 0.285, 0.295$ left to right respecitively). Supercritical/subcritical transition coincides with bend-CCFL. Note the increased intensity of ADE-CCFL that becomes of an equal importance to bend-CCFL at $J_{L,in} = 0.295$. The periodic behavior at the onset of ADE-CCFL (periodic froths at the water inlet, annular flow) is marked by little spikes in pressure difference and air flow rate. Red circle: Onset of bend-CCFL, purple circle: deflooding

The parameters values were normalized using to the maximum value of each parameter in each experiment. The water level decrease resulting from ADE-CCFL is marked by a rectangular.

7.3.4.1 Fourth region, Onset of CCFL

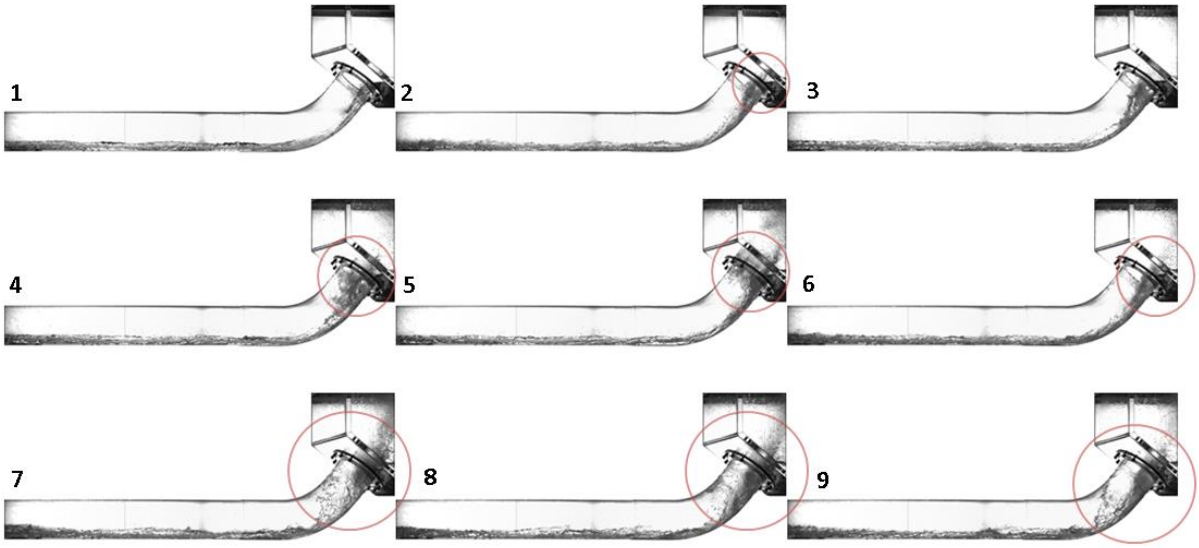

Figure 7.9 A set of successive images that show the air/water interface during the onset of ADE-CCFL in the fourth region. Images were recorded with 10 frames/second frequency using a wide-angle objective. The red circles show the onset of the ADE-CCFL at the water inlet and the periodic formation of froths and annular flow (instance number 8).

At low air velocities the flow is a supercritical flow. The water thickness is higher and the water stream a 3D structure is visible even in small pictures of Figure 7.9, 1. The wavy flow pattern is visible from this side view. As said before, the water stream periodic divergence and convergence cause this phenomenon (see section 7.4 for more detailed Figures).The descriptions of the events in this region are rather similar to the ones in the third region. It incorporates also dual mechanisms of onset of CCFL. However, when $J_{w,in}^{*0.5} > 0.275$, a remarkable phenomenon starts to occur and differentiates it from the previous region. Droplets at the water inlet appear at quite low air velocities ($J_G^{*0.5} \approx 0.41$) and the water film is already disturbed at low air velocities $J_G^{*0.5} \approx 0.44 - 0.41$ (Figure 7.9,, 2). Consequently, active droplets entrainment at the water inlet starts at $J_G^{*0.5} = 0.44 - 0.45$. Droplets near the water exit appear at $J_G^{*0.5} \approx 0.47$ and active droplets entrainment starts at $J_G^{*0.5} = 0.44 - 0.48$ followed by the onset of ADE-CCFL at $J_G^{*0.5} = 0.50 - 0.48$ (value decreases as $J_{w,in}^{*0.5}$ increases, Figure 7.9, 2-3). The recirculation near the water exit appears at higher air flow values compared to the previous region $J_G^{*0.5} = 0.55 - 0.58$ accompanied with small roll-waves at the water surface. Shear forces play a larger role in initiating these roll-waves that travel as far as the middle of the pipe before disappearing. The flow becomes highly disturbed. Droplets at the horizontal part appear at $J_G^{*0.5} = 0.48 - 0.51$ and the water film becomes disturbed, and rippled (Figure 7.9, 7-9). The annular flow at the riser starts to appear with a periodic behavior at $J_G^{*0.5} = 0.55 - 0.51$, (value decreases as $J_{w,in}^{*0.5}$ increases) as a result of water film disturbances and active droplets entrainment (Figure 7.9,, 4-6 red

circles). As the inlet water velocity increases ($J_{w,in}^{*0.5} \geq 0.285$) the annular flow switches periodically into annular churn flow for short time (Figure 7.9, 7-9 red circles). The flow is accompanied by periodic froths pushed into the SGs causing small spikes in the pressure difference (Figure 7.8, red line, especially the right plot).

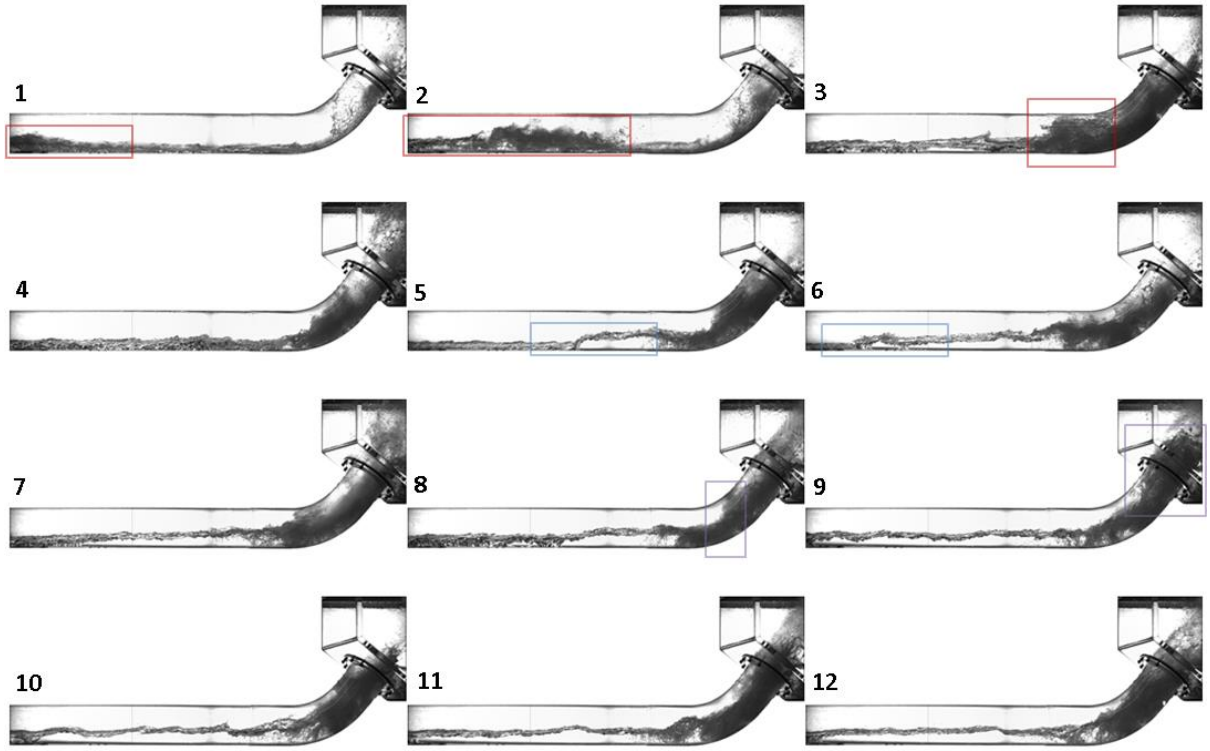

Figure 7.10 A set of successive images that show the air/water interface during the onset of bend-CCFL in the fourth region. Images were recorded with 10 frames/second frequency using a wide-angle objective. The red rectangles show the advancing large roll-wave from the water exit towards the bend, blue rectangle: shows the retreating water front after the onset of bend-CCFL, and purple rectangle: shows a large blockage at the bend.

The active droplets entrainment at the water exit, and the roll-waves at the water surface increase as the air velocity increases. As the roll-waves gets large enough they form a blockage that is pushed at once into the bend, transforming the flow into subcritical flow immediately (Figure 7.10, 1-3, red rectangle). This leads eventually into the onset of an intensive, sudden, and violent bend-CCFL (Figure 7.10, 1-6 $J_G^{*0.5} \approx 0.60 - 0.62$). Figure 7.10,, 5 and 6, shows the retreating water front towards the water exit after being pushed with the blockage into the bend. Figure 7.10,, 7 shows the established bend-CCFL. The bend-CCFL is accompanied with an intense foamy annular churn flow, large turbulent roll-waves and an intensive periodic plugging (Figure 7.10, 7-12). Large roll-waves start to appear at the middle of the pipe (Figure 7.10, 10, and 11) due to the high water level that exist after onset of bend-CCFL. The waves' amplitude reach the top of the hot-leg pipe as it reach the bend, forming a nearly complete blockage of the air flow, this cause the blocking to be pushed by the air pressure behind as a lump of water droplets, wave crest, and foam into the SG (Figure 7.10, 8 and 9, purple rectangle) forming the periodic plugging that characterize the bend-CCFL in this region of water inlet velocities.

7.3.4.2 Fourth region, Deflooding

Decreasing the blower rotational speed decreases the intensity of the bend-CCFL. Periodic plugging persists longer than in previous region. Large roll-waves keep appearing at middle of the pipe due to elevated water depth in the horizontal part of the hot-leg. A further decrease of the air velocity will cause the periodic plugging to disappear; however, bend-CCFL persists through annular churn flow and large roll-waves breaking into the SGs. The intensity of the roll-waves decreases gradually and finally the annular churn flow disappears. Only large roll-waves remain at the bend ($J_G^{*0.5} \approx 0.41$). A further decrease of the air velocity decreases the amplitude of the roll-waves and shifts them toward the near-bend region. Eventually only a hydraulic jump with small waves remains at the bend. Finally a sudden transition into supercritical flow occurs. The hydraulic jump moves towards the water exit and vanishes there. This happens at a constant blower power (=constant pressure difference).

7.3.5 Overview of the four recognized regions

The Previous sections classification is based upon the type of events and phenomena found in each region and not only upon the main CCFL mechanisms in that region. If the classification is to be done according to CCFL mechanisms, then the fourth region can be merged with the third one since it incorporates dual CCFL mechanisms. However, the appearance of the annular churn flow periodically at the riser during the ADE-CCFL even before onset of bend-CCFL, the increased role of ADE-CCFL, and the strong periodic plugging, differentiate it from the third region. The water level reduction caused by the ADE-CCFL is so pronounced in the fourth region that it is equal to that caused by the bend-CCFL (see figure 7.8, right picture, blue line). Since the ADE-CCFL occurs at the water inlet, it is independent from the conditions that exist within the hot-leg itself. As the critical air velocity at which the ADE-CCFL occurs decreases as water inlet velocity increases (see Figure 7.65), the importance of ADE-CCFL at high inlet water velocities is higher since it will be the mechanism by which the CCFL will occur first and much earlier as the bend-CCFL. The shear forces play an important role into the occurrence of the ADE-CCFL. Additionally, the 3D water stream structure is very important for a correct prediction of this mechanism, and thus experiments and simulation performed in rectangular cross section geometry will not be able to reflect the real conditions of the ADE-CCFL. Table 7.1 gives a brief summary of the over-described four regions. The main two CCFL mechanisms are bend-CCFL (gradual or sudden) and it dominates at low-medium water inlet velocities and ADE-CCFL (slight, intense with periodic behavior).

Table 7.1: An overview of the four experimentally recognized regions for CCFL occurrence.

$J^{*0.5}_{w,in}$	Bend-CCFL*	ADE-CCFL*	Notes
$\mathbf{0.085 - 0.125}$	Main mechanism	Not existent	Bend-CCFL happens gradually after the transition from a supercritical into a subcritical flow
$\mathbf{0.135 - 0.175}$	Main mechanism	Not existent	Bend-CCFL occurs suddenly and coincides with supercritical/subcritical transition.
$\mathbf{0.185 - 0.265}$	Mechanism of higher importance	Initiates with slight intensity prior to bend-CCFL	Bend-CCFL occurs suddenly and coincides with supercritical/subcritical transition. Slight ADE-CCFL starts at lower air velocities
$\mathbf{0.275 - 0.295}$	Mechanism of an equal importance	Mechanism of an equal importance	Bend-CCFL happens suddenly, ADE-CCFL is more pronounced and accompanied by periodic behavior

*Importance is evaluated according to the amount of backflow water resulting from corresponding mechanism.

7.4 A detailed look into the air/water interface in the four CCFL regions

Section 7.3 provided a detailed phenomenological description of the four recognized CCFL regions as summarized within table 7.1 Although a visual description was provided via a set of successive pictures for each region, these pictures were small, and recorded at low frequency 10 frame/s. The aim of those Figures was to show the onset of CCFL within the full hot-leg geometry, and thus a wide-angle objective (24 mm) was implemented. The use of the wide-angle objective causes distortions of the pictures near the frames edge. The use of a low frequency does not allow capturing a detailed air/water interface due to the fast existing velocities and changes of the interface. The current chapter will introduce Figures that were acquired using higher frequency (500 frame/s) and a 50 mm objective. They provide clearer pictures of the air/water interface and explain a lot of the terminology used within the descriptions in section 7.3. The Figures will follow the same classification used in previous sections according to the inlet water velocities.

7.4.1 Visual observations of the flow patterns

Figures 7.11-7.63 Shows high quality images of the air/water interface for a representative case for each of the previously four recognized CCFL regions. A description of some specific observations is provided within the caption of each figure.

1. First region

   - Supercritical flow

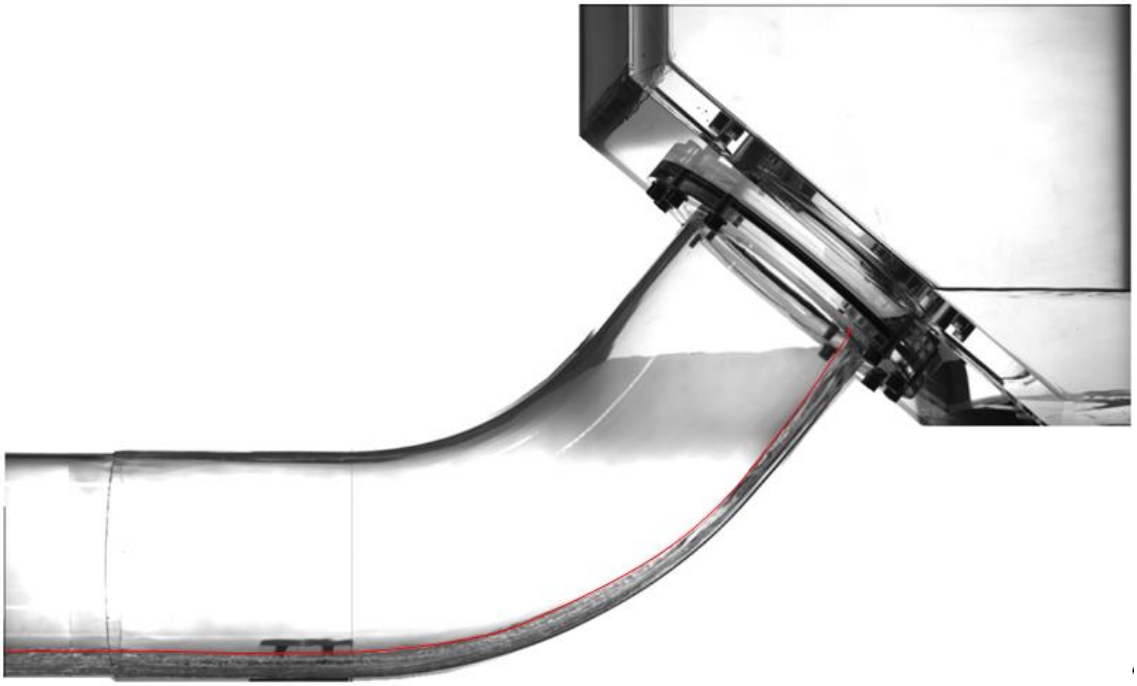

Figure 7.11 Supercritical flow at the bend. A smooth and undisturbed water stream flows from the SGs towards the hot-leg. $J_w^{*0.5} = 0.105$. The actual water surface is marked by a red line.

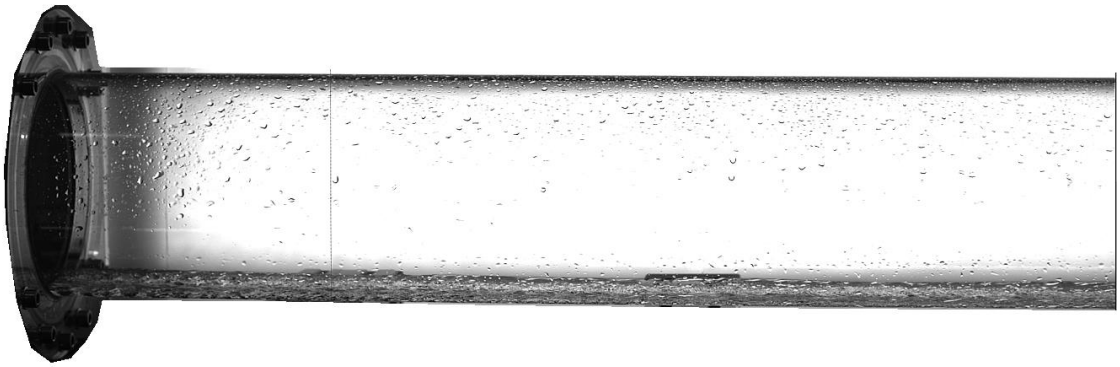

Figure 7.12 Supercritical flow near the water exit. A smooth undisturbed water stream flows towards the water exit. The droplets at the upper section of the pipe originate from a previous test (they are not accompanied with this flow condition). $J_w^{*0.5} = 0.105$.

- Appearance of the hydraulic jump

Figure 7.13 The approach of the hydraulic jump coming from the water exit towards the bend. . $J_w^{*0.5} = 0.105$.

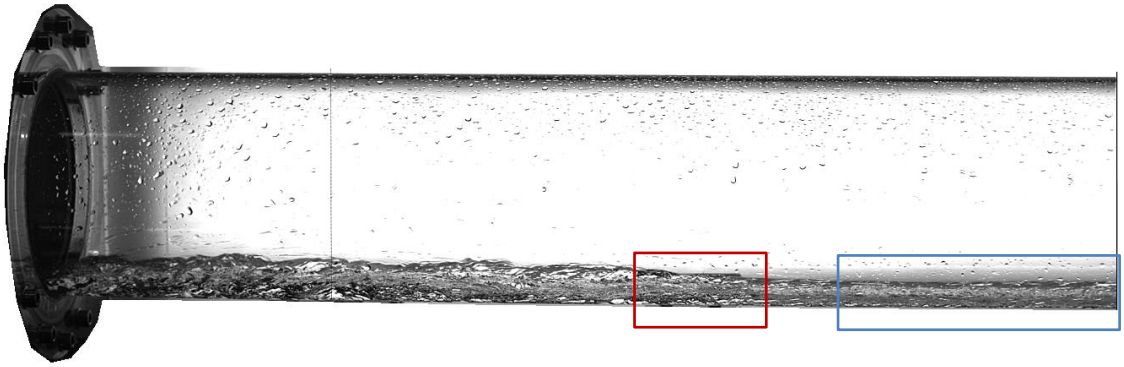

Figure 7.14 The appearance of the hydraulic jump at the water exit. The front of the hydraulic jump is clearly seen (red rectangle). Downstream of jump, the flow is still in a supercritical condition (blue rectangle). . $J_w^{*0.5} = 0.105$.

- The onset of the hydraulic jump

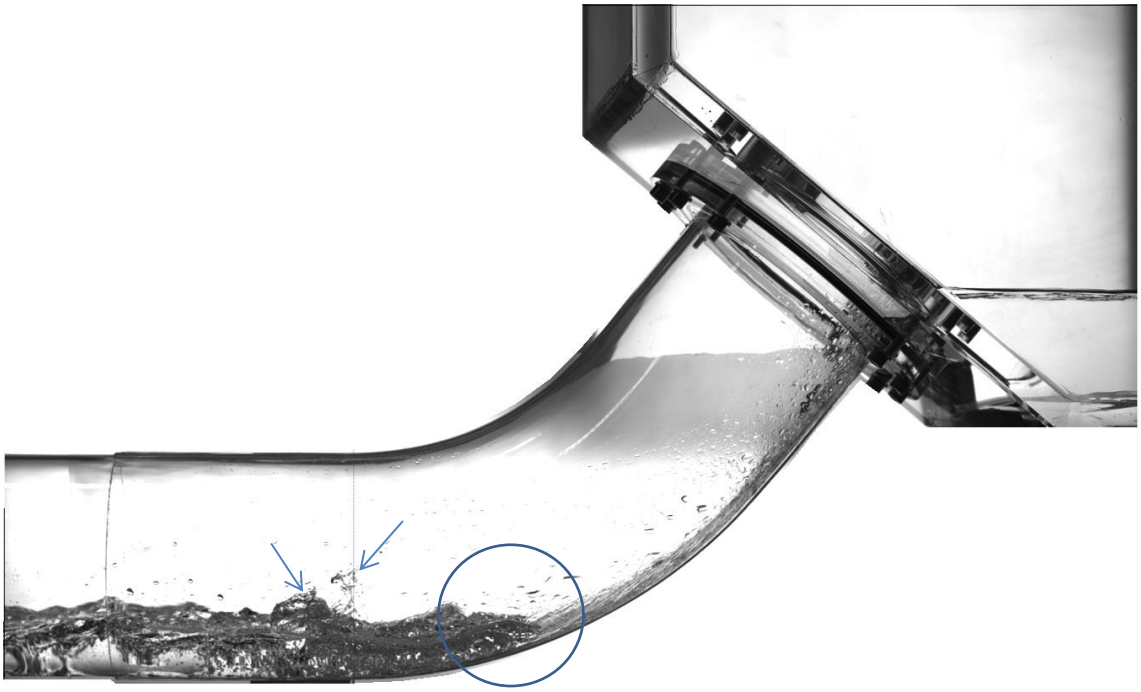

Figure 7.15 The hydraulic jump at the bend. Note the wavy air/water interface and the shedding of some droplets out of the water surface. . $J_w^{*0.5} = 0.105$.

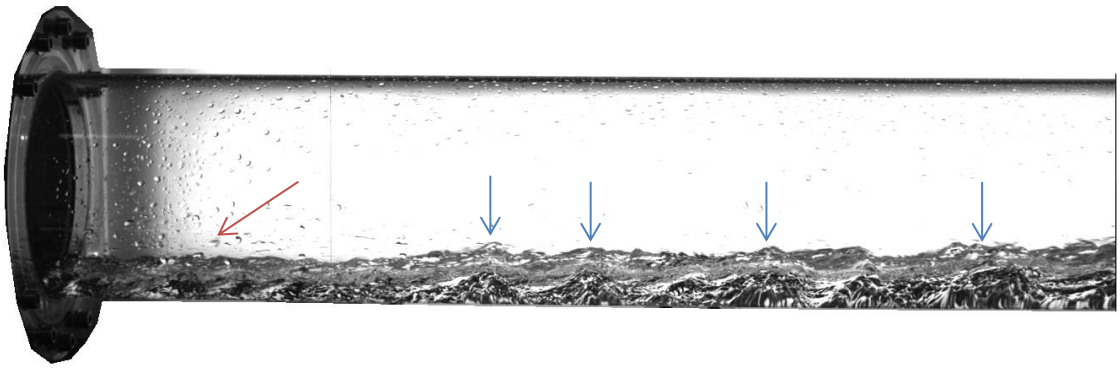

Figure 7.16 The hydraulic jump at the water exit. The wavy air/water interface is wavy and peaks of the moving waves can be clearly recognized (blue arrows). The red arrow indicates formation of droplets near the exit. The gradual decrease of the water thickness towards the water exit is also clear. . $J_w^{*0.5} = 0.105$.

- The onset of bend-CCFL

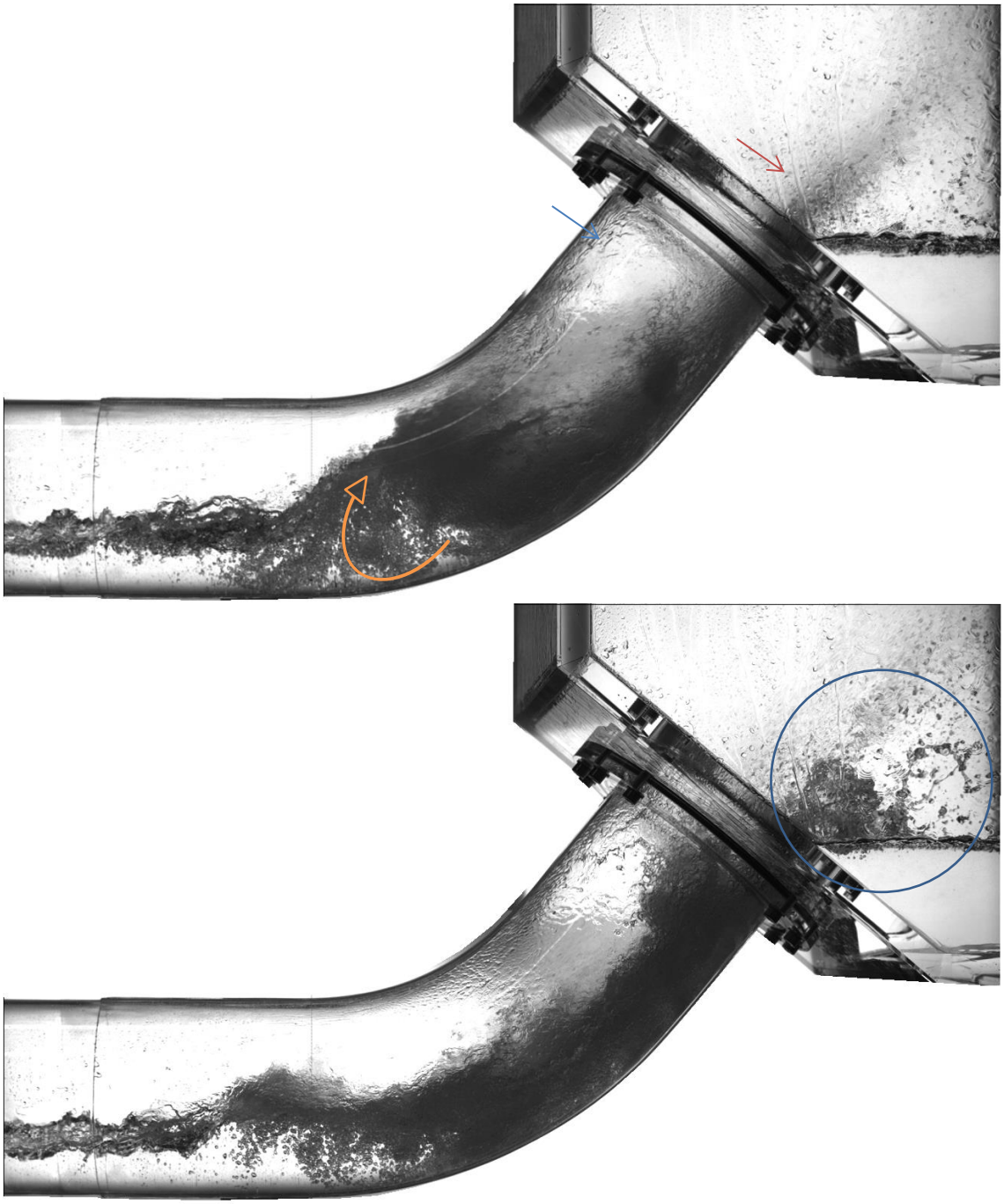

Figure 7.17 The onset of bend-CCFL in the first region. Top: The orange curved arrow shows the recirculation area and the trapped bubbles inside. The top of the roll-wave crest approaches the upper side of the bend. The blue arrow indicates the film water layer of the annular flow layer. The red arrow shows foam and droplets mix pushed towards the SGs. Bottom: the remaining of the wave crest as it is pushed into SGs, indicated by a blue circle. . $J_w^{*0.5} = 0.105$.

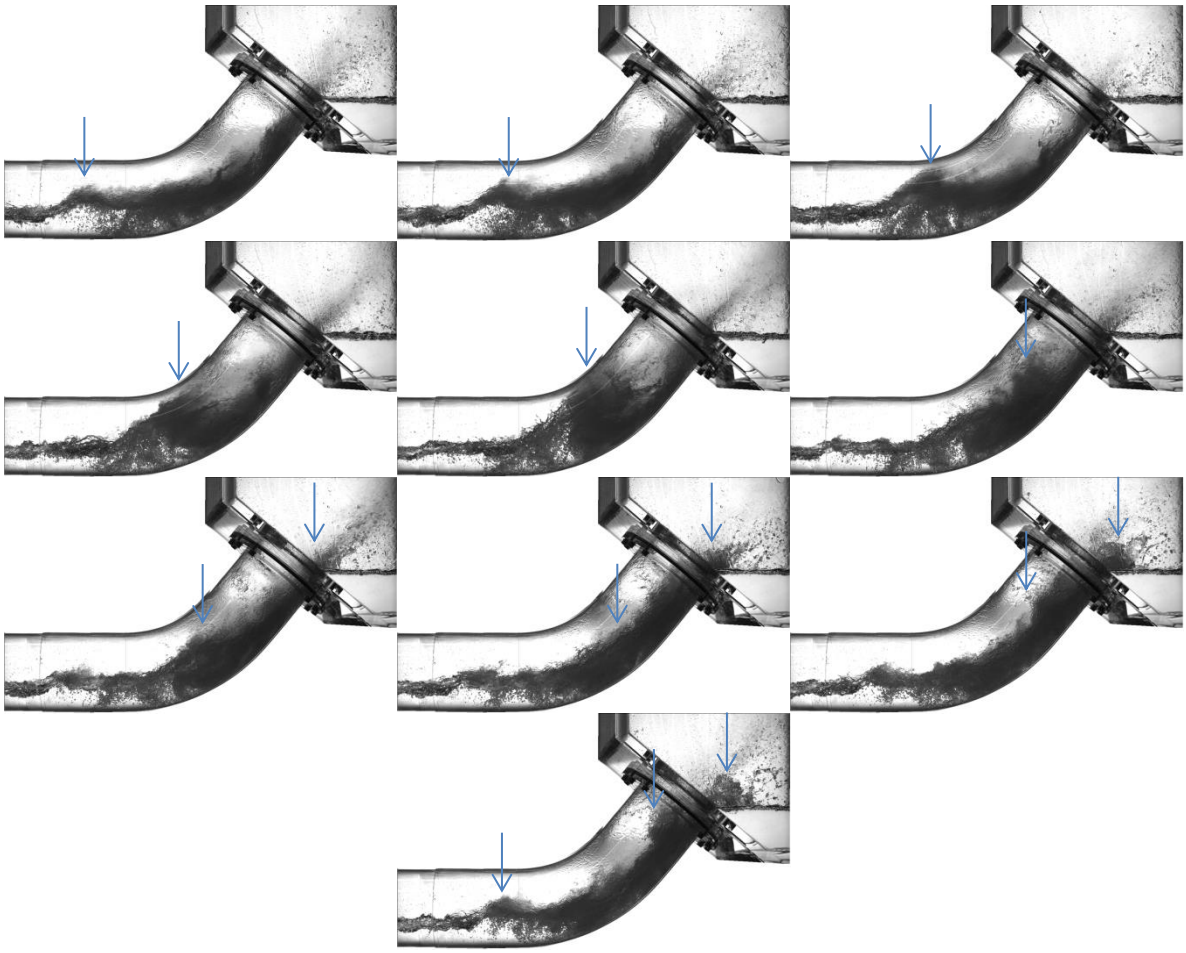

Figure 7.17 A set of successive images that illustrates the formation of a roll-wave near the bend and tracks it until it breaks into the SGs. These images illustrates the main mechanism by which the CCFL occurs in this region. Time step: 2 ms. $J_w^{*0.5} = 0.105$.

- Deflooding

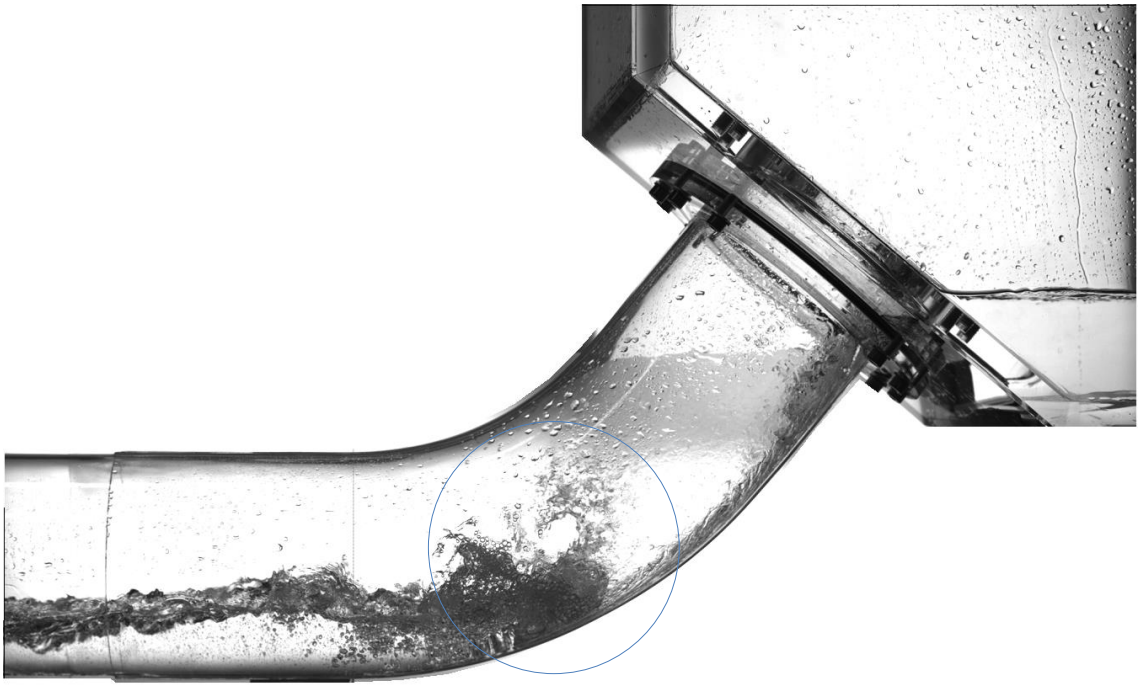

Figure 7.18 Deflooding at the bend. Despite that some small waves are still forming and crashing into the bend, they do not reach the SGs, and thus no carryover of the water happens in the opposite direction. This condition indicates the end of CCFL or the deflooding . $J_w^{*0.5} = 0.105$.

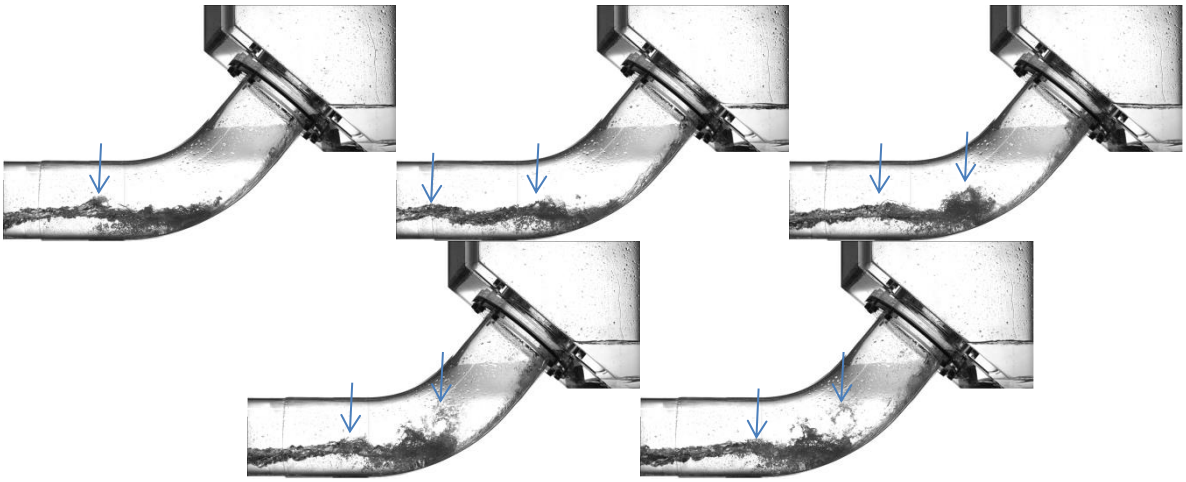

Figure 7.19 A set of images that illustrates the air/water interface near the bend during deflooding. Note that small waves are still forming within the horizontal part but they cannot create a sufficient blockage at the bend. They breaks completely within the riser. $J_w^{*0.5} = 0.105$.

2. Second region
   - Supercritical flow

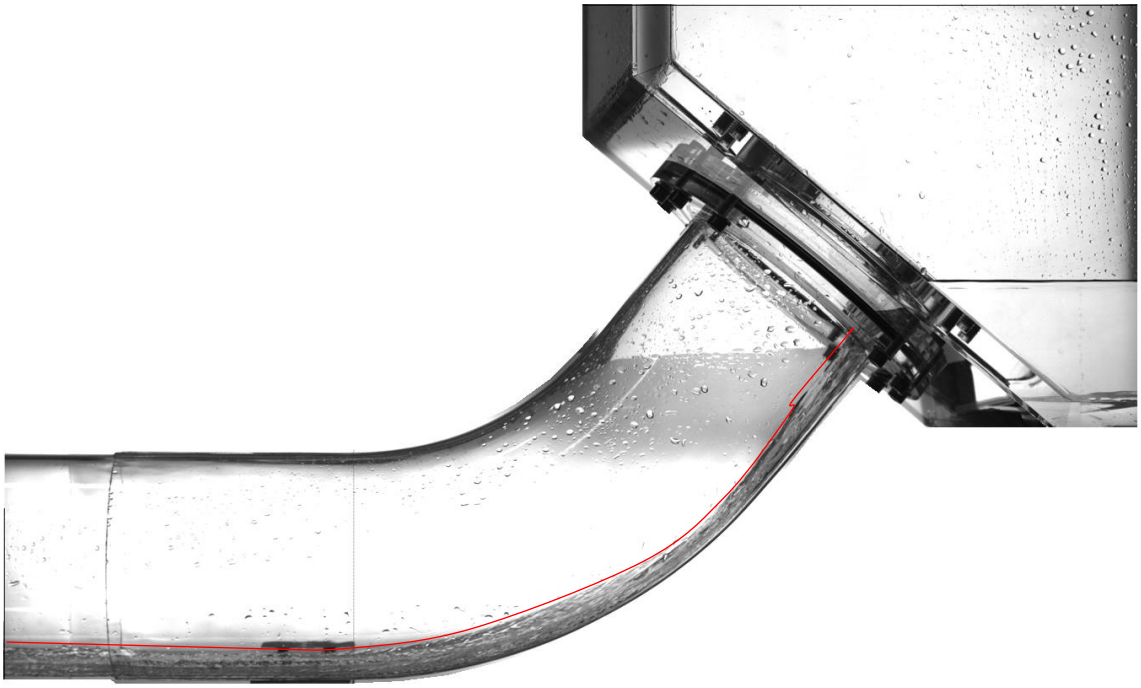

Figure 7.20 Supercritical flow at low air velocity. $J_w^{*0.5} = 0.155$. The water level is thicker as in the case of $J_w^{*0.5} = 0.105$. The actual water surface is marked by a red line.

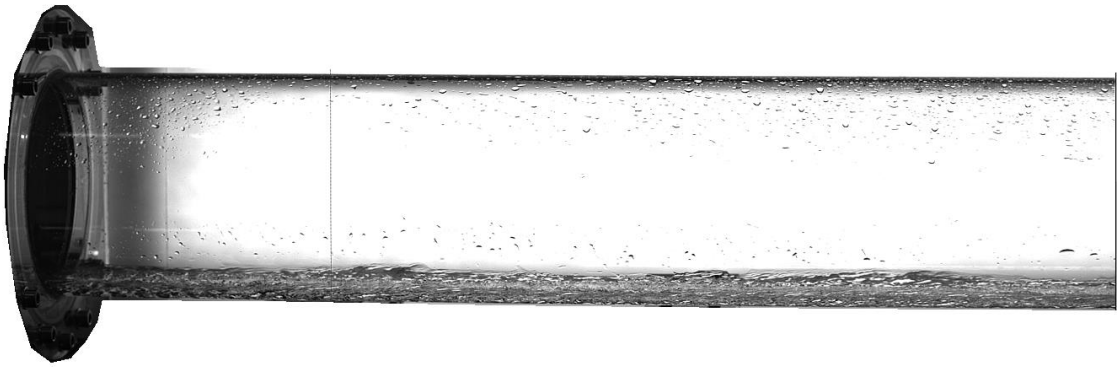

Figure 7.21The air/water interface near the water exit during supercritical flow. $J_w^{*0.5} = 0.155$. A smooth water stream flows into the water exit.

   - Prior to bend-CCFL

Figure 7.22 The air/water interface at the bend just prior to the occurrence of bend-CCFL. No hydraulic jump happens, however the water stream is highly disturbed with an intensive formation of water droplets. $J_w^{*0.5} = 0.155$.

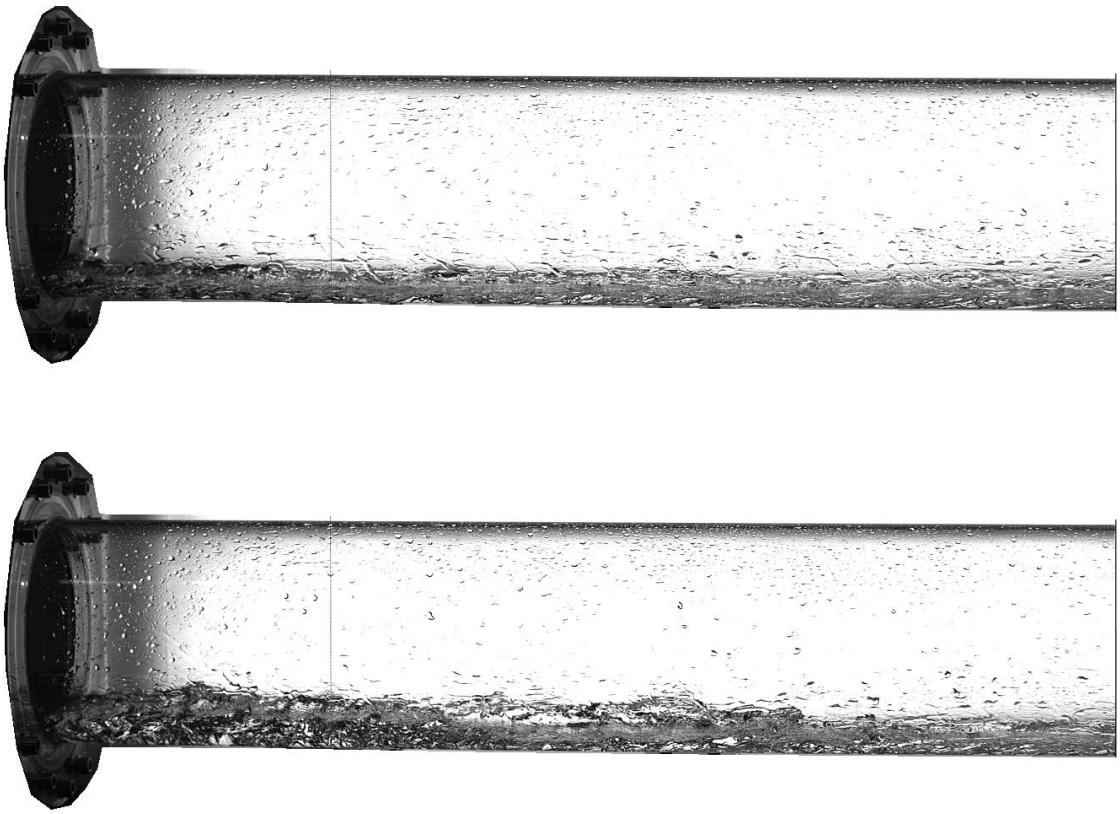

Figure 7.23 The air/water interface at the water exit just prior to the occurrence of bend-CCFL. Upper image: No hydraulic jump occurs, the water stream is highly disturbed with an intensive formation of water droplets. Bottom Image: At the beginning of small roll-waves formation. The roll-waves travel at once towards the bend transforming the flow into a subcritical flow immediately. $J_w^{*0.5} = 0.155$.

- Bend-CCFL

Figure 7.24 The air/water interface during the bend-CCFL. Upper image: A large roll-waves approaching the bend and blocking almost the entire cross section of the pipe. A strong annular churn flow occurs at the bend/riser region. Lower image: The remaining of the wave crest, droplets, and the foam after it crashes into the SGs. The intensity of the CCFL mechanism is remarkably higher as in the first region. $J_w^{*0.5} = 0.155$

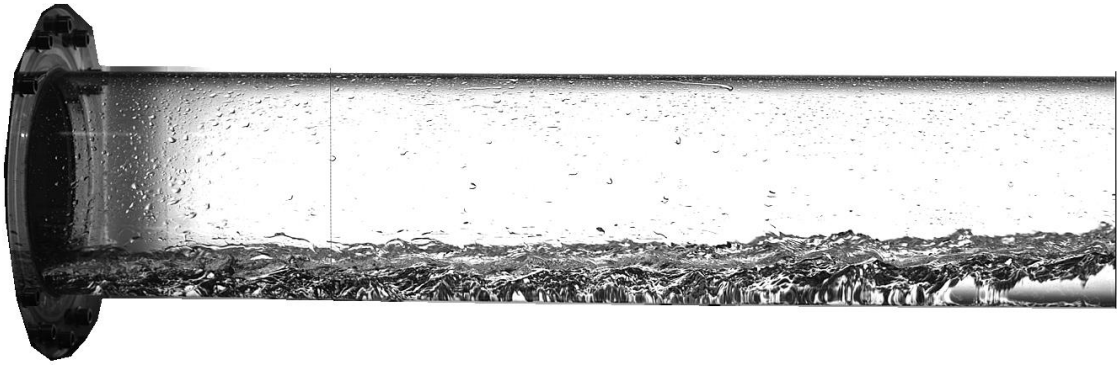

Figure 7.25 The air/water interface during the bend-CCFL near the water exit. The flow is wavy and the water depth is larger than the first region. $J_w^{*0.5} = 0.155$

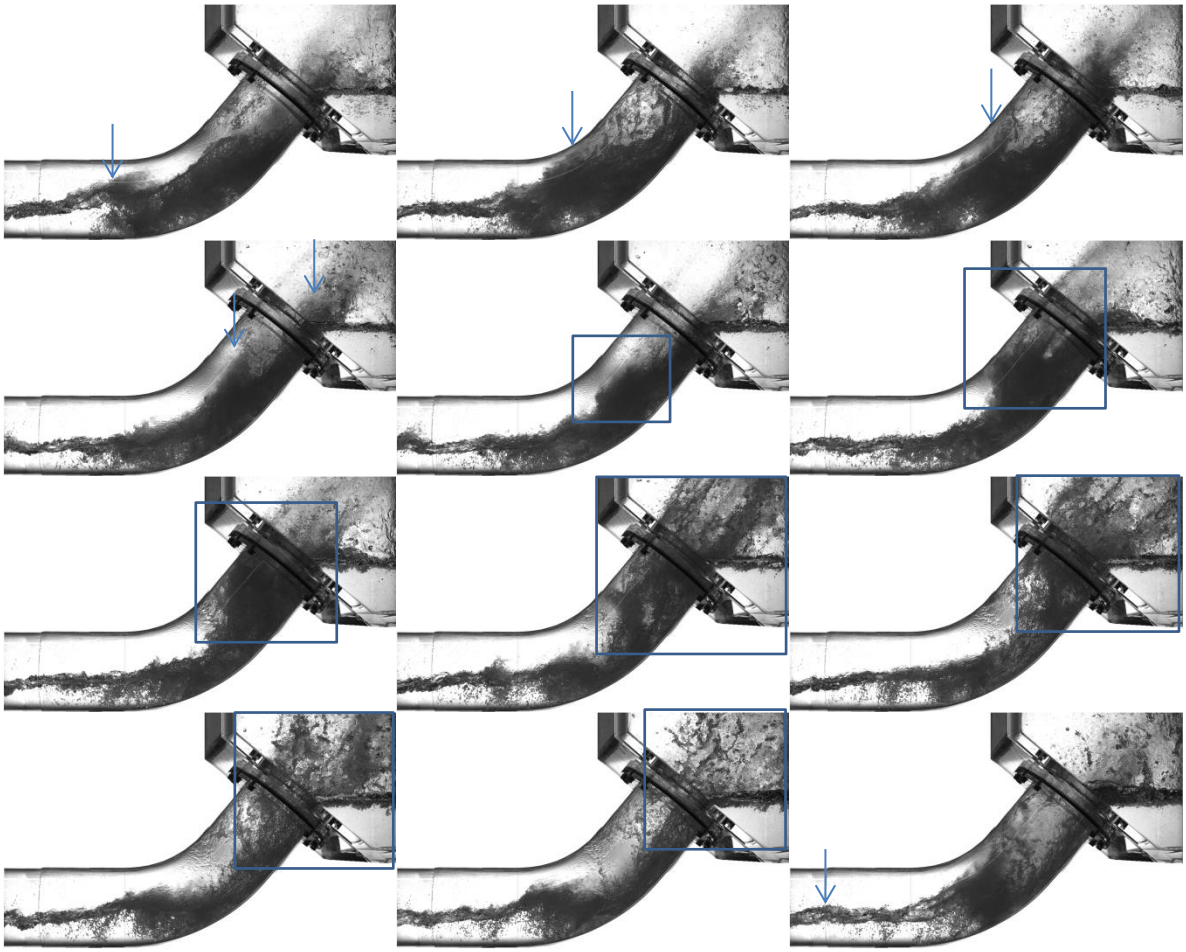

Figure 7.26 A set of successive images that illustrate the air/water interface during bend-CCFL. Time step: 4 ms. The arrow follows the tip of the large roll-wave and the rectangle follows the blockage that occurs at the riser, and the subsequent breaking of the air/water mixture into the SGs. $J_w^{*0.5} = 0.155$

- Deflooding

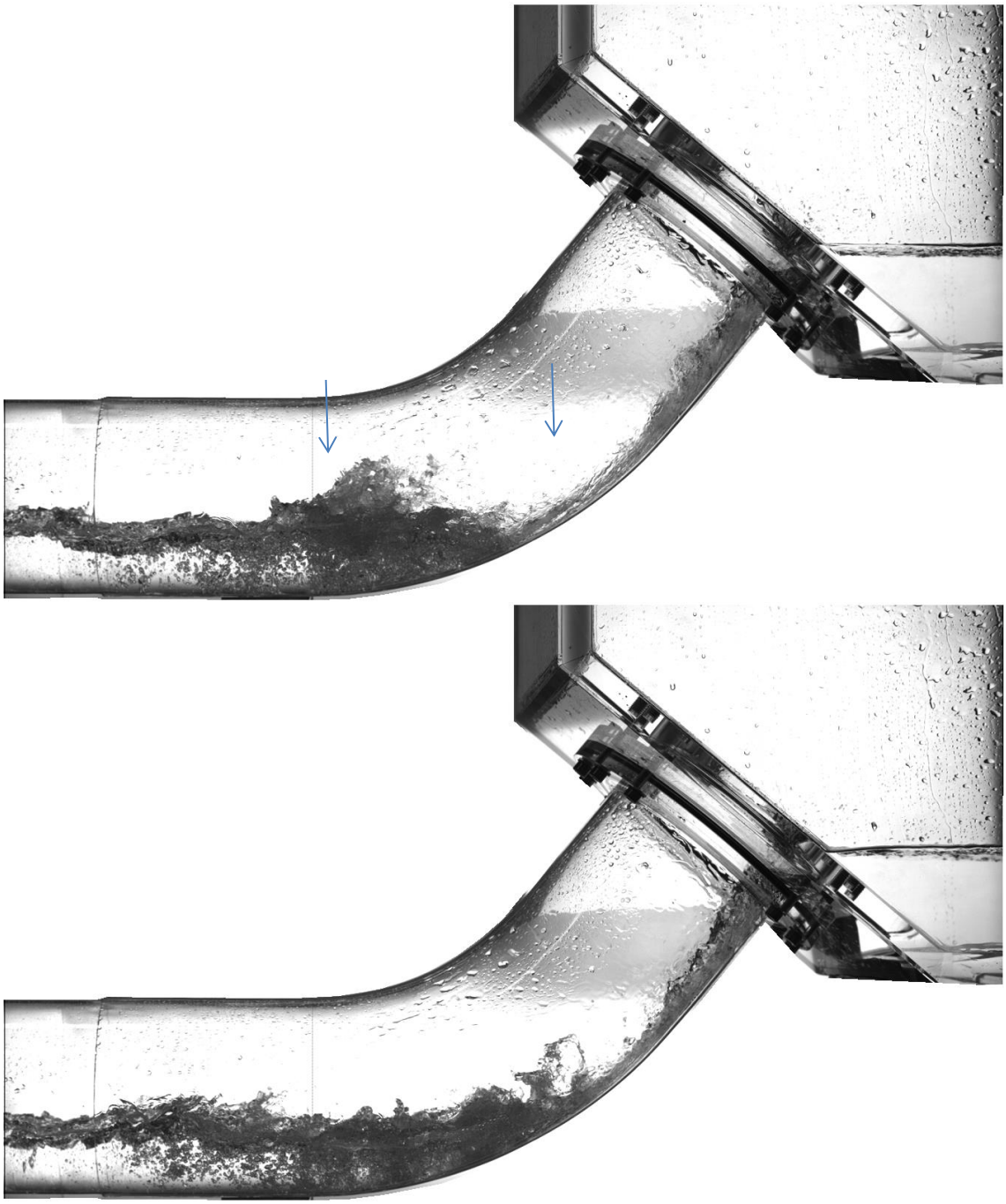

Figure 7.27 The air/water interface at the bend during deflooding. Upper image: some small waves are still forming at the bend . Bottom image: the small waves do not reach the SGs after they break into the riser. $J_w^{*0.5} = 0.155$

3. Third region

- Supercritical flow

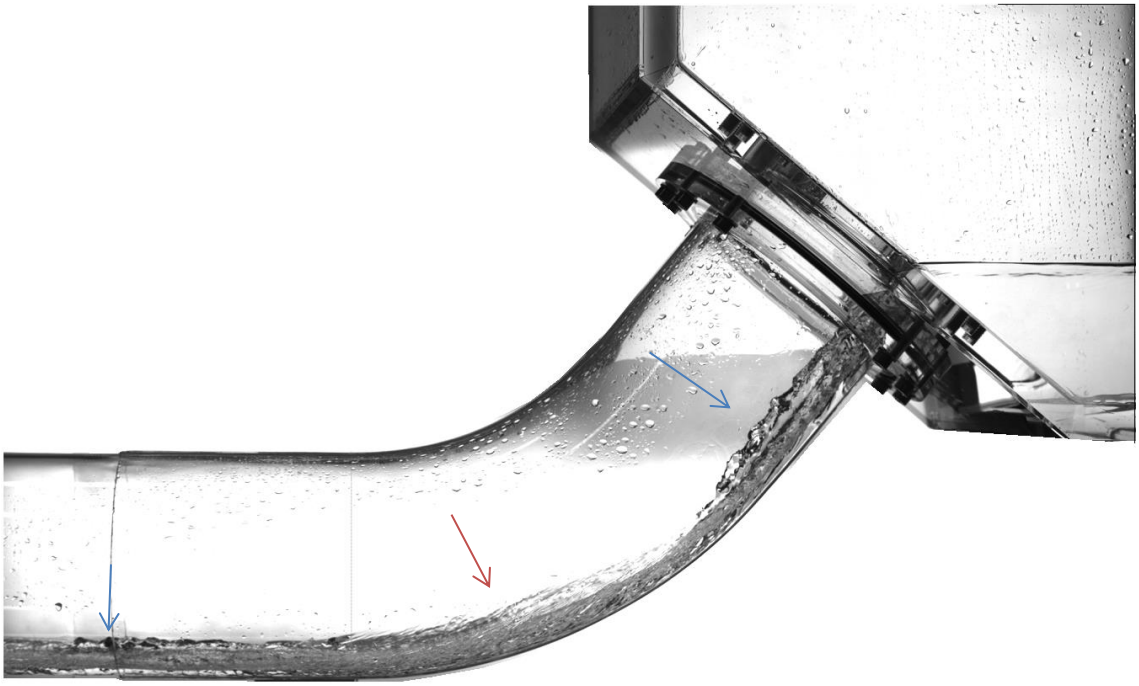

Figure 7.28 Supercritical flow at the bend. The 3D structure of the water stream is visible: blue arrows: the convergent stream creating a peak at the center of the pipe, red arrow: diverging stream, the water surface is flat and stretch into both sides. The turbulent water surface at the inlet is also clear. This helps initiating the ADE-CCFL and is a clear difference from experiments with a rectangle cross section. $J_w^{*0.5} = 0.255$.

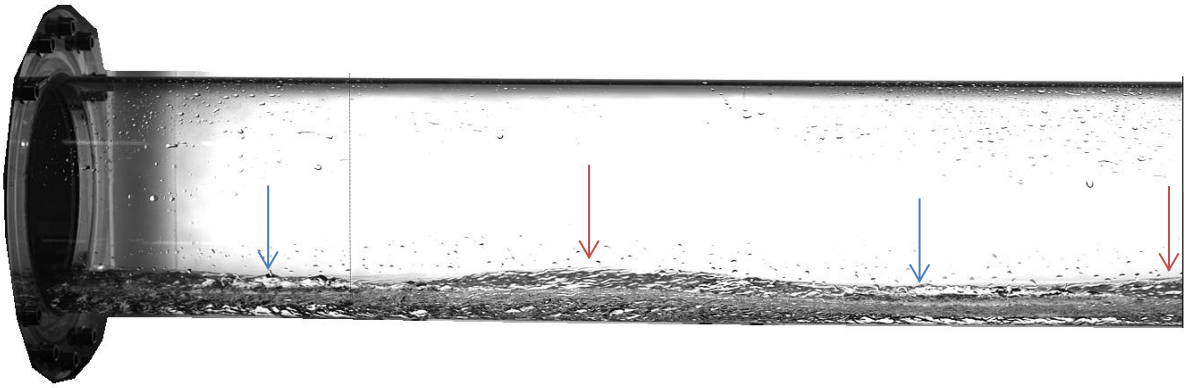

Figure 7.29 Supercritical flow near the water exit. The flow pattern that consists of converging/diverging water stream can be easily seen. Blue arrow: converging stream. Red arrow: diverging stream. $J_w^{*0.5} = 0.255$.

- ADE-CCFL

Figure 7.30 The air/water interface during ADE-CCFL at the bend. A jet of water droplets can be seen at the inlet, this jet transports water back into the SGs which forms the second mechanism of CCFL occurrence.. $J_w^{*0.5} = 0.255$

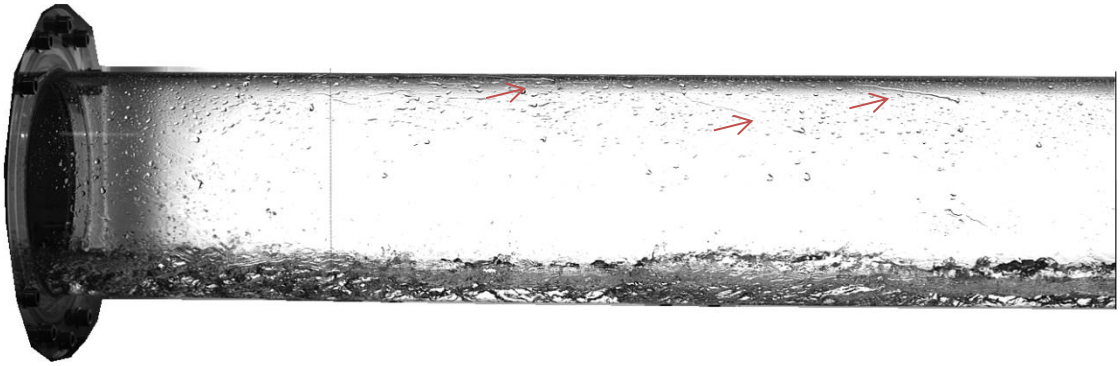

Figure 7.31 The air/water interface during ADE-CCFL near the water exit. The water stream surface is turbulent and rough. There is a strong formation of water droplets at the water exit and inside the pipe. $J_w^{*0.5} = 0.255$. Note some droplets smearing on the inner surface of the pipe after being pushed to it from the water exit.

- Prior to Bend-CCFL

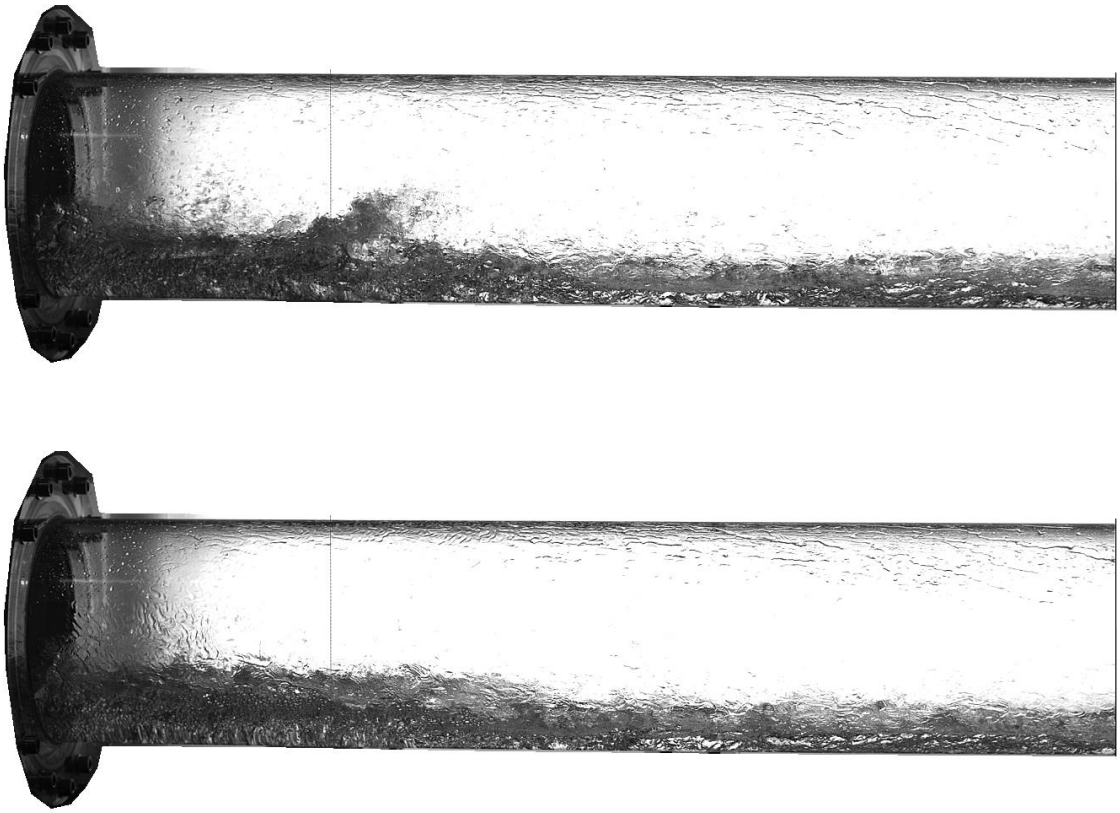

Figure 7.32 The air/water interface near the water exit prior to the bend-CCFL. Upper image: Large waves appear near the water exit and start to form a blockage. Lower Image: The beginning of the transition into a subcritical flow, a clear water thickening can be seen near the water exit. $J_w^{*0.5} = 0.255$

- Bend-CCFL

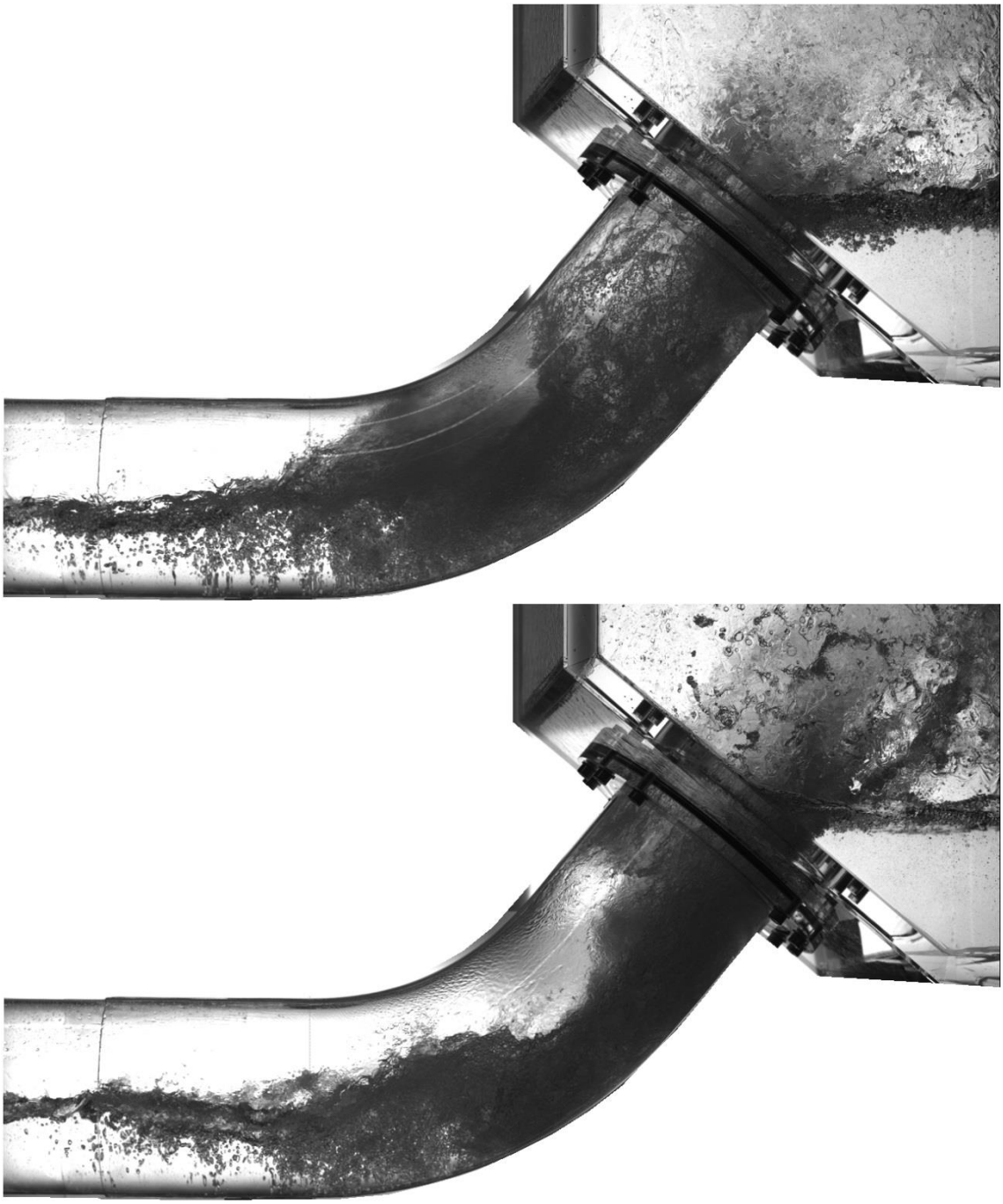

Figure 7.33 The air/water interface during the bend-CCFL. Upper image: A large roll-waves blocking the entire cross section of the pipe. An intense annular churn flow accompanied with a large amount of foam formation occurs at the bend/riser region. Lower Image: The remaining of the two-phase mixture after it is pushed into the SGs. The bend-CCFL mechanism remains the same, however the intensity and amount of water carried backwards is increasing $J_w^{*0.5} = 0.255$

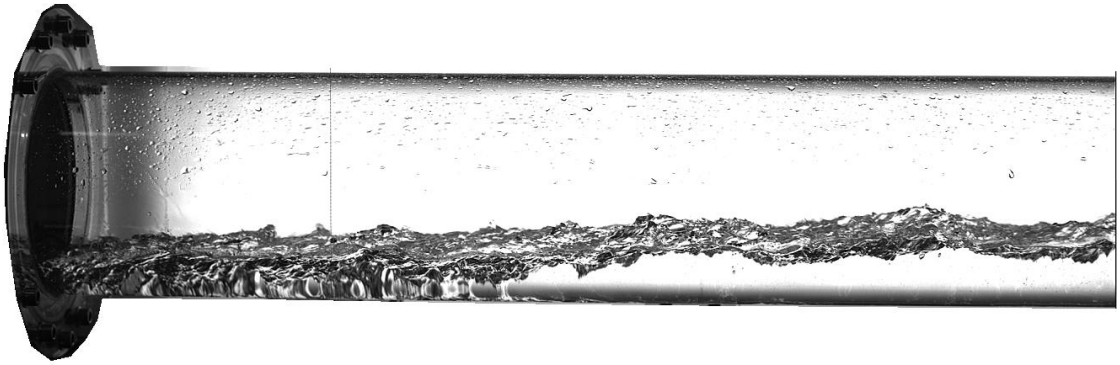

Figure 7.34 The air/water interface near the water exit during the bend-CCFL. The water depth is remarkably higher than previous cases and is caused by the higher blockage at the bend. . $J_w^{*0.5} = 0.255$.

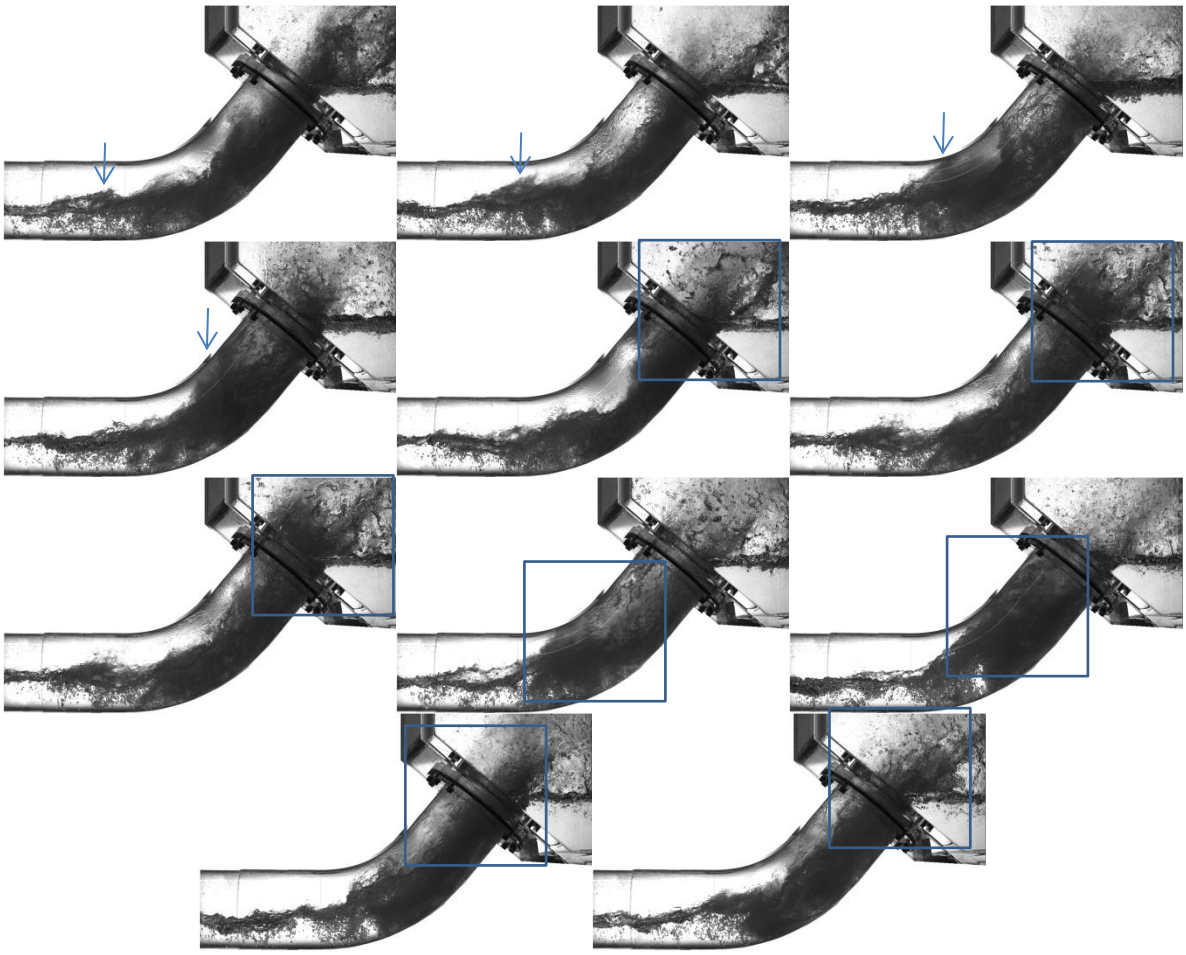

Figure 7.35 A set of successive images that illustrates the air/water interface during the bend-CCFL. Time step: 4 ms. The arrow tracks a large roll-wave approaching the bend and the rectangle tracks the formation of a large blockage at the riser. The subsequent breaking of the air/water mixture into the SGs is intense and occurs twice before a second roll-waves arrives.. $J_w^{*0.5} = 0.255$. Blower rotation speed at 75%.

- Blower at 55% of rotational speed, bend-CCFL persist

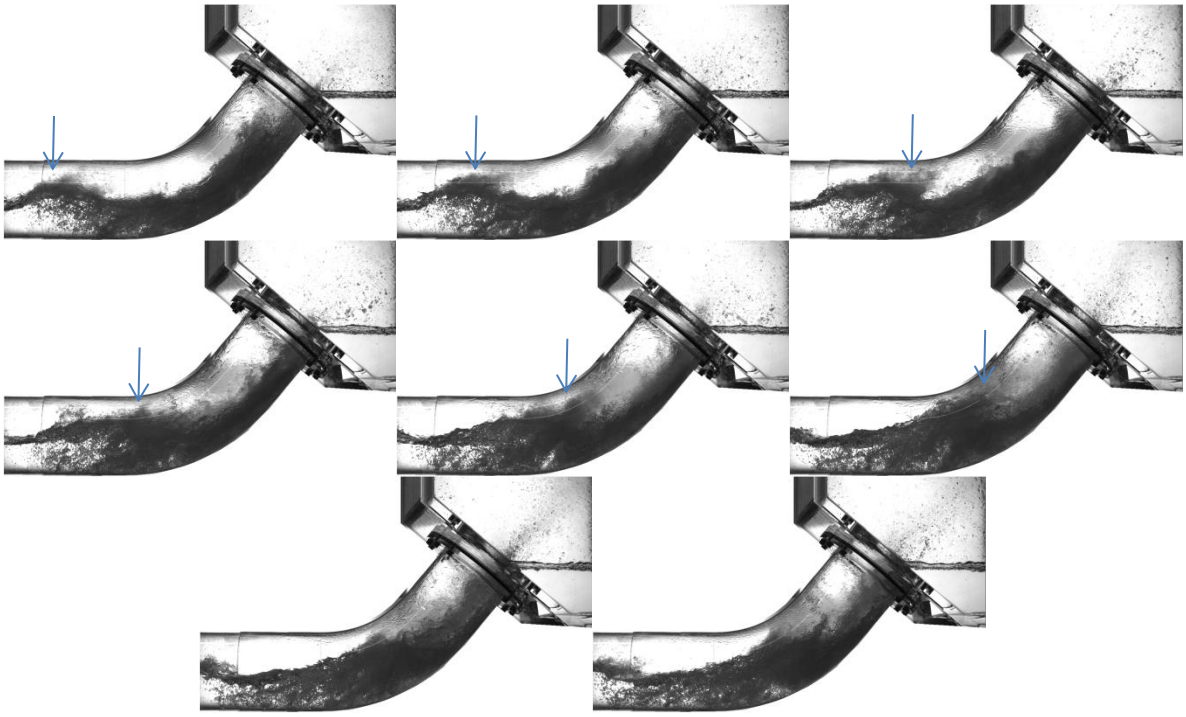

Figure 7.36 A set of successive images that illustrates the air/water interface during the reduction of blower rotation speed (55%). Large roll-waves start to emerge away from the bend (near the middle of the pipe). They move towards the bend increasing their amplitude and touch the upper edge of the pipe forming a blockage. This maintains the CCFL at the bend although its intensity is reduced and a periodic plugging is less frequent. $J_w^{*0.5} = 0.255$

- Deflooding, rotational speed (40%)

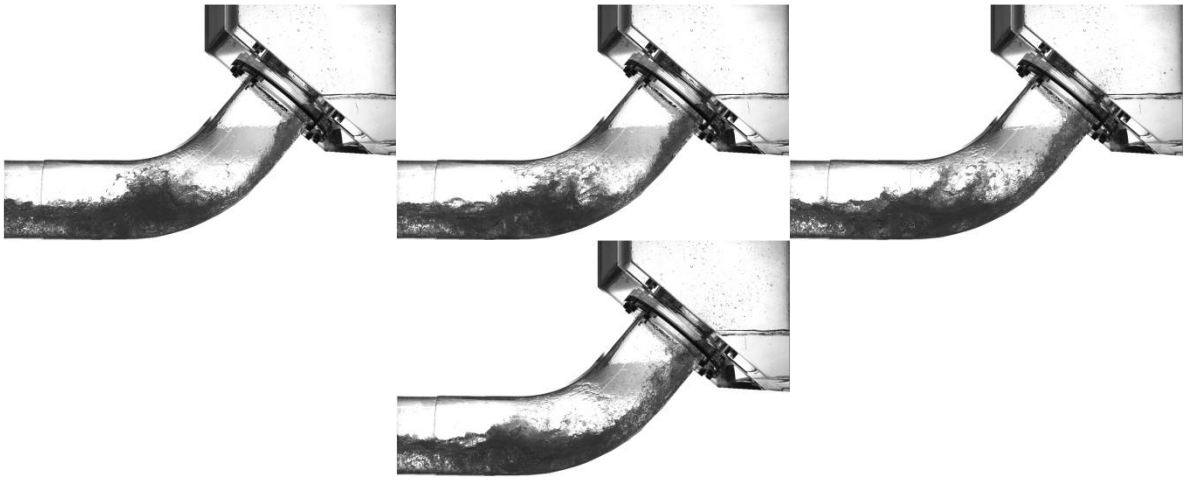

Figure 7.37 A set of successive images that illustrates the air/water interface during deflooding. Blower rotation speed (40%). the formation of large roll-waves near the bend stops. Some smaller waves can still emerge at the water surface but they break into the riser and are not able to reach the SGs. $J_w^{*0.5} = 0.255$

- Deflooding, rotational speed (35%)

Figure 7.38 The air/water interface during deflooding. blower rotation speed (35%). Only a hydraulic jump remains at the bend with some droplets shedding off the surface. Eventually, the hydraulic jump moves towards the water exit transforming the flow back into a supercritical flow. $J_w^{*0.5} = 0.255$.

4. Fourth Region
   - "Supercritical flow", Or flow at low air velocity

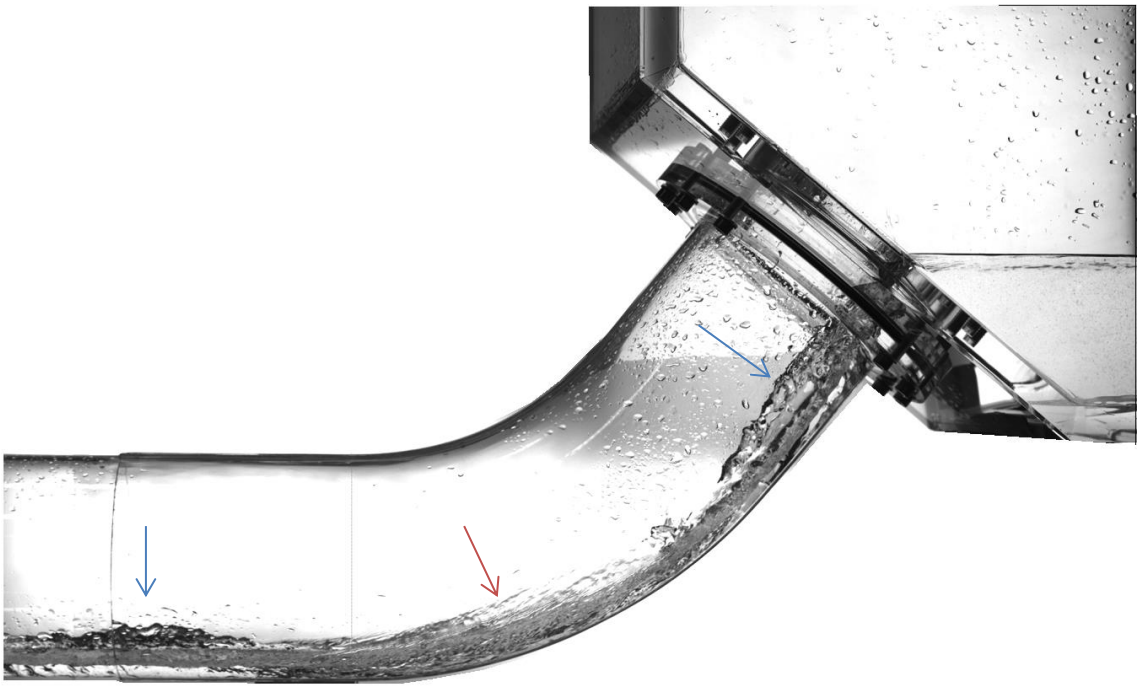

Figure 7.39 Supercritical flow at the bend. The 3D structure of the water stream is more visible than in the third region: Blue arrows: the convergent stream creating a peak at the center of the pipe, red arrow: diverging stream. The water surface at the inlet is more turbulent and instable with a sensible formation of a droplets jet even at low air velocity. $J_w^{*0.5} = 0.305$.

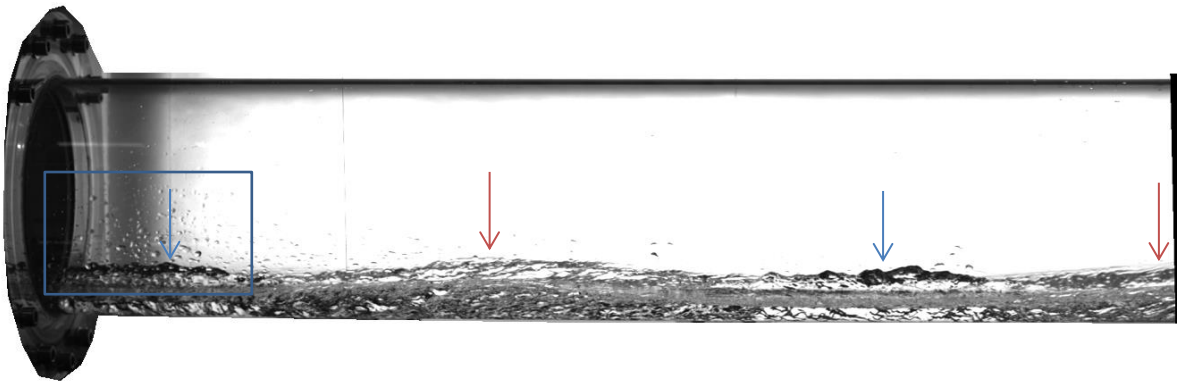

Figure 7.40 Supercritical flow near the water exit. The 3D structure of the water stream is more apparent than in previous region: blue arrows: the convergent stream, red arrow: diverging stream. The water surface is turbulent with a strong formation of droplets at the exit (blue rectangle). $J_w^{*0.5} = 0.305$.

- ADE-CCFL

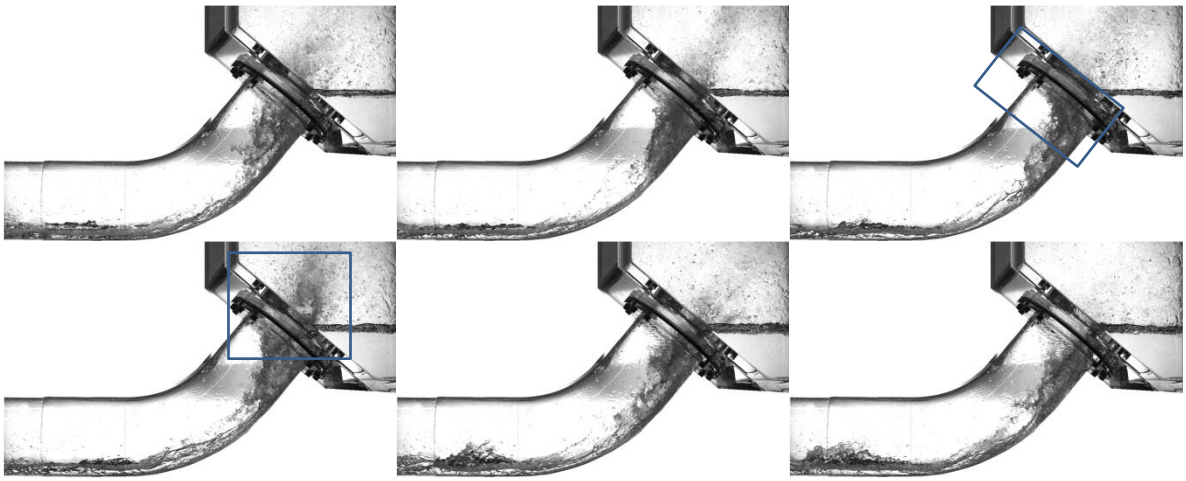

Figure 7.41 A set of successive images that illustrates the air/water interface during the onset of ADE-CCFL. A strong jet of water droplets occurs at the water inlet. A periodic blocking of the entire cross section of the pipe entrance happens leading into a sporadic occurrence of the annular flow at the water inlet (blue rectangle). $J_w^{*0.5} = 0.305$.

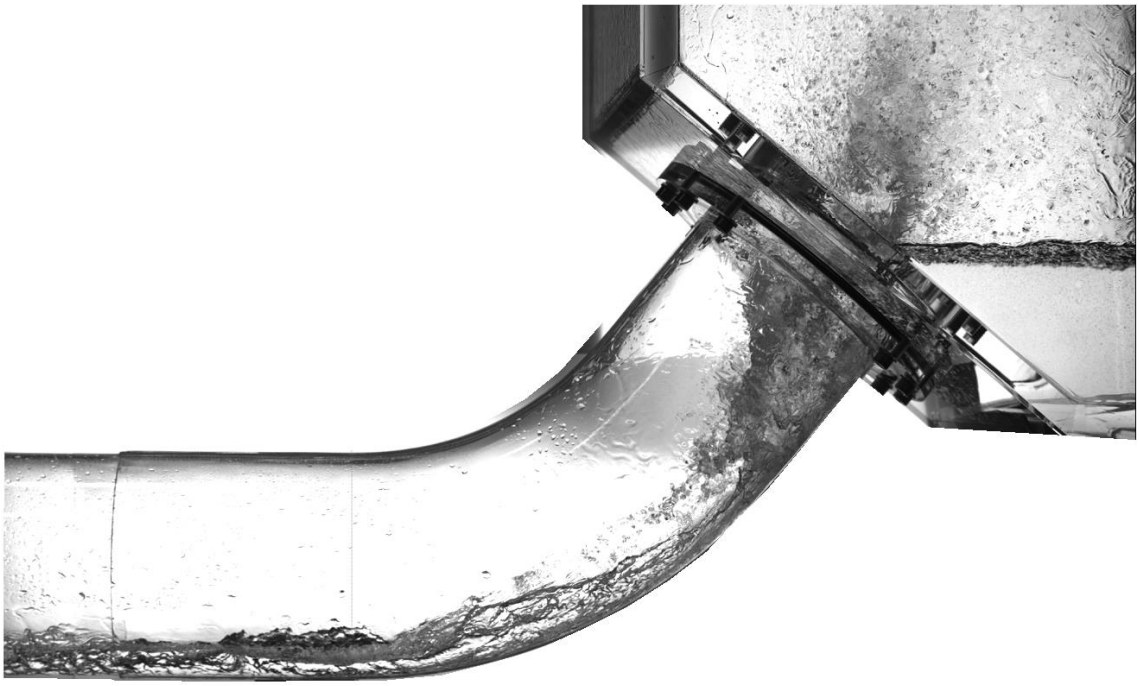

Figure 7.42 The air/water interface during the onset of ADE-CCFL. The droplets jet after the formation a sporadic annular flow at the water inlet can be clearly seen. $J_w^{*0.5} = 0.305$

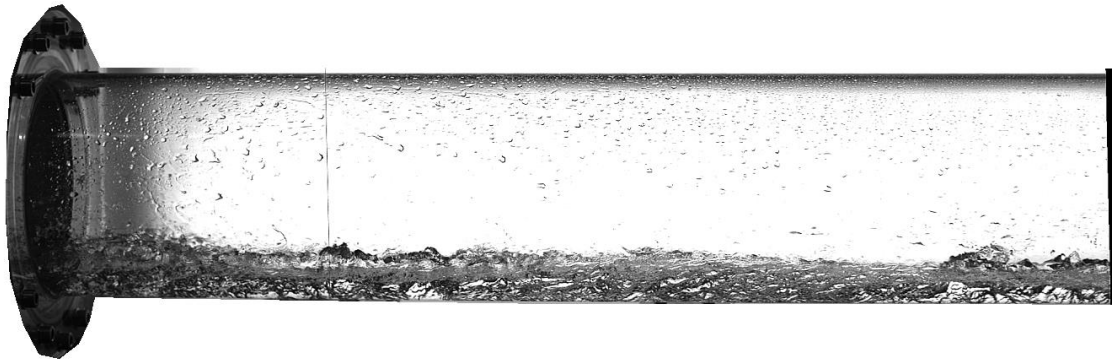

Figure 7.43 The air/water interface near the water exit during the onset of ADE-CCFL. The water stream surface is highly turbulent (though not subcritical), with a strong formation of droplets inside the entire horizontal section. $J_w^{*0.5} = 0.305$.

- Prior to bend-CCFL

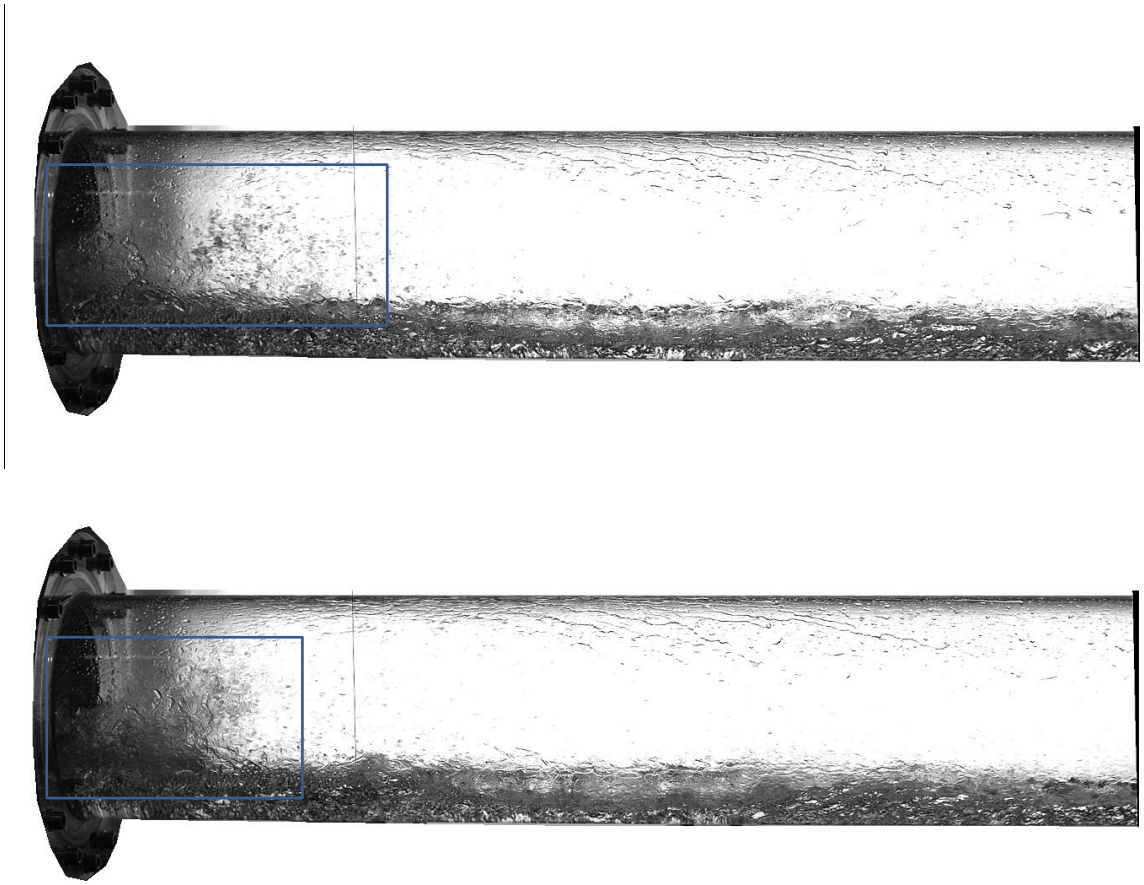

Figure 7.44 The air/water interface near the water exit prior to the onset of bend-CCFL. Top: A strong active droplets entrainment occurs near the water exit. The surface of the water stream is highly turbulent. Droplets of water are happening along the entire horizontal section. Bottom: A large roll-wave emerges at the water exit, it moves fast towards the bend transforming the flow into a subcritical flow immediately. $J_w^{*0.5} = 0.305$

- During the onset of the bend-CCFL

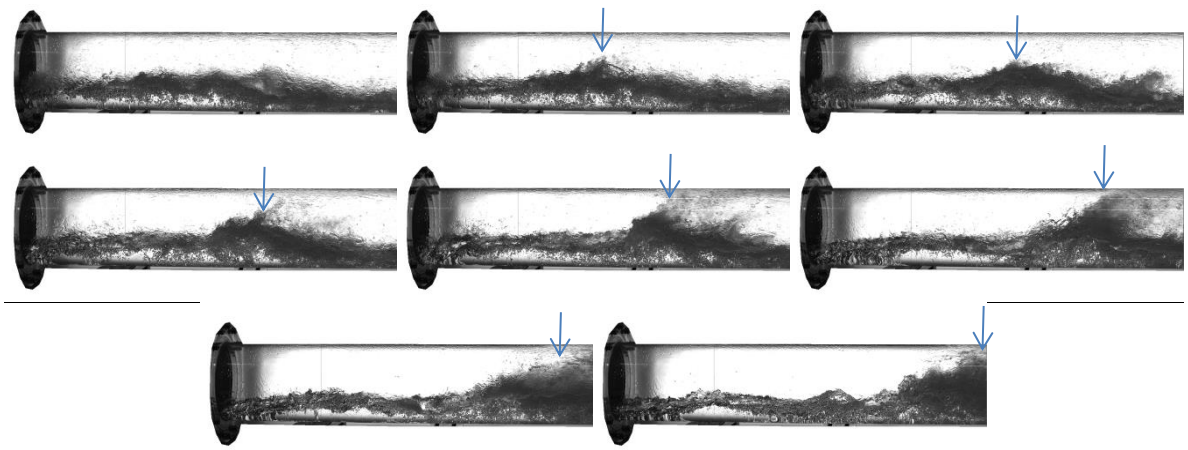

Figure 7.45 A set of successive images that illustrates the air/water interface near the water exit during the onset of bend-CCFL. The flow becomes highly turbulent and water droplets build a water thickening, at the surface of this water thickening a large roll-wave (blue arrow) that blocks the air flow is pushed violently towards the bend transforming the flow upstream instantly into a subcritical flow. $J_w^{*0.5} = 0.305$.

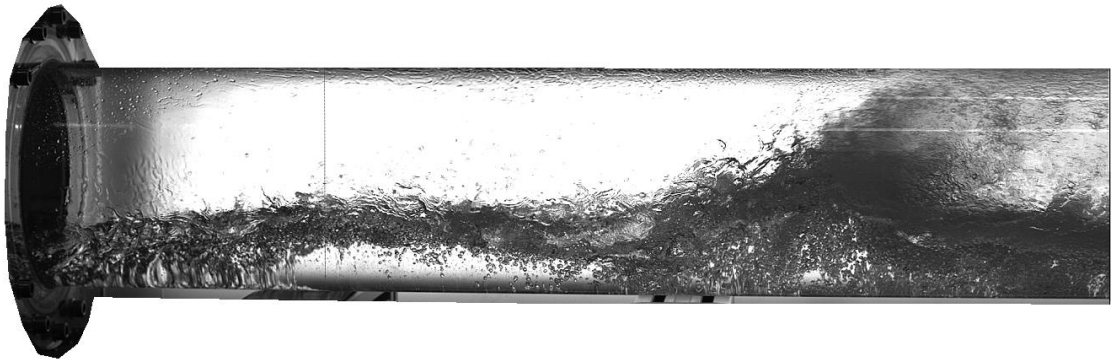

Figure 7.46 A large and turbulent roll-wave advances towards the bend transforming the flow behind into a subcritical flow. This mechanism differs significantly from the formation of a hydraulic jump that moves towards the bend before the onset of the bend-CCFL (as in the first region). $J_w^{*0.5} = 0.305$.

- Bend-CCFL: Large roll-waves appears near at the middle of the horizontal part:

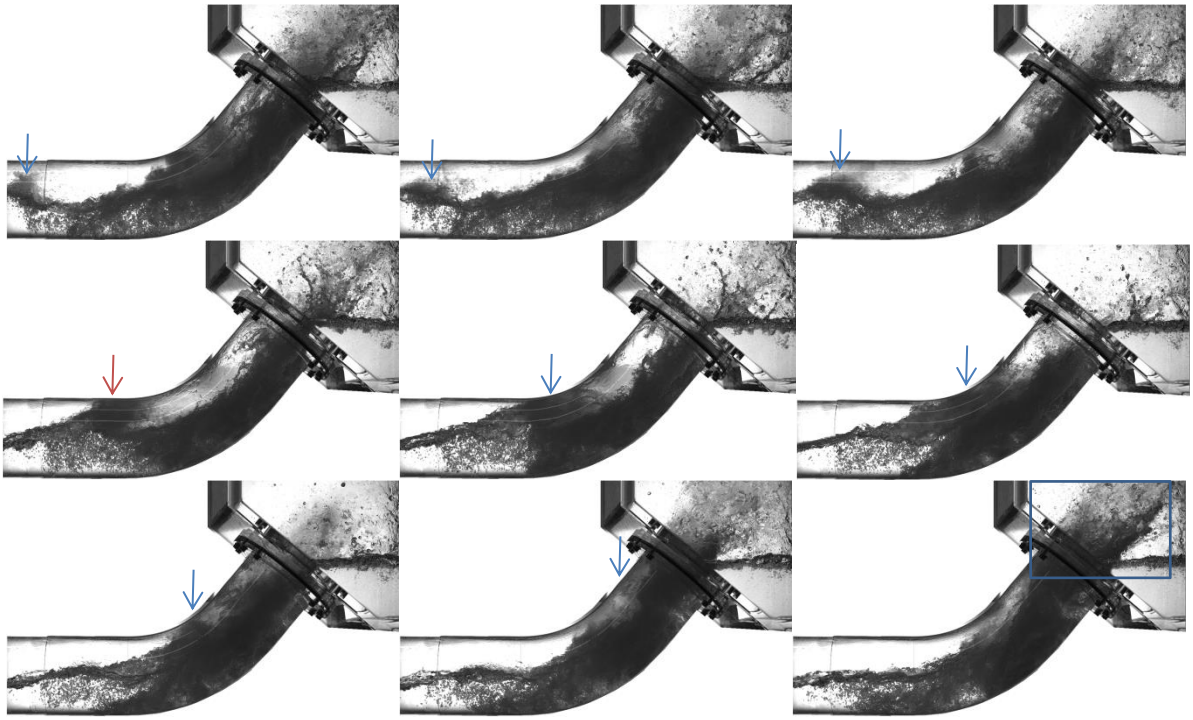

Figure 7.47 A set of successive images that illustrates the air/water interface and formation of large roll-waves during the Bend-CCFL. The waves start to appear near the middle of the pipe, its amplitude grows as it advances towards the bend. It Blocks the entire cross-section even before it reaches the bend (red arrow). A large blockage happens within the riser and it is pushed violently with a large amount of water into the SGs. $J_w^{*0.5} = 0.305$.

Figure 7.48 A set of successive images that illustrates the air/water interface after the breaking of a large roll-wave into the riser. An intense, violent and turbulent annular churn flow occurs, transporting a large amount of water in the form of droplets, small lumps of water, and foam into the steam generator creating a periodic plugging at the riser. $J_w^{*0.5} = 0.305$.

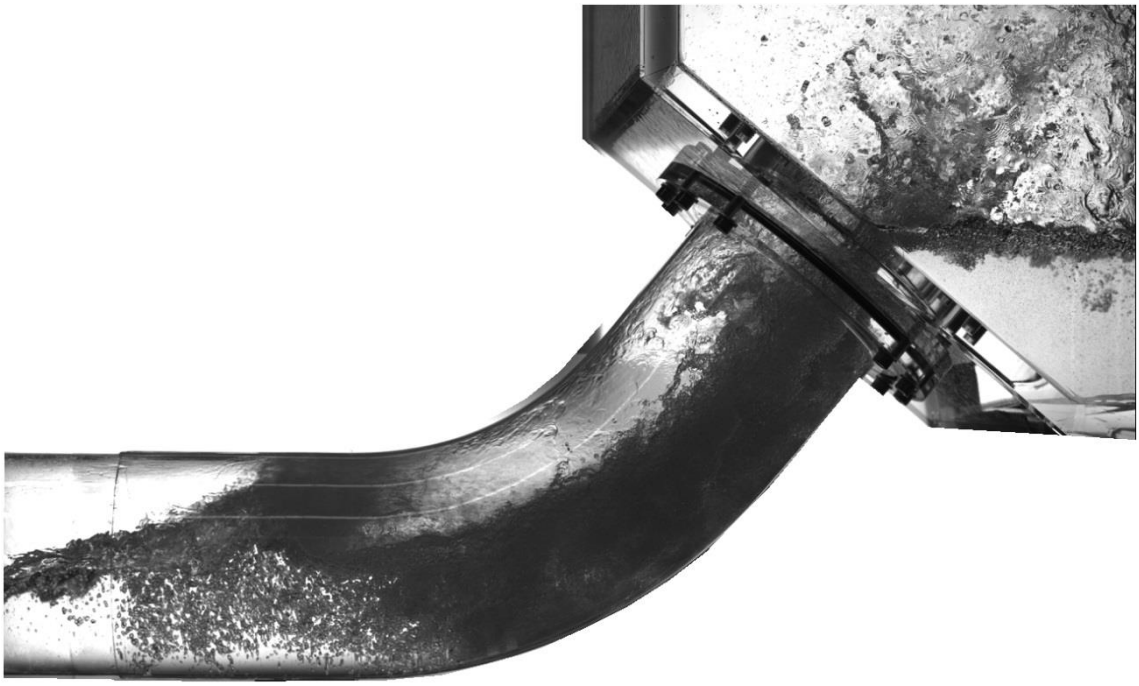

Figure 7.49 A large roll-waves that blocks the air flow during the Bend-CCFL. $J_w^{*0.5} = 0.305$.

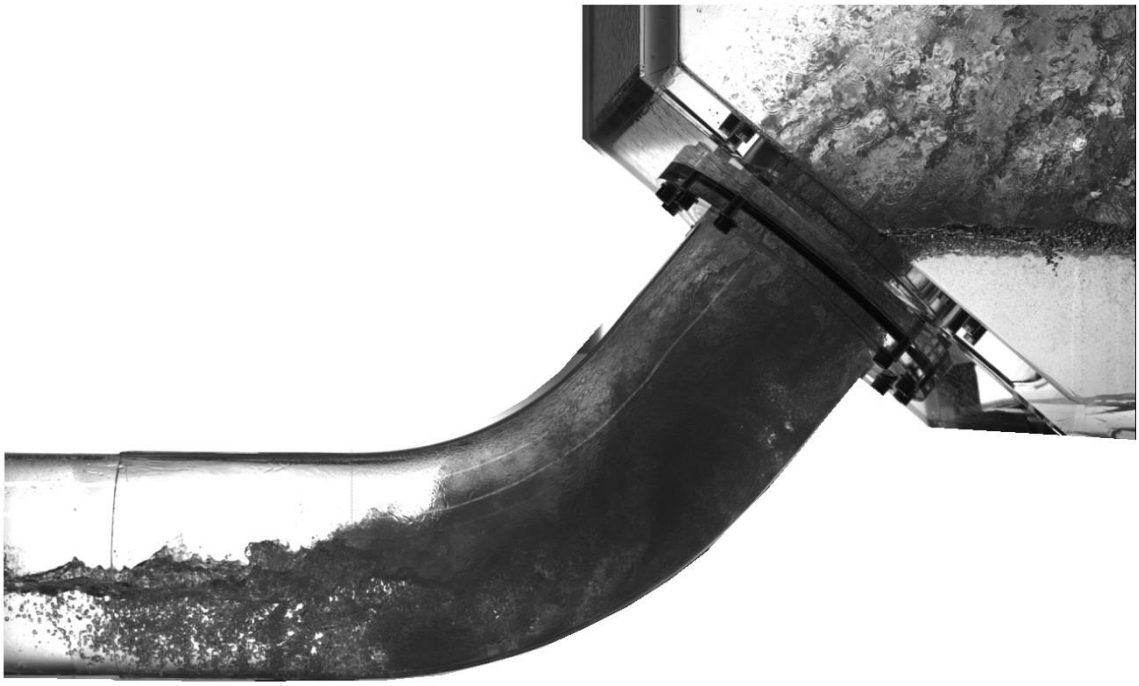

Figure 7.50 An intense, violent and turbulent annular churn flow during the Bend-CCFL. $J_w^{*0.5} = 0.305$.

- bend-CCFL: air/water interface at the exit;

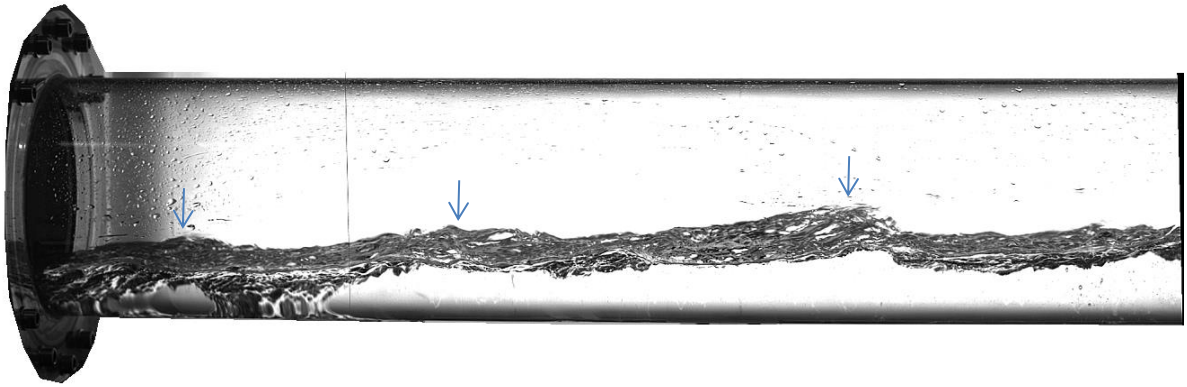

Figure 7.51 The air/water interface near the water exit during the bend-CCFL. $J_w^{*0.5} = 0.305$. The waves grow in amplitude as the water depth increases.

- Reduction of the blower's rotational speed (65%)

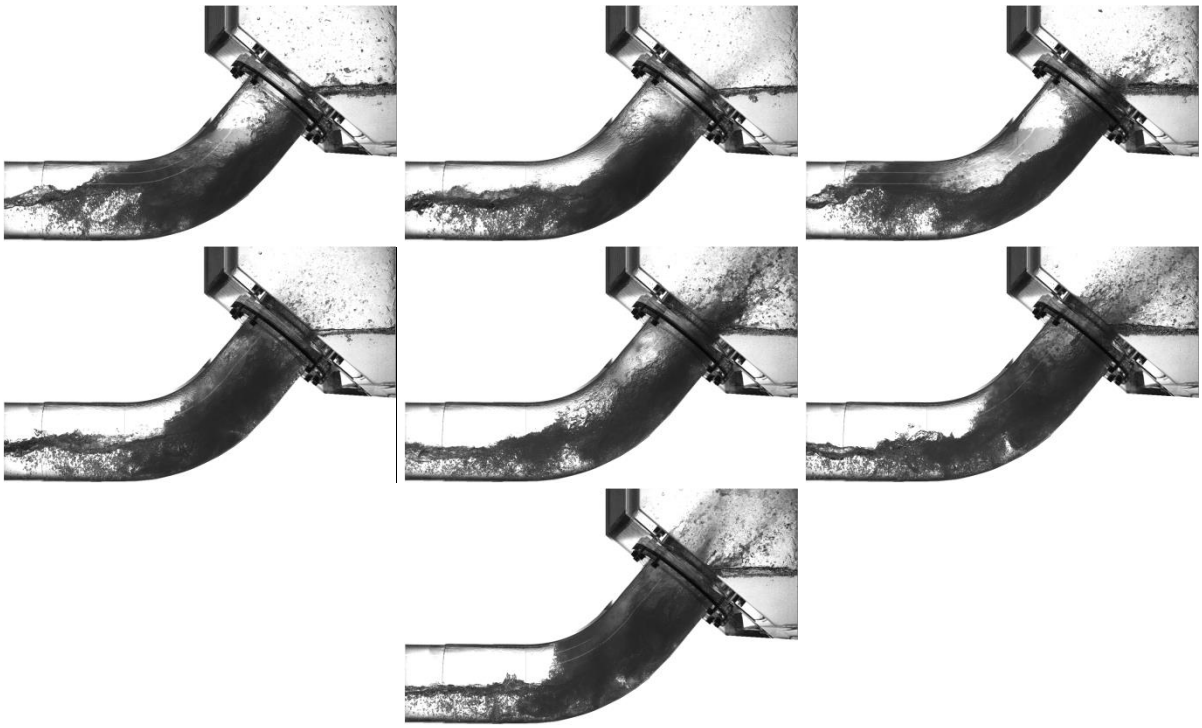

Figure 7.52 A set of successive images that illustrates the air/water interface during reduction of the. blower rotation speed (65%). The bend-CCFL becomes less intense but still occurring at the bend. $J_w^{*0.5} = 0.305$.

- Reduction of the blower's rotational speed (55%)

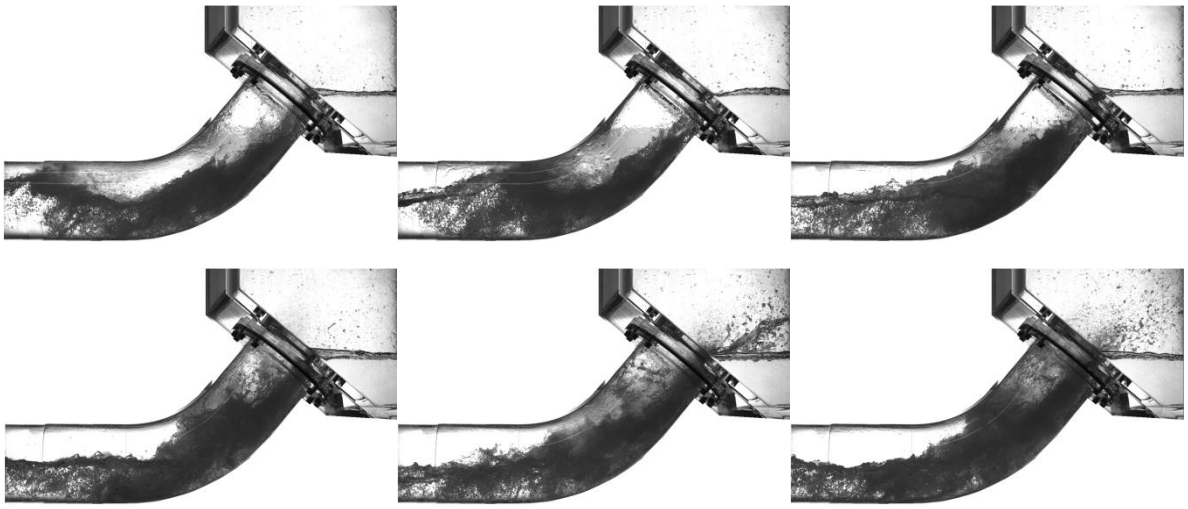

Figure 7.53 A set of successive images that illustrates the air/water interface during reduction of the. blower rotation speed (55%). The bend-CCFL intensity is remarkably reduced. Large roll-waves are still forming at the middle of the horizontal part, however no intense blockage is happening at the riser anymore (Plugging). $J_w^{*0.5} = 0.305$

- Reduction of the blower's rotational speed, start of the deflooding (50%)

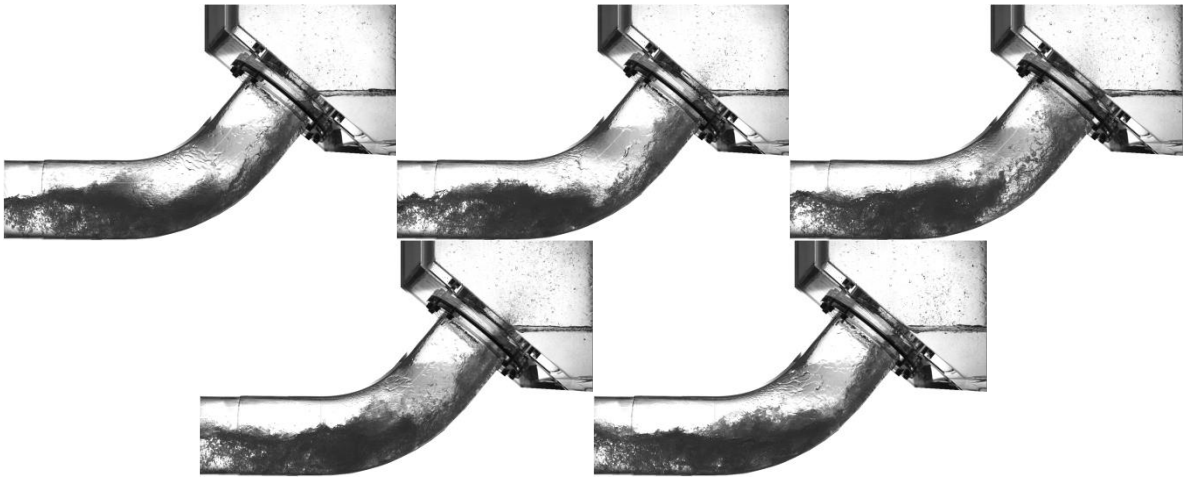

Figure 7.54 A set of successive images that illustrates the air/water interface during reduction of the blower rotation speed (50%). The annular churn flow disappears, only large roll-waves are breaking into the riser transporting small amounts of water as droplets into the SGs. This situations marks the beginning of deflooding. $J_w^{*0.5} = 0.305$.

- Reduction of the blower's rotational speed, deflooding (40%)

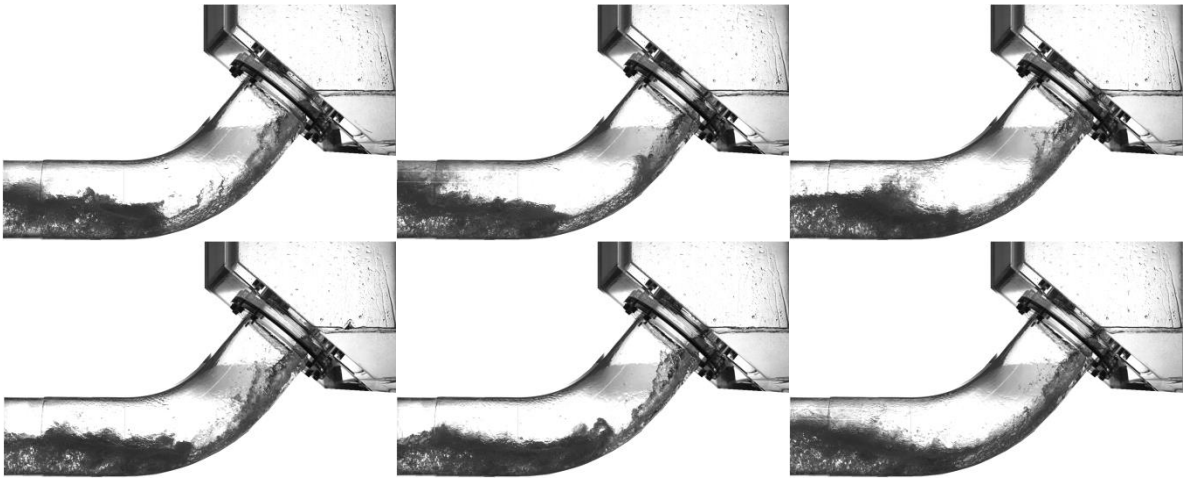

Figure 7.55 A set of successive images that illustrates the air/water interface during reduction of the. blower rotation speed (40%, deflooding). No large roll-waves are breaking into the SGs anymore. Only small waves are still forming on the surface of the remaining hydraulic jump at the bend. $J_w^{*0.5} = 0.305$.

7.4.2 A comparison of the flow patterns among the four CCFL regions

7.4.2.1 Supercritical flow

- Figure 7.56 shows that as $J_{w,in}^{*0.5}$ increases:
  - The water level increases.
  - The water stream starts to show a 3D pattern with a distinctive difference from experiments performed in narrow rectangle cross-section shape.
  - The water stream becomes turbulent with a rough surface at the inlet. Water droplets appears at the highest $J_{w,in}^{*0.5}$. even at low air velocities during which the flow is considered a "supercritical"

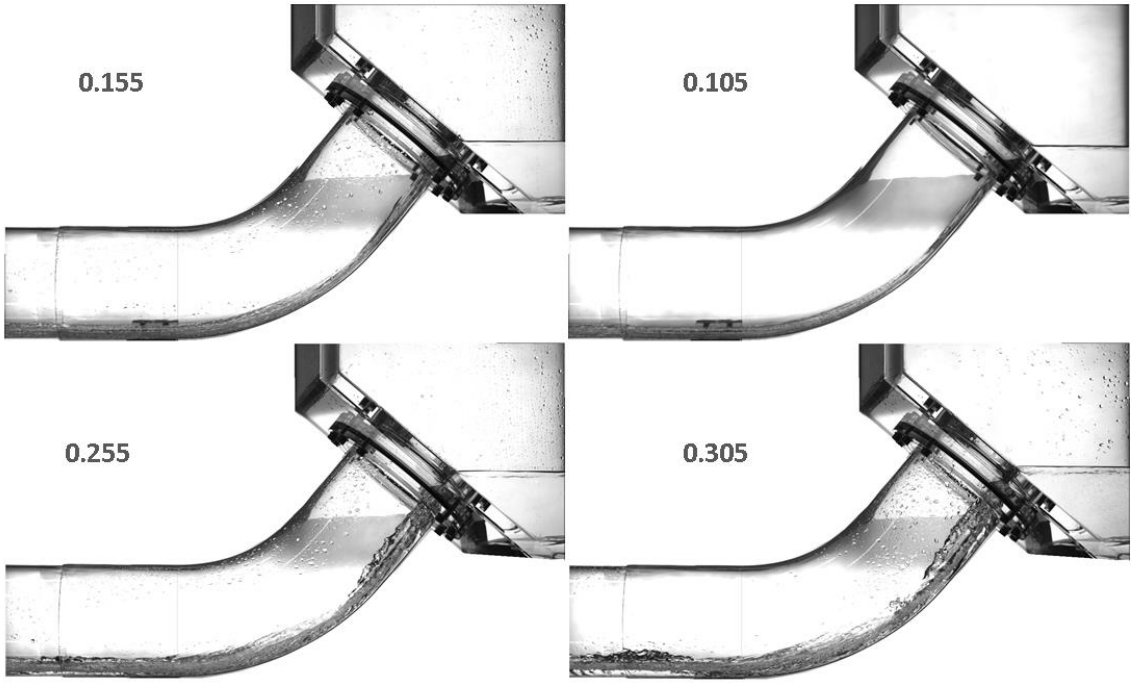

Figure 7.56 A comparison of the air/water interface during supercritical flow at the bend. $J_{w,in}^{*0.5}$ is used to indicate each image.

- Supercritical flow near the exit. Figure 7.57 shows that as $J_{w,in}^{*0.5}$ increases:
  - The water level increases.
  - Flow pattern appears: The water surface becomes rough and turbulent, shedding droplets.

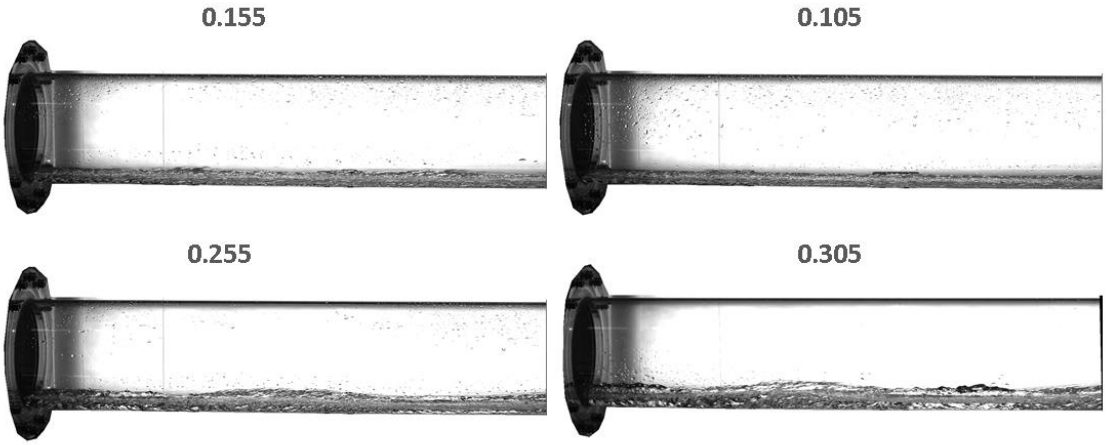

Figure 7.57 A comparison of the air/water interface during supercritical flow near the water exit. $J_{w,in}^{*0.5}$ is used to indicate each image.

7.4.2.2 The air water interface just prior to the onset of the B-CCFL.

Figure 7.58 shows that as $J_{w,in}^{*0.5}$ increases:

- The formation of hydraulic jump ($J_{w,in}^{*0.5} = 0.105$) is replaced by the formation of roll-waves with growing amplitude that transform the flow into the subcritical condition suddenly.
- The water surface becomes turbulent with an increased rate of droplets formation.

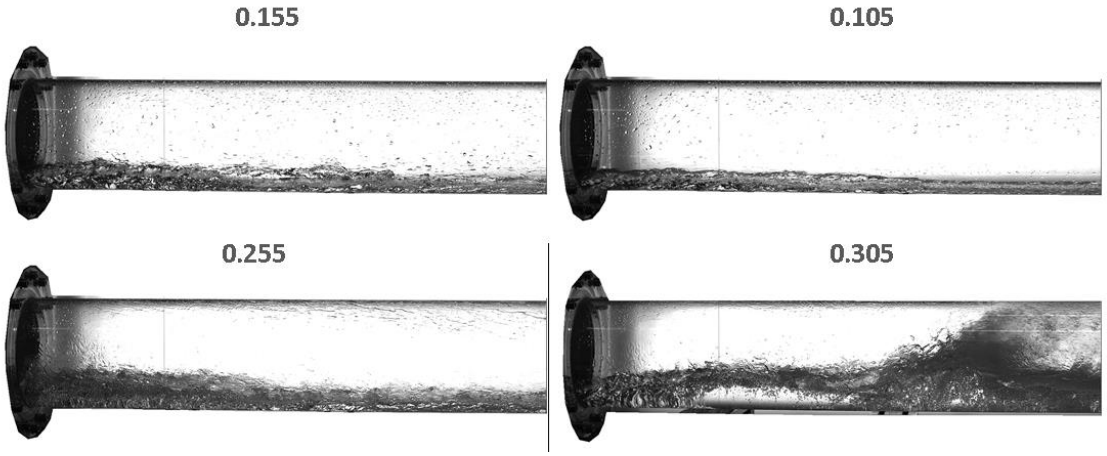

Figure 7.58 A comparison of the air/water interface near the exit just prior to the onset of the bend-CCFL . $J_{w,in}^{*0.5}$ is used to indicate each image.

7.4.2.3 Bend-CCFL

Figure 7.59 shows that as $J_{w,in}^{*0.5}$ increases:

- The intensity of the CCL increases.

- The large roll-waves amplitude grows and thus the blockage at the bend
- The annular-churn flow becomes more turbulent and thus the mixing of the two-phases and amount of "foam" becomes larger.
- A blockage of the entire cross section occurs at high values and plugging starts.

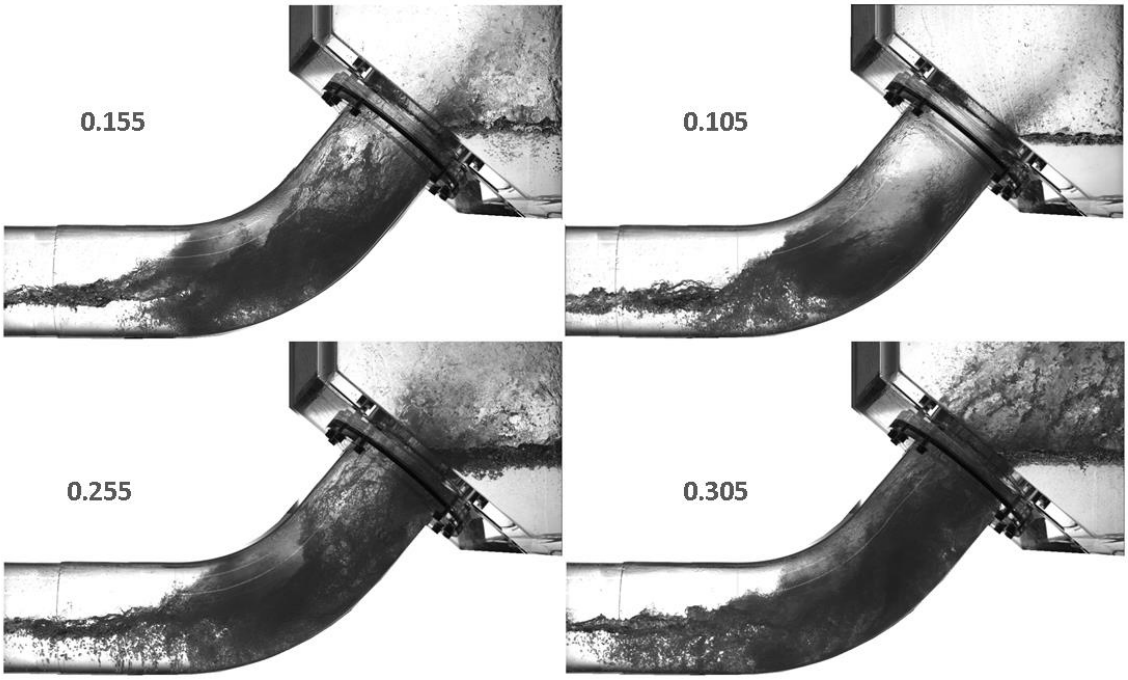

Figure 7.59 A comparison of the air/water interface at the bend just prior to the onset of the bend-CCFL. $J_{w,in}^{*0.5}$ was used to indicate each image.

- Bend CCFL near the exit. Figure 7.60 shows that as $J_{w,in}^{*0.5}$ increases:
  - The water depth increases and also the water depth gradient.
  - The amplitude and length of the waves increases.

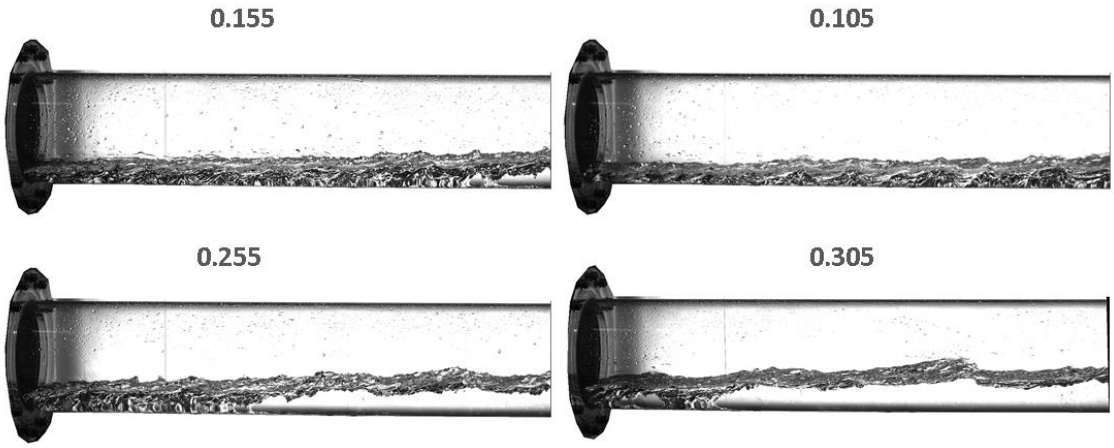

Figure 7.60 A comparison of the air/water interface near the exit during bend-CCFL. $J_{w,in}^{*0.5}$ is used to indicate each image.

7.4.2.4 ADE-CCFL at the bend and near the exit

Figure 7.61 shows that as $J_{w,in}^{*0.5}$ increases:

- The intensity of the droplets jet increases.
- A sporadic blockage of the entire cross section occurs, transforming the flow into annular/annular-churn periodically ($J_{w,in}^{*0.5} = 0.305$).
- At the water's exit: the interface becomes more rough and turbulent with an increased rate of droplets formation.

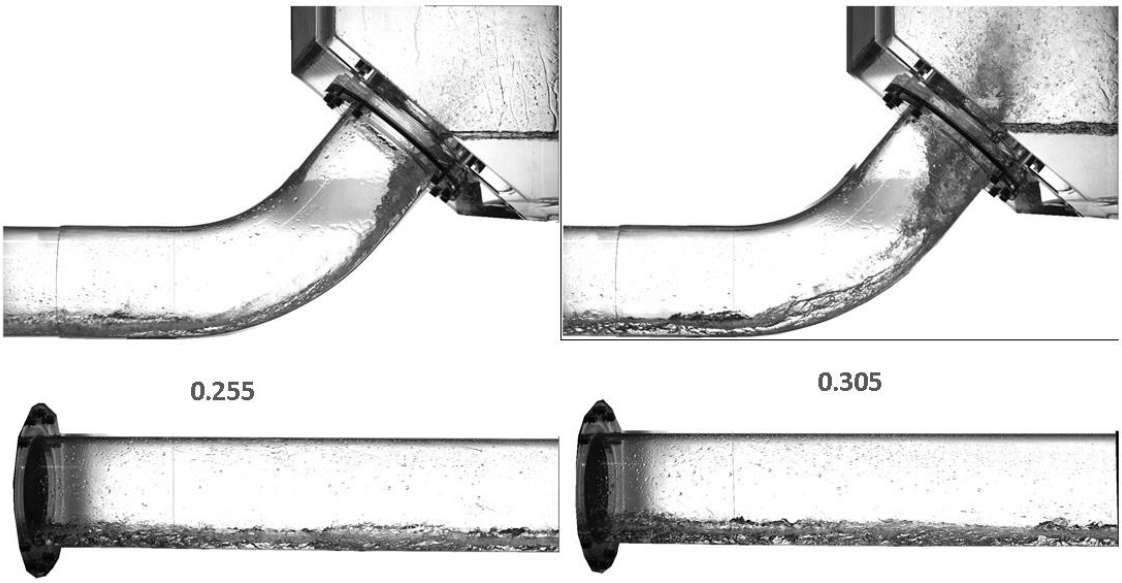

Figure 7.61 A comparison of the air/water interface at the bend/near the water exit during ADE-CCFL. $J_{w,in}^{*0.5}$ was used to indicate each image.

7.4.2.5 Hydraulic jump

- The hydraulic jump at the bend as observed during the deflooding: Figure 7.62 shows that as $J_{w,in}^{*0.5}$ increases:
  - The depth of the jump increases.
  - The surface becomes more turbulent and small roll-waves appears $J_{w,in0}^{*0.5} > 0.175$ increases.

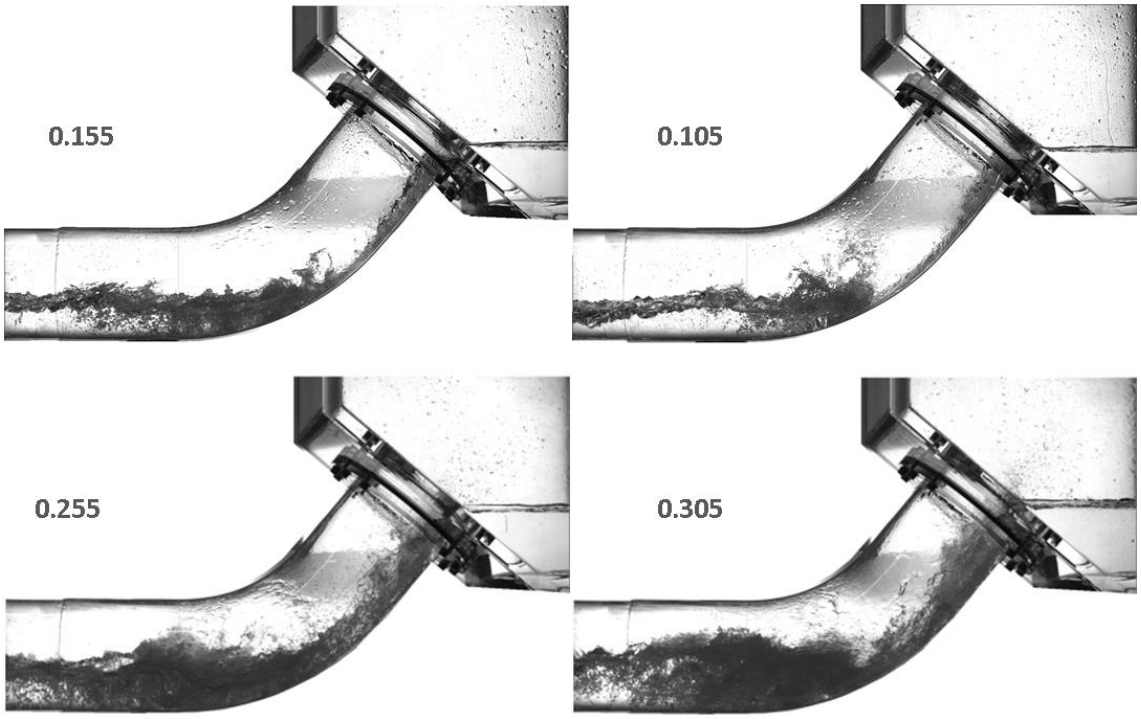

Figure 7.62 A comparison of the air/water interface at the bend during deflooding. $J_{w,in}^{*0.5}$ was used to indicate each image.

- The hydraulic jump at the bend in the first region. Figure 7.63 shows that the difference between the situation before the onset of the bend-CCFL (left image) and during the deflooding (right image). This illustrates the hysteresis and the dependency of the flow pattern upon the history of the flow.

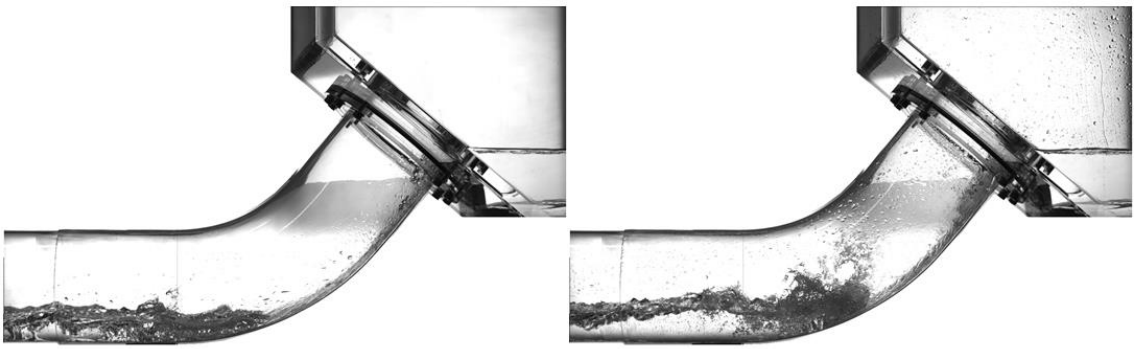

Figure 7.63 A comparison of the air/water interface at the bend before the onset of bend-CCFL(left) and during deflooding(right) $J_{w,in}^{*0.5} = 0.105$. The figure is a good example of the hysteresis characteristic of the CCFL. During bend-CCFL the blockage at the bend becomes larger and faster air happens locally at the bend holding the blockage larger than the one before the occurrence of the bend-CCFL.

7.5 The Onset of CCFL as a function of the water inlet velocity

7.5.1 Measurement method of the onset of CCFL and deflooding limits.

One important aspect of CCFL investigation is to determine the critical gas velocity at which the onset of CCFL is happening. The air flow rate, the water inlet flow rate, the water level within the reactor vessel simulator and the pressure difference between the RVs and SGs were logged during the entire experiment time. The experiments starts from supercritical flow at low air velocity until the onset of bend-CCFL and then back until returning into the initial condition of supercritical flow. Since the air velocity was increased stepwise using small steps:$\Delta J_G^{*0.5} = 0.01$, the onset of CCFL can be determined with more accuracy. The onset of CCFL can be determined either visually or using the water level within the RVs. As the water was pumped from the RVs into the hot-leg and then back into the RVs, the water level within the RVs will remain constant until the CCFL occurs. At the onset of CCFL, the water level begins to decrease continuously until deflooding happens, and then it start to increase again. The increase after deflooding is caused by the backflow of the trapped water within the hot-leg into the RVs. Following this description, the following limits were defined:

- The onset of ADE CCFL (when relevant): is the air velocity at which the water level within the RVs decreases below the average initial constant value by double the maximum perturbation of the level during the time in which it maintains a constant average value. Mathematically this can be interpreted as follows:

$$lw = \overline{lw} \pm \Delta lw \qquad t_0 < t < t_s$$

$$\overline{lw} = \frac{1}{t_s - t_0} \int_{t0}^{t_s} lw(t)dt \tag{7.1}$$

$$\delta lw = Max\left(\left|lw - \overline{lw}\right|\right)\Big|_{t=t_0 \to t_s} \tag{7.2}$$

Where t_s is the time during which the flow is supercritical.

$$J_{G,c}^{*0.5} = J_G^{*0.5}(lw < \overline{lw} - 2 \times \delta lw) \tag{7.3}$$

- The onset of Bend-CCFL: is the air velocity at which the bend-CCFL occurs (Visual identification). Practically, this coincides with the maximum air inlet velocity reached within the experiment. After the occurrence of bend-CCFL the actual air velocity provided by the Blower decreases due to the large blockage of air path and large increase of pressure difference.
- Deflooding: is the air velocity at which the water level reaches its minimum:

$$J_{G,deflooding}^{*0.5} = J_G^{*0.5}(lw = Min(lw)|_{t=t_0 \to t_{max}}) \tag{7.4}$$

Figure 7.64 illustrates the determination of ADE-CCFL and the deflooding for $J_{w,in}^{*0.5} = 0.255$

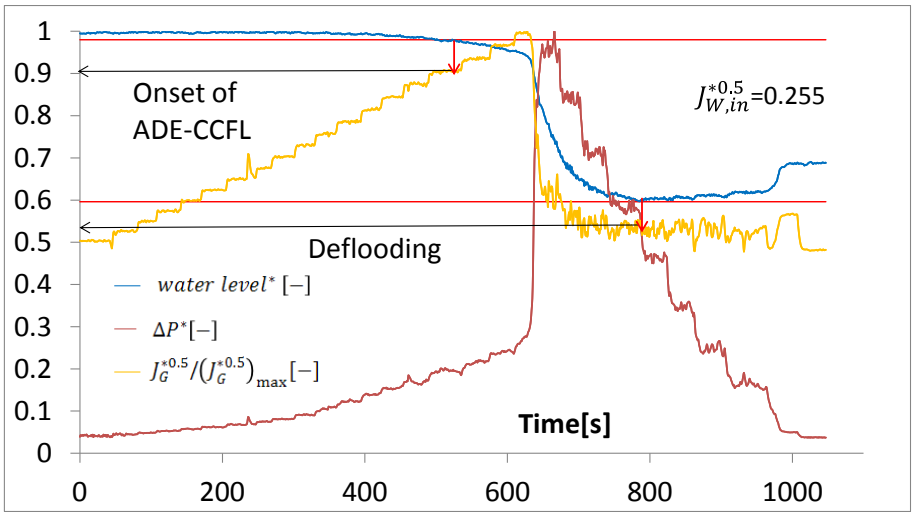

Figure 7.64 An example that shows the determination of the onset of ADE-CCFL limit and the deflooding limit out of the experimental data.

Adopting the over mentioned definitions, the onset of CCFL can be determined very precisely. In the case of an ADE-CCFL, the decrease of the water level is slight and cannot be determined visually. Active droplets entrainment can be identified ahead of ADE-CCFL, ,however, without being certain if the mechanism transports a sensible amount of water back into the SGs or not. On the other hand, the bend-CCFL is easy to determine visually. Bend-CCFL occurs after even one step $\Delta J_G^{*0.5} = 0.01$ increase and after that the air velocity will be decreased, thus no ambiguity can be inferred from the visual determination.

7.5.2 A statement about the measured values

Within the already reviewed literature there was a lot of ambiguity about “CCFL correlation” or “CCFL data”. The ambiguity comes mainly from the fact that some investigations were performed at low water inlet velocities region ($J^{*0.5}_{W,in} < 0.2$). Within this range the hysteresis effect is minimal and the value at which the onset of CCFL occurs coincides, or is very close to the value at which the deflooding occurs. Consequently, many studies developed “CCFL Correlations” relying on data obtained for “Onset of CCFL” and were used also for “deflooding’ and vice versa. Here, it should be once more emphasized that the onset of CCFL is different from the deflooding, and the air velocity value at which the onset of CCFL occurs differs from the value at which the deflooding does. Furthermore, the onset of CCFL should be tightly linked to the place of occurrence (bend, water entrance), and more importantly, to the corresponding mechanism: CCFL at the water inlet (ADE-CCFL) differs completely from the CCFL at the bend (bend-CCFL). Following points are to be considered within current work:

1. Within this study, the onset of ADE-CCFL at the water inlet, the onset of bend-CCFL at the bend, and the deflooding are three distinguished and different limits that should be never be mixed.
2. Any linear correlation that is provided is representing the limit at which the deflooding occurs.

3. For the onset of CCFL, the limit should be obtained only from the experimental plot provided.
4. At low water inlet velocities $J_{W,in}^{*0.5} < 0.185$, there is one limit for the onset of CCFL: the onset of bend-CCFL
5. At medium water inlet velocities$J_{W,in}^{*0.5} > 0.185$ there are two limits for the onset of CCFL: the onset of ADE-CCFL, and the onset of bend-CCFL
6. The intensity of ADE-CCFL increases with increasing the inlet water velocity and thus the significance of ADE-CCFL must not be neglected as $J_{W,in}^{*0.5} > 0.265$, as it starts to occurs much earlier as bend-CCFL.

7.5.3 Experimental values of the onset of CCFL, and deflooding limits.

The onset of CCFL and deflooding limits were determined according to methods described in 7.5.1. The Wallis parameters defined in equation (1.9) were used for air and water non-dimensional velocities. Figure 7.65 shows the critical air velocities at which the onset of the bend-CCFL (red marks), the onset of ADE-CCFL (green marks), and deflooding (blue marks) occur. Deflooding follows a clear linear trend, while the onset of CCFL trend is a function of the water inlet velocity. As it can be clearly seen, The onset of CCFL and deflooding limits are very close to each other –rather identical- at low inlet water velocities ($J_{w,in}^{*0.5} < 0.125$). When $J_{w,in}^{*0.5} \geq 0.135$, the deflooding occurs only when the air velocity is sufficiently lower that the value at which the onset of CCFL occurred (bend-CCFL or ADE-CCFL). ADE-CCFL appears at $J_{w,in}^{*0.5} > 0.185$. It does not play a significant role compared to bend-CCFL until $J_{w,in}^{*0.5} > 0.265$ (see discussion in section 7.3).

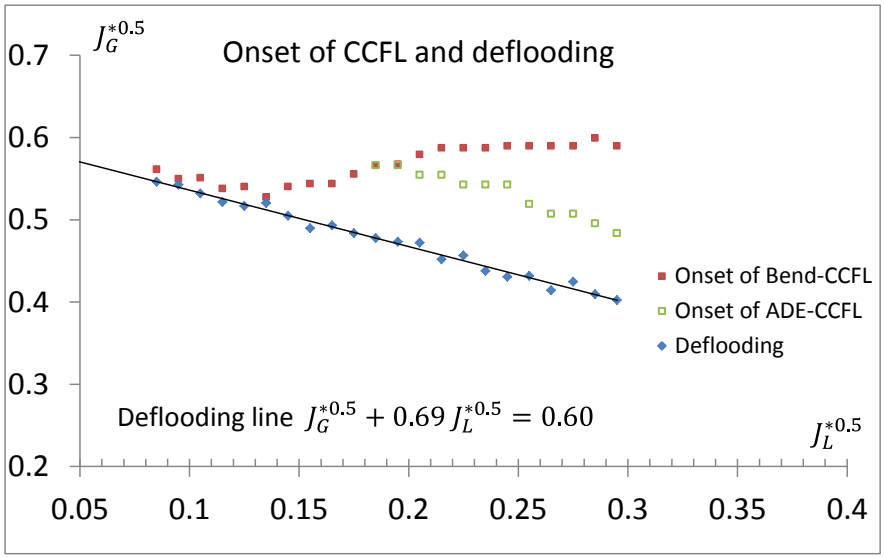

Figure 7.65 Experimental determination of: Onset of bend-CCFL (red dots), ADE-CCFL(green dots), and Deflooding (blue dots). Hysteresis effect is slight for $J_{w,in}^{*0.5} < 0.135$ and grows thereafter. The correlation shown within the graph corresponds to the deflooding line. The onset of bend-CCFL and ADE-CCFL coincides at $J_{w,in}^{*0.5} = 0.185$, and 0.195

The trend of the onset of bend-CCFL (Figure 7.65, red marks) is decreasing until $J_{w,in}^{*0.5} = 0.135$. In this region, the water thickening, the appearance of a recirculation area, and the hydraulic jump formation near the water exit become easier as the inlet water velocity increases. This is mainly due to the increased water depth near the water exit, and the increased local air velocity there. Meanwhile, the kinetic energy of water is still low and plays a minor effect. As a result, the critical air velocity needed to trigger the subcritical/supercritical transition, and the onset of CCFL will decrease with the increasing inlet water velocity. As $J_{w,in}^{*0.5} > 0.135$ The trend of the onset of bend-CCFL becomes an increasing one. The change of the trend follows the change of the mechanism by which the bend-CCFL occurs. The sudden bend-CCFL starts to take place. The higher inlet water velocities increase the water kinetic energy, and larger air velocities are needed to create roll-waves that can reach the bend and induce a bend-CCFL. Water droplets formation, and shear force start to play a larger role in the events that leads into the onset of bend-CCFL near the water exist. It is expected that at very high water inlet velocities ADE-CCFL will be the main mechanism for CCFL occurrence. Within current experiments, the deflooding line was found to follow following correlation:

$$J_{G,deflooding}^{*0.5} = -0.69\, J_{w,in}^{*0.5} + 0.60 \qquad (7.5)$$

Figure 7.66 compares the onset of CCFL from different experimental investigations. It shows the dependency of the onset of CCFL upon the inlet water velocity. The effect of different geometrical parameters upon the results is noticeable. The region where the trend of onset of CCFL against the inlet water velocity is a decreasing/increasing differs from one study to another. The onset of CCFL is very sensitive to scaling, and geometrical parameters. Even if some geometrical parameters were similar, (L/D ratio in particular), the results will differ if the diameters or the cross section geometry is different. Comparison between the current experimental data and data from UPTF (full-scale facility, no Hutze data) and MHERESA (with close geometrical parameters), shows close results especially at low inlet water velocities $J_{w,in}^{*0.5} < 0.135$.

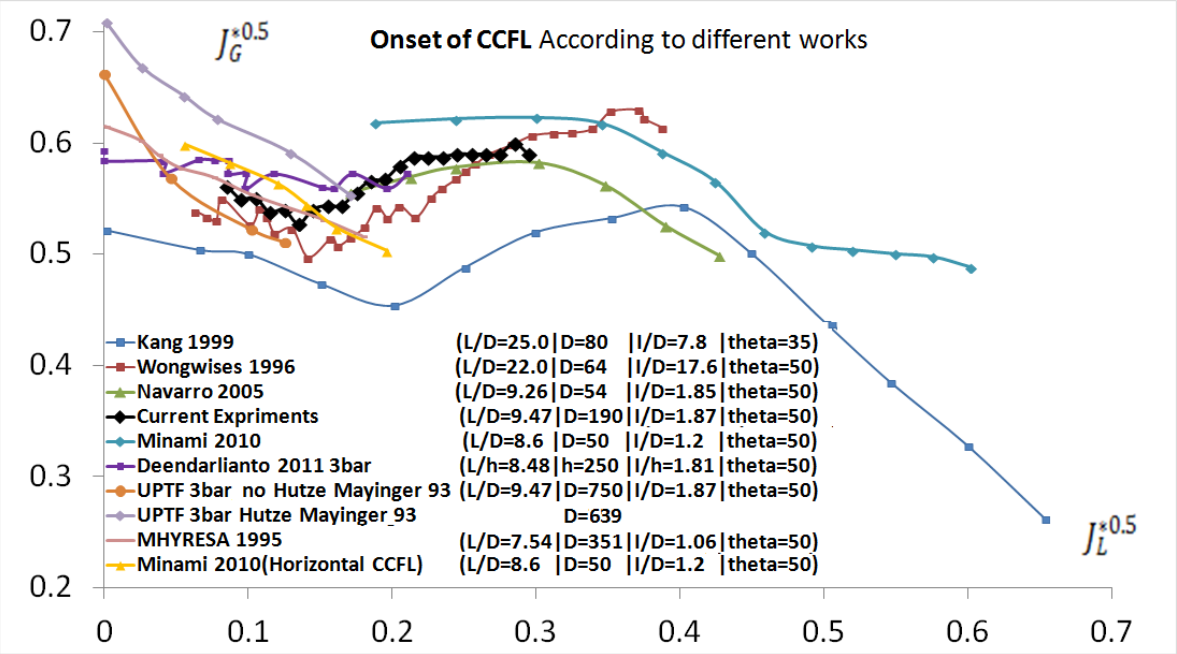

Figure 7.66 A comparison between current experiments and previous works on the onset of bend-CCFL (ADE-CCFL is not recognized in previous works).

Figure 7.67 compares deflooding from different experiments (Minami 2010a and Deendarlianto 2011 experiments were performed in rectangular cross sections). The difference that happens due to a different experimental set-up and geometrical parameters can be clearly seen. The data of Deendarlianto 2011 has close geometrical parameters and scale to the current experiments; however they used a rectangle cross section which resulted in a noticeable difference form current experiments.

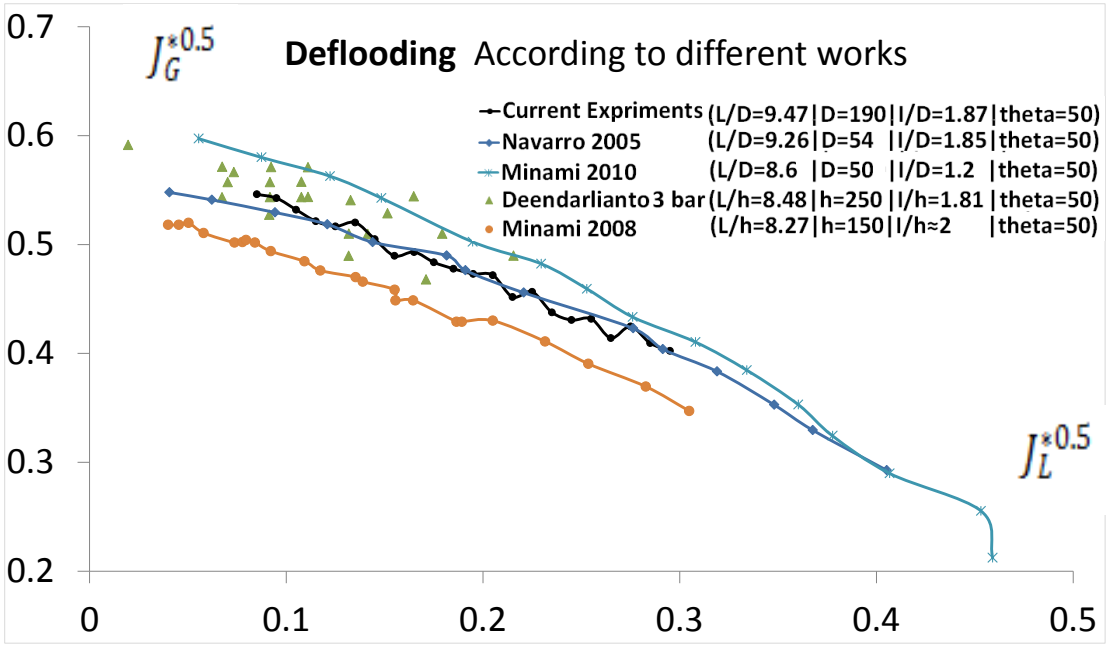

Figure 7.67 A comparison between current experiments and previous works on the deflooding line

7.6 Summary and discussion of COLLIDER experimental results

The test facility COOLIDER was built and experimental investigations were performed in order to investigate the CCFL in large diameter hot-leg geometry. The geometrical parameters of COLLIDER test facility were scaled to a real PWR hot-leg geometry in order to get as much as close flow similarity with a full-scale model as possible. Experimental investigations covered low and medium water inlet velocities, which are of most important for CCFL occurrence during a LOCA/SBLOCA accidents. Out of the experimental investigations, following conclusions can be stated:

- COLLIDER construction was proved to deliver reliable results over CCFL phenomenon. At low inlet water velocities the results were close to the 1:1 scale experiments.
- High-quality images that illustrate the observed flow patterns during CCFL/deflooding occurrence were provided for the first time in a full-length and a large-diameter hot-leg geometry. These images provide a valuable CFD validation data of the interfacial structure.
- Two main CCFL mechanisms were identified and described in detail: bend-CCFL, and ADE-CCFL. Four CCFL regions were recognized according to the sub-mechanisms involved and the contribution of each mechanism. The four regions are classified according to the inlet water velocity.
- The combination of the high-quality imaging and flow parameters logging allowed an enhanced and a more precise knowledge over this phenomenon.
- The results shows the importance of investigations in a real large-diameter pipe geometry and the flow characteristics that cannot be seen in experimental investigations in other small or rectangular geometries
- Form a safety point of view, the onset of ADE-CCFL precedes the occurrence of the bend-CCFL for $J_{w,in}^{*0.5} > 0.185$. It becomes of a significant importance as $J_{w,in}^{*0.5} > 0.265$ and its influence cannot be neglected.

Chapter 8 CFD validation using COLLIDER experimental results

One main objective of the experimental work carried out at COLLIDER test facility is to provide validation data for CFD codes. The use of the HSC along with well set-up experiments can deliver clear and high quality images of the air/water interface which is the main parameter to validate in CFD simulations of CCFL. As already presented within the previous chapter, experiments can also provide measurements of: the water level within the reactor tank simulator, the pressure difference between the reactor tank simulator and the steam generator simulator, the air flow rate, and the water inlet flow rate. These parameters can be validated within the calculations as well. Since the HSC camera is placed in front of the hot-leg which is illuminated from behind, the captured air/water interface corresponds to the projected interface into the camera's chip plane with all the distortions coming from the pipe geometry. However these projections are a good approximation of the the air/water distribution within the mid-plane of the hot-leg. The pressure difference is the result of the blockage/water level distribution within the entire hot-leg, and a well-predicted pressure difference indicates a better predicted air/water interface.

8.1 Validation of CFD using COLLIDER experimental results

One main objective of the experimental work carried out at COLLIDER test facility is to provide validation data for CFD codes. CFD simulations of CCFL are among the most challenging two-phase flow CFD simulations. The reason comes mainly from the complexity of the phenomenon itself. As already shown within the previous chapters, the air/water interface at the onset of CCFL is highly complex incorporating a vast variety of flow regimes and patterns:

- Turbulent churn-flow: Within the riser.
- Annular flow: In the bend region.
- Bubbly flow: In the recirculation area within the water at the bend.
- Droplets: within the air flow into the steam generator.
- Waves: within the horizontal part until they break into the riser.

This variety of flow patterns and regimes make it nearly impossible to simulate each single pattern, since they occur at the same place. Additionally all these phenomena occur at relatively high flow velocities accompanied with large amount of turbulence production and high change rate of the air/water interface. If the case will contains heat and mass transfer (steam/water flows), the complexity will be just elevated into another level. Another difficulty comes from the fact that each flow pattern requires different correlations for interfacial transfer terms. 1D safety codes usually use the experimentally developed correlations to determine the occurrence of CCFL within the hot-leg during LOCA accidents. However, due to the dependency of the phenomenon on many factors and its sensitivity to the geometry and instantaneous flow conditions, it is not unsuitable to use this simple approach. The results can be either too conservative limiting an efficient operation of the power plant or risking the occurrence of a CCFL during one of most important safety-related accidents in a PWR.

Consequently a more elaborated CFD simulations are required. In recent years many authors started to set up 3D CFD models for this phenomenon, with a various amount of success. A review of some of these works show that the modeling approach (Euler-Euler, VOF, etc), the development of suitable momentum-transfer models, and turbulence modeling are among the most important issues to be worked upon. However, an important part of all these modeling attempts is to rely on high quality experimental data for validation and development of the adopted models. The increased work on the coupling of 1D safety system codes and 3D codes opens the door for more applications of CCFL CFD simulations. In this case a 1D modeling is done for the entire system, while a 3D model for the hot-leg. This arrangement delivers a more accurate prediction of the CCFL during accidental conditions since the system 1D model receives results for the complex component (the hot-leg) from a 3D two-phase simulation while the 3D model updates the boundary conditions constantly from the 1D model.

8.1.1 Validation Data from COLLIDER

The use of the HSC along with well set-up experiments can deliver clear and high quality images of the air/water interface which is the main parameter to validate in CFD simulations of CCFL. As already presented within the previous chapters, experiments can also provide measurements of: the water level within the reactor tank simulator, the pressure difference between the reactor tank simulator and the steam generator simulator, the air flow rate, and the water inlet flow rate. These parameters can be validated within the calculations as well. Since the HSC camera is placed in front of the hot-leg which is illuminated from behind, the captured air/water interface corresponds to the projected interface into the camera's chip plane with all the distortions coming from the pipe geometry. The captured interface in this case will be however close to the air/water distribution within the mid-plane of the hot-leg (with the norm perpendicular to the camera's chip plane). Consequently, all comparisons of the air/water interface shall be considered as a "good approximate". The pressure difference is the result of the blockage/water level distribution within the entire hot-leg, and a well-predicted pressure difference indicates a better predicted air/water interface. The measured water level in the reactor vessel simulator along with the inlet water flow allows calculating the backflow water flow rate and comparing it with the simulations. A good prediction of the backflow water also gives a good indication about the calculated air/water interface and the momentum-transfer. A better experimental approach would be to use a planar laser and to capture images exactly from the experimental mid-plane. Within the current experiments no planar laser could have been used and thus only the projected images were used for the validation. However, some authors [Utanohara et al. 2011] used similar data to compare with CFD calculation since it will be very close to the more accurate data from the hot-leg mid-plane. Additionally, the exact air/water interface cannot be exactly reproduced by the simulations due to the complexity of the case, the ever-changing and highly-turbulent interface, and the numerous factors that affect the final results.

8.2 An overview of CFD Modeling approaches of the CCFL phenomenon

8.2.1 Volume of fluid approach (VOF)

Here, one mixture conservation equation is used for all phases. All variables and properties are calculated as volume-averaged values. The volume fractions are determined by the continuity equations. The interfacial forces are replaced by smoothly varied volumetric forces The motion of the interfaces can be tracked indirectly after resolving the motion of all phases. This makes the VOF approach suitable when the interface and the flow patterns near the interface are most important. This approach was adopted in many investigations [Minami et al 2008b, and 2010b, Utanohara et al 2011, Murase et al. 2010, Kinoshita et al. 2010, Bartosiewicz et al. 2008, Gorai et al. 2005].

8.2.2 Large interface model (LIM)

The large interface model takes into account large interfaces which can be smooth, wavy or rough. The models are written within a three-cell stencil around the large interface position. This stencil is used to calculate, on both the liquid and gas sides, the distance from the first computational cell to the large interface. Both distances are used in the models written in a wall law-like format. Some assumptions are deduced from experimental data used for the CFD validation [Coste 2013].

8.2.3 The two-fluid approach

The two-fluid approach was considered for this study. The choice was made due to the fact that this model allows to link experiments with CFD calculation via modeling of the momentum transfer (a future goal of this project). Within this approach, separate equations for mass, momentum and energy are used for each phase. Predefined models and user expressions are required in order to model the interfacial interactions between the two phases [ANSYS CFX-Pre User's Guide]. Free surface model is widely applied within this approach. Different phases are separated by density differences using the buoyancy force. The interfacial momentum transfer is defined by the friction force F_i :

$$F_i = \tau_i a_i = -0.5 C_D \rho_l |v_r| v_r a_i \grave{} \quad (8.1)$$

ρ_l is the density of the continuous phase (ρ_G is to be used for an annular flow), v_r is the relative velocity between the gas and liquid phases, and a_i is the interfacial area concentration per unit volume. The modelling of the drag coefficient is the central point of this approach and many models exist in literature. Among these models are:

- The algebraic interfacial area density (AIAD) applied by [Höhne et al 2011]: this model accounts for the bubbles and droplets besides free surface region and this it incorporates four phases: the liquid phase, the gas phase, droplets, and bubbles. It provides different correlations for the interfacial area concentration and the drag coefficient according to the existent phase. The different phases are recognized by the

value of the interfacial area concentration. A special treatment was applied at the free surface.

- Modeling the momentum exchange via a phase exchange model and the two-fluid Reynolds stresses [Wintterle et al 2008]. A statistical time averaging of the surface was applied to smear the wavy free surface by the application of a dispersion force F_S proportional to the gradient of the void fraction. The dispersion force is balanced by the buoyancy force to resolve the void fractions. The drag coefficient is calculated depending on a length scale. A special treatment was considered near the interface for the length scale and the turbulence.

- Utanohara11 et al. used a combination of different drag coefficients in different flow patterns (bubbly, slug, annular).

Within this work only the applied drag model of Utanohara et al. (2011) will be explained. The adoption of this model was due to its good results and simplicity. The use of the more elaborated AIAD will require more time and less experimental cases can be validated.

8.3 CFD modeling of COLLIDER

8.3.1 Geometry

Most of the 3D models of the hot-leg simulate the entire facility. This means that no symmetry conditions were used to simplify the geometry and reduce the total number of volume elements/nodes. The reason is the complexity of the phenomenon and the numerous 3D effects that can be eliminated once a symmetry condition is applied. Another reason is the building of the mesh. High quality meshes are required for this kind of simulations which can be only built by using advanced meshing tools such as ICEM. The meshing of the entire geometry (i.e. the hot-leg with the full circle cross section) is technically much less complicated than meshing half of the geometry. 3D COLLIDER geometry was already shown in Figure 3.10; however some simplifications were made in order to make the meshing process of the facility easier. These simplifications do not affect the accuracy final results since they are mostly away from the hot-leg boundaries.

- The air inlet into the reactor vessel simulator was simplified. The divergent entrance was omitted and replaced by a simple pipe which is similar to the size of the hot-leg pipe. This makes the blocking process much easier. Additionally the level of the air inlet was adjusted to the level of the hot-leg pipe for the same reason. The fact that the air entrance is a bit higher than the hot-leg pipe is due to some preliminary design ideas that applied an inclined plate to direct the air flow smoothly into the hot-leg pipe (avoiding a direct blow into the water surface inside the hot-leg.
- The length of the steam generator where the water rise within into the hot-leg entrance was shortened in order to minimize the number of calculation elements (this part was cut horizontally below the level of the hot-leg entrance). Furthermore, the water

inflow into the steam generator will not be via the two DN50 pipes at the bottom as in the experiments but through the entire square bottom of the trimmed water entrance.

- The air outlet was changed from a circle into a rectangle preserving the area of the experimental outlet.
- The inclined plate was not considered since its effect was found to be neglected even upon the experimental results.

Figure 8.1 shows the final geometry adopted within the current simulations.

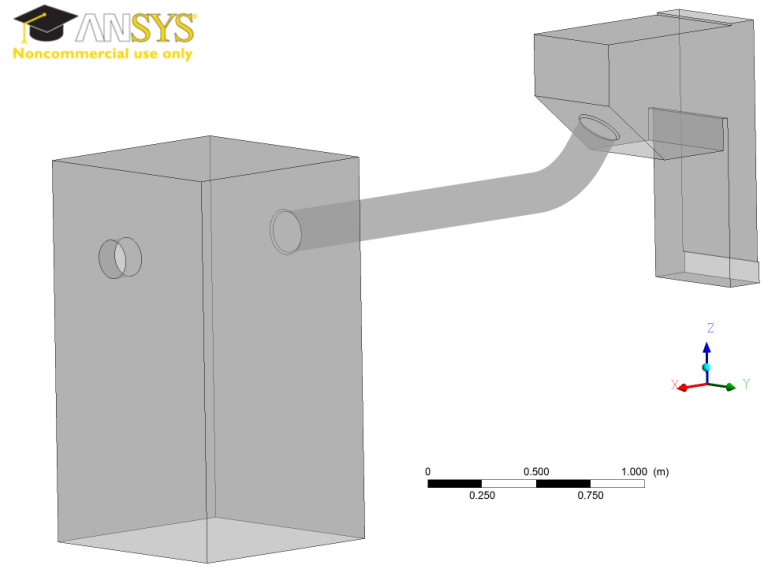

Figure 8.1 Geometry of COLLIDER in CFX simulations.

8.3.2 Meshing

The meshing was accomplished using the advanced meshing tool ANSYS ICEM CFD 12.1. It provides advanced geometry acquisition, mesh generation, mesh optimization, and post-processing tools to meet the requirement for integrated mesh generation and post processing tools for today's sophisticated analyses. Maintaining a close relationship with the geometry during mesh generation and post-processing, it is used especially in computational fluid dynamics and structural analysis and offers the capability to parametrically create meshes from geometry in numerous formats [ANSYS ICEM CFD, Tutorial Manual, Release 11.0]. The most important aspect of using this tool is that it provides a direct link between geometry and analysis through blocking, nodalization and mesh generation. The tool allows checking the quality of the generated mesh, and controlling numerous numbers of its characteristics (refinement, inflation near edges, edges angle etc.). For Two-phase flows accompanied with a high turbulence and mixing, hexahedral mesh elements are preferred by most studies. Hexahedral elements have more nodes per element as tetrahedral ones (5 to 1) resulting in more accurate calculation of the flow parameters. The memory increase for the same number of elements is higher for tetrahedral elements when more than one phase is considered. A correct discretization refines the mesh where the interface is complicated and accompanied

with large or fast changes of flow parameters. However, this should be done without an unnecessary increase of the total number of the calculation elements (calculation time). The quality of the final mesh affects the numerical solution regarding its accuracy and convergence. Poorly-built meshes can lead into unphysical results or creates problems with convergences (no convergence or increased time until convergence). The meshing process for such a large geometry is a time-consuming technical process, and should be done carefully to provide the correct discretization for solving the flow equations; consequently this task was accomplished in the frame of a Master work that was supervised extensively under the current project. The meshing process includes the following steps [Zamorano 2013]:

- Creating parts out of the COLLIDER geometry by dividing the geometry volume into several parts to facilitate the meshing procedure. Additionally the calculation 3D domain and the 2D parts for setting boundary conditions are specified.
- Blocking: defining the faces, edges, and vertices where the meshing parameters such as number of nodes and inflation are specified. A careful blocking makes the final mesh conforms closely to the original geometry.
- Pre-mesh parameters: Number of nodes for each part, for each edge and the separation between nodes are specified. Refinement of some regions of interest can be specified here as well.
- Pre-mesh quality and smoothing: A final overall quality over 0.3 was achieved (98 % of the nodes are over 0.7, A minimum of 0.2 should be achieved). The minimum angle criteria were over 18 ° was achieved (more than 97 % of the nodes are over 36 °).
- Building an unstructured mesh: a structured mesh generate a mesh for each block which can results in some difficulties (Conforming a single block to a complicated shape). Unstructured mesh produce one mesh for the entire calculation domain and merge common nodes on blocks interfaces. Most investigations used unstructured meshes for CCFL studies.

Finally an unstructured hexahedral mesh consisting of 203503 elements and 192823 nodes was generated for CFD calculation. Figures 8.2-8.6 shows the final mesh and its details. Within the final mesh, a special care was paid to the discretization of the following parts:

- The air entrance into the hot-leg: here the air velocity suffers large changes of both direction and amplitude. This area was refined to yield an accurate calculation.
- The near wall region within the hot-leg was refined as much as possible (keeping the total number of elements small enough for a reasonable calculation time).
- The junction between the bend and the steam generator was discretized in order to achieve a smooth transition between the mesh within the hot-leg bend region and the steam generator where the most complicated phenomena occurs at the onset of CCFL.

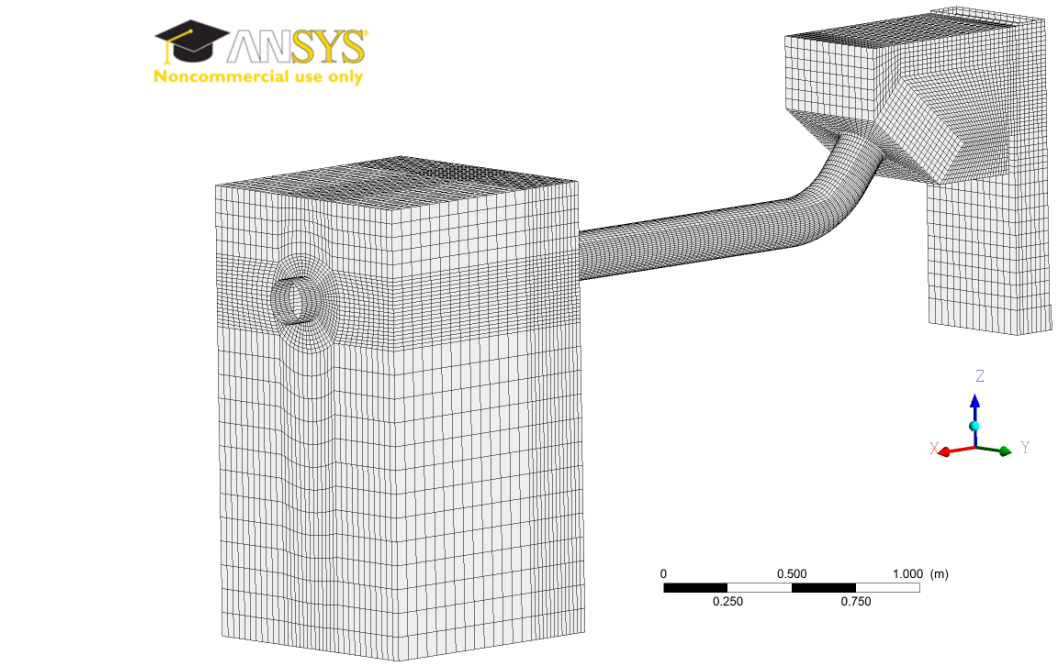

Figure 8.2 Top: a general view of the final accomplished mesh of COLLIDER test facility..

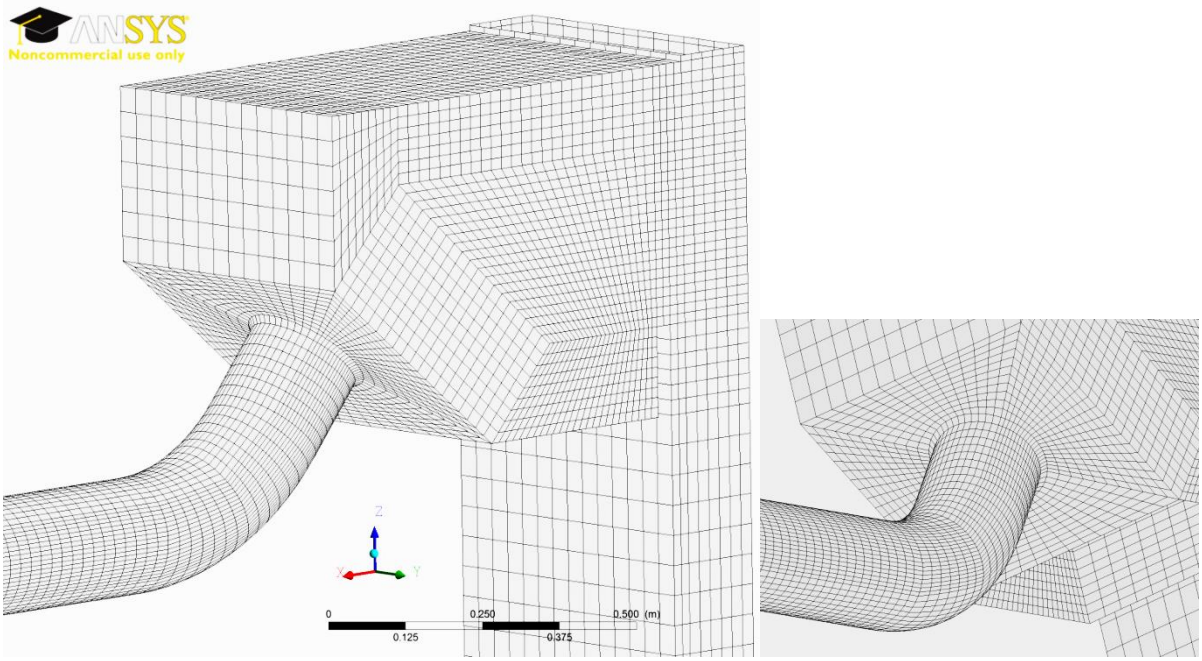

Figure 8.3 Mesh details of the junction between the hot-leg and the steam generator simulator. A detailed view of the hot-leg/SGs junction is shown on the right.

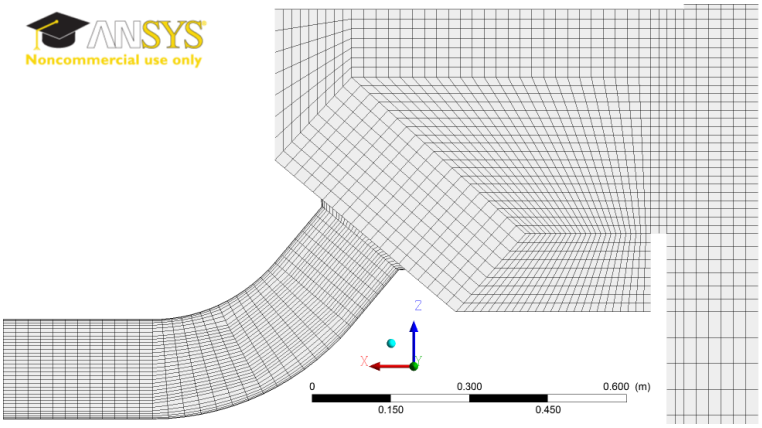

Figure 8.4 Mesh details of the junction between the hot-leg and the steam generator simulator (side view).

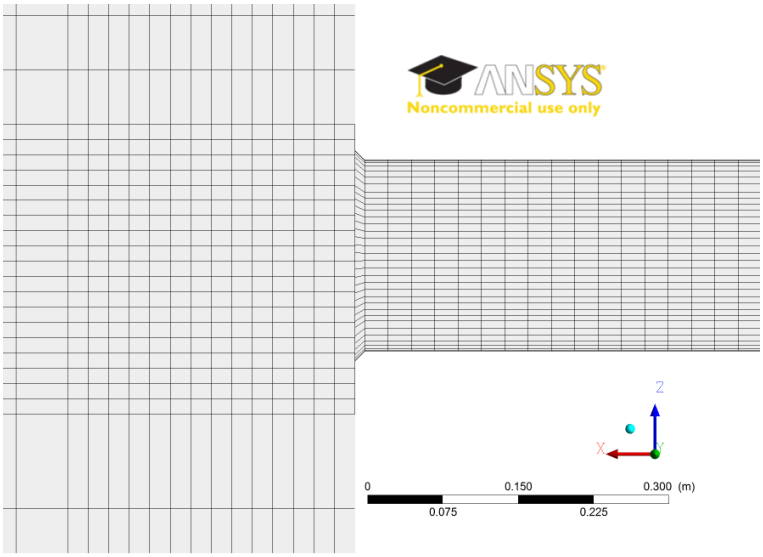

Figure 8.5 Mesh details of the junction between the hot-leg and the reactor vessel simulator.

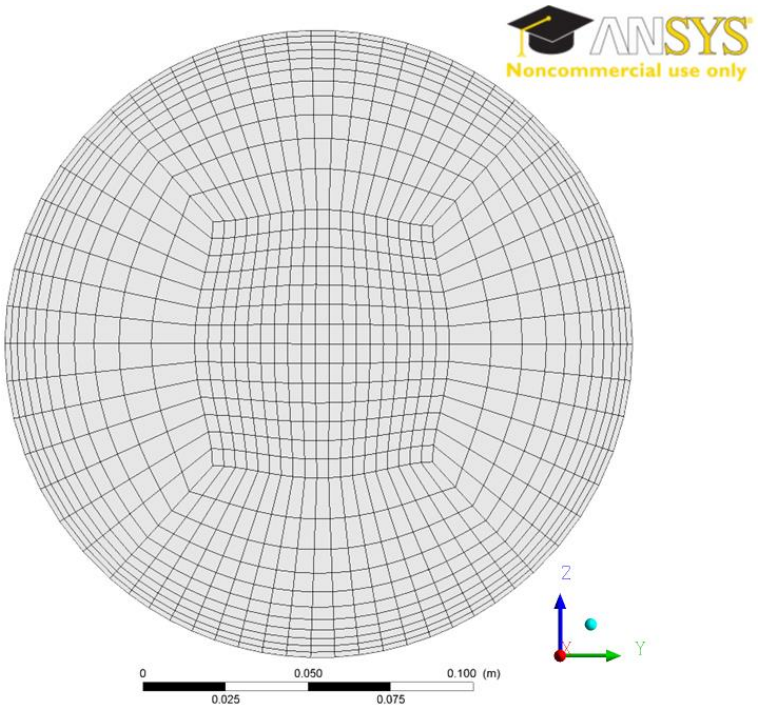

Figure 8.6 Mesh details of the cross section of the hot-leg.

8.3.3 Boundary conditions

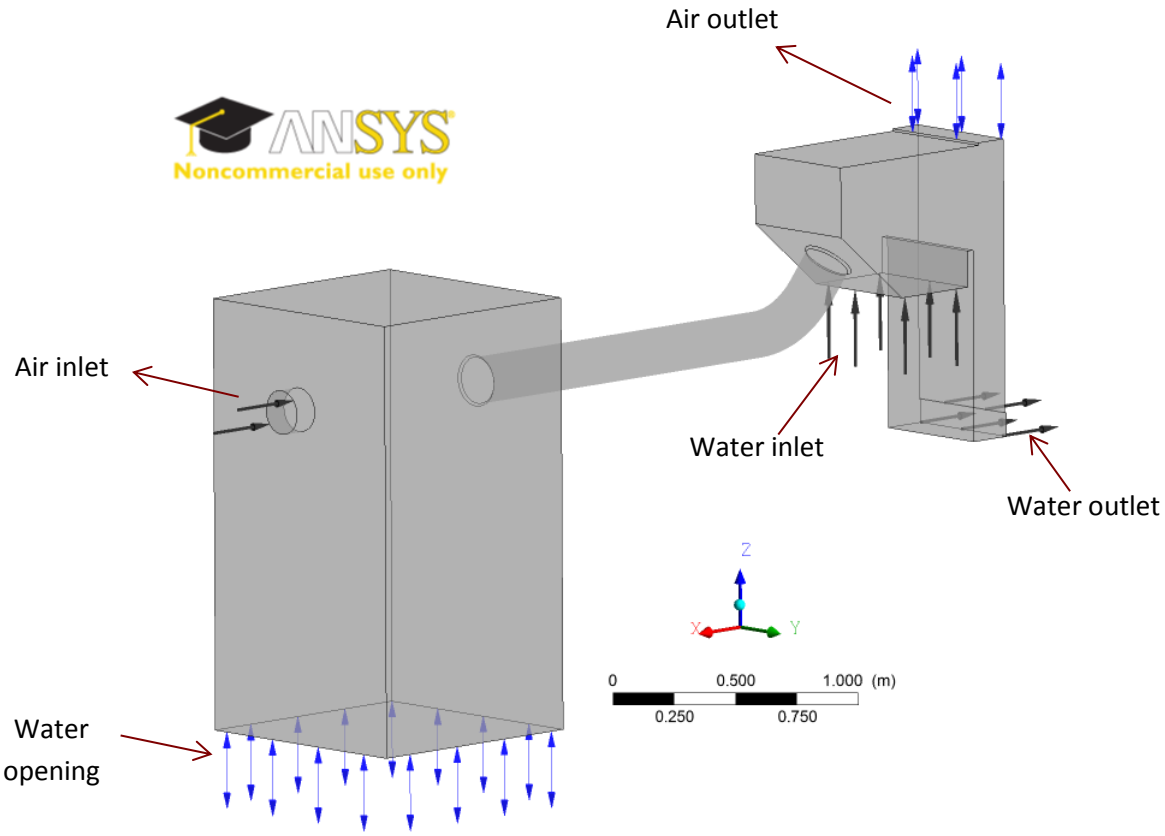

Figure 8.7 Boundary conditions adopted in COLLIDER CFX simulations.

Figure 8.7 illustrates the set of boundary conditions for current simulations:

- An air inlet with a constant flow rate for the steady state simulations and a time function for transient simulations.
- A water inlet with a constant flow rate for all simulation cases.
- An opening at the air outlet: using the opening allows to specify the escaping phase (only air).
- An opening at the bottom of the reactor vessel simulator: this is to help maintain a constant water level within the reactor tank and thus minimizing convergence issues within this volume regarding its coarse mesh (see Figure 8.2).
- An outlet for the water at the bottom of the steam generator. A reference pressure of 0 Pa was applied.
- A non-slip wall condition was applied to the entire domain walls.

The over-mentioned set of boundary conditions was found to be the most convenient to achieve convergence through judging the results of many trials through the modeling process. Also these conditions were the best to maintain a low percent of mass balance at the end of the simulations. Considering the complexity of this case, convergence was a major issue upon which boundary conditions have also its influence.

8.3.4 Physical models

An Euler-Euler two-fluid approach within the CFD code CFX12.1was adopted. The free surface model was chosen. According to CFX manuals [ANSYS CFX-Solver Modeling Guide], the density of the lighter phase (air) was made as a reference density for buoyancy force. A single domain consisting of one hexahedral unstructured mesh was considered. Air at 25° C and water were adopted as working phases. No heat transfer is present and thus an adiabatic model was considered for both phases. Since the case has geometry of large dimensions along with flows of high velocities, it becomes important to consider turbulence generation near the walls and inside the flow. The best choice will be using the shear stress transport which gives good results in all flow regions. The momentum transfer was considered through definition of a drag coefficient. The applied drag coefficient within current simulations was developed by [Minami et al. 2008b, Minami et al 2010b] and it was validated for 1/15 and 1/5 downscaled tests at Kobe university. The current study will validates it at 1/3.9 scaled COLLIDER. The coefficient is defined implicitly as a product between the drag coefficient and the interfacial area concentration $C_D a_i$. In order to adapt into different flow regimes, a combination of different drag coefficients was considered as follows:

$$C_D a_i = \min\left(C_D a_i|_{Bubbly}, \max(C_D a_i|_{Slug}, C_D a_i|_{Annular})\right) \quad (8.2)$$

$$C_D a_i|_{Bubbly} = \frac{2\alpha(1-\alpha)g}{v_d^2} \quad (8.3)$$

$$C_D a_i|_{Slug} = 9.8(1-\alpha)^3 \left(\frac{4.5\alpha}{D_H}\right) \quad (8.4)$$

$$C_D a_i|_{Annular} = \frac{0.02\left(1+75(1-\alpha)\right)\alpha^{0.5}}{D_H} \quad (8.5)$$

The correlation for the bubbly flow (or low void fractions) was proposed by Andersen (1982). The correlation for slug flow was proposed by Ishii and Mishima (1984) and the Annular flow correlation by Wallis (1969). The correlation for the slug flow was simplified by setting the void fraction of small bubbles (α_s) into zero within the original correlation 8.6 (D_{sm} is the Sauter mean diameter).

$$C_D a_i|_{Slug} = 9.8(1-\alpha)^3\left(\frac{4.5(\alpha-\alpha_s)}{D_H(1-\alpha_s)} + \frac{6\alpha_s(1-\alpha)}{D_{sm}(1-\alpha_s)}\right) \quad (8.6)$$

The drift velocity was calculated by a correlation given by Kataoka et al (1987)

$$v_d = 1.4(D_H^*)^{0.125}\left(\frac{g\sigma(\rho_L-\rho_G)}{\rho_L^2}\right)^{0.25} \quad (8.7)$$

Where $D_H^* = D_H\left(\frac{g(\rho_L-\rho_G)}{\sigma}\right)^{0.5}$

Figure 8.8 shows the resulting drag coefficient at two pipe diameters: 0.05 m and 0.75 m. A comparison between the resulting drag in the two cases reflects the fact that drag has lower values at high channel diameters which is in accordance with the theoretical review (see section 1.2).

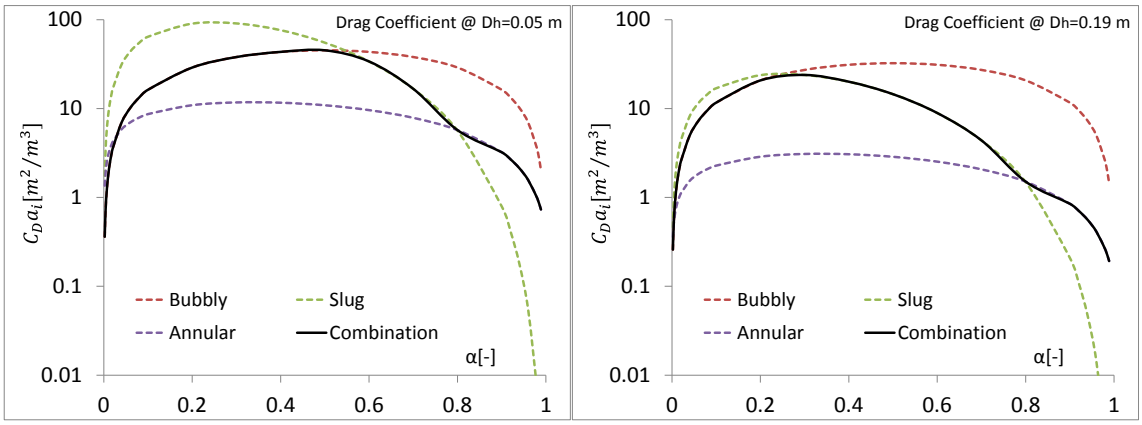

Figure 8.8 Drag coefficient as modeled by Minami et al. 2008b, 2010b at two different pipe diameters. $D_H = 0.05\,m$ (left); $D_H = 0.19\,m$ (COLLIDER diameter). The drag is remarkably lower at higher diameters.

8.4 Simulations results

Following the experimental procedure, a supercritical flow is established at low air velocity as a starting point. This provides an excellent starting point for transient conditions since it has low turbulent values and almost a stationary flow conditions (some turbulences and disturbances occurs at high water velocities). The air/water interface is well stratified and this suite the free surface model adopted within the current investigations. Consequently it was decided to conduct a steady state simulation at low air velocities to get an initial air/water

distribution for the transient cases. As for the simulated cases, four representative cases of the four recognized regions in section 7.3 were chosen as investigation cases. Initial conditions were taken out of experiments.

8.4.1 Initial conditions

Two cases were chosen for CFD simulations the case with $J_{w,in}^{*0.5} = 0.105$ as a representative of the low water inlet velocities and gradual onset of bend-CCFL. It also represent a case within the range of water inlet velocities where reflux condensation occurs ($J_{w,in}^{*0.5} < 0.2$). The second case is $J_{w,in}^{*0.5} = 0.305$ and it selected because of the onset of a strong ADE-CCFL. Simulations were performed in two steps:

- Steady state simulations: were carried out at low air velocities where the flow is supercritical one. The air/water interface is rather stable and steady state calculation can reproduce the initial void fraction distribution for transient simulations.
- Transient simulations: were carried out when the input air velocity was increased/decreased.

Table 8.1 shows the initial conditions for steady state simulations. All simulations were carried out at low air velocity (matching the experimental value) in order to produce the condition of supercritical flow in each case.

Table 8.1 Initial conditions for the steady state simulations.

$J_{w,in}^{*0.5}$	$J_{w,in}[\mathrm{m.s^{-1}}]$	$J_a[\mathrm{m.s^{-1}}]$
0.105	0.0146	~7.4
0.305	0.1266	

The result of the steady state simulations will represent the initial condition for the transient simulations except for the input air velocity which will be changed according to the experimental procedure that leads into the onset of CCFL in each case. Within the original experimental procedure (see section 7.2), the air velocity was increased by small steps ($\Delta J_a^{*0.5} = 0.01$) in order to search and identify the occurrence of CCFL and preceding phenomena precisely. This experimental procedure will require a long acquisition time (20-25 min) which results in large number of images for each case (ca. 12000-15000 image). However the main problem is the simulation time. The time requirement for 20 minutes of transient calculation using the previously described mesh is beyond reasonable realization. Practically running the transients on i7 quad core processor (local parallel calculation on 7 processors @ 2.4 GHz) will yield 10s of simulation per day. In order to make the calculations more feasible, new experiments were executed in which the air velocity was changed according to limited major steps following the acquired experimental pre-knowledge about the onset of CCFL in each case. The resulting experiments were short in time (~2 min) allowing each of the transients to run within 1-2 weeks of time (depending on the behaviour of convergence, sometimes the time step was further reduced after the simulation crash or does not converge with the initial time step). Table 8.2 shows these changes and their

correspondence. Table 8.3 shows the time intervals which were applied for each change during simulations. The last change of the air velocity always corresponds to the air reduction caused by the large increase of pressure loss (between the RVs and SGs) after the onset of bend-CCFL (as the blower characteristics cannot afford the air velocity at the occurring pressure difference). As such, the last air change was made in order to "mimic" the experiments rather than it was an action executed during the experiments.

Table 8.2 Air changes and their correspondence during transient's simulations

$J_{w,in}^{*0.5}$	$\Delta J_{a1}[\mathrm{m.s^{-1}}]$	Correspondence	$\Delta J_{a2}[\mathrm{m.s^{-1}}]$	Correspondence	$\Delta J_{a3}[\mathrm{m.s^{-1}}]$	Correspondence
0.105	$7.7-10.2$	Transition into subcritical flow	$10.2 \rightarrow 14.2$	Onset of bend-CCFL	$14.2 \rightarrow 14$	Blower characteristics
0.305	$7.7 \rightarrow 13$	Onset of ADE-CCFL	$13.5 \rightarrow 15.7$	Onset of end-CCFL	$15.7 \rightarrow 8$	Blower characteristics

Table 8.3 Air changes and their corresponding time intervals.

$J_{w,in}^{*0.5}$	$J_{w,in}[\mathrm{m.s^{-1}}]$	$\Delta J_{a1}[\mathrm{m.s^{-1}}]$	$\Delta t_1[\mathrm{s}]$	$\Delta J_{a2}[\mathrm{m.s^{-1}}]$	$\Delta t_2[\mathrm{s}]$	$\Delta J_{a3}[\mathrm{m.s^{-1}}]$	$\Delta t_3[\mathrm{s}]$	$\Delta J_{a\hat{3}}[\mathrm{m.s^{-1}}]$	$\Delta t_{\hat{3}}[\mathrm{s}]$
0.105	0.0146	$7.7-10.2$	8	$10.2-14.2$	8	$14.2 \rightarrow 14$	0	-	-
0.305	0.1266	$7.7 \rightarrow 13$	8	$12.8 \rightarrow 15$	8	$15 \rightarrow 10.4$	4	$10.4 \rightarrow 8$	8

8.4.2 Steady state simulations

Figures 8.9 and 8.10 show a comparison between the water fraction distribution obtained from experiments and the one obtained out of the steady state simulations in the mid-plane of the facility. The experimental images were acquired using a wide-angle 24mm objective. In order to make the comparisons more feasible, the extra pixels that do not belong to the water presence was manually removed, and the scale of the images was adjusted to match the simulation results.

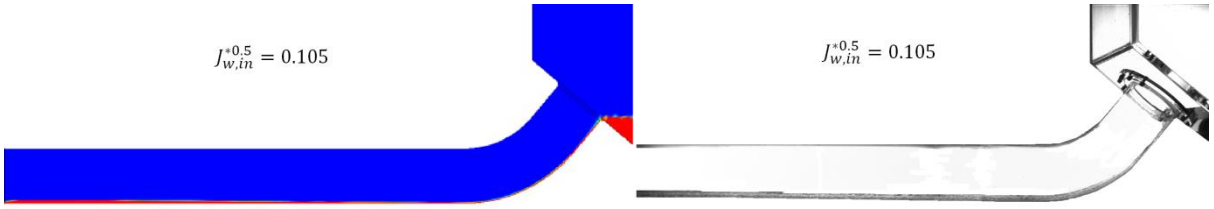

Figure 8.9: A comparison of the water volume fraction between simulation and experimental data at $\mathrm{J_{w,in}^{*0.5}} = 0.105$. Simulation results: shown at mid-plane, experiments: a side view projection.

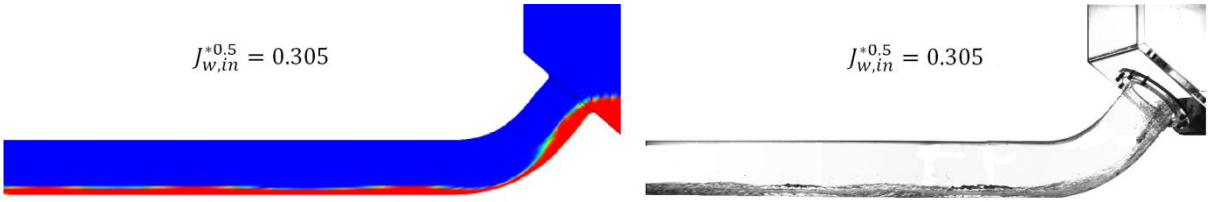

Figure 8.10 A comparison of the water volume fraction between simulation and experimental data at $\mathrm{J_{w,in}^{*0.5}} = 0.105$. Simulation results: shown at mid-plane, experiments: a sideview projection.

The resulting interface from simulations at $J_{w,in}^{*0.5} = 0.105$ represents an undisturbed stratified air/water interface at low inlet water velocities while a stratified flow with some surface disturbances and 3D structure appears at $J_{w,in}^{*0.5} = 0.305$ which is in accordance with the experimental observations. The comparison shows also that the steady states simulation was able to predict the characteristics of the supercritical flow. In particular the increase of the water depth towards the water exit at $J_{w,in}^{*0.5} = 0.105$. For $J_{w,in}^{*0.5} = 0.305$, the water stream begins to get disturbed even at low air velocities. his can be identified within the simulation results by a smeared void fraction at the surface, which indicates an increased mixing and thus an increased turbulence production. The water stream starts to get thicker at the entrance into the riser; the surface within the horizontal part shows a wavy pattern (not a wavy flow). The apparent experimental water depth at the bend is thicker. This is because the experimental images are 2D projection of the air/water interface into the camera plane, while the simulations are obtained exactly at the mid-plane of the facility. If the water stream is divergent (see figure 8.11), it will spread into the side wall of the pipe creating a thin film that climb higher and results in a higher projected water depth. If the water stream is convergent a peak appears near the center of the pipe's cross section. The projection of the convergent stream results in a lower apparent water level as in the case of the divergent stream. However, the results stay comparable to a high extent and these are going to be used as an initialization for the transient simulations. Future experimental work should be able to illuminate a thin sheet around the mid-plane of the facility during experiments using a planar laser. This will allow obtaining more accurate experimental data for comparison.

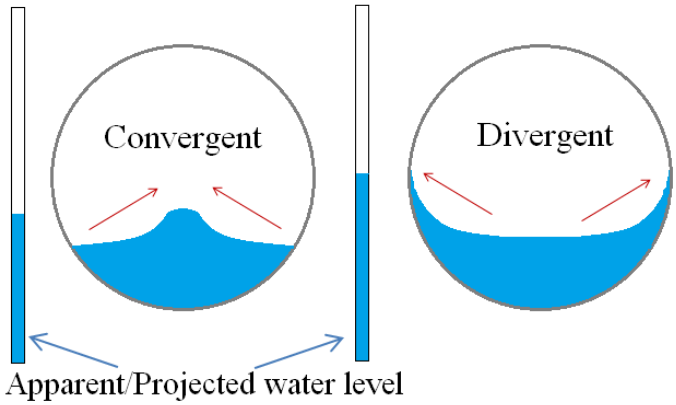

Figure 8.11 An illustration of water level 3D structure within the hot-leg pipe (horizontal section).

8.4.3 Validation of the onset of CCFL in transient calculations

8.4.3.1 Case of low water inlet velocity $J_{w,in}^{*0.5} = 0.105$

Figure 8.12 shows the experimental and the approximated air input velocity used as an input for CFX simulations (air superficial velocity within the hot-leg pipe). The transient was made in three stages according to tables 8.2 and 8.3. The first transient tries to simulate the transition from a supercritical flow into a subcritical flow and the formation of the hydraulic jump at the bend. The results of this stage are shown in Figure 8.13 (Water fraction's distributions). As it can be seen the CFX predicts the transition a little bit earlier as within the

experiments. The Result at $t = 14.4$ s shows that the jump has moved towards the bend within the simulations, while it is still closer to the water exit in experiments. However the match between the simulations and experiments is good and the final case at $t = 30$ s is well comparable to the experiments. The development of the pressure difference between the RVs and the SGs agrees well with the experimental value (see figure 8.12 the first step of the pressure difference change).

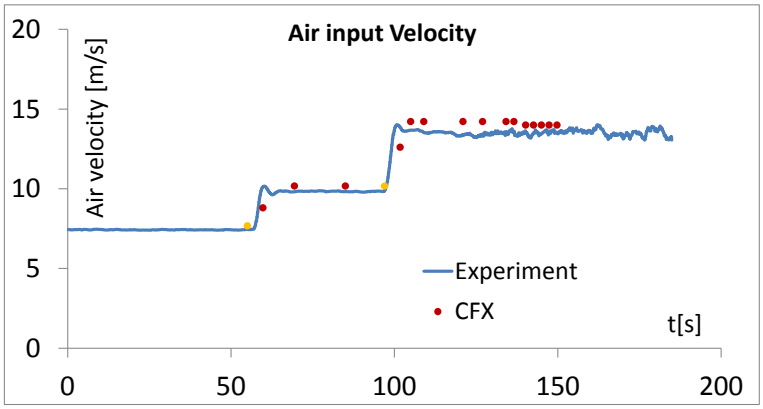

Figure 8.12 The air inlet velocity during experiments. The red points show the approximated change in simulations. The orange point indicates the start point of each of the two performed transients' calculations.

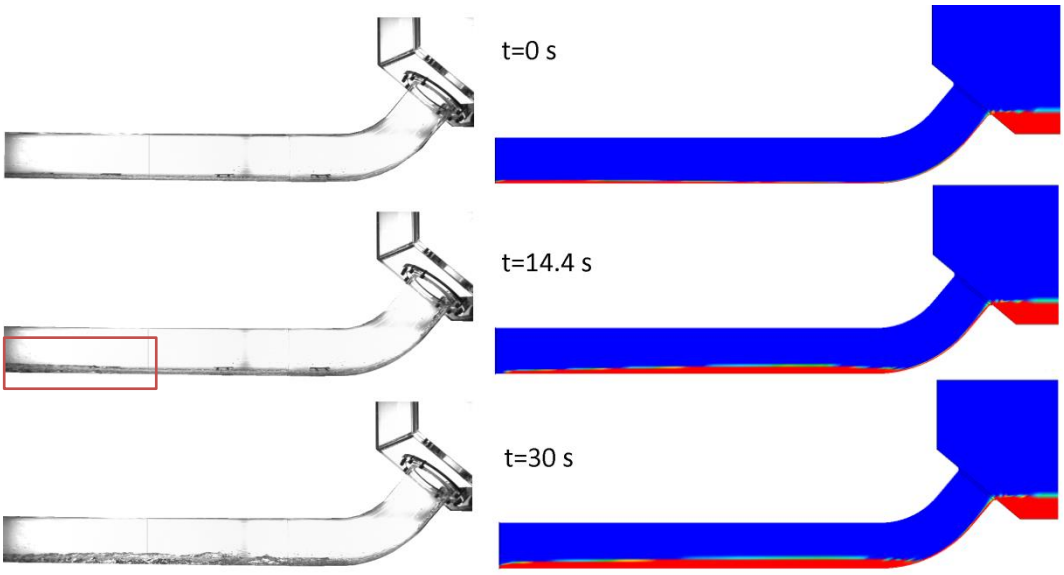

Figure 8.13 The air/water interface during the first air velocity increase at different time steps. The transient shows the transition from a supercritical into a subcritical flow and the formation of a hydraulic jump at the bend. Left column: experiments, right column: CFX. $t = 0$ corresponds to the start point of the air input velocity increase (left orange point in figure 8.12).

Figure 8.14 shows the development of the air/water interface during the second stage of the simulation. This stage corresponds to the onset pf the bend-CCFL. As it can be seen from the comparison between the experiments and the simulations at different time steps, the prediction of the transition agrees well with the experiments. This indicates an adequate drag

coefficient. A major difference between experiments and simulations is the amount of two-phase mixture at the bend during the transition. Within experiments (marked with red rectangles in figure 8.14), the amount of two-phase mixture is larger and this related to the amount of air entrainment and turbulence mixing at that area. The use of the free surface model limits the reproduction of such regions within the simulations.

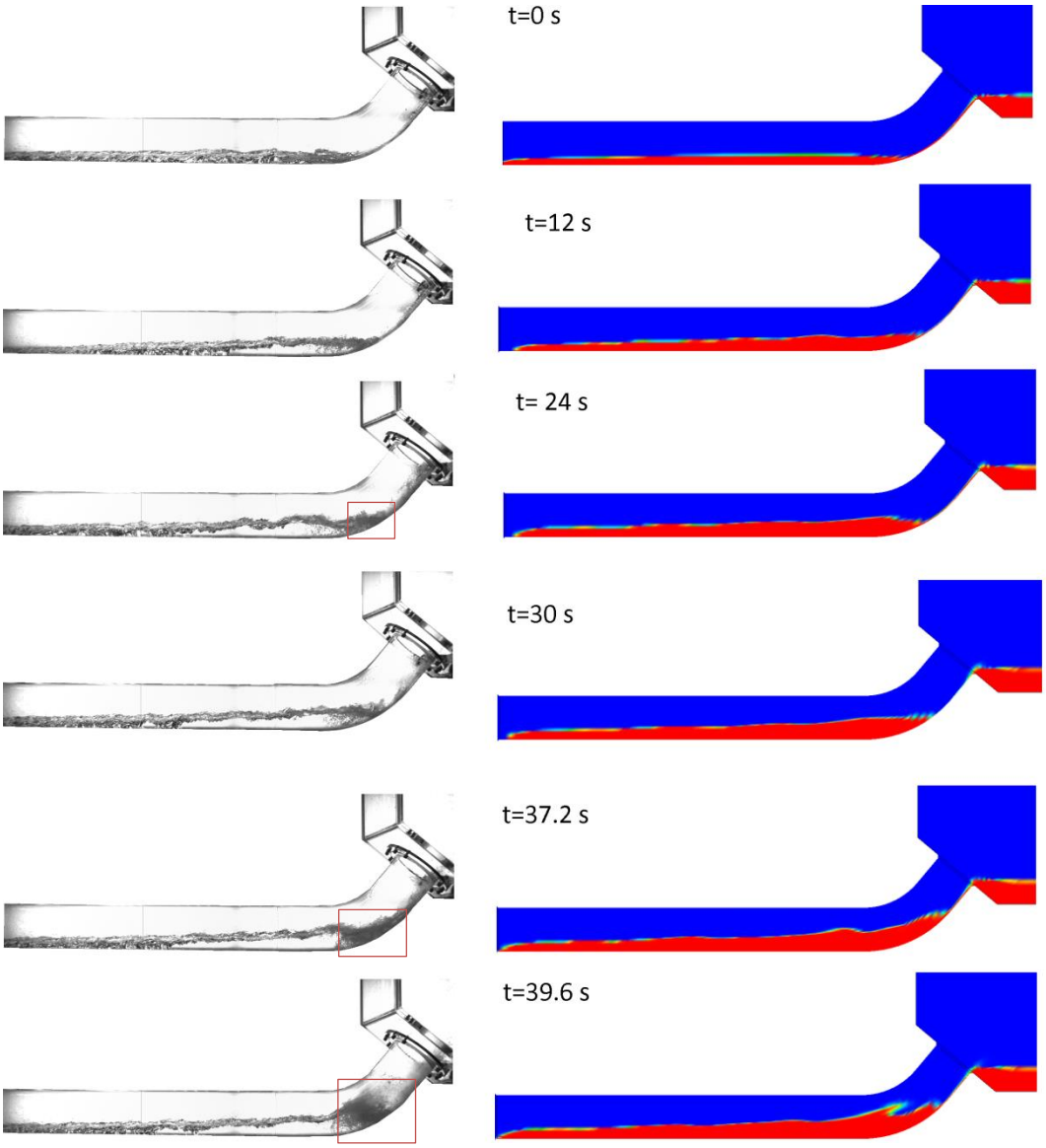

Figure 8.14 The air/water interface during the second air velocity increase at different time steps. The transient shows the onset of bend-CCFL at the bend. Left column: experiments, right column: CFX. $t = 0$ corresponds to the start point of the second air velocity increase (right orange point in figure 8.12).

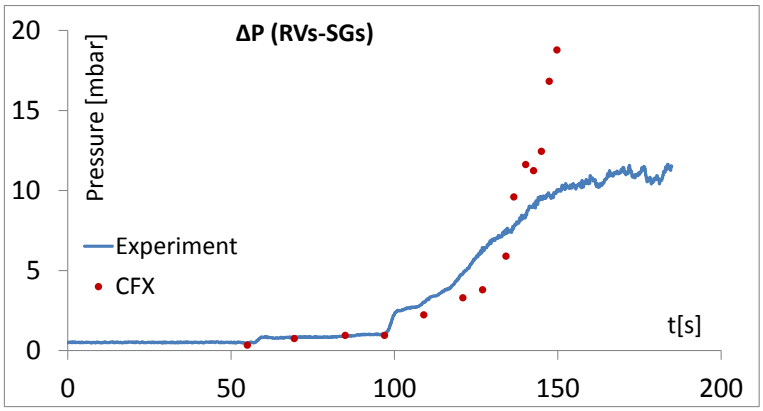

Figure 8.15 the development of the pressure difference between the RVs and SGs during experiments and CFX simulations. CFX simulations overestimate the pressure loss after the onset of bend-CCFL.

The development of the pressure difference can be seen in Figure 8.15 . The CFX predicted pressure difference agrees with the experimental value until a certain point ($\Delta P \approx 7.5$ mbar) and then it exceeds the experimental values even after the reduction of the air input velocity. This indicates that the drag and the momentum transfer is overestimated at low void fractions ($\equiv$ high water volume fractions). Although the overall comparison is still showing a good agreement between simulations and experiments and especially the air/water interface, this overestimation will cause an earlier transition into bend-CCFL at higher water velocities ($\equiv$ higher water volume fractions) as it will be shown in the case of $J_{w,in}^{*0.5} = 0.305$. Many aspects of the CCFL occurrence were well predicted and in particular the formation of large-roll waves that breaks into the steam generator and forms the main mechanism of water backflow. Figure 8.16 shows a set of successive images obtained during the third stage of the simulation (reduction of the air velocity, see table 8.3). The time shown within this figure is not the absolute time calculated from the start point of the velocity increase because the flow in this stage is not stationary of even transient and cannot be compared with experiments directly. This is because the formation of the large-roll waves and breaking into the steam generator is completely chaotic. The successive images show a good agreement between the prediction of this phenomenon in experiments and in simulations. As a conclusion, it can be said that the adopted drag coefficient and modeling of the momentum transfer is acceptable at low water inlet velocities an can be used to predict the onset of bend-CCFL in this range of velocities. However, it should be mentioned that in order to assert this fact a simulation that mimic the experimental procedure should be made. this means that the air input velocity should be increased within small steps and allowing the simulation to run for sufficient time after each increase (at least 30 seconds). The occurrence of CCFL should be then checked within the results weather it agrees with experiments or not. The main obstacle of such a simulation is the time cost. Such a simulation can require 500-600 s of simulation which is beyond current capabilities of available calculating resources to be done within a reasonable time.

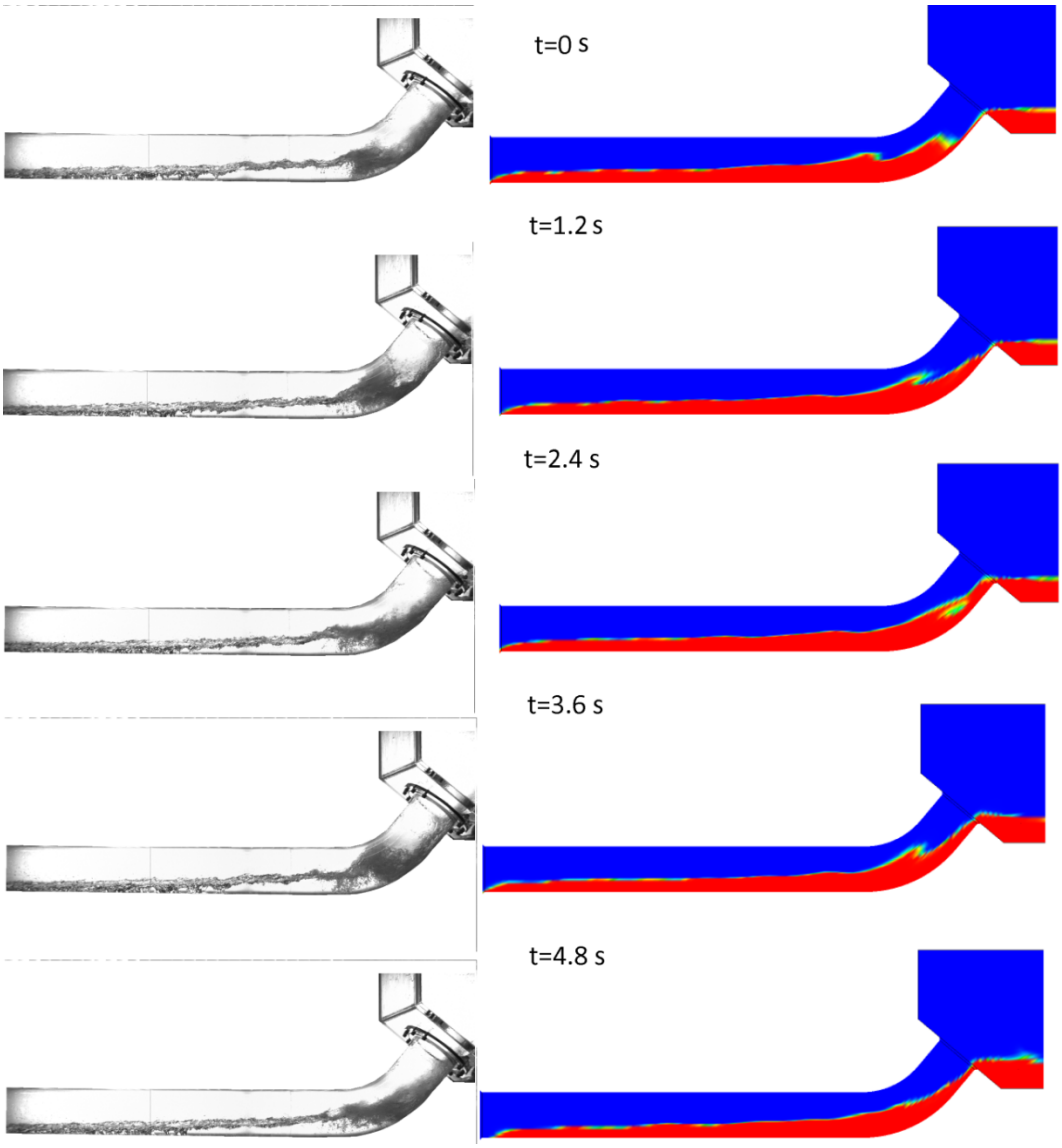

Figure 8.16 The air/water interface during the formation of a large roll-wave at the bend after the onset of bend-CCFL. The transient shows the approach aof the wave into the bend and its breaking into the SGs. Left column: experiments, right column: CFX. $t = 0$ corresponds to the first shown image.

8.4.3.2 Case of high water inlet velocity $J_{w,in}^{*0.5} = 0.305$

Figure 8.17 shows the experimental and the approximated air input velocity (air superficial velocity within the hot-leg pipe). This simulation was done also in three stages according to tables 8.2 and 8.3. The third stage (reduction of the air inlet velocity according to the experimental values) is done in two steps in order to match the experimental values. The orange points indicate the start point of each of these three stages.

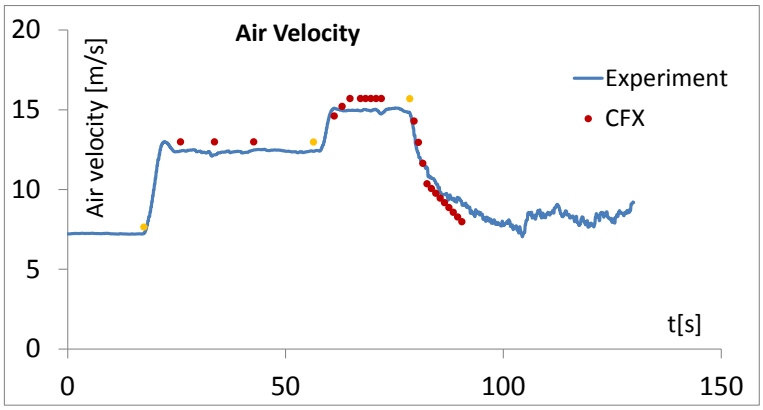

Figure 8.17 The air inlet velocity during experiments. The red points show the approximated change in simulations. The orange point indicates the start point of each of the two performed transients' calculations.

Figure 8.18 shows the results of the water volume fraction for the first simulation stage. This stage corresponds to the onset of ADE-CCFL that is the strong formation of water-droplets jet at the water entrance. The figure shows the air/water interface after 25 s of simulation. As it can be seen there is a slight change of the interface within the simulations. No visible jet is seen in the CFX simulations (very slight and barely visible). Figure 8.19 shows the same results after reduction of the scale of the void fraction down to 0.1 instead of 1. As it can be seen from this figure there is a jet formation at higher air velocities but it is slight that it does not match the experiments. Even after the second increase of the air velocity (that simulates the onset of bend-CCFL) this jet stays weak during the transition. Here an improvement of the definition is required in order to predict the second mechanism of CCFL (ADE-CCFL) at high water inlet velocities. Such a simulation cannot be found in literature at all, since most of attempts were made to predict the onset of bend-CCFL. It seems that the momentum transfer does not depend upon the local void fraction alone- as most of the correlations in literature tries to set- but also on the specific topology of the air/water interface, the amount of turbulence near the interface, and the attack angle of the air in regard to the falling water stream (relevance to the gravity vector). A more advanced definition is required.

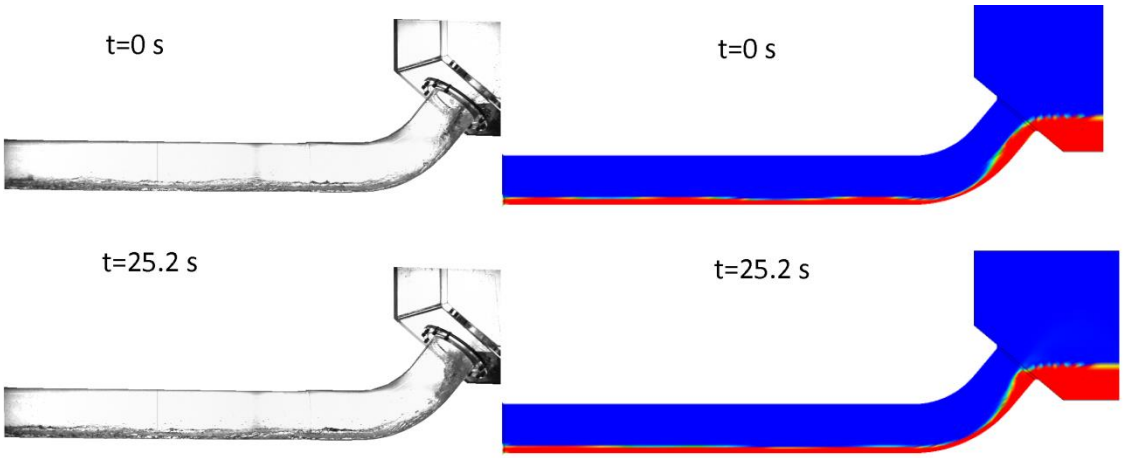

Figure 8.18 The air/water interface during the first air velocity increase at different time steps. The transient shows the slight change at the water entrance but no visible ADE-CCFL (see figure 8.19). Left column: experiments, right column: CFX. $t = 0$ corresponds to the start point of the first air velocity increase (left orange point in figure 8.17).

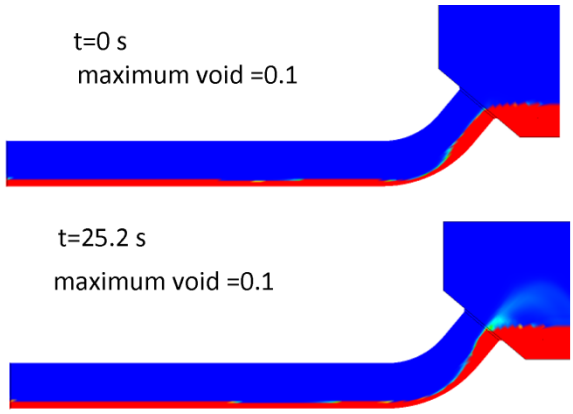

Figure 8.19 The air/water interface during the first air velocity increase. Within these Figures the scale was changed to show a slight formation of ADE-CCFL at the water entrance (maximum water volume fraction =0.1 instead of 1) . Although being small, it shows a difference form the initial condition. Current drag formulation cannot predict ADE-CCFL.

Figure 8.20 shows the air/water interface during the second stage of this simulation (second increase of the air velocity). This Figure illustrates the formation of a large roll-wave that moves fast towards the bend transforming the flow into a subcritical one immediately. Within this simulation the transition was faster in CFX simulation as in experiments. In order to show the transition development in simulations and experiments the experimental images were shifted back by 5.6 seconds. The shifted results agrees well with the experiments As mentioned before, it can be seen that no growth of the water jet occurs at the water entrance even after the this large increase of the air velocity. The simulations show also the change of the mechanism by which the transition into subcritical flow happens. Instead of the formation of a hydraulic jump a clear formation of large waves happens. This agrees well with experiments.

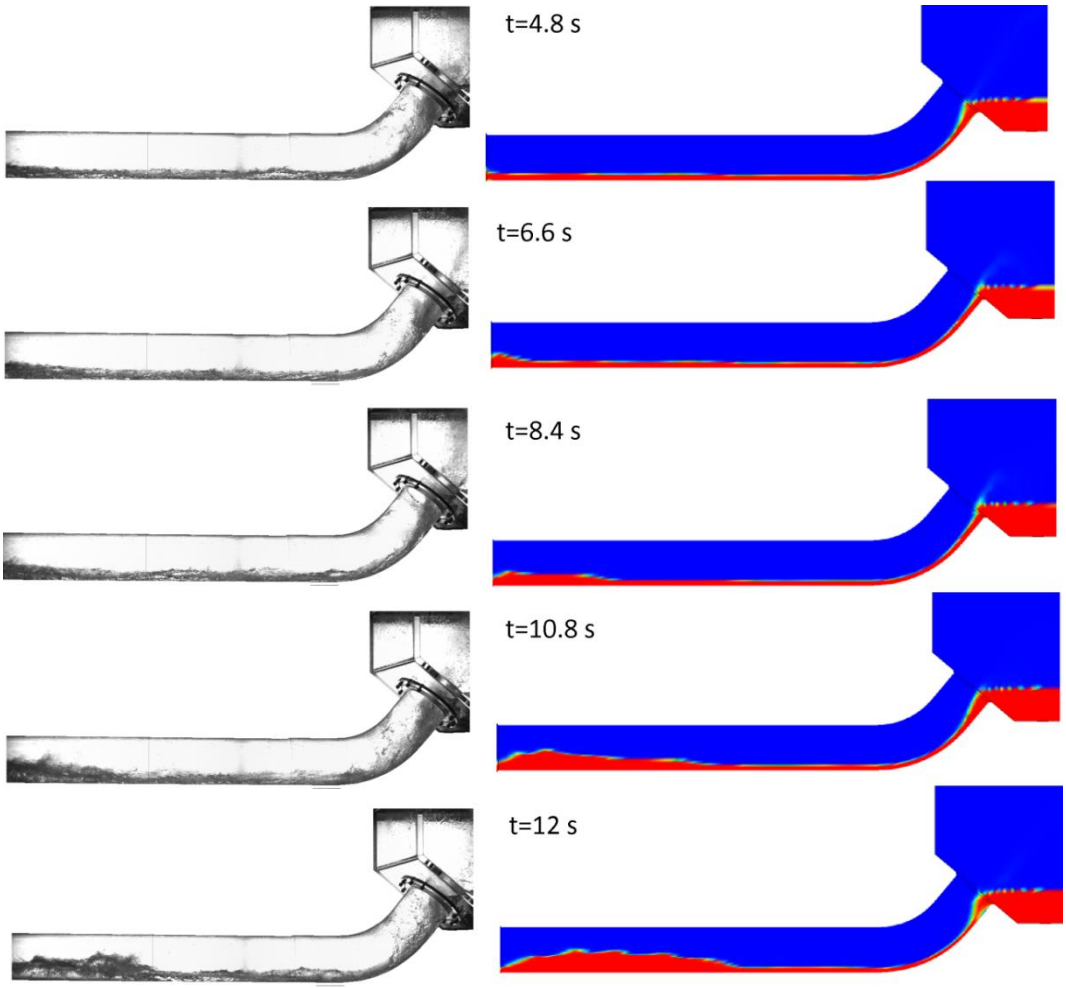

Figure 8.20 The air/water interface during the second air velocity increase at different time steps. The transient shows the formation of a large roll-wave near the water exit that moves towards the bend. Left column: experiments, right column: CFX. $t = 0$ corresponds to the start point of the second increase air input velocity (second orange point from left in figure 8.17).Because the drag definition was not ideal, the transition occurs earlier within CFX simulations, experimental data are shifted by 5.6 s to match simulations.

Figure 8.21 shows the approach of the large wave towards the bend and the transition of the flow in the entire hot-leg into a subcritical flow. The occurrence of a large blockage at the riser is well depicted within the simulations. The flow back of large amount of water can be seen at t=15.6 s. However, as it was said before, the two-phase mixture and formation of a lot of foam at the bend cannot be seen within simulations. The transition occurs about 5.6 seconds earlier within simulations, this can be seen in the development of the pressure difference in figure 8.22 The sharp increase of the pressure difference –which correspondes to the onset of bend-CCFL- happens clearly earlier in simulations.

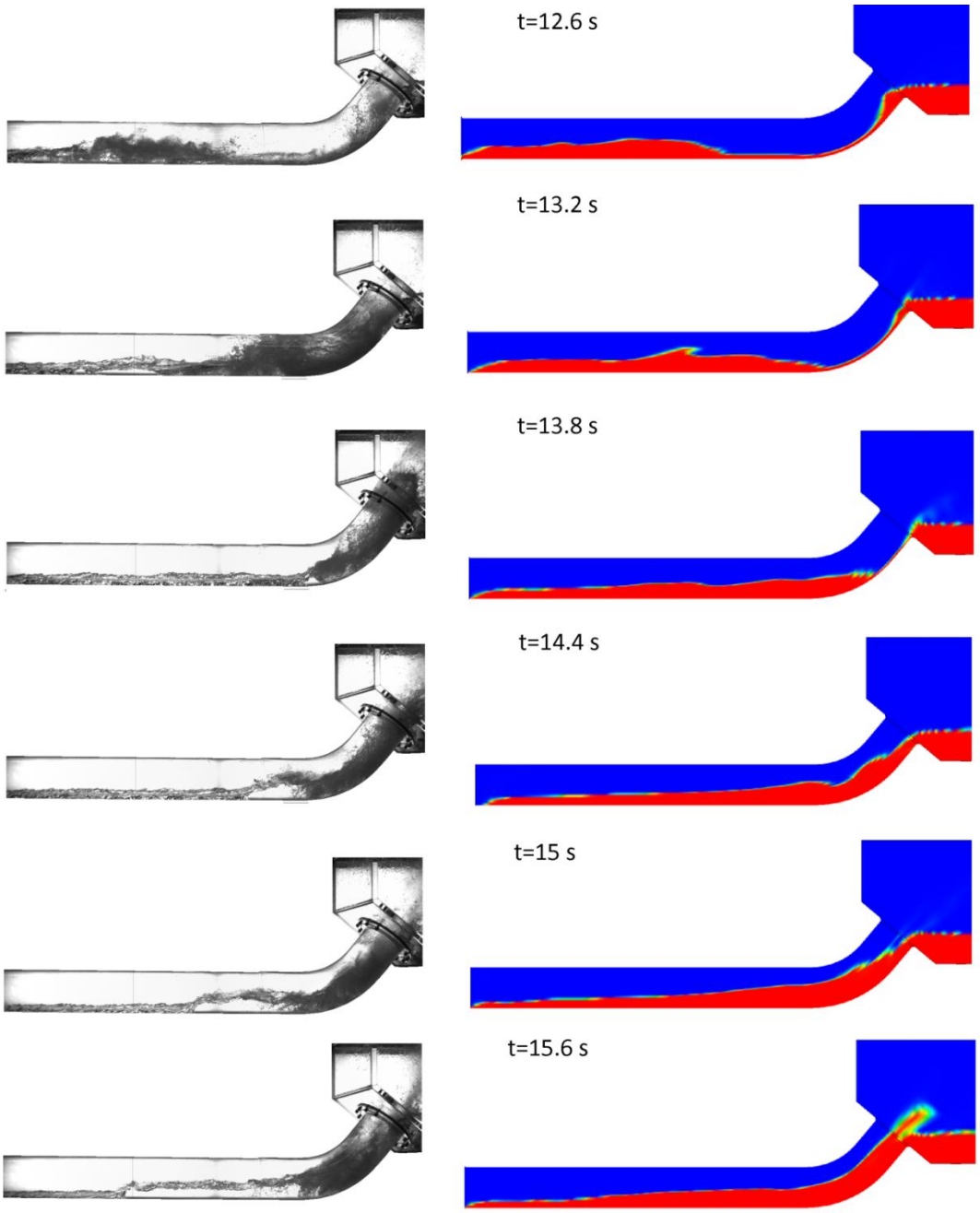

Figure 8.21 The air/water interface during the second air velocity increase at different time steps. The transient shows the arrival of the large roll-wave at the bend and the onset of intense bend-CCFL. Left column: experiments, right column: CFX. $t = 0$ corresponds to the start point of the second increase air input velocity (second orange point from left in figure 8.17). Experimental data are shifted by 5.6 s to match simulations.

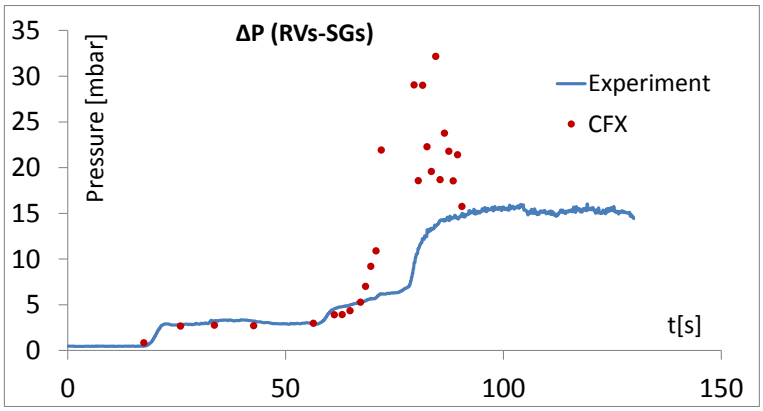

Figure 8.22 the development of the pressure difference between the RVs and SGs during experiments and CFX simulations. CFX simulations overestimates the pressure loss after the onset of bend-CCFL. The start of the sharp increase of the pressure drop (that marks the onset of bend-CCFL) is earlier in CFX simulations.

The early occurrence of the bend-CCFL in simulations indicates that the drag coefficient starts to overestimates the momentum transfer at specific void fraction. This can be seen from the large overestimation of the values of pressure difference in simulations against experimental values after the onset of the bend-CCFL. They stay higher even after the reduction of the air inlet velocity (third stage of the simulation). Figure 8.23 shows a set of successive images that shows the prediction of the bend-CCFL mechanism. The Formation of large roll-waves that can start even near the middle of the pipe (t=7.5 s, see the approaching wave before the bend) is well predicted. In this case a higher amount of two-phase mixture that is pushed into the steam generator can be clearly seen (at t=1,4, 5, and 6 s). The formation of large roll-waves that reach the upper part of the pipe at the bend can also be seen (t=3 , 4.5, 5.5, and 7 s). All these observations can be seen in Figure 7.53 section 7.4.

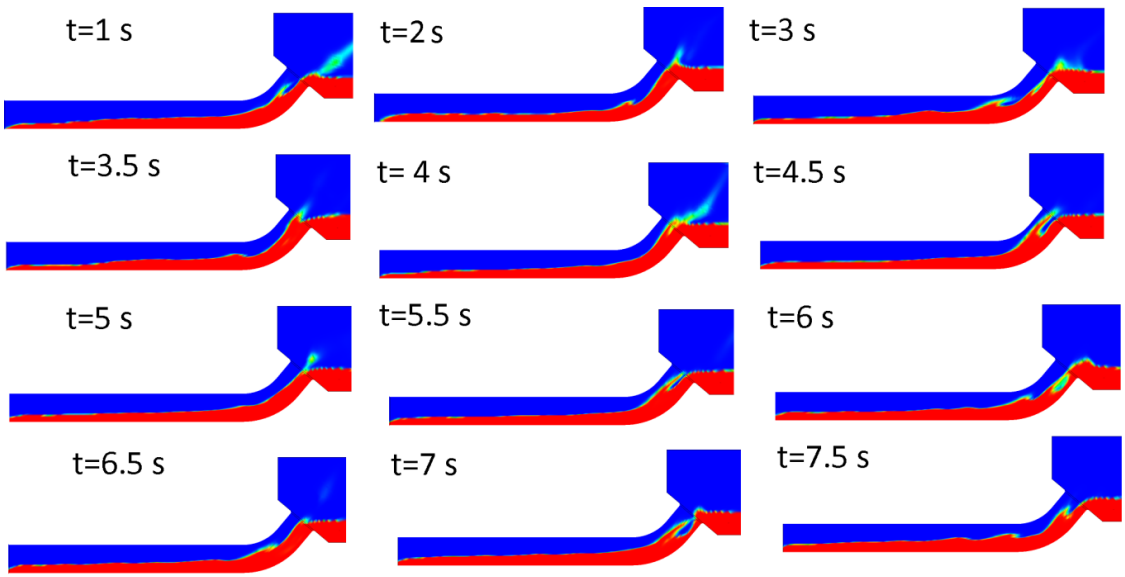

Figure 8.23 The air/water interface during the air velocity decrease at different time steps. The transient shows the intense bend-CCFL at the bend, the formation of large roll-waves close to the bend and their movement towards the bend. $t = 0$ Corresponds to the first image.

8.5 Conclusion of the CFD simulations of the COLLIDER test facility.

CFD simulation of the COLLIDER test facility using commercial code CFX. were performed. The aim is to validate the performance of these codes and to test the existing models of momentum transfer against existing experimental data. Simulation results were compared against experimental full-length images of the air/water interface within the hot-leg besides the pressure difference between the RVs and the SGs. These simulations were the first to be validated against data from a facility of large diameter geometry with 1/3 scale and realistic circular cross section. As such these results are valuable for further development of CFD codes. The current simulations were performed at two representative points: $J_{w,in}^{*0.5} = 0.105 \text{ and } 0.305$. The first point lies within the range of water flow rate that exist during reflux-condensation phase after a LOCA and the second is a good representative for the onset of the second CCFL mechanism: ADE-CCFL. The simulations show the following:

- The onset of bend-CCFL was generally well predicted at low and high inlet water velocities. However transient calculations shows that the transition was faster in simulations than in experiments specially at high water velocity which can be returned to the overestimation of the drag at low void fractions.
- The conclusion of the first point is supported by the overestimated pressure difference (RVs-SGs) after the onset of the bend-CCFL.
- The ADE-CCFL was not predicted adequately at $J_{w,in}^{*0.5} = 0.305$. Even when the air velocity was increased during the second increase of air velocity. This was an indication of the need for another approach to reproduce this phenomenon.
- Despite shortcomings following observed phenomena were well predicted:
    - The Formation of large roll-waves at the bend and their crash into the SGs at $J_{w,in}^{*0.5} = 0.105$.
    - The formation of large-roll waves within the hot-leg and their approach into the bend forming a large sporadic blockage at $J_{w,in}^{*0.5} = 0.305$.
    - The transitions that lead into the bend-CCFL were predicted plausibly.

It is clear that further development is required. The main point is the construction of a new approach and drag coefficient that can predict ADE-CCFL and does not overestimate the amount of momentum transfer. Since a fine mesh was created, no mesh study was conducted, however further development of the mesh –especially at the bend region- can improve the results. Further transients that apply small increment of the air velocity in order to find the onset of CCFL using simulations and comparing it with results in Figure 7.65 should be considered. Such simulations will need a considerable amount of calculation resources.

Chapter 9 Further work

SCUBA is a versatile facility for investigation of bubbly flows using HSC technique. It is possible to expand the quality and range of acquired data via implementation of new measuring techniques. The use of the HSC gives a unique look into the actual behavior of the bubbles which was a decisive factor in investigating the steam bubble condensation. Further developments of the current investigations can be achieved via:

- Local measurement of the water velocity distribution.
- Application of double imaging techniques.
- Mixing steam with air and the investigation of the mixing ratio effect upon the condensation process.
- Application of different injection nozzles in order to produce even smaller bubbles.

SCUBA can be used for investigation of air/water flows in a large diameter and relatively long test section (~3.5 m length).

COLLIDER is a unique facility in its size, scale, real geometry, and full transparency. It is also built to be flexible for further geometrical modifications. Further works on COLLIDER can include:

- Performing more elaborated CFD simulations and further development of the momentum transfer models depending on the comparison with experimental data.
- Obtaining more experimental data for CFD validation: PIV measurements of the velocity field within the hot-leg.
- Construction of a new hot-leg pipe that includes a simulator of the Hutze pipe and testing its effect in experiments and simulations.
- Construction of an aquarium around the hot-leg to improve the quality of the acquired air/water interface.

Acknowledgments

I would like to thank all people who participated in one way or another to the success of this work. My utmost and sincere thanks go to my Prof. Rafael Macian-Juan. He provided me with an invaluable support and a unique chance to build such a laboratory. I recall all those valuable discussions that we had together. I gained lot of knowledge from him; I say: thanks for everything. My father, your soul was accompanying me through all delights and hardships; your light is still illuminating inside me. I thank my mother, whom without her love and dedication, I was not to reach this point of my life. I remember with a lot of gratefulness the support of my beloved uncle; may your soul rest in peace. Many thanks go to my family, to their love and support.

I would like to thank all students and assistants who participated to this work, especially I would name Andreas Hibler, and Tyll Bodden, who provided a valuable technical support to the work. I want to thank all colleagues at the department of nuclear engineering whom at one day or another gave a hand to the laboratory. My thanks go also to many people in industry who did their best to provide our lab with the required equipment. I want also to be grateful to all my teachers and professors who granted me knowledge and support.

The two-phase thermalhydraulic laboratory at the department of nuclear engineering of the Technical University Munich has been funded by a grant from E.ON Kernkraft, Germany.

References

Al Issa, S.; Macian, R., Experimental investigation of countercurrent flow limitation (CCFL) in a large-diameter hot-leg pipe geometry: A detailed description of CCFL mechanisms, flow patterns and high-quality HSC imaging of the interfacial structure in a 1/3.9 scale of PWR geometry, Nuclear Engineering and Design, 280 (2014) pp. 550-563.

Al Issa S., Weisensee P., Macián-Juan R. , Experimental investigation of steam bubble condensation in vertical large diameter geometry under atmospheric pressure and different flow conditions, International Journal of Heat and Mass Transfer 70 (2014) 918–929.

Al Issa, S., Moreno-Prosper, M., Developing a procedure for calculation of bubble parameters, diameter, velocity, aspect ratio and path depending upon shadowgraph technique and high speed camera recordings for multiple bubbles and diluted bubbly flows. The 15th International Topical Meeting on Nuclear Reactor Thermal - Hydraulics, Pisa, Italy, May 12-17, 2013.Paper no. NURETH15-045.

Al Issa, S., Weisensee P., Experimental investigation of steam bubble condensation in flowing subcooled water in vertical large diameter geometry under atmospheric pressure. The 15th International Topical Meeting on Nuclear Reactor Thermal - Hydraulics, Pisa, Italy, May 12-17, 2013. Paper no. NURETH15-362.

Al Issa S., Weisensee P., Experimental investigation of steam bubble condensation in flowing subcooled water with two different injection nozzle geometries, Proceedings of the 21th International Conference on Nuclear Engineering ICONE21-16494 July 29-August 2, 2013, Chengdu, China, ICONE21-16494.

Al Issa, S., Macian R., Experimental investigation of CCFL in large diameter hot-leg geometry, Proceedings of the 21th International Conference on Nuclear Engineering ICONE21-16494 July 29-August 2, 2013, Chengdu, China, ICONE21-16510.

Al Issa, S.; Macian, R., A review of CCFL phenomenon, Annals of Nuclear Energy vol. 38 issue 9 September, 2011. p. 1795-1819.

Andersen, J.G.M., 1982. Interfacial shear for two-fluid models. American Nuclear Society Transactions 41, 669–671

ANSYS CFX-Pre User's Guide, Release 12.1 © 2009 ANSYS, Inc.

ANSYS CFX-Solver Modeling Guide, Release 12.1 © 2009 ANSYS, Inc.

ANSYS CFX-Solver Theory Guide, Release 12.1 © 2009 ANSYS, Inc.

ANSYS ICEM CFD, Tutorial Manual, Release 11.0 © 2007, ANSYS, Inc.

Ardron, K.H., Banerjee, S., 1986. Flooding in an elbow between a vertical and a horizontal or near-horizontal pipe. Part II: theory.Int. J. Multiphase Flow 12 (4), 543–558

Baik S., and Hanratty T. J., Effects of a drag reducing polymer on stratified gas–liquid flow in a large diameter horizontal pipe, International Journal of Multiphase Flow 29 (2003) 1749–1757

Bankoff S.G. and Lee S.C., A critical review of the flooding literature, in Hewitt G.F., Delhaye J.M. and Zuber N. (eds.), Multiphase Science and Technology, Vol. 2, Hemisphere, New York, 1986, pp. 95-180.

Barnea, D., A unified model for predicting flow pattern transitions for the whole range of pipe inclination, Int. J. Multiphase Flow 13, p. 1-12 (1987)

Bartel M. D., Ishii M., Masukawa T., Mi Y., Situ R., Interfacial area measurements in subcooled flow boiling, Nuclear Engineering and Design 210 (2001) 135–155

Bartosiewicz, Y., Lavieville, J., Seynhaeve, J.M., 2008. A first assessment of the NEPTUNE CFD code: instabilities in a stratified flow. Comparison between the VOF method and a two-field approach. Int. J. Heat Fluid Flow 29, 460–478.

Bharathan D. and Wallis G.B., Air-water countercurrent annular flow, Int. J. Multiphase Flow 9 (1983) 349-366.

Bharathan D., Wallis G.B. and. Richter H.J, Air-water countercurrent annular flow, EPRI NP-1165, 1979.

Brucker G.G., Sparrow E.M., Direct contact condensation of steam bubbles in water at high pressure, Int. J. Heat Mass Transfer 20 (1977) 371–381

Celata G. P., Cumo Maurizio, Francesco D'Annibale, Paolo Oi Marco, Akio Tomiyama, Chiara Zovini. Effect of gas injection mode and purity of liquid on bubble rising in two-component systems. Experimental Thermal and fluid Science 31 pp. 37-53. (2005).

Chen, Y. M., Mayinger, F., Measurement of heat transfer at the phase interface of condensing bubbles. International Journal of Muliphase Flow, Volume 18 (1992.), pp. 877-890.

Cheng L., Suk Woo K., Ishii M., Lim J., Suppression pool mixing and condensation tests in puma facility, Proceedings of ICONE14 International Conference on Nuclear Engineering July 17-20 2006, Miami, Florida, USA.

Choi K.Y., and No H .C., 'Experimental Studies of Flooding in Nearly Horizontal Pipes," Int. J. Multiphase Flows 21(3),419(1995).

Chun M. H. and Kim Y.-S., A semi empirical correlation for adiabatic interfacial friction factor in horizontal air-water countercurrent stratified flow, Int. Comm. Heat Mass Transfer, Vol. 22, No. 5, pp. 617~528, 1995

Chun M. H. and Lee B.-R., Nam H. Y., Theoretical and experimental investigation of the onset of slugging in horizontal stratified air-water countercurrent flow, Int. Comm. Heat Mass Transfer, Vol. 23, No. 1, pp. 11-22, 1996

Chun M.-H., and Yu S.-O., A Theoretical and Experimental Study of the Steam Condensation Effect on the CCFL in Nearly Horizontal Two-phase Flow, Journal of the Korean Nuclear Society Volume 31, Number 6, pp.618-630, December 1999

Clift R., Grace J.R., Weber M.E., Bubbles, Drops, and Particles, Academic Press, New York, 1978.

Coste P., A Large Interface Model for two-phase CFD, Nuclear Engineering and Design 255 (2013) 38– 50.

De Bertodano M. L., Counter current flow Gas-Liquid Flow in o Pressurized .water Reactor Hot leg, Nuclear Science and engineering 117 126-133 (1994)

De Sampaio P. A.B., Faccini J. L.H., Su J., Modeling of stratified gas–liquid two-phase flow in horizontal circular pipes, International Journal of Heat and Mass Transfer 51 (2008) 2752–2761

Deendarlianto, Vallée C., Lucas D., Beyer M., Pietruske H., Carl H., Erratum to "Experimental study on the air/water counter-current flow limitation in a model of the hot leg of a pressurized water reactor". Nuclear Engineering and Design 241 3359–3372. (2011).

Didier J., Fundamental issues related to the numerical simulation of two-phase flows with phase-change, Proceedings of FEDSM2006, ASME Joint U.S. - European Fluids Engineering Summer Meeting July 17-20, Miami, FL, 2006.

Duckler A. E. and Hubbard M. G., A Model for Gas-Liquid Slug Flow in Horizontal and Near Horizontal Tubes, Ind. Eng. Chem., Fundam., Vol. 14, No. 4, 1975 337

Engineering Progress 48 (3), 141.

Fan L.-S., Tsuchiya K., Bubble Wake Dynamics in Liquids and Liquid-Solid Suspensions, Butterworth-Heinemann,Oxford, (1990).

Gardner G.C., Flooded Countercurrent Two Phase Flowing Horizontal Tubes and Channels , Int. J. Multiphase flow 9,4,367(1983)

Gargallo M., Schulenberg T., Meyer L., Laurien E., Counter-current flow limitations during hot leg injection in pressurized water reactors, Nuclear Engineering and Design 235 (2005) 785–804

Geffraye, G., Bazin, P., Pichon, P., Bengaouer, A., 1995. CCFL in hot legs and steam generators and its prediction with the CATHARE Code. In: Proceedings of the Seventh NURETH, Saratoga Springs, NY.

Ghiaasiaan S. M., Wu X., Sadowski D. L. and Abdel-Khalik S. I. , Hydrodynamic characteristics of counter-current two-phase flow in vertical and inclined channels: effects of liquid properties, Int. J. Multiphase Flow Vol. 23, No. 6, pp. 1063-1083, 1997

Ghiaasiaan S.M., Turk R.E., Abdel-Khalik S.I., Countercurrent flow limitation in inclined channels with bends, Nuclear Engineering and Design 152 (1994) 379-388

Ghorai, S., K.D.P. Nigam, 2005. CFD modeling of flow profiles and interfacial phenomena in two-phase flow in pipes. Chemical Engineering and Processing 45, 55–65.

Gumerov, N. A., 1996. The heat and mass transfer of a vapor bubble with translatory motion at high Nusselt numbers. International Journal of Multiphase Flow, Volume 22, pp. 259-272

Ha K.-S., Lee Y.-B., No H.-C., Comparison of subcooled boiling models, Proceedings of ICAPP '05 Seoul, Korea, May 15-19, 2005, paper 5134.

Hari S., Hassan Y. A., Improvement of the subcooled boiling model for low-pressure conditions in thermal-hydraulic codes, Nuclear Engineering and Design 216 (2002) 139–152.

Herdtle Felix, Konstruktion eines Vertikal-Hydraulikkreislaufs zur Untersuchung von Dampfblasenkondensation, Semesterarbeit, (2011). Technichal university Munich.

Hihara E., Soejima H. and Salto T., Slugging of countercurrent gas-liquid flow in a horizontal channel, Nippon Kikai Gakkal Ronbunshu (B) 51 (1985) 394-397, in Japanese.

Höhne, T., Deendarlianto. , Lucas D. Numerical simulations of counter-current two-phase flow experiments in a PWR hot leg model using an interfacial area density model. International Journal of Heat and Fluid Flow 32 (2011), 1047–1056.

Hughmark, G.A., 1967. Mass and heat transfer from rigid spheres. AlChE Journal 13, 1219.

Ishii, M., Mishima, K., 1984. Two-fluid model and hydrodynamic constitutive relations. Nuclear Engineering and Design 82, 107–126.

Jeong H. Y., Prediction of counter-current flow limitation at hot leg pipe during a small-break LOCA, Annals of Nuclear Energy 29 (2002) 571–583

Jeong J. H., Development of Counter-Current Flow Limitation Model Applicable to a Sharp-Edged Liquid Entrance, Korean J. Chem. Eng., 181(1), 824·830 (2001)

Kadri U., Mudde R.F. , Oliemans R.V.A. , Bonizzi M., Andreussi P., Prediction of the transition from stratified to slug flow or roll-waves in gas/liquid horizontal pipes, International Journal of Multiphase Flow 35 (2009) 1001–1010

Kalman H., Condensation of a bubble train in immiscible liquids, International Journal of Heat and Mass Transfer 49 (2006) 2391–2395.

Kalman H., Condensation of bubbles in miscible liquids, International Journal of Heat and Mass Transfer 46 (2003) 3451–3463

Kalman H., Mori Y. H., Experimental analysis of a single vapor bubble condensing in subcooled liquid, Chemical Engineering Journal 85 (2002) 197-206

Kang S.-K., Chu L.-C., NO H. C., and Chun M.-H., air-water countercurrent flow limitation in a horizontal pipe connected to an inclined riser, Journal of the Korean Nuclear Society Volume 31, Number 6, pp.548-560, December 1999

Kawaji M., Anoda Y., Nakamura H. and Tasaka K., Phase and velocity distributions and holdup in high-pressure steam/water stratified flow in a large diameter horizontal pipe, Int. J. Multiphase Flow 13 (1987) 145-159.

Kawaji M., Thompson L.A. and Krishnan V.S., Countercurrent flooding in vertical to inclined pipes, Exp. Heat Transfer 4 (1991) 95-110

Kawaji, M., Thomson, L.A., Krishnan, V.S., 1989. Countercurrent flooding in an elbow between a vertical pipe and a downwardly inclined pipe. In: Proceedings of the Fourth NURETH, Karlsruhe, Germany, 20–27.

Kim H.J., Lee S.C. and Bankoff S.G., Heat transfer and interracial drag in countercurrent steam-water stratified flow, Int. J. Multiphase Flow 11 (1985) 593-606.

Kim H.T., No H. C., Assessment of RELAP5/MOD3.2.2g against flooding database in horizontal-to-inclined pipes, Annals of Nuclear Energy 29 (2002) 835–850

Kim S.-J., Park G.-C., Interfacial heat transfer of condensing bubble in subcooled boiling flow at low pressure, Int. J. of Heat and Mass Transfer 54 (2011) 2962-2974

Kinoshita, I., Murase, M., Utanohara, Y., Minami, N., Tomiyama, A., 2010. Numerical simulation of countercurrent gas-liquid flow in a PWR hot leg under reflux cooling. J. Nucl. Sci. Technol. 47 (10), 963–972.

Koncar B.,Mavko B., Modelling of low-pressure subcooled flow boiling using the RELAP5 code, Nuclear Engineering and Design 220 (2003) 255–273.

Koncar, Kljenak I, Mavko B., Modelling of local two-phase flow parameters in upward subcooled flow boiling at low pressure, International Journal of Heat and Mass Transfer 47 (2004), 1499– 1513.

Krolewski S.M. Flooding Limit in a Simulated Nuclear Reactor Hot-Leg, BS Thesis, Massachusetts Institute of Technology (1980)

Lee S.C. and Bankoff S.G., Stability of steam-water countercurrent flow in an inclined channel: flooding, J. Heat Transfer105 (1983) 713-718.

Lee T.H., Park G.C., Lee D.J., Local flow characteristics of subcooled boiling flow of water in a vertical concentric annulus, International Journal of Multiphase Flow 28 (2002) 1351–1368

Lin P. Y. and T. J. Hanratty, The effect of pipe diameter on flow patterns for air-water flow in horizontal pipes, Int. J. Multiphase Flow, 13, p.549-563 (1987)

Linehan J.H., The interaction of two-dimensional stratified, turbulent air-water and steam-water flows, Ph.D. dissertation, Dept. of Mech. Engng., Univ. of Wisconsin (1968).

Lucas D., Prasser H.-M., Steam bubble condensation in sub-cooled water in case of co-current vertical pipe flow, Nuclear Engineering and Design 237 (2007) 497-508

Lucas, D. et al., 2009. Condensation of steam bubbles injected into subcooled water. The 13th international topical meeting on nuclear reactor thermal hydraulics (NURETH-13); Kanazawa City, Ishikawa Prefecture, Japan, September 27-October 2, 2009

Lucic A., Mayinger F., Transportphenomena in subcooled flow boiling, Heat Mass Transfer 46 (2010) 1159-1166

Lucic, A., Emans, M., Mayinger, F. & Zenger, C. Interferometric and numerical study of the temperature field in the boundary layer and heat transfer in subcooled flow boiling. International Journal of Heat and Fluid Flow, Volume 25 (2004), pp. 180-195.

Maurus R., Ilchenko V., Sattelmayer T., Automated high-speed video analysis of the bubble dynamics in subcooled flow boiling, International Journal of Heat and Fluid Flow 25 (2004) 149–158

Mayinger F., Chen Y. M., Heat transfer at the phase interface of condensing bubbles, Heat Transfer 86, Proc. of the 8th Int. Heat Transfer Conf. San Francisco, Calif., Aug. 17-22, (1986), 1913-1918

Minami, N., Nishiwaki, D., Kataoka, H., Tomiyama, A., Hosokawa, S., Murase, M. Countercurrent gas–liquid flow in a rectangular channels simulating a PWR hot leg (1) flow pattern and CCFL characteristics. Japanese Journal of Multiphase Flow 22 (4), 403–412, (2008a) [in Japanese].

Minami, N., Murase, M., Nishiwaki, D., Tomiyama, A. Countercurrent gas–liquid flow in a rectangular channels simulating a PWR hot leg (2) analytical evaluation of

countercurrent flow limitation. Japanese Journal of Multiphase Flow 22 (4), 413–422, (2008b) [in Japanese].

Minami, N., Nishiwaki, D., Nariai, T., Tomiyama, A., Murase, M. Countercurrent gas–liquid flow in a PWR hot leg under reflux cooling (I) air–water tests for 1/15th scale model of a PWR hot leg. Journal of Nuclear Science and Technology 47 (2), 142–148. , (2010a).

Minami, N., Murase, M., Tomiyama, A. Countercurrent gas–liquid flow in a PWR hot leg under reflux cooling (II) numerical simulation of 1/15-scale air–water tests. Journal of Nuclear Science and Technology 47 (2), 149–155, (2010b).

Minato A. et al., An extended Two-Fluid model for interface behaviour in gas-liquid two-phase flow, 8th Int. Conf. on nuclear engineering (ICONE8), paper 8045 (2000).

Murase, M., Kinoshita, I., Utanohara, Y., Lucas, D., Vallée, C., Tomiyama, A., 2010. Numerical calculations for air-water tests on CCFL in different-scale models of a PWR hot leg. In: 18th International Conference on Nuclear Engineering (ICONE18-29092), Xi'an, China, May 17–21.

Navarro M. A., Study of countercurrent flow limitation in a horizontal pipe connected to an inclined one, Nuclear Engineering and Design 235 (2005) 1139–1148

Ohnuki a., Adachi H. and Murao Y., Scale effects on countercurrent gas-liquid flow in a horizontal tube connected to an inclined riser, Nuclear Engineering and Design 107 (1988) 283-294

Ohnuki A., Experimental Study of Counter-Current Two-Phase Flow in Horizontal Tube Connected to Inclined Riser, Journal of Nuclear Science And Technology 23 (1986) 219-232.

Okawa T., Ishida T., Kataoka I., Mori M., On the rise paths of single vapor bubbles after the departure from nucleation sites in subcooled upflow boiling, International Journal of Heat and Mass Transfer 48 (2005) 4446–4459

Okawa T., Tanaka T., Kataoka I., Mori M., Temperature effect on single bubble rise characteristics in stagnant distilled water, International Journal of Heat and Mass Transfer 46 (2003) 903–913

Okawa Tomio, Tanaka Tomoe, Kataoka Isao, Michitsugu Mori. Temperature effect on single bubble rise characteristics in stagnant distilled water. International Journal of Heat and Mass Transfer 46,pp. 903–913. (2002).

Osakabe M. and Kawasaki Y., Top flooding in thin rectangular and annular passages, Int. J. Multiphase Flow 15 (1989) 747-754.

Park C. K, Jun H. G., Yoon Y. J., Kim y. s., Song C. H., Analysis of steam condensation phenomenon in multi-hole spargers, proceedings of icapp '05 Seoul, Korea, May 15-19, 2005 paper 5129.

Park H.-S., Lee T.-H., Hibiki T., Baek W.-P., Ishii M., Modeling of the condensation sink term in an interfacial area transport equation, International Journal of Heat and Mass Transfer 50 (2007) 5041–5053

Patro R., Leifer I., and Bowyer P. A study on the temperature variation of rise velocity for large clean bubbles. Journal of atmospheric and oceanic 17 (2000).

Pradel Sebastian, Aufbau und Konstruktion eines Heißstrang-DWR-Simulatores für Untersuchungen des Gegenstrom-Begrenzungs-Phänomenes.,Diplomarbeit, (2011). Technichal university Munich.

Prodanovic V., Fraser D., Salcudean M.,Bubble behavior in subcooled flow boiling of water at low pressures and low flow rates, International Journal of Multiphase Flow Volume 28, Issue 1, January 2002, Pages 1-19

Pushkina, O.L., Sorokin, L., Breakdown of liquid film motion in vertical tubes. Heat Transfer Soviet Res. 1,(1969) 56–64.

Ranz, W.E., Marshall, W.R., 1952. Evaporation from drops, part I, part II. Chemical

Richter H. J.,"Flooding in Tubes and Annuli " lnt.J.MultiphaseFlow,7(6),647(1981)

Richter H.J., Wallis G.B., Carter K.H. and Murphy S.L., Deentrainment and countercurrent air-water flow in a model PWR hot leg, NRC-0193-9 (September 1978).

Sam A., Gomez C.O., Finch J.A. Axial velocity profiles of single bubbles in water/frother solutions. Department of Mining and Metallurgical Engineering, McGill University, Montreal, Que. H3A2A7, Canada.(1995).

Siddiqui H., Banerjee S. and Ardron K.H., Flooding in an elbow between a vertical and a horizontal or near-horizontal pipe, part I: experiments, Int. J. Multiphase Flow 12 (1986) 531-541.

Suzuki, S. and Ueda, T. (1977) Behavior of liquid films and flooding in counter-current two-phase flow-Part I. Flow in circular tubes. Int. J. Multiphase Flow 3, 517-532.

Taitel Y. and Dukler A. E., A model for predicting flow regime horizontal and near horizontal transitions horizontal Gas-liquid Flow, AlChE Journal (Vol. 22, No. 1) January, 1976

Tien C. L, A Simple Analytical Model for Countercurrent Flow Limiting Phenomena with Vapor Condensation, Letters in Heat and Mass Transfer, 4, 231 (1977).

Tomiyama A., Celata G.P., Hosokawa S., Yoshida S. Terminal velocity of single bubbles in surface tension force dominant regime. International Journal of Multiphase Flow 28, 1497–1519. (2002).

Tomiyama A., Yoshida S., Hosokawa S., Surface tension force dominant regime of single bubbles rising through stagnant liquids, in: Proceedings of the UK-Japan Seminar on Multiphase Flow, Bury St Edmunds, (2001).

Vallée C., Höhne T., Prasser H.-M., Sühnel T., Experimental investigation and CFD simulation of horizontal stratified two-phase flow phenomena, Nuclear Engineering and Design 238 (2008) 637–646

Wallis G.B. and Dobson J.E., The onset of slugging in horizontal stratified air-water flow, Int. J. Multiphase Flow 1 (1973) 173-193.

Wallis G.B., flooding velocities for air and water in vertical tubes. UKAEA Report, AAEW-R123 (1961).

Wallis G.B., Richter H.J. and Bharathan D., Air-water countercurrent annular flow in vertical tubes, EPRI NP-786, 1978.

Wallis, G. B., One Dimensional Two-Phase Flow, McGraw Hill (1969).

Wan P.T. and Krishnan V.S., Air-water flooding in an 90^o elbow with a slightly inclined lower leg, Proc. CNS 7th Annual Conf., Toronto, June 1986

Wang H. And Kondo S., a study on the stratified horizontal counter-current two-phase flow, Nuclear Engineering and Design 121 (1990) 45-52 45

Wang M.J., Mayinger F., Simulation and analysis of thermal-hydraulic phenomena PWR hot leg related to SBLOCA, Nuclear Engineering and Design 155 (1995) 643 652

Warrier G. R., Basu N., Dhir V. K., Interfacial heat transfer during subcooled flow boiling, International Journal of Heat and Mass Transfer 45 (2002) 3947–3959

Weiss P.A., Hertlein R.J., UPTF test results first 3 separate effect tests, NUREG/CP-0082 Vol. 4 (February 1987)

Wintterle T., Laurien E., Stäbler T., Meyer L., and Schulenberg T., Experimental and numerical investigation of counter-current stratified flows in horizontal channels, Nuclear Engineering and Design 238 (2008) 627–636

Wong T.N. and Yau Y.K., Flow patterns in two-phase air-water flow, INT. Comm. Heat Mass Transfer, Vol. 24, No. 1, pp. 111-118, 1997

Wongwises S., Effect of inclination angles and upper end conditions on the countercurrent flow limitation in straight circular pipes, Int. Comm. Heat Mass Transfer, Vol. 25, No. 1, pp. 117-125, 1998(a) [30]

Wongwises S., Interfacial friction factors in countercurrent stratified two-phase flow in a nearly-horizontal circular pipe, Int. Comm. Heat Mass Transfer, Vol. 25, No. 3, pp. 369-377, 1998(b) [15]

Wongwises S., Two-phase countercurrent flow in a model of a pressurized water reactor hot leg, Nuclear Engineering and Design 166 (1996) 121-133

Wu M., Gharib M., Experimental studies on the shape and path of small air bubbles rising in clean water. Department of Physics, Occidental College, Los Angeles, California 90041. (2002).

Yeoh G.H., Tu J.Y., A unified model considering force balances for departing vapor bubbles and population balance in subcooled boiling flow, Nuclear Engineering and Design 235 (2005) 1251–1265

Young S. B., Kap K., Kwang W. S., and Hho J. K., Loss of Coolant Accident Analysis During Shutdown Operation of YGN Units 3/4, Journal of the Korean Nuclear Society Volume 31, Number 1, pp.17-28, February 1999.

Yuan D. W., Pan L. M., Chen D.-Q., Wang X.-J., Condensation heat transfer coefficient at vapour–liquid interface of subcooled flow boiling in vertical narrow rectangular channel, Nucl. Power Eng. (China) 30 (2009) 30–34

Zamorano J. CFD modeling of COLLIDER test facility using CFX 12.1 for investigation and validation of counter current flow limitation (CCFL) in a large-diameter PWR hot-leg

pipe geometry. Master Thesis (2013). Institute of nuclear engineering, Technichal university Munich.

Zapke, A., Kröger, D.G., 1996. The influence of fluid properties and inlet geometry on flooding in vertical and inclined Tubes. Int. J. Multiphase Flow 22 (3), 461–472.

Zeitoun O. M., Subcooled flow boiling and condensation, Ph.D. Thesis, McMaster University, Canada, 1994

Zeitoun O., Shoukri M., Axial void fraction profile in low pressure subcooled flow boiling, Int. J. Heat Mass Transfer, vol. 40, No. 4, pp. 869 879, 1997.

Zeitoun O., Shoukri M., Chatoorgoon V., Measurement of interfacial area concentration in subcooled liquid-vapour flow, Nuclear Engineering and Design 152 (1994) 243-255.

Appendix A

This appendix provides a detailed look into the behavior of large steam bubbles during condensation in flowing subcooled water. It introduces sets of figures; each of them illustrates a specific observation or effect. Each set consists of a number of successive images that track a specific condensing bubble preceded by a comment explaining the tracked effect. The bubble -which is the subject of the comment-, is indicated by a red little square placed exactly at its calculated center-of-mass. The time step between the successive images was chosen to illustrate the desired effect; and thus the time-step varies between different figures' sets according to the tracked observation. The corresponding time-step is shown within each figure inside a white box next to the variable named "Step". Number 2 means that the successive images are shown each two time steps (1 time step $=1/1500$ s) and so on. The flow conditions for each Figure are also shown next to the variables "Js", "Jw" which represent the steam and water superficial velocities respectively. The value next to the variable "dtsub" represents the water temperature. The bubble diameter $D_{B,eq}$ is not relevant since it indicates the diameter of the bubble in the last instance. The variables "nbub" and "t_abs" are also irrelevant. Each set of figures is provided with two additional plots: the left plot represents the path of the tracked bubble and right plot represents the bubble diameter against time. The purpose of these two plots is to show the general trend of the plotted variable and link it to the visual observations. Therefore, no special care was paid to make the axis' numbering visible. Finally, these sets of figures were selected arbitrarily, and thus they are not a representative of the statistical behavior of all tracked bubble for each injection nozzle. They were selected to show the specific behavior include inside each of them.

Cases out of the CIN4mm Nozzle

1. Fast condensation at the end of the bubbles lifetime: the bubble's surface become more rough and deformed which fastens the condensation rate.

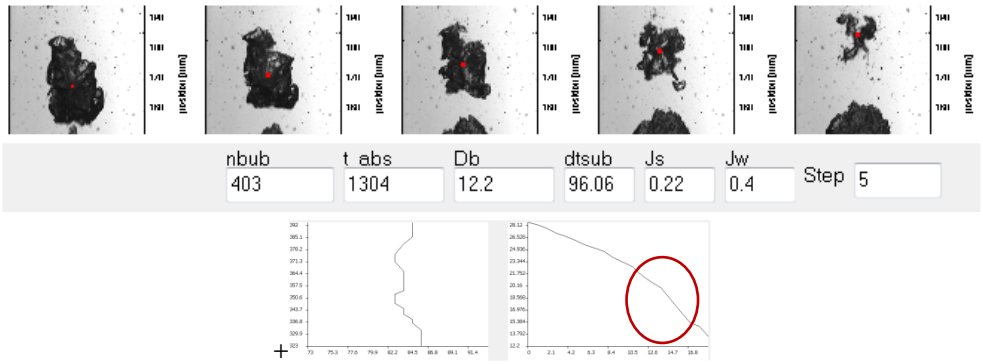

2. Tailed bubble: The remaining jet part (the tail) condense very fast (due to initial velocity) which affects the bubble's diameter at the beginning of the condensation.

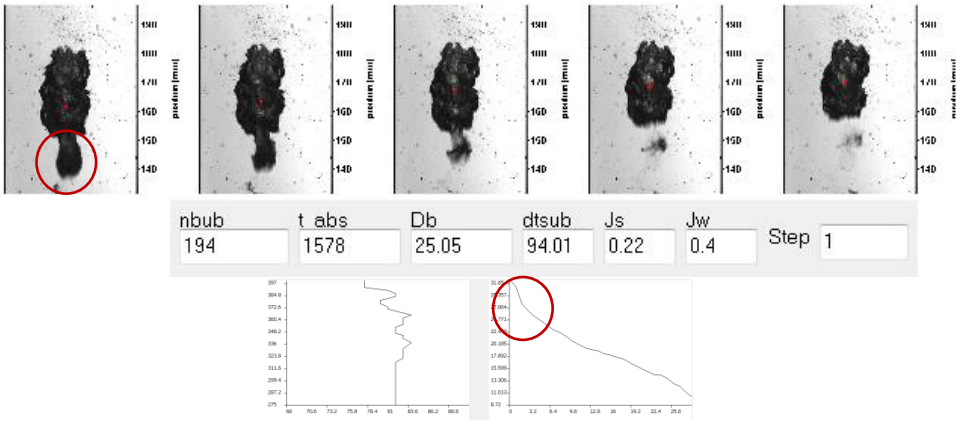

3. Tailed bubble: Development of the bubble's shape

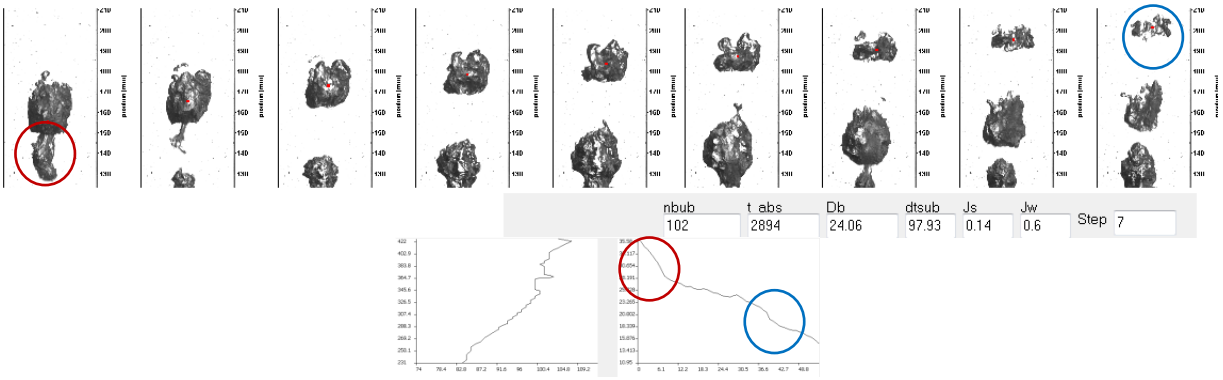

4. Large bubble: relatively smoother and elongated at the beginning, the bubble becomes rougher and rounded as it condenses. This affects the bubble diameter slope against time.

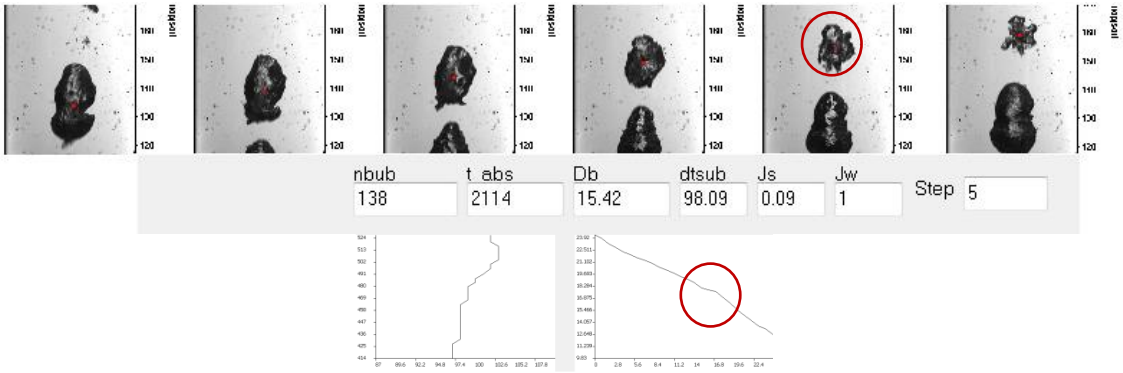

5. Large bubble: The bubble suffers a larger deformation and becomes a narrow and elongated as it condenses. This results in a large change of the bubble diameter slope against time, as well as the displacement of the center of mass rightwards.

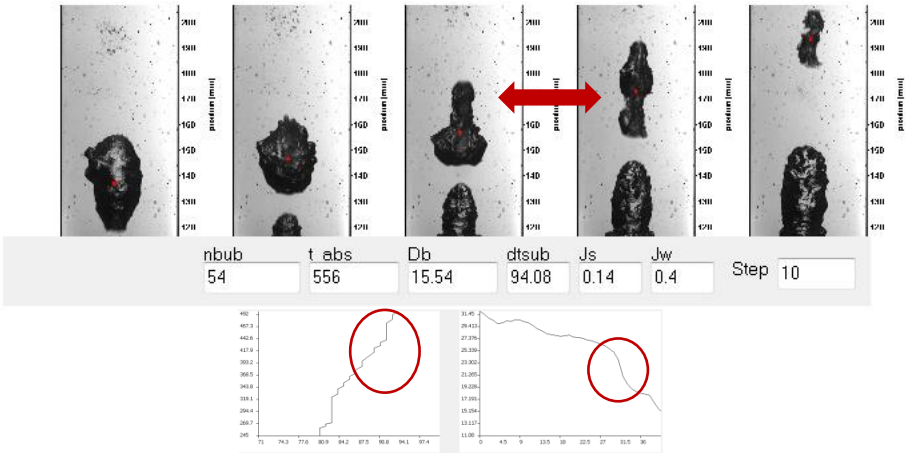

6. Large bubble: A chaotic change of the bubble's shape through condensation. The bubble suffers multiple breakups. This cannot be fully avoided within the tracking procedure. The effect upon the bubble diameter can be seen through the abrupt change of the diameter.

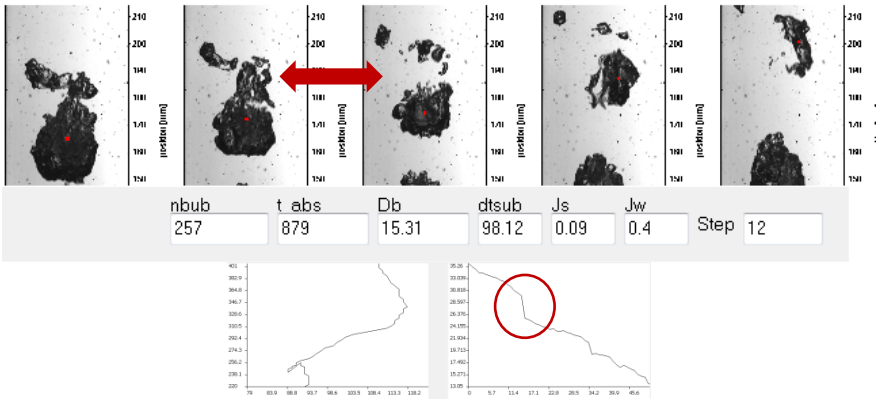

7. Large bubble: A chaotic change of the bubble's shape through condensation and multiple breakups. Even with a limit set upon the volume change, some bubbles with a considerable defragmentation can be still tracked.

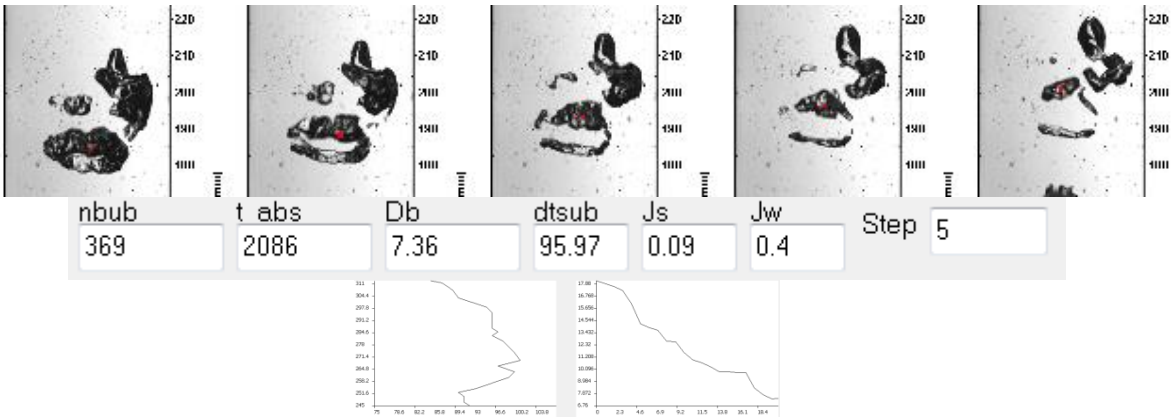

8. Large bubble: A gradual condensation with small shape changes.

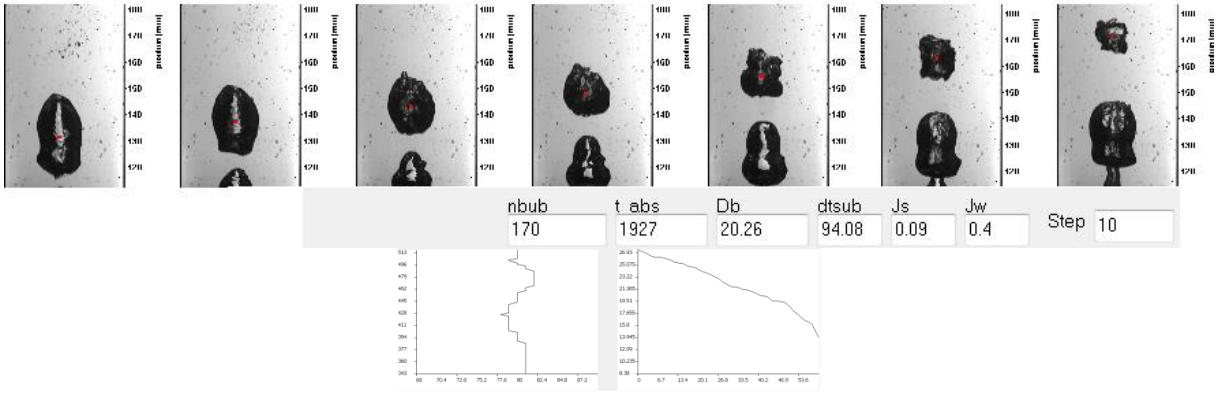

9. Large bubble: Chaotic change of the bubble shape. Bubbles can take any arbitrary shape during condensation. The displacement of the bubbles' center-of-mass rightwards after the shape deformation can be also seen.

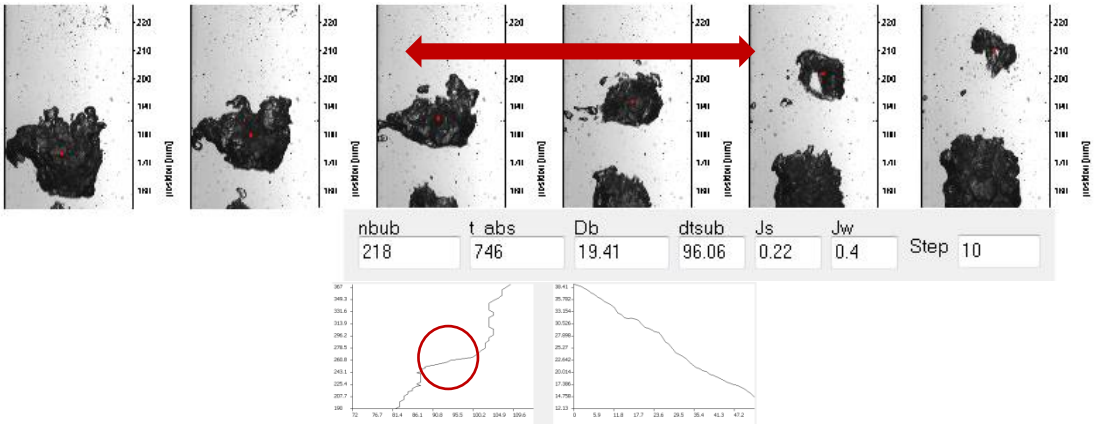

10. Bubble fragment condensation: fragments that break from condensing bubbles can take any shape upon break-up.

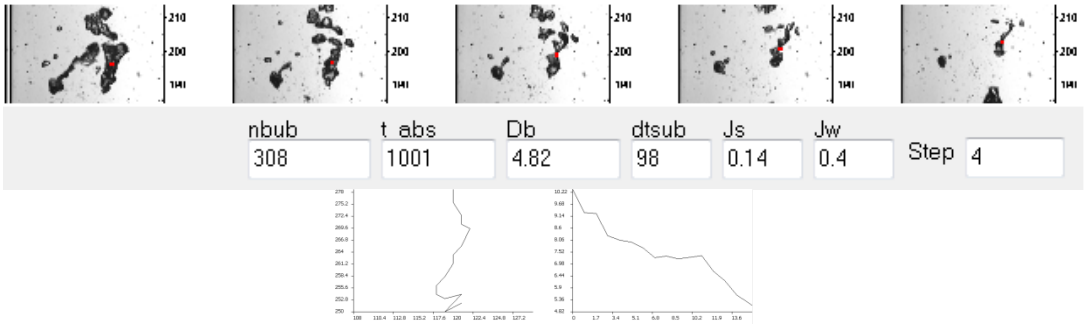

11. Bubble fragment: the fast condensation of the left parts shifts the center of mass to the right as it can be seen from the plot of the bubble's path.

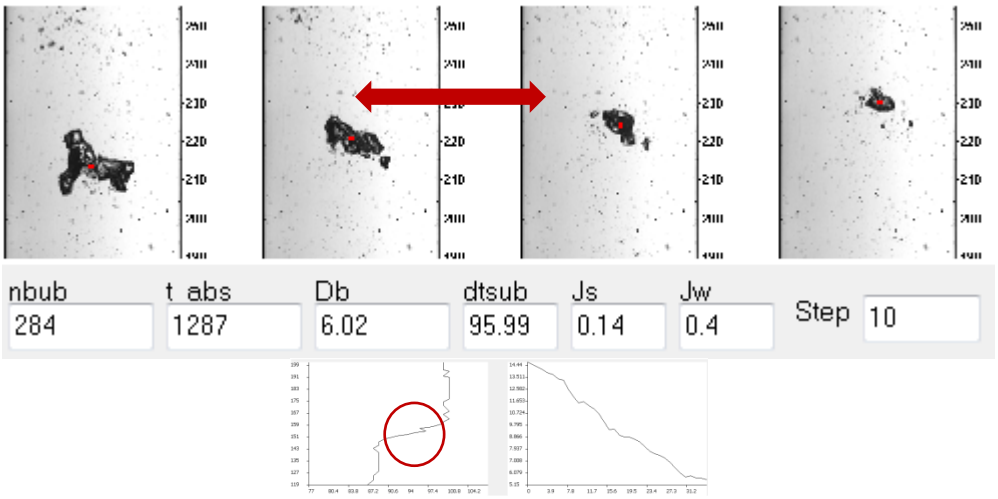

12. Medium size bubble: One can notice the rapid decrease of the diameter along with the bubble's rough surface.

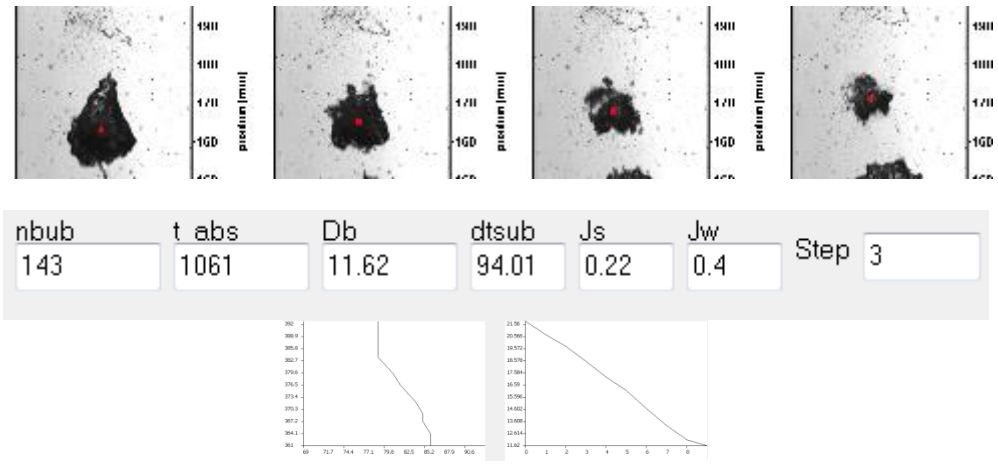

13. Medium size bubble: The bubble has an extension on its upper side. Extensions are susceptible to break-up as the narrow junction to the main bubble body condenses earlier as the main bubble volume. A sudden change of the bubble diameter occurs.

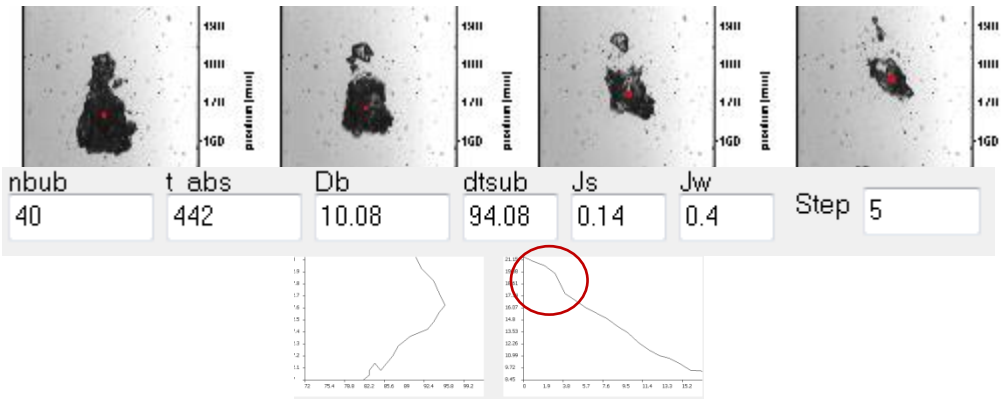

14. Large tailed bubble. The tail can either separate or condense rapidly. In this case, a gradual condensation occurs.

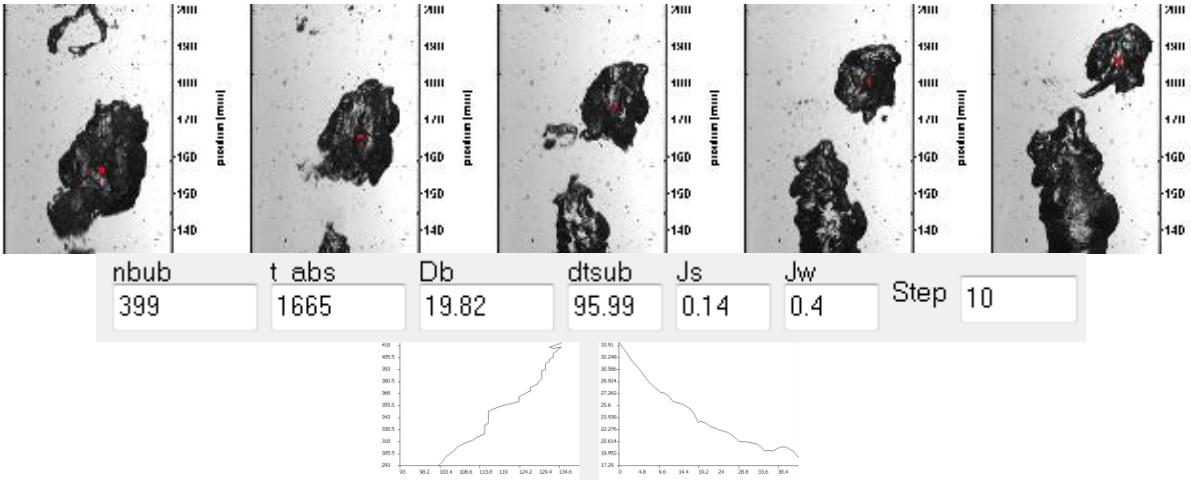

15. Medium size bubble: A gradual condensation followed by a slight increase of the condensation rate at the end due to the increased deformation the bubble.

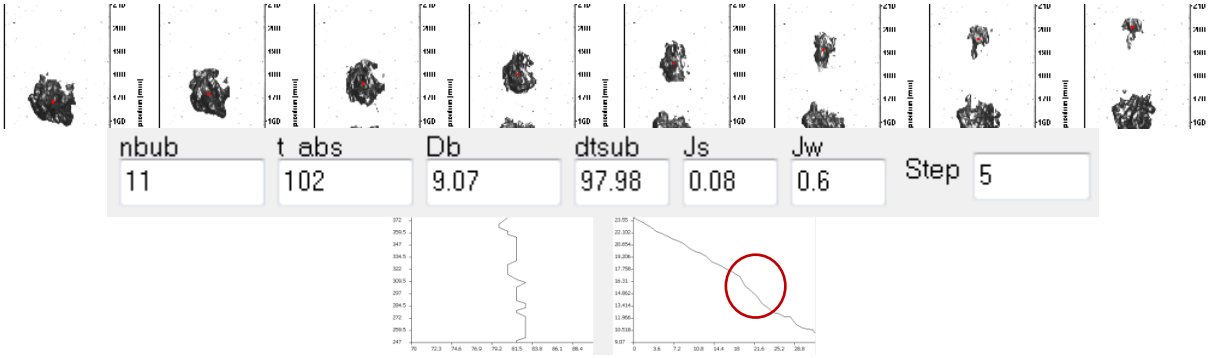

16. Medium size bubble: A gradual condensation occurs at the beginning followed by a faster condensation as the bubble surface gets rougher. The slope of the bubble's diameter against time becomes higher accordingly.

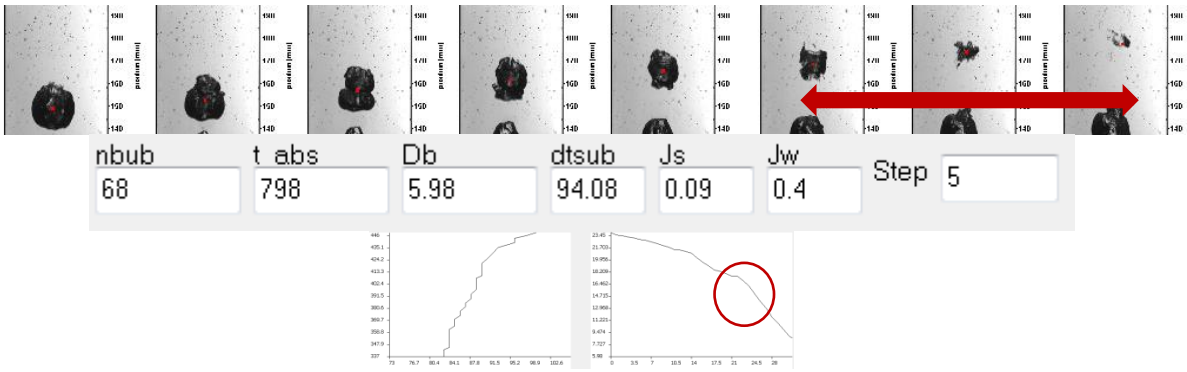

17. Medium size bubble: The bubble transforms into a flat shape after an initial condensation. The condensation rate slows down after this shape change.

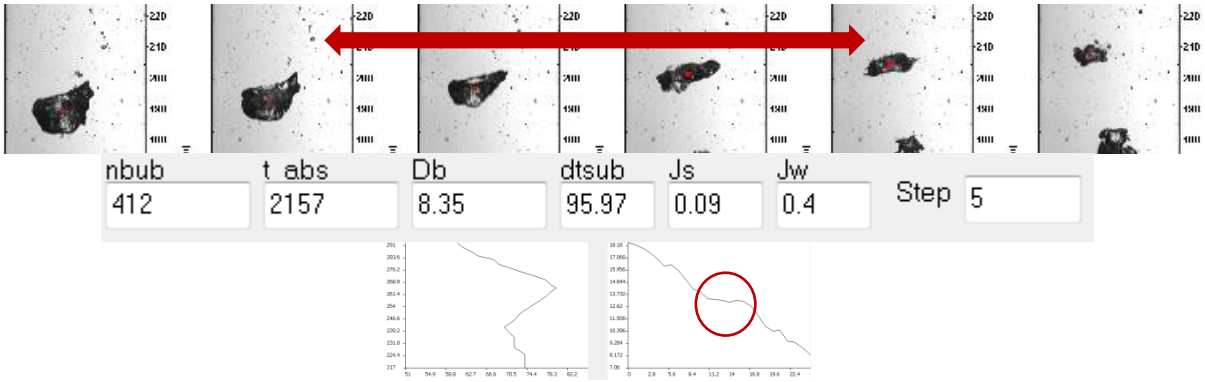

18. Medium size bubble: Reduced rate of condensation after the bubble changes its shape into a flat.

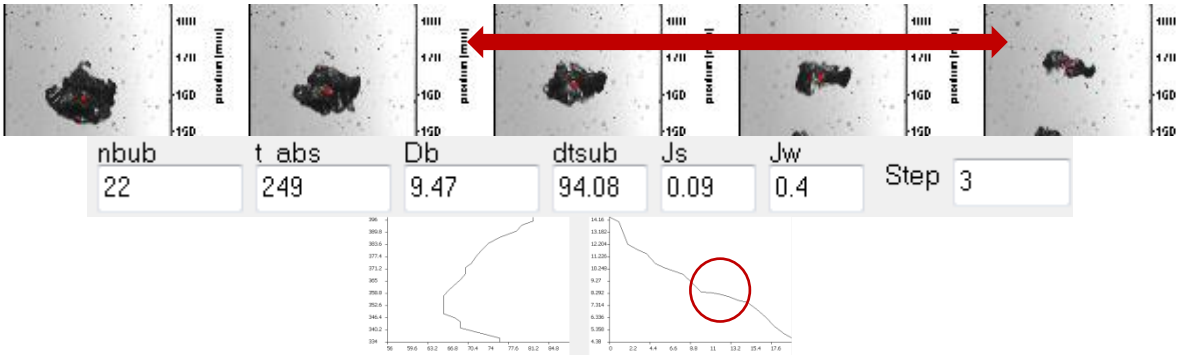

19. Medium size bubble: a gradual condensation of without a large change of the bubble's shape

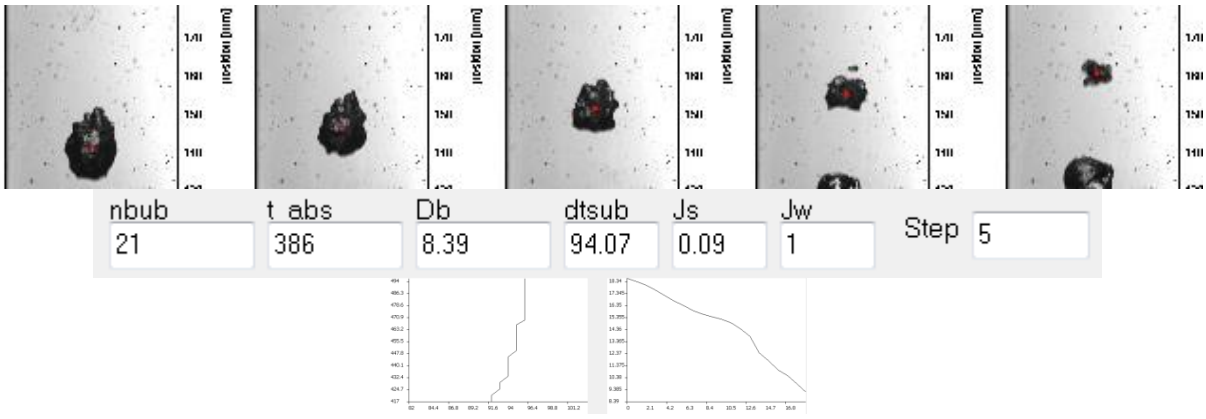

20. Medium size bubble: a gradual condensation without a large change of the bubble's shape.

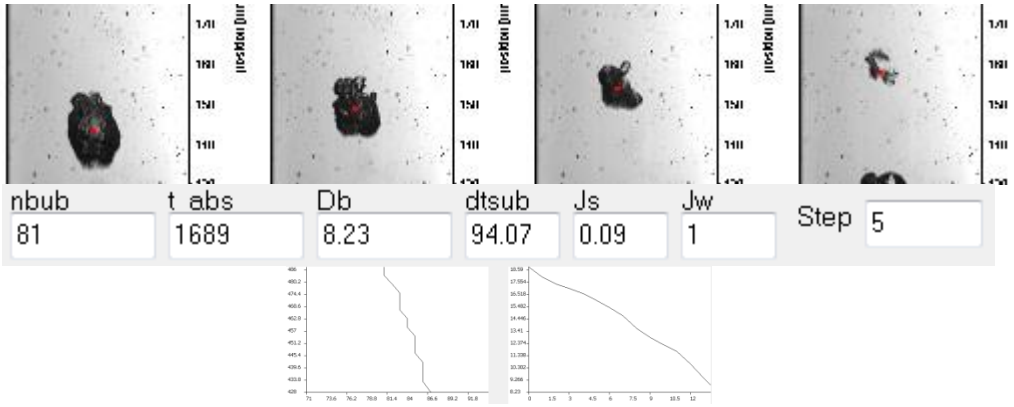

21. Small bubble: slow condensation of the bubble due to the air content.

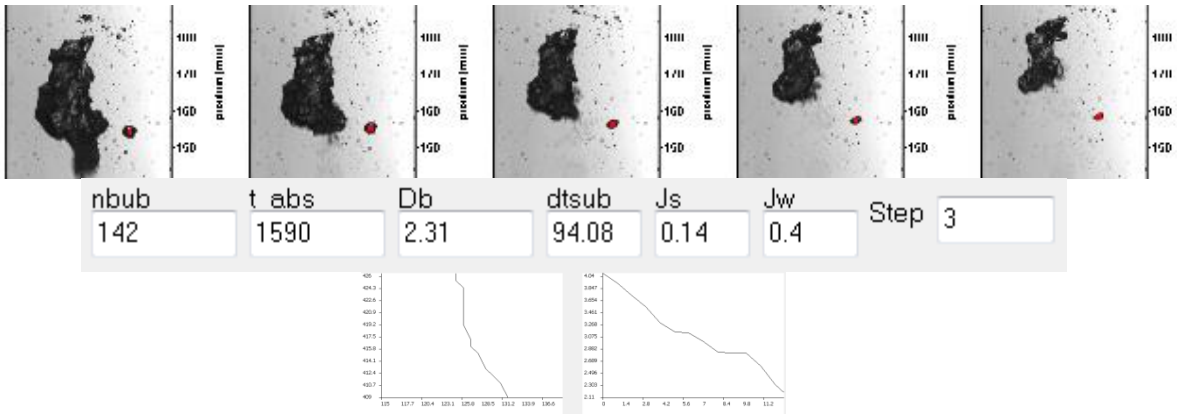

22. Small bubble fragment

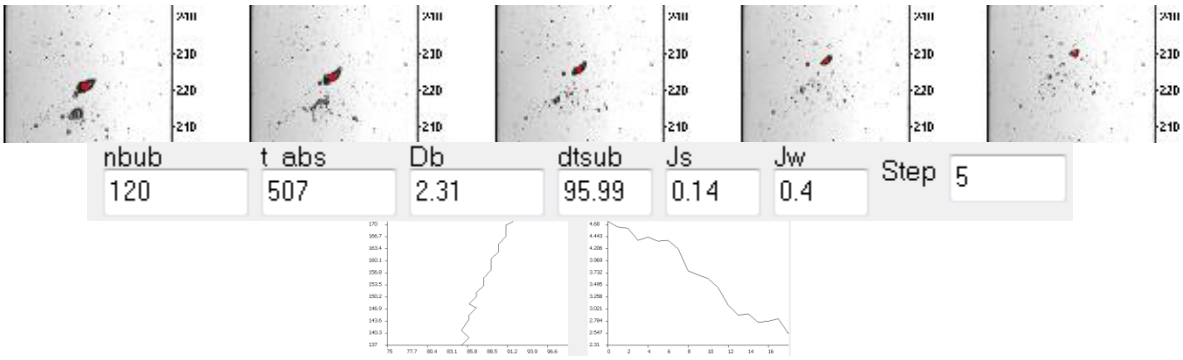

23. Small bubble fragment

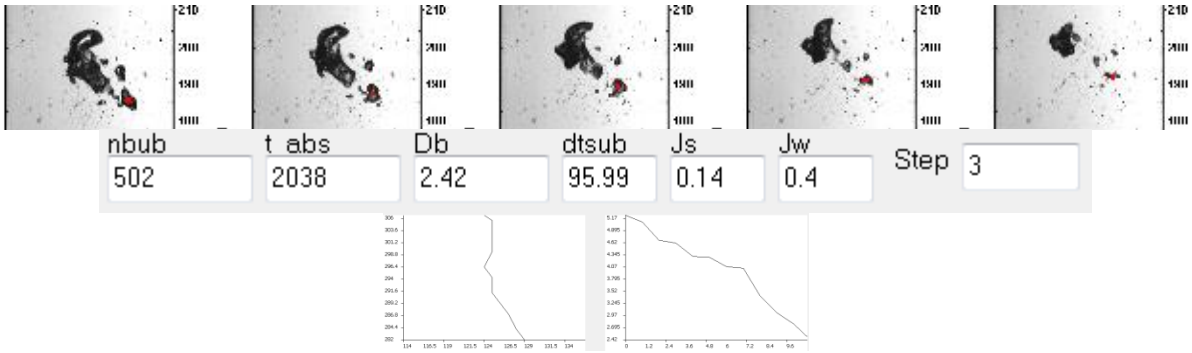

Cases from the HIN2X4mm nozzle

1. Tailed medium-size bubble. Bubble tails results from the initial jet upon detachment. The steam inside them moves quicker and condenses faster. This is accompanied with a rapid decrease in bubble's diameter at the beginning of the condensation, and a displacement of the bubble's center-of-mass

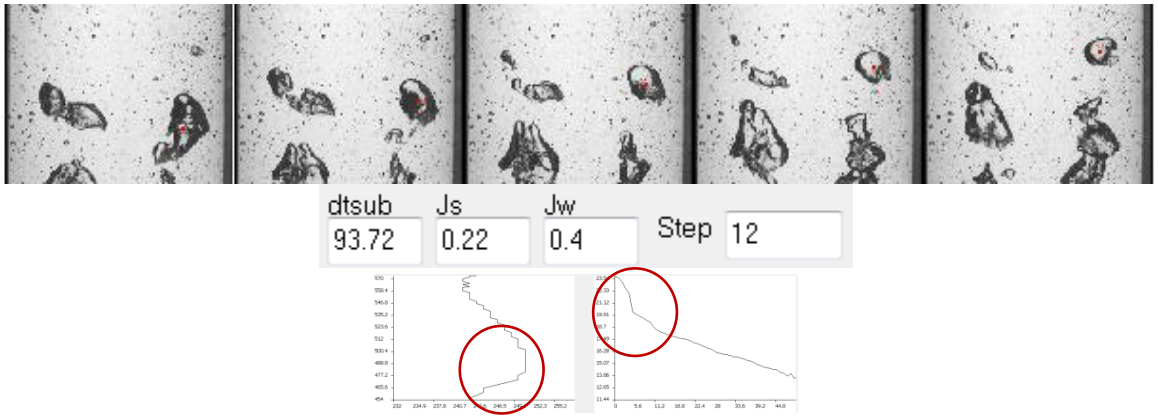

2. Tailed medium-size bubble. The initial jet from the injection nozzle can still be seen at the beginning. A transition from a rounded into flat shape occurs near the end of the condensation..

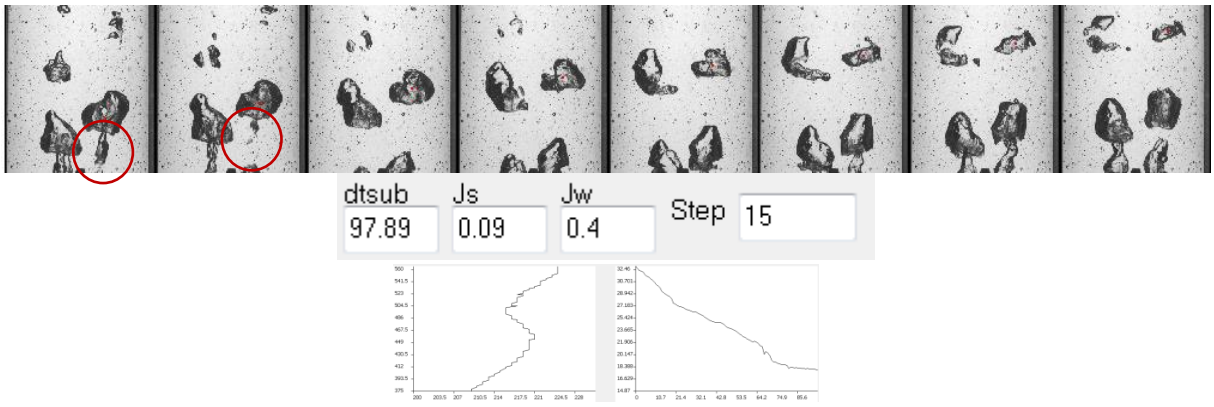

3. Tailed bubble the initial jet moves through the bubble's volume bubble volume and emerges at the top (instance 3).

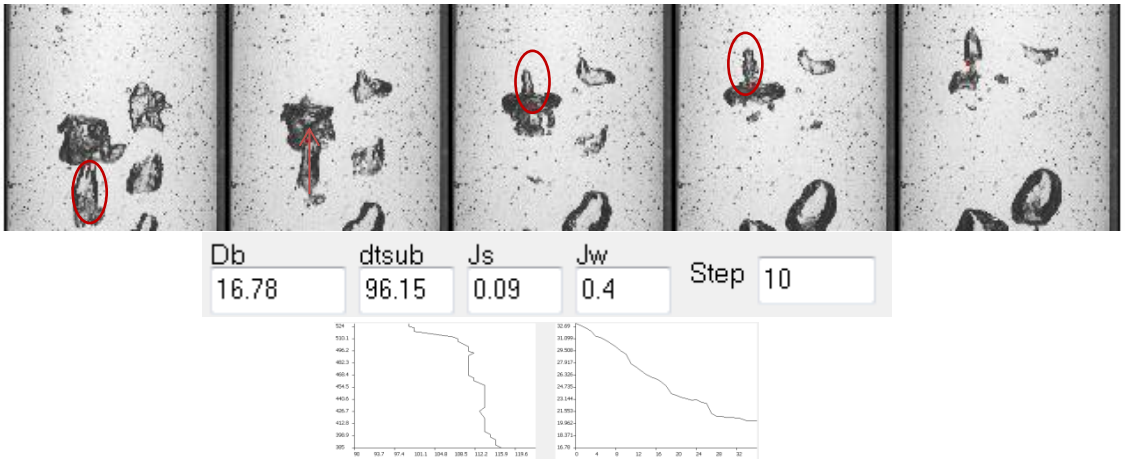

4. Small bubble fragment

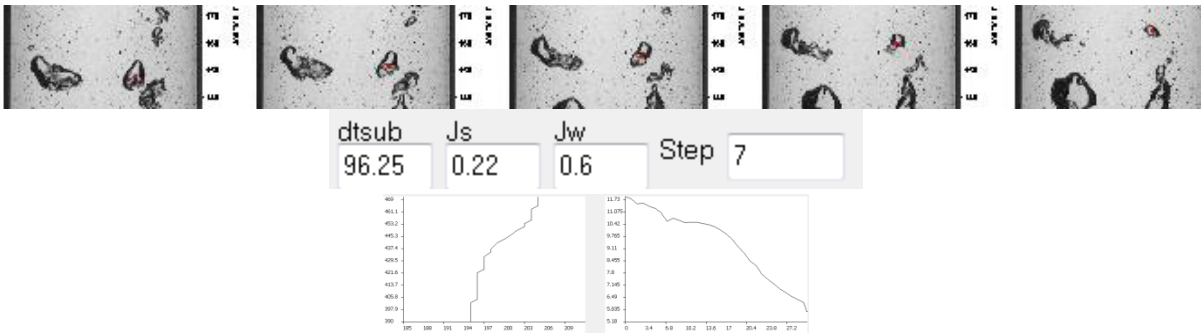

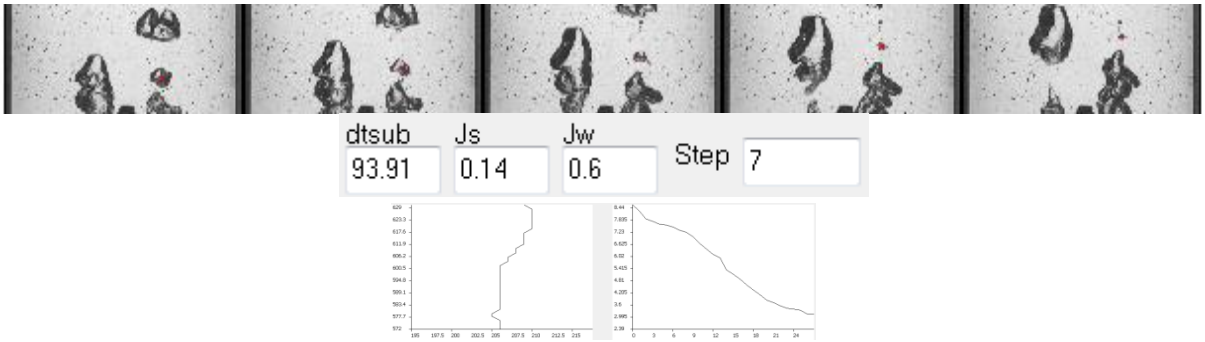

5. Small bubble fragment: slow condensation. due to: the increased air-content in this fragment after an initial condensation phase, and sliding near the pipes wall with a low rising velocity.

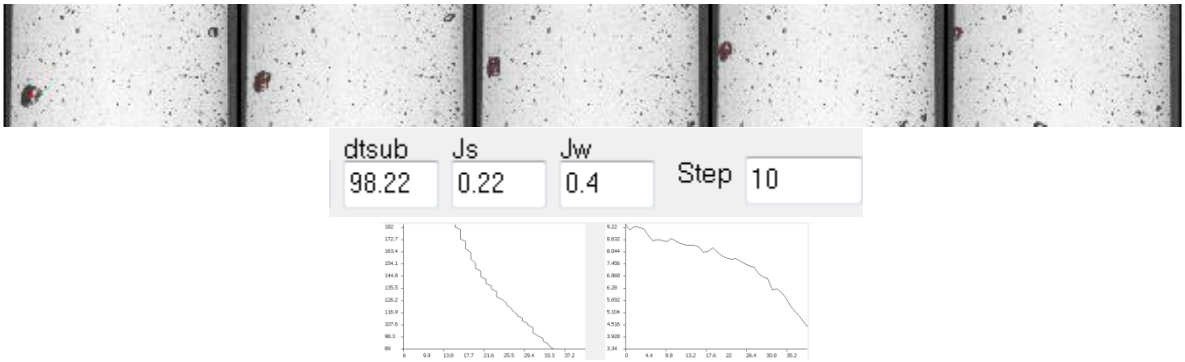

6. A medium size bubble. The bubble changes into a small shell near the end of the condensation.

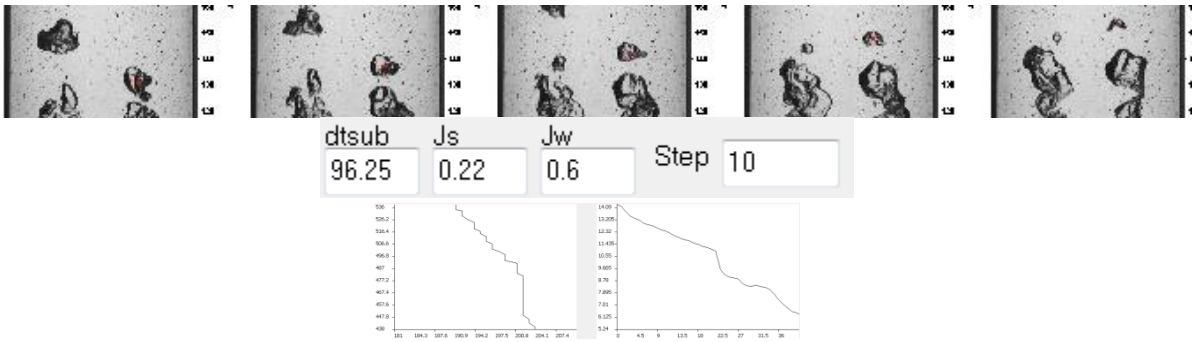

7. A medium size bubble. The transition from long shape into a more rounded shape is accompanied with a reduced rate of the bubble condensation.

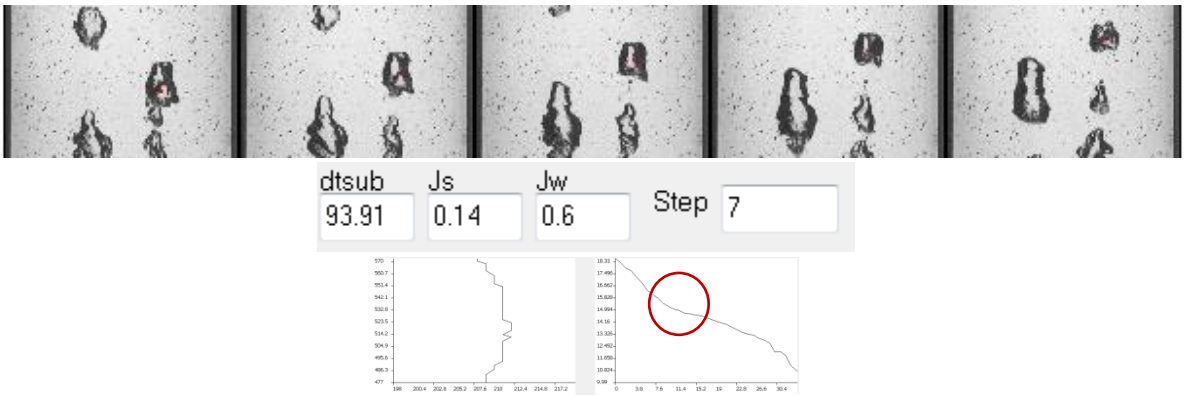

8. A medium size bubble: the bubble deformation causes the bubble to move rightwards.

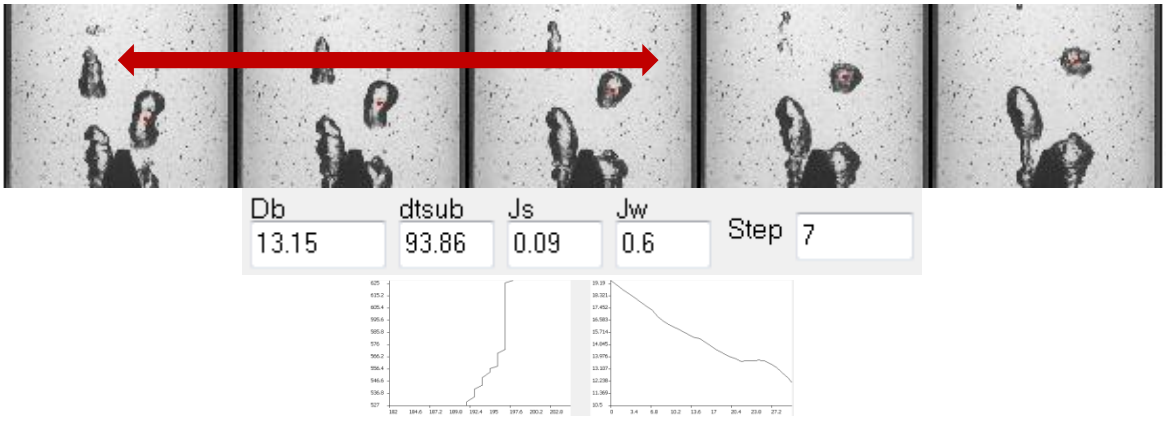

9. Medium-size bubble A gradual condensation.

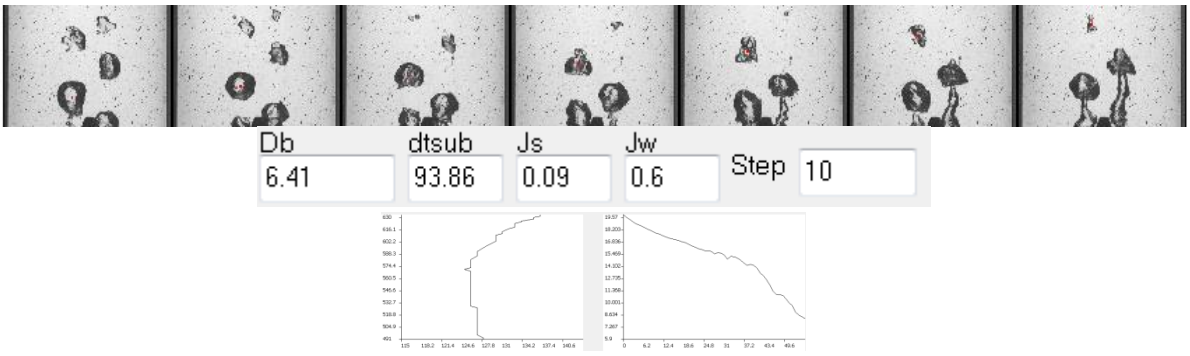

10. Medium-size bubble: The increased surface roughness increases the bubble condensation rate. Note the increased diameter slope against time.

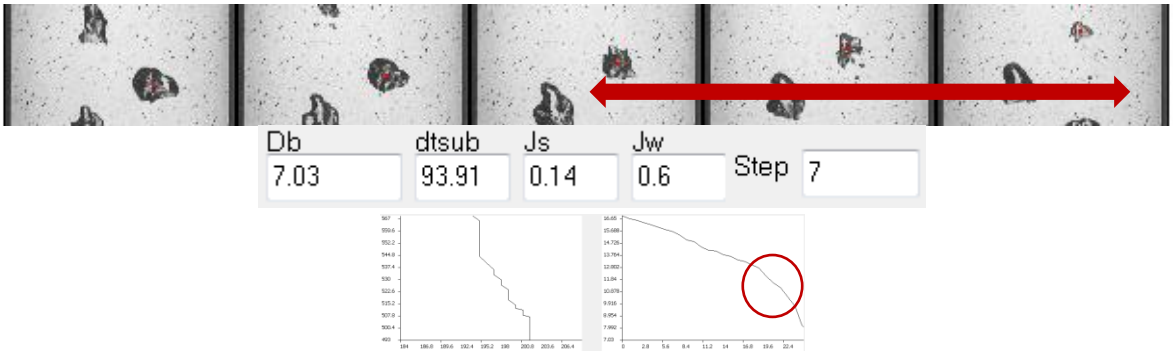

11. A long-shaped bubble moves leftwards. The initial diameter drop is due to the breakup.

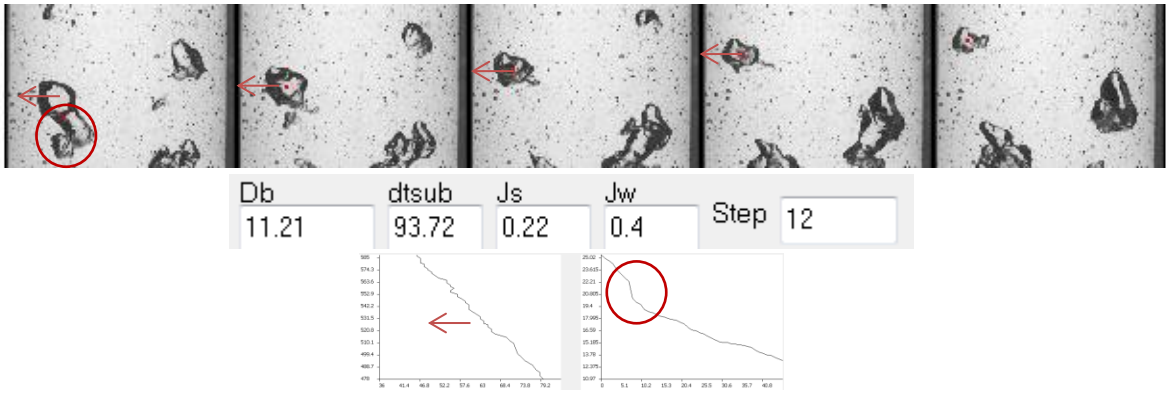

12. A long shaped bubble moves rightwards. Lateral movements are sometimes induced by bubble shape deformation.

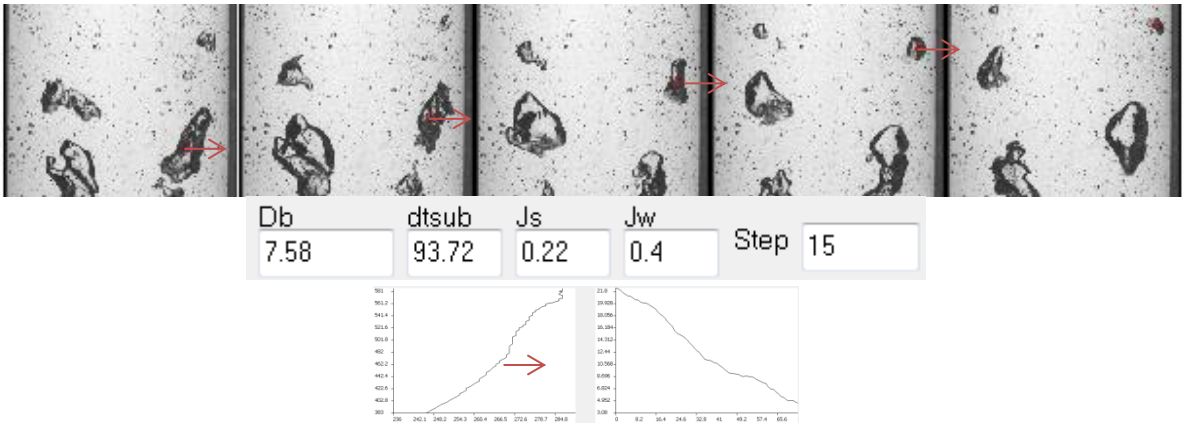

13. Large bubble. A large break-up follows the elongation and shape deformation of the bubble.

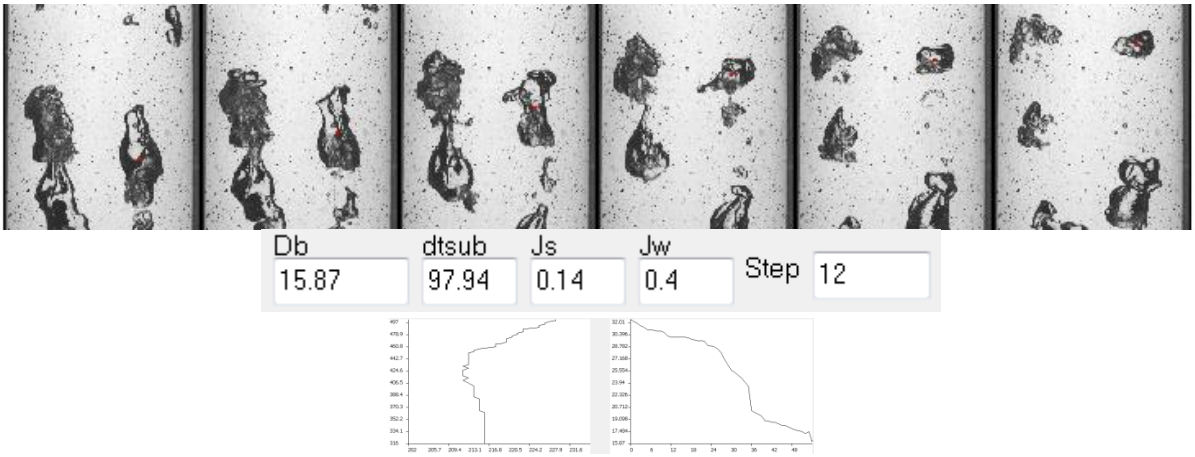

14. Large bubble: the shape deformation affects both: the diameter and the path.

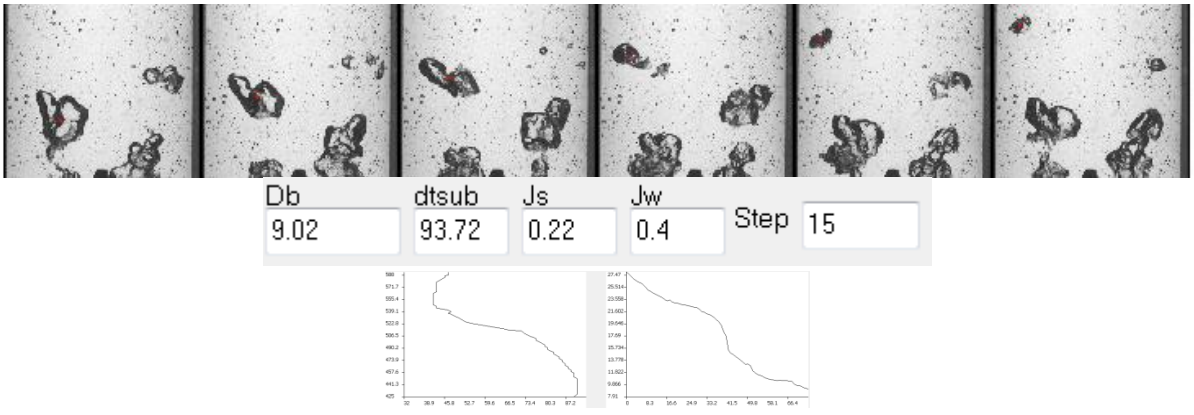

15. Large bubble: Shape deformation results in fluctuations of the bubble diameter.

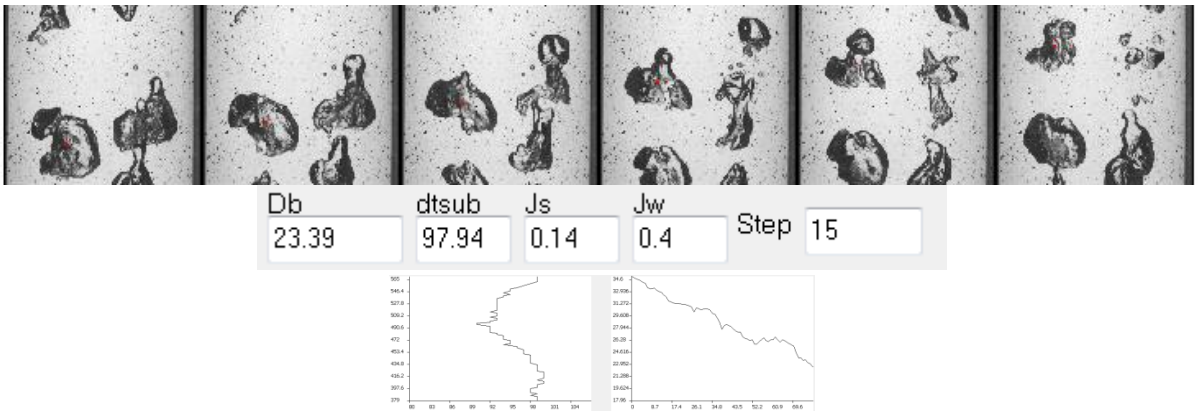

16. Small bubble.

17. Long-shaped bubble without breakup.

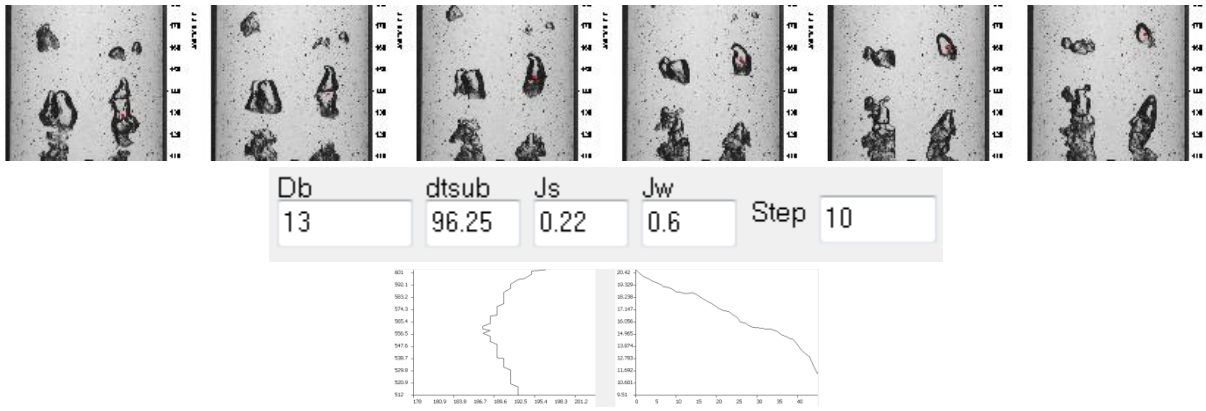

18. Cap-shaped bubble